

FY 2006

**Oak Ridge National Laboratory
Annual Progress Report for the Power Electronics and
Electric Machinery Program**

Prepared by:

Oak Ridge National Laboratory

Mitch Olszewski, Program Manager

Submitted to:

**Energy Efficiency and Renewable Energy
FreedomCAR and Vehicle Technologies
Vehicle Systems Team**

Susan A. Rogers, Technology Development Manager

October 2006

Engineering Science and Technology Division

**Oak Ridge National Laboratory
Annual Progress Report for the Power
Electronics and
Electric Machinery Program**

Mitch Olszewski, Program Manager

October 2006

Prepared by the
OAK RIDGE NATIONAL LABORATORY
Oak Ridge, Tennessee 37831
managed by
UT-BATTELLE, LLC
for the
U.S. DEPARTMENT OF ENERGY
Under contract DE-AC05-00OR22725

Contents

List of Figures	v
List of Tables	xiii
Acronyms and Abbreviations.....	xv
1. Introduction	1
2. Thermal Control for Power Electronics and Motors	7
2.1 Thermal Control for Inverters and Motors	7
2.2 Identifying the Barriers and Approaches to Achieving High-Temperature Coolants	31
3. Electric Machinery Research and Technology Development	43
3.1 Uncluttered CVT Machine	43
3.2 Interior Permanent Magnet Reluctance Machines.....	53
3.2.1 Interior Permanent Magnet Reluctance Machines with Brushless Field Excitation—16,000 rpm.....	53
3.2.2 High-Power-Density Reluctance Interior Permanent Magnet Machines—6,000 rpm.....	65
3.3 Control of Fractional-Slot Surface Mounted Permanent Magnet Motors with Concentrated Windings	71
3.4 Extending the CPSR of Synchronous Reluctance Motors.....	123
3.5 Advanced Traction Motor Development	141
4. Power electronics Research and Technology Development	153
4.1 Wide Bandgap Materials	153
4.2 Integrated dc-dc Converter for Multi-Voltage Bus Systems	177
4.3 Cascaded Multilevel Inverter.....	193
4.4 Advanced Converter Systems for High-Temperature HEV Environments.....	211
4.5 dc/dc Converter for Fuel Cell and Hybrid Vehicle.....	227
5. Systems Research and Technology Development.....	237
5.1 Fully Integrated HEV Traction Motor Drive Development Using Thermoelectrics and Film Capacitor Innovations.....	237
5.2 Studies of Competitive Products	263
5.2.1 Benchmarking of Competitive Technologies.....	263
5.2.2 Component Characterization.....	279

Figures

	Page
2.1 Thermal Control for Inverters and Motors	
1. Photo of inside of motor housing showing spray nozzle locations	9
2. SEMIKRON Model 400IGD06 82-kW inverter	11
3. ORNL floating loop schematic diagram	12
4. Curve tracer data showing Semikron current capability	13
5. Comparison of Semikron 82-kW dc link capacitor and Custom Electronics and SBE cylindrical capacitors for ORNL half-size inverter.....	14
6. Core of first FY 2006 ORNL prototype inverter.....	15
7. Power IGBT subassembly	15
8. Semikron power IGBT board.....	15
9. One of three sections of the Semikron board used to produce subassemblies for prototype	15
10. A three-dimensional model of the ORNL prototype showing assembly components	16
11. Model showing tighter packaging	16
12. Side view and top view of ORNL prototype internal components	17
2.2 Identifying the Barriers and Approaches to Achieving High-Temperature Coolants	
1. Modular capacitor position and size in the Prius inverter/converter casing.....	34
2. Ripple current vs ambient temperature for high-temperature capacitors	35
3. Flux strength of a selected NdFeB magnet vs temperature.....	37
4. Average motor insulation life vs winding temperature for four insulation types	37
5. General PMSM design approach applicable for high-temperature cooling	38
3.1 Uncluttered CVT Machine	
1. Shaft torque and stator torque of a motor.....	44
2. Doubling shaft torque at a given shaft speed	44
3. ORNL technology does not have brushes and slip rings	44
4. Example of an 18-pole, axial-gap, 2-phase uncluttered rotor	45
5. One side of the proof-of-concept uncluttered rotor with rings.....	46
6. The opposite side of the proof-of-concept uncluttered rotor with teeth	46
7. Two-phase excitation core for the uncluttered rotor	47
8. An example of an uncluttered CVT	48
9. A possible axial-gap example of an uncluttered CVT	48
10. Experimental setup for proving the brushless rotating armature concept.....	49
11. The proof-of-uncluttered-rotor-concept prototype completed in FY 2006.....	50
12. Cut view of the uncluttered rotor proof-of-concept prototype	50
3.2.1 IPMR Machines	
1. Assembly of ORNL 16,000-rpm motor design.....	54
2. Location of bridge in a rotor punching	54
3. Flexibility provided by adjustable field excitation.....	55
4. Rotor of ORNL's 16,000-rpm motor	55
5. Air-gap flux density distributions with various excitation amperetums (AT)	56
6. Three-phase line-to-neutral back-emfs at 5000 rpm with and without field excitation	56
7. Stronger field excitation that can enhance output torque	57
8. Vibration analysis obtained from test	57

9.	Line-to-neutral back-emf voltage vs speed	58
10.	No-load core and friction losses vs field current for each speed.....	58
11.	No-load core and friction losses vs speed for each field current.....	59
12.	Finite-element stress analysis of 16,000-rpm rotor	59
13.	Radial displacement analysis of 16,000-rpm rotor.....	60
14.	Shear stresses at the support columns of an 0.018-in. thick 16,000-rpm laminate rotor.....	60
15.	Wound stator core	61
16.	Rotor punching.....	61
17.	Rotor core stack and shaft	61
18.	Completed rotor	61
19.	Excitation coil housing.....	61
20.	Excitation coil inside the coil housing	61
3.2.2	High-Power-Density Reluctance Interior Permanent Magnet Machines—6,000 rpm	
1.	PM arrangement of Toyota Prius rotor	66
2.	Various PM arrangements for increasing air gap flux density	67
3.	Prototype motor showing locations of side poles and side magnets	67
4.	Three-dimensional simulation results for rotor flux density distributions	68
5.	Comparison between simulation and test results of air gap flux densities produced by PMs for various PM arrangements	68
3.3	Control of Fractional-Slot Surface Mounted Permanent Magnet Motors with Concentrated Windings	
1.	Distributed and concentrated windings	74
2.	Calculation of the winding function for an idealized motor with a uniform gap	75
3.	Relation between conductor count and winding function	76
4.	Winding function for the 36-slot, 30-pole concentrated winding being studied for possible use as a hybrid electric vehicle traction motor.....	77
5.	Redistribution of the coils from the concentrated winding shown in Figure 4 into an ideal distributed winding for a rotor with p pole pairs	78
6.	Definition of slot dimensions for inductance calculations	81
7.	Cross-section of the basic repeating unit of the 55-kW (peak), 36-slot 30-pole (2/5 s/p/ph) SPM2 machine design	83
8.	SPEED rendition of the 36-slot, 30-pole SPM2 with concentrated windings	84
9.	Magnetic loss at 2,000 rpm (The motor is drawing 275 A ISP under load.....)	88
10.	Magnet loss at 10,000 rpm	88
11.	Effect of speed on skin depth penetration	89
12.	Approach taken by SPEED to determine skin depth penetration.....	89
13.	The effect of frequency on magnetic losses	90
14.	Zero current losses of the FSCW-1 prototype.....	100
15.	Fundamental frequency model of a permanent magnet motor driven by a pulse-width modulation controlled voltage source inverter	102
16.	Closed-loop speed control block diagram	102
17.	Amplitude modulation index versus pseudo amplitude modulation index for a frequency modulation index of 39.....	103
18.	Rated current limiting control (left) and rated current plus rated power limiting control (right).....	106
19.	Analytical predictions of the spatial air-gap flux density distribution for a slotted version of the SPM1 machine for a rotor angular position of 5 mechanical degrees	109

20.	Predicted flux density waveform in different parts of the stator based on the assumption of uniform tooth flux density	109
21.	Comparison of predicted air gap magnetic flux density distribution at radius R_s — using closed-form (B_r_Code) and finite-element (B_r_FEA) analysis.....	110
22.	Comparison of predicted iron losses in different parts of the <i>SPMI</i> machine at 2000 rpm in an open-circuit condition using closed-form analysis and point-by-point finite-element analysis technique.....	110
23.	Finite-element-analysis-predicted iron eddy current losses at 2000 rpm with a peak armature current of 200 A.....	111
24.	Cross section of two-pole machine illustrating a stator current vector and its decomposition into d - and q -axis components to achieve vector control of a surface permanent magnet machine	112
25.	Maximum torque/amp current vector trajectory for <i>SPMI</i> machine at 20% of rated torque.....	113
26.	Maximum torque/volt current vector trajectory for <i>SPMI</i> machine at 20% of rated torque.....	113
27.	Comparison of predicted copper losses for 20% of rated torque with $\max T/A$ and $\max T/V$ algorithms.....	114
28.	Comparison of predicted iron losses for 20% of rated torque with $\max T/A$ and $\max T/V$ algorithms.....	114
29.	Predicted efficiency of <i>SPMI</i> machine at 20% of rated torque for $\max T/A$ and $\max T/V$ algorithms, plus specified minimum efficiency line.....	114
30.	Variation of <i>SPMI</i> efficiency at 2000 rpm as a function of i_d with i_q adjusted to hold the torque constant at 20% of rated torque.....	114
31.	Current vector trajectory for <i>SPMI</i> machine to deliver maximum partial-load efficiency at 20% of rated torque.....	115
32.	Predicted efficiency of <i>SPMI</i> machine at 20% of rated torque for maximum partial-load efficiency, plus specified minimum efficiency line.....	115
33.	Predicted stator tooth magnetic flux density waveform at 2000 rpm and 20% rated output torque under $\max T/A$ operating conditions	116
34.	Predicted stator tooth magnetic flux density waveform at 2000 rpm and 20% rated output torque under $\max T/V$ operating conditions	116
35.	Predicted stator tooth magnetic flux density waveform at 2000 rpm and 20% rated output torque under \max efficiency operating conditions.....	116
36.	Predicted harmonic spectra for stator tooth magnetic flux density at 2000 rpm, 20% rated torque for the three operating conditions.....	116
37.	Danfoss VLT 5252 inverter on mobile base	117
38.	Open door shows Danfoss control unit at top and power switching section at bottom.....	117
39.	Interface card with fiber optics and dead time insertion prepared at Aalborg University to allow control of a commercial inverter while maintaining its fault protection features	117
40.	New OPAL RT target PC and connection box	118
41.	Pre-test diagnostic verification signal bypass card	118
42.	Voltage (black-left), motor current (red-middle) and direct current supply current (orange-right) sensors.....	118
43.	6-kW fractional-slot SPM motor with concentrated windings.....	118
3.4	Extending the CPSR of Synchronous Reluctance Motors	
1.	Schematic of a synchronous reluctance motor (4 poles, 12 slots, 40-cm diameter, 100 cm long, no permanent magnets)	125

2.	Magnetic flux lines generated by the stator's rotating field in a reluctance motor with a solid rotor	129
3.	Distribution of magnetic flux crossing the air gap generated by the stator's rotating field in a motor with a solid rotor	130
4.	Total torque in the motor with a solid rotor made of nonconductive steel as a function of time for a quarter turn	131
5.	Modified synchronous reluctance motor types with PMs added between the rotor's steel layers	132
6.	Torque as a function of stator current angle, γ	133
7.	Torque as a function of stator current angles from 0 to 360 eDeg	134
8.	Average flux at the rotor surface for stator current angles from 0 to 360 eDeg	134
9.	Permeability dependence on flux for study on the effect of saturation	135
10.	Torque vs control angle, γ , with and without saturation	135
11.	Average radial and tangential rotor surface flux components vs control angle, γ , with and without saturation	136
12.	Permeability and flux lines in a type A motor with no shoes on the stator teeth	136
13.	Radial flux distribution along the rotor periphery for $\gamma = 0$ to 360 eDeg	137
14.	Tangential flux distribution along the rotor periphery for $\gamma = 0$ to 360 eDeg	137
15.	Radial flux distribution along the rotor periphery for $\gamma = 0$ to 45 eDeg	138
16.	Tangential flux distribution along the rotor periphery for $\gamma = 0$ to 45 eDeg	138
17.	Radial and tangential flux distributions along the rotor periphery for optimal control angle	139
3.5	Advanced Traction Motor Development	
1.	Physical topology, three designs	142
2.	U-barrier, two bridges, three magnets per pole	144
3.	Six-pole pair machine configuration	146
4.	Current and torque profile at 200-Vdc, peak power	147
5.	Power density comparison—FreedomCAR design vs Prius motor	148
6.	Motor parameter comparison—FreedomCAR design vs Prius motor	149
7.	Motor assembly—exploded view	150
8.	Cost vs volume for the FreedomCAR motor	151
4.1	Wide Bandgap Materials	
1.	Experimental I-V curves of the 75-A SiC Schottky diode	154
2.	R_D and V_D obtained from the experimental data in Figure 1	154
3.	Test circuit for dynamic characterization	155
4.	Current and voltage waveforms of SiC JFET S3—double pulse test	155
5.	Temperature-controlled box used for high-temperature testing	155
6.	Reverse recovery current waveforms of the SiC Schottky diode for different forward current values	156
7.	Switching energy losses of SiC diode at different temperatures	156
8.	Static characteristics of GaN Schottky diode	157
9.	V_d forward voltage drop of GaN Schottky diode	157
10.	R_d on-state resistance of GaN Schottky diode	157
11.	Comparison of i-v curves of SiC and GaN Schottky diodes	157
12.	Comparison of reverse recovery currents between SiC and GaN at 25°C	158
13.	Turn-off energy losses of GaN diode at different temperatures	158
14.	Energy losses comparison between Si and GaN diodes at 125°C	158
15.	i-v curves of JFET S1	159

16.	i-v curves of JFET S2.....	159
17.	i-v curves of JFET S3.....	159
18.	On-resistance of S3.....	159
19.	Transfer characteristics of JFET S3.....	159
20.	Transfer characteristics of several SiC JFET samples.....	159
21.	Total switching energy losses of JFET S3 at different currents and temperatures.....	160
22.	Block diagram of the system level model.....	160
23.	i-v characteristics of IGBT at different temperatures.....	161
24.	Turn-on switching energy losses of IGBT with Si and SiC diodes at 25°C.....	162
25.	Turn-off switching energy losses of IGBT with Si and SiC diodes at 25°C.....	162
26.	Total switching energy losses of IGBT at different currents and temperatures.....	162
27.	i-v characteristics of Si pn diode at different temperatures.....	163
28.	Turn-off energy losses of Si pn diode at different currents and temperatures.....	163
29.	Side view of the cross section of the inverter.....	163
30.	The equivalent circuit of the thermal model.....	164
31.	Efficiency vs output power of three different inverters at 150 N-m load.....	165
32.	Efficiency versus output power of three different inverters at 200 N-m load.....	165
33.	Temperature profile of devices over FUDS cycle.....	166
34.	Heat sink volume vs device junction temperatures for all-Si and all-SiC inverters.....	166
35.	TO-220 through-hole high-temperature package of 75-A SiC Schottky diode.....	167
36.	Case temperature of 75-A diode at different current level measured at 200°C ambient.....	167
37.	Voltage drop across the diode at different currents.....	168
38.	A 450-A high-temperature SiC diode module with six 75-A Schottky diodes in parallel.....	168
39.	i-v curves of the 450-A diode module.....	169
40.	Voltage drop across the diode module at different currents.....	169
41.	Case temperature of 75-A diode at different current levels measured at 200°C ambient.....	170
42.	Three-phase inverter built at ORNL.....	170
43.	R-L load test setup.....	171
44.	Efficiency vs. output power at 325-V dc voltage.....	172
45.	Efficiency of inverters at 325 V dc voltage and 50 Hz output.....	173
4.2	Integrated dc-dc Converter for Multi-Voltage Bus Systems	
1.	Power management in future fuel cell vehicles.....	178
2.	Original topology with LC filter.....	179
3.	Modified topology that eliminates the LC filter.....	179
4.	Schematic of the 4 kW dc-dc converter.....	180
5.	Transformer terminal voltages and currents waveforms illustrating the operating principle.....	181
6.	Simulation results showing power transfer from 42 V to 14 V and HV.....	182
7.	Simulation results showing power transfer from HV to 42 V and 14 V.....	183
8.	Photo of the planar transformer. Footprint: 4.875 × 2.125 in.....	184
9.	Photo of the DSP control board. Size: 7.0 × 3.5 in.....	184
10.	Three-dimensional assembly layout.....	185
11.	The 4-kW prototype. Footprint: 10.7 in. wide × 11.0 in. deep × 2.7 in. maximum height.....	186
12.	Typical testing waveforms for power transfer from 42 V to 14 V and HV.....	187
13.	Typical testing waveforms for power transfer from HV to 42 V and 14 V.....	188
14.	Efficiency chart.....	189
15.	Possible electrical power system architectures for fuel cell vehicles.....	189
4.3	Cascaded Multilevel Inverter	
1.	One leg of a three-leg inverter connected to a full H-bridge with a capacitor dc source.....	194
2.	Five-level output waveform of the multilevel inverter.....	194

3.	To make the output voltage zero for $\theta_1 = \theta = \pi$, one can either set $v_1 = +V_{dc}/2$ and $v_2 = -V_{dc}/2$ (bottom left) or $v_1 = +V_{dc}/2$ and $v_2 = +V_{dc}/2$ (bottom right).	195
4.	Top level Simulink block diagram.	196
5.	Rotor speeds achievable using a standard three-leg inverter (left) and the proposed multilevel inverter (right).	197
6.	Left: Voltage using a standard three-leg inverter. Right: Voltage obtained using the proposed multilevel inverter.	197
7.	Left: Motor torque using standard three-leg inverter. Right: Motor torque using proposed multilevel inverter.	197
8.	Left: Stator current for the standard three-leg inverter. Right: Stator current for the proposed multilevel inverter.	198
9.	Capacitor voltage vs time.	198
10.	Expanded view of the capacitor voltage as a function of time.	199
11.	Fundamental frequency waveform.	199
12.	θ_1 and θ_2 vs m .	200
13.	Rotor speed in rad/s vs time in seconds.	201
14.	Commanded and computed fundamental voltage in volts vs time in seconds.	201
15.	Computed fifth-harmonic of the voltage in volts vs time in seconds.	202
16.	Torque in N-m vs time in seconds.	202
17.	Enlarged view of the phase 1 voltage in volts vs time in seconds.	203
18.	Phase 1 stator current vs time.	203
19.	Capacitor voltage in volts vs time in seconds.	203
20.	An enlarged view the capacitor voltage in volts vs time in seconds.	204
21.	Scaled capacitor voltage, stator current, and stator voltage vs time in seconds.	204
22.	$0 < \varphi < \theta_1$.	205
23.	$\theta_1 < \varphi < \theta_2$.	206
24.	$\theta_2 < \varphi < \pi/2$.	206
4.4	Advanced Converter Systems for High-Temperature HEV Environments	
1.	The dc-dc power conversion system and dc-dc converter module	212
2.	10-kW dc-dc converter module.	213
3.	Experimental results of the converter. 1X means the output voltage equals to input voltage; 2X means the output voltage is twice the input voltage.	214
4.	The proposed 5-level MMCCC with four modular blocks	215
5.	The modular block	215
6.	The proof-of-concept six-level MMCCC.	215
7.	Schematic of the gate driver circuit	216
8.	Complete layout of the gate driver chip.	217
9.	Layout of the logic part of the gate driver chip.	218
10.	Layout of the high-voltage output stage.	218
11.	Capacitance and loss for a BaZrO ₃ prototype capacitor manufactured at TRS Technologies	221
12.	Temperature dependence of capacitance and loss for a commercial multilayer ceramic capacitor	222
13.	Temperature dependence of capacitance and loss for a commercial multilayer Y5V ceramic capacitor under an applied dc voltage of 200 V	222
4.5	dc/dc Converter for Fuel Cell and Hybrid Vehicle	
1.	The novel interleaved dc/dc converter topology	228
2.	Alpha dc/dc converter under test.	229

3.	Efficiency test results at $V_i = 200\text{ V}$, 300 V , 350 V , and 400 V	230
4.	Alpha and Beta power module layout.....	230
5.	The Beta version of dc/dc converter (5.1 L).....	231
6.	Beta dc/dc converter interfaces.....	232
7.	Alpha baseplate pin-fin design with pin-fin.....	233
8.	Beta baseplate design without pin-fin.....	233
9.	Coolant channel fluid simulation.....	234
10.	The thermal simulation results.....	234
11.	Baseplate leak test setup.....	234
12.	Baseplate leaks with initial seal design.....	235
5.1	Fully Integrated HEV Traction Motor Drive Development Using Thermoelectrics and Film Capacitor Innovations	
1.	Cutaway view of integrated motor and inverter utilizing silicon carbide power electronics, thermoelectric temperature boundaries, silicon electronics and film capacitors.....	240
2.	Motor concept section view showing detail of component arrangement and proposed heat flow path.....	241
3.	Exploded view of ProEngineer mechanical model used to analyze the thermal performance of the ORNL SiC-TE motor/inverter integration concept.....	242
4.	First model analyzed showing the “cold zone” heat flows—the top layer (just a copper heat spreader) interfaces with the rest of the system through the TE layer (not in this model).....	243
5.	Second model showing the “hot zone” heat flows.....	244
6.	This third model shows the whole assembly where Model 1 and Model 2 structures are basically joined together using the TE boundary layer.....	245
7.	Cold zone produced by TE layer.....	246
8.	Power flow schematic in the SiC/TE/silicon/film capacitor integration concept.....	247
9.	The effect of layering on maximum temperature difference.....	247
5.2.1	Benchmarking of Competitive Technologies	
1.	Accord motor with custom-designed end plates and shaft.....	266
2.	Preparation of test cell for Accord performance testing.....	266
3.	Accord/Prius locked-rotor torque vs electrical position at varying levels of stator current.....	267
4.	Comparison of Accord and Prius motor efficiency contour maps.....	268
5.	Comparison of Accord and Prius inverter efficiency contour maps.....	269
6.	Comparison of Accord and Prius motor plus inverter efficiency contour maps.....	270
7.	PM configurations and dimensions for three hybrid rotor designs.....	272
8.	Volume of entire Prius inverter/converter assembly.....	273
9.	Conceptual change to inverter/converter casing for excluding the buck/boost converter.....	273
10.	2004 Prius gear assembly in an open casing.....	274
11.	Components making up the Prius gear box.....	274
12.	Approximate volume estimation and planetary gear assembly.....	275
13.	Dimensions for planetary gear, the first reducer gear, and extension.....	275
14.	Uncoupled, energized spin test of the Accord motor to assess core losses.....	276
5.2.2	Component Characterization	
1.	Static test input screen.....	280
2.	Dynamic test input screen.....	281

3.	Single Prius film capacitor test set up	282
4.	Single Prius film capacitor tested in the static mode at 5 kHz	283
5.	Single Prius film capacitor ESR frequency response	283
6.	Single Prius film capacitor DF frequency response	284
7.	Single Prius film capacitor frequency response	284
8.	Kemet ceramic capacitor static test at 5 kHz	285
9.	Penn State ceramic high-temperature static test at 5 kHz	286
10.	Temperature rise over ambient at 5 kHz	287
11.	Single Prius film capacitor leakage current vs temperature	288
12.	Circuit used to calculate ESL	288
13.	Hysteresis plot of the Prius sintered benchmark magnet at 183°C	290
14.	Hysteresis plot of the Shin-Etsu N43TS sintered magnet at 182°C	291
15.	Hysteresis plot of the ANL sintered magnet at 175°C	292
16.	Hysteresis plot of Arnold Magnetics Plastiform 2205 bonded benchmark magnet at 200°C	294
17.	Hysteresis plot of the Ames MQP-11 HTP magnet at 200°C	295
18.	Hysteresis plot of the Ames MQP-O bonded magnet at 202°C	296

Tables

	Page
2.1 Thermal Control for Inverters and Motors	
1. Comparison of cooling methods	8
2. Loop pressures	9
3. Motor winding electrical parameters	10
4. Temperatures.....	10
5. Comparison of key specifications	12
6. One-half size inverter test results	18
2.2 Identifying the Barriers and Approaches to Achieving High-Temperature Coolants	
1. Characteristic of Delco Remy MQ2° NdFeB magnets.....	36
2. Estimate of life-shortening hours accrued during 15 years of city driving	38
3. Itemized listing of costs of eliminated components	39
4. Estimations of additional costs to resolve barriers in components/subsystems	40
5. Multiparameter, temperature-based qualitative comparison	41
3.2.1 IPMR Machines	
1. Comparison of dimensions of the ORNL 16,000-rpm motor and the Toyota/Prius motor	54
3.3 Control of Fractional-Slot Surface Mounted Permanent Magnet Motors with Concentrated Windings	
1. Fourier coefficients of winding function for a stator with 36 slots	77
2. FreedomCAR traction motor targets	83
3. Comparison of UWM and ORNL design parameters for the proposed 55 kW (PEAK) SPM.....	84
4. Speed software loss equation coefficient definitions	85
5. Core losses for ARNON 7 laminations in the 55-kW FSCW-SPM motor	86
6. Magnet losses for a 36-slot, 30-pole 55-kw FSCW-SPM motor	91
7. MatLab program to calculate magnet losses	92
8. SPEED design sheets for FSCW-SPM motor delivering 30 kW at 2000 rpm	93
9. SPEED design sheets for FSCW-SPM motor delivering 55 kW at 10,000 rpm	96
10. SPMI machine dimensions and parameters	108
3.4 Extending the CPSR of Synchronous Reluctance Motors	
1. SPEED performance data for a synchronous reluctance motor whose stator has four turns per pole	125
2. SPEED performance data for synchronous reluctance motor whose stator has eight turns	126
3. Design sheet for the reluctance motor shown in Figure 1	126
3.5 Advanced Traction Motor Development	
1. Comparison of three design performances with specification	143
2. Motor parameters, six-pole pair, 3.4 in. (final design)	145
3. Parts included in MFG cost estimate	150
4. Comparison of FreedomCAR motor with target	152

4.1	Wide Bandgap Materials	
1.	Ratings of the devices used in the inverters	161
4.4	Advanced Converter Systems for High-Temperature HEV Environments	
1.	U.S. capacitor industry products for high-temperature capacitors	219
2.	Summary of high-temperature materials survey (taken from a study of more than 50 materials)	220
3.	General commercial capacitor classes (Note the trade-off between dielectric constant and temperature dependence of dielectric constant)	221
4.5	dc/dc Converter for Fuel Cell and Hybrid Vehicle	
1.	The percentage of goals achieved as of FY 2005 through Alpha design	229
2.	The BOM and weight of Beta design	232
3.	Status summary from the Beta design during FY 2006	236
5.1	Fully Integrated HEV Traction Motor Drive Development Using Thermoelectrics and Film Capacitor Innovations	
1.	TE device manufacturer comparison data	239
2.	TE comparisons showing normalized cost per unit of heat flux	240
3.	Thermal model calculations and assumptions	243
4.	Capacitor power dissipation (W) due to voltage and power factor effects	248
5.	COP in terms of number of layers and temperature gradient	249
5.2.1	Benchmarking of Competitive Technologies	
1.	Differences between the hybrid Accord and the Prius	265
2.	Comparison of design parameters for Prius and Accord	271
5.2.2	Component Characterization	
1.	Maximum ripple current for the single Prius film capacitor	287
2.	Sintered magnet test results	289
3.	Bonded magnet test results	293

Acronyms and Abbreviations

A	ampere
A_{RMS} or A_{rms}	ampere rms
AC	air-conditioning
ac	alternating current
AIPM	automotive integrated power module
AMES	Ames Laboratory
ANL	Argonne National Laboratory
BCD	bipolar CMOS DMOS
BDCM	brushless direct current motor
BFE	brushless field excitation
CAD	computer-aided drafting
CAN	controller area network
CFC	chlorofluorocarbon
COP	coefficient of performance
CPA	conventional phase advance
CPSR	constant power speed range
CSI	current-source inverter
CTE	coefficient of thermal expansion
DAC/DAQ	data acquisition system
d-axis	direct-axis
DF	dissipation factor
DMIC	dual-mode inverter control
DOE	U.S. Department of Energy
DSP	digital signal processor
EERE	Energy Efficiency and Renewable Energy
emf	electromotive force
EMI	electromagnetic interference
ESL	effective series inductance
ESR	equivalent series resistance
FC	fuel cell
FCV	fuel cell vehicle
FCVT	FreedomCAR and Vehicle Technologies
FEA	finite-element analysis
FreedomCAR	Freedom Cooperative Automotive Research
FSCW	fractional slot concentrated windings
GaN	gallium nitride
GT	Georgia Institute of Technology
GWP	global warming potential
HC	hydrocarbon
HCFC	hydrochlorofluorocarbon
HEV	hybrid electric vehicle
HFC	hydrofluorocarbon
HFE	hydrofluoroether
HSUPM	hybrid-secondary-uncluttered permanent magnet
HV	high voltage
HVAC	heating, ventilating, and air-conditioning
ICE	internal combustion engine
ID	inner diameter

IGBT	insulated gate bipolar transistor
IM	induction motor
IMA	integrated motor assist
IPM	integrated power module
IPM	interior permanent magnet
I-source	current-source
ISR	Isothermal Systems Research
JFET	junction field-effect transistor
JIC	jet impingement cooling
MLCC	multilayer ceramic capacitor
MMCCC	multilevel modular clamped dc/dc converter
mmf	magneto-motive force
MOSFET	metal oxide semiconductor field-effect transistor
MS	methylsiloxane
MSU	Michigan State University
NASA	National Aeronautics and Space Administration
NMOS	negative-channel MOS
NTRC	National Transportation Research Center
OD	outer diameter
ODP	ozone-depleting potential
OFCVTs	Office of FreedomCAR and Vehicle Technologies
ORNL	Oak Ridge National Laboratory
PEEM	Power Electronics and Electric Machines
PEEMRC	Power Electronics and Electric Machinery Research Center
Penn State	Pennsylvania State University
PFC	perfluorocarbon
PHEV	plug-in HEV
PM	permanent magnet
PMDC	permanent magnet brushless dc
PMDC	permanent magnet direct current
PMOS	positive-channel MOS
PMSM	permanent magnet synchronous motor
PWM	pulse-width modulation
q-axis	quadrature-axis
R&D	research and development
rad/s	rotational speed
RFP	request for proposals
RIPM	reluctance interior permanent magnet
rms	root-mean-square
RSC	Rockwell Scientific Company
RTFC	real time flux control
SCR	silicon-controlled rectifier
SDPR	switching device power rating
Si	silicon
SiC	silicon carbide
SKAI	Semikron Advanced Integration
SMPM	surface mounted permanent magnet
SOC	state-of-charge
SOI	silicon on insulator
SPM	surface permanent magnet
SUV	sport utility vehicle

TE	thermoelectrics
THS II	Toyota hybrid system (2004)
toff	turn-off times
ton	turn-on
UT	University of Tennessee
UWM	University of Wisconsin–Madison
V	volt
VIBE	vibration-induced bubble ejection
V-source	voltage-source
VSI	voltage source inverter
W	watt
WBG	wide bandgap
WEG	water–ethylene glycol
ZSC	zero-sequence circuit
ZVS	zero-voltage-switching

1. Introduction

The U.S. Department of Energy (DOE) and the U.S. Council for Automotive Research (composed of automakers Ford, General Motors, and DaimlerChrysler) announced in January 2002 a new cooperative research effort. Known as FreedomCAR (derived from "Freedom" and "Cooperative Automotive Research"), it represents DOE's commitment to developing public/private partnerships to fund high-risk, high-payoff research into advanced automotive technologies. Efficient fuel cell technology, which uses hydrogen to power automobiles without air pollution, is a very promising pathway to achieve the ultimate vision. The new partnership replaces and builds upon the Partnership for a New Generation of Vehicles initiative that ran from 1993 through 2001.

The Vehicle Systems subprogram within the FreedomCAR and Vehicle Technologies Program provides support and guidance for many cutting-edge automotive and heavy truck technologies now under development. Research is focused on understanding and improving the way the various new components of tomorrow's automobiles and heavy trucks will function as a unified system to improve fuel efficiency. This work also supports the development of advanced automotive accessories and the reduction of parasitic losses (e.g., aerodynamic drag, thermal management, friction and wear, and rolling resistance).

In supporting the development of hybrid propulsion systems, the Vehicle Systems subprogram has enabled the development of technologies that will significantly improve fuel economy, comply with projected emissions and safety regulations, and use fuels produced domestically.

The Vehicle Systems subprogram supports the efforts of the FreedomCAR and Fuel Partnership and the 21st Century Truck Partnership through a three-phase approach intended to

- Identify overall propulsion and vehicle-related needs by analyzing programmatic goals and reviewing industry's recommendations and requirements and then develop the appropriate technical targets for systems, subsystems, and component research and development activities;
- Develop and validate individual subsystems and components, including electric motors, emission control devices, battery systems, power electronics, accessories, and devices to reduce parasitic losses; and
- Determine how well the components and subsystems work together in a vehicle environment or as a complete propulsion system and whether the efficiency and performance targets at the vehicle level have been achieved.

The research performed under the Vehicle Systems subprogram will help remove technical and cost barriers to enable the development of technology for use in such advanced vehicles as hybrid and fuel-cell-powered automobiles that meet the goals of the FreedomCAR Program.

A key element in making hybrid electric vehicles practical is providing an affordable electric traction drive system. This will require attaining weight, volume, and cost targets for the power electronics and electrical machines subsystems of the traction drive system. Areas of development include these:

- Novel traction motor designs that result in increased power density and lower cost;
- Inverter technologies involving new topologies to achieve higher efficiency and the ability to accommodate higher-temperature environments;
- Converter concepts that employ means of reducing the component count and integrating functionality to decrease size, weight, and cost;
- More effective thermal control and packaging technologies; and
- Integrated motor/inverter concepts.

The Oak Ridge National Laboratory's (ORNL's) Power Electronics and Electric Machinery Research Center conducts fundamental research, evaluates hardware, and assists in the technical direction of the DOE Office of FreedomCAR and Vehicle Technologies Program, Power Electronics and Electric Machinery Program. In this role, ORNL serves on the FreedomCAR Electrical and Electronics Technical

Team, evaluates proposals for DOE, and lends its technological expertise to the direction of projects and evaluation of developing technologies.

ORNL also executes specific projects for DOE. The following report discusses those projects carried out in FY 2006 and conveys highlights of their accomplishments. Numerous project reviews, technical reports, and papers have been published for these efforts, if the reader is interested in pursuing details of the work.

Below are summaries of major accomplishments for each technical project.

Thermal Control for Inverters and Motors

- An oil spray cooling system for a 6000-rpm drive motor was designed, fabricated, and tested. The cooling was significantly improved from similar motors that incorporate oil-sling cooling systems.
- ORNL has designed, built, and tested an inverter half the size of a commercially available module of the same power rating. The dc test reached 600-A capability (200 A per leg) and the ac switching test achieved 250 Arms for a 3-phase output.

Identifying the Barriers and Approaches to Achieving High-Temperature Coolants

- The study was performed to identify practical approaches, technical barriers, and cost impacts for achieving high-temperature coolant operation for certain traction drive subassemblies and components of hybrid electric vehicles (HEVs). The results of the study showed it to be evident that a few formidable technical and cost barriers exist, and no effective approach for mitigating the barriers was evident in the near term.
- All significant barriers that pertain to the inverter, dc link capacitor, and motor were identified.
- Approaches for resolving many of the barriers were discussed in the study.
- Component-level issues were addressed in the study for operation at a significantly higher coolant temperature. These issues generally pertained to the cost and reliability of existing or near-term components that would be suitable for use with 105°C coolant. The assessed components included power electronic devices/modules such as diodes and insulated gate bipolar transistors (IGBTs), inverter-grade high-temperature capacitors, permanent magnets (PMs), and motor-grade wire insulation. The need for potentially modifying/resizing subassemblies such as inverters, motors, and heat exchangers was also addressed in the study.

Uncluttered CVT Machine

- The design of the proof-of-concept uncluttered rotor without windings and a half stator wound core to couple to the uncluttered rotor was completed. The uncluttered rotor and its half stator were fabricated, and the uncluttered rotor teeth were machined out of solid steel instead of laminations in order to lower costs for the proof-of-concept prototype. The uncluttered rotor concept for the brushless rotating stator (or armature) was proved through tests conducted on the prototype.

Interior Permanent Magnet Reluctance Machines with Brushless Field Excitation—16,000 rpm

- The 16,000-rpm motor design was completed and the prototype fabricated. Initial testing was performed and a dimensional and cost analysis was made based upon the Toyota Prius motor. This motor design enables better motor performance with system cost savings. Also, if used in a vehicle architecture requiring a boost converter, this motor can produce 250-kW output at 16,000 rpm. This significantly widens the possible applications for this type of motor.

High-Power-Density Reluctance Interior Permanent Magnet Machines—6000 rpm

- The new technology derived from this project shows that the air-gap flux density produced by the new PM arrangement can be doubled compared with that of the Toyota/Prius motor. The PM torque

component is proportional to the product of the PM fundamental air-gap flux density and the current of the motor. Therefore, the higher PM fundamental air-gap flux density produces higher torque at a given current of the motor and hence a higher power density of the motor.

Control of Fractional-slot Surface-mounted PM Motors with Concentrated Windings

- Two 55-kW surface permanent magnets (SPMs) with fractional slot concentrated windings (FSCW) incorporating FreedomCAR targets were designed and studied. SPM1 was selected for developing an analytical model to accurately predict the stator tooth and yoke iron losses in FSCW-SPM machines. SPM2 was selected for an analytical model comparison study.
- The SPM2 motor was modeled with SPEED software, and ORNL collaborated with the University of Wisconsin at Madison (UWM) to compare design parameters calculated using SPEED's PC-BDC module with those calculated by UWM.
- A rapid motor/inverter simulator was created using MatLab. Its verity was checked with time domain calculations using PSPICE software to show that the algorithms in the simulator are fast enough to use in a control circuit.
- A closed-form analytical model was successfully developed that can accurately predict the stator tooth and yoke iron losses in FSCW-SPM machines during open-circuit operation.
- A detailed point-by-point finite-element analysis (FEA) of FSCW-SPM machines was completed and is proving very useful in identifying the relative contributions of hysteresis and eddy-current losses in different parts of the machine as a function of rotor speed.
- Three control schemes were developed.
 - The UWM scheme controls to ensure maximum motor efficiency and shows how motor losses under load may be sufficiently reduced by field weakening, which increases total current, to offset the additional I^2R losses and thereby improve motor efficiency.
 - The first ORNL scheme is a low-cost scheme because it eliminates current sensors. The ORNL simulator assumes losses that increase with the square of the speed.
 - The second ORNL scheme uses a set of antiparallel silicon controlled rectifiers in each phase to ensure that any load is accommodated with minimum current, which ensures that it is a maximum overall efficiency scheme.
- UWM performed a successful FEA-based verification of a significant efficiency improvement (>5% at some speeds) that can be achieved in FSCW-SPM machines by using a modified vector control algorithm during partial-load operating conditions.
- ORNL evaluated its first control scheme with the simulator for two constraints, first so that rated current is not exceeded and second so that rated power is not exceeded. The limiting current constraint allows considerably more power to be delivered over a large part of the power speed curve.

Extending the CPSR of Synchronous Reluctance Motors

- FLUX2D software was applied to a model of a PM motor that was created by ORNL to determine the phase advance, which is the angle between the center of a rotor pole and the stator current orientation that will produce maximum torque. The model of the PM motor was created with inset magnets, and the magnets were turned off to simulate a synchronous reluctance motor with doubly salient poles. The torque produced was then calculated for a fixed rotor as the current in the stator was varied over one pole, and for current fixed in the stator with the rotor turned through one pole angle. Definite maxima were found with only rough agreement between the two approaches. A similar exercise with COMSOL demonstrated good agreement between the two approaches for estimating the phase advance for maximum torque.
- Using SPEED as a design tool, two synchronous reluctance motors were modeled to attempt to meet FreedomCAR targets. The first model with four turns per pole could not deliver maximum power at 2000 rpm. Adequate power at 2000 rpm required eight turns per pole, which doubled the amount of

copper to increase both cost and weight. The motor was too heavy and too expensive to meet FreedomCAR goals.

- A per-phase model was designed by applying a winding function to a synchronous reluctance motor with salient rotor and stator poles to determine the inductance that should be used. This approach yielded direct and quadrature inductances, which had to be added for use in the model. Unfortunately, flux fringing, verified by a COMSOL analysis, indicated that use of the winding function was clearly an approximation. Later work showed that a reliable model should include not only flux fringing but also saturation.
- Detailed models of switched reluctance motors were constructed to study flux behavior in a synchronous reluctance motor. Variations in the study included (1) a solid rotor to study the effect of eddy currents on the rotor; (2) regular reluctance rotors turning inside stators with and without shoes in their teeth; and (3) a comparison of synchronous reluctance motor performance, assuming no saturation with performance, that included saturation as part of the model. Overall results strongly suggested that any reliable model of a synchronous reluctance motor must incorporate flux fringing as well as saturation.

Advanced Traction Motor Development

- The technical report entitled *FreedomCAR Advanced Traction Drive Motor Development Phase 1* was issued in September 2006. The report documents the design effort and conclusions reached by UQM Technologies, Inc. during the Phase 1 task. A 6 pole-pair machine with 36 slots in a 3-slot-per-pole configuration was determined to be the final design choice. The final design met or exceeded most of the 2010 FreedomCAR goals and traction motor technical targets.

Wide Bandgap Materials

- Several silicon carbide (SiC) Schottky diodes, junction field effect transistors (JFETs) and gallium nitride (GaN) Schottky diodes were acquired.
- SiC Schottky diodes, JFETs, and GaN Schottky diodes were tested, characterized, and modeled.
- A 55-kW all-SiC inverter was modeled and its performance was compared with that of similarly rated all-Si and Si-SiC hybrid inverters.
- High-temperature packages were built for SiC power devices to operate at 200°C.
- All-Si and Si-SiC (Si IGBTs and SiC Schottky diodes) hybrid inverters were built and tested and the results compared.

Integrated dc/dc Converter for Multi-Voltage Bus Systems

- Topology development
 - A half-bridge-based dc/dc converter was developed that can interconnect the 14-V, 42-V and high-voltage buses and can reduce the component count by 50% over the conventional full-bridge-based technologies. Further refinements have eliminated the inductor capacitor (LC) filter for the 14-V bus.
 - Interleaved modular configurations using the half-bridge as building blocks share the capacitor legs and provide a greater degree of component count reduction as the number of modules increases when scaling up the power level.
 - The capacitor leg current in the interleaved configurations can be significantly reduced, thus decreasing the capacitance.
 - A novel control scheme was also devised that can control the power flow among the three buses and reduce the flux density of the transformers.
- Prototype demonstration
 - A 4-kW prototype was designed and built using two 2-kW modules.
 - The prototype was successfully tested at load power levels of up to 4.6 kW.

- Efficiencies were measured between 93.0 and 95.8% over a wide power range of 0.5 to 4.6 kW.
- Evaluation of the prototype indicates that it exceeds the 2015 FreedomCAR targets for specific power and power density and the 2010 cost target.
- dc/dc converter requirements study for fuel cell vehicle applications
 - Several possible power system configurations and the requirements for dc/dc converters were identified.

Cascaded Multilevel Inverter

- A control algorithm was developed to keep the capacitors charged.
- The inverter/converter was simulated in PSpice and Simulink.
- A design simulation of an electrical drive system with the inverter/converter was developed.
- A 1.2-kW prototype was designed.

Advanced Converter Systems for High-Temperature HEV Environments

- Michigan State University designed and fabricated a 10-kW dc/dc converter module based on one of its earlier topologies.
- The University of Tennessee (UT) and ORNL devised an alternative dc/dc converter topology and fabricated a low-power proof-of-concept circuit to demonstrate its feasibility.
- UT and ORNL designed a high-temperature gate drive using a new silicon-on-insulator process by Atmel.
- Pennsylvania State University evaluated capacitors for high-temperature applications.

dc/dc Converter for Fuel Cell and Hybrid Vehicle

- Ballard focused on the production beta design to address differences between the DOE goals and the Alpha design results. The major achievement in FY 2006 was the design and verification of the final beta unit to meet the targets. Tasks included
 - Electrical improvements over the Alpha design
 - Cost reduction
 - Volume reduction
 - Weight reduction
 - Thermal design improvement
 - Manufacturing process improvements

Fully Integrated HEV Traction Motor Drive Development Using Thermoelectrics and Film Capacitor Innovations

- The thermoelectrics (TE) research that was performed was used to produce a comparison chart of commercially available TE devices. Many manufacturers' products were evaluated, and the data have been pulled together for comparison of costs and capabilities. Informative results were obtained that provide good insight into how the available TEs perform, and how some emerging TE technologies are improving performance in some helpful areas.
- A motor type was chosen in order to provide a tangible basis for design concepts and packaging innovations. The design chosen was a commercially available General Electric 5-kW induction motor.
- Physical packaging design ideas were introduced and developed. These ideas resulted in the concept of a layered SiC/TE packaging that allows silicon electronics and film capacitors to be packaged closely with the SiC. This approach uses TEs to keep the silicon and film capacitors cool while allowing the SiC to operate at much higher ambient temperatures.

Benchmarking of Competitive Technologies

- The efficiency mapping tests of the Prius PM synchronous motor (PMSM) and inverter were completed in a specially prepared test cell using an ORNL controller system developed for this project.
- The benchmarking design and packaging evaluation was completed for the Accord subsystems.
- The Accord motor was prepared with a new rotor shaft design and motor end plates, and the inverter was prepared through analysis of the circuit and the construction of auxiliary circuitry.
- Tests were completed on the Accord subsystems that included back-electromotive force, locked rotor, and efficiency mapping.
- Prius and Accord technical evaluations and test results were documented, and technical reports were issued for both during the year.

Component Characterization

- Commercial film and ceramic capacitor benchmarks were defined and characterized.
- Capacitor test samples were tested in two modes, statically and dynamically. Capacitor testing in the static mode requires a thermal cycling process that must continue uninterrupted for extended periods of time. Capacitor testing in the dynamic mode requires testing at thermal extremes and requires ripple current and bias voltage input from the operator.
- Magnet benchmarks for bonded and sintered magnets were defined and characterized.
- Magnet test samples were tested over a temperature range from 20 to 235°C.
- The development of a data acquisition system using LABView was completed to control the environmental chamber and to log data from the measuring instruments for capacitor evaluations.

2. Thermal Control for Power Electronics and Motors

2.1 Thermal Control for Inverters and Motors

Principal Investigator: John Hsu, Curtis Ayers, Chester Coomer
Oak Ridge National Laboratory
National Transportation Research Center
2360 Cherahala Boulevard
Knoxville, TN 37932
Voice: 865-946-1325; Fax: 865-946-1210; E-mail: hsujs@ornl.gov

DOE Technology Development Manager: Susan A. Rogers
Voice: 202-586-8997; Fax: 202-586-1600; E-mail: Susan.Rogers@ee.doe.gov

ORNL Program Manager: Mitch Olszewski
Voice: 865-946-1350; Fax: 865-946-1262; E-mail: olszewskam@ornl.gov

Objectives

The objective of the Thermal Control for Inverters and Motors project is to reduce the size of the inverter by 50% in FY 2006 (based on the current size of the SemiKron 400-A, 160-kW inverter) and then reduce it to one-third of the original size in FY 2007 without negatively impacting the cost, life expectancy, and performance of the entire system.

Motor cooling is also addressed in this project. A cooler motor is particularly needed for plug-in hybrid vehicles because the demand on the motor is higher for providing sufficient torque and power without constantly relying on the help of the engine.

Approach

Much effort has been exerted within the electronics research community to improve semi-conductor die cooling, but little or no attention has been given to improving cooling for dc-link bus capacitors. Oak Ridge National Laboratory (ORNL) has recognized the importance of cooling all the components in the traction drive system, especially the dc-link capacitor. In this project, ORNL uses the passenger air conditioning (AC) coolant to aid in the cooling of the power electronics circuitry. Tapping into the AC system can enable cooling of the insulated gate bipolar transistors (IGBTs), diodes, dc-link capacitor, digital signal processors (DSPs), gate drives, and control power supply without relying on the AC compressor. Note that not all the components need to be submerged in the liquid refrigerant, because the refrigerant vapor and the hermetic housing of the refrigerant provide separate cooling environments for the different components of the inverter/motor drive system.

As part of this project, an oil-spray cooling method was investigated to improve motor cooling.

Approach in FY 2006

- Design and test motor heat exchanger with oil spray
- Design and fabricate hermetic container
- Fabricate film capacitor with tapered metal distribution and bare metal end connections
- Mount silicon dies in prototype cascade inverter
- Assemble and test inverter
- Perform initial integration of floating loop, inverter, and motor

Major Accomplishments

1. An oil spray cooling system for the drive motor was designed, fabricated, and tested. The cooling was significantly improved compared with oil-sling cooling systems.
2. ORNL designed, built, and tested a half-size, full-power inverter. The dc test reached 600-A capability (200 A per leg), and the ac switching test achieved 250 A_{RMS} for 3-phase output.

Technical Discussion for Motor Cooling

Motor windings will heat up in operation because of the finite resistance of the wire and the amperage load. Two primary motor cooling strategies have been used in the Power Electronics and Electric Machinery Research Center laboratory. The first, the "slinger" method, is patterned after the mechanism used in the Toyota Prius electric traction motor. The second method, the "pumped-spray" method, uses an external pump to spray cooled lubricant directly on the electric windings of the motor.

The "slinger" mechanism places a disk with a few slots cut radially into the outer edge adjacent to and rotating with the motor rotor. A portion of the disk periphery is immersed into cooling lubricant in the motor lower internals (the sump) so that during motor/disk rotation, the lubricant is picked up in the slots and hurled by centrifugal force onto the other motor internals, hence the name "slinger." This slinger arrangement has the advantage of simplicity and low cost. An obvious disadvantage is that the lubricant flow is not spread uniformly on the motor windings around the periphery of the motor internals. (However, this simple, inexpensive method may be better in some sense under low loads or short transients than a more complicated method.) A test apparatus was assembled to mirror as closely as possible the configuration of the Prius traction motor, and then operated at load to evaluate the performance of the simple slinger cooling method. The tests were conducted in 2004.

An external pump was used to spray cooling lubricant directly onto the motor windings to evaluate this more direct spray cooling method. This pumped-spray cooling method uses a dedicated external pump that takes coolant from the motor sump, passes it through a heat exchanger, and sprays the coolant through 18 nozzles distributed uniformly over the top half of the motor casing. The sprayed coolant impinges directly onto the motor stator windings, where the coolant drips off the windings back into the sump. To compare the results of the slinger tests with the pumped spray tests, the results were made as comparable as possible. They are shown in Table 1. The laboratory ambient temperature was approximately 20°C for both test series.

Table 1. Comparison of cooling methods

	Pumped spray	Slinger
Total electrical power (W)	2270	2070
Maximum winding temperature (°C)	59.2	142.0
Lubricant sump temperature (°C)	31.9	65.0
Pumping power (W)	104.0	96.0

The pumping power for the pumped-spray method was measured by the current and voltage draw of the dc motor that powered the rotary gear pump. The pumping power for the slinger method was measured by the load on the motor that powered the rotating slotted disk. Thus even though the pumped-spray method required an independent pump, a power increase of only approximately 8% was required for the increased cooling. The viscous drag and momentum transfer experienced by the rotating disk slinger method is not as effective in pumping cooling fluid as is the rotary gear pump.

Based on an inspection of Table 1, the pumped-spray method clearly reduced the maximum winding temperature by a considerable amount compared with the slinger, while removing approximately 10% more heat. This significant improvement in cooling is no doubt a result of the higher coolant flow rate and more uniform coolant distribution of the pumped-spray method. Although this method is more involved

than the simple slinger method, the results show a distinctly advantageous lower motor winding temperature.

Details of the Pumped-Spray Cooling Method

- It uses hydraulic fluid as the coolant, sprayed directly on windings and adjacent internal structure.
- The cooling subsystem uses commercially available components.
- A stainless steel brazed plate heat exchanger is used.
- Transmission oil is used.
- A gear pump is used.
- Screen filters are used.
- Multiple spray nozzles are aimed at hot spots

The motor cooling subsystem uses spray nozzles, as shown in Figure 1. The electric motor cooling test loop was designed, assembled, debugged, and tested on August 28, 2006. The test loop circulates the coolant through a heat exchanger, pumps the coolant, and sprays the cooled fluid on the motor windings. The cooling fluid is a synthetic hydraulic fluid, manufactured by Amsoil and designated as ATH. There were 12 spray nozzles on each of the two sides of the ORNL 6000-rpm BFE test motor; 3 were horizontally aimed at the excitation coil, and the remaining 9 were radially aimed at the stator windings in the upper half of the motor casing.



Figure 1. Photo of inside of motor housing showing spray nozzle locations.

For the electrical power levels tested, the motor stator windings were cooled well below the temperature limit of $\sim 180^{\circ}\text{C}$. Test results are presented in Table 2, which reports the measured pressures; Table 3, which reports the measured phase currents, voltages, and total power; and Table 4, which reports the measured temperatures. The motor was wired in a delta configuration. There were three tests at the stated power levels. The loop pressures experienced by the cooling fluid for all power levels are given in Table 2. The pump dc motor was set to an 8-V and 13-A draw.

Table 2. Loop pressures

Place in loop	Gauge pressure (psi)
Pump discharge	26.0
HX inlet	26.0
HX outlet	19.5
Motor inlet	19.5

Table 3. Motor winding electrical parameters

Maximum line current (A)	Leg A-B		Leg B-C		Leg A-C		Total power (W)
	Current (A)	Potential (V)	Current (A)	Potential (V)	Current (A)	Potential (V)	
109.0	48.9	16.3	59.5	16.0	57.5	16.4	1535
205.4	86.0	27.9	109.7	27.2	105.3	27.1	6970
266.0	103.9	33.6	138.0	32.3	134.2	33.7	9439

Table 4. Temperatures

Thermocouple location	Test at 1448 W	Test at 5860 W	Test at 7491 W
1. Oil sump	26.0°C	32.8°C	42.0°C
2. Motor front, 1:00 outside stator	42.3°C	91.7°C	133°C
3. Motor back, 10:00 outside stator	34.5°C	60.0°C	81.2°C
4. Motor back, 12:00 inside stator	43.0°C	81.6°C	133°C
5. Motor front, 9:00 inside stator	34.2°C	77.5°C	79.0°C

The tests were conducted by first electrically powering the windings to yield the approximate maximum line current shown in Table 3 with the hydraulic pump off. The maximum line current is seen in the third line for the delta leg configuration given in Table 3. After less than a minute, the winding temperatures started to increase noticeably, and then the hydraulic pump was energized. This heatup procedure was used to decrease the time needed for a steady state to occur. The first trial procedure had the oil flowing before the ac current was initiated, and the elapsed time to a steady-state was much longer than desired. The oil was allowed to flow until no perceived change in the winding temperatures was noticed, approximately 10–15 minutes. The ac motor current was then shut off, and the temperatures decreased quickly. The dc pump motor was shut off after a few more minutes.

Although the power supply had the capability of providing higher power, further testing at higher power was not completed because the winding fibrous insulation external to the motor case started to smoke at currents higher than the maximum reported in Table 3. This smoke was probably from residual cooling fluid on the fibrous insulation. The spray cooling system was designed to cool only the inside of the motor and not the outside. Further tests could be conducted at higher powers if cooling external to the case were provided, such as simply using a fan to blow laboratory ambient air over the external motor leads.

As seen from the data in Table 3, the delta configuration was not perfectly balanced. The total power was calculated by squaring each leg current, multiplying by the leg resistance, and then adding the three leg powers. The measured resistance for Leg A-B is 0.162 ohm, for Leg B-C is 0.154 ohm, and for Leg A-C is 0.156 ohm, all measured at the laboratory ambient temperature of approximately 19°C. The resistance values were calculated based on the average temperature of the windings for the three maximum line-current cases, respectively. Table 1 shows that the coolant pumping power was 104 W for 2270 W total system power. It is important to note that for all total powers shown in Table 3, the coolant pumping power remained at 104 W.

The heat generation rate in the windings should be uniform at any position. Referring to Table 4 data, note that the maximum stator temperature occurred at the topmost positions for all tests. Also note that the winding temperature decreased as the thermocouple position became more horizontal. The spray nozzles, which had the same orifice diameter, were evenly spaced over the top half of the motor and were fed coolant from a common supply tube. This would imply that the coolant flow experienced by the windings increased with an increasingly more horizontal position. In addition, since the lower part of the stator is immersed in the oil sump, thermal conduction through the iron core and copper in the stator transports heat from the upper part of the stator to the oil sump. To lower this maximum winding temperature, it would be advantageous to bias the flow more toward the top of the motor by increasing the

orifice size at the topmost positions, decreasing the orifice size at the more horizontal positions, or perhaps eliminating the most horizontal orifice. This topmost orifice size bias might increase the other temperatures, but the objective of the spray cooling arrangement should be to decrease the maximum temperature no matter where it occurs.

Of particular note is that the temperature rise across the water side of the heat exchanger was on the order of 10°C above laboratory ambient for all tests, and the water pump head pressure was 26 psi for all tests. This low temperature rise might indicate that the heat load on the heat exchanger was low; it might also indicate that there was a fair amount of heat loss to ambient. The heat exchanger was noticeably warm to the touch but not hot, and there may have been a significant heat loss from the bare metal of the heat exchanger to ambient. The heat exchanger was oriented vertically, which might increase any natural convection to the lab ambient.

The ORNL tests described show that the hydraulic fluid motor cooling loop will keep the stator winding temperatures well below the temperature of concern for the power levels listed for these tests, even with the coolant pumping power maintained at a low level. The cost for the ORNL approach will be slightly higher because of the additional pump. However, an effort is ongoing to attempt to modify the exchanger and to incorporate the pump with the shaft to reduce costs.

Technical Discussion for Inverter Size Reduction

The goal for FY 2006 was to reduce the size of the inverter by 50%, using the Semikron inverter (Model 4001GD06) as a baseline (Figure 2).

Data published by Semikron rate this inverter at 160 kW using 25°C coolant, and 82 kW with 70°C coolant, with the *specific power* at 9.9 kW/kg and the *volumetric power density* at 9.5 kW/liter. The derated current for the 70°C condition is about 250 A_{RMS}. For purposes of comparison with the ORNL inverter that is based on a 50–60°C maximum coolant temperature (bulk liquid temp in a 2-phase system), the Semikron rating at 70°C will be used to provide a more even rating comparison. The ORNL inverter is rated at approximately 65 kW (based on dc test results and cooling capabilities), with 19 kW/kg and 21 kW/L power capabilities. Key specifications are compared in a tabular form in Table 5.



Figure 2. SEMIKRON Model 4001GD06 82-kW inverter.

Table 5. Comparison of key specifications

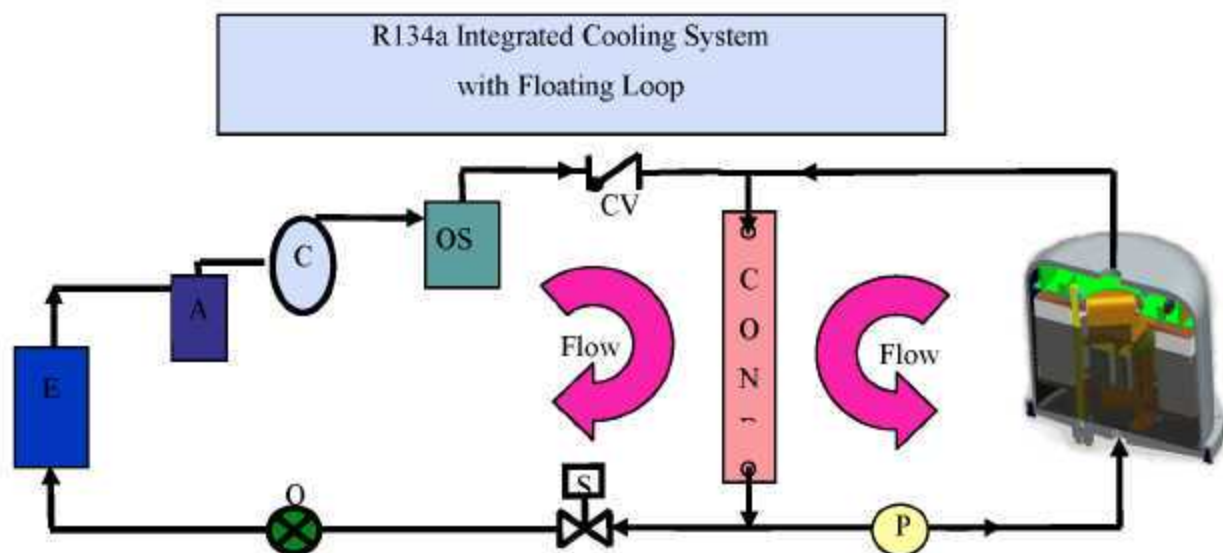
	Semikron 82 kW	ORNL 65 kW	FreedomCar targets 55 kW
Volume (l)	8.6	3.1	6.1
Full load amps	252	250	
kW/kg	9.9	19	11
kW/liter	9.5	21	9

Approach to Size Reduction

- Direct-contact 2-phase cooling technique (ORNL floating loop)
- Capacitor size reduction through shape innovation and lower-temperature environment
- Shift from conventional power electronics packaging methods

1. Direct two-phase cooling technique

The ORNL floating loop cooling system (refer to Publications section and related patents in the Patents section) is a direct contact 2-phase cooling technique that improves cooling sufficiently to partially enable a reduction in size from existing conventionally cooled inverters (Figure 3). The improved heat transfer coefficient achieved by directly submerging the power electronics devices and conductors in refrigerant (R134a in this research) allows the silicon devices to be pushed to higher current levels than conventional cooling will allow, with the same or reduced junction temperatures.

**Figure 3. ORNL floating loop schematic diagram.**

Conventional design (e.g., the Semikron design) depends on conduction cooling from one side of the silicon power chip to transfer heat through an electrically insulating layer (usually aluminum nitride) into the heat sink. The thermal resistance of this setup is high compared with direct 2-phase liquid cooling, in which the coolant itself completely surrounds the chips and the associated electrical conductors near the chips. Heat fluxes of as much as 95 W/cm^2 (using both sides of the silicon chip as heat transfer areas) have been achieved in the laboratory during testing of the ORNL FY 2006 half-size inverter. This result is based on dc load testing in which up to 167 W has been dissipated from each of 12 IGBT chips at the

peak dc loading. Similar calculations for the Semikron inverter indicate about 42 W per chip of heat dissipated, which equates to less than 50 W/cm² (using one side of the chip as conduction heat transfer area). These data indicate that about four times as much heat is being removed from each chip using the direct-cooling technique.

The current test results were limited at this stage by the loading equipment capabilities presently available at ORNL. Testing will continue for higher currents when the loading capability is increased in the near future. The gate driver circuitry, which was designed for a lower-current-capability IGBT, presently exhibits a saturation voltage protection that is too low. This situation is also limiting some of our output current tests. The protection enables around 250 A for a given leg of the 3-phase circuit, which is made up of two IGBT chips. The IGBTs themselves have been tested using a Tektronix high-power curve tracer and do not show any current saturation in this range. The saturation curve in Figure 4 shows that the pair of chips can handle a collector current of 384 A and that the V_{ce}/I_c curve is still linear at the 384-A point. This indicates that the pair of chips can exceed this value by a significant amount, allowing the chips to be pushed to a higher current than previous tests have used.

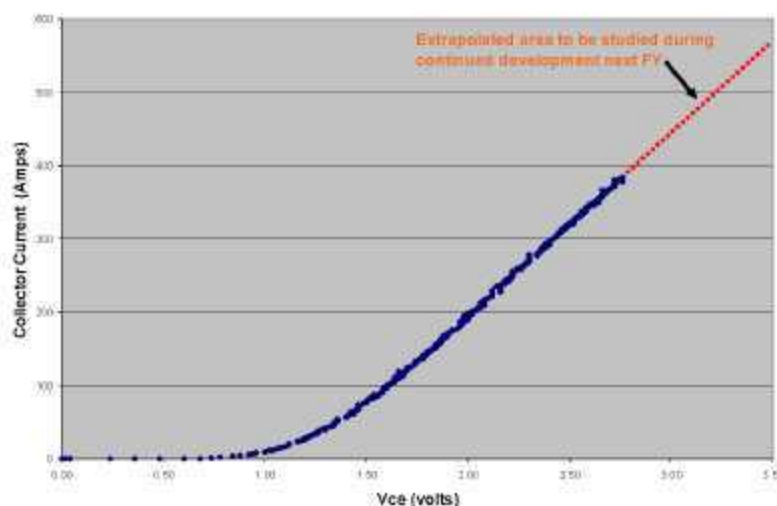


Figure 4. Curve tracer data showing Semikron current capability.

During the next fiscal year, the gate drive circuits will be fully matched to the IGBTs that are chosen for the final 1/3-size prototype. This modification will enable maximum power density to be drawn from that assembly. The loading equipment will be upgraded to handle the needed inverter current and power output to complete the full-power testing.

2. Capacitor size reduction

The dc link capacitor design that was chosen for this project has resulted in a much smaller capacitor for the ORNL cylindrical half-size inverter. The capacitors being used are polypropylene film, 900 V and 500 microfarads (μf). Polypropylene capacitor has been undergoing various types of tests while submerged in R134a over the past 2 years. The actual inverter capacitor being used has been tested in a submerged manner over the past 6 months for ripple current capability and is now being tested in the actual full-power inverter configuration in dc and ac tests. These tests prove the viability of the capacitor for this type of use and thus enable the size and volume of the required dc link capacitance to be significantly reduced. Tests to date indicate we can achieve a 50% size reduction, and ongoing ripple current tests will determine what the maximum reduction in capacitance for inverter usage can be.

Laboratory capacitor performance tests

- Maximum ripple current: 300 A_{RMS}
- Resonance frequency: 8 kHz

Figure 5 shows the Semikron inverter capacitor on the left and the cylindrical inverter capacitor on the right. Not only is the configuration significantly different, but also the volume and thus the mass are very different. The Semikron capacitor depends on conduction heat transfer through the bottom of the package and acceptable ambient conditions around the top of the inverter housing. The ORNL capacitor configuration, along with the design concept, allows the capacitor to be directly surrounded by liquid coolant. This insulates it from ambient conditions to a large degree and maintains the capacitor core temperature close to bulk liquid temperature. The typical operating temperature for the capacitor in this design will be less than 60°C, as opposed to temperatures under the hood of around 90–125°C.

Capacitor comparison:

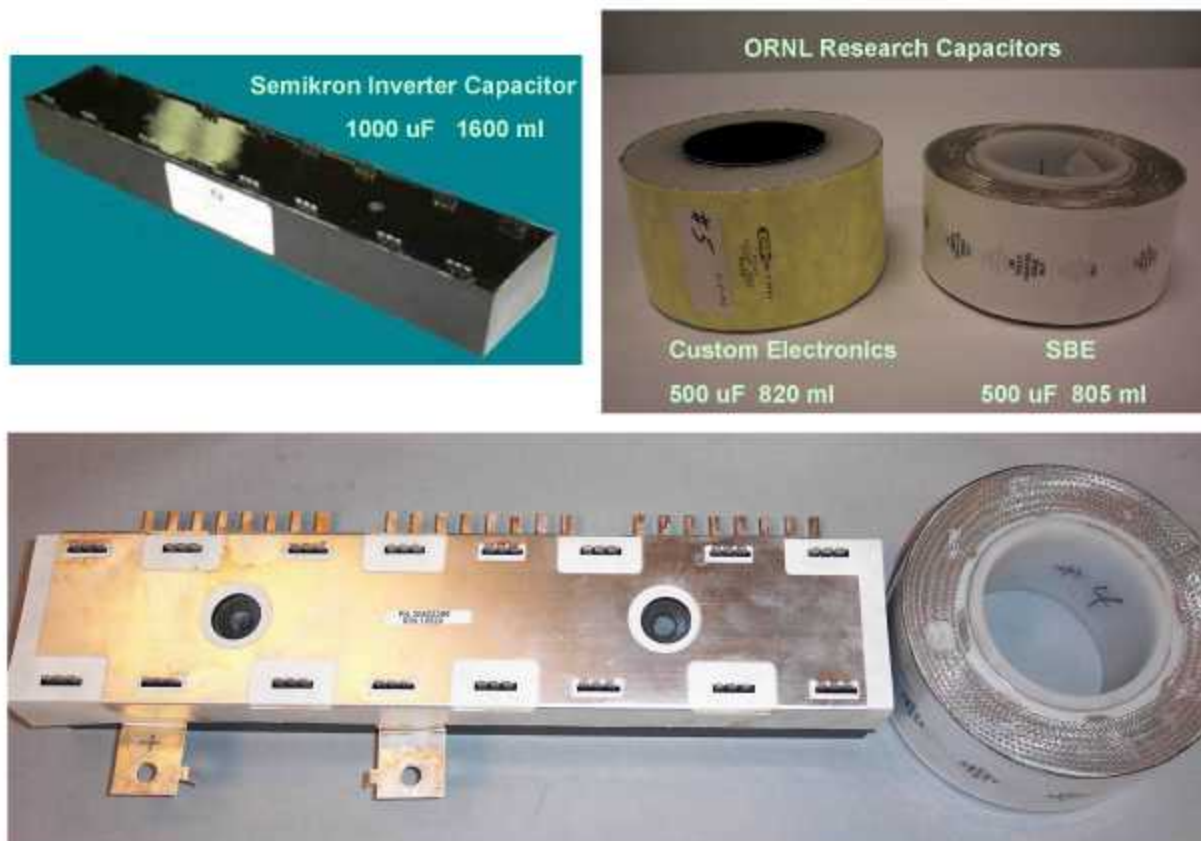


Figure 5. Comparison of Semikron 82-kW dc link capacitor and Custom Electronics and SBE cylindrical capacitors for ORNL half-size inverter. The ORNL design reduces capacitance and volume by 50%.

3. Shift from conventional electronics packaging methods

The long, rectangular block shape of the Semikron capacitor fits the conventional inverter design, which is typically planar and rectangular. Heat removal from the typical inverter is unidirectional through the bottom of the package to a cold plate cooled with water or air. The ORNL approach is to achieve the most volume-efficient shape, which is a sphere or cube. The cylindrical capacitor with a hollow core enables this type of 3-dimensional design.

The first ORNL FY 2006 prototype was developed to perform dc load testing. Figure 6 shows the core of the power section of the inverter, which is built from subsections of the Semikron DBC power electronics cards (Figure 7). The dc link capacitor was not needed for these tests, so it is not installed in this prototype.



Figure 6. Core of first FY 2006 ORNL prototype inverter.



Figure 7. Power IGBT subassembly.

ORNL chose to use the Semikron DBC power board for the FY 2006 half-size inverter prototype for expediency in building and testing the whole inverter geometry to meet the FY 2006 goals. In the meantime, plans and modeling efforts are ongoing to develop the final substrate geometry that will be used to help complete the final 1/3-size inverter. The full board used by Semikron provides power to one of the three phases of the inverter. ORNL was able to cut the full board into three discrete subsections to efficiently turn one board into three boards to serve for all three phases on the new inverter. Figures 8 and 9 show the full board and the subsection used by ORNL. The subsection is the power section used in

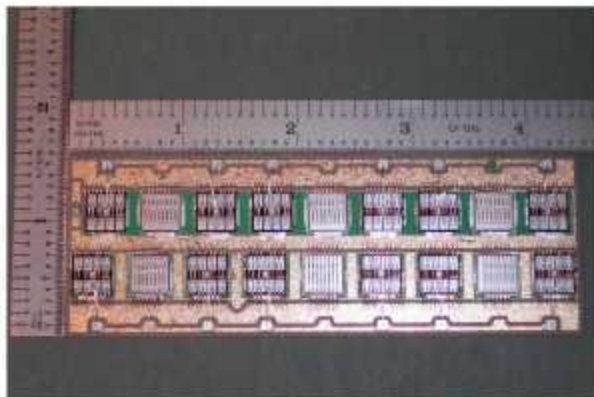


Figure 8. Semikron power IGBT board.

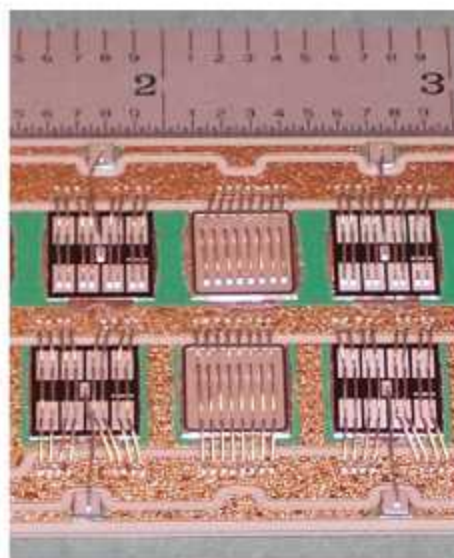


Figure 9. One of three sections of the Semikron board used to produce subassemblies for prototype.

the power subassembly shown in Figure 7. It uses 1/3 of the silicon chips required in the full Semikron board but provides essentially the same current and power performance.

The first row seen in Figure 8 makes up one of the six legs of a full inverter with an IGBT-diode-IGBT arrangement. The second row of chips makes up a second leg in one phase of the inverter—the pair can be represented by A_{upper} and A_{lower} , for example, for the A phase. The 3-dimensional shape that is the core of ORNL's design can begin to be seen in this assembly. It becomes even more evident with the final prototype half-size inverter design seen in the 3-dimensional model shown in Figure 10.

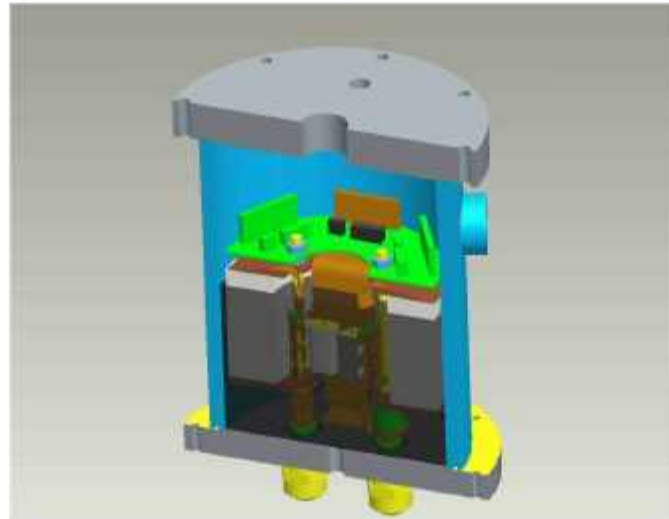


Figure 10. A three-dimensional model of the ORNL prototype showing assembly components.

In the cross-section view in Figure 10 can be seen the dc link cylindrical capacitor; the power electronics subassemblies are packaged in the hollow core of the capacitor. The dc links, disks mounted on the top and bottom ends of the capacitor, feed dc power from the external feed-throughs (seen at bottom) to the power electronics subassemblies in the center. The 3-phase output from the subassemblies exits the housing through the bottom alongside the dc input feeds. The dark shaded area shows an approximate liquid level for the coolant, and the gate driver and interface card can be seen on the top of the assembly.

Liquid feed to the system is through the bottom in the center, and vapor removal (to the condenser) is through the center of the top. This design depicts our test vessel, not a "final" design. A model of a standalone inverter might look like the unit shown in Figure 11. This model has been used to calculate the specific power and volumetric power density, and a plastic vessel/assembly has been built to verify packaging possibilities.

This model was developed with ProEngineer Wildfire software, and materials and densities of each of the parts were supplied to the software. Using this information, the software was used to provide volume and mass information for the whole model.

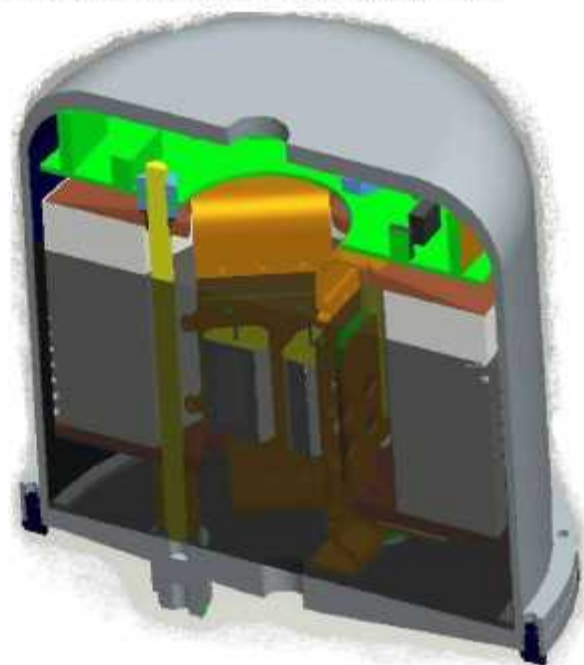


Figure 11. Model showing tighter packaging.

The FY 2006 ORNL model, which is calculated to provide approximately 65 kW of power output, has an estimated volume of 3.1 L and an estimated mass of 3.5 kg. The size and mass calculations include the DSP controller, accessory power supplies, and an interface board, estimated using the solid modeling software. For this phase of the development, these components were placed outside the pressure housing. Future developments can show the feasibility of internal or external mounting for these components. The finished inverter core is shown in Figure 12. The subassembly is complete, ready for insertion into the housing in preparation for full-power ac output. The system power is fed into a dummy R-L load on the 3-phase output to test for maximum current capability.

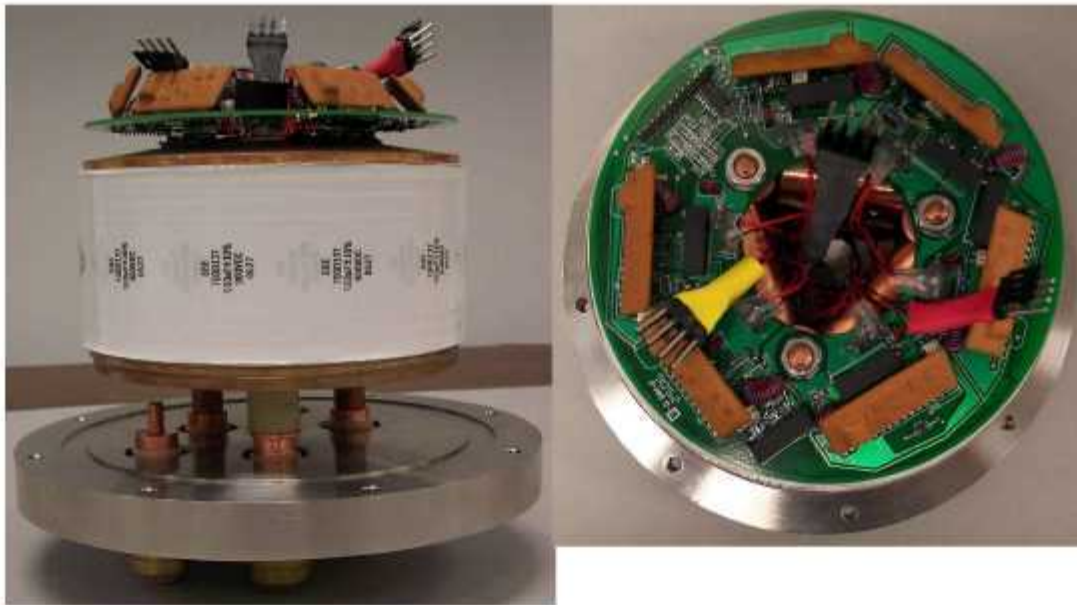


Figure 12. Side view and top view of ORNL prototype internal components.

Laboratory Testing for the ORNL Inverter Prototype

The first prototype was built early in the year to provide testing and data, using the re-sized Semikron boards. This unit primarily served as the dc loading prototype, but lessons learned in construction and mounting of the dies were used to improve the final half-size prototype design built later in the year. dc load testing was performed in the following manner. The inverter was built as a full-fledged 3-phase inverter with individual gate controls as usual. For the dc test, the plus and minus dc link were wired directly into the power supply with no load in between. The phase outputs of the inverter were left open-circuited since no ac output was being created. The gates for all the legs of the inverter were turned fully on for the duration of the test, and the chips themselves served as the load for the test in a short-circuit configuration. This configuration would cause the IGBTs to fail if the current during the test were not controlled, so the power supply was operated in current control mode. The voltage was allowed to float as the current was increased for the dc tests. This method produces heat in the IGBTs without the need to produce controlled ac output currents, and it was appropriate for the initial year's load testing. The IGBTs heated up with increasing dc current, and a temperature-to-current capability was determined. A dc test setup was developed to provide a method of measuring junction temperatures based on forward voltage drops, in order to correlate surface-mounted temperature measurement methods (such as thermistors or thermocouples). We hope to develop this method so that it can be used directly in operating inverters; but at this point, it requires a more steady-state operating condition (dc instead of ac output).

ac load testing was set up in a much more conventional manner: a full-fledged inverter with a DSP controller connected to a 3-phase R-L output load. The power was supplied to the inverter by a dc power supply at voltages up to 350 V_{dc}. The existing load equipment at ORNL at this time prevented full power

(full calculated power is 65 kW), but it reached approximately the full load current required of 250 A. The FreedomCAR inverter output capability was reached (55 kW), but higher values are expected from this inverter design that will produce the high specific power and volumetric power density that were calculated based on dc test results. Some trouble was experienced above 225 A_{RMS}, but only because of a mismatch of the gate driver and the particular IGBTs that were used for this prototype. A false saturation condition was detected, causing the gate drivers to shut down at around 250 A_{RMS}. As seen in the Semikron saturation curve (Figure 4), this value can be increased significantly (hopefully to ~ 400 A_{RMS}) when the gate drive problems are resolved.

The test results for this project year are listed in Table 6. Data sheets from the power analyzer taken at the various test levels are found in Appendix A. These results, along with the calculated specific power and volumetric power densities, show that the goal of a 50% reduction from the baseline for inverter size was reached.

Table 6. One-half size inverter test results

dc OUTPUT TEST (all gates turned on, current controlled):		
— used to determine overall cooling capability for the IGBTs, and maximum current capability		
dc link (volts)	dc current (A)	Power losses (W)
3.3	400	1430
3.6	500	2000

ac OUTPUT TEST (operated with DSP controller with R-L output load):				
— these tests help determine overall operability of the inverter, and maximum power capability				
dc link (V)	Modulation index	V_o output	A_{RMS} output	Power out (kW)
350	0.95	255	153	55
150	0.15	25	200	4 (load reconfigured)
104	~0.2	45	225	8.1

Conclusions

- Tests on the oil spray cooling of the motor confirm that oil-spray cooling is a more effective cooling system than oil-sling cooling system in the same motor structure.
- Motor cooling test data are as follows:
 - Maximum power: 9.4 kW @ 266 A, 104 W pump power
 - Maximum temperature: 133°C @ 7.5 kW
- Coolant pump power can be tailored to the cooling load demand. For lower cooling demand periods, the pump speed (and thus power) can be reduced. When higher system power is needed, and thus more motor cooling, the coolant pump flow rate can be increased as needed.
- There is at least a 4.5 : 1 increase in motor heat removal with no change in the required input coolant pumping power.
- The 500-μF dc link film capacitor functions well while submerged in refrigerant.
- The dc link capacitor tests reveal no limitations so far in handling of ripple current of up to 300 A_{rms}. These tests will continue in order to determine the maximum ripple current capability. Results of the ripple current capability tests will determine the final size for the capacitor. It appears that the capacitor can be reduced in size and volume.

- Tests on the half-size full rated inverter, including dc load and ac tests were conducted. The dc load tests confirmed that the inverter meets the full-load half-size objective. The output capability was successfully tested at up to 55 kW and is expected to be higher based on load calculations from dc test data. Loading capability limitations prevented testing at a higher power for this fiscal year.
- The size of the FY 2006 inverter is calculated at 3.1 L, including the DSP controller, accessory power supplies, interface electronics, and the inverter core itself. This is a reduction of more than 50% from the published Semikron size of 8 L.

ORNL One-half size inverter dc load testing

A_{dc} input	490
A_{RMS} output	347 (calculated)
Max power	110 kW (calculated)
Chip T	70 C
Delta T	38 C
Chip cooling	167 W/chip

ORNL One-half size inverter ac load testing

Maximum A_{RMS} output: 250
 Maximum power output: 55 kW (limited only by output loading capability)
 Inverter chip temp

- Specific power density for the FY 2006 prototype inverter = 19 kW/kg
 — Semikron baseline is 9.9 kW/kg; improvement is 92%
- Volumetric power density for the FY 2006 prototype inverter = 21 kW/liter
 — Semikron baseline is 9.5 kW/L; improvement is 121%

Future Direction

- Complete prototype design of ORNL substrate/IGBT mounting
- Redesign gate driver to match new IGBTs
- Use double-side die mounting without wire bonds
- Complete capacitor ripple current testing to determine final size/volume
- Integrate suitable components inside inverter shell
- Prototype and test new feedthrough concept for I/O connections

Publications

Curt Ayers and Kirk Lowe, "Fundamentals of a Floating Loop Concept Based on R134a Refrigerant Cooling of High Heat Flux Electronics," presented at SemiTherm22 Conference, Dallas, March 2006.

Kirk Lowe and Curt Ayers, "Operating Controls and Dynamics for Floating Refrigerant Loop for High Heat Flux Electronics," presented at SemiTherm22 Conference, Dallas, March 2006.

Patents

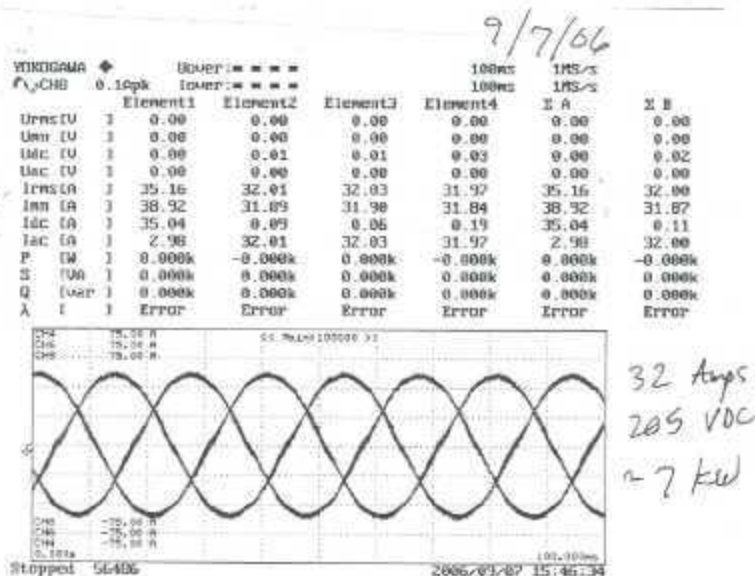
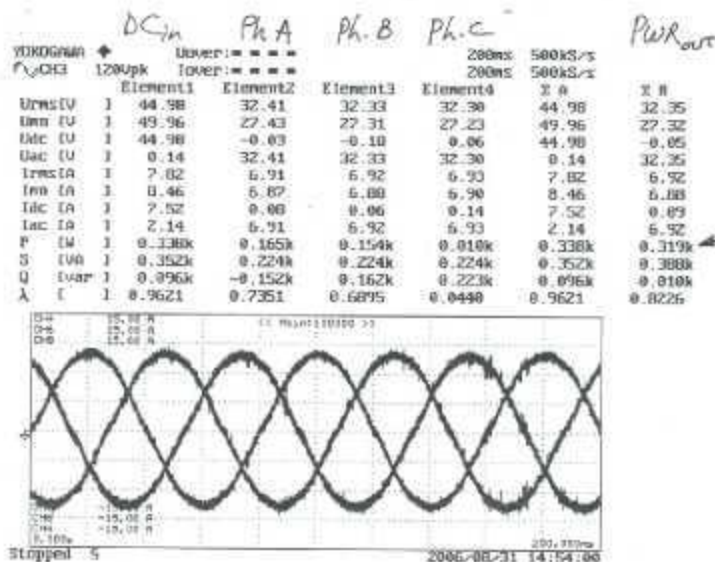
John Hsu, Curtis Ayers, Chester Coomer, and Laura Marlino, "Floating Loop System for Cooling Integrated Motors and Inverters Using Hot Liquid Refrigerant," U.S. Patent 6,993,924 B2, February 7, 2006.

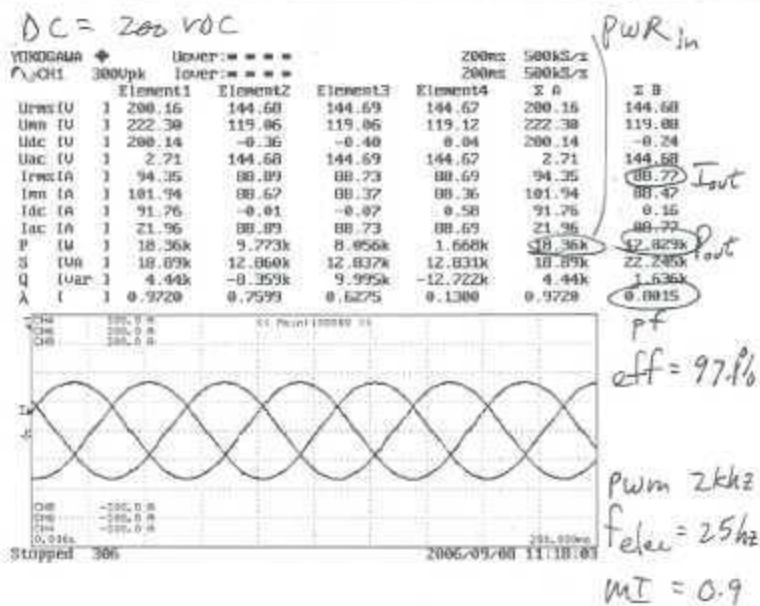
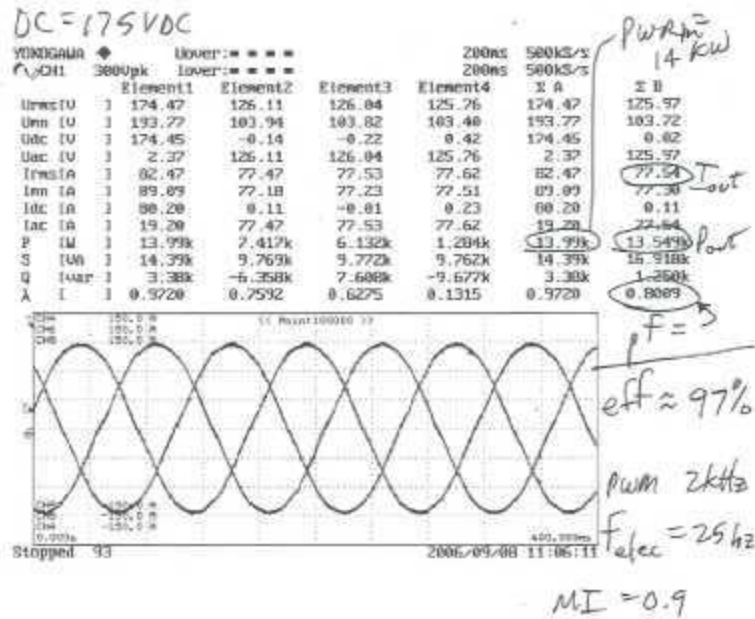
John S. Hsu, Donald J. Adams, Gui-Jia Su, Laura D. Marlino, Curtis W. Ayers, and Chester Coomer, "Cascaded Die Mountings with Spring-Loaded Contact-bond Options," U.S. Patent 6,930,385, August 16, 2005.

John S. Hsu, Donald J. Adams, Gui-Jia Su, Laura D. Marlino, Curtis W. Ayers, and Chester Coomer, "Total Thermal Management System for Hybrid and Full Electric Vehicles," U.S. Patent 6,772,603, August 10, 2004.

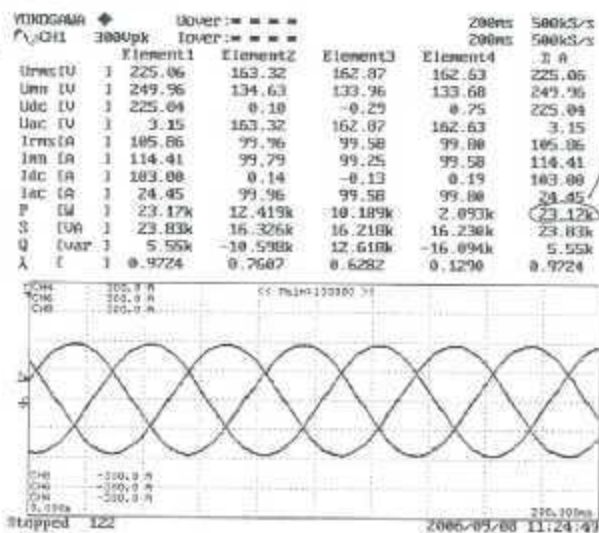
John S. Hsu and William S. Schwenterly, "Superconducting PM Undiffused Machines with Stationary Superconducting Coils," U.S. Patent No. 6,700,297, March 2, 2004.

Appendix A. Power Analyzer Data Sheets from ac Testing of the ORNL Half-size Inverter





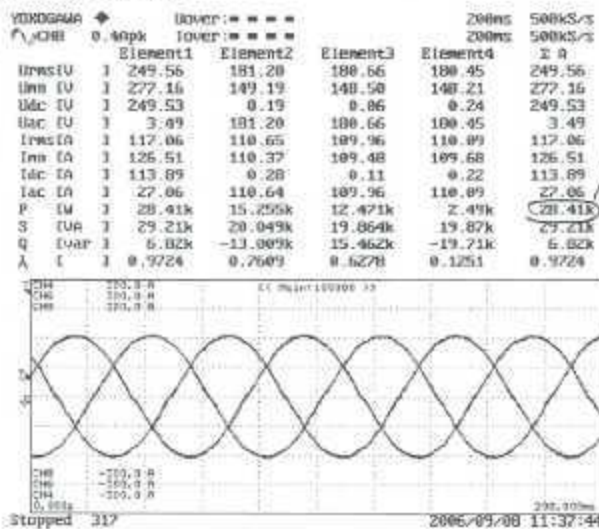
DC = 225 VDC



PWR in
 Z B
 162.94
 134.07
 0.19
 162.94
 99.70
 99.54
 0.07
 24.45
 23.12k
 23.83k
 5.55k
 0.9724

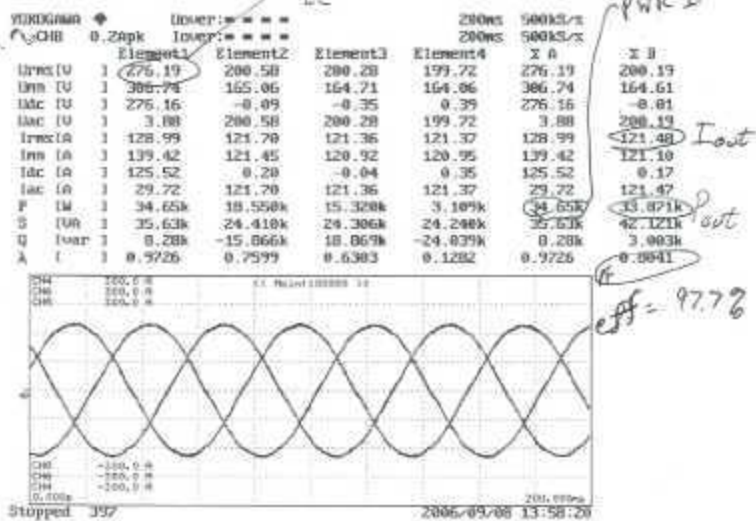
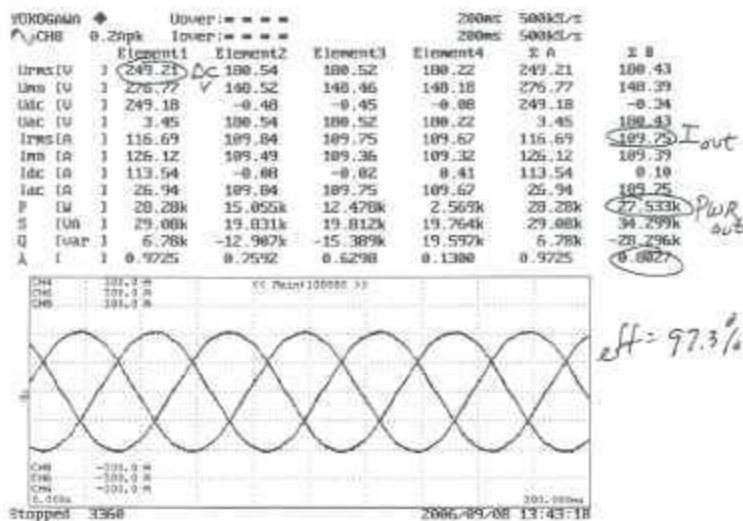
Pf
 eff = 97.6%

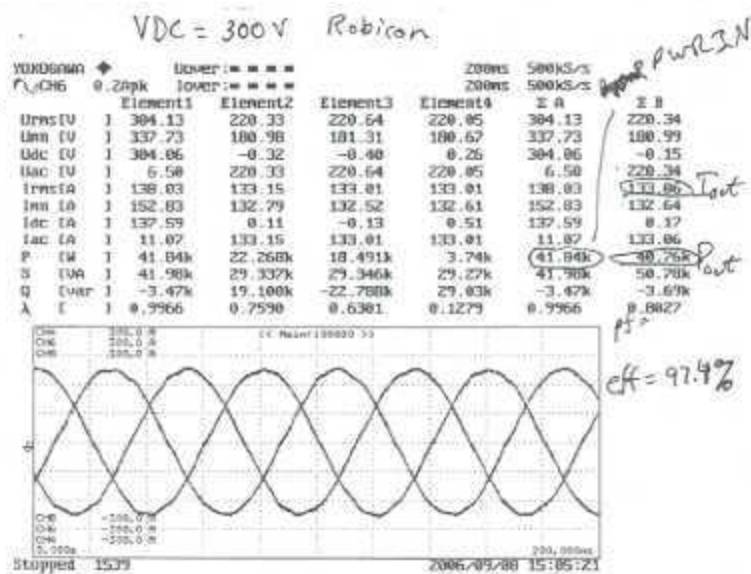
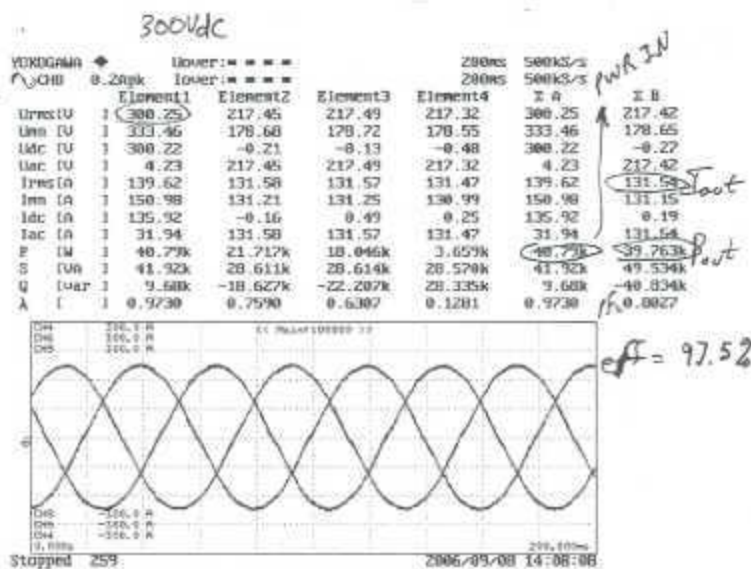
DC = 250 VDC



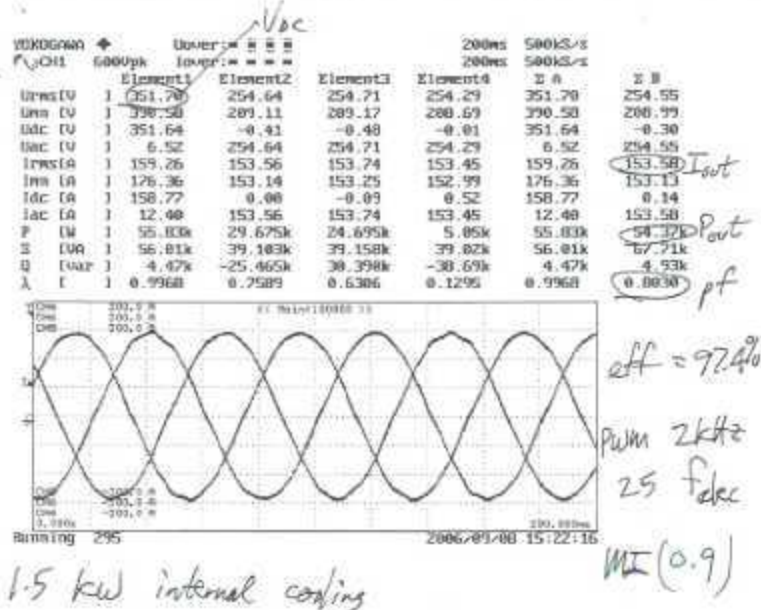
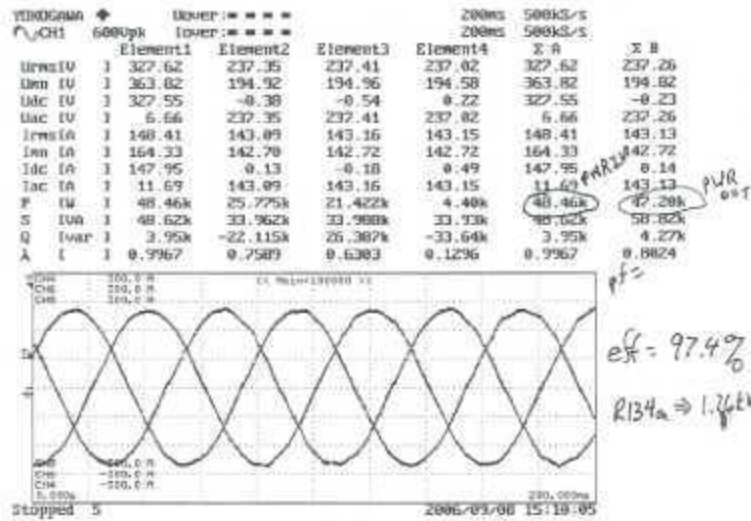
PWR in
 Z B
 180.77
 148.64
 0.16
 180.77
 110.23
 109.84
 0.20
 27.06
 28.41k
 29.21k
 6.82k
 0.9724

Pf
 eff = 97.6%

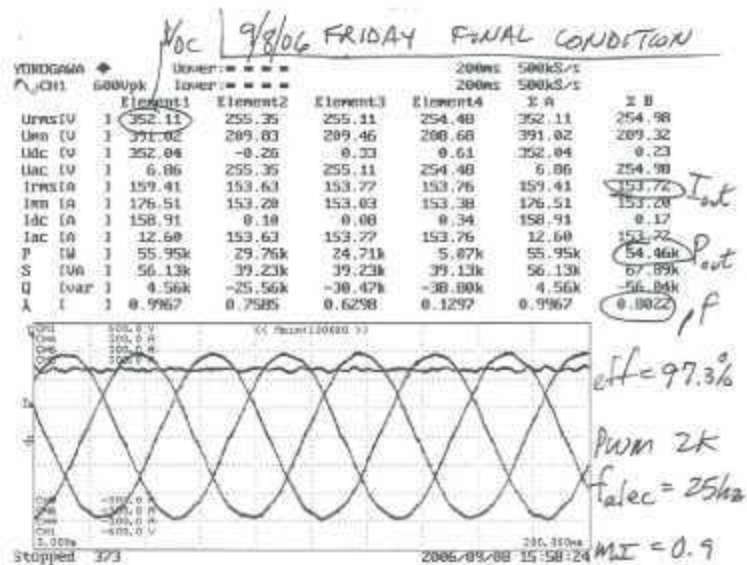




325Vdc Robicon

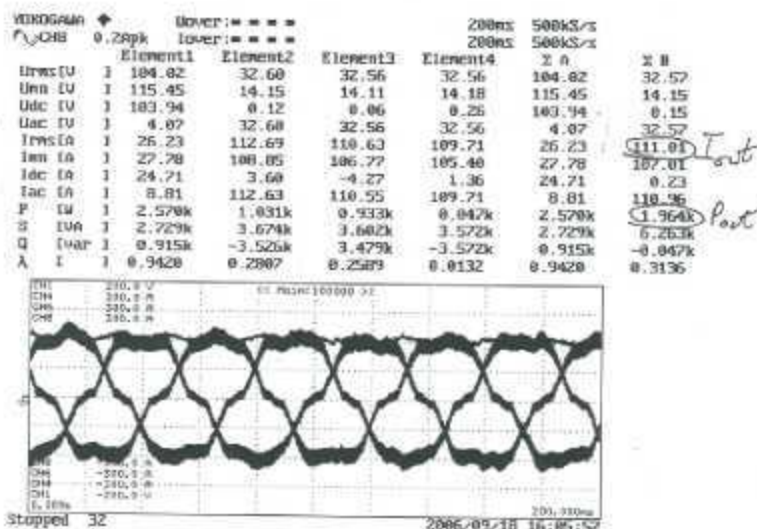
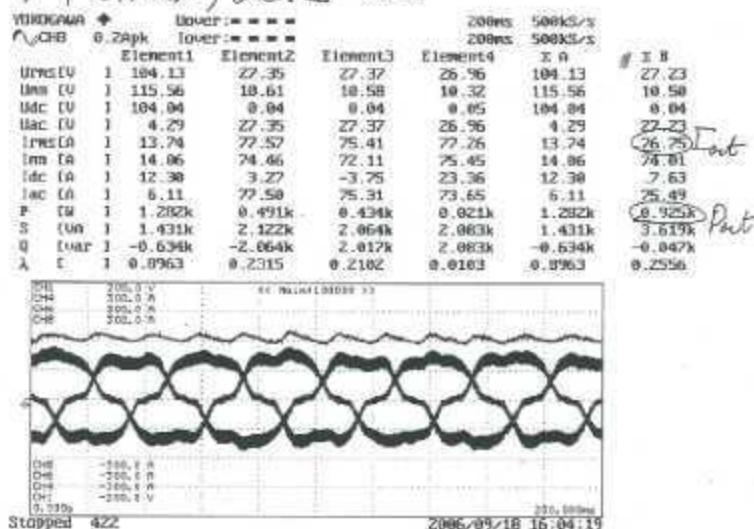


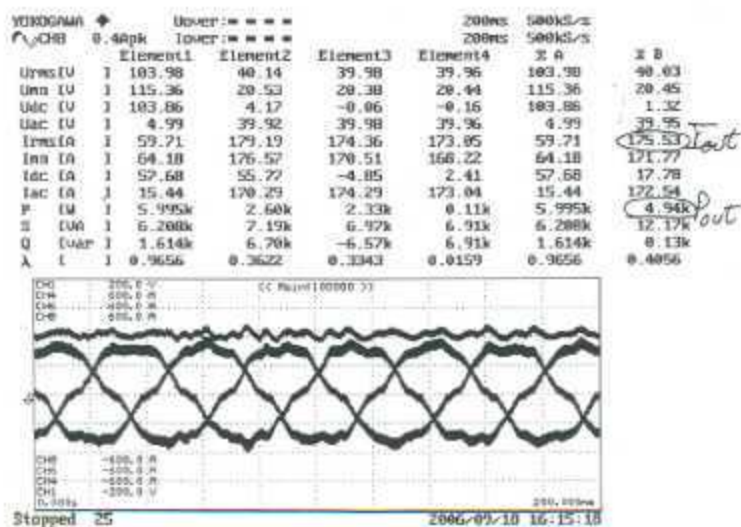
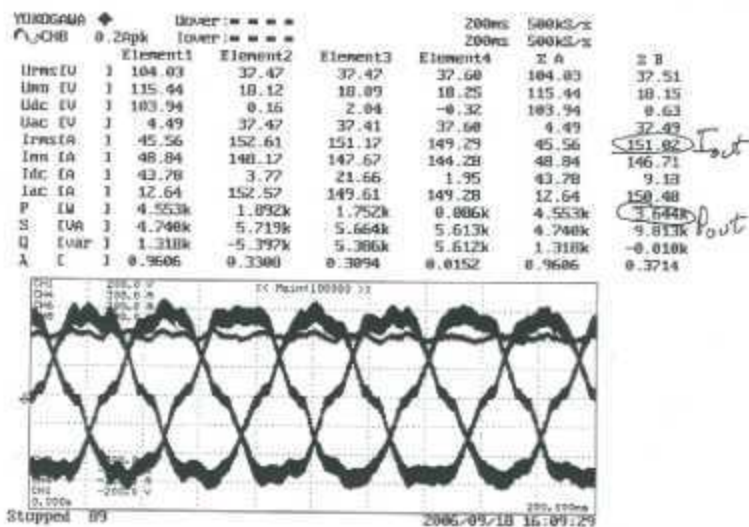
1.5 kw internal cooling

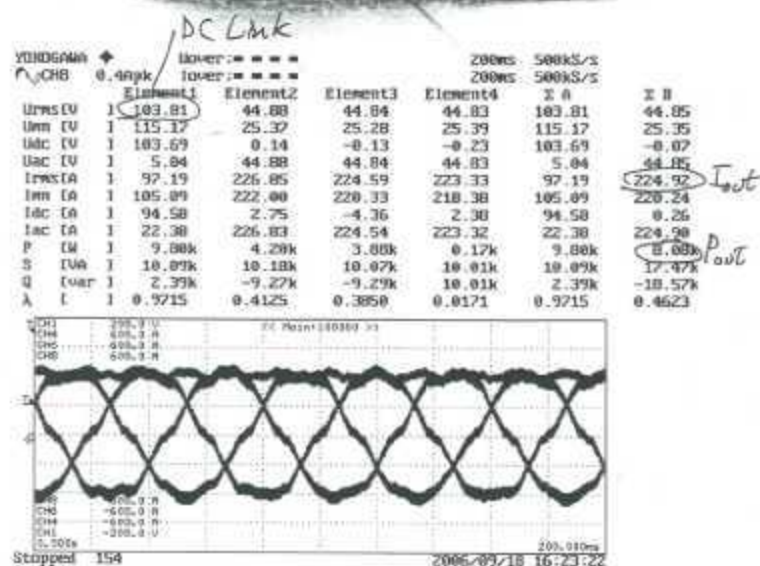
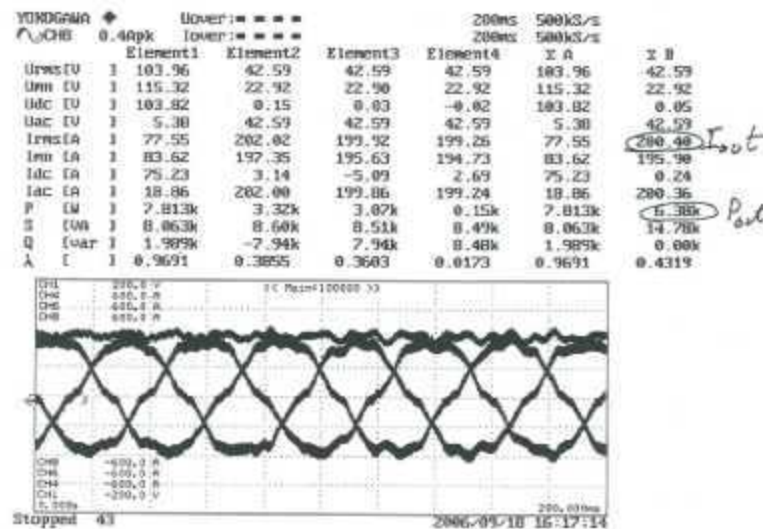


ROBICON PWR

Y-Y trfmr, delta load







2.2 Identifying the Barriers and Approaches to Achieving High-Temperature Coolants

Principal Investigator: John Hsu

Oak Ridge National Laboratory

National Transportation Research Center

2360 Cherahala Boulevard

Knoxville, TN 37932

Voice: 865-946-1325; Fax: 865-946-1262; E-mail: hsujs@ornl.gov

DOE Technology Development Manager: Susan A. Rogers

Voice: 202-586-8997; Fax: 202-586-1600; E-mail: Susan.Rogers@ee.doe.gov

ORNL Program Manager: Mitch Olszewski

Voice: 865-946-1350; Fax: 865-946-1262; E-mail: olszewskim@ornl.gov

Objectives

The goal of this project is to identify the barriers and approaches to achieving high-temperature coolant operation for the traction drive components of a hybrid vehicle and to identify the cost benefits/penalties when moving from a dedicated cooling loop at 65°C to the use of 105°C coolant from the engine radiator.

This assessment is important because automotive manufacturers are interested in utilizing the existing water/glycol engine cooling loop to cool hybrid electric vehicle (HEV) subassemblies to eliminate an additional coolant loop with its associated reliability, space, and cost requirements. In addition, the cooling of power electronic devices, traction motors, and generators is critical in meeting the FreedomCAR and Vehicle Technology (FCVT) goals for power rating, volume, weight, efficiency, reliability, and cost.

System tradeoffs will be taken into account in studying the use of high-temperature coolants. Corresponding radiator size, electronics packaging issues, motor housing size, pumps, hoses, power electronics, reliability of components, and meeting the 15-year FreedomCAR lifetime goal will be assessed against cost. The result of this effort will be a definitive analysis of the issues and tradeoffs involved with increasing the coolant temperature so as to ascertain the feasibility of moving ahead with 105°C coolant in hybrid vehicles.

Approach

The approach in this project is to review available literature and data to identify the barriers and approaches to achieving high-temperature coolants. A 50/50 water/glycol mixture will be used as a baseline coolant at 105°C in this investigation. Information will be collected from technical literature and industry.

Because heat flux is proportional to the temperature difference between the device's hot surface and the coolant, a device that can tolerate higher temperatures enables the device to be smaller while dissipating the same amount of heat. Trench insulated gate bipolar transistors (IGBTs) with higher-junction-temperature (175°C) silicon dies are gradually emerging into the market. This is an option that could provide more cooling margin in using 105°C coolant. Additionally, the permissible ripple current of various types of dc bus capacitors decreases rapidly as temperatures increase. New film dc-bus capacitors with higher-temperature capabilities are also emerging in the market. Necessary modifications to the existing cooling loop will be studied; cost, size, volume and weight tradeoffs assessed; and the results of the study reported.

The cooling of the power electronic devices, traction motors, and generators is critical in meeting the FreedomCAR goals for volume, weight, efficiency, reliability, and cost. Currently, the most commonly used coolant in automotive applications is a 50/50 water/glycol liquid mixture. The combustion engine is normally cooled by $<100^{\circ}\text{C}$ and reach 105°C or higher. Commercially available automotive-grade silicon electronic components have maximum junction temperature limits of 125°C . Therefore, the temperature difference between the junction and the 50/50 mix coolant of these devices is 20°C (i.e., $125^{\circ}\text{C} - 105^{\circ}\text{C}$). The less temperature difference that exists between the coolant and the dies' permissible junction temperature, the less margin there is to dissipate heat to the coolant environment.

This investigation focuses on identifying the barriers and approaches to achieving high-temperature coolants by analyzing the benefits and tradeoffs to using high-temperature coolants from the component, module, and system level perspectives.

Major Accomplishments

This study was performed by Oak Ridge National Laboratory (ORNL) to identify practical approaches, technical barriers, and cost impacts to achieving high-temperature coolant operation for certain traction drive subassemblies and components of HEVs. HEVs are unique in their need for the cooling of certain dedicated-traction drive subassemblies/components that include the electric motor(s), generator(s), inverter, dc converter (where applicable), and dc link capacitors. The new coolant system under study would abandon the dedicated 65°C coolant loop, such as used in the Prius, and instead rely on a 105°C engine cooling loop.

Because there is high interest by original equipment manufacturers (OEMs) in reducing manufacturing cost to enhance their competitive standing, the approach taken in this analysis was designed to be a positive, "can-do" approach that would be most successful in demonstrating the potential or opportunity of relying entirely on a high-temperature coolant system. Nevertheless, it proved to be clearly evident that a few formidable technical and cost barriers exist, and no effective approach for mitigating the barriers was evident in the near term.

The goals of the project were fully met by the identification of all significant barriers that pertain to the inverter, dc link capacitor, and motor. Approaches for resolving many of the barriers were also discussed; however, the full range of solutions will only come from additional R&D.

For operation at a significantly higher coolant temperature, component-level issues had to be addressed in this study. These issues generally pertained to the cost and reliability of existing or near-term components that would be suitable for use with the 105°C coolant. The assessed components include power electronic devices/modules such as diodes and IGBTs, inverter-grade high-temperature capacitors, permanent magnets (PMs), and motor-grade wire insulation. The need for potentially modifying/resizing subassemblies, such as inverters, motors, and heat exchangers, was also addressed in the study.

To obtain pertinent information to assist ORNL researchers to address the thermal issues at the component, module, subassembly, and system levels, preexisting laboratory test data obtained at varying temperatures were analyzed in conjunction with information obtained from technical literature searches and industry sources.

Technical Discussion

This project considers the potential temperature-related impacts on the performance of materials, components, and subsystems used in a Prius-like HEV traction system based on increasing the cooling loop temperature from 65°C to 105°C . The sections below focus on (1) the inverter power electronic devices, (2) inverter dc link capacitors, and (3) selected PM synchronous motor (PMSM) components that have the highest vulnerability to operation at elevated temperatures. The barriers that will be identified in each of these three main subsections will be those barriers that may prevent the components and subsystems from operating reliably during a 15-year service life when cooled by a 105°C cooling loop.

Note: The potential need for resizing the radiator was assessed, and it was determined that (1) the HEV heat load is small compared with that of the engine and (2) the air-to-coolant differential

temperature would be much higher, improving heat dissipation. Therefore, the need for a size change is considered minor or nonexistent.

Inverter/Converter Power Electronics Circuitry

This section considers what barriers may exist to operating the inverter and converter packages at 105°C. The analysis will consider inverter bus voltages of up to 500 Vdc for meeting peak power operation. Similarly, the Prius uses a 500-V boost converter, and the short-duration peak current in each leg of the inverter is ~200 A_{RMS}.

Conventional silicon-based materials and power device packaging designs are clearly challenging barriers to the use of a high-temperature coolant because junction temperatures will need to increase in high-temperature-coolant-based inverters to ~150°C. For this reason, currently marketed but not fully life-tested devices will be considered in this analysis: silicon-based trench IGBTs and high-temperature diodes, both with junction temperature ratings of up to 175°C. These IGBTs and diodes are presently available from several manufacturers.

Although device specifications list "175°C" maximum junction temperatures, the technology for these trench IGBTs and diodes is not mature; consequently, many design details must be considered that would normally have less importance. These include the determination of ratings for the actual parallel-device module packaging, observing current-dependent thermal deratings, observing temperature ratings for switching vs conductance, and the need to consider exactly how the module will be cooled in the final design.

On a positive note, Semikron's recent efforts at developing a 133-kW high-temperature inverter system show the high potential of using even presently available power electronic devices. Their analysis showed¹ that the 40°C coolant rise did not require an increase in inverter size or in the number of power electronic devices. This was based on (1) using new high-temperature devices, (2) using devices with lower losses, (3) increasing the power density, and (4) improving the heat sink. Only a modest cost increase was projected for the power electronics.

This assessment of high-temperature power electronics did not identify any serious barriers, except for the use of conventional silicon-based power electronics. Instead, a listing was developed of what might best be characterized as weak barriers for the cooling of the inverter and converter subsystems at 105°C. This is based on individual assessments of the thermal performance of trench IGBTs and the potential for thermal fatigue and wire bonding failures in the power electronics device packaging.

The following describes both *potential* barriers for the inverter/converter and certain design considerations that merit mentioning:

1. As expected, conventional silicon-based materials and power device packaging cannot support the use of a high-temperature coolant because junction temperatures will need to increase to ~150°C.
2. Recent literature² indicates that new 600-V IGBTs, using a trench metal oxide semiconductor top cell with ultra-thin 70-μm wafer technology, may be qualified for 175°C junction temperature, but the maximum operating temperature under switching conditions is reduced to 150°C. Because 150°C is much better than 125°C and most likely adequate based on development efforts, the thermal derating issue is a design consideration. More recently and subsequent to this study, Infineon Technologies announced 200°C junction temperature trench IGBTs.
3. There appears to be a significant potential for a solder-related fatigue issue that would limit the lifetime of IGBTs below 15 years if the use of a high-temperature coolant is implemented. This must be further investigated so that appropriate high-temperature solders, sintering, or other known technologies are employed.
4. The cooling requirements of the inverter driver board must be thoroughly evaluated and/or certain driver circuit components may have to be upgraded to maintain reliability/expected life at elevated temperatures.

Thermal Assessment of High-Temperature dc Link Capacitors

The capacitors used at the high-voltage dc-link-to-inverter interface are of interest because, within the bounds of current technology, it is very challenging to manufacture capacitors that provide adequate ripple current at the elevated temperatures. Even in a 65°C system, the present technology can barely meet this high-temperature application with acceptable volume, mass, cost, and reliability/lifetime. Highlighting this fact, the Prius capacitor module has a mass of 3.1 kg (almost 7 lb). In the case of the Prius, the modular polymer film capacitor takes up a significant portion of the volume inside the inverter/converter housing, as indicated in Figure 1.

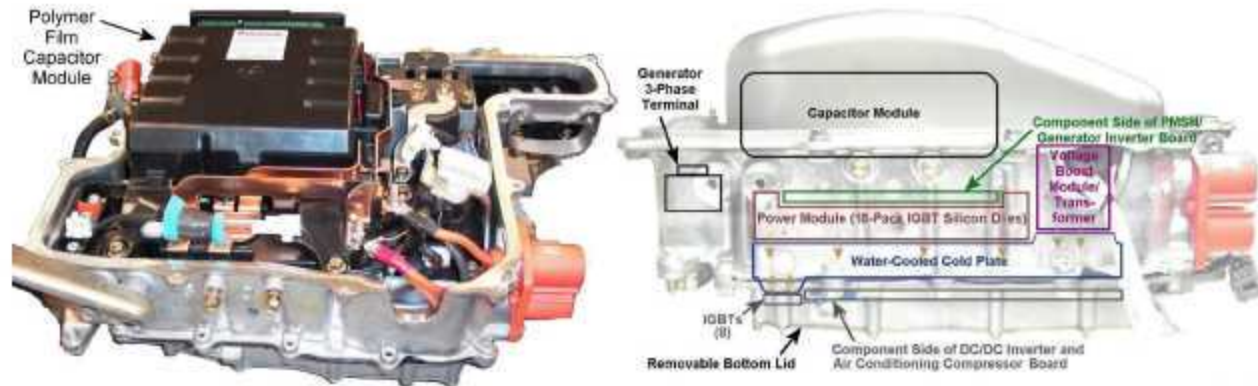


Figure 1. Modular capacitor position and size in the Prius inverter/converter casing.

The above concerns are certainly less of an issue for inverters placed in the much cooler passenger compartment as Honda does in its HEV line; however, that is outside the scope of this assessment, which considers only the use of a 105°C coolant for cooling of the HEV components and subsystems.

An engine compartment temperature of 140°C is considered applicable in the inverter design where a coolant-filled “cold plate” covers the base of a fully enclosed aluminum case in which the dc link capacitor is housed. Adopting a 105°C inverter coolant loop will increase the temperature of all the components in the casing, including the capacitor. There is also the potential for active capacitor cooling in some future HEV design.

Although many types of dielectrics exist, polymer film capacitors are generally produced with polypropylene, polyester, polycarbonate, or polystyrene. The temperature effects of these dielectrics result in changes in the capacitance, dissipation factor, and lifetime of film capacitors. High temperatures limit the available ripple current levels. Alterations in capacitance and dissipation factor play a large role in the amount of power dissipated and ultimately in the efficiency of the capacitor.

The amount of power dissipated across a capacitor is given as

$$P = V_{AC}^2 * 2\pi f * C * DF = \frac{I_{AC}^2}{2\pi f * C} * DF \quad (1)$$

The maximum heat removal capacity is

$$P = \frac{\Delta T}{R_{th}} \quad (2)$$

Solving these two equations for the current ripple yield

$$I_{AC} = \sqrt{\frac{(T_R - T_A) * 2\pi f * C}{R_{th} * DF}} \quad (3)$$

Assuming that a 500- μ F capacitor has a case thermal resistance, R_{th} , of 130W/°C and that the capacitor is operated at a 5-kHz inverter switching frequency at rated temperature, the plots in Figure 2 show the maximum available ripple current of the capacitor vs temperature for polymer film and ceramic capacitors.

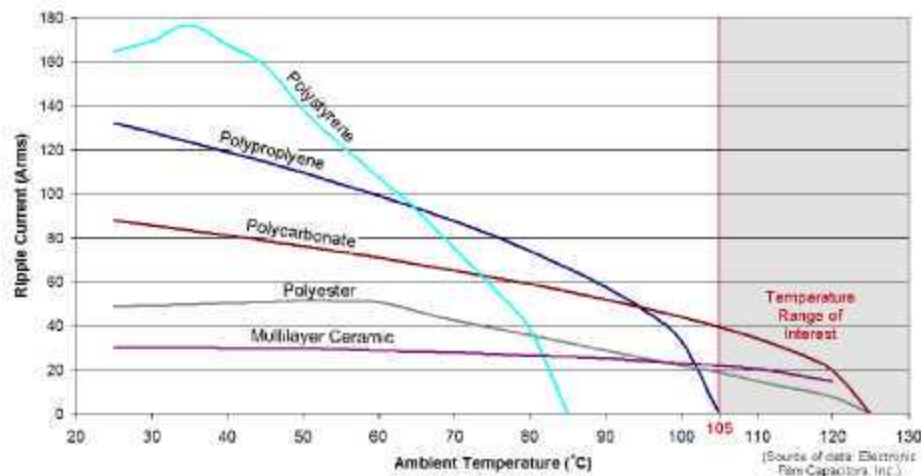


Figure 2. Ripple current vs ambient temperature for high-temperature capacitors.

Clearly, the adverse affect of temperature on ripple current is a serious issue. Even the polycarbonate, polyester, and ceramic capacitors do not appear to be of any potential use within the shaded range of interest. This leads to the question of what capacitors are being developed in laboratories or in the process of entering into production. Unfortunately, products in development are shrouded in secrecy, and details are considered to be proprietary. This has provided a serious obstacle to the assessment of high-temperature capacitors.

ORNL is able to report that a leading ceramic capacitor manufacturer produces a high-temperature capacitor for which the specifications are reportedly: 16 μ F per module, 400-V continuous, $I_{ripple} = 25A @ 125^{\circ}C$ maximum, and the cost is \$20/module. Based on the required ripple current in an inverter, ~7 modules would be needed in parallel at a total cost of \$140 in large-quantity purchases. However, the 400-V limit is problematic because a 600-V rating for an appropriate margin in HEV systems includes a 500-V boost converter.

Other, higher-cost 400-V capacitors were reported, but there were no reports of newly developed 600-V, high-temperature, inverter-grade capacitors being available other than prohibitively expensive Teflon capacitors. However, Semikron³ reports that in the process of their development of a high-temperature inverter, they reached the conclusion that commonly available, 600-V capacitors can be used if three are placed in parallel. Using this approach instead of utilizing a high-temperature capacitor increases the volume, mass, and cost by a factor of 3; this is considered a serious penalty.

New capacitors with improved specifications and significantly lower cost are expected in 1 to 2 years—or in 10 years—depending on which technical or industry source is consulted.

The design barriers for dc-link capacitors include the following:

1. Temperature increases in the dc-link capacitor application have a strong and detrimental effect on the ripple current specification for many types of polymer capacitors.

2. High-temperature (125°C or higher) capacitors with adequate ripple current and a 600-V continuous rating can be found today by taking existing capacitors and using three in parallel. This approach triples cost and size, which is a serious penalty and a major barrier. There is a need for low-cost, high-temperature capacitors, and it is important that these be brought to the market soon.
3. The reliability and lifetime of any newly released, high-temperature capacitors must be well established through testing before they are introduced into vehicles.
4. Ceramic capacitors have superior high-temperature performance compared with polymer film capacitors; however, presently the cost is high, and an unacceptable energetic and flammable failure mode exists.
5. Teflon capacitors have excellent high-temperature performance, but cost is clearly prohibitive.

Thermal Characterization of Magnets

Neodymium-iron-boron (NdFeB) magnets are the most powerful of all the magnets commonly used in industry and are made of advanced rare-earth materials. They provide high performance and resilience against demagnetization. However, these magnets are extremely sensitive to temperature and susceptible to oxidation if not properly coated.^{4,5}

NdFeB magnets are frequently selected for HEV applications, including the Prius, because of their high magnetic strength and acceptable cost. Unique Mobility (UQM), a major manufacturer and researcher of PM motors, also uses NdFeB PMs.⁶⁻¹⁰

An increase in temperature of NdFeB PMs reduces the magnetic strength linearly up to 100°C as follows:¹¹

$$B_r = B_{rA} + s(T - T_A) \quad .$$

where B_{rA} is the residual flux density at normal ambient temperature T_A , and s is the slope of the B_r temperature characteristic (for NdFeB this tends to be -0.1% per °C). Above 100°C, the magnetic field strength begins to fall more rapidly as indicated in Table 1.^{7,12}

Table 1. Characteristic of Delco Remy MQ2^a NdFeB magnets

Residual induction	0.8T
Intrinsic coercive force	1.43 ma/m
Temperature coefficient of remanence to 100°C	-0.10%
Temperature coefficient of remanence to 125°C	-0.11%
Temperature coefficient of remanence to 175°C	-0.15%

^aMQ2—Delco Remy Magnequench Division

For an NdFeB PM with the above characteristics, Figure 3 shows the reduced strength of the magnet in per unit form vs temperature. It is estimated that there will be a 20–30% reduction in flux strength for motor operation at the higher coolant temperature as PM temperature approaches 200°C. This temperature-induced effect represents a very significant barrier. This reduction in magnetic field strength due to temperature is reversible because the magnetization will return to the original value once the temperature is decreased.

If the operating temperature of the motor exceeds a certain critical temperature, irreversible demagnetization of the magnet will result.⁹ This critical temperature is ~150°C for many types of NdFeB magnets, but 220°C for the particular type of NdFeB PM selected for the Prius.¹³ However, the reversible, temperature-induced reduction in field strength is more significant because the motor performance (i.e., shaft power) will be significantly reduced at temperatures that will be frequently reached during vehicle operation (assuming a 105°C coolant).

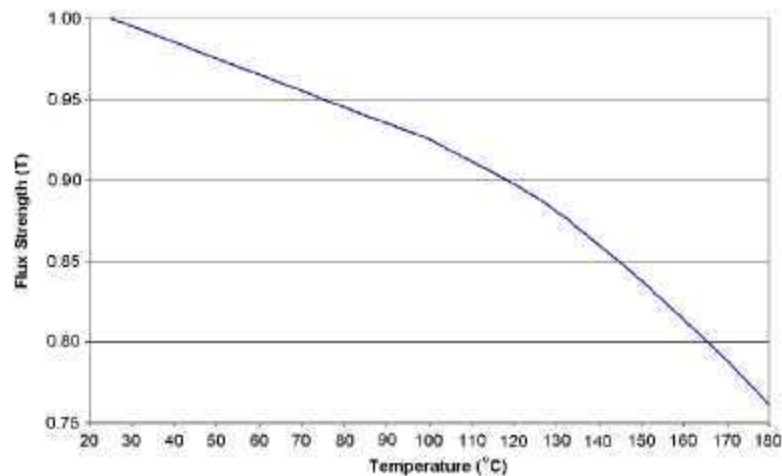


Figure 3. Flux strength of a selected NdFeB magnet vs temperature.

Stator Winding Insulation

Magnet wire used in many applications today is inverter spike resistant (ISR). This Class H wire has excellent resistance to damage from high-voltage spikes that commonly result from rapidly changing pulse-width modulated (PWM) currents in inductive circuits.

Motor wire insulation is a well-developed technology that is not expected to change significantly in the next several years. That is not to imply that major strides have not been made in the last 25 years. Today's motors operate at significantly higher temperatures while meeting 20,000-h lives or greater. The most common types of insulation, in order of increasing quality, are Class A, Class B, Class F, and Class H. These insulations are rated for maximum temperature in 25°C increments as indicated in Figure 4. Less common insulations are available such as Class S (240°C) and Class C (over 240°C); however, the use of these would create a cost increase, which may be avoidable.

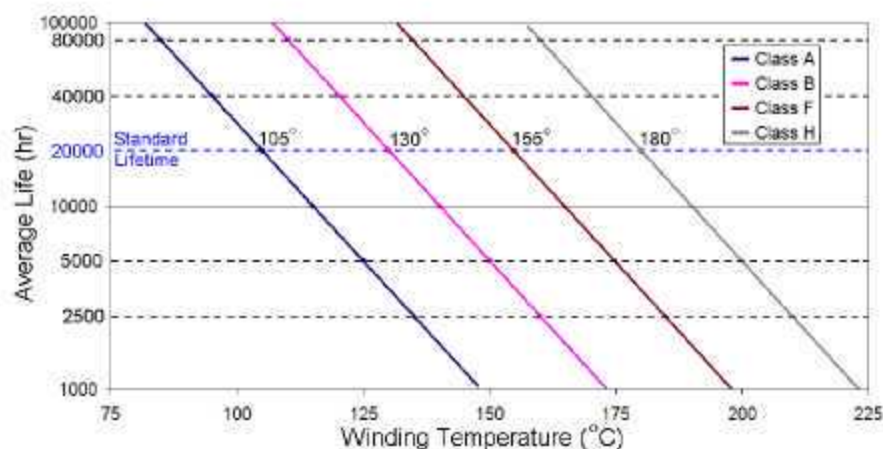


Figure 4. Average motor insulation life vs winding temperature for four insulation types.

For HEV applications, it is essential to fully understand the duty cycle and rate of accrued time on the motor when estimating motor insulation life. For instance, the Prius is considered to be a "strong hybrid" since the motor is relied upon 100% for accelerations from a full stop. It is also used to assist the engine for accelerations and high torque demands such as passing vehicles at highway speeds and for driving up a grade. Table 2 shows an estimate of the required number of hours that may be expected from the motor during a 15-year period. The example numbers reflect heavy usage of the vehicle with an accrued

Table 2. Estimate of life-shortening hours accrued during 15 years of city driving

Daily vehicle operation (h/day)	Days in a year	Number of years	Fraction of vehicle-operation time when the stator insulation is at a life-shortening temperature	Accrued life-shortening hours in 15 years	Accrued miles in the 15 years @ 35 mph
1.25	365	15	0.75	5,100	240,000

240,000 miles. If one assumes the fraction of time when the motor temperature is hot (near or above 180°C) to be 0.75, then the number of life-shortening hours on the insulation is 5,100 h. This high fraction would reflect stop-and-go city driving rather than highway usage where the motor may be seldom used. The 5,100 h is far below the 20,000-h standard for motor insulation life. Referring to Figure 4, this would necessitate the use of Class H insulation at 200°C instead of the 180°C standard.

PMSM Barriers

Before identifying design barriers, the following observations are made concerning an unmodified PMSM that is cooled with a 105°C cooling loop:

1. Heat will not be removed from the casing as effectively as in the case of a 65°C coolant design.
2. Because of (1), the oil temperature, stator temperature, and rotor temperatures will be higher.
3. There will be significant time periods when the 105°C coolant will be *heating* the motor casing.
4. There will also be times when the 105°C coolant will provide *cooling* due to (a) the temperature floor of the PMSM being raised and (b) motor operation in engine compartment temperatures of up to 140°C.

Figure 5 shows the general design approach for a PMSM cooled by 105°C coolant. Because the temperature floor is raised substantially, a design response is needed to lower and stiffen the temperature ceiling by making the heat exchanger, and possibly other components, more effective in responding to thermal excursions that occur during vehicle operation.

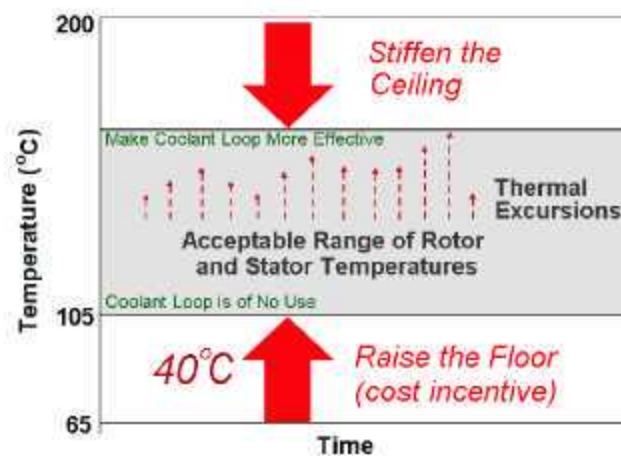


Figure 5. General PMSM design approach applicable for high-temperature cooling.

The following are the PMSM barriers:

1. The primary barrier for the PMSM is that the flux strength of the PMs will decrease 20–30% whenever the PMs are at elevated temperatures consistent with operation based on a high-temperature coolant. This will reduce PMSM/vehicle performance and/or require higher, compensating motor current. Higher motor current will compound the thermal control problem.

2. As determined in the electrical assessment, higher temperatures result in a very substantial 29% increase in losses due to temperature-induced changes in back-emf and stator winding copper losses. This will result in unacceptable temperatures for the stator insulation and PMs unless the cooling system is significantly improved and/or the size of the motor is increased to facilitate heat transfer. Detailed thermal studies will be required to produce a high-temperature motor design.
3. During those times when heat flows from the motor to the coolant, the temperature gradient between the coolant and casing will be low, reducing the effectiveness of the heat exchanger.
4. Because of increased stator winding operating temperatures, Class H insulation will be operated beyond its conventional limits. This may be acceptable based on total hours of operation at high temperatures, but some level of detailed verification/study may be needed.
5. Higher-temperature stator insulation (Class C) can be used but at higher cost.
6. One design approach to better controlling PM temperature entails the design of a more effective water/glycol-coolant-to-oil heat exchanger. Increasing the size of the heat exchanger and locating it at the bottom of the PMSM are desirable approaches but will increase volume, mass, and cost. Encircling the stator with a cooling jacket is another option. These approaches are considered to be "a beginning" that must be followed by other, yet-undefined improvements.
7. The acceptability of raising coolant temperature can only be fully verified by selecting detailed candidate designs and performing thermal analysis and performance modeling. This will involve developmental costs.

System-Level Assessment

In considering numerous design changes that must be or could be pursued to eliminate a dedicated, low-temperature cooling loop, it is important to weigh the cost requirements of each proposed design against the cost savings of eliminating the dedicated cooling loop.

The Prius uses a \$480 radiator (2.05 g and 4.19 L) that is partitioned to provide a low-temperature, 1.14-L, dedicated coolant loop radiator. This loop also uses a \$142 12-Vdc electric pump (344 g) and miscellaneous hoses. The elimination of this system may entail simply eliminating the partitioning in the radiator, eliminating the pump, and reconfiguring a few hoses. Table 3 shows the predicted cost savings. Using an unpartitioned radiator would save ~\$80 and, with the elimination of the pump and two hoses, the total savings would be ~\$250, based on the retail prices of new components. The wholesale cost would be ~\$187.50.

Table 3. Itemized listing of costs of eliminated components

Eliminated components or features	Cost savings (\$)	Source used as basis of estimation
Electric pump	142	Toyota of Knoxville
Partitioning of the radiator	80	—
Hoses (2) associated with eliminated components (pump and partitioned radiator)	28	toyotapartscheap.com
Total retail	250	
Minus 25% retail store profit	-62.5	
Wholesale	187.50	

Conclusion

This study consisted of a technical/engineering evaluation and literature search designed to investigate the feasibility of raising the coolant temperature of a Prius-like HEV system from 65°C to 105°C. The study focused on subsystems and components that were deemed most vulnerable to operation at higher temperatures. These included the inverter power electronics, the dc link capacitor for the inverter, and stator insulation and PMs in the PMSM.

There is high interest among the OEMs in reducing manufacturing cost to enhance their competitive standing. One candidate means of accomplishing this is eliminating the HEV-dedicated coolant loop. In

light of this high interest, a positive, “can-do” approach was used in this study to the fullest extent possible to fairly assess the potential or opportunity of relying entirely on a high-temperature coolant system. Nevertheless, it proved to be clearly evident that a few formidable technical and cost barriers exist, and no effective approach for mitigating the barriers was identifiable in the near term.

The major barriers encountered in this study are

1. **Inverter dc link**—High-temperature (125°C or higher) capacitors with adequate ripple current and a 600-V continuous rating can be found today only by taking existing capacitors and using three in parallel or by using prohibitively expensive Teflon film capacitors. The first approach triples cost and size, which is a serious penalty and a major barrier. There is a need for low-cost, high-temperature capacitors, and it is important that these be brought to the market soon.
2. **PMSM1**—The primary barrier for the PMSM is that the flux strength of the PMs will decrease by 20–30% whenever the PMs are at elevated temperatures consistent with operation based on a high-temperature coolant. This will reduce PMSM/vehicle performance and/or require higher, compensating motor current. Higher motor current will compound the thermal control problem.
3. **PMSM2**—Higher temperatures result in a very substantial 29% increase in losses due to temperature-induced changes in back-emf and stator winding copper losses. This will result in unacceptable temperatures for the stator insulation and PMs unless the cooling system is significantly improved and/or the size of the motor is increased to facilitate heat transfer. Detailed thermal studies will be required to produce a high-temperature motor design.

Although there were no “major barriers” for the inverter/converter power electronics, one issue remains. New 600-V IGBTs, using a trench MOS top cell with ultra-thin 70- μ m wafer technology, may be qualified for 175°C junction temperature, but the maximum operating temperature under switching conditions is reduced to 150°C. Because 150°C is much better than 125°C and most likely adequate, the thermal derating issue is mainly a design consideration. Furthermore, very recently, Infineon Technologies released new devices that can reportedly operate with a 200°C junction temperature without the need for current derating.

Table 4 lists the potential cost increases that would result from resolving the barriers for the major critical subsystems/components identified in this assessment. Other costs may be incurred for such things as inverter driver circuit improvements, the buck/boost converter high-temperature capacitor, improved oil spray design for stator cooling, etc. However, the costs of the items listed in Table 4 already exceed the \$188 cost savings of eliminating the dedicated coolant loop by a substantial amount. Even the summation of the *minimum* estimated costs exceeds the cost savings.

Table 4. Estimations of additional costs to resolve barriers in components/subsystems

Subsystem or component	Constraints specified by the assessment	Estimates of additional cost
Inverter power electronics	The <i>future</i> cost increase for high-temperature power electronic modules when they become available for full rated switching current without thermal derating.	\$25–125/inverter \$4–21/converter
dc link capacitors	The cost increase of using three times the capacitance prior to new products becoming available with adequate ripple current and a 600-Vdc continuous rating.	\$210–250 ^a
PMSM (protecting PM and stator insulation)	The cost increase for additional casting in the heat exchanger and other as-yet unknown improvements necessary for control of PM temperatures and dissipating higher losses.	\$30–200
Total		\$269–596

^aThis assumes the cost of a low-temperature capacitor, similar to that used in the Prius, is ~\$100

Table 5 is a qualitative comparison matrix of various parameters of interest for each of the critical components and subsystems. The parameters of interest include availability of components, mass, volume, performance, reliability, lifetime, and cost. For temperatures lower and higher than the 65°C base case, the potential thermal effect is designated as either being positive (+) or negative (-), where applicable. Major barriers are designated with double negatives. As an example using stator insulation, adopting a 105°C coolant would have negative impacts on mass, volume, and cost if it were necessary to use a different type of insulation, such as Class C. This assessment considered remaining with Class H to be potentially feasible, depending on whether heat transfer can be significantly improved, in which case those negatives would not apply. This illustrates how some designations in the table are only *potentially* applicable.

Table 5. Multiparameter, temperature-based qualitative comparison

Parameter	50°C	65°C	105°C
<i>Elimination of HFV-dedicated cooling system</i>			
Cost		Base case	+
<i>Inverter power electronics</i>			
Availability of components		Base case	
Mass		Base case	
Volume		Base case	
Vehicle performance		Base case	
Reliability	+	Base case	-
Attaining a 15-year life		Base case	-
Cost		Base case	
<i>dc link capacitor</i>			
Availability of components		Base case	--
Mass		Base case	-
Volume		Base case	-
Vehicle performance		Base case	
Reliability	+	Base case	-
Attaining a 15-year life	+	Base case	-
Cost	+	Base case	--
<i>PMSM PMs</i>			
Availability of components	+	Base case	-
Mass		Base case	
Volume		Base case	
Vehicle performance	+	Base case	--
Reliability	+	Base case	-
Attaining a 15-year life	+	Base case	-
Lack of a new PMSM design ^a		Base case	--
Cost	+	Base case	-
<i>PMSM stator insulation</i>			
Availability of components		Base case	
Mass		Base case	-
Volume		Base case	-
Vehicle performance		Base case	-
Reliability		Base case	
Attaining a 15-year life		Base case	-
Lack of a new PMSM design ^a		Base case	--
Cost		Base case	-

^aA new design is needed for significantly improved heat dissipation

Future Direction

The high-temperature barrier study is complete as of the end of FY 2006. The study served to highlight a number of areas needing attention, and there are potential areas in which the FCVT program may see a new (or renewed) need to support development. These areas include the development of low-cost, high-temperature components and packaging concepts that meet all the required specifications. The components include IGBTs, diodes, inverter-grade capacitors, and PMs. Innovations in cooling systems, such as oil-spray cooling of the rotor/stator, are also needed for the development of a viable high-temperature PMSM.

Publications

R. H. Staunton, J. S. Hsu, and M. R. Starke, *Barriers to the Application of High-Temperature Coolants in Hybrid Electric Vehicles*, ORNL/TM-2006-514, Oak Ridge National Laboratory, 2006.

References

1. Communication from J. Mookken, Semikron, to R. H. Staunton (ORNL) via email, *Inverters for High Temperature*, and phone on August 7, 2006.
2. P. Kanschä, H. Ruthing, et al., "600V-IGBT: A Detailed Analysis of Outstanding Static and Dynamic Properties," presentation at PCIM Europe Conference, 2004.
3. John Mookken, Semikron, "High-Temperature (105°C) Inverter Development," presentation at DOE FreedomCAR Vehicle Technology Program Annual Review, Oak Ridge, Tennessee, August 2006.
4. R. H. Staunton, S. C. Nelson, P. J. Otaduy et al., *PM Motor Parametric Design Analyses for a Hybrid Electric Vehicle Traction Drive Application*, ORNL/TM-2004/217, Oak Ridge National Laboratory, Oak Ridge, Tennessee, September 2004.
5. Anil Naji, "High Performance Permanent Magnets 7," Catalog, Magnet Sales and Manufacturing Inc, 1995.
6. Arnold Technologies, "TechNotes: How to Select the Appropriate Permanent Magnet Material," December 2002.
7. J. G. West, "Propulsion Systems for Hybrid Electric Vehicles," *Electrical Machine Design for All-Electric and Hybrid-Electric Vehicles (Ref. No. 1999/196)*, IEE Colloquium, pp.1/1-1/9, 1999.
8. *Annual Report 2005*, UQM Technologies, Frederick, Colorado, 2005.
9. T. Sebastian "Temperature Effects on Torque Production and Efficiency of PM Motors Using NdFeB Magnets," *IEEE Transactions on Industrial Applications*, 31(2), April 1995.
10. F. Crescimbeni, A. D. Napoli, L. Solero, and F. Caricchi, "Compact Permanent-Magnet Generator for Hybrid Vehicle Applications," *IEEE Transactions on Industrial Applications*, 41(5), October 2005.
11. Akira Kawahashi, "A New Generation Hybrid Electric Vehicle and Its Supporting Power Semiconductor Devices," Toyota Motor Corporation, *Proceedings of 2004 International Symposium on Power Semiconductor Devices and ICs*, 2004.
12. J. F Gieras and M. Wing, *Permanent Magnet Motor Technology*, Marcel Dekker, 2002.
13. Verbal communication from Dr. Hitoshi Yamamoto, Neomax America, Inc., to J. S. Hsu, ORNL, during the 2005 Permanent Magnet Conference, 2005.

3. Electric Machinery Research and Technology Development

3.1 Uncluttered CVT Machine

Principal Investigator: John Hsu

Oak Ridge National Laboratory

National Transportation Research Center

2360 Cherahala Boulevard

Knoxville, TN 37932

Voice: 865-946-1325; Fax: 865-946-1210; E-mail: hsujs@ornl.gov

DOE Technology Development Manager: Susan A. Rogers

Voice: 202-586-8997; Fax: 202-586-1600; E-mail: Susan.Rogers@ee.doe.gov

ORNL Program Manager: Mitch Olszewski

Voice: 865-946-1350; Fax: 865-946-1262; E-mail: olszewskm@ornl.gov

Objectives

Develop a new machine that combines motor and generator into one unit with a continuously variable transmission (CVT).

- The design enables additional torque coupling between the two rotors for producing more wheel torque.
- The combination of a motor and generator into one machine with only a single permanent magnet rotor has the potential to be simpler and less costly than conventional CVTs.
- The output power of the uncluttered rotor can be doubled.

Approach

- The uncluttered rotor CVT machine project has an ultimate multi-year goal of producing an electric machine with double the power density of current-technology machines at a given rotor speed.
- The principle of the uncluttered rotor was proved in FY 2001 through modification and testing of an induction machine with a specially wound rotor. The FY 2006 effort completed the second step of the proof-of-concept machine and eliminated the windings in the uncluttered rotor.
- The specific FY 2006 goal was to design and build a proof-of-concept uncluttered rotor without windings and a half stator that couples with the uncluttered rotor.

Major Accomplishments

- The design of the proof-of-concept uncluttered rotor without windings and a half stator wound core to couple to the uncluttered rotor was completed. The uncluttered rotor and its half stator were fabricated, and the uncluttered rotor teeth were machined out of solid steel instead of laminations in order to lower costs for the proof-of-concept prototype. The uncluttered rotor concept for the brushless rotating stator (or armature) was proved through tests conducted on the prototype.

Technical Discussion

The physics of the uncluttered CVT can be understood through an examination of a conventional motor. Figure 1 shows that for any conventional motor, the stator sees a counter-torque to the shaft torque. The magnitude of the stator torque is the same as that of the shaft torque. Anchor bolts are used to hold the stator down in practically all motor installations.

Figure 2 shows that the stator counter-torque can be used to double the shaft torque at a given rotor speed by removing the mounting bolts, allowing the stator to rotate on the added bearings, and transferring the stator torque to the shaft through gears, such as a set of planetary gears. Figure 2 also

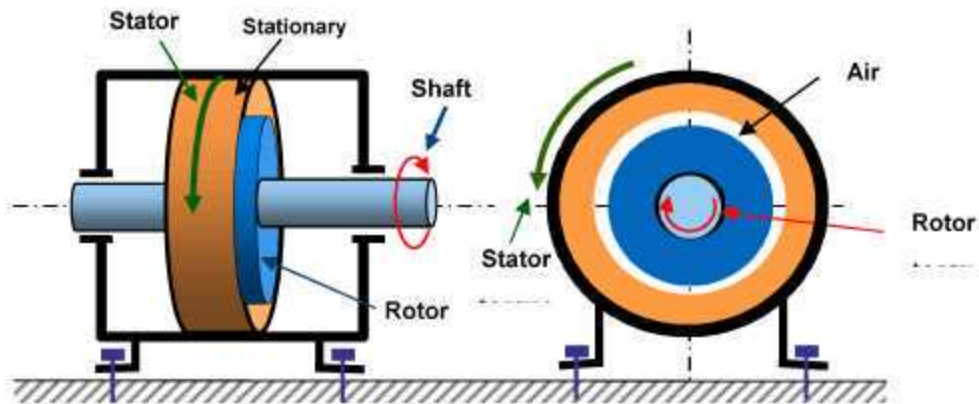


Figure 1. Shaft torque and stator torque of a motor.

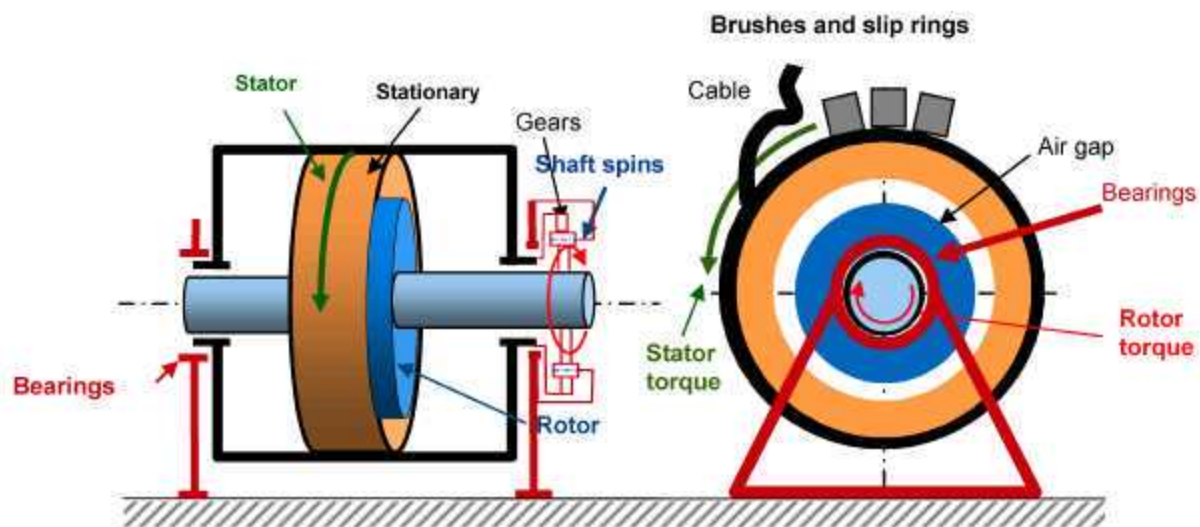


Figure 2. Doubling shaft torque at a given shaft speed.

shows that to harvest the torque of a rotating stator (or armature), brushes and slip rings would normally be required. Oak Ridge National Laboratory's (ORNL's) uncluttered CVT is a novel approach that doubles the torque at a given rotor speed and eliminates the brushes and slip rings. The absence of brushes and slip rings in the ORNL technology is emphasized in Figure 3.

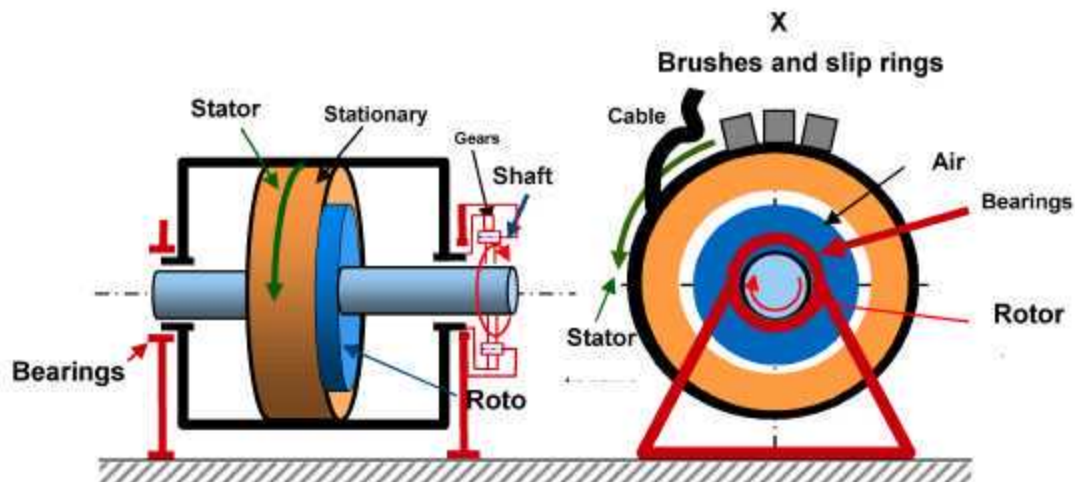


Figure 3. ORNL technology does not have brushes and slip rings.

Uncluttered Rotor

The ORNL technology for eliminating the brushes and slip rings is derived from the uncluttered rotor concept, which is explained through a conventional wound-stator core. When 3-phase currents are fed to the windings of a conventional wound-stator core, a rotating magnetic flux is produced, which goes through the air gap and reaches the rotor to return the rotating flux. The rotating speed of this rotating flux observed from the stator, regardless of whether the stator is stationary or rotating, is determined only by the frequency and number of poles of the winding. Therefore, the function of an uncluttered rotor is to produce a rotating flux. The rotating speed of this flux observed from the uncluttered rotor is determined only by the excitation frequency and by the number of poles of the uncluttered rotor. There are no brushes and slip rings for the excitation of the uncluttered rotor. The excitation wound core for the uncluttered rotor is stationary. The uncluttered rotor has no conductor; hence, no brushes and slip rings are required. The term “uncluttered” arises from the fact that when the current frequency is fed to the stationary excitation coil, the rotor speed does not change the corresponding rotating flux speed viewed from the rotor. The rotor speed influence is totally isolated to prevent a cluttered outcome.

Many variations of the uncluttered rotor and its excitation can be achieved. For example, Figure 4 shows an 18-pole, axial-gap, 2-phase uncluttered rotor that has two sides. The side facing the uncluttered rotor excitation core has rings. The flux has a tangential coupling between the excitation core and the rings. Because the rotation of the rings does not cause a change in the flux entering or leaving the rings, no torque is produced for this tangential magnetic coupling.

The opposite side of the sample axial-gap rotor has conventional teeth. When this side is coupled to a permanent magnet rotor with poles or to a conventional stator with teeth, the radial coupling produces torque. Figure 5 shows the ring side of the actual prototype uncluttered rotor. The opposite side of the rotor with teeth is shown in Figure 6.

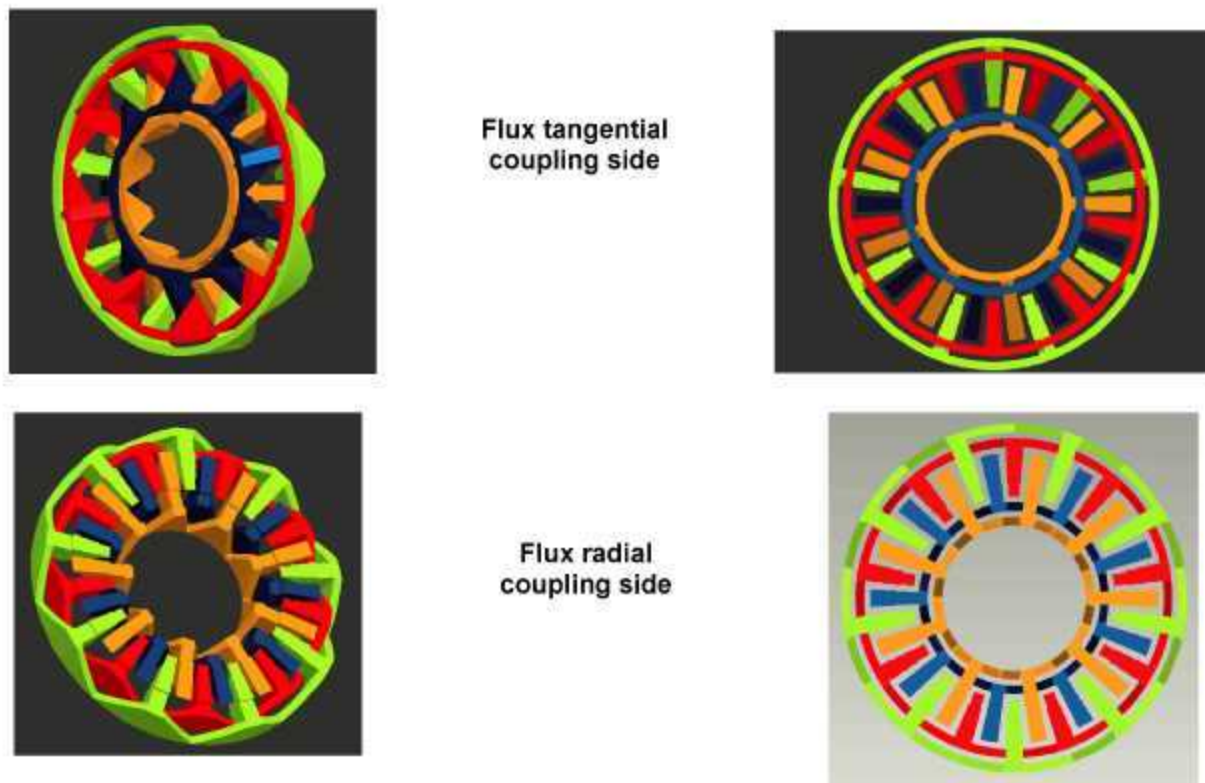


Figure 4. Example of an 18-pole, axial-gap, 2-phase uncluttered rotor.



Figure 5. One side of the proof-of-concept uncluttered rotor with rings.



Figure 6. The opposite side of the proof-of-concept uncluttered rotor with teeth.

The excitation core for the uncluttered rotor is shown in Figure 7. The two circular slots are for the 2-phase excitation coils. The resistance values and the inductance values of these 2-phase coils are designed to be equal for balanced 2-phase operation. The resistance value can be controlled by the wire size and the inductance value by the ring and slot dimensions. For the 3-phase option, three rings would be required, instead of the four rings required for the 2-phase option. In short, the uncluttered rotor made of flux-conducting material produces an equivalent rotating armature without brushes and slip rings.



Figure 7. Two-phase excitation core for the uncluttered rotor.

Uncluttered CVT

An uncluttered CVT offers these benefits:

- Rotating stator for harvesting the reaction torque
- Brushless operation
- Combination motor and generator
- Single set of permanent magnets
- Smaller size, lighter weight, and lower cost

Figure 8 shows an example of the uncluttered rotor concept used for a CVT. The portion marked “Completed in FY 06” was to prove the brushless rotating armature concept. Inside this portion, the uncluttered rotor is sandwiched between the uncluttered rotor excitation core on the left and an air gap facing the rotating field of the permanent magnet rotor on the right. The combination of the excitation core and the uncluttered rotor is equivalent to a rotating stator without brushes. The energy going into the stationary excitation core is transferred through the air gap to the uncluttered rotor. Because the magnetic coupling at this air gap is a tangential coupling, no torque is produced during the transfer. The other side of the uncluttered rotor has a radial coupling between the uncluttered rotor and the permanent magnet rotor. Torque would be produced between the uncluttered rotor and the permanent magnet rotor in this air gap.

For the initial concept validation, the permanent magnet rotor was taken out and the wound stator used on the right side was substituted to produce a rotating field.

A possible axial-gap example of an uncluttered CVT is shown in Figure 9. For FY 2006, the experimental setup for using the uncluttered rotor concept to prove the brushless rotating armature concept is shown in Figure 10.

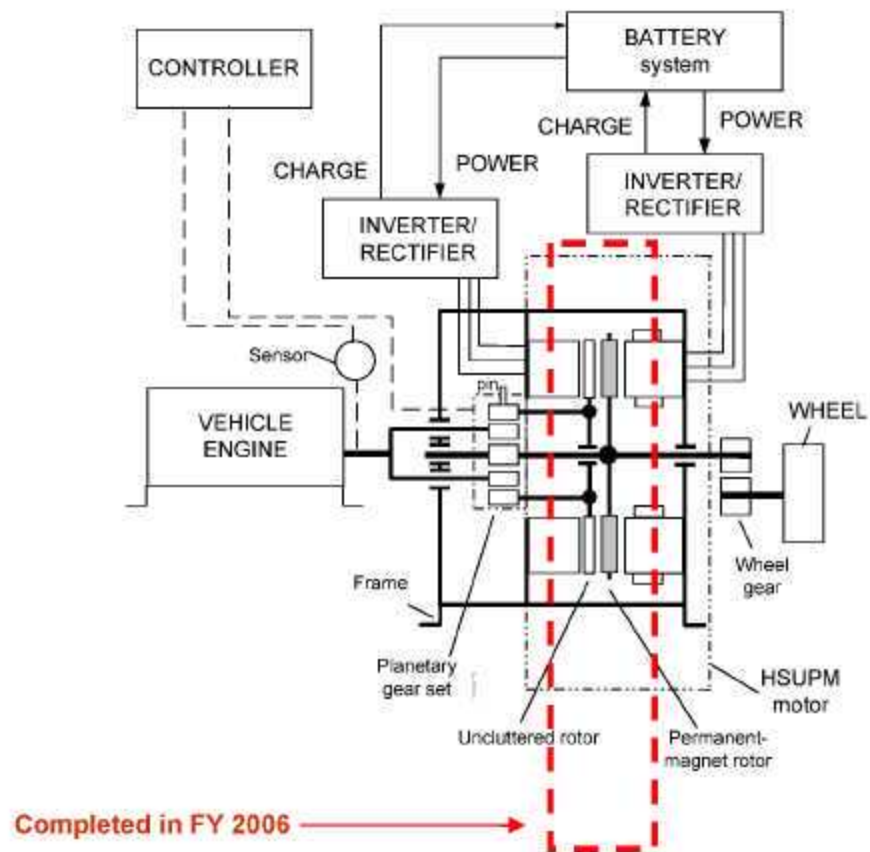


Figure 8. An example of an uncluttered CVT.

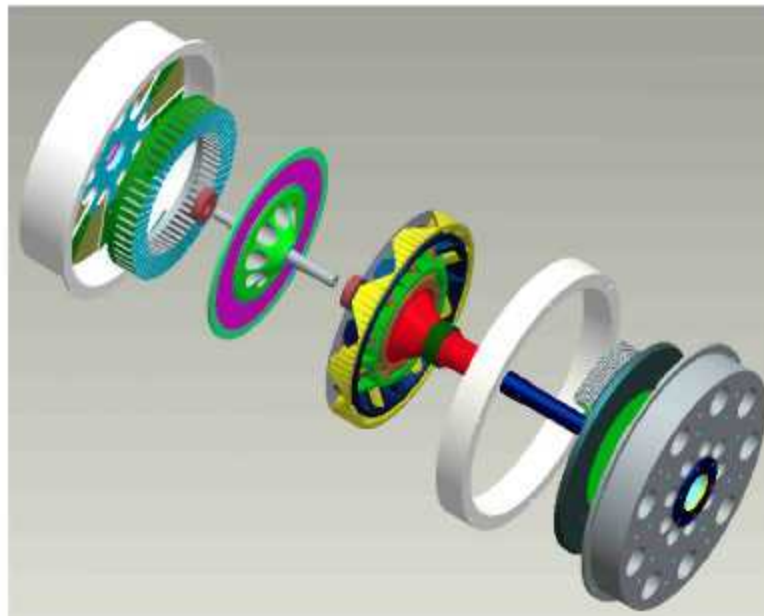


Figure 9. A possible axial-gap example of an uncluttered CVT.

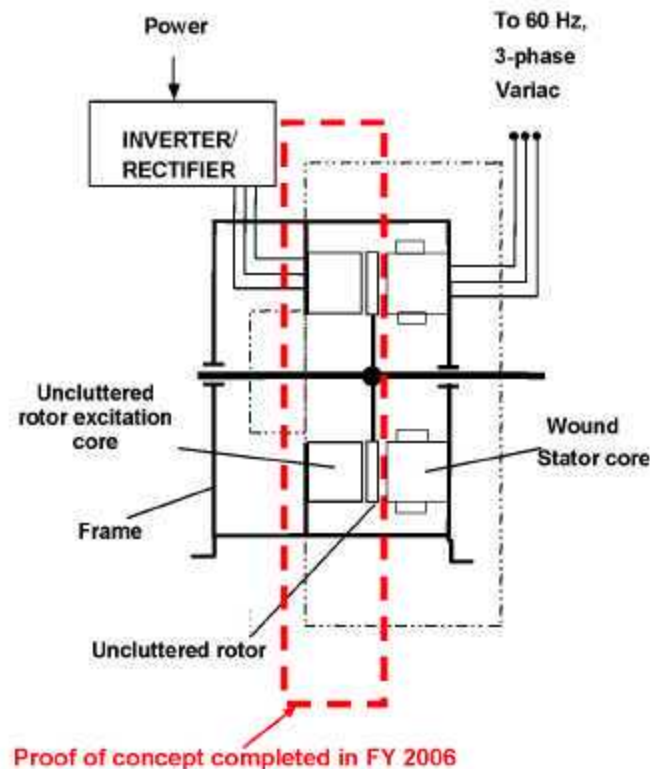


Figure 10. Experimental setup for proving the brushless rotating armature concept.

Figure 11 shows the prototype for the uncluttered rotor proof of concept completed in FY 2006. There are no brushes or slip rings in the machine. The 3-phase wound stator leads are connected to one side of the conventional axial-gap stator that provides a rotating field for the emulation of the rotating permanent magnet rotor. The uncluttered rotor shaft and the uncluttered rotor brushless excitation leads are also shown. The cut view of the proof-of-concept uncluttered rotor prototype is shown in Figure 12.

Tests on the Uncluttered Rotor

The following tests were performed on the prototype.

Induction Mode Test

In this test, the uncluttered rotor and its stator were viewed as a rotating stator or as a rotating wound armature. This rotating wound armature was magnetically coupled to another rotating field produced by the permanent magnet. In this test, the rotating field produced by the permanent magnets was replaced by the rotating field produced by a 3-phase wound core. If the frequency going into the 3-phase wound core is changed, the synchronous speed of the rotating field will be equivalent to the speed of the permanent magnet rotor. Therefore, the rotating wound armature coupled to the rotating field at a synchronous speed will actually be equivalent to an induction motor. In this equivalent setup, the rotating armature will act like a rotor of an induction motor, and the permanent magnet rotor will act like a stator of an induction motor that produces a synchronous magnetic field. The speed of the uncluttered rotor acting as the rotor of an induction motor would have a slip that is lower than the synchronous speed. The speed could be controlled by varying the resistance of the stationary uncluttered- rotor excitation coils. This expectation was clearly confirmed by the test.

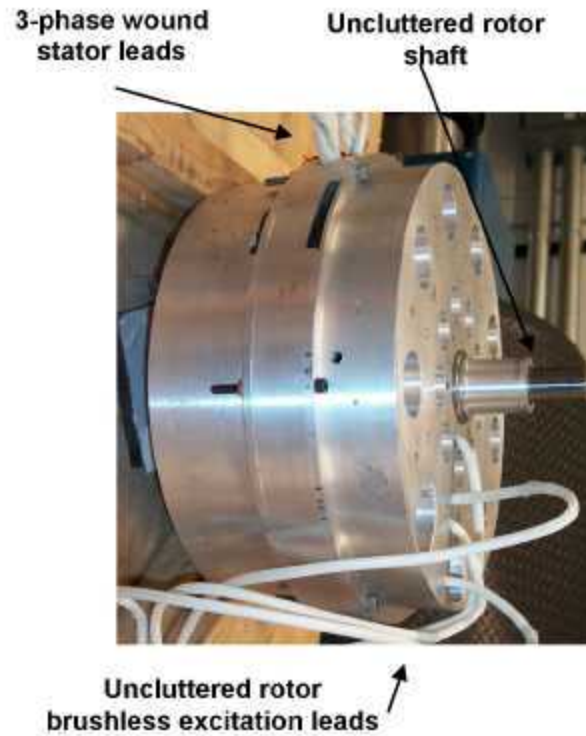


Figure 11. The prototype for the uncluttered rotor proof of concept completed in FY 2006.

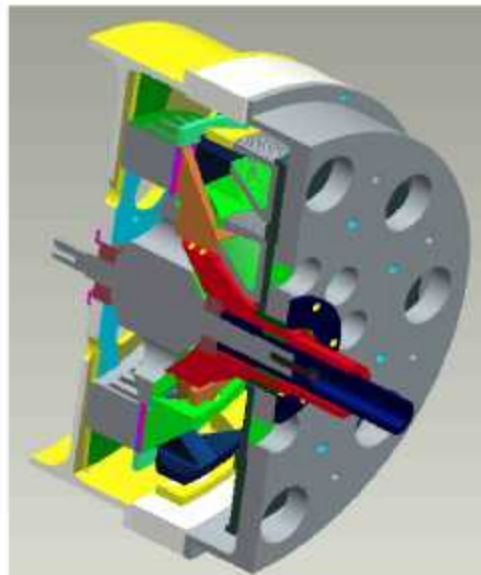


Figure 12. Cut view of the uncluttered rotor proof-of-concept prototype.

dc Mode Test

In this test, a dc current was fed to the stationary uncluttered-rotor excitation coils. The dc flux produced by the dc current went through the flux rings of the uncluttered rotor and turned into 8-pole flux on the other side of the rotor. This 8-pole flux interacted with the rotating flux produced by the 3-phase wound core that resulted in a synchronous motor. The rotor speed should be the synchronous speed of 400 rpm. This expectation was confirmed by the test.

Variable Frequency Mode Test

In this test, a set of variable-frequency two-phase currents was fed to the stationary uncluttered-rotor excitation coils. The variable-frequency flux produced by the variable-frequency currents went through the flux rings of the uncluttered rotor and transformed into an 8-pole rotating flux on the other side of the rotor. The speed of the uncluttered rotor went higher than the synchronous speed of the 3-phase wound core when the 2-phase sequence was opposite to the 3-phase sequence. If the 2-phase sequence is the same as the 3-phase sequence, the speed of the uncluttered rotor would go lower than the synchronous speed of the 3-phase wound core. This expectation was confirmed by the test.

Note that the number of phases of the uncluttered rotor excitation coils can be changed to two, three, or other practical numbers.

Conclusion

The concept of using an uncluttered rotor for the rotating brushless stator armature was proved through induction mode, dc mode, and variable-frequency mode tests. In FY 2006, a prototype was built and the concept for the rotating brushless stator armature was validated.

Future Direction

The next step is to simulate the performance of the uncluttered rotor and subsequently the uncluttered CVT assembly through design iteration and to start work on control of the uncluttered rotor.

Patents

John Hsu, "Hybrid-Secondary Uncluttered Permanent Magnet Machine and Method," U.S. Patent 6,977,454, December 20, 2005.

John Hsu, "Simplified Hybrid-Secondary Uncluttered Machine and Method," U.S. Patent 6,891,301, May 10, 2005.

John Hsu, "Hybrid Secondary Uncluttered Induction Machine," U.S. Patent No. 6,310,417, October 30, 2001.

References

1. J. Hsu, "Hybrid-Secondary Uncluttered Induction (HSUI) Machine," *IEEE Transactions on Energy Conversion* 16(2), ITCNE4, (ISSN 0885-8969), 192-197 (June 2001).
2. J. Perahia, "Discussion of Hybrid-Secondary-Uncluttered Induction (HSUI) Machine," *IEEE Transactions on Energy Conversion* 17(1), ITCNE4, (ISSN 0885-8969), 150 (March 2002).
3. J. Hsu, "Closure on Hybrid-Secondary-Uncluttered Induction (HSUI) Machine," *IEEE Transactions on Energy Conversion* 17(1), ITCNE4, (ISSN 0885-8969), 150 (March 2002).

3.2 Interior Permanent Magnet Reluctance Machines

3.2.1 Interior Permanent Magnet Reluctance Machines with Brushless Field Excitation—16,000 rpm

Principal Investigator: John Hsu

Oak Ridge National Laboratory

National Transportation Research Center

2360 Cherahala Boulevard

Knoxville, TN 37932

Voice: 865-946-1325; Fax: 865-946-1210; E-mail: hsujs@ornl.gov

DOE Technology Development Manager: Susan A. Rogers

Voice: 202-586-8997; Fax: 202-586-1600; E-mail: Susan.Rogers@ee.doe.gov

ORNL Program Manager: Mitch Olszewski

Voice: 865-946-1350; Fax: 865-946-1262; E-mail: olszewskim@ornl.gov

Objective

Develop an interior permanent magnet (IPM) reluctance motor with brushless field excitation that offers high torque per ampere per core length by using a brushless excitation coil to enhance the flux. The motor does not require a dc/dc boost converter at medium and high speeds. The core loss is low, because the flux can be weakened by not supplying current to the excitation coil.

Approach

Increase motor speed to reduce size, weight, and cost.

- Achieve field weakening and enhancement by incorporating an additional flux path using external field excitation.
- Improve existing IPM design by adding side magnets without additional brushless field excitation.

Positives

1. The system does not require a dc/dc boost converter, resulting in a reduction in system costs.
2. Sufficiently higher torque per ampere per core length can be attained at low speeds.
3. Lower core losses at low torque regions, especially at high speeds, are attained.
4. Safety and reliability are increased because burning is prevented under the fault condition of a shorted winding.

Negatives

The system has an unconventional rotor structure and unconventional brushless field excitation.

Barriers/Challenges

For 16,000-rpm motors, mechanical stress is a challenge. Thicker bridges that link the rotor punching segments have to be increased. Consequently, the rotor flux leakages significantly lower the motor performance. This barrier can be overcome by the use of external excitation to ensure sufficient rotor flux.

Tasks

- Perform electromagnetic simulations and mechanical analysis.
- Complete fabrication of motor.
- Conduct evaluation tests upon completion of motor assembly.
- Complete testing in FY 2007.

Accomplishments

The assembly of the ORNL 16,000-rpm motor design is shown in Figure 1. Table 1 compares the dimensions of the ORNL 16,000-rpm motor and those of the Toyota/Prius motor.^{1,2} The masses and sizes derived from this table provide a basis for a cost comparison with the Prius motor. The extra excitation coils and cores of the ORNL motor are made of copper wires and mild steel. The savings realized by a shorter stator core (1.875 in. compared with 3.3 in. for the Prius) and shorter stator winding compensate for their total cost. The low-current (5 A, maximum) control of the field excitation cost is minimal because of the low-current components required. This motor design enables better motor performance with system cost savings. Additionally, if used in a vehicle architecture requiring a boost converter, this motor can produce 250-kW output at 16,000 rpm. This significantly widens the possible applications for this type of motor.

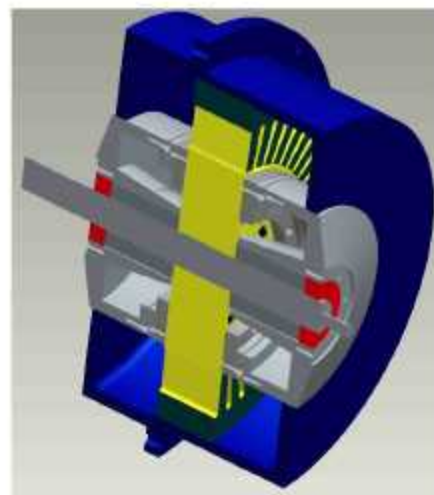


Figure 1. Assembly of ORNL 16,000-rpm motor design.

Table 1. Comparison of dimensions of the ORNL 16,000-rpm motor and the Toyota/Prius motor

	Prius	ORNL
Speed_	6000 rpm	16,000 rpm
Stator Lam. OD_	10.6"	same
Rotor OD_	6.375"	same
Core length_	3.3"	1.88"
Bearing to Bearing outer face_	7.75"	7.45"
Magnet Weight lbs_	2.75	2.57
Estimated field adj. ratio_	none	2.5
Rating_	33/50 kW	same
Boost converter_	yes	No
High speed core loss_	high	low

Technical Discussion

The design for the 16,000-rpm motor not only optimizes torque capability but also incorporates the ability to weaken the air gap flux density by having no excitation coil current. The need for low core losses across a wide range of speeds was also addressed in this design. The design maximizes the thickness of

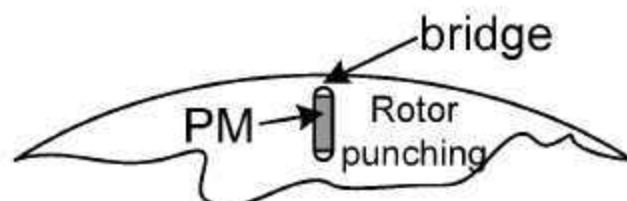


Figure 2. Location of bridge in a rotor punching.

the rotor punching bridges (material between the magnet slots in the rotor) (Figure 2) to satisfy the mechanical stress requirements at the high speeds required of this machine. More leakage flux produced by the PMs can go through these bridges, so the air-gap flux density produced by the PMs will be lower than in other, similar IPM machines such as the lower-speed Prius motor.

The 16,000-rpm motor with brushless field excitation provides flexibility for a drive system design to meet field strength requirements that vary at different loads and speeds. In general, the brushless field excitation approach can provide field enhancement and weakening for strong or weak PMs, as shown in Figure 3.

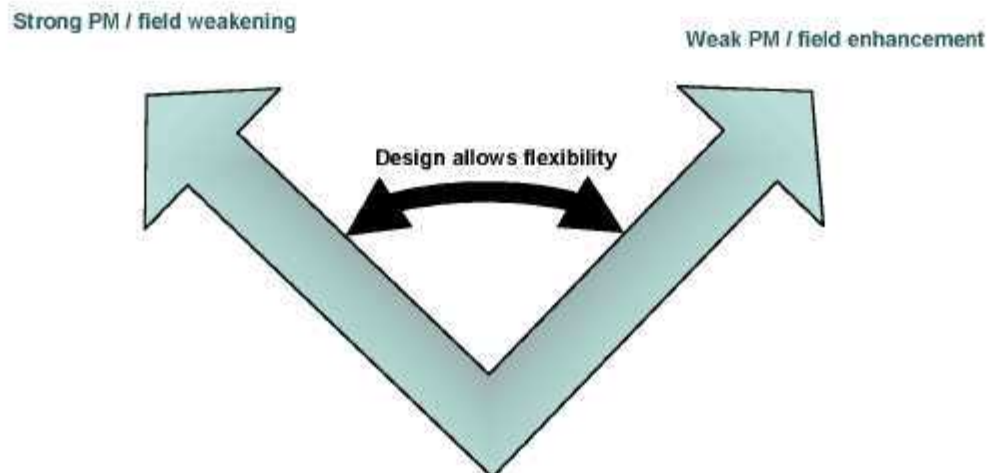


Figure 3. Flexibility provided by adjustable field excitation.

This motor is intentionally designed for low air-gap flux density at high speeds with no field excitation current applied. This solves the problem of high core loss seen in existing high-PM-flux-density, high-speed motors of the type used in Prius and Highlander automobiles, which are plagued with both high core and high d-axis current losses necessary for field weakening. Figure 4 shows the rotor punching, the locations of PMs, and the completed rotor.

Figure 5 shows the air-gap flux density distributions at various excitation ampereturns (ATs). The excitation coil has 865 turns. The excitation current is the ATs, divided by the turns (865). The air-gap flux density of this motor can be adjusted with the external excitation coils to tailor the torque output. When high torque is required, the air-gap flux density is enhanced. When low torque and high efficiency are required, the excitation current is reduced to zero.

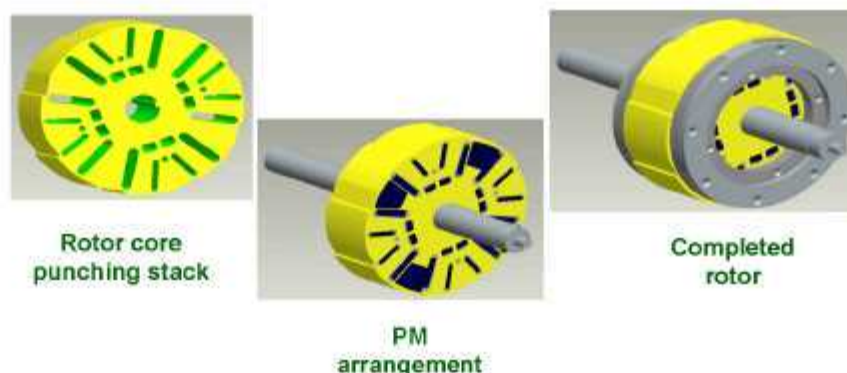


Figure 4. Rotor of ORNL's 16,000-rpm motor.

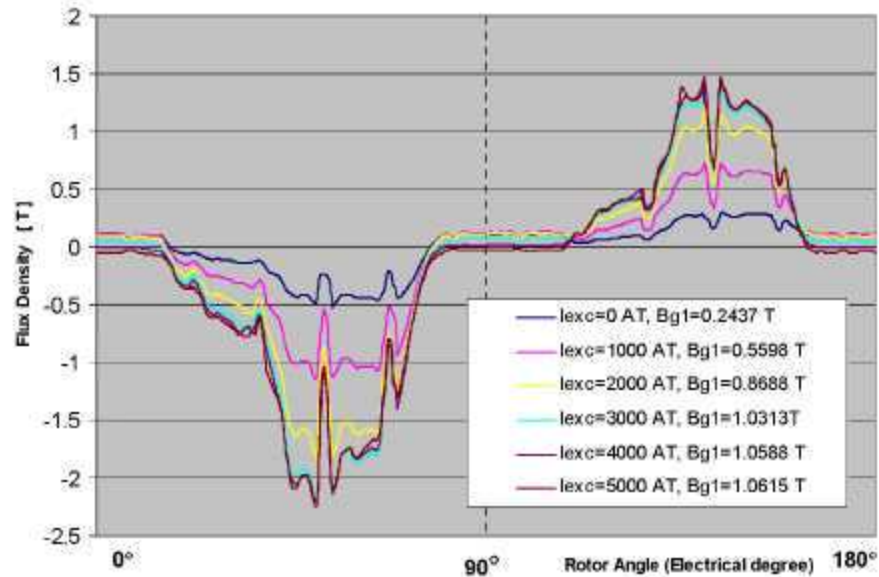


Figure 5. Air-gap flux density distributions with various excitation ampereturns (AT).

Figure 6 shows test results for three-phase, line-to-neutral back-electromotive force (emf) at 5000 rpm with 5-A and 0-A excitation currents, respectively. The asymmetry of the air-gap flux density distribution shown in Figure 5 does not affect the symmetry of the induced back-emf waveform. The expected output torque at 141 A_{RMS} (i.e., 200-A magnitude value) is shown in Figure 7. It clearly shows that the stronger field excitation can enhance the output torque.

The vibration analysis obtained from testing is shown in Figure 8. Vibration analysis will be conducted at each subsequent speed tested.

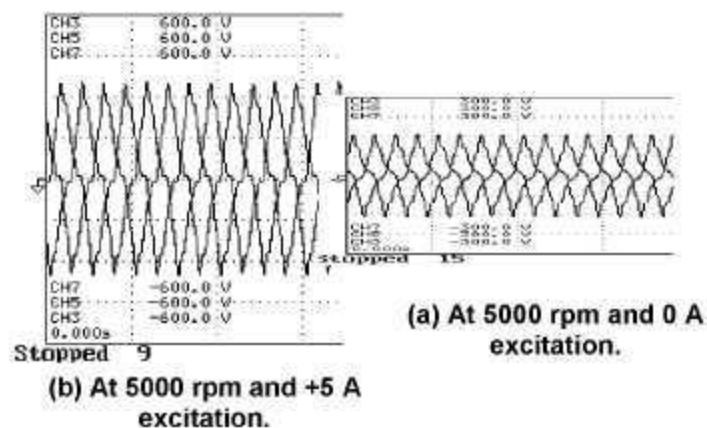


Figure 6. Three-phase line-to-neutral back-emfs at 5000 rpm with and without field excitation.

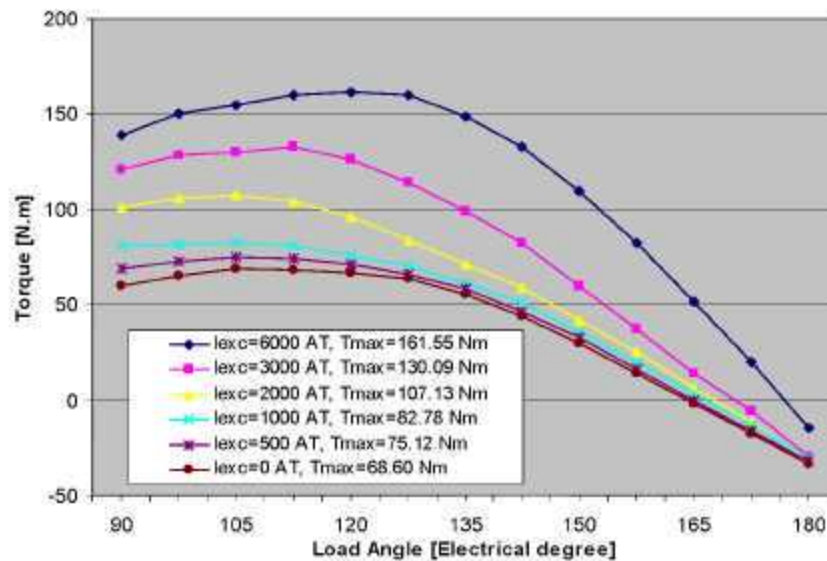


Figure 7. Stronger field excitation that can enhance output torque.

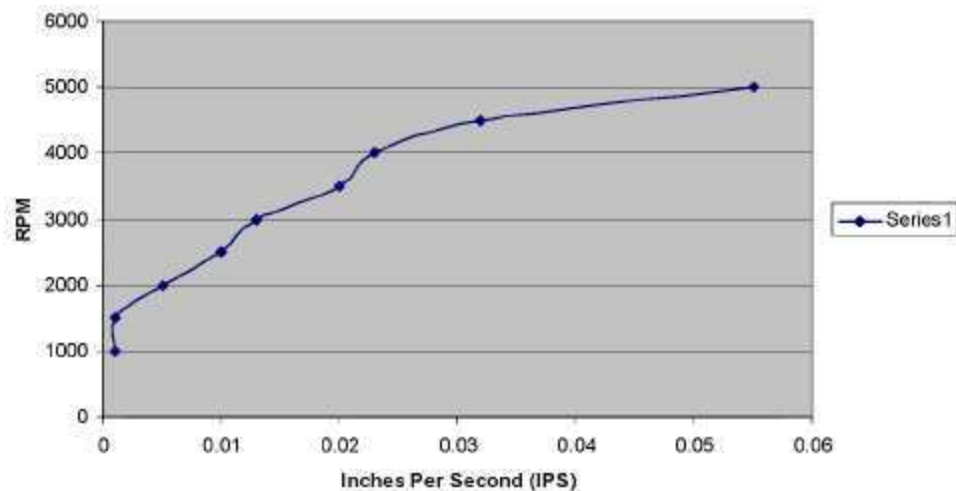


Figure 8. Vibration analysis obtained from test.

Figure 9 shows that the back-emf can be controlled effectively through the external field excitation current with a range of current from 0 to 5 A, thus negating the necessity of using a boost converter to overcome high back-emf. The initial tests show that the air-gap flux density can change up to 2.5 times at a given speed. This enables the motor to have all the advantages of both the existing strong PM reluctance motors (i.e., high power density, high back-emf at high speed, high core loss) and the weak PM reluctance motors (i.e., low power density, low back-emf, lower core loss) without their disadvantages. The additional circuitry necessary to supply the excitation current to the coils should cost less than \$10 in production quantities.

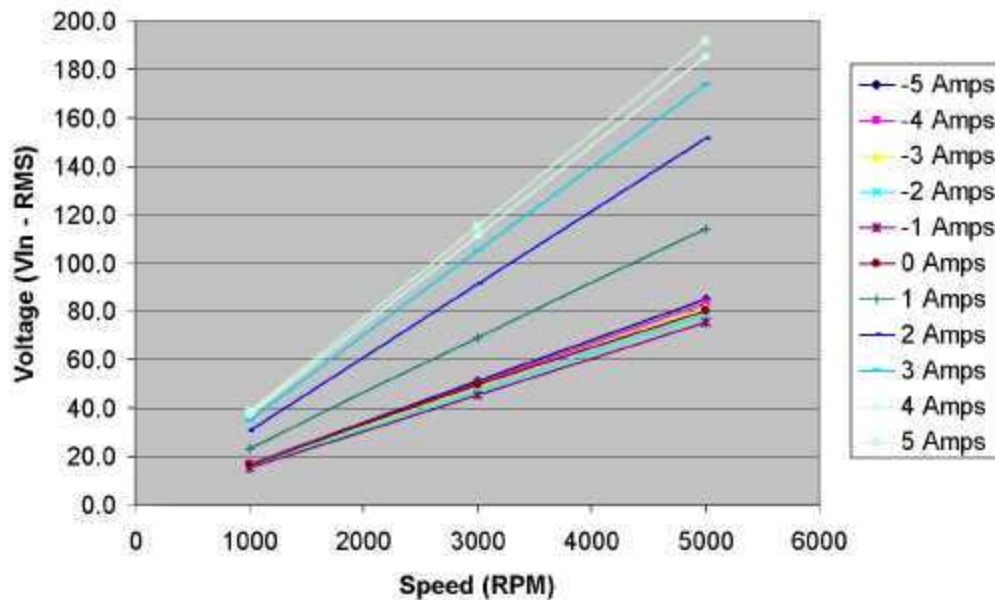


Figure 9. Line-to-neutral back-emf voltage vs speed.

The core and friction loss tests conducted show the benefits of lower air-gap flux density (Figure 10). For example, at 5000 rpm, the core and friction loss is 200 W with zero field excitation, compared with 600 W at high field excitation for a high air-gap flux density. This inherently low air-gap flux density motor design enables significantly lower core losses at high speeds (Figure 11). Yet at low speeds, when high torque is needed, the ability to enhance the field can dramatically boost the torque. The excitation coils coupled with this low air-gap flux design enable the motor to be controlled or “fine tuned” to operate in its highest-efficiency areas across the torque/speed curve.

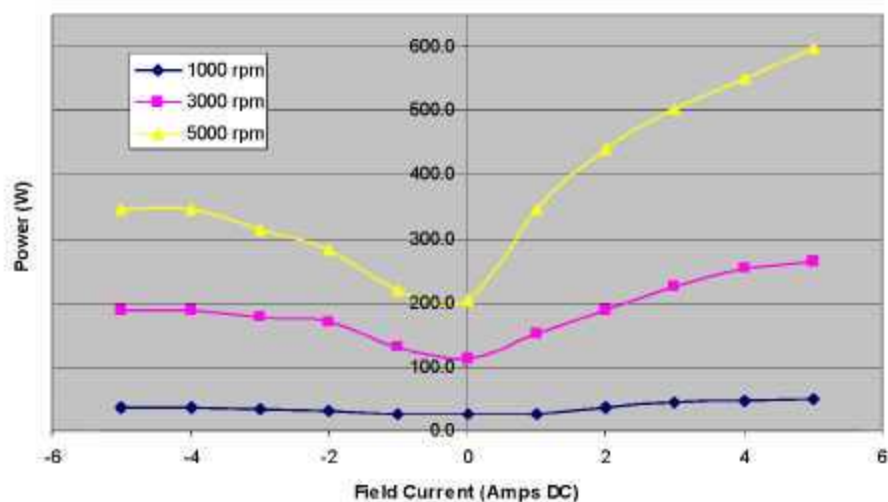


Figure 10. No-load core and friction losses vs field current for each speed.

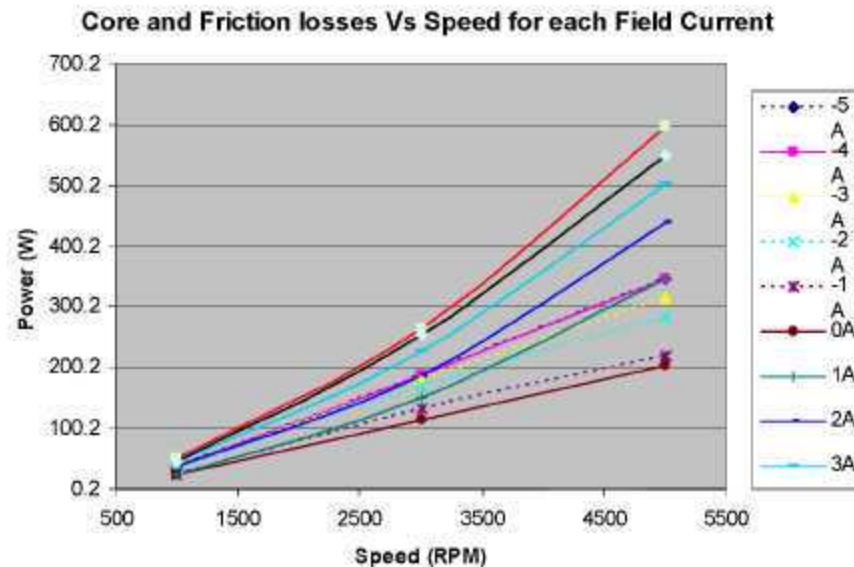


Figure 11. No-load core and friction losses vs speed for each field current.

Mechanical Analyses of 16,000-rpm Rotor

Extensive effort was expended on the high-speed, 16,000-rpm critical speed and three-dimensional (3-D) mechanical stress analyses. A transfer matrix approach was used to estimate the critical speed. The 3-D softwares used for stress analyses were ALGOR, ANSYS, and Pro/E. The analytical results are as follows.

- Estimated critical speed of 16,000-rpm rotors: 24,960 rpm (safety factor = 1.56).
- Stress analyses of rotor:
 - Figure 12(a) shows the solid models with only a quarter of the PMs having properly defined contact surfaces (i.e., the upper right quarter that shows the gaps between PM and rotor punching).
 - Figure 12(b) shows that when contact surfaces are bonded to the lamination, the stresses become unrealistically low. This demonstrates the importance of having the contact surfaces properly defined.

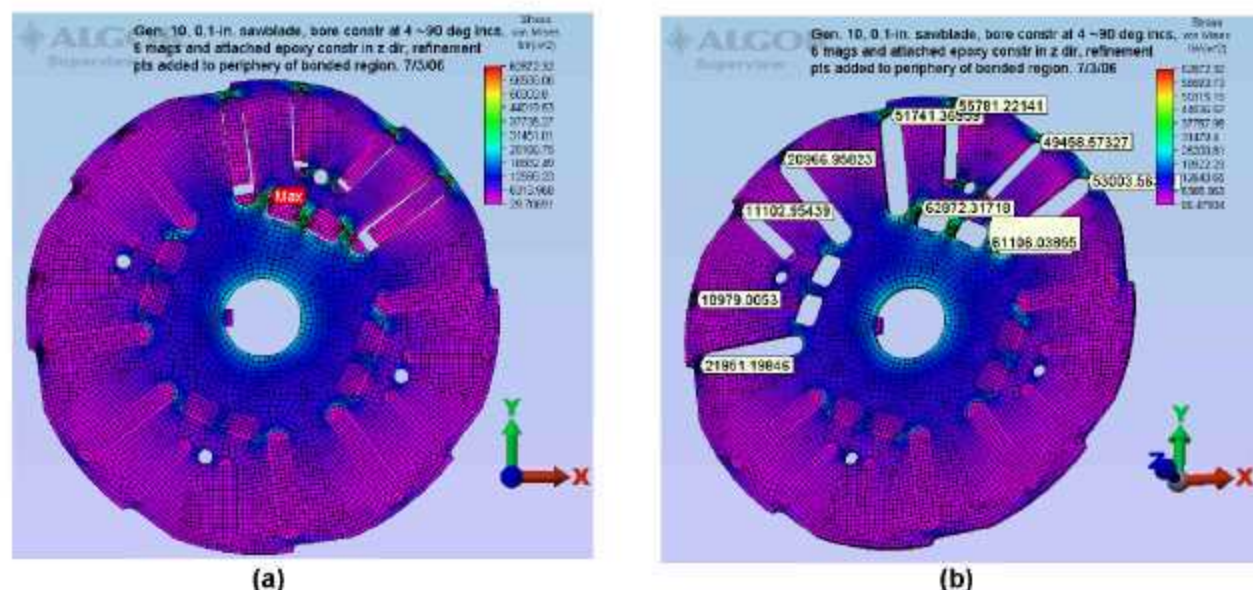


Figure 12. Finite-element stress analysis of 16,000-rpm rotor.

Figure 13 shows that, from the simulation, the radial displacement at the rim of a 0.018-in.-thick 16,000-rpm laminate rotor ranges from 0.00066 to 0.00124 in., which is less than the air gap of 0.029 in. Figure 14 shows that, although acceptable, the shear stresses at the support columns of a 0.018-in.-thick 16,000-rpm laminate rotor are slightly larger because the side of the small magnet nearest to the radial magnet is not along a radius.

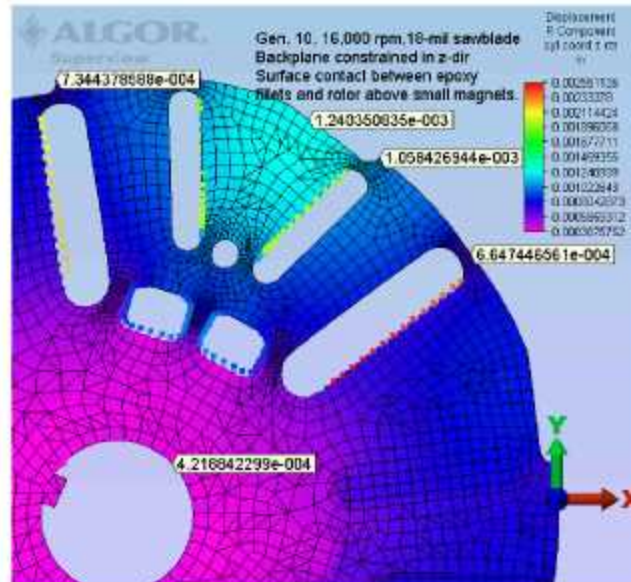


Figure 13. Radial displacement analysis of 16,000-rpm rotor.

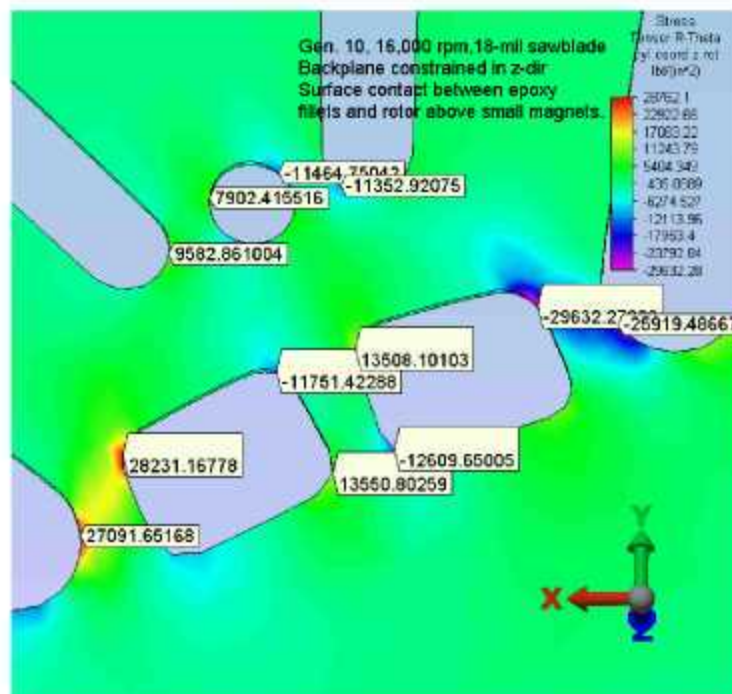


Figure 14. Shear stresses at the support columns of an 0.018-in. thick 16,000-rpm laminate rotor.

Parts fabricated

Figures 15 through 20 show the parts that have been fabricated for the prototype motor.

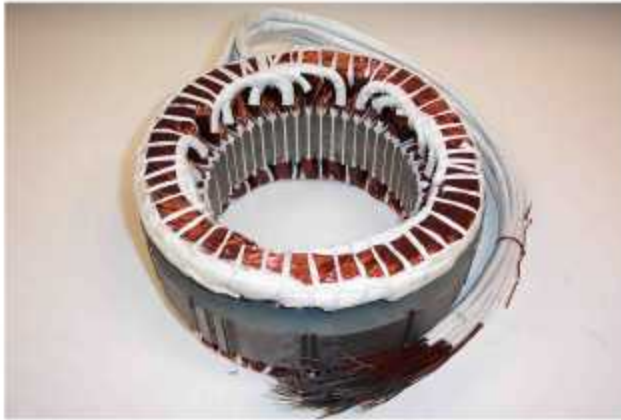


Figure 15. Wound stator core.



Figure 16. Rotor punching.



Figure 17. Rotor core stack and shaft.



Figure 18. Completed rotor.



Figure 19. Excitation coil housing.



Figure 20. Excitation coil inside the coil housing.

Based on the experience of building the prototype at ORNL, it is anticipated that the motor will not present any complicated manufacturing issues. This is certainly a concern with any design undertaken at ORNL. No issues with added gearbox complexity are expected. We do not foresee a more complex gearbox than the planetary gearbox that is currently used by some automotive manufacturers.

The prototype motor can be further reduced in mass and volume by redesigning the interface between the excitation coils and the motor housing. This improvement will reduce the cost to manufacture the motor by eliminating some machining steps as well as raw materials.

Conclusion

The design of the 16,000-rpm motor not only optimizes torque capability but also incorporates the ability to weaken the air-gap flux density. It also addresses the need for low core losses across a wide range of speeds.

This design maximizes the thickness of the rotor punching bridges (material between the magnet slots in the rotor) to satisfy the mechanical stress requirements at the high speeds required of this machine. More leakage flux produced by the PMs can go through these bridges, so the air-gap flux density produced by the PMs will be lower than in other, similar IPM machines such as the lower-speed Prius motor.

Our motor is intentionally designed for low air-gap flux density at high speeds with no field excitation current applied. This solves the problem of high core losses seen in existing high-PM-flux-density, high-speed motors of the type used in the Prius and Highlander automobiles, which are plagued with both high core and high d-axis current losses necessary for field weakening.

This motor is still in the development stage. Validation data will be available after initial testing is completed this year. Initial test results show the following:

- The back-emf can be controlled effectively through the external field excitation current with a range of current from 0 to 5 A, thus negating the necessity of using a boost converter to overcome high back-emf. The air-gap flux density can change up to 2.5 times at a given speed. This enables the motor to have all the advantages of both existing strong PM reluctance motors (i.e., high power density, high back-emf at high speed, high core loss) and weak PM reluctance motors (i.e., low power density, low back-emf, lower core loss) without their disadvantages. The additional circuitry necessary to supply the excitation current to the coils should cost less than \$10 in production quantities.
- The core and friction loss tests conducted show the benefits of lower air-gap flux density. For example, at 5000 rpm, the core and friction loss is 200 W with zero field excitation, compared with 600 W at high field excitation for a high air-gap flux density.

This inherently low air-gap flux density motor design enables significantly lower core losses at high speeds. Yet at low speeds, when high torque is needed, the ability to enhance the field can dramatically boost the torque. The excitation coils, coupled with this low air-gap flux design, enable the motor to be controlled or fine tuned to operate in its highest-efficiency areas across the torque/speed curve.

It is not anticipated that the motor will present any complicated manufacturing issues. Redesigning the interface between the excitation coils and the motor housing will further reduce the mass and volume of the prototype motor, reducing the manufacturing cost.

In addition to the low loss performance improvement, this motor design eliminates the requirement for a boost converter, simplifying the power electronics and enabling cost savings in the total drive system. Comparing mass and size provides a basis for a cost comparison with the Prius motor. The extra excitation coils and cores of the 16,000-rpm motor are made of copper wires and mild steel. The savings realized by a shorter stator core (1.875 in. compared with the 3.3 in. of Prius) and shorter stator winding compensate for their total cost. The low-current (5-A, maximum) control circuit for the field excitation coils cost is minimal because of the low-current components required. This motor design enables better performance with system cost savings. Additionally, if used in a vehicle architecture requiring a boost

converter, this motor can produce 250-kW output at 16,000 rpm, significantly widening possible applications.

Future Direction

In FY 2007 the research goal is to produce a motor with significantly reduced size, weight, and volume from that of current technology. The higher power density and lower system cost will provide industry with a greater cost vs performance ratio. A dramatic system cost savings will be realized by eliminating the dc/dc boost converter as well. Through reductions in core losses at high speeds by using the field weakening capability improvements in vehicle fuel efficiency will also be realized.

In FY 2007 performance testing will be completed. Performance calculations for the 3-D RIPM-BFE motors will be verified and adjustments made in the models depending on testing results. These tests will include the back-emf data with no field excitation as well as with enhancement and weakening of the field. Locked rotor testing will be completed with the same conditions as the back-emf tests (no field excitation and enhancement/weakening of the field). Performance and efficiency mapping will also be completed during FY 2007. Testing will take place at various voltage increments, and speed and torque ranges, similar to the benchmarking tests performed on the Prius motor at ORNL. This motor will be driven by a dynamometer system to facilitate data measurements. Revisions to the motor, due to unforeseen issues, will be resolved, and the motor will be retested as necessary.

Patents

J. S. Hsu et al., "Rotor Apparatus for High Strength Undiffused Brushless Electric Machine," U.S. Patent 6,989,619, January 24, 2006.

J. S. Hsu et al., "Hybrid-Secondary Uncluttered Permanent Magnet Machine and Method," U.S. Patent 6,977,454, December 20, 2005.

J. S. Hsu et al., "Permanent Magnet Machine and Method with Reluctance Poles for High Strength Undiffused Brushless Operation," U.S. Patent 6,972,504, December 6, 2005.

J. S. Hsu et al., "Simplified Hybrid-Secondary Uncluttered Machine and Method," U.S. Patent 6,891,301, May 10, 2005.

J. S. Hsu et al., "High Strength Undiffused Brushless (HSUB) Machine," U.S. Patent 6,573,634, June 3, 2003.

J. S. Hsu et al., "Hybrid Secondary Uncluttered Induction Machine," U.S. Patent 6,310,417, October 30, 2001.

J. S. Hsu et al., "Permanent Magnet Energy Conversion Machine," U.S. Patent 5,952,756, September 14, 1999.

References

1. M. Kamiya, "Development of Traction Drive Motors for the Toyota Hybrid System," Toyota Motor Corporation, 1, Toyota-cho, Toyota, Aichi, Japan.
2. M. Okamura, E. Sato, and S. Sasaki, "Development of Hybrid Electric Drive System Using a Boost Converter," Toyota Motor Corporation, 1, Toyota-cho, Toyota, Aichi, Japan.

3.2.2 High-Power-Density Reluctance Interior Permanent Magnet Machines—6,000 rpm

Principal Investigator: John Hsu

Oak Ridge National Laboratory

National Transportation Research Center

2360 Cherahala Boulevard

Knoxville, TN 37932

Voice: 865-946-1325; Fax: 865-946-1210; E-mail: hsujs@ornl.gov

DOE Technology Development Manager: Susan A. Rogers

Voice: 202-586-8997; Fax: 202-586-1600; E-mail: Susan.Rogers@ee.doe.gov

ORNL Program Manager: Mitch Olszewski

Voice: 865-946-1350; Fax: 865-946-1262; E-mail: olszewskim@ornl.gov

Objective

- The objective is development of a high-power-density motor technology for reluctance interior permanent magnet (RIPM) motors, using side magnets located at the motor's end turns.

Approach

- To improve the power density of existing RIPM motors, the rotor of this new design was modified to have additional side magnets. Because this new motor does not use any additional external field excitation, it is more in line with conventional motor structures than other recent Oak Ridge National Laboratory (ORNL) motor projects. This project involved the development of a 6000-rpm motor. However, the new technology resulting from this project can be used for either higher- or lower-speed motors. A dc/dc boost converter and/or a strong direct-axis current for field weakening might be needed for this motor at high speeds because of the high back-electromotive force (emf) produced by the strong permanent magnet (PM) air-gap flux density.
- The unique design of this motor necessitated highly intensive, time-consuming computational modeling. Traditional two-dimensional finite element analyses could not be used effectively in the simulations, so three-dimensional simulations had to be performed.

Major Accomplishments

- The new technology derived from this project shows that the air-gap flux density produced by the new PM arrangement can be doubled compared with that of the Toyota Prius motor. The PM torque component is proportional to the product of the PM fundamental air-gap flux density and the current of the motor. Therefore, higher PM fundamental air-gap flux density produces higher torque at a given current and hence a higher power density of the motor.

Future Direction

This project was completed in FY 2006.

Technical Discussion

The power input of an RIPM motor is shown in Equation (1). The output power of the motor is the input power minus the losses of the motor. If the losses that include the copper loss, core loss, stray loss, and mechanical loss of the motor are neglected for simplification, the output power is represented by the input power.

$$P_m = \frac{3}{2} \left[\frac{EV}{X_d} \sin \delta - \frac{V^2}{2} \left(\frac{1}{X_q} - \frac{1}{X_d} \right) \sin 2\delta \right] \quad (1)$$

In Equation (1), E is the back-emf that is proportional to the no-load air-gap flux density. V is the phase voltage, δ is the load angle, and X_d and X_q are the direct and quadrature inductances, respectively. Based on this equation, power can be increased by raising the E value.

Because E is produced by the PMs without excitation from the stator currents, the higher the air-gap flux density is at no load, the higher the E value is. The target for this investigation is to find practical ways to increase the air-gap flux density produced by the PMs. Various novel PM arrangements are compared with the arrangement of the Toyota Prius PM rotor, which is shown in Figure 1. The PMs are situated inside the V-shaped grooves [1–2]. There is an air gap between the rotor and the stator. The air-gap flux density of this motor is used as the base value for the normalized comparison for various novel PM arrangements.

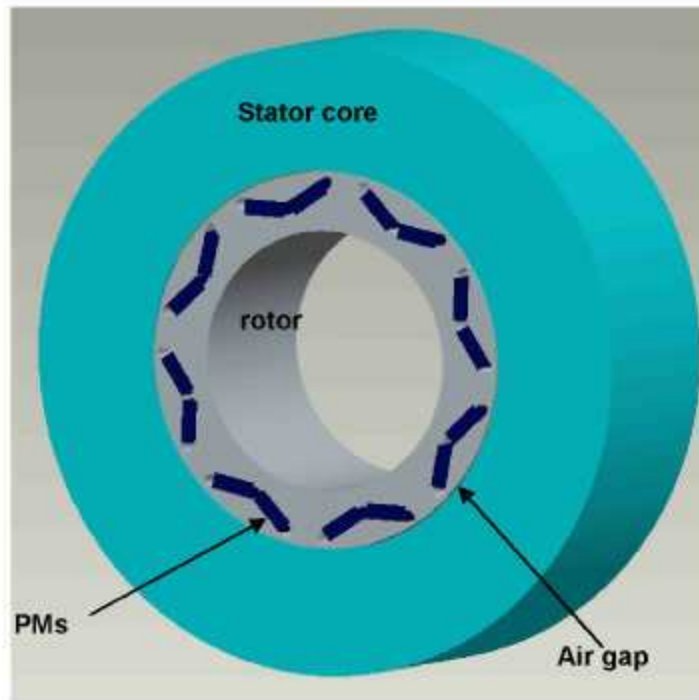


Figure 1. PM arrangement of Toyota Prius rotor.

Figure 2 shows various PM arrangements of an RIPM motor that has no additional field excitation. Figure 2(a) shows the U-shaped PMs that are symmetrically arranged for the north and south poles of the rotor. There is no side PM for this arrangement. Figure 2(b) shows that in addition to the U-shaped PMs, there can be either partial side PMs (represented by the blue magnets) or full side PMs (represented by both the blue and brown magnets). For the partial side-PM arrangement, the side PM and side pole piece are alternately located at the ends of the rotor poles. For the full side-PM arrangement, PMs are located at the ends of the rotor poles. A soft magnetic end ring (not shown) is attached to the ends of the side PMs to provide a flux return path for the side PMs.

Figure 3 shows the locations of the side poles and side PMs of a partial side-PM prototype motor. The magnetic end rings are not shown in this figure. For a full side-PMs arrangement, the side poles are replaced by side PMs. The prototype uses an aluminum non-magnetic spacer to mechanically secure the side poles and side PMs.

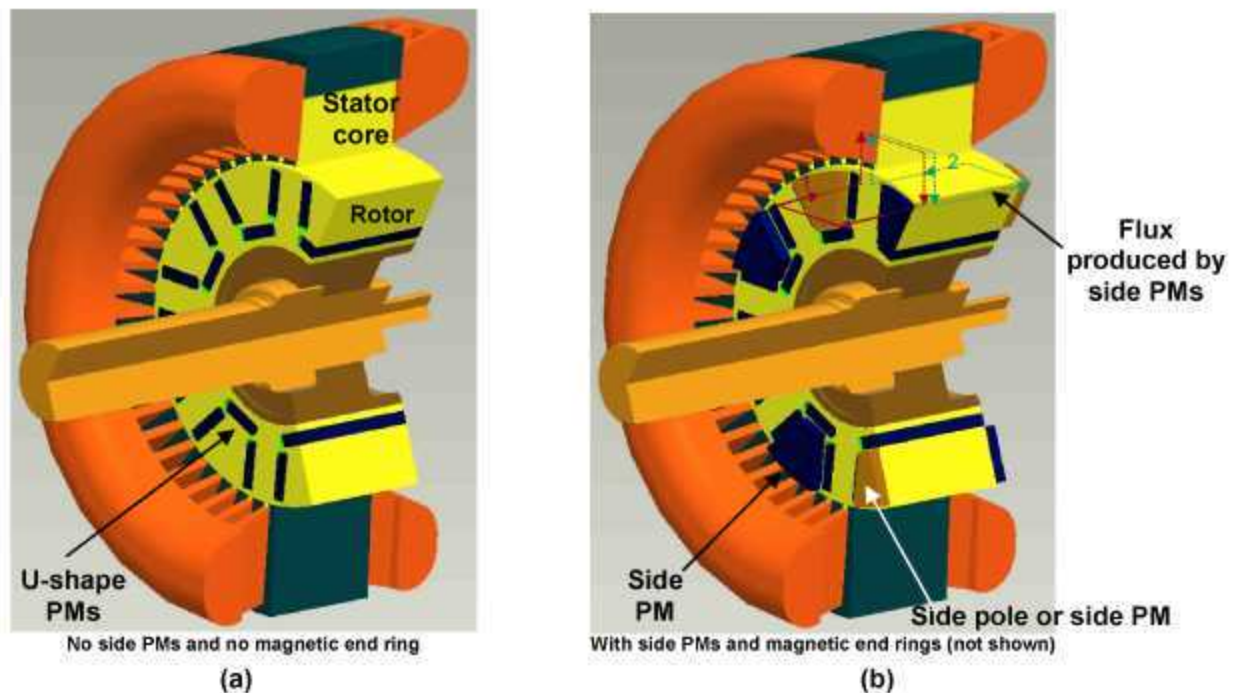


Figure 2. Various PM arrangements for increasing air-gap flux density.

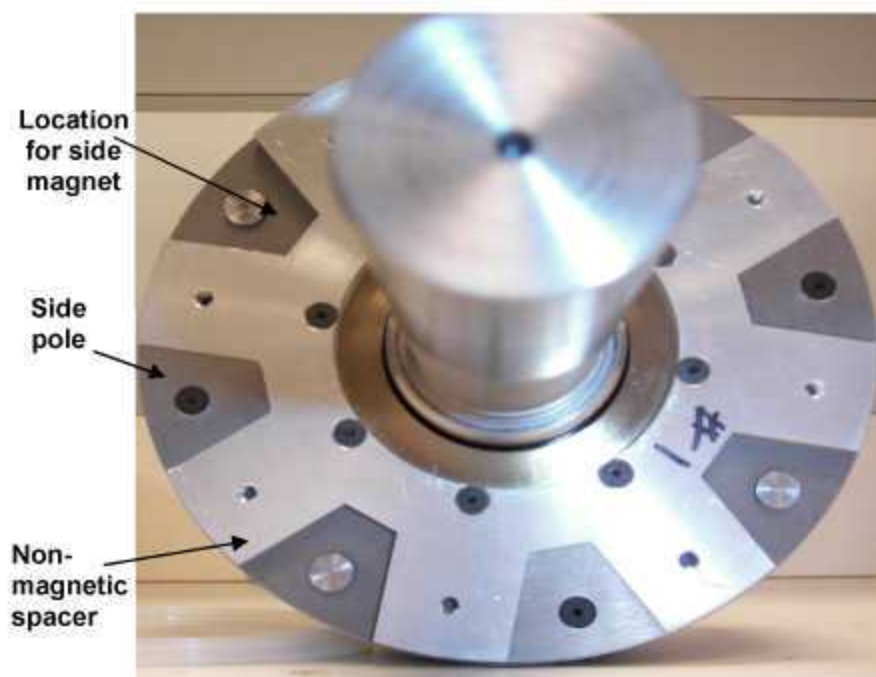


Figure 3. Prototype motor showing locations of side poles and side magnets.

Figure 4 shows the 3-dimensional finite element simulation results for the rotor flux density distributions produced by PMs only for the Toyota Prius; it shows no side-PM, partial side-PM, and full side-PM arrangements. Note that the very high flux density of the rotor is located in the narrow punching bridges on top of the PM grooves. The bridges magnetically short-circuit the PMs and become very saturated. These magnetically saturated bridges limit the flux that leaks from a rotor pole to its adjacent

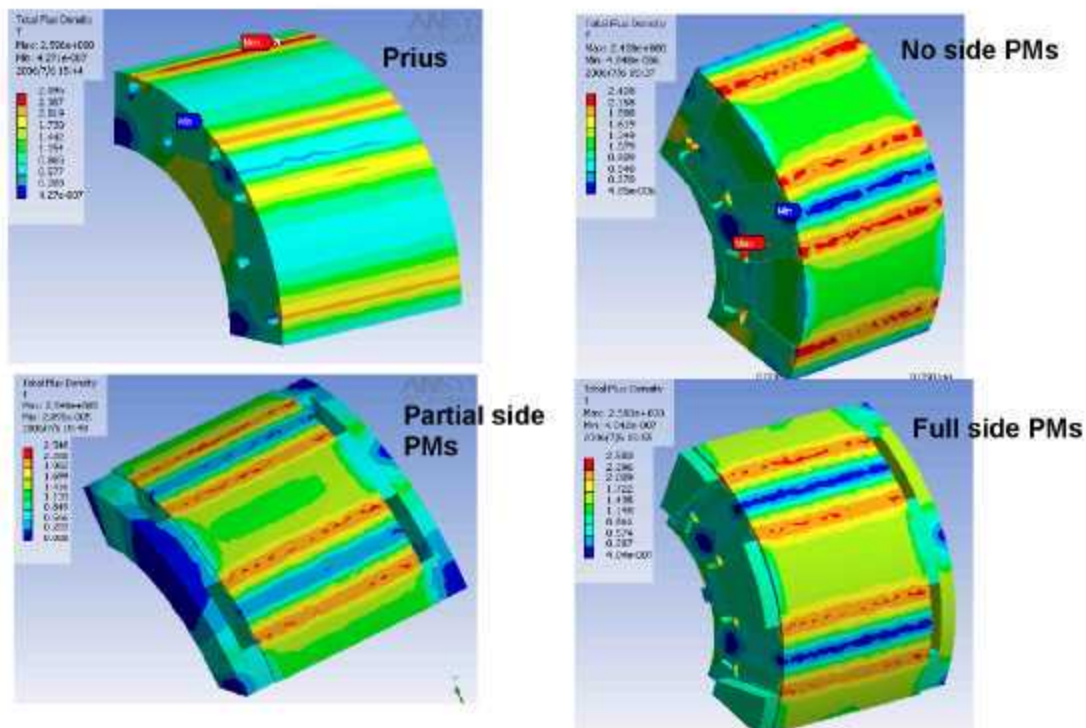


Figure 4. Three-dimensional simulation results for rotor flux density distributions.

pole. Because the bridge flux inside the bridge is mainly in the rotor peripheral direction, the radial air-gap fluxes at the bridge locations are relatively lower.

Figure 5 shows the radial air-gap flux distributions produced by the PMs for the four cases shown in Figure 4. The air-gap no-load flux density for the case of the U-shaped magnets plus full side PMs can reach double the value of the Prius air-gap no-load flux density.

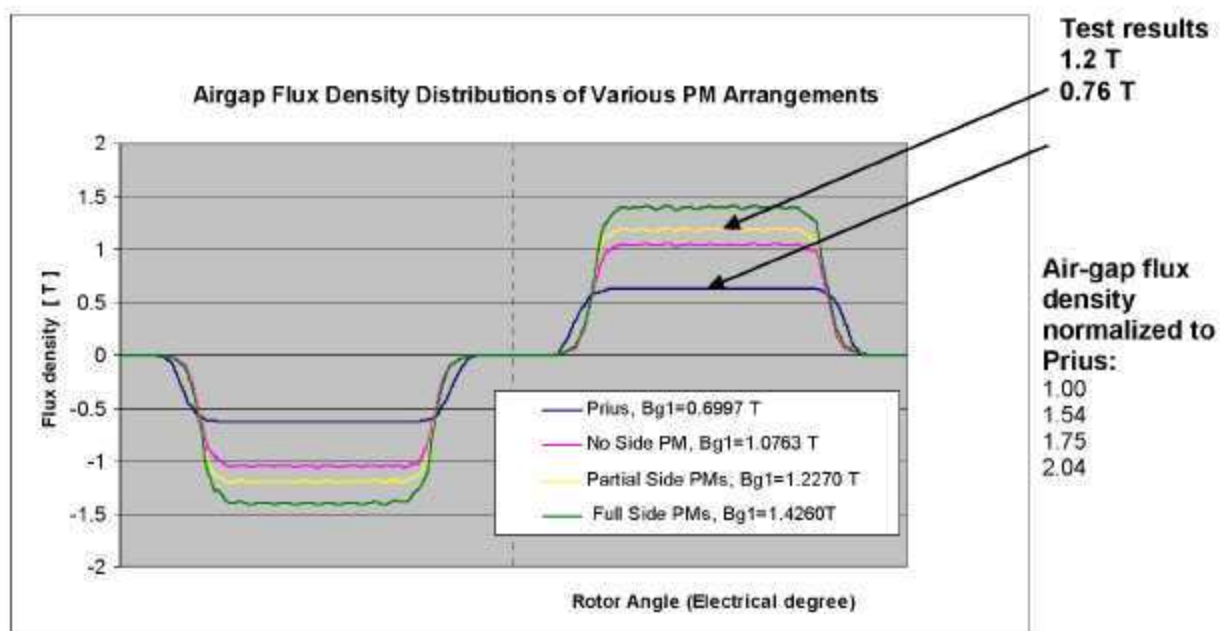


Figure 5. Comparison between simulation and test results of air-gap flux densities produced by PMs for various PM arrangements.

Conclusion

To improve the power density of existing RIPM motors, the rotor of an existing traditional machine was modified to contain additional side magnets. Because the motor being studied in this project does not use any additional external field excitation, it is more in line with conventional motor structures. The new technology resulting from this project can be used for either high- or low-speed motors. A dc/dc boost converter and/or a strong direct-axis current for field weakening might be needed for this motor at high speeds because of the high back-emf produced by the strong PM air-gap flux density.

The new technology derived from this project shows that the air-gap flux density produced by the PMs can be doubled compared with that of the Toyota Prius motor. Because the PM torque component is proportional to the product of the PM fundamental air-gap flux density and the current of the motor, higher PM fundamental air-gap flux density produces higher torque at a given current, yielding a higher-power-density motor.

This project was completed in FY 2006.

Future Direction

Beyond FY 2006, assistance to original equipment manufacturers for commercial prototypes will be provided as needed.

Patents

John Hsu, "Rotor Apparatus for High Strength Undiffused Brushless Electric Machine," U.S. Patent 6,989,619, January 24, 2006.

References

1. Munehiro Kamiya, "Development of Traction Drive Motors for the Toyota Hybrid System," Toyota Motor Corporation, 1, Toyota-cho, Toyota, Aichi, 471-8571, Japan.
2. Masaki Okamura, Eiji Sato, and Shoichi Sasaki, "Development of Hybrid Electric Drive System Using a Boost Converter," Toyota Motor Corporation, 1, Toyota-cho, Toyota, Aichi, 471-8572, Japan.

3.3 Control of Fractional-Slot Surface Mounted Permanent Magnet Motors with Concentrated Windings

Principal Investigator: John W. McKeever

Oak Ridge National Laboratory

National Transportation Research Center

2360 Cherahala Boulevard

Knoxville, TN 37932

Voice: 865-946-1316; Fax: 865-946-1262; E-mail: mckeeverjw@ornl.gov

DOE Technology Development Manager: Susan A. Rogers

Voice: 202-586-8997; Fax: 202-586-1600; E-mail: Susan.Rogers@ee.doe.gov

ORNL Program Manager: Mitch Olszewski

Voice: 865-946-1350; Fax: 865-946-1262; E-mail: olszewskim@ornl.gov

Objectives

The overall objective of this project is to develop techniques to analyze, design, and control fractional-slot concentrated-winding (FSCW) surface permanent magnet (SPM) synchronous machines; to investigate their possible use as a hybrid electric vehicle (HEV) traction motor; and if appropriate, to bring them into competition with internal permanent magnet motors. FSCW motors have potential for fault tolerant, wide constant power speed range (CPSR) operation because of their high inductance. They also have features that can reduce copper costs through improved slot utilization and elimination of copper end turns and reduce fabrication costs through simplified assembly methods.

A second objective, which is a subset of analysis and design, is to improve the model for calculating iron losses in the stator teeth and yoke, in the rotor, and in the magnets. Until more accurate estimates of these losses are available, reliable evaluation of the impact of minimizing them requires laboratory measurements.

Approach

The approach was to use closed-form analytical tools and commercial software to investigate and propose a design for a 55-kW FSCW motor. Originally, the plan was to build the 55-kW traction motor for testing. That approach was changed as it was felt that enough research had been completed on the FSCW motor that original equipment manufacturers could make the transition to market if they thought it had sufficient merit. Consequently, the product at the end of the year was a proposed 55-kW FSCW design whose analysis indicated that it could meet near term FreedomCAR targets.

We also developed a motor/inverter simulator to evaluate control schemes developed to improve efficiency of the FSCW-SPM motor. The approach was to test control schemes using the 6-kW FSCW prototype motor developed and tested at the University of Wisconsin, Madison (UWM), in FY 2005, mounted in a new frame that allowed liquid to cool the stator.

ORNL collaborated with UWM to test the control schemes developed. ORNL has a low cost scheme that controls at rated current or rated power to achieve maximum torque per amp below base speed and maximum power per amp above base speed. It is low cost because it eliminates current sensors. UWM has a modified vector control scheme to maximize motor efficiency at partial load. It determines the machine excitation that will provide the most favorable trade-off between copper losses and iron losses to achieve the highest possible efficiency under light-load conditions.

In FY 2006 the iron loss and magnet loss models were modified to extend the loss calculations to higher frequencies where skin effects alter the results. Plans call for this iron loss model to be

incorporated into the UWM FSCW-SPM machine design program. Point-by-point finite-element analysis (FEA) is being used to verify the iron loss predictions of the closed-form model whenever experimental test results are not available to provide this verification.

Major Accomplishments

1. Incorporated FreedomCAR targets to design and propose two 55-kW SPM motors with FSCWs for study in FY 2006. *SPM2* was selected for an analytical model comparison study. *SPM1* was selected for developing an analytical model to accurately predict the stator tooth and yoke iron losses in FSCW-SPM machines.
2. Modeled the *SPM2* motor with SPEED software and collaborated with UWM to compare design parameters calculated using SPEED's PC-BDC (brushless direct current) module with those calculated by UWM.
3. Created a rapid motor/inverter simulator using MatLab and checked its verity with time domain calculations using PSPICE software to show that the algorithms in the simulator are fast enough to use in a control circuit.
4. Successfully developed a closed-form analytical model that can accurately predict the stator tooth and yoke iron losses in FSCW-SPM machines during open-circuit operation. The status of this work will be included in this report.
5. Completed a detailed point-by-point FEA of FSCW-SPM machines that are proving very helpful in identifying the relative contributions of hysteresis and eddy-current losses in different parts of the machine as a function of rotor speed.
6. Developed three control schemes.
 - a. The UWM scheme controls to ensure maximum motor efficiency. It shows how motor losses under load may be sufficiently reduced by field weakening, which increases total current, to offset the additional I^2R losses and thereby improve motor efficiency. This work is described in this report.
 - b. The first ORNL scheme is a low-cost scheme because it eliminates current sensors. The ORNL simulator assumes losses that increase with the square of the speed.
 - c. The second ORNL scheme uses a set of antiparallel silicon-controlled rectifiers (SCRs) in each phase to ensure that any load is accommodated with minimum current, which ensures that it is a maximum overall efficiency scheme.
7. Performed a successful FEA-based verification of a significant efficiency improvement ($>5\%$ at some speeds) that can be achieved in FSCW-SPM machines by using the modified vector control algorithm during partial-load operating conditions.
8. Evaluated the first ORNL control scheme with the simulator for two constraints, first so that rated current is not exceeded and second so that rated power is not exceeded. The limiting current constraint allows considerably more power to be delivered over a large part of the power speed curve.

Technical Discussion

Benefit and Use of Concentrated Windings

Introduction

Until John Hsu began research on motors with flux generated by an external coil and then directed into the rotor to modulate or even replace conventional magnet flux,¹ most of ORNL's PM motor research centered on axial- and radial-gap PM motors with distributed windings with one slot per pole per phase. To operate these motors above base speed, where the back-electromotive force (back-emf) equals the source voltage, making it difficult to deliver power from the source, a technique known as phase advance² had to be used. This technique had limitations that could be overcome by adding antiparallel SCRs in each of the three phases thereby increasing the maximum speed but also slightly increasing the cost because of the additional components. This new control technique, called dual mode inverter control,³

was simulated using a “per-phase” model to show that the SCRs could be represented by a variable inductance.⁴ For PM motors, it has been recognized that one way to increase the maximum speed at which rated power is reached is to increase their inductance. A brute force way to do this was to add an inductor in each line, but a much better way would be to design the inductance into the motor itself. Designing the required inductance into the motor with distributed windings has been difficult as will be discussed later in this report.

In May 2004 an interim report prepared by UWM discussed significant benefits when a distributed winding is replaced by a concentrated winding.⁵ The primary benefit is that the inductance necessary to allow high speed operation may be easily designed into the motor. Other benefits included improved fault tolerance, improved slot utilization because stator segments can be bobbin wound to achieve a higher fill factor, easier assembly because the segments can be assembled after winding, and a large reduction in the volume of copper used in end windings.

In FY 2005 ORNL’s Power Electronics and Electric Machinery Research Center, in collaboration with UWM’s Prof. Tom Jahns and his student, Dr. Ayman M. El-Rafaie, investigated applications of concentrated windings for use in HEV and fuel cell permanent magnet (PM) traction drives. During FY 2005 a 6-kW motor was designed and tested up to 4000 rpm⁶ to validate the design procedure developed at UWM.⁷ ORNL, a member of the SPEED Consortium at the University of Glasgow in Scotland, modeled the 6-kW design using SPEED software, a detailed motor development tool. The results generally agreed well. In FY 2006 UWM designed a 55-kW traction drive which met the 2010 FreedomCAR targets.⁸ ORNL modeled the 55-kW motor, again getting good agreement except for the high speed magnet losses. During e-mail exchanges with the University of Glasgow we found that the algorithm used by SPEED does not consider skin effect, which would lead to increased resistance as the speed increases, and does not consider the effects of circumferential or axial magnet segmentation. The next release will use a 2-D finite-element program linked to a transient solver that produces files read by SPEED to calculate iron and magnet losses to solve the problem.

Distributed windings and concentrated windings

Technology for distributed stator windings has been around for 100 years and is well understood; consequently, it has long been the winding of choice for motor development. The amount of fundamental magnet flux linked by the stator winding coils determines the torque and power produced and is therefore the most important parameter of a PM motor. The reference winding that passes maximum flux is a distributed winding like the one shown in Figure 1(a). For each phase, full pitch coils bypass two slots for the other two phases. Two coils from adjacent poles are overlapped in one slot. This pattern is repeated for each pole and the coils are connected in series to complete the phase. The number of slots per pole per phase is 1. The back-emf is the algebraic rather than vector sum of each coil in a phase. An example of a concentrated winding similar to the one being investigated for use as an HEV traction motor is shown in Figure 1(b). Each coil winding is concentrated in two adjacent slots. After the first coil is wound in one direction, 4 slots are skipped, two for each of the other two phases, before the next concentrated coil is wound in the opposite direction to complete the stator pole pair. The 6-kW FSCW motor built and tested in FY 2005 and the 55-kW FSCW motor designed in FY 2006 have 36 slots and 30 pole pairs.

Winding function

The winding function is a representation of idealized stator coils. It is estimated from a process for counting conductors (personal communication between Professor Tom Jahns, UWM, and John McKeever, ORNL). First, Ampere’s law is applied along closed curves to determine $H_\phi(\theta)$ referenced to $H(0)$. Then Gauss’ law is applied to determine $H(0)$. All the wires are assumed to be at the center of the slot for convenience in analysis.

Both laws come from Maxwell’s equations:

$$\nabla \times H = J \text{ and } \nabla \cdot B = 0 \quad (1)$$

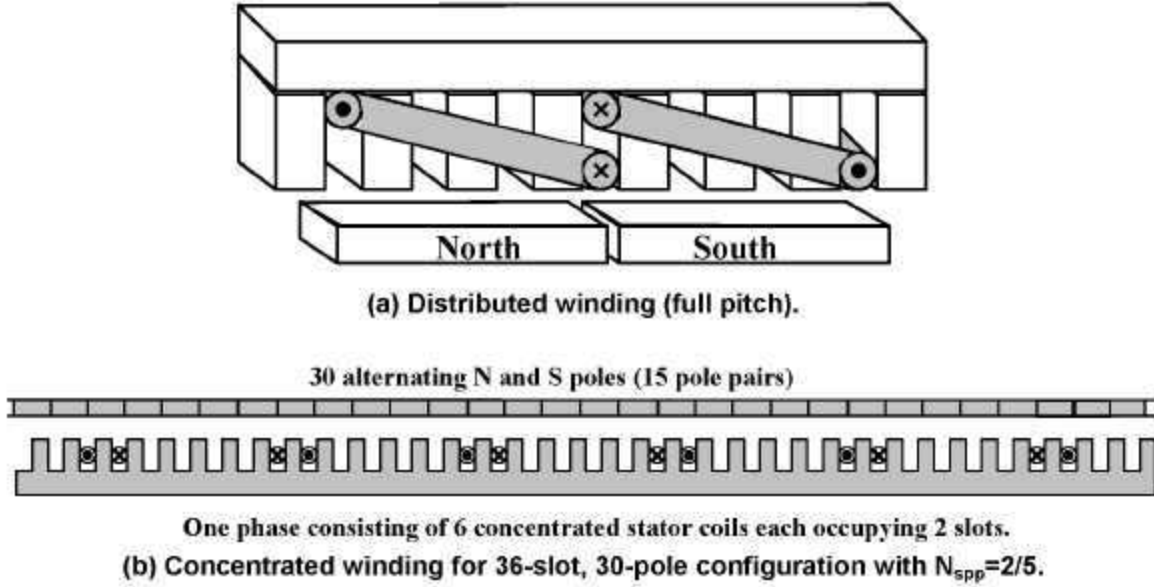


Figure 1. Distributed and concentrated windings.

Stokes' theorem is applied to the surface integral of the left equality in Equation (1), producing a line integral on the left and the product of the number of turns inside the surface times the current in the turns, which is expressed as

$$\oint H(\theta) \cdot d\mathbf{l} = n(\theta)i \quad (2)$$

The divergence theorem is applied to the volume integral on the right equality in Equation (1), which transforms the divergence of B over a volume to the integral of B over the surface of the volume, which says that the total flux crossing the surface sums to zero. This is expressed as

$$\int_{Surface} B \cdot d\mathbf{A} = \int_{Surface} \mu_o H(\theta) L_{stack} r_{gap} d\theta = 0 \quad (3)$$

where

r_{gap} is the radius of the gap,
 L_{stack} is the axial dimension of the rotor.

This technique is applied to a simple example shown in Figure 2.

The line integral of Equation (2) follows the contour abcd in the counterclockwise direction. Evaluation of the line integral in the stator or rotor is negligible because the value of μ , the magnetic permeability, is very large. Evaluation of the line integral in the gap where the value of μ is μ_o provides the primary contribution. Every line integral passes through H_{ref} , which is a constant whose value will be determined so that the total flux through the gap is zero. The direction of H_{ref} is arbitrarily chosen to be radial inward. The actual flux, which is proportional to $H(\theta)$, is radial inward and outward. The number of wires with current, i , encircled by the contour is expressed by $n(\theta)$. Wires with current into (minus) and out (plus) of the page are represented by the symbols "x" and "•," respectively. Contour integral evaluation is

$$H_{ref}g + H(\theta)g = n(\theta)i \quad (4)$$

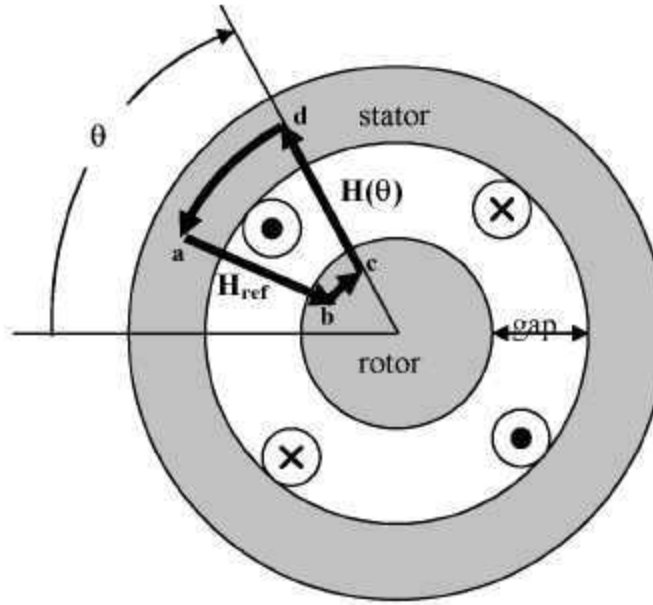


Figure 2. Calculation of the winding function for an idealized motor with a uniform gap.

where g is the gap between the rotor and stator.

This leads to

$$H(\theta) = \frac{n(\theta)i}{g} - H_{ref} \quad (5)$$

From Equation (3) it follows that

$$\oint_{\text{Surface}} B \cdot dA = \mu_0 r_{\text{gap}} L_{\text{stack}} \int_0^{2\pi} H(\theta) d\theta = 0 \quad (6)$$

Substituting the values from Equation (5) into Equation (6) leads to the value:

$$\int_0^{2\pi} \left[\frac{n(\theta)i}{g} - H_{ref} \right] d\theta = 0 \quad (7)$$

from which we get

$$H_{ref} = \frac{i}{g} \frac{1}{2\pi} \int_0^{2\pi} n(\theta) d\theta = \frac{i}{g} \overline{n(\theta)} \quad (8)$$

The bar over $n(\theta)$ denotes an average value. If we now substitute Equation (8) into Equation (5), we find that

$$H(\theta) = \frac{i}{g} [n(\theta) - \overline{n(\theta)}] = \frac{i}{g} N(\theta) \quad (9)$$

The term in brackets defines the winding function $N(\theta)$. From Equation (4), recall that $n(\theta)$ is the number of wires enclosed by the contour, counting wires into the page as minus and wires out of the page as plus. For the example shown in Figure 2, Figure 3(a) shows a plot of $n(\theta)$, the conductor count versus angle, and Figure 3(b) shows a plot of $N(\theta)$, the winding function.

The winding function indicates the regions in which flux would be produced by current in the conductors and the direction of the flux. None of the preceding discussion has mentioned the magnet pole pairs, which would be attached on the surface of the rotor to interact with the stator conductors. When p pole pairs are introduced, $N(\theta)$ determines the stator regions that link the magnets' flux. The motor's torque is determined by the flux linkages, which will be discussed shortly.

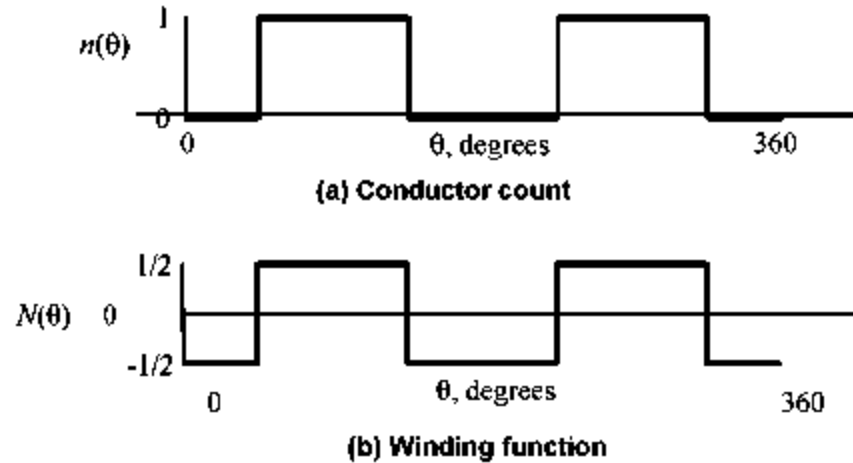


Figure 3. Relation between conductor count and winding function.

Winding factor

The winding function discussed in the previous section is related only to the number of slots and assumes that all of the conductors are placed at the midpoint of each slot to produce a square wave like the one shown in Figure 3(b). The winding factor, which is the subject of this section, is the ratio of actual flux links, ψ_{actual} , to the ideal flux links, ψ_{ideal} , across the gap. The flux links are proportional to the integral from 0 to 2π of the product of the winding function with the magnetic field. In this explanation the magnetic field is approximated by $B = B_{\text{max}} \cos(p\theta)$, where p is the number of magnet pole pairs. The actual and ideal winding functions are both expressed as Fourier series.

Recall that the form of the Fourier expansion is

$$N(\theta) = \sum_{n=1}^{\infty} a_n \cos(n\theta) + \sum_{n=1}^{\infty} b_n \sin(n\theta) \quad , \quad (10)$$

where

$$a_n = \frac{\int_0^{2\pi} N(\theta) \cos(n\theta) d\theta}{\pi} \quad \text{and}$$

$$b_n = \frac{\int_0^{2\pi} N(\theta) \sin(n\theta) d\theta}{\pi} \quad .$$

Figure 4 shows the actual winding function, which is a square wave positioned symmetrically so that only the coefficients of the cosine terms survive. The expansion of the actual concentrated winding function is

$$N_{actual}(\theta) = \sum_{n=1,3,5,\dots}^{\infty} a_n \cos(n\theta) \quad (11)$$

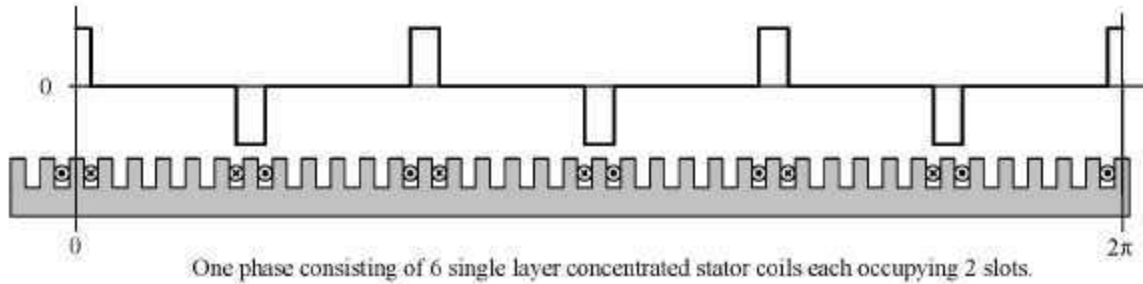


Figure 4. Winding function for the 36-slot, 30-pole concentrated winding being studied for possible use as a hybrid electric vehicle traction motor.

As an illustration, Fourier coefficients of the winding function for the concentrated winding in Figure 4 with $N(\theta) = \pm 1$ inside the coils and 0 elsewhere are shown in Table 1.

Table 1. Fourier coefficients of winding function for a stator with 36 slots

n	a_n	b_n	n	a_n	b_n	n	a_n	b_n
1	0	0	7	0	0	13	0	0
2	0	0	8	0	0	14	0	0
3	0.32954	0	9	0.30011	0	15	0.24597	0
4	0	0	10	0	0	16	0	0
5	0	0	11	0	0	17	0	0
6	0	0	12	0	0	18	0	0

The quantity, N_{spp} , which is the number of slots per pole per phase, is a useful design parameter. It provides the following useful relations for a three-phase winding with p equal to the number of magnet pole pairs and the $N_{slots/coil}$ equal to the number of slots per coil:

$$N_{coils/phase} = \frac{N_{spp}(2p)}{N_{slots/coil}} \quad ,$$

$$N_{slots} = N_{spp} 3(2p) \quad ,$$

$$N_{slots/phase} = N_{spp}(2p) \quad ,$$

and

$$N_{slots/pole} = N_{spp} 3 \quad .$$

Because an equivalent distributed winding with $N_{spp} = 1$ produces maximum flux links, it is used to estimate the ideal flux links used in the denominator of the winding factor. The six concentrated winding coils, N_{conc} , shown in Figure 4, are reconfigured with no change in coil dimension over one pole pair in the form of a distributed winding ($N_{spp} = 1$) as shown in Figure 5(a). N_{spp} is the number of slots per pole

per phase. When the magnetic field is symmetrically positioned within the coils, this is the configuration that has the maximum flux linkages as shown in Figure 5(b).

Equation (12) gives the ideal number of flux links for one pole pair and Equation (13) the actual number of flux links for the concentrated winding.

$$\Psi_{ideal} = L_{stack} \frac{N_{coils/phase}^{conc}}{2} 2 \int_0^{\pi/p} B_{max} \sin(p\theta) r_{gap} d\theta = [r_{gap} L_{stack} B_{max}] \frac{N_{coils/phase}^{conc}}{2} \frac{4}{p} \quad (12)$$

$$\Psi_{actual} = L_{stack} \int_0^{2\pi} \sum_{n=1,3,5,\dots}^{\infty} a_n \cos(n\theta) B_{max} \cos(p\theta) r_{gap} d\theta = [r_{gap} L_{stack} B_{max}] p \pi \quad (13)$$

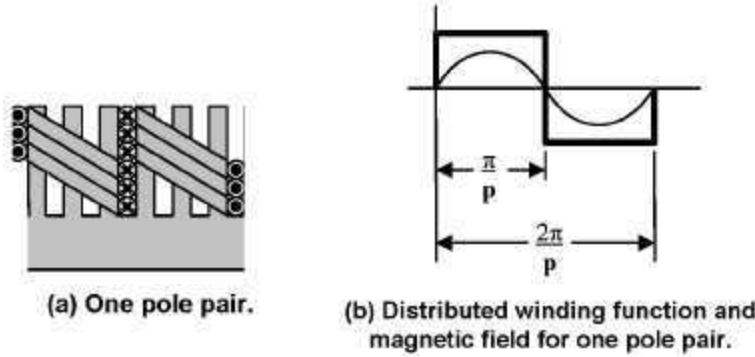


Figure 5. Redistribution of the coils from the concentrated winding shown in Figure 4 into an ideal distributed winding for a rotor with p pole pairs.

Noting that the Fourier coefficient, a_p , is a function of the number of slots, we find that the expression for the winding factor is

$$k_w(N_{slots}, p) = \frac{\Psi_{actual}}{\Psi_{ideal}} = \frac{a_p \pi}{2N_{spp}} \quad (14)$$

The winding factor for the concentrated winding with 36 slots and 15 pole pairs is

$$k_w(36, 15) = \frac{0.24597\pi}{2\frac{2}{5}} = 0.9659,$$

which indicates that this configuration, whose $N_{spp} = 2/5$, yields flux links close to the ideal value.

Concentrated winding (fluxmate) equivalent of a motor with distributed windings

The purpose of this section is to relate a distributed winding for which $N_{spp} = 1$ to a corresponding single layer concentrated winding and to quantify the amount by which the inductance of the concentrated winding is increased. $N_{spp} = 2/5$ for the corresponding concentrated winding being examined for use as an HEV traction motor. Another configuration that has the same winding factor has $N_{spp} = 2/7$. Equations will be used to illustrate how the concentrated winding may be used to design increased inductance into

an SPM motor. As $N_{spp} = 1$ for distributed windings, the quantity N_{spp} in the following equations will refer to the fractional value for the concentrated windings.

For the first step we start with a distributed winding with p magnetic pole pairs and $6p$ slots and determine the number of slots for the concentrated winding specified by its N_{spp} . The corresponding concentrated winding has $N_{slots}^{conc} = N_{spp}(6p)$ slots. For a distributed winding with $6p$ slots and 15 magnetic pole pairs, the corresponding concentrated winding with $N_{spp} = 2/5$ has 36 slots.

Next we ensure that the flux linking the coil for each phase is the same for the two configurations. For the distributed winding, the flux links in one phase are

$$\psi^{dist} = \int_0^{2\pi} \frac{N_{turns}^{dist}}{2} B_{max} [\cos(p\theta)] L_{stack} r_{gap} d\theta \quad (15)$$

The magnet flux is symmetrically positioned in the winding function so that the product of their signs results in the absolute value of the cos term. This may be evaluated with the integral

$$\psi^{dist} = 4p \int_0^{\frac{2\pi}{p}} \frac{N_{turns}^{dist}}{2} B_{max} L_{stack} r_{gap} \cos(p\theta) \frac{d(p\theta)}{p} = 2N_{turns}^{dist} B_{max} L_{stack} r_{gap} \quad (16)$$

For the concentrated winding, the flux links in one phase are

$$\psi^{conc} = \int_0^{2\pi} N_{turns}^{conc} \sum_{n=1,3,\dots}^{\infty} a_n \cos(n\theta) B_{max} \cos(p\theta) L_{stack} r_{gap} d\theta = N_{turns}^{conc} B_{max} L_{stack} r_{gap} \pi a_p \quad (17)$$

When Equation (16) is equal to Equation (17), the ratio of turns for the concentrated winding to the distributed winding is

$$\frac{N_{turns}^{conc}}{N_{turns}^{dist}} = \frac{2}{\pi a_p} \quad (18)$$

Equation (14) relates the value of a_p to the value of the winding factor. Also in Equation (14) the number of coils/phase for the concentrated winding, which is a single layer winding with $N_{slots/coil}^{conc} = 2$, is $N_{coils/phase}^{conc} = N_{spp} p$. From these relations, Equation (18) may be expressed as

$$\frac{N_{turns}^{conc}}{N_{turns}^{dist}} = \frac{1}{N_{spp} k_w} \quad (19)$$

For our study example, $N_{spp} = 2/5$ and $k_w = 0.9659$ yielding a ratio of 2.588. This value is also obtained from Equation (18) by using the value of a_{15} from Table I.

Next we discuss inductance and the relation between the inductance of distributed windings and that of concentrated windings. Inductance is the proportionality constant between the current flowing in one set of coils and the flux that it produces, which may link the coil producing the flux (self-inductance) or another coil (mutual inductance). The mutual inductance between phases for distributed windings is 1/3 the self-inductance because only 1/3 of any pair of coils from different phases overlap; however, the mutual inductance between phases of concentrated windings is zero because the concentrated winding

coils have no overlap. This may be seen by inspection of Figure 4 and with the addition of the other phase coils. No rectangle in one phase intersects a rectangle in another phase.

We shall consider the two main types of inductance in a PM motor, self-inductance and slot-leakage inductance. Self-inductance is related to flux that crosses the gap and interacts with the magnet. Slot-leakage inductance links wires in each slot but does not contribute to torque production. Both inductances are additive, producing the reactive impedance that must be overcome in the electrical circuit. End turn leakage inductance makes a much smaller contribution to the total inductance and is not included in this discussion. The following equations show the relationship between self-inductance and leakage inductance for the distributed and concentrated windings.

Self-Inductance

Self-inductance over one phase is

$$L_{self} = c \int_0^{2\pi} (N_{self}(\theta))^2 d\theta^2, \quad (20)$$

where $c = \mu_o r_{gap} L_{stack}/g$ and g is the gap between the magnets and the stator teeth. For the distributed winding function the value in parentheses in Equation (20) contributes a constant value, $\left(\frac{N_{turns}^{dist}}{2}\right)^2$, over an angular distance, $2\pi/p$, a total of p times, which by inspection is

$$L_{self}^{dist} = c \left(\frac{N_{turns}^{dist}}{2}\right)^2 \left[\frac{2\pi}{p}\right] \text{rad per pole } [p] \text{poles} = c (N_{turns}^{dist})^2 \frac{\pi}{2}. \quad (21)$$

For a concentrated winding, the value in brackets for Equation (20) contributes a constant value, $(N_{self}^{conc})^2$, over $1/3$ of the stator so that

$$L_{self}^{conc} = c (N_{turns}^{conc})^2 \left[\frac{\pi}{3}\right]. \quad (22)$$

The ratio of the inductance of the concentrated winding to that of the distributed winding is

$$\frac{L_{self}^{conc}}{L_{self}^{dist}} = \frac{2}{3} \frac{1}{[N_{spp} k_w]}. \quad (23)$$

For the concentrated winding of interest this ratio is 4.47.

Slot-leakage inductance

Slot-leakage inductance over one phase is

$$L_{slot_leakage} = \mu_o L_{stack} N_{spp} (2p) [N_{turns}]^2 \left[\frac{h_s^2}{3A_s} + \frac{d_2}{(b_o + w_s)/2} + \frac{d_1}{b_o} \right], \quad (24)$$

where the dimensions of the slot are shown in Figure 6. A_s is the area of the slot and r_s is the outer radius of the slot.

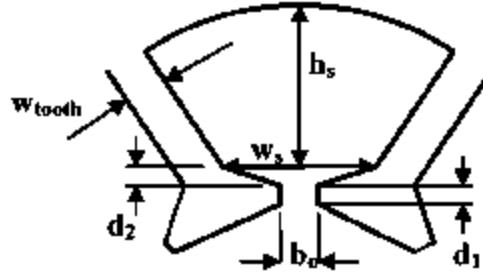


Figure 6. Definition of slot dimensions for inductance calculations.

The area of the slot is

$$A_s = \frac{\pi(r_s^2 - (r_s - h_s)^2)}{N_{spp} 3(2p)} - h_{tooth} w_{tooth} \quad (25)$$

Flux is carried by all teeth adjacent to a pole and is channeled in both directions in the back iron. The tooth width is chosen to be wide enough to prevent saturation. Its width is given by

$$w_{tooth} = \frac{2w_{back_iron}}{3N_{spp}} \quad (26)$$

where $3N_{spp}$ is the number of slots per magnet pole to carry the flux. The fact that the back iron handles half the flux is described by the equation

$$w_{back_iron} = \frac{\phi_g}{2B_{max} L_{stack}} \quad (27)$$

The final equation for the width of the tooth is

$$w_{tooth} = \frac{\phi_g}{3N_{spp} B_{max} L_{stack}} \quad (28)$$

which leads to the ratio for the width of a tooth in a concentrated winding to the width of a tooth in a distributed winding:

$$\frac{w_{tooth}^{conc}}{w_{tooth}^{dist}} = \frac{1}{N_{spp}} \quad (29)$$

Using Equation (29) with Equation (25) and a similar procedure for the slot's arc radius, we find that both the ratio of the slot area in a concentrated winding to the slot area in a distributed winding and the ratio of the slot arc width in a concentrated winding to the arc width in a distributed winding are the same:

$$\frac{A_s^{conc}}{A_s^{dist}} = \frac{1}{N_{spp}} = \frac{w_{slot}^{conc}}{w_{slot}^{dist}} \quad (30)$$

When these relations are substituted into Equation (24) for the slot leakage of the concentrated winding and for the distributed winding, the ratio of the two inductances is

$$\frac{L_{slot_leak}^{conc}}{L_{slot_leak}^{dist}} = \left[\frac{1}{k_w} \right]^2 \frac{\left[\frac{h_s^2}{3A_s^{dist}} + \frac{d_2 2}{(N_{spp} b_o + w_s^{dist})} + \frac{d_1}{N_{spp} b_o} \right]}{\left[\frac{h_s^2}{3A_s^{dist}} + \frac{d_2 2}{(b_o + w_s^{dist})} + \frac{d_1}{b_o} \right]} \quad (31)$$

The value of $1/(k_w)^2$ is 1.07. The ratio of the terms in brackets shows that the $N_{spp} b_o$ term has the effect of reducing the effective slot width. Using the parameters $h_s = 25.4$ cm, $A_s^{dist} = 125$ mm, $w_s^{dist} = 4$ mm, $d_2 = 3$ mm, $d_1 = 3$ mm, and $b_o = 2$ mm, which represent the slot of the 55-kW motor with concentrated windings being studied, we find that the three terms in the upper right bracket of Equation (31) are $1.72 + 1.25 + 3.75$, and the three terms in the lower right bracket are $1.72 + 1.0 + 1.5$. The ratio is 1.59, caused by the impact that N_{spp} has on the effective slot opening, b_o . The ratio of the bracketed terms cannot be ignored. The contribution of the slot opening to the slot-leakage inductance is large. For the example under study, the ratio of concentrated to distributed slot-leakage inductances is

$$\frac{L_{slot_leak}^{conc}}{L_{slot_leak}^{dist}} = 1.07 \times 1.59 = 1.70 \quad (32)$$

The total inductance is the sum of the self-inductance and slot-leakage inductance. From Equations (23) and (31), the total inductance is

$$L_{total} = \frac{2}{3} \left[\frac{1}{N_{spp} k_w} \right]^2 L_{self}^{dist} + \frac{1}{k_w^2} L_{slot_leak}^{dist} \quad (33)$$

which for the case of interest is $L_{total} = 4.47 L_{self}^{dist} + 1.70 L_{slot_leak}^{dist}$; clearly showing the increase in inductance from the concentrated windings—mainly in the self-inductance, but also in the slot-leakage inductance.

Finally, we examine the larger slot area of the concentrated winding, which has a fill factor of 0.7 compared to 0.5 for a distributed winding, to see whether it can accommodate the larger number of turns. First recognize that the useable area of the slot for the distributed winding is $A_{useable}^{dist} = 0.5 A_s^{dist}$ and that the useable area of the slot for the concentrated winding is $A_{useable}^{conc} = 0.7 A_s^{conc} = 0.7 \frac{A_s^{dist}}{N_{spp}}$. The ratio of useable areas is

$$\frac{A_{useable}^{conc}}{A_{useable}^{dist}} = \frac{1.4}{N_{spp}} \quad (34)$$

which for the case of interest is 3.5, meaning that the slot in the concentrated winding can handle 3.5 times the number of turns in the slot of the distributed winding. This will work because the number of distributed turns from Equation (19) must be multiplied by 2.588 to have the same flux links. In fact, only a small improvement in fill factor from 0.5 to 0.5176 will allow the desired 2.588 useable area ratio.

Analysis and Design of Motors with Fractional-Slot Concentrated Windings

Design of an FSCW HEV traction drive motor

A summary of the FreedomCAR targets shown in Table 2 was incorporated by UWM and ORNL to scale the design of a 6-kW FSCW motor built and tested in FY 2005⁶ to 55-kW for use as an HEV traction drive motor.⁸ The design is a 36 slot-30 pole configuration built from six repeating units, each having six slots and five poles, which can be wound separately and then assembled into the final stator for ease of manufacturing (Figure 7). At the same time, the fractional-slot concentrated winding develops sufficient inductance to allow the required CPSR of 5 from base speed of 2000 rpm to top speed of 10,000 rpm.

Table 2. FreedomCAR traction motor targets

Requirement	Target specification
Minimum top speed [rpm]	10,000
Peak power at 20% of max speed for 18 s and nominal voltage [kW]	55
Continuous power at 20 to 100% of maximum speed and nominal voltage [kW]	30
Battery operating voltage [V_{dc}]	Nominal: 325 Range: 200 to 450
Maximum current at motor [A_{rms}]	400
Characteristic current [A_{rms}]	< Max current
Efficiency at 10 to 100% of max speed rated power	>93%
Efficiency at 10 to 100% of max speed for 20% of rated torque	>93%
Torque pulsations—not to exceed at any speed [% of peak torque]	<5
Peak power to weight ratio for active materials [kW/Kg]	>2.75
Peak power to volume ratio for active materials [kW/liter]	>12.5

UWM has developed its own software design methodology⁷ while ORNL has used the SPEED software from Motorsoft. The design parameters have been developed using the UWM software and verified using SPEED software. The motor as sketched by the SPEED software in Figure 8 consists of six of the segments shown in Figure 7. There are some differences, including the following.

1. SPEED has 30 turns per phase of AWG #19 wire with each turn consisting of 47 conductors and a fill factor of 70%, whereas UWM fills each slot with copper at the same fill factor.
2. SPEED uses ARNON 7 for the laminations, while UWM uses a general lamination model.⁹
3. The present version of SPEED does not consider skin effects nor does it allow segmentation in the circumferential direction, while UWM segments each magnet circumferentially into five pieces.⁸

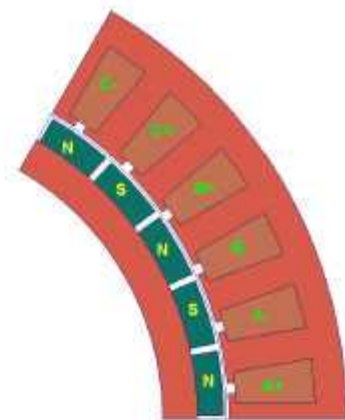


Figure 7. Cross-section of the basic repeating unit of the 55-kW (peak), 36-slot 30-pole (2/5 s/p/ph) SPM2 machine design.

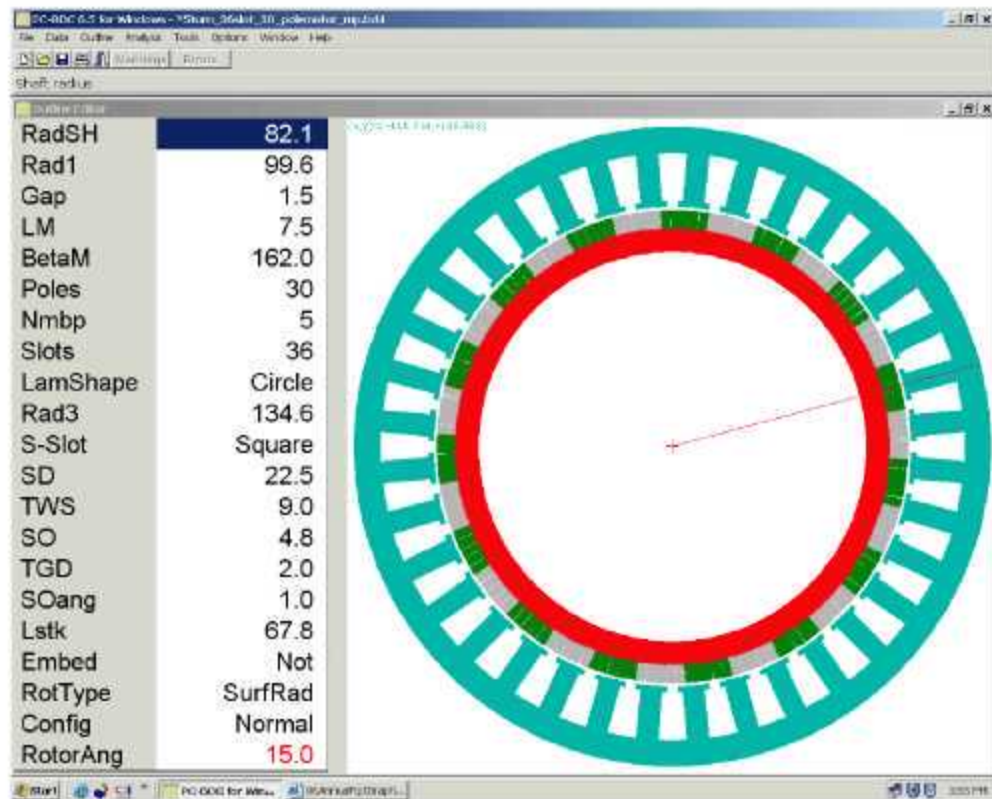


Figure 8. SPEED rendition of the 36-slot, 30-pole SPM2 with concentrated windings.

A comparison of the results of the two programs is shown in Table. 3.

Table 3. Comparison of UWM and ORNL design parameters for the proposed 55 kW (PEAK) SPM

Design parameter	UWM	ORNL	Remarks
Inductance, [μ h]			
Self	25.5	29	
Slot	41	40	
End	—	4	
Total	66.5	73	
Phase resistance, [mohms]	4.9	4.15	
Fundamental magnet flux linkages [mWebers]	17.5	18.42	
Characteristic current [A_{rms}]	264	252	
Line-to-line back-emf [V_{rms}]	120	124	@ 2000 rpm
Rated current [A_{rms}]	230	181	
Current density [A_{rms}/mm^2]	6.7	5.9	
Base speed efficiency [%]	93	97	@ 2000 rpm
Top speed efficiency [%]	92	87.7	@ 10,000 rpm
Core loss [W]	1676	206	@ 2000 rpm
Armature loss [W]	780	309	@ 2000 rpm
Magnet loss [W]	1288	882	@10000 rpm
Mass [kg]			
Iron	10.3	11.1	
Copper	8.8	4.6	
Magnet	2.2	2.1	
Total	17.3	17.8	

The most significant difference between the two design calculations is the losses. The two methods are explained in the next section.

Core loss calculations

Core loss data from steel suppliers is almost always sinusoidal data and may be characterized by the Steinmetz equation with separate terms for hysteresis and eddy current losses:

$$P = C_h f B_{pk}^n + C_e f^2 B_{pk}^2, \quad (35)$$

where

- P is the power per unit mass, W/kg,
- B_{pk} is the peak flux density, T,
- f is the frequency, Hz,
- C_h is the hysteresis loss coefficient,
- C_e is the eddy current loss coefficient.

The exponent, n , is often assumed to be 1.6 to 1.8 but varies some with B_{pk} and SPEED allows a linear variation in the form $n = a + b B_{pk}$, in which both a and b should be positive.

The flux density in motor laminations may be far from sinusoidal. SPEED uses a modified Steinmetz equation

$$P = C_h f B_{pk}^{a+b B_{pk}} + C_{el} \left| \frac{dB}{dt} \right|^2. \quad (36)$$

The hysteresis loss component is unchanged, but the eddy-current component is taken to be proportional to the mean squared value of dB/dt over one cycle of the fundamental frequency. SPEED programs apply Equation (36) in the respective sections of the magnetic circuits after calculating the relevant flux-density waveforms.

The eddy current loss coefficient, C_{el} , in the modified form can be derived from the sine wave coefficient, C_e , if we assume that Equation (36) is true when $B = B_{pk} \sin(2\pi f t)$. If so, then

$$\left| \frac{dB}{dt} \right|^2 = 4(\pi f B_{pk})^2 \cos^2(2\pi f t) \text{ whose mean value is } \left| \frac{dB}{dt} \right|^2 = 2(\pi f B_{pk})^2. \text{ For the sine wave flux density,}$$

Equations (35) and (36) give the same result if $C_{el} = \frac{C_e}{2\pi^2}$. The loss coefficients in the SPEED program

have names related to the quantities in Equation (36) as shown in Table 4. The core losses versus speed for ARNON 7 laminated steel are shown in Table 5.

Table 4. Speed software loss equation coefficient definitions

Name in design program	Name in Equation (36)
C/C_h	C_h
Cfa	a
Cfb	b
C/C_e	C_{el}

Table 5. Core losses for ARNON 7 laminations in the 55-kW FSCW-SPM motor

RPM	Loss, W
2000	206
4000	577
6000	1113
8000	1814
10,000	2681

The UWM core loss method follows that of Mi, Slemon, and Bonert.⁹ UWM uses a revised approximate model for tooth eddy-current loss. For an m-phase PM motor with q slots per pole per phase, there are mq slots per pole. The time, Δt , required for the magnet to pass one tooth is

$$\Delta t = T \frac{I}{m2q}, \quad (37)$$

where

T is the time for a pole pair to pass a slot pitch, which is $2\pi/\omega_{\text{elect}}$,

m is the number of phases,

$2q$ is the number of slots per pole pair,

ω_{elect} is the electrical rotational speed of the rotor, rad/s.

Under linear trapezoidal assumptions of the waveforms, the time rate of tooth flux change is

$$\frac{dB}{dt} = \frac{B_{\text{tooth}}}{\Delta t}. \quad (38)$$

The change of tooth flux density occurs four times per time period, T . The average eddy current loss density in the teeth can now be expressed as

$$P_{\text{eddy_current}} = 2k_e \left(\frac{dB_{\text{tooth}}}{dt} \right)^2 = 2k_e \left(\frac{B_{\text{tooth}}}{\Delta t} \right)^2 \left(\frac{4\Delta t}{T} \right) = 16k_e mq \left(\frac{B_{\text{tooth}}}{T} \right)^2. \quad (39)$$

Multiplying by the number of phases and expressing T in terms of the electrical frequency we obtain the expression,

$$P_{\text{eddy_current}} = 12k_e q \left(\frac{\omega_{\text{elect}} B_{\text{tooth}}}{\pi} \right)^2. \quad (40)$$

From Equation (39) it can be seen that the eddy current loss is proportional to the number of slots per pole.

The equation for the eddy current losses in the teeth used by UWM⁷ is

$$p_{el} = \frac{4m}{\pi^2} q k_q k_r k_e (\omega_e B_{tooth})^2, \quad (41)$$

where

k_q is the motor geometry correction factor,

k_r is a correction factor to account for the contribution of the circumferential component,⁹

k_e is the eddy current constant that depends on the lamination material.

The value of flux density in the tooth is estimated by the equation

$$B_{th} = \frac{w_t + w_s}{w_t} B_{gap}^{pk}, \quad (42)$$

where B_{gap}^{pk} is the peak air gap magnetic flux density. Its value is estimated by

$$B_{gap}^{pk} = \frac{V_{ag}^{rms} P}{\sqrt{2} R_s L_{stack} k_{wj} \omega_e}, \quad (43)$$

where

w_t is the tooth width,

w_s is the slot width,

V_{ag}^{rms} is the rms air gap voltage supply,

k_{wj} is the fundamental winding factor,

ω_e is the electrical frequency in rad/s.

The corresponding equation for the eddy current losses in the yoke is

$$p_{ey} = \frac{l}{\alpha} \frac{8}{\pi^2} k_s k_r (\omega_e B_y)^2, \quad (44)$$

where α is the ratio of the magnet span to the pole pitch, B_y is the peak magnetic flux in the stator yoke, and

$$k_r = 1 + \frac{8 k_q d_y^2}{27 \alpha q \lambda_2^2}, \quad (45)$$

where d_y is the stator yoke thickness and λ_2 is the projected slot pitch at the middle of the yoke.

Tooth hysteresis loss and yoke hysteresis loss can be expressed as a function of the maximum flux density in each area. In the teeth the hysteresis loss density is

$$p_{ht} = k_h \omega_{elect} B_{th}^\beta. \quad (46)$$

In the yoke the hysteresis loss density is

$$p_y = k_h \omega_{elect} B_{yk}^\beta \quad (47)$$

These are the forms used by UWM.

Magnet loss calculations

The magnet loss algorithm in the SPEED software does not account for the effect of skin depth on magnet loss. A finite-element transient solver has been added to the SPEED software package for its next release. Output from the new package has been provided for ORNL's 55-kW FSCW motor by SPEED's technical support at the University of Glasgow in Scotland. That output is shown in Figures 9 through 13.

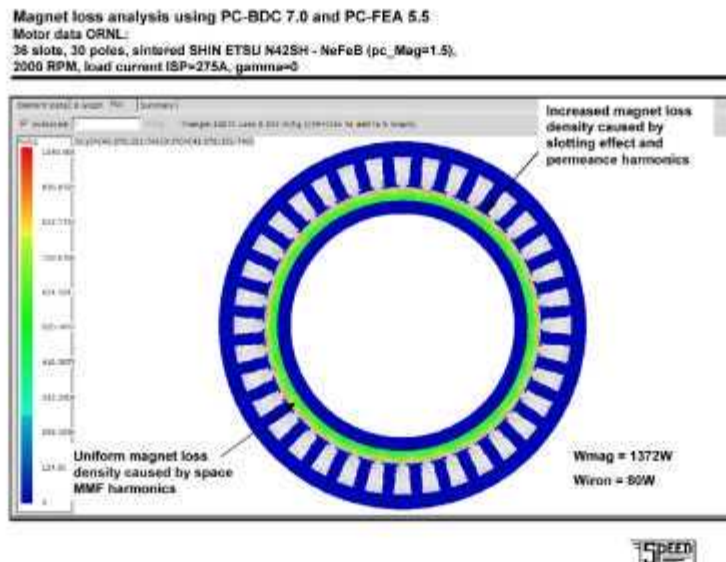


Figure 9. Magnetic loss at 2,000 rpm. (The motor is drawing 275 A ISP under load. Losses are the result of space harmonics, slotting, and permeance. At 2000 rpm the electrical frequency is 500 Hz.)

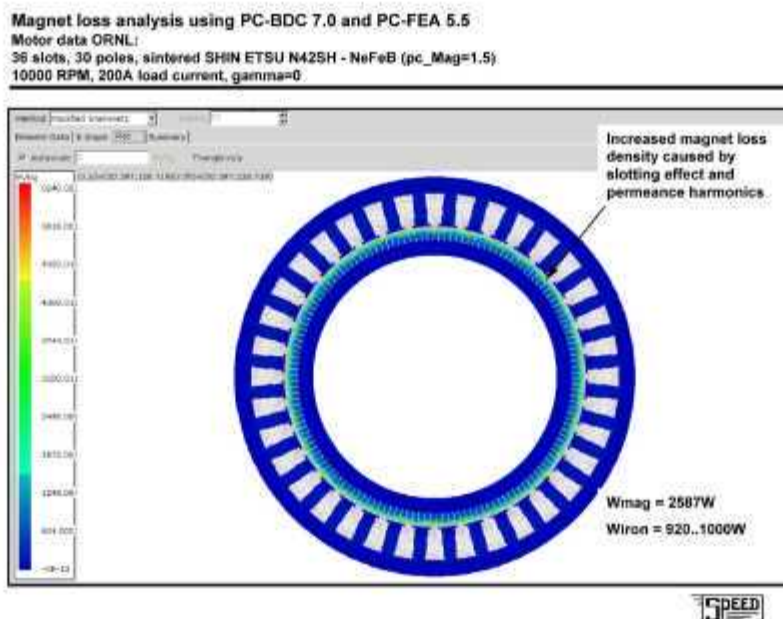


Figure 10. Magnet loss at 10,000 rpm.

Magnet loss analysis using PC-BDC and PC-FEA

Motor data ORNL:

36 slots, 30 poles, sintered SHIN ETSU N42SH - NeFeB (pc_Mag=1.5), On load

• Magnets skin depth penetration per space MMF harmonics [mm]

NOTE: LM (length of magnet slot along the magnetization direction) = 7.5mm

$$\delta = \frac{1}{\sqrt{\pi f \sigma \mu}}$$

MMF Harmonic order	2000 RPM/275A Skin depth [mm]	10000 RPM/200A Skin depth [mm]
5	10.53	4.70
7	8.90	3.98
11	7.10	3.17

At lower speed, i.e. 2000RPM:

- the eddy-current losses determined by the space MMF harmonics within the magnets are mainly resistance limited;
- the eddy-current losses determined by slotting effect and permeance variation within the magnets are mainly resistance limited, but with important inductance influence from the higher harmonics – transient solver is necessary

At higher speed, i.e. 10000RPM:

- the eddy-current losses determined by slotting effect and permeance variation within the magnets are essentially inductance limited;
- the eddy-current losses determined by space MMF harmonics within the magnets are essentially inductance limited – transient solver is necessary

**Figure 11. Effect of speed on skin depth penetration.****Theory**

- Use PC-BDC i-psi GoFER, Elements table
- Assumptions:
 - A series of magnetostatic (for resistance limited cases) or transient (for inductance limited) solutions in PC-FEA contains the A-values step-by-step
- Calculate losses using $dA/dt = (A[k] - A[k-1])/\Delta t$ $J_e = \sigma \frac{\partial A}{\partial t}$
- We can also use Fourier decomposition of A $J_e = -\sigma \sum_1^N (n \omega c_n \sin(n \omega t - \varphi))$
- PC-BDC plots the loss density, the waveforms of B, A and Je in each mesh element
- Use for estimation of losses in the magnets and any retaining cans

**Figure 12. Approach taken by SPEED to determine skin depth penetration.**

Theory

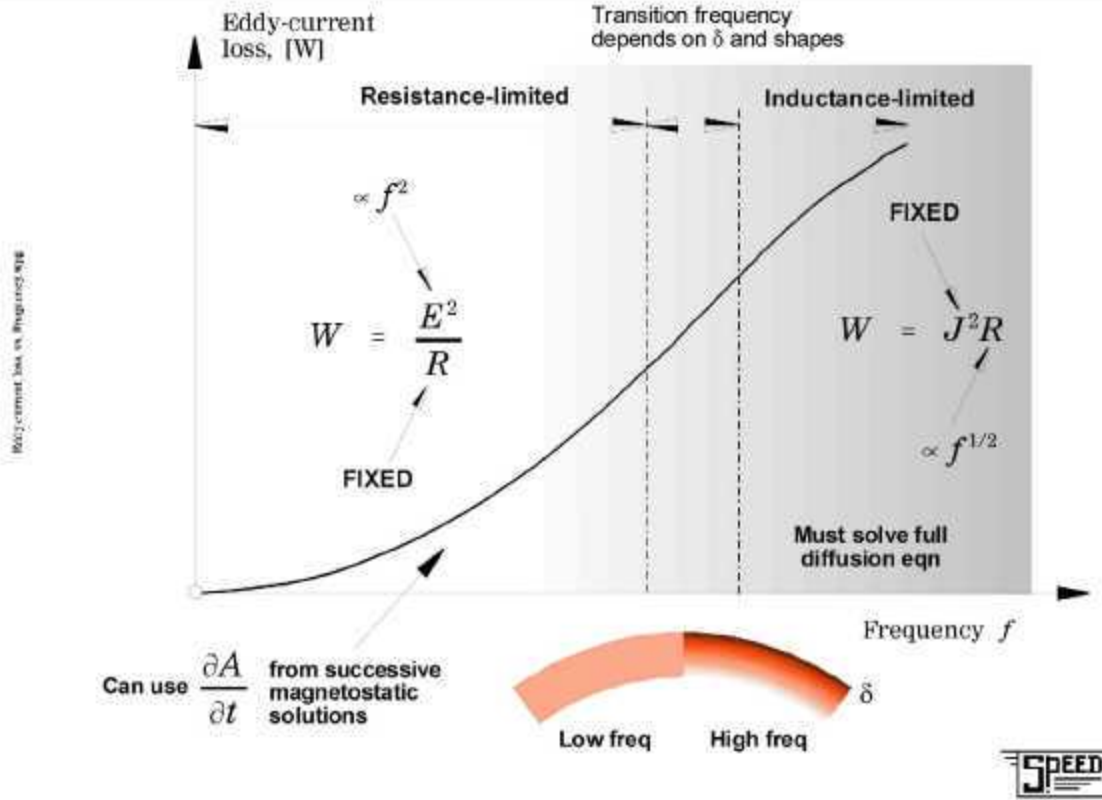


Figure 13. The effect of frequency on magnetic losses.

While the speed has increased fivefold, the loss has increased by a factor of about 2. This is because of the skin effect, shown in Figure 11.

UWM has almost the same procedure as shown in Figures 12 and 13 except for the addition of skin depth penetration. Figure 13 shows that skin effect lowers the magnet loss at high frequencies. This explains why the UWM magnet loss at 10,000 rpm in Table 6 is higher than the value obtained by SPEED.

The procedure used by UWM¹⁰ characterizes the stator winding as a current sheet in the rotor reference. The time dependent expression for current density in the sheet in terms of the angle, θ_r , in the rotor is

$$\begin{aligned}
 J_s(\theta_r, t) &= \frac{q}{2} \sum_n J_n \cos(np_s \theta_r + (np_s - mp_r)\Omega t) \text{ for } n = qk + m, \\
 J_s(\theta_r, t) &= \frac{q}{2} \sum_n J_n \cos(np_s \theta_r + (np_s + m^* p_r)\Omega t) \text{ for } n = qk - m, \\
 J_s(\theta_r, t) &= 0 \text{ for } n \neq qk \pm m,
 \end{aligned} \tag{48}$$

where

- q is the number of phases,
- $m = -1$ when $N_{spp}=2/5$ and $+1$ when $N_{spp}=2/7$,
- $k = 0, 1, 2, 3, 4, 5, \dots$,
- p_s is the number of stator pole pairs,

p_r is the number of rotor pole pairs,
 n is the summation index, which is not even for a cosine expansion like the one in Equation (9).
 Ω is the rotational speed of the rotor, radians/second.

The value of J_n is

$$J_n = \frac{2N_s I_{pk}}{\pi R_s} k_{wn} \quad (49)$$

where

N_s is the number of turns in series per phase,
 I_{pk} is the peak phase current,
 R_s is the radius of the current sheet,
 k_{wn} is the n^{th} winding factor.

The expression for the n^{th} winding factor is

$$k_{wn} = \frac{\left| 1 - \exp \left(j \frac{2\pi n}{N_{sphase}} \right) \right|}{2} \quad (50)$$

where N_{sphase} is the number of slots per phase.

Table 6 presents the magnet losses calculated by the MatLab program listed in Table 7. Table 8 is a presentation of output from the SPEED calculation for the 36-slot, 30-pole motor delivering 30 kW at 2000 rpm. Table 9 is a presentation of output from the SPEED calculation for the same motor delivering 55 kW at 10,000 rpm.

Summary of Design Analysis

In summary, the 55-kW design has been compared for two design methodologies and all differences have been resolved leading to a viable design for an HEV traction drive motor. The 55-kW motor was designed with 30 poles according to the developed design process. With this knowledge, there is mounting evidence that FSCW motors with low pole and slot count can be feasible in some cases and are worthy of further investigation.

Table 6. Magnet losses for a 36-slot, 30-pole 55-kw FSCW-SPM motor

Angular speed, rpm	Loss from Atallah equations ¹⁰ used by UWM, W	Loss calculated by Popescu at SPEED Consortium scaled by current ratio, W
2000	256	898
1018	1018	
2291	2291	
4073	4073	
6364	6364	1693

Table 7. MatLab program to calculate magnet losses

```

%Calculating Magnet Losses in case of SPM machines equipped with concentrated windings
clear all
close all
clc
m=-1; %m=1 in case of 2/7 S/P/Ph %m=-1 in case of 2/5 S/P/Ph
q=3; %Number of phases
Ps=3; %Number of stator pole pairs
Pr=15; %Number of rotor pole pairs
Mu_0=4*pi*10^(-7);
Rho_mg=1.5*10^(-6); %Resistivity of the magnet material sintered magnets, Ω-m
%Rho_mg=20*10^(-6); %Resistivity of the magnet material bonded magnets, Ω-m
Alpha_p=0.95; %Ratio of magnet span to pole pitch
N_segments=1; %Number of magnet segments/pole
Alpha=2*pi*Alpha_p/(2*Pr*N_segments);
% Rs=0.1031; %Stator outer radius
% Rr=0.0993; %Rotor outer radius
% Rm=0.1025; %Magnet outer radius
Rs=0.1346; %Stator outer radius
Rr=0.0921; %Rotor outer radius
Rm=0.0996; %Magnet outer radius
n=1; %Space harmonic order
Ns=30; %Number of series turns per phase
Irms=180;
Im=Irms*sqrt(2); %Peak phase current
Kwn=abs(1-1*exp(sqrt(-1)*150*(n/5)*pi/180))/2;
Jn=(2*Ns*Im/(1*pi*Rs))*Kwn;
speed=2*pi*10000/60; %Rotor speed in rad/sec
leff=0.0678; % Machine active length [m]
if n*Ps==1
    Fn=log(Rm/Rr);
else
    Fn=((Rm/Rr)^(2*n*Ps+2)-1)/(-2*n*Ps+2);
end
Pcn=((q^2*Mu_0^2*Alpha/(8*Rho_mg))*((Jn^2/(n^2*Ps^2))*((n*Ps-m*Pr)^2*speed^2*...
    ((Rm/Rs)^(2*n*Ps))*((Rs^2*Rm^2)/(2*n*Ps+2))*((1-(Rr/Rm)^(2*n*Ps+2))...
    +((Rr/Rs)^(2*n*Ps))*Rs^2*Rr^2*Fn+((Rr/Rs)^(2*n*Ps))*Rs^2*(Rm^2-Rr^2))...
    / (1-((Rr/Rs)^(2*n*Ps)))^2);
if n*Ps==2
    Gn=log(Rm/Rr);
else
    Gn=((Rm/Rr)^(-1*n*Ps+2)-1)/(-1*n*Ps+2);
end
Pan=(-q^2*Mu_0^2/(Alpha*Rho_mg))*((Jn^2/(n^4*Ps^4))*((n*Ps+m*Pr)^2*speed^2*...
    ((Rm/Rs)^(n*Ps))*((Rs*Rm^2/(n*Ps+2))*((1-(Rr/Rm)^(n*Ps+2))...
    +((Rr/Rs)^(n*Ps))*Rs*Rr^2*Gn)^2 ...
    * (sin(n*Ps*Alpha/2))^2/(Rm^2-Rr^2)*(1-(Rr/Rs)^(2*n*Ps))^2);
P=(Pcn+Pan)*leff
P_magnet=P*N_segments*2*Pr

```

Table 8. SPEED design sheets for FSCW-SPM motor delivering 30 kW at 2000 rpm

PC-BDC 6.5 for Windows (6.5.2.8) 9/15/2006 3:58:41 PM
 c:\program files\speed\magnet dbm\5turn_36slot_30_polemotor_mp.bd4
 UT-Battelle LLC
 PC-BDC main title
 PC-BDC sub-title

1 Dimensions:-----

RotType	SurfRad	Embed	Not	Poles	30
Stator..					
StatorOD	269.200 mm	LamShape	Circle	Slots	36
SYoke	11.000 mm	ASD	22.500 mm	SP	1.200
Rad3	134.600 mm	Rad2	123.600 mm	S-Slot	Square
TWS	9.000 mm	SD	22.500 mm	SO	4.800 mm
TGD	2.000 mm	SOang	1.000 mDeg	Stf	0.970
Rotor..					
MOH	0.000 mm	Nmbp	5	Skew	0.000
RotorOD	199.200 mm	Rad1	99.600 mm	Gap	1.500 mm
LM	7.500 mm	BetaM	162.000 eDeg	pupa	0.900
RYoke	10.000 mm			RadSH	82.100 mm
DHub	184.200 mm	wNeck	0.386 mm		
MEdge	7.500 mm	LM_min	7.500 mm		
wMag	3.755 mm				
Lstk	67.800 mm	Lrotor	67.800 mm	Lstator	76.800 mm

2 Magnet Data:-----

Magnet	SHIN-ETSU N42SH-nd-fe-Br Magnet				
Br	1.000 T	Hc	955.000 kA/m	MuRec	1.050
CBr	-0.100 %/DegC	CHc	-0.540 %/DegC	DMag	7600.000 kg/m3
BrT	1.004 T	HcT	975.628 kA/m		
Nuisance	0.000 mm	BrTnu	1.004 T	MuRecnu	1.050

3 Control Data:-----

RPM	2000.000 rpm	Vs	292.500 V	Drive	Sine
ISP	255.500 A	gamma	0.000 deg	Sw_Ctl	ISP_HB
HBA_act	ISP/300	HB%	0.333	HBtype	Constant
FixfChop	No	fChop	0.000 kHz	fChopAct	598.000 kHz
EMFCalc	BLV	dq0	false		
Vq	0.000 V	Rq	0.000 ohm	Vd	0.600 V
t_q	0.000 us			Freq1	500.000 Hz
ISP_Act	255.500 A	Tol_Act	ISP/20	ISLA_Act	1/128

4 Winding Data:-----

Connex	Wye				
WdgType	Custom				
Offset	8	CPP	0.200		
Tph	30.000	PPATHS	1	SPP	0.400
Layers	1.000	CSidesPh	12	Z	180.000
MLT	187.393 mm	LgthOEnd	84.286 mm	Ext	0.000 mm
EndFill	0.500	LaxPack	87.399 mm	Liner	0.200 mm
WireSpec	AWGTable	Gauge	19		
NSH	47	WireDia	0.912 mm	InsThick	0.000 mm
SFg	0.695	SFn	1.093	MaxSFn	1.093
Aslot	220.890 mm^2	ASlotLL	208.410 mm^2	ACond	30.693 mm^2

Table 8. SPEED design sheets for FSCW-SPM motor delivering 30 kW at 2000 rpm (continued)

GPAslot	230.490 mm ²	ATstick	0.253 mm ²	TopStick	false
TwjWid	2.000 mm	TwjLeg	3.500 mm	TwjThk	0.000 mm
PhsWid	2.000 mm	PhsLeg	3.500 mm	PhsThk	0.000 mm
ATwj	0.000 mm ²	APhs	0.000 mm ²		
XET	1.000	ETCalc	BDC 6.0	Rext	0.000 ohm
Nse	36.896	X_R	1.000	Ax1	15.000 mDeg
T_Wdg	100.000 DegC	Rph0	4.150E-03 ohm	R_LL	8.301E-03 ohm
T_c	20.000 DegC	Rph	3.158E-03 ohm/ph	TFRho	1.000
Inductances...					
Lph	0.073 mH	Mph	0.000 mH	XL	1.000
Lg	0.029 mH	LSlot	0.040 mH	Lendt	4.449E-03 mH
Mg	0.000 mH	MSlot	0.000 mH	LDiff	0.024 mH
Lsigma	0.068 mH	Msigma	2.639E-03 mH	XLdiff	1.000
Lgg	0.133 mH	Mgg	0.000 mH	PCSlot	1.551
LL_d	0.147 mH	LL_q	0.147 mH	L_LL	0.147 mH
Lg_0	5.279E-03 mH	Lg_2	2.059E-05 mH	Laa_d	0.073 mH
Ld	0.073 mH	Lq	0.073 mH	Laa_q	0.073 mH
Xd	0.230 ohm/ph	Xq	0.230 ohm/ph	Xsigma	0.205
ohm/ph					
XCd	1.000	XCq	1.000	Lext	0.000 mH
Gd	0.177	Gq	0.176	XLendt	1.000
kw1	0.966	Xm0	0.141 ohm/ph		
ks1	1.000	kpl	1.000	kd1	1.000
keg	0.182	fz	1.133	PSSlot	S-Closed
Saliency	Auto	CalcLdLq	Auto	muPlug	1.000
i1_Ang	2.023 A	i2_Ang	-222.394 A	i3_Ang	220.371 A

5 Magnetic Circuit Design:

T_Mag	100.000 DegC	T_r	16.000 DegC	XBrT	1.000
BrT	1.004 T	BgOC	0.898 T	Hca	760.912 kA/m
BgAvOC	0.676 T	PhiG	0.964 mWb	BgA/BgOC	0.753
Bg1OC	0.964 T	PhiM1	0.874 mWb	Bg1/BgOC	1.073
BmOC	0.828 T	Bm/BrT	0.825	XBtpk	1.000
HmOC	-133.421 kA/m	Hm/HcT	-0.137	PC	4.938
Bst	1.474 T	Bsy	0.666 T	Bry	0.711 T
XTw	0.000	XSyoKe	0.000	XRYoke	0.000
kT	0.570 Nm/A	kE	0.641 Vs/Rad	krpmNL	4.679 krpm
kSat	1.000	XSatn	1.000	CalcSatn	Fixed
SatnTol	0.000				
Xks	0.000	ks	0.000	XTTarc	1.000
EffWst	9.000 mm	EffLst	20.410 mm	ukCL	0.000
XBgap	1.000	X_EMF	1.000	k_rpf	1.000
Btpk_OC	1.508 T	Btpk_Ld	1.541 T	Btpk_LdS	1.541 T
Bypk_OC	0.661 T	Bypk_Ld	0.961 T	Bypk_LdS	0.961 T
eLLpk	134.285 V	eTmax	2.277 V	Belot	4.879E-03 T
IBk	2853.421 A	Bk	0.000 T	Hk	-760.912 kA/m
ILR	46315.717 A	BmLR	-15.255 T	HmLR	-1.23E+04 kA/m
IC180	67578.987 A	BmC180	-22.718 T	HmC180	-1.80E+04 kA/m
BHmag	110.467 kJ/m3	Carter	1.027	Xrm	0.500
Amhp	612.481 mm ²	Aghp	641.236 mm ²	Rghp	1.912E+06 At/Wb
Pm0	0.108 uWb/At	Xrl	1.000	prl	0.256
apEnd	1.000	Pend	0.000	Lme	7.500 mm
u_LKG	0.000	f_Lkg	0.950	if_Lkg	1.053
Fringing	ON	XPringe	1.000	XBetaM	1.000
SlotMod	No	XSlotMod	1.000		

**Table 8. SPEED design sheets for FSCW-SPM motor delivering 30 kW at 2000 rpm
(continued)**

7 Dynamic design (time-stepping simulation):-----

OpMode	Motoring	Vs	292.500 V	RPM	2000.000 rpm
Tshaft	143.249 Nm	Pshaft	30001.993 W	Eff	97.384 %
WCu	309.103 W	WFe	256.306 W	WWP	0.000 W
WCan	0.000 W	WMagnet	240.576 W	WShaft	0.000 W
WTotal	805.984 W	TempRise	0.000 DegC	Jrms	5.885
A/mm^2					
IWpk	255.948 A	IWav	162.624 A	IWrms	180.637 A
ILpk	255.948 A	ILav	162.623 A	ILrms	180.637 A
IQchpk	255.951 A	IQchav	58.267 A	IQchrm	108.823 A
IQcmpk	255.951 A	IQcmav	58.267 A	IQcmrm	108.823 A
IDchpk	255.927 A	IDchav	23.050 A	IDchrm	66.884 A
IDcmpk	255.927 A	IDcmav	23.050 A	IDcmrm	66.884 A
IDC_W	105.652 A	WConv	82.979 W	EffDCSh	97.122 %
IDC_P	105.610 A	WSwitch	0.000 W	Pelec	30807.978 W
Tgap	145.621 Nm	Tei	145.622 Nm	Trel	-0.001 Nm
Tloop	145.617 Nm	WFeCalc	OC	CalcVwfm	None
Virms	0.000 V	Ilrms	180.635 A	phi_1	-0.739 deg
phV1	90.000 deg	phI1	90.739 deg	phEq1	90.247 deg
Vld	0.000 V	Ild	-2.329 A		
Vlg	0.000 V	Ilg	180.651 A		

8 Steady-State Thermal Model:-----

TempCalc	DegCW	FixTMag	IterX	Ambient	20.000 DegC
DegCW	0.000 degC/W	HTCyl	0.000 W/m2/C	HTCend	0.000
W/m2/C					
TempRise	0.000 DegC	T_c	20.000 DegC	T_r	16.000 DegC
T_f	20.000 DegC	T_y	20.000 DegC	HeatFlux	3.980
kW/m^2					
SlotPeri	57.597 mm	Liner	0.200 mm	ct_Liner	0.200 W/mC
SSArea	3905.110 mm^2	C_motor	17.751 kJ/C	ThRSlot	7.113E-03 C/W
FSArea	2.025E+05 mm^2	ThermTC	0.000 min	R_fa	0.000 C/W

9 Miscellaneous:-----

Weights...					
wt_Cu	4.602 kg	wt_Fe	11.154 kg	wt_Mag	2.095 kg
wt_Tot	17.851 kg	wt_Shaft	13.310 kg	wt_Frame	2.880 kg
wt_FeS	8.313 kg	wt_FeR	2.841 kg	wt_RSS	18.496 kg
Inertia components...					
RotJ	0.086 kg-m2	RotJSS	0.088 kg-m2	RotJSh	0.045 kg-m2
RotJFe	0.022 kg-m2	RotJMag	0.019 kg-m2	LShaft	80.000 mm
sigma	4.997 psi				
Wf0	0.000 W	RPM0	1000.000 rpm	NWFT	1.000
Fringing	ON	XFringe	1.000	NHx	21
CanStyle	None				
Ecc	0.000	UMPavg	-6.11E-15 kg	UMPmax	-4.31E-15 kg
TRFrms	21.667 kg	TRFavg	17.038 kg	TRFmax	37.738 kg
CForce	29.935 kg			LamThk	0.500 mm
NLams	132	pcLam	3.000 %	RFe1	1.000E+06

10 Core loss analysis:-----

WFeCalc	OC	LossFE	Mech	XFe	1.000
---------	----	--------	------	-----	-------

Table 8. SPEED design sheets for FSCW-SPM motor delivering 30 kW at 2000 rpm (continued)

DFekgS	7656.829	kg/m ³	St.Steel	Arnon 7	3.25% Si		
DFekgR	7656.829	kg/m ³	Ro.Steel	Arnon 7	3.25% Si		
DFekgSh	7857.007	kg/m ³	Sh.Steel	Low Carbon Steel	26g		
wt_Teeth	3.820	kg	wt_Yoke	4.493	kg	wt_Troot	0.897 kg
Specific core losses...							
cFe_E50	0.192	W/kg	cFe_H50	3.176	W/kg	cFe_50	3.368 W/kg
cFe_E_F	19.182	W/kg	cFe_H_F	31.758	W/kg	cFe_F	50.941 W/kg
cFe_T_E	17.299	W/kg	cFe_T_H	29.856	W/kg	cFe_T	47.155 W/kg
cFe_Y_E	3.405	W/kg	cFe_Y_H	4.134	W/kg	cFe_Y	7.539 W/kg
Core loss analysis...							
WFe_T_E	81.600	W	WFe_T_H	140.832	W	WFe_T	222.432 W
WFe_Y_E	15.299	W	WFe_Y_H	18.574	W	WFe_Y	33.873 W

End of Design sheet-----

Table 9. SPEED design sheets for FSCW-SPM motor delivering 55 kW at 10,000 rpm

PC-BDC 6.5 for Windows (6.5.2.8) 9/29/2006 10:41:46 AM
 c:\program files\speed\magnet dbm\Sturn_36slot_30_polemotor_mp.bd4
 UT-Battelle LLC
 PC-BDC main title
 PC-BDC sub-title

1 Dimensions:-----

RotType	SurfRad	Embed	Not	Poles	30
Stator..					
StatorOD	269.200 mm	LamShape	Circle	Slots	36
SYoke	11.000 mm	ASD	22.500 mm	SP	1.200
Rad3	134.600 mm	Rad2	123.600 mm	S-Slot	Square
TWS	9.000 mm	SD	22.500 mm	SO	4.800 mm
TGD	2.000 mm	SOang	1.000 mDeg	Stf	0.970
Rotor..					
MOH	0.000 mm	Nmbp	5	Skew	0.000
RotorOD	199.200 mm	Rad1	99.600 mm	Gap	1.500 mm
LM	7.500 mm	BetaM	162.000 eDeg	pupa	0.900
RYoke	10.000 mm			RadSH	82.100 mm
DHub	184.200 mm	wNeck	0.386 mm		
MEdge	7.500 mm	LM_min	7.500 mm		
wMag	3.755 mm				
Lstk	67.800 mm	Lrotor	67.800 mm	Lstator	76.800 mm

2 Magnet Data:-----

Magnet	SHIN-RTSU N42SH-nd-fe-Br Magnet				
Br	1.000 T	Hc	955.000 kA/m	MuRec	1.050
CBR	-0.100 %/DegC	CHc	-0.540 %/DegC	DMag	7600.000 kg/m3
BrT	0.920 T	HcT	542.440 kA/m		
Nuisance	0.000 mm	BrThu	0.920 T	MuRecnu	1.050

3 Control Data:-----

RPM	10000.000 rpm	Vs	292.500 V	Drive	Sine
ISP	325.000 A	gamma	77.500 deg	Sw_Ctl	ISP_HB
HBA_act	ISP/300	HB%	0.333	HBtype	Constant
FixfChop	No	fChop	0.000 kHz	fChopAct	0.000 kHz
EMFCalc	BLV	dq0	false		

**Table 9. SPEED design sheets for FSCW-SPM motor delivering 55 kW at 10,000 rpm
(continued)**

Vg	0.000 V	Rg	0.000 ohm	Vd	0.600 V
t _g	0.000 us			Freq1	2500.000 Hz
ISP_Act	325.000 A	Tol_Act	ISP/20	ISLA_Act	1/128
4 Winding Data:-----					
Connex	Wye				
WdgType	Custom				
Offset	8	CPP	0.200		
Tph	30.000	PPATHS	1	SPP	0.400
Layers	1.000	CSidesPh	12	Z	180.000
MLT	187.393 mm	LgthOEnd	84.286 mm	Ext	0.000 mm
EndFill	0.500	LaxPack	87.399 mm	Liner	0.200 mm
WireSpec	AWGTable	Gauge	19		
NSH	47	WireDia	0.912 mm	InsThick	0.000 mm
SFg	0.695	SFn	1.093	MaxSFn	1.093
ASlot	220.890 mm ²	ASlotLL	208.410 mm ²	ACond	30.693 mm ²
GPASlot	230.490 mm ²	ATstick	0.253 mm ²	TopStick	false
TwjWid	2.000 mm	TwjLeg	3.500 mm	TwjThk	0.000 mm
PhsWid	2.000 mm	PhsLeg	3.500 mm	PhsThk	0.000 mm
ATwj	0.000 mm ²	APhs	0.000 mm ²		
XET	1.000	ETCalc	BDC 6.0	Rext	0.000 ohm
Nse	36.896	X_R	1.000	Ax1	15.000 mDeg
T _{wdg}	100.000 DegC	Rph0	4.150E-03 ohm	R_LL	8.301E-03 ohm
T _c	100.000 DegC	Rph	4.150E-03 ohm/ph	TFRho	1.314
Inductances:-----					
Lph	0.073 mH	Mph	0.000 mH	XL	1.000
Lg	0.029 mH	LSlot	0.040 mH	Lendt	4.449E-03 mH
Mg	0.000 mH	MSlot	0.000 mH	LDiff	0.024 mH
Lsigma	0.068 mH	Msigma	2.639E-03 mH	XLdiff	1.000
Lgg	0.133 mH	Mgg	0.000 mH	PCSlot	1.551
LL_d	0.147 mH	LL_q	0.147 mH	L_LL	0.147 mH
Lg_0	5.279E-03 mH	Lg_2	2.059E-05 mH	Laa_d	0.073 mH
Ld	0.073 mH	Lq	0.073 mH	Laa_q	0.073 mH
Xd	1.152 ohm/ph	Xq	1.151 ohm/ph	Xsigma	1.027 ohm/ph
XCd	1.000	XCq	1.000	Lext	0.000 mH
Gd	0.177	Gq	0.176	XLendt	1.000
kw1	0.966	Xm0	0.704 ohm/ph		
ks1	1.000	kp1	1.000	kdi	1.000
ksg	0.182	fz	1.133	PSSlot	S-Closed
Saliency	Auto	CalcLdLq	Auto	muPlug	1.000
i1_Ang	-174.622 A	i2_Ang	324.691 A	i3_Ang	-150.068 A
5 Magnetic Circuit Design:-----					
T_Mag	100.000 DegC	T_r	100.000 DegC	XBrT	1.000
BrT	0.920 T	BgOC	0.829 T	Hca	697.250 kA/m
BgAvOC	0.624 T	PhiG	0.889 mWb	BgA/BgOC	0.753
BgIOC	0.890 T	PhiM1	0.807 mWb	Bg1/BgOC	1.073
BmOC	0.764 T	Bm/BrT	0.831	XBtpk	1.000
HmOC	-117.999 kA/m	Hm/HcT	-0.218	PC	5.154
Bst	1.361 T	Bsy	0.615 T	Bry	0.656 T
XTW	0.000	XSyoce	0.000	XRYoke	0.000
kT	0.526 Nm/A	kE	0.592 Vs/Rad	krpmNL	5.069 krpm
kSat	1.000	XSatn	1.000	CalcSatn	Fixed
Xks	0.000	ks	0.000	XTarc	1.000
EffWst	9.000 mm	EffLst	20.410 mm	ukCL	0.000
XBgap	1.000	X_EMF	1.000	k_rpf	1.000
eLLpk	619.807 V	eTmax	10.508 V	Bslot	2.052E-03 T

Table 9. SPEED design sheets for FSCW-SPM motor delivering 55 kW at 10,000 rpm (continued)

IBk	2614.688 A	Bk	0.000 T	Hk	-697.250 kA/m
ILR	35237.155 A	BmLR	-11.450 T	HmLR	-9375.134 kA/m
IC180	1.099E+05 A	BmC180	-37.658 T	HmC180	-2.92E+04 kA/m
BHmag	90.187 kJ/m3	Carter	1.027	Xrm	0.500
Amhp	612.481 mm ²	Aghp	641.236 mm ²	Rghp	1.912E+06 At/Wb
Pm0	0.108 uWb/At	Xrl	1.000	prl	0.256
apEnd	1.000	Pend	0.000	Lme	7.500 mm
u_LKG	0.000	f_Lkg	0.950	if_Lkg	1.053
Fringing	ON	XFringe	1.000	XBetaM	1.000

6 Sine-wave static design [phasor diagram]:-----

OpMode	Motoring	Vs	292.500 V	RPM	10000.000 rpm
Tshaft	28.683 Nm	Pshaft	30036.330 W	Eff	76.255 %
WCu	657.587 W	WFe	2681.160 W	WWF	0.000 W
WCan	0.000 W	WMagnet	6014.394 W	Jrms	7.487 A/mm ²
WTotal	9353.141 W	TempRise	80.000 DegC	IWrms	229.810 A
IWpk	325.000 A	IWav	206.900 A	ILrms	229.810 A
ILpk	325.000 A	ILav	206.900 A	Pelec	39389.470 W
IDC_P	134.665 A	WFeCalc	OC	VLL1	100.788 V
Eq1	259.780 V	Vph1	58.190 V	gamma	77.500 deg
Iq1	49.740 A	Id1	-224.362 A	delta	88.435 eDeg
Vq1	1.589 V	Vd1	-58.168 V	PF	0.982
BglLoad	0.794 T	phi	10.935 eDeg	Phiqa1	0.019 mWb
Bgad	0.000 T	Phida1	-0.087 mWb	Fda1	-585.342 At/gap
BmLoad	0.679 T	Bma	-0.085 T	Trel_PS	-0.031 Nm
Tgap_PS	36.986 Nm	TEI_PS	37.017 Nm	Trel	-0.031 Nm
Tgap	36.986 Nm	Tei	37.017 Nm		
Tloop	36.986 Nm				
Available voltage...					
Vs120	197.507 Vrms	Vs1	228.061 Vrms	Vs1Lin	179.119 Vrms

8 Steady-State Thermal Model:-----

TempCalc	DegCW	FixTMag	IterX	Ambient	20.000 DegC
DegCW	0.000 degC/W	HTCcyl	0.000 W/m2/C	HTCend	0.000 W/m2/C
TempRise	80.000 DegC	T_c	100.000 DegC	T_r	100.000 DegC
T_f	100.000 DegC	T_y	100.000 DegC	HeatFlux	0.000 kW/m ²
SlotPeri	57.597 mm	Liner	0.200 mm	ct_Liner	0.200 W/mC
SSArea	3905.110 mm ²	C_motor	17.751 kJ/C	ThRSlot	7.113E-03 C/W
FSArea	2.025E+05 mm ²				

9 Miscellaneous:-----

Weights...

wt_Cu	4.602 kg	wt_Fe	11.154 kg	wt_Mag	2.095 kg
wt_Tot	17.851 kg	wt_Shaft	13.310 kg	wt_Frame	2.880 kg
wt_FeS	8.313 kg	wt_FeR	2.841 kg	wt_RSS	18.496 kg

Inertia components...

RotJ	0.086 kg-m2	RotJSS	0.088 kg-m2	RotJSh	0.045 kg-m2
RotJFe	0.022 kg-m2	RotJMag	0.019 kg-m2	LShaft	80.000 mm
sigma	1.269 psi				
Wf0	0.000 W	RPM0	1000.000 rpm	NWFT	1.000
Fringing	ON	XFringe	1.000	NHx	21
CanStyle	None				
Ecc	0.000	UMPavg	-9.64E-16 kg	UMPmax	1.166E-14 kg
TRFrms	18.464 kg	TRFavg	14.519 kg	TRFmax	32.158 kg
CForce	748.387 kg			LamThk	0.500 mm
NLams	132	pcLam	3.000 %	RPei	1.000E+06

Table 9. SPEED design sheets for FSCW-SPM motor delivering 55 kW at 10,000 rpm (continued)

10 Core loss analysis:-----					
WFeCalc	OC	LossFE	Mech	XFe	1.000
DFekgS	7656.829 kg/m ³	St.Steel	Arnon 7 3.25% Si		
DFekgR	7656.829 kg/m ³	Ro.Steel	Arnon 7 3.25% Si		
DFekgSh	7857.007 kg/m ³	Sh.Steel	Low Carbon Steel 26g		
wt_Teeth	3.820 kg	wt_Yoke	4.493 kg	wt_Troot	0.897 kg
Specific core losses...					
cFe_E50	0.192 W/kg	cFe_H50	3.176 W/kg	cFe_50	3.368 W/kg
cFe_E_F	479.560 W/kg	cFe_H_F	158.791 W/kg	cFe_F	638.350 W/kg
cFe_T_E	368.532 W/kg	cFe_T_H	113.605 W/kg	cFe_T	482.137 W/kg
cFe_Y_E	72.541 W/kg	cFe_Y_H	18.015 W/kg	cFe_Y	90.556 W/kg
Core loss analysis...					
WFe_T_E	1738.393 W	WFe_T_H	535.885 W	WFe_T	2274.278 W
WFe_Y_E	325.937 W	WFe_Y_H	80.945 W	WFe_Y	406.882 W
End of Design sheet-----					

Differences between the results of UWM and SPEED have been resolved. Such differences, which concern magnet losses, are because of the skin effect at higher speeds and are essentially inductance limited at higher speeds. These results emphasize the necessity of circumferentially segmenting the magnets and do not detract from the results of El Refaie, Jahns, and McKeever.⁸

Speed Control of Fractional-Slot Concentrated Winding PM Motors

A wide and theoretically infinite CPSR can be achieved with a PM synchronous motor if the winding inductance is sufficiently large.¹¹⁻¹³ Recent work at UWM⁶ has shown that winding inductance of FSCW-SPM machines can easily be made sufficiently large to achieve satisfactory CPSR performance. Electric/hybrid electric vehicles require not only wide CPSR operation but also high efficiency. While CPSR performance can be resolved through proper machine design using FSCW technology, the efficiency of traction drives can depend on how they are controlled. Of particular concern is the efficiency of the traction drive when operating at fractional load conditions. In the present work the effect of control on the efficiency of the overall drive system and on the efficiency of the motor alone is considered.

Introduction

At ORNL investigators have analyzed the requirements of a speed control scheme whose objective is to minimize the motor current magnitude at all operating conditions.¹³ Below base speed, in the constant torque operating mode, a traction drive with this type of control maximizes the motor shaft torque (Nm) produced per amp of motor current. Above base speed in the constant power operating mode, this type of control maximizes the power (watts) per amp of motor current. During FY 2006 the ORNL team developed a closed-loop speed control for an FSCW machine which implements motor current magnitude minimization. A 6-kW, 30-pole, FSCW motor developed by UWM, FSCW-1, is to be tested using the closed-loop speed control system developed by ORNL and drive/motor efficiency will be determined experimentally. Details of the speed control and test setup and procedures are described below.

In companion work, investigators at UWM have shown that minimum motor current control does not necessarily ensure maximum motor efficiency.¹⁴ Their work showed that, for a specific FSCW design, a blend of maximum torque per amp and maximum torque per volt control may improve overall motor efficiency by reducing motor core losses.¹⁴ In the light load condition cited in the reference, the motor current magnitude for maximum motor efficiency was approximately three times larger than for the maximum torque per amp control at the same condition. The overall reduction in core losses was sufficient to overcome a ninefold increase in motor copper losses. Because loss mechanisms in the inverter are approximately linear in motor current magnitude, it is not clear whether the maximum motor

efficiency condition will also result in maximum overall system efficiency. The testing of the 6-kW FSCW prototype may be extended to study whether the minimum motor current control or minimum motor loss control has the best overall system efficiency. Further details of the UW maximum motor efficiency control concept are contained in the section entitled “Enhanced Partial Load Efficiency Control Algorithm.”

Parameters of the 6-kW prototype FSCW motor

The 6-kW FSCW prototype was laboratory tested by ORNL to determine the values of key machine parameters and to characterize speed dependent zero current losses. The winding resistance, inductance, and fundamental back-emf constant are

$$\begin{aligned} R &= 0.075 \, \Omega \text{ per phase} \\ L &= 1.2 \text{ mH per phase} \\ K_v &= 0.05494 \text{ volts per rpm} \\ &\quad (49.45 \text{ V rms at 900 rpm}) \end{aligned} \tag{51}$$

The zero current speed sensitive losses are shown in Figure 14. The figure shows data points taken from dynamometer measurements and a least squares fit to the experimental data. Dynamometer measurements were taken only up to 4000 rpm, which is the highest speed at which the 6-kW prototype has been driven, but the least squares fit predicts losses of 1867 W at 6000 rpm. The ORNL model of motor losses includes only speed sensitive effects.

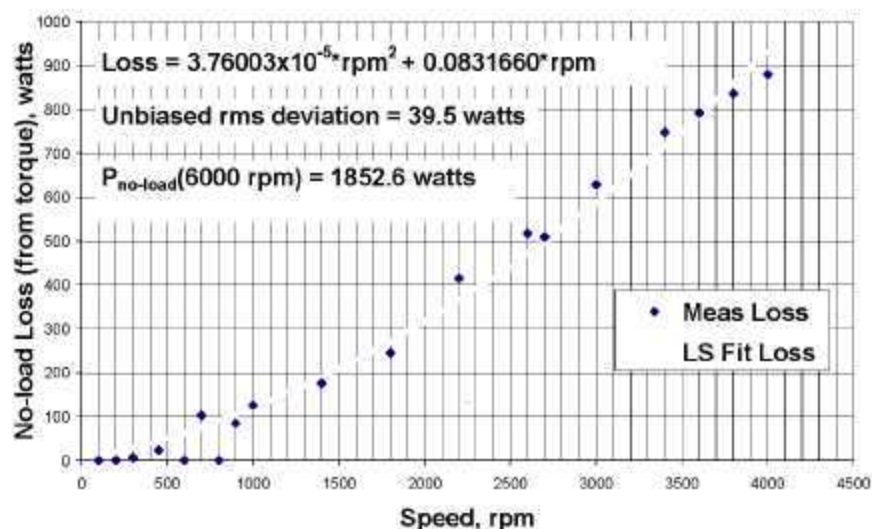


Figure 14. Zero current losses of the FSCW-1 prototype.

The prototype machine has 30 poles, a base speed of 900 rpm, and a rated output power of 6 kW. Let “subscript b,” b , denote “at base speed” and let n denote speed relative to base speed. Then the reactance of the winding inductance and magnitude of the back-emf at base speed and at any relative speed, n , are given by the following:

$$\begin{aligned} p &= 30 \text{ poles,} \\ N_b &= 900 \text{ rpm,} \end{aligned}$$

N = speed in rpm.

$$n = \frac{N}{N_b} = \text{normalized speed,}$$

$\Omega_b = 1413.7$ electrical radians/second,

$X_b = \Omega_b L = 1.6965$ Ohms reactance at base speed,

$X = nX_b$ reactance at relative speed, n , and

$E = nE_{b\text{back}}$ —emf magnitude at relative speed, n .

Let “subscript capital R,” R , denote “rated” values so that rated useful average output power and rated rms motor current are

$$\begin{aligned} P_R &= 6,000 \text{ W} \\ \text{and} \quad I_R &= \frac{P_R}{3E_b} = 40.44 \text{ A rms} \end{aligned} \quad (52)$$

The minimum dc supply voltage necessary to support rated power at base speed for this motor is given by

$$V_{dc-\min} = \pi \sqrt{\frac{(E_b + RI_R)^2 + (X_b I_R)^2}{2}} = 192 \text{ V} . \quad (53)$$

Simplified Per-Phase Model

ORNL has used simplified per phase models with considerable success to study the performance of PM machine drives with either trapezoidal or sinusoidal back-emf wave shapes. The per-phase model represents only the fundamental frequency component response of the machine; consequently, some factors such as torque ripple cannot be studied while using this simplification. In general the fundamental frequency component dominates the motor current response and accurately preserves power. The main advantage of the simplified fundamental frequency model is that it eliminates the need for simulating the pulse-width modulation (PWM) switching actions. Although the effects of switching are not explicit in this model, it was recently extended to predict all of the inverter loss mechanisms.¹³ The model is shown in Figure 15. This model was used extensively in the development of the closed-loop control schemes described below.

Closed-loop speed control system for FSCW PM traction motors

An objective in the development of the closed-loop speed control was to have low complexity and minimum use of sensors. The control structure selected is a proportional speed control (Figure 16). The speed command, labeled as “spdcmd” in the figure, is processed through a simple gain, K_s in the figure, and the actual speed is subtracted to form a speed error. The speed error is multiplied by a gain, K_e in the figure, and the output is a desired rms motor current, I_d . The desired current is processed through a saturation function whose upper limit is the specified rms current rating of the motor, I_R , and whose lower limit is zero because a negative rms value makes no physical sense. The output of the saturation function is the commanded rms current, I_{crmt} . This commanded current and the measured instantaneous shaft speed and position are all that are required in this controller to generate inverter commands. It is presumed that sinusoidal PWM control will be used to generate inverter switching commands;

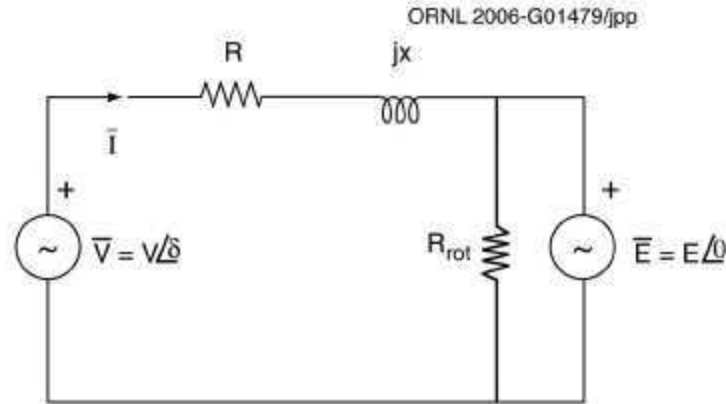


Figure 15. Fundamental frequency model of a permanent magnet motor driven by a pulse-width modulation controlled voltage source inverter.

consequently, the required control variables are the amplitude modulation index, denoted as M_a , and the inverter lead angle, δ . Values of M_a between 0 and 1 are referred to as the linear modulation region. In this region the rms value of the fundamental frequency component of the line-to-neutral voltage applied to the motor is given by

$$V_1 = \frac{M_a V_{dc}}{2\sqrt{2}} \text{ for } 0 \leq M_a \leq 1 \quad (54)$$

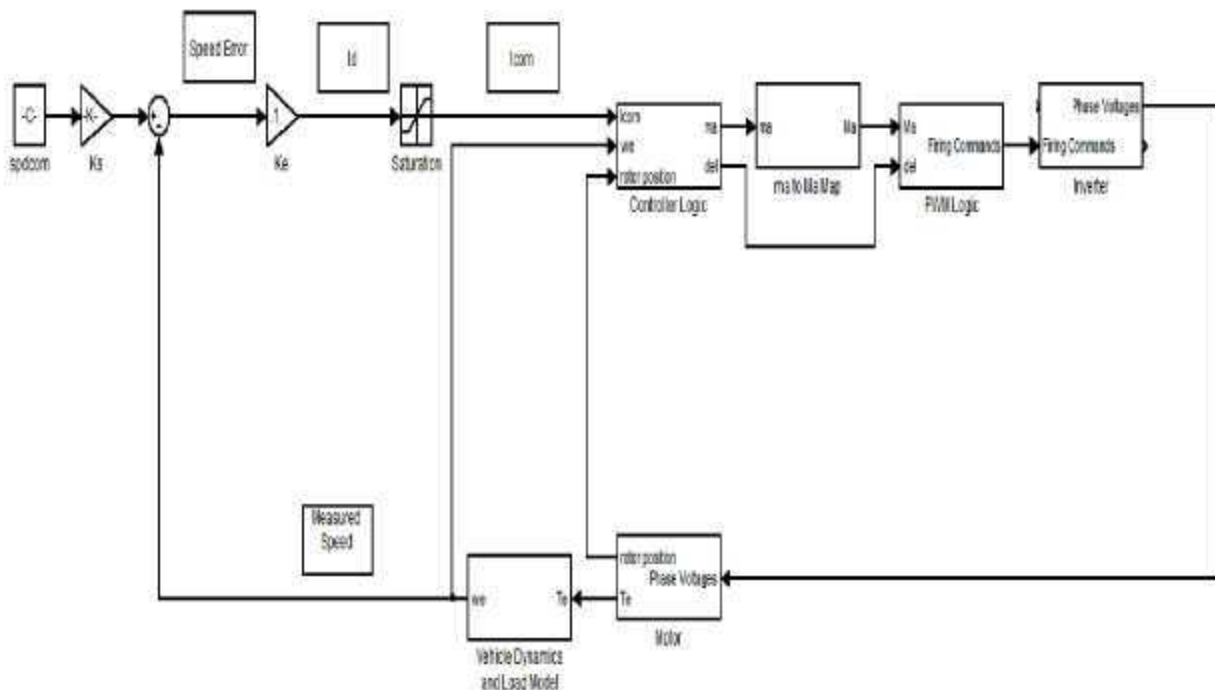


Figure 16. Closed-loop speed control block diagram.

Values of M_a greater than 1 are called the nonlinear modulation region, and in this region the high frequency switching of PWM degenerates towards six-step operation. The value of the rms fundamental

component increases with values of M_a greater than 1 but less than linearly, and in fact, once the PWM has degenerated to six-step switching, no further increase is observed in fundamental voltage. The fundamental voltage for a six-step waveform is the maximum possible value and is given by

$$V_{l-max} = \frac{\sqrt{2}V_{dc}}{\pi} \quad (55)$$

The controller logic block calculates a “pseudo amplitude modulation index,” ma , which is the ratio of the rms fundamental voltage to the rms fundamental voltage at the end of linear modulation; that is

$$ma = \frac{V_l}{\frac{V_{dc}}{2\sqrt{2}}} = \frac{2\sqrt{2}V_l}{V_{dc}} \quad (56)$$

Values of ma lie between 0 and $\frac{4}{\pi}$. For a given ma , the value of the corresponding M_a is dependent on the frequency modulation index. The frequency modulation index is the ratio of the frequency of the triangular carrier wave of the PWM logic to fundamental frequency. Because the fundamental frequency of the motor increases with motor speed, the frequency modulation index is not constant unless the carrier frequency is varied in proportion to any change in motor speed. Generally the carrier frequency is not fixed but held constant at the highest switching frequency that can be tolerated by the inverter switches. A map of ma into M_a is shown in Figure 17 for a frequency modulation index of 39. The ma to M_a map in the control block diagram is implemented as a table lookup. If necessary, several maps can be stored for various values of frequency modulation index and interpolation can be used to account for changes in frequency modulation arising from changes in motor speed. Once amplitude modulation index, M_a , and lead angle, δ , are determined, the control function is complete, and the remaining components in the diagram would be the same as for any other PWM controlled drive and include the PWM switching logic to firing commands block, the inverter, the motor, and the vehicle and load dynamics blocks.

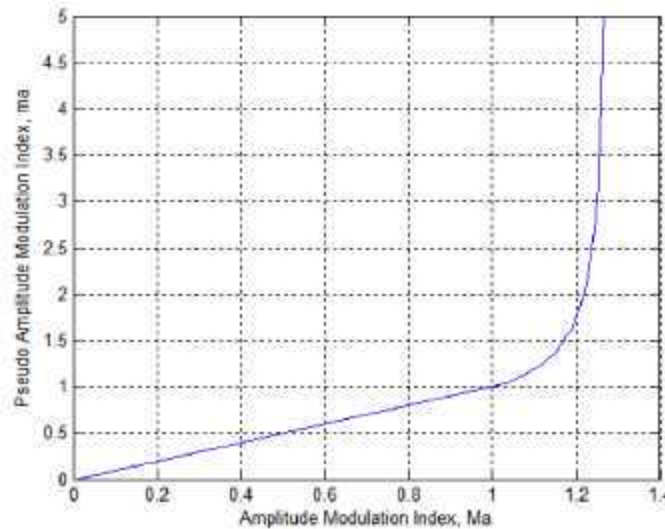


Figure 17. Amplitude modulation index versus pseudo amplitude modulation index for a frequency modulation index of 39.

Notice that current sensing is not used in this control. This does leave the performance of the controller vulnerable to variations in machine and drive parameters, especially the direct current supply voltage, the winding inductance, and the back-emf voltage constant. The direct current supply voltage is easily measured and consequently variation in V_{dc} is readily accounted for. Handling variations in the back-emf constant and winding inductance will be studied in the future. For the experiments at hand, the laboratory measurements of inductance and back-emf constant will suffice.

The core of the control strategy is contained in the Figure 16 block labeled "Controller Logic," which processes the current command, I_{com} ; measured speed, ω_e ; and measured rotor position into the pseudo amplitude modulation index, ma , and the inverter lead angle, δ , which appears as δ in the equations. Two variations of the controller logic block are discussed below.

Rated Current Limiting Controller Logic

The specified rms current rating of the motor, I_R , is not to be exceeded at any operating condition. PM machines with low speed and core losses may be able to develop more power in the constant power zone than at base speed without exceeding the rms current rating. For such machines, the onboard direct current supply may have to provide power in excess of its rating if the motor is allowed to approach rated current during operation above base speed. The controller logic can be adapted to preclude exceeding rated power as discussed in the section entitled "Rated Current and Rated Power Limiting Controller Logic." In this section the constraint is to limit motor current to be no greater than the rated value.

Consider operating at relative speed, n , at pseudo amplitude modulation index, ma , and inverter lead angle, δ . The linear model of Figure 15 has rms current

$$I = \frac{\sqrt{V^2 - 2nVE_b \cos \delta + n^2 E_b^2}}{Z} \quad (57)$$

where

$$V = \frac{maV_{dc}}{2\sqrt{2}}$$

and

$$Z = \sqrt{R^2 + (nE_b)^2}$$

If the rms current is to be no greater than the rated value, I_R , then the inverter lead angle must be limited to a value no larger than

$$\delta_{\max} = \cos^{-1} \left[\frac{V^2 + n^2 E_b^2 - Z^2 I_R^2}{2nVE_b} \right] \quad (58)$$

Maximum power transfer between the inverter and the motor occurs when the inverter lead angle is equal to β where

$$\beta = \tan^{-1} \left(\frac{nX_b}{R} \right) \quad (59)$$

If the value of δ_{\max} exceeds the value of β , then more power can be produced at a lower current than the rated current. It isn't reasonable to maintain rated current if more power can be developed at a lower current level. As the objective of the control is to meet the load condition at the minimum current, the best value of δ_{\min} is

$$\delta_{\min} = \min \left(\beta, \cos^{-1} \left[\frac{V^2 + n^2 E_b^2 - Z^2 I_R^2}{2nV E_b} \right] \right) . \quad (60)$$

Rated current and rated power limiting controller logic

Above base speed a PM motor may be capable of developing more power than the rated value while operating below rated current. If it is desired to restrict developed power to a value no greater than rated, then the inverter lead angle must be restricted to a lower value than required for current limitation. At relative speed n (greater than one), such that the pseudo amplitude modulation index is at the maximum value of $\frac{4}{\pi}$ and the applied rms motor voltage at fundamental frequency is likewise at its maximum,

$$V_1 = V_{1-\max} = \frac{\sqrt{2}V_{dc}}{\pi} . \quad (61)$$

Then the total developed power per phase, including useful load power and speed sensitive losses, is given by

$$\frac{P}{3} = \frac{nE_b V_1}{Z} \cos(\beta - \delta) - \frac{n^2 E_b^2}{Z} \cos \beta , \quad (62)$$

where

$$\beta = \tan^{-1} \left(\frac{nX_b}{R} \right) .$$

To limit this power to be no greater than rated power, P_R , requires that the inverter lead angle be limited to

$$\delta_{\max} = \beta - \cos^{-1} \left(\frac{ZP_R / 3 + n^2 E_b^2 \cos \beta}{nV_1 E_b} \right) . \quad (63)$$

Under some conditions, particularly low supply voltage, it may be necessary to restrict δ to be no larger than the value of β . In such cases, the rated power cannot be developed and having $\delta = \beta$ allows maximum possible power.

To avoid having the motor enter regeneration mode during coasting operation, such as when the vehicle is in motion but the speed command is temporarily reduced to zero, the value of lead angle, δ , must be larger than

$$\delta_{\min} = \beta - \cos^{-1} \left(\frac{ZP_{rd}(n) + n^2 E_b^2}{nV_1 E_b} \right) . \quad (64)$$

This limit should also be applied in the rated current magnitude limiting logic described in the previous section.

Simulation of the closed-loop speed control

The speed control system described in the preceding section was simulated using the fundamental frequency model developed in previous work.¹³ This eliminates the need to include the PWM switching logic and greatly decreases the simulation time required to investigate vehicle response to speed commands. Even though the details of PWM switching are suppressed, the model is still able to capture the inverter losses described in Lawler.¹³

Only the step response to large speed commands is considered here. One simulation is shown for the current limiting control logic and the same simulation is shown for the power limiting control logic. The simulations are done for standing start conditions, zero initial vehicle speed, and a step command to one-half full speed (or 3000 rpm). It is assumed that the vehicle load is quadratic in speed with the full 6-kW rated power required for 6000 rpm. The equivalent rotational inertia was selected so that the vehicle driven by the 6-kW prototype weighed approximately 500 kg. Although this is a very heavy vehicle for the size of the motor, the use of a large rotational moment of inertia will decrease the speed of response to speed commands and make the comparison of the rated current limiting control and the rated power limiting control clearer.

Figure 18 displays the response of motor revolutions per minute, commanded and root-mean-square motor current, and developed power to the step command from 0 rpm to 3000 rpm for both the rated current limiting logic [Figure 18(a), (c), and (e)] and the rated current and rated power limiting logic [Figure 18(b), (d), and (f)]. Notice that in steady state both cases have a steady state error because of the

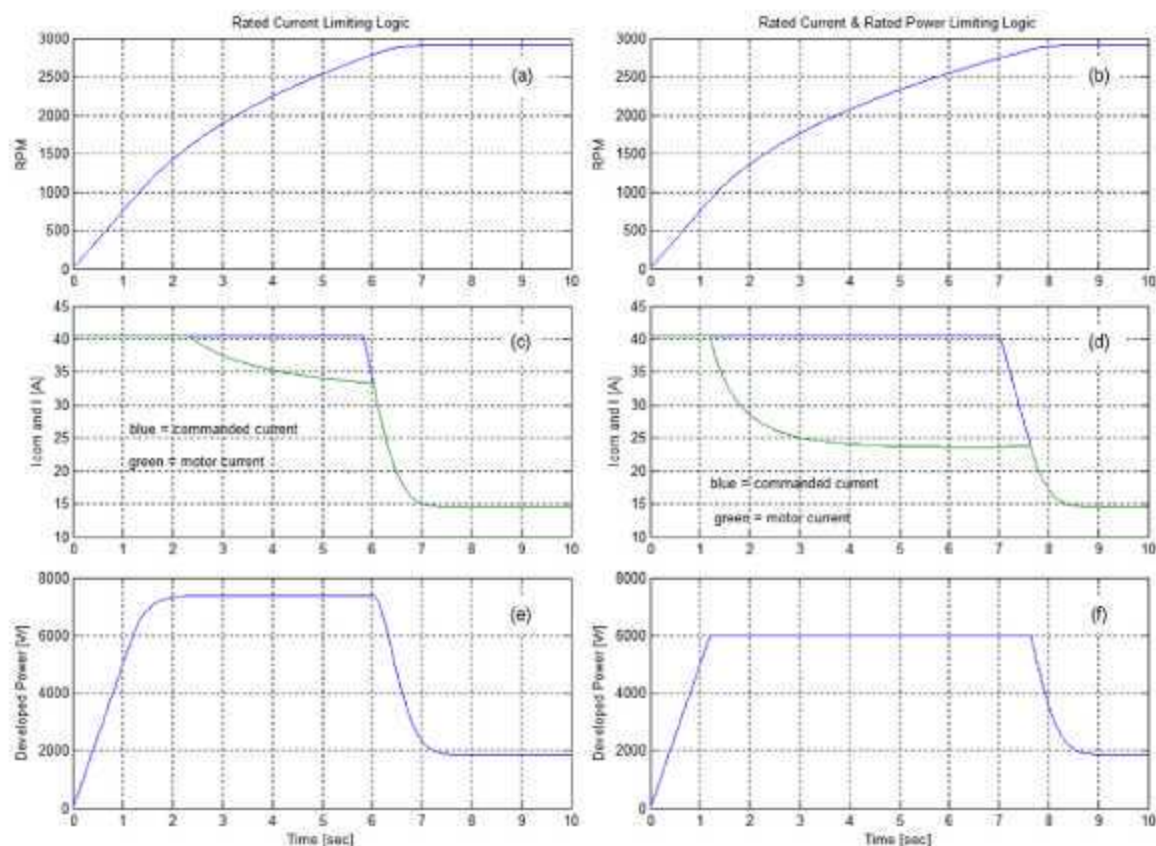


Figure 18. Rated current limiting control (left) and rated current plus rated power limiting control (right).

use of a simple proportional control. This error could be suppressed by increasing the proportional gain, K_s , of Figure 16 by adding an integrator to the controller or by the vehicle operator simply increasing the speed command slightly.

Notice that for the rated current limiting logic [Figure 18(a), (c), and (e)] the actual motor current begins decreasing at about 2.4 s despite the fact that the commanded current remains at the rated value. This is an instance where forcing the motor current to remain at rated power would result in less developed power. Figure 18(e) demonstrates that despite the reduction in current between 2.4 and 5.8 s, the developed power remains constant at 7400 W.

For the rated current and rated power limiting logic, the acceleration of the motor is slower than for the rated current limiting logic. This is because the developed power is limited to 6000 W, whereas, with only current limiting control, the developed power peaked at 7400 W. The current and power limited control took more than 8 s to reach steady state, whereas the current limiting control took less than 7 s. In the rated current and rated power limiting control, the motor current begins decreasing at 1.3 s and this decrease is associated with limiting the developed power to 6000 W.

The final steady state condition of the two cases is identical. The two methods will differ in response during transient conditions, but the steady states will be the same for any load condition that does not exceed rated power.

Conclusion

A simple proportional speed control has been developed for FSCW-SPM motors. Detailed simulation of the control shows that it can be effective in controlling motor speed while minimizing the motor current magnitude during operation above and below base speed. Laboratory testing of this method and the maximum motor efficiency control described below will allow comparisons to be made as to which method results in the greatest overall drive efficiency.

Iron Loss Model Development

As noted in the objectives, significant effort is being devoted to the development of closed-form analytical models of the iron losses in the FSCW-SPM machine. This section will summarize the nature of the analytical models and the progress that has been achieved towards verifying their accuracy.

Two FSCW-SPM machines designed to meet the FreedomCar advanced traction motor performance targets were proposed for use in analytical studies during FY 2006.⁸ The first, named *SPM1*, exhibited a 900-V back-emf at top speed (10,000 rpm), which was above the 600-V target. *SPM1* has been used as the basis for comparisons between iron loss predictions of the closed-form analytical model and more detailed predictions from FEA. The second, named *SPM2*, exhibited a 600-V back-emf at top speed and had the best match between target values and performance estimates; consequently, it was chosen for the "Analysis and Design of Motors with Fractional-Slot Concentrated Windings" part of this study.

This 55-kW (peak) machine, *SPM1*, is used as an example for exploring the proposed analytical approach for calculating the iron losses. A cross-section of the basic repeating unit of this machine was shown in Figure 7, and some key machine dimensions and parameters are summarized in Table 10. More details about this machine can be found in El-Refaie, Jahns, and McKeever.⁸

The electromagnetic FEA programs MagNet2D (Infolytica) and JMag (JRI, Inc.) have been used to provide more accurate predictions of the magnetic fields and iron losses in the FSCW-SPM machine. In particular, the JMag program is capable of providing a point-by-point frequency spectrum calculation of the iron losses over the complete cross-section of the machine. Both hysteresis and eddy-current losses are calculated for *SPM1*, using iron loss characteristics provided by the lamination steel manufacturer. This approach provides the highest possible accuracy for predicting the iron losses in such a machine, but the calculations are very time-consuming.

Table 10. *SPM1* machine dimensions and parameters

Slots/pole/phase	2/5	Slots	36
Poles	30	Rotor outer radius [mm]	92.1
Stator OD [mm]	269	Active length [mm]	63.5
Total length [mm]	75.4	Magnet thickness [mm]	7.5
Air-gap thickness [mm]	1.5	Magnet remanent flux density [T]	1.0 @ 140°C
Copper mass [kg]	4.6	Magnet mass [kg]	2.0
Iron mass [kg]	9.7	Total mass [kg]	16.3

Open-Circuit Machine Model and Loss Predictions

SPM1, summarized in the preceding section, was analyzed to determine its magnetic flux density distribution and losses under open-circuit conditions. The major parts of the machine that contribute to the iron losses include

1. stator iron tooth and yoke,
2. rotor iron inner yoke, and
3. rotor magnets.

Under open-circuit conditions for which there is no stator excitation, the rotor losses are minimal¹⁵ because the rotor back-iron that carries the magnet flux does not see much temporal change in flux density as the rotor moves.

Closed-form expressions for the magnetic flux density distribution under open-circuit conditions have been derived as a function of radius inside the air gap by solving the associated Laplace equations.^{16,17} The accuracy of this technique depends on the assumption that magnetic saturation is not significant in the machine iron, an assumption that is typically quite reasonable for this type of machine. These equations determine the spatial harmonic components of the flux density distribution for a specified machine configuration. In particular, attention is paid to three different radii—the rotor iron outer radius (R_r+), the rotor magnet outer radius (R_m+), and stator inner radius (R_s-).

Figure 19(a) shows the predicted spatial distribution of the air-gap flux density at these three different radii inside the air gap for a slotted version of the *SPM1* machine. The harmonic spectrum for the flux density distribution at radius, R_s- , is shown in Figure 19(b). The effect of the slots is to introduce even harmonics into the distribution as well as lowering the amplitude of the fundamental component. More details about the analytical model including mathematical expressions have been included in a separate report.

The tooth flux density can be approximately calculated by assuming that the flux density¹⁸ is uniform across the width of each tooth, TW , for all of its length, h_g , excluding the tooth tip. The resulting flux density in the tooth can then be approximately determined by integrating the flux density waveform over the tooth pitch and dividing by the tooth width, TW . Figure 20(a) shows the resulting tooth flux density distribution predicted using the approach described above as the rotor is rotated. Higher-order harmonic components are attenuated in the spatial flux density distribution so that the resulting waveform in Figure 20(a) is dominated by its fundamental component. The peak value of the tooth flux density, B_{th} , as the rotor rotates through a complete pole pitch is approximately 0.62 T for the *SPM1* machine.

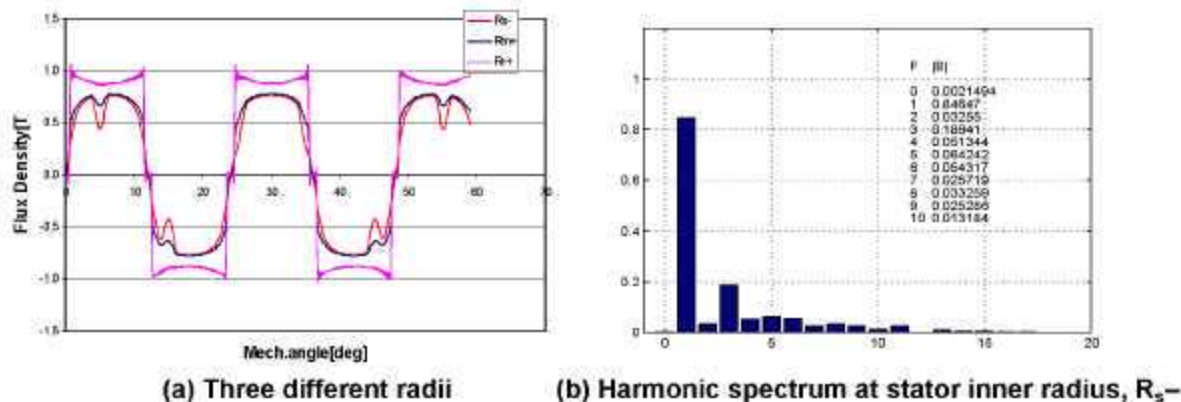


Figure 19. Analytical predictions of the spatial air-gap flux density distribution for a slotted version of the SPMI machine for a rotor angular position of 5 mechanical degrees.

The same type of simplifying assumption made about the uniformity of the flux density across the tooth width can be extended to the stator yoke, for which it will be assumed that the flux density is the same everywhere in the cross-sectional area of the stator yoke behind each stator slot. Figure 20(b) shows the predicted yoke flux density distribution waveform as the rotor is rotated. As in the case of the tooth flux density waveform, the amplitudes of the harmonic components are significantly attenuated. The peak amplitude of the SPMI yoke flux density B_{ykn} as the rotor rotates through a complete pole pitch is determined to be approximately 1.32 T.

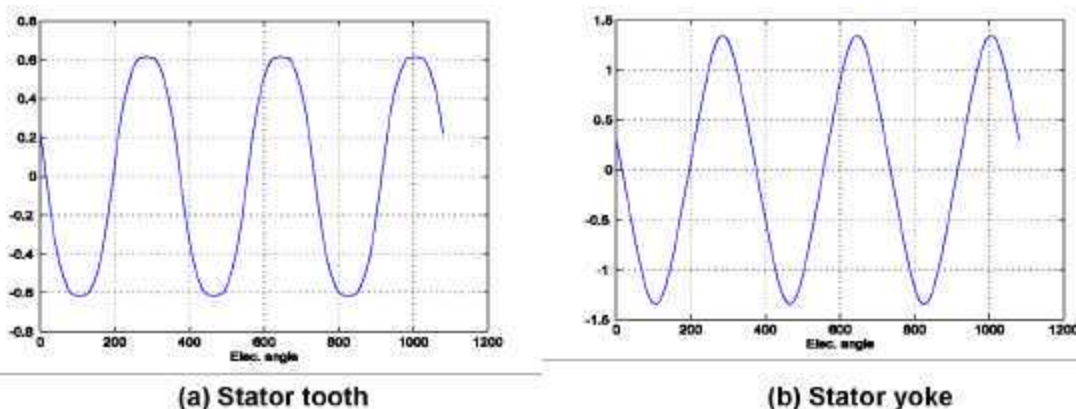


Figure 20. Predicted flux density waveform in different parts of the stator based on the assumption of uniform tooth flux density.

Figure 21 provides a direct comparison of the predicted spatial flux density distributions at radius, R_{s-} , for the closed-form analytical model and FEA. The high-quality agreement between the two waveforms and their dominant frequency components indicates that the closed-form analytical approach can do an excellent job of predicting the air-gap flux density distributions for this type of SPM machine.

The stator iron core loss can be predicted using the stator tooth and yoke flux density waveforms that have been calculated using closed-form analysis based on the uniform flux density principle as described above. The analytical model for determining the stator core losses is based on summing the loss contributions of each of the dominant harmonic components in the frequency spectra for the tooth and yoke flux densities.

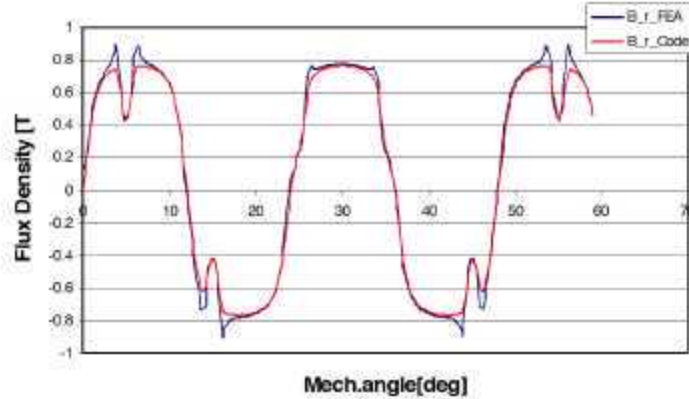


Figure 21. Comparison of predicted air gap magnetic flux density distribution at radius R_s – using closed-form (B_r_Code) and finite-element (B_r_FEA) analysis.

The familiar Steinmetz equation⁹ for calculating the hysteresis loss associated with each of the frequency components in the flux density waveform is given by

$$P_{ht} = k_h B_{th}^\beta \omega_s \text{ [W/m}^3\text{]} \quad (65)$$

The corresponding eddy current loss equation is given by

$$P_{et} = k_e B_{th}^2 \omega_s^2 \text{ [W/m}^3\text{]} \quad (66)$$

Typical values have been adopted for the coefficients and exponents that appear in the above loss equations for grades of silicon iron laminations commonly used in small and medium induction motors. They are $k_h = 48$, $\beta = 2$, and $k_e = 0.055$.

Figure 22 provides a comparison of the predicted total iron losses in different parts of the machine using the closed-form analytical model and the more accurate point-by-point FEA technique described previously. There are several observations that can be made from this figure.

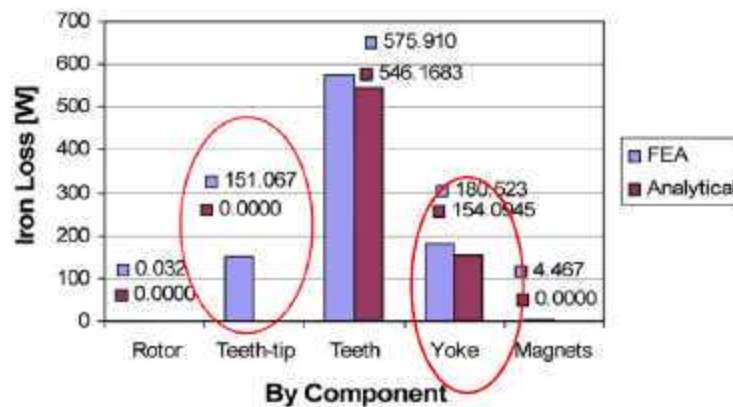


Figure 22. Comparison of predicted iron losses in different parts of the *SPM1* machine at 2000 rpm in an open-circuit condition using closed-form analysis and point-by-point finite-element analysis technique.

On the positive side, the agreement between the iron loss predictions, including both hysteresis and eddy current losses, for the closed-form analysis and point-by-point FEA is quite good, with the closed-form predictions approximately 5% and 14% below the FEA predictions for the teeth and yoke portions of the machine, respectively.

Figure 22 also highlights the fact that a technique for predicting the iron losses in the stator tooth tips along the inner stator bore has not yet been developed for the closed-form analysis, explaining why this bar is absent from the figure. The tooth tips are exposed to a richer harmonic mix of spatial flux density components than the rest of the teeth or yoke. These harmonics explain why the FEA predictions for the tooth-tip iron losses are nearly as high as for the yoke in the *SPMI* machine. As a result of these additional losses, which are not accounted for using the closed-form analysis, the total error between the predicted iron losses using the two techniques is approximately 23%. **This clearly identifies an area where further work is needed to improve the closed-form analytical model.**

Finally, the FEA-predicted iron loss results in Figure 22 confirm that the rotor magnet and iron yoke losses are very low in the *SPMI* machine for open-circuit conditions.

Armature Reaction Loss Predictions

The next major step in developing the iron loss model for the FSCW machine is to predict the iron losses associated with magnetic flux density components induced by the presence of current in the stator coils. This type of loss is called armature reaction loss. Progress has been made towards predicting these armature reaction iron losses using the point-by-point FEA technique.

Figure 23(a) shows the FEA-predicted iron losses in the *SPMI* machine, broken down by the major sections of the machine, when it is rotating at 2000 rpm with alternating current stator currents of 200 A.

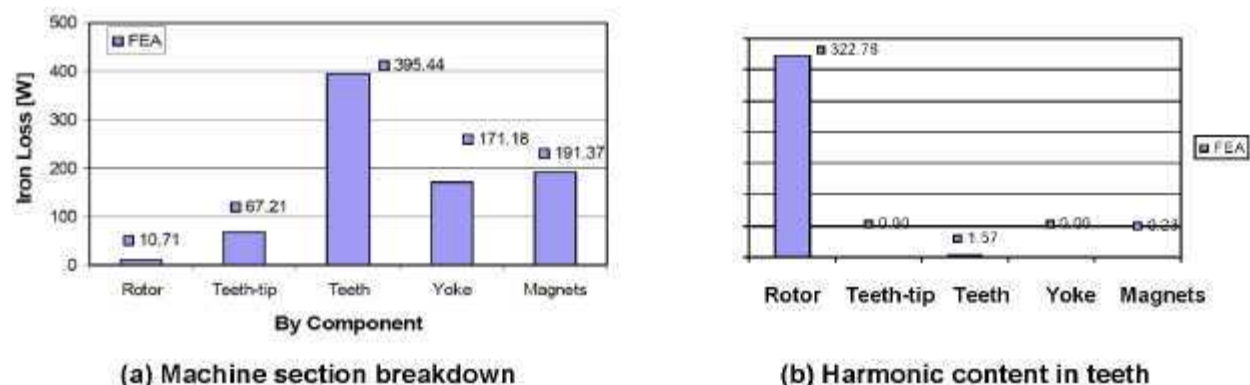


Figure 23. Finite-element-analysis-predicted iron eddy current losses at 2000 rpm with a peak armature current of 200 A.

The magnets were physically present for this analysis, but they were assumed to be completely demagnetized for this analytical exercise to focus attention exclusively on the armature reaction effects. For this analysis, it has been assumed that each magnet pole piece is broken into five identical pieces along the circumferential direction. This was done on the basis of previous work,¹⁹ which showed that the magnet losses can be reduced by more than 80% when this kind of segmented magnet structure is adopted.

Among all of the laminated steel components except for the magnets the predicted iron losses are highest in the stator teeth and lowest in the rotor yoke [Figure 23(a)], following trends similar to those observed in the preceding section for the open-circuit conditions. The major difference between the previous open-circuit and the armature reaction case studied here is that the eddy current losses in the magnets become a significant loss component in the machine when substantial stator currents are flowing.

These magnet losses would have been considerably higher if the magnet poles had not been broken into multiple pieces.

Figure 23(b) presents a different perspective on the FEA-predicted eddy current losses in the teeth caused by the stator currents, broken down in this part of the figure by harmonic component. It is clear from this breakdown that iron losses for the armature reaction operating condition are attributable almost completely to the fundamental component. Additional results not included here show that this is true for the stator yoke and tooth-tips as well. This is good news because it is likely to simplify the task of developing a closed-form analytical model that can predict these iron losses contributed by the stator currents with reasonable accuracy. Efforts to develop this feature of the iron loss prediction method using closed-form analysis are presently under way.

Enhanced Partial Load Efficiency Control Algorithm

High-performance torque control in SPM machines can be achieved using current-regulated vector control. According to this technique, the amplitudes of the instantaneous currents in the three stator phases are controlled so that their combined effect can be represented on a cross-section of the machine as a vector that has an amplitude and angle. A simple representation of this concept that illustrates a current vector, \vec{i}_s , for a two-phase alternating current machine is provided in Figure 24. Newcomers to this concept are referred elsewhere for more details.²⁰

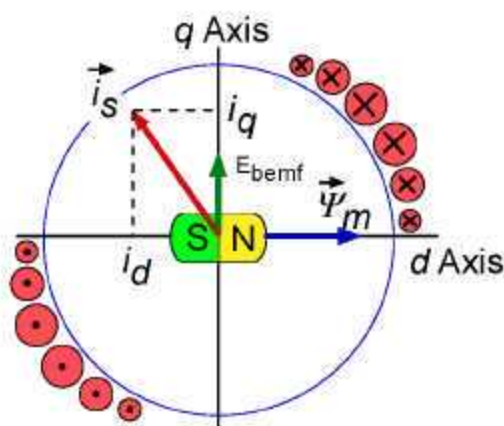


Figure 24. Cross section of two-pole machine illustrating a stator current vector and its decomposition into d - and q -axis components to achieve vector control of a surface permanent magnet machine.

According to the basic concept of vector control, the amount of torque that is produced by an SPM machine is determined by both the amplitude of the current vector and, very importantly, by its angle with respect to the orientation of the rotor magnets. In Figure 24 the rotor magnet orientation is represented by the magnet flux linkage vector, $\vec{\psi}_m$, aligned with the north pole of the rotor magnets. A two-axis plane can be uniquely defined that is locked to the rotor's instantaneous angular position at every time instant so that the orientation of $\vec{\psi}_m$ is defined to be the direct or d -axis, and an orthogonal axis is defined as the quadrature or q -axis. As a result, any current vector such as \vec{i}_s in Figure 24 can be uniquely decomposed into an i_d component along with the d -axis and an i_q component aligned with the q -axis. The torque and the terminal voltage developed by the SPM machine are determined by the values of i_d and i_q , so controlling these two orthogonal current components provides the basis for controlling the torque production of the machine.

Conventional vector control algorithms for SPM machines are based on minimizing the stator copper losses by adjusting the stator current in the rotor-based dq frame to achieve maximum torque-per-amp

(*max T/A*) operation.^{12,21} Figure 25 shows the calculated current vector trajectory line for maximum torque/amp operation of the *SPMI* machine over a wide range of rotor speeds in the i_q - i_d plane when delivering 20% of rated torque. According to this algorithm, the value of i_q is essentially constant while i_d is gradually increased (with negative polarity) as the speed is increased beyond the corner point value to accomplish the necessary flux weakening. Flux weakening is required at elevated speeds to counteract the effect of the magnet flux linkage, sufficiently so that the terminal voltage of the machine at each speed will remain within the maximum limit set by the available source voltage.

It is useful to identify an alternative version of this vector control algorithm to minimize the machine's terminal voltage under all operating conditions by using as much negative d -axis current as available to accomplish this objective. The current vector trajectory for this maximum-torque-per-volt strategy is shown in Figure 26 for the *SPMI* machine at 20% of rated torque, exhibiting very little motion over the full speed range. That is, the same current vector amplitude is applied at all speeds, adjusted so that its amplitude equals the rated continuous current value. This algorithm is referred to as maximum torque-per-volt (*max T/V*).

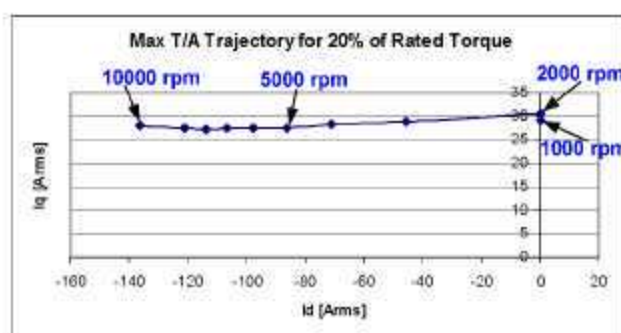


Figure 25. Maximum torque/amp current vector trajectory for *SPMI* machine at 20% of rated torque.

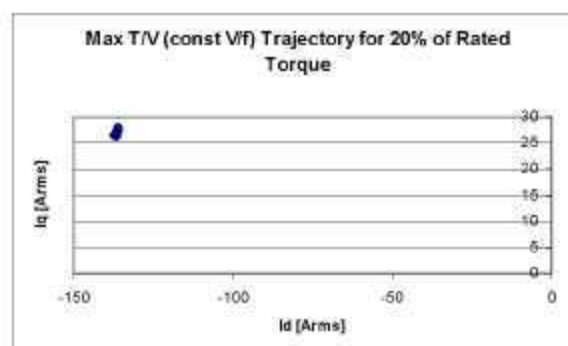


Figure 26. Maximum torque/volt current vector trajectory for *SPMI* machine at 20% of rated torque.

This *max T/V* algorithm is useful for illustration purposes in this discussion because it has the special feature of minimizing the stator core loss by minimizing the stator flux density at all speeds. However, its practical usefulness is very limited because this iron loss minimization is accomplished at the price of maximizing the copper loss.

Some valuable insights are also available by comparing the calculated loss components with each of these two vector control algorithms. Figure 27 confirms that the maximum torque-per-amp algorithm (*max T/A*) delivers lower copper losses at all speeds below maximum speed (10,000 rpm) compared to the *max T/V* algorithm. On the other hand Figure 28 shows that the roles reverse for iron core losses,⁹ with the *max T/V* algorithm achieving significantly lower core losses than the *max T/A* algorithm at all speeds below 10K rpm.

An important observation from this exercise is that the *max T/V* algorithm tends to yield higher efficiency at speeds where the iron losses are dominant, while the *max T/A* algorithm tends to achieve higher efficiency at speeds where copper losses are dominant. Figure 29 confirms this observation by comparing the predicted efficiency of the *SPMI* machine at 20% of rated torque for the two algorithms over a wide speed range. More specifically, Figure 29 shows that the *max T/A* algorithm is significantly better for minimizing the total machine losses at low speeds where the iron losses tend to be the lowest, but the *max T/V* algorithm demonstrates its superiority at higher speeds above approx. 2000 rpm, where iron losses are much higher. Unfortunately, Figure 29 also shows that neither algorithm is capable of achieving the 93% efficiency target for the FreedomCAR traction motor, with the largest deficiencies appearing at low speeds.

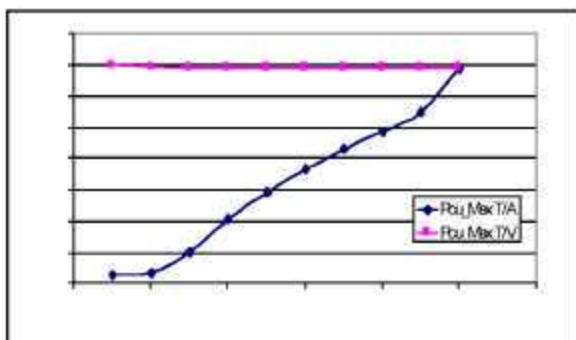


Figure 27. Comparison of predicted copper losses for 20% of rated torque with $\max T/A$ and $\max T/V$ algorithms.

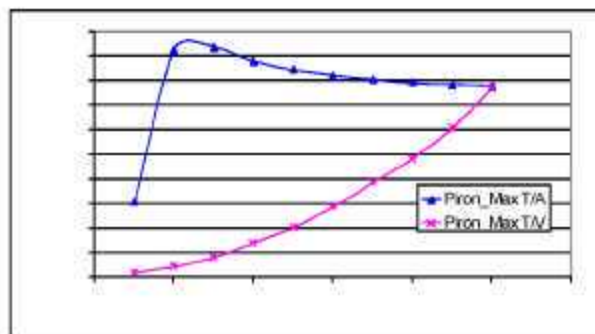


Figure 28. Comparison of predicted iron losses for 20% of rated torque with $\max T/A$ and $\max T/V$ algorithms.

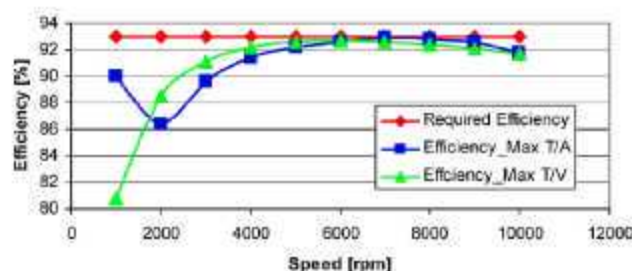


Figure 29. Predicted efficiency of SPM1 machine at 20% of rated torque for $\max T/A$ and $\max T/V$ algorithms, plus specified minimum efficiency line.

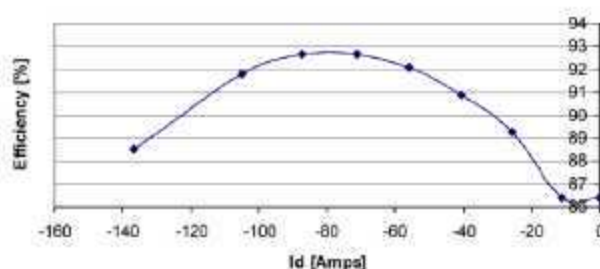


Figure 30. Variation of SPM1 efficiency at 2000 rpm as a function of i_d with i_q adjusted to hold the torque constant at 20% of rated torque.

A critical observation at this stage is that the $\max T/A$ and $\max T/V$ algorithms represent two distinct extremes in the vector control spectrum. In between these two extremes are an infinite number of alternative formulations. Each candidate algorithm represents a different weighted blending of the two extreme algorithms, raising the possibility that a blended algorithm might perform better than either $\max T/A$ or $\max T/V$ alone.

An investigation was launched to determine whether there might be another combination of I_q , which determines the resulting torque, and I_d , which is used to adjust the flux level in the machine, that will lead to higher machine efficiency values than either the pure $\max T/A$ or $\max T/V$ algorithms.

The results of this investigation have been very promising, indicating that the appropriate blend of the two algorithms can yield significant improvements in the machine efficiency, particularly at those speeds that exhibit the largest deficiencies in Figure 29. As an example, Figure 30 shows the variation of predicted SPM1 efficiency at 2,000 rpm and 20% of rated torque as a function of I_d . The predicted efficiency is approx. 86.5% for the $\max T/A$ algorithm (when I_d is zero), while the efficiency is approx. 88.5% for the $\max T/V$ algorithm ($I_d = -140$ A_{rms}). In between these extremes, the partial-load machine efficiency peaks when $I_d = -80$ A_{rms} at a value very close to the specified value of 93%. This is a clear indication that choosing the optimum combination of I_d and I_q can have a very significant effect on maximizing the partial-load efficiency of the machine. These results will be discussed further based on the FEA results presented in the following section.

Figure 31 presents the calculated current vector trajectory for achieving the highest partial-load efficiency as the rotor speed is increased from 1000 to 10,000 rpm. By comparing this trajectory to the *max T/A* and *max T/V* current vector trajectories in Figures 25 and 26, it can be observed that the new trajectory adds a higher-level of negative *d*-axis current as a function of rotor speed compared to the *max T/A* trajectory in order to reduce the iron losses, but not as much I_d as the *max T/V* algorithm would require.

Figure 32 shows the new predicted efficiency curve for the *SPMI* machine at 20% of rated torque when the current vector trajectory in Figure 31 is applied as a function of rotor speed. The partial-load efficiency values are boosted at every speed compared to the values plotted in Figure 29 for the *max T/A* and *max T/V* trajectories. In fact, the results in Figure 32 predict that the *SPMI* machine will be able to meet the minimum efficiency requirements (93%) for 20% rated torque over the complete speed range.

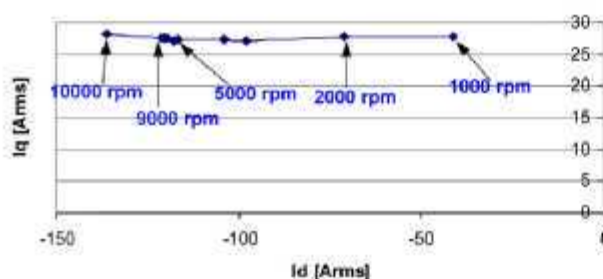


Figure 31. Current vector trajectory for *SPMI* machine to deliver maximum partial-load efficiency at 20% of rated torque.

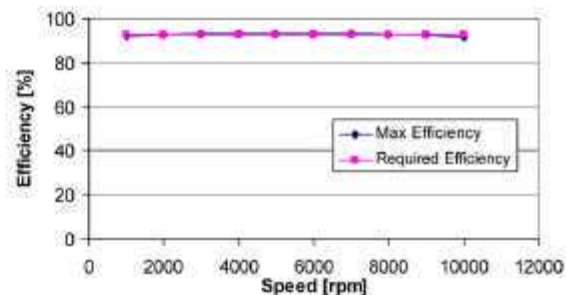


Figure 32. Predicted efficiency of *SPMI* machine at 20% of rated torque for maximum partial-load efficiency, plus specified minimum efficiency line.

Finite-Element Analysis Results

To verify the assumptions used in the analytical calculations of core losses and to gain more insights into the tradeoffs between the copper and core losses for maximizing the partial-load efficiency, FEA simulations using *MagNet 2D* (Infolytica) were carried out. Three operating points at 2000 rpm and 20% rated torque are considered. These points correspond to three distinct points on the partial-load efficiency curve shown in Figure 30, representing *max T/A* (far right), *max T/V* (far left), and *max efficiency* operation at the peak of the curve.

The FEA-predicted magnetic flux density time-domain waveforms in the stator teeth are shown in Figures 33 to 35 for the three highlighted operating points. The harmonic spectrum of the stator-tooth flux density waveform is presented in Figure 36.

The first key observation drawn from these figures is that the magnetic flux density waveforms in the stator teeth are almost purely sinusoidal, as confirmed by the harmonic spectrum in Figure 36. This result is striking because the fractional-slot concentrated windings produce many spatial harmonics in the air-gap flux density waveform.²² The sinusoidal wave shapes in Figures 33 to 35 justify the sinusoidal approximation adopted for calculating the peak air gap magnetic flux density and, subsequently, for calculating the peak magnetic flux density in the stator teeth and yoke.

The second key observation, drawn from comparing Figures 33 and 34, is that there is an 80% reduction of the peak magnetic flux density in the stator tooth for the *max T/V* algorithm compared to the *max T/A* algorithm. This flux density reduction leads to a significant reduction of the predicted core losses in the stator teeth. This reduction in the stator core loss comes at the expense of an increase in the rms phase current from 30.6 to 139.3 A_{rms} and a corresponding increase in the copper losses, as discussed in the previous section. This result is consistent with the results shown earlier in Figures 27 and 28.

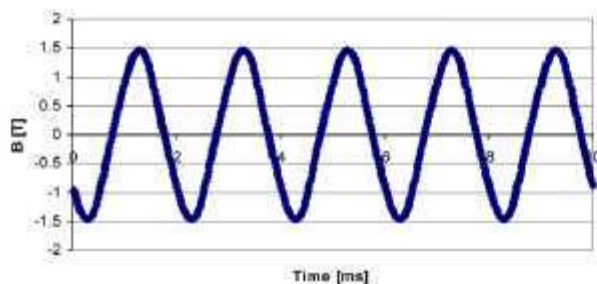


Figure 33. Predicted stator tooth magnetic flux density waveform at 2000 rpm and 20% rated output torque under *max T/A* operating conditions.

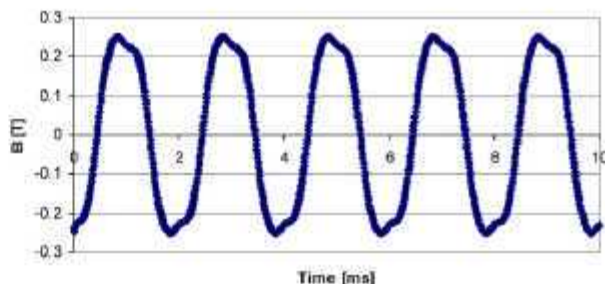


Figure 34. Predicted stator tooth magnetic flux density waveform at 2000 rpm and 20% rated output torque under *max T/V* operating conditions.

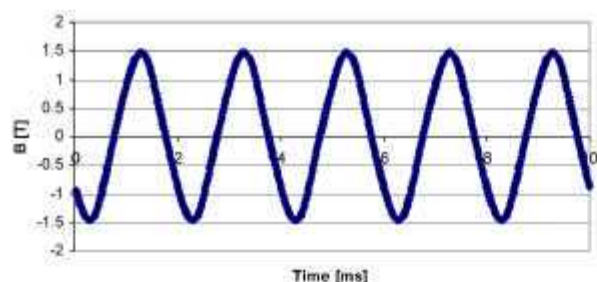


Figure 35. Predicted stator tooth magnetic flux density waveform at 2000 rpm and 20% rated output torque under *max efficiency* operating conditions.

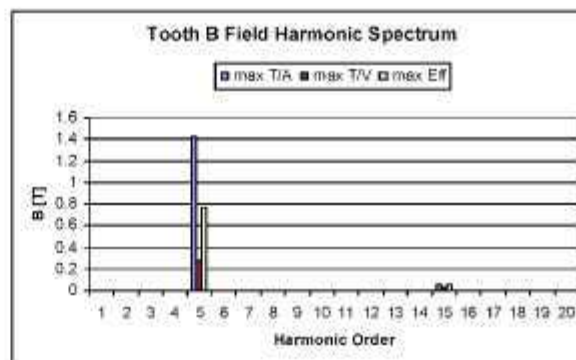


Figure 36. Predicted harmonic spectra for stator tooth magnetic flux density at 2000 rpm, 20% rated torque for the three operating conditions.

Figure 35 shows the predicted stator tooth magnetic flux density waveforms under the *max efficiency* operating conditions. It can be observed that there is almost a 50% reduction in the stator tooth peak magnetic flux density compared to the *max T/A* case. At the same time, there is an increase in the phase current from 30.6 to 76.4 A_{rms}. This blend of the *max T/A* and the *max T/V* algorithms yields the maximum partial-load efficiency for operation at 20% rated torque with a rotor speed of 2000 rpm.

Preparations to Test Control Schemes for the FSCW-SPM Motor

Upgraded hardware and software for use with OPAL-RT have been acquired during FY 2006 to conduct efficiency tests on the 6-kW FSCW-SPM motor for evaluating several control schemes developed by UWM and ORNL. An inverter and an interface card with dead time insertion capability, which communicates with the inverter's control unit while maintaining internal fault protection, allow a rapid prototype system such as OPAL-RT to control the semiconductor device gates while the motor is under actual load. Results of these tests will be used to compare and evaluate the control schemes. The new inverter is a Danfoss VLT 5252, which was purchased to deliver a range of powers up to the 55-kW target of an HEV traction drive system. The VLT 5252 has a typical shaft output power of 200 to 250 kW with normal 110% overload torque and 160 to 200 kW for high 160% overload torque. Figures 37 and 38 show the portable inverter and the internal arrangement of its control unit and power switching section.



Figure 37. Danfoss VLT 5252 inverter on mobile base.



Figure 38. Open door shows Danfoss control unit at top and power switching section at bottom.

Figure 39 shows the special interface card provided by Aalborg University in Denmark. It replaces a card in the Danfoss, which allows gate signals generated by the OPAL-RT system to control inverter switching. This is an effective way of bypassing an inverter's control unit to impress a new control scheme on a motor so that its effect on the motor/inverter system may be evaluated during actual operation.



Figure 39. Interface card with fiber optics and dead time insertion prepared at Aalborg University to allow control of a commercial inverter while maintaining its fault protection features.

ORNL's old OPAL-RT system encountered a problem generating stable PWM signals. It was necessary to upgrade the ORNL target computer and the OPAL-RT software to remedy this problem. The new target PC uses a QNX Version 6.2 operating system with a significantly faster bus speed. Field-programmable-gate-array-based I/O cards, which are expected to solve the unstable PWM problem, are part of the acquisition. Figure 40 shows the new target computer with its two white terminal buses mounted on the front, and Figure 41 shows one terminal bus replaced by a card used during the OPAL-RT pre-test check-out procedure to verify that all cards and software are working properly. Voltage, current, and speed sensor signals will enter the white terminal bus, and gate drive signals for the Aalborg



Figure 40. New OPAL RT target PC and connection box.

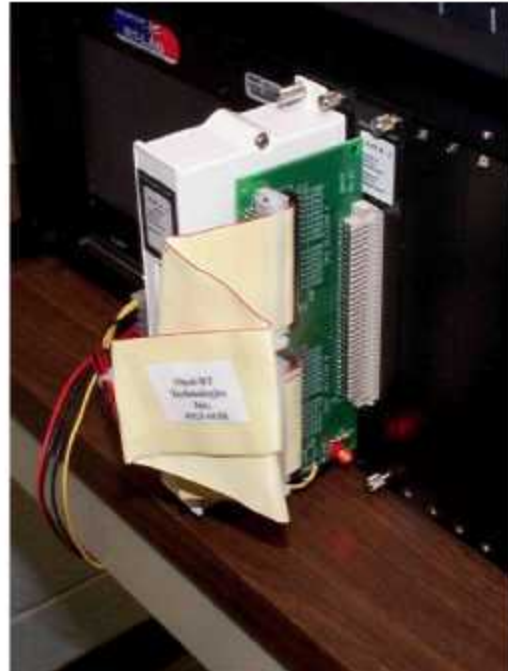


Figure 41. Pre-test diagnostic verification signal bypass card.

card will leave the bus. Current and voltage sensors are shown in Figure 42. The 6-kW motor in its new frame that allows water cooling of the stator is shown in Figure 43.

The checkout procedure for the inverter is in the approval cycle and the pre-test check-outs of the OPAL-RT target computer are in progress. Preparation of the final test plan for efficiency measurements as a function of speed for several partial loads will begin in FY 2007. This plan will be prepared in collaboration with UWM because it must be compatible with their control scheme so that a meaningful comparison of the two schemes may be made.



Figure 42. Voltage (black-left), motor current (red-middle) and direct current supply current (orange-right) sensors.

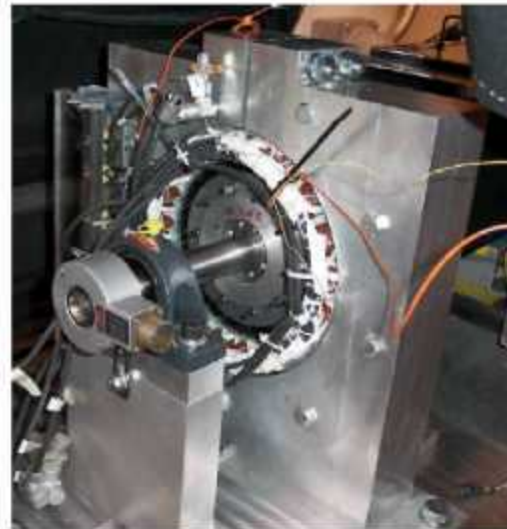


Figure 43. 6-kW fractional-slot SPM motor with concentrated windings.

Conclusions

Equations have been presented showing how a concentrated winding may be used to design increased inductance into an SPM motor with distributed windings. A distributed winding with $N_{sp} = 1$ has the maximum flux linkage with the stator; consequently, to produce comparable torque, a stator with concentrated windings must be able to produce a comparable number of flux links. A relation between the SPM motor with concentrated windings and its fluxmate with distributed windings emerges from the equations. Further, these equations show that there is always sufficient room in the slots of the concentrated windings to add the wire turns necessary to ensure that the flux across the gap for the concentrated windings is the same as that of its corresponding distributed winding, thus the name fluxmate.

The 55-kW design, *SPM2*, proposed by UWM has been evaluated using two design methodologies. The result is a viable design for an HEV traction drive motor. Two such motors, the other being *SPM1*, were designed according to the UWM methodology with a similar pole and slot count to UWM's 6-kW FSCW-SPM prototype now being used to evaluate control schemes at ORNL. With this knowledge, there is mounting evidence that FSCW motors with low pole and slot count are worthy of further investigation for traction applications.

Slight differences between the design results from UWM's application of its design methodology and ORNL's application of commercially available SPEED software have been identified and resolved. These differences relate to methods used to calculate magnet losses. At higher speeds these losses are reduced because more of the current flows at the surface of the conductor, thereby increasing its resistance. This effect is described by saying that the losses at high speeds are inductance limited. These results emphasize the importance of circumferentially stacking the magnets. The differences do not alter the conclusions or the designs proposed by UWM.

A simple proportional speed control has been developed at ORNL for FSCW-SPM motors. Detailed simulation of the control shows that it can effectively control motor speed while minimizing the motor current magnitude during operation above and below base speed. Laboratory testing of this control method and UWM's maximum motor efficiency control will allow comparison and determination of which method exhibits the greatest overall drive efficiency.

Significant progress has been achieved during the past year in the development of advanced machine analysis/design and control techniques that will improve the operating efficiency of future FSCW-SPM machines. In particular, the work is contributing to a much-improved understanding of the sources and distribution of FSCW-SPM machine iron losses that play a major role in determining machine efficiency. This new knowledge is being put to use immediately in other programs to design more powerful FSCW-SPM machines for electric traction applications with improved efficiency characteristics.

Future Directions

Setup of the prototype 6-kW FSCW-SPM machine for dynamometer testing at ORNL is in progress. We will prepare a detailed plan to present the specifics for measuring the inverter and motor efficiencies so that the different control schemes may be compared. Each of the control schemes will be programmed in MatLab, compiled for use with OPAL RT, and used to drive the motor.

The detailed test plan will precede efficiency measurements of ORNL's low-cost control scheme to achieve maximum torque per amp below base speed and maximum power per amp above base speed at various speeds and partial loads. Similar test regimens will be used to test UWM's modified vector control algorithm under partial-load operating conditions so that the results may be used to compare control schemes.

During the first quarter of FY 2007 the prototype machine will be exercised under OPAL RT control to obtain the necessary comparative tests. Work is continuing at UWM to enhance the capabilities of the closed-form analytical model for accurately predicting iron losses in FSCW-SPM machines during operation over wide ranges of speed and load conditions. This improved iron loss model will be used to

develop an optimized design of a 55-kW (peak) FSCW-SPM machine to meet the demanding performance requirements for the FreedomCar.

Publications

A. M. EL-Refaie, T. M. Jahns, P. J. McCleer, and J. W. McKeever, "Experimental Verification of Optimal Flux Weakening in Surface PM Machines Using Concentrated Windings," in *Rec. of 2005 IEEE Ind. Appl. Soc. Ann. Mtg.*, Hong Kong, October 2005. *Accepted for publication in IEEE Trans. on Ind. Applications.*

A. M. EL-Refaie, T. M. Jahns, and J. W. McKeever, "Effect of Back-EMF Constraints on Fractional-Slot Surface PM Machines Designed for Wide Constant-Power Speed Range Operation," in *Proc. of 2006 Intl. Conf. on Electrical Machines*, Chania, Greece, September 2006.

A. M. EL-Refaie, T. M. Jahns, and J. W. McKeever, "Modified Vector Control Algorithm for Increasing Partial-Load Efficiency of Fractional-Slot Concentrated Winding Surface PM Machines," in *Rec. of 2006 IEEE Ind. Appl. Soc. Ann. Mtg.*, Tampa, October 2006.

References

1. J. S. Hsu, *Permanent Magnet Energy Conversion Machine*. U. S. Patent No. 5,952,756, September 14, 1999.
2. Cambier et al., *Brushless DC motor Using Phase Advance Timing Advancement*, U.S. Patent 5,677,605, October 14, 1997.
3. J. S. Lawler, J. M. Bailey, and J. W. McKeever, "Extended Constant Power Speed Range of the Brushless DC Motor Through Dual Mode Inverter Control," ORNL/TM-20000/130, July 2000.
4. J. S. Lawler, J. M. Bailey, and J. W. McKeever, "Minimum Current Magnitude Control of Surface PM Synchronous Machines during Constant Power Operation," *IEEE Power Electronics Letters* 3(2) (June 2005).
5. T. M. Jahns, *Cost Reduction Opportunities for Permanent Magnet Synchronous Machines*, Interim Report prepared for ORNL Technical Project Manager, May 24, 2005.
6. A. M. EL-Refaie, T. M. Jahns, P. J. McCleer, and J. W. McKeever, "Experimental Verification of Optimal Flux Weakening in Surface PM Machines Using Concentrated Windings," *IEEE Ind. Appl. Soc. Annual Meeting*, Oct. 2-6, 2005, Hong Kong.
7. Ayman M. EL-Refaie, *High Speed Operation of Permanent Magnet Machines*, Electrical and Computer Engineering Ph.D. Thesis at the University of Wisconsin-Madison, 2005.
8. A. M. EL-Refaie, T. M. Jahns, and J. W. McKeever, "Effect of Back-EMF Constraints on Fractional-Slot Surface PM Machines Designed for Wide Constant-Power Speed Range Operation," *Intl. Conf. on Electric Machines*, September 2006, Greece.
9. C. Mi, G. R. Slemon, and R. Bonert, "Modeling of Iron Losses of Permanent-Magnet Synchronous Motors," *IEEE Transactions on Industry Appl.* 39(2) (May/June 2003).
10. K. Atallah, D. Howe, P. H. Mellor and D. A. Stone, *Rotor Loss in Permanent-Magnet Brushless AC Machines*, *IEEE Tran. on Ind. Appl.* 36(6) (November/December 2000).
11. T. Sebastian and G. R. Slemon, "Operating Limit of Inverter Driven Permanent Magnet Motor Drives," *IEEE Trans. Ind. Appl.* 1A-23(2) 327-333 (March 1987).
12. W. Soong and T. J. E. Miller, "Field Weakening Performance of Brushless Synchronous AC Motor Drives," *IEE Proc. Of the Electronics Power Applications* 141(6), 331-340 (November 1994).
13. J. S. Lawler, "Control of Surface Mounted Permanent Magnet Motors with Special Application to Fractional-slot Motors with Concentrated Windings," ORNL/TM-2005-184, September 2005.
14. A. M. EL-Refaie, T. M. Jahns, J. W. McKeever, "Modified Vector Control Algorithm for Increasing Partial-Load Efficiency of Fractional-slot Concentrated Winding Surface PM Machines," *IEEE Ind. Appl. Soc. 41st Annual Mtg.*, Marriott Waterside Hotel, Tampa, FL, October 8-12, 2006.
15. V. Zivotic-Kukolj, W. L. Soong, N. Ertugrul, "Iron Loss Reduction in an Interior PM Automotive Alternator," pp. 1736-43 in *Rec. of 2005 IEEE Ind. Appl. Soc. Ann. Mtg.*, Hong Kong, October 2005.

16. Z. Q. Zhu, D. Howe, C. C. Chan, "Improved Analytical Model for Predicting the Magnetic Field Distribution in Brushless Permanent-Magnet Machines," *IEEE Trans. Magnetics* **38**(1) (January 2002).
17. Z. Q. Zhu, and D. Howe, "Instantaneous Magnetic Field Distribution in Brushless Permanent Magnet dc Motors, Part I: Open-Circuit Field," *IEEE Trans. Magnetics* **29**(1) (January 1993).
18. D. Zarco, *A Systematic Approach to Optimized Design of Permanent Magnet Motors with Reduced Torque Pulsations*, Ph.D. Thesis, Department of Electrical and Computer Engineering, University of Wisconsin-Madison, 2004.
19. A. M. EL-Refaic and T. M. Jahns, "Comparison of Synchronous PM Machine Types for Wide Constant Power Speed Range Operation," in *Rec. of 2005 IEEE Ind. Appl. Soc. Annual Meeting*, Hong Kong, Oct. 2005.
20. D. W. Novotny and T. A. Lippo, *Vector Control and Dynamics of AC Drives*, New York, Oxford University Press, 1996.
21. Z. Q. Zhu, U. S. Chen, and D. Howe, "Iron Loss in Permanent-Magnet Brushless AC Machines Under Maximum Torque per Ampere and Flux Weakening Control," *IEEE Trans. Magnetics*, **38**, 3285-3287, September (2002).
22. A. M. EL-Refaic, T. E. Jahns, and D. W. Novotny, "Analysis of Surface Permanent Magnet Machines Equipped with Concentrated Windings," *IEEE Trans. Energy Conversion*, **21**, 34-43, March 2005.

3.4 Extending the CPSR of Synchronous Reluctance Motors

Principal Investigator: John W. McKeever

Oak Ridge National Laboratory

National Transportation Research Center

2360 Cherahala Boulevard

Knoxville, TN 37932

Voice: 865-946-1316; Fax: 865-946-1262; E-mail: mckeeverjw@ornl.gov

DOE Technology Development Manager: Susan A. Rogers

Voice: 202-586-8997; Fax: 202-586-1600; E-mail: Susan.Rogers@ee.doe.gov

ORNL Program Manager: Mitch Olszewski

Voice: 865-946-1350; Fax: 865-946-1262; E-mail: olszewskim@ornl.gov

Objectives

The objective of this project was to determine if a reliable per-phase analytical model could be developed for a synchronous reluctance motor. A per-phase model, which has been developed for brushless dc permanent magnet (PM) motors and for switched reluctance motors, has been used to show that both of these motor types have unbounded constant power speed ratios (CPSRs) if resistance and speed sensitive losses are neglected. If a reliable per-phase model could be developed, it could be used to determine if a synchronous reluctance motor also has an unbounded CPSR. During the development of a per-phase model of the switched reluctance motor, detailed computer modeling revealed that, as the speed of the model increased, saturation did not impact its performance. The question is whether saturation-independent behavior is true for a synchronous reluctance motor, considering the different drive mechanisms.

Another objective was to model a synchronous reluctance motor using available commercial motor design software to determine performance targets that may be compared with the FreedomCAR targets. This would provide an idea of the extent to which performance targets had to be improved to make this motor an a hybrid electric vehicle (HEV) traction drive candidate.

Approach

Commercial software was used extensively during this part of the project. ORNL is a member of the SPEED Consortium, based at the University of Glasgow, Scotland. Consequently, SPEED software was used to model two synchronous reluctance motor inverter designs and to check their performance characteristics. Two other software packages employed were FLUX2D and COMSOL. Although FLUX2D has a good magnetic solution capability, construction of models was difficult, requiring extensive technical support from Magsoft. COMSOL proved to be far more versatile and, because of its ability to represent saturation, was helpful in determining how important it is that saturation be a part of any model we develop.

An attempt was made to define a per-phase model like the one used for brushless dc motors and switched reluctance motors. The winding function, which assumes an idealized machine with uniform air gap, was applied to a reluctance motor with salient rotor and salient stator poles. The double salient poles have a very nonuniform gap. This nonuniformity caused flux fringing at all positions of the rotor pole from its aligned to unaligned positions, making use of the winding function an approximation. A model of a synchronous reluctance motor using COMSOL showed that flux fringing effects are significant. Use of the winding function as an approximation gave equations for direct and quadrature inductances

corresponding to the aligned and unaligned positions of the rotor. A detailed finite-element analysis will be necessary to quantify the reliability of the per-phase model.

Meaningful analyses were provided by using COMSOL to examine the flux patterns between the rotor and stator during operation of a synchronous reluctance motor. The results and conclusions of this analysis are included in this report.

Major Accomplishments

1. We applied FLUX2D software to determine the phase advance, which is the angle between the center of a rotor pole and the stator current orientation, that will produce maximum torque. ORNL created a model of a PM motor with inset magnets and turned off the magnets to simulate a synchronous reluctance motor with doubly salient poles. The torque produced was then calculated for a fixed rotor as the current in the stator was varied over one pole and for current fixed in the stator with the rotor turned through one pole angle. Definite maxima were found with only rough agreement between the two approaches. A similar exercise with COMSOL demonstrated good agreement between the two approaches for estimating the phase advance for maximum torque.
2. Using SPEED as a design tool, two synchronous reluctance motors were modeled to try to meet FreedomCAR targets. The first model with four turns per pole could not deliver maximum power at 2000 rpm. Adequate power at 2000 rpm required eight turns per pole, which doubled the amount of copper to increase both cost and weight. The motor was too heavy and too expensive to meet FreedomCAR goals.
3. We defined a per-phase model by applying a winding function to a synchronous reluctance motor with salient rotor and stator poles to determine the inductance that should be used. This approach yielded direct and quadrature inductances, which had to be added for use in the model. Unfortunately, flux fringing, verified by a COMSOL analysis, indicated that use of the winding function was clearly an approximation. Later work showed that a reliable model should include not only flux fringing but also saturation.
4. We constructed detailed models of switched reluctance motors to study flux behavior in a synchronous reluctance motor. Variations in the study included (1) a solid rotor to study the effect of eddy currents on the rotor; (2) regular reluctance rotors turning inside stators with and without shoes in their teeth; and (3) a comparison of synchronous reluctance motor performance, assuming no saturation with performance, that included saturation as part of the model. Overall results strongly suggested that any reliable model of a synchronous reluctance motor must incorporate flux fringing as well as saturation.

Technical Discussion

Modeling a Synchronous Reluctance Motor using SPEED Software

Two SPEED models of a synchronous reluctance motor

Two similar synchronous reluctance motor designs were studied to assess their potential to meet the targets of the FreedomCAR program. The two designs differ in the number of turns used in the stator. Their rotors are identical and consist of four poles made of six U-shaped plates of magnetic steel separated by five air gaps. Figure 1 shows a schematic drawing of the synchronous reluctance motor design considered.

Table 1 contains the performance data for a synchronous reluctance motor with four stator turns per pole. Top speed is 10,000 rpm, and performance values are at 20% of top speed.

Table 2 contains the performance data for a synchronous reluctance motor with eight stator turns per pole. Again top speed is 10,000 rpm, and performance values are calculated at 20% of top speed.

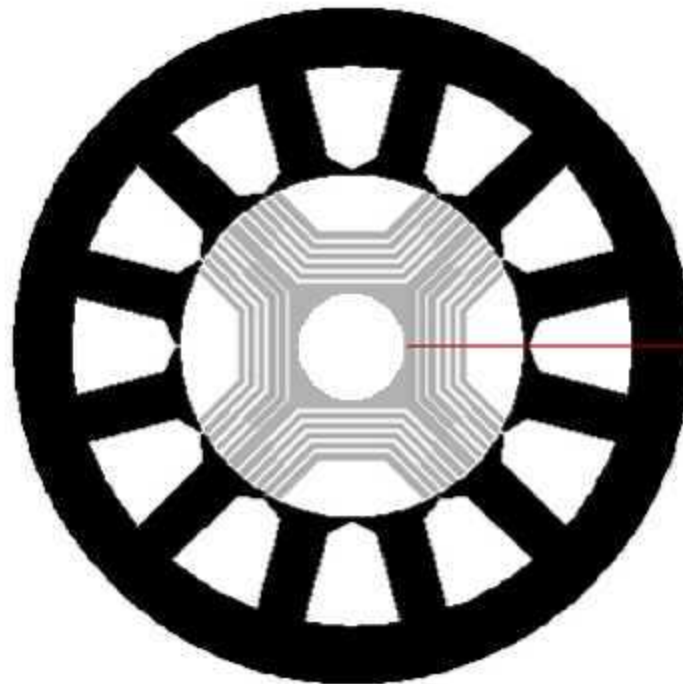


Figure 1. Schematic of a synchronous reluctance motor (4 poles, 12 slots, 40-cm diameter, 100 cm long, no permanent magnets).

Table 1. SPEED performance data for a synchronous reluctance motor whose stator has four turns per pole

25 kW at 2,000 rpm with 93% efficiency using $\gamma = 65$ eDeg 565-A peak current, 400-A _{rms} current, 92 V _{LL} => 118 V _{dc} Current density = 5.1 A/mm ²
55 kW at 10,000 rpm with 96% efficiency using $\gamma = 49.5$ eDeg 322-A peak current, 228-A _{rms} current, 342 V _{LL} => 438 V _{dc} Current density = 2.9 A/mm ²
30 kW at 10,000 rpm with 96% efficiency using $\gamma = 46$ eDeg 233-A peak current, 165-A _{rms} current, 262 V _{LL} => 336 V _{dc} Current density = 2.1 A/mm ²
Total weight 65.6 kg (30 kg of Cu and 45 kg of Fe) Total volume = 12.6 L Peak power/weight = 0.73 kW/kg [<2.75] Peak power/volume = 4.4 kW/L [<12.5] (i.e., about factor of 3 below target for power density)

Table 2. SPEED performance data for synchronous reluctance motor whose stator has eight turns

 55 kW at 2,000 rpm with 94% efficiency using $\gamma = 75$ eDeg
565-A peak current, 400-A_{rms} current, 297 V_{LL} => 381 V_{dc}Current density = 5.1 A/mm²30 kW at 2,000 rpm with 96% efficiency using $\gamma = 65$ eDeg330-A peak current, 233-A_{rms} current, 203 V_{LL} => 260 V_{dc}Current density = 2.9 A/mm²7.5 kW at 10,000 rpm with 96% efficiency using $\gamma = 45$ eDeg58-A peak current, 41-A_{rms} current, 262 V_{LL} => 336 V_{dc}Current density = 0.5 A/mm²

Total weight 106 kg (61 kg of Cu and 45 kg of Fe)

Total volume = 12.6 L

Peak power/weight = 0.52 kW/kg [<2.75]Peak power/volume = 4.4 kW/L [<12.5]

(i.e., about 5 and 3 times below targets for power density)

A sample SPEED design sheet for the Table 2 case is contained in Table 3.

Table 3. Design sheet for the reluctance motor shown in Figure 1

PC-SREL 1.5 for Windows (1.5.2.1) 2/8/2006 11:50:00 AM					
F:\My Documents\jjo_srel_motor55kwFC2krp syl					
UT-Battelle, LLC					
PC-SREL main title					
PC-SREL sub-title					
1 Dimensions					
RotorRad	100.000 mm	BoreRad	102.000 mm	Gap	2.000 mm
FrameRad	200.000 mm	ShaftRad	34.000 mm	POLES	4
SLOTS	12	TWS	28.000 mm	SD	64.000 mm
SO	2.000 mm	TGD	2.000 mm	TGANG 4	0.000 mDeg
RNSQ	Square	Stf	0.970	RotType	As Lam
LStator	100.000 mm	LRotor	100.000 mm	LShaft	150.000 mm
LMotor	175.000 mm	1stLayer	Guide	PoleMat	Insulation
NLayers	12	B_Thick	2.000 mm	G_Thick	4.000 mm
NunGuide	6	NunBarrs	6	PoleArc	42.200 mDeg
2 Control Data					
RPM	2000.000 rpm	I(rms)	233.000 A	Gamma	65.000 eDeg
Vs(dc)	450.000 V	Rtrans	0.000 Ohms	Vdiode	0.600 V
Vtrans	0.000 V				
3 Winding Data					
WdgType	Lap	Connex	Wye	Throw	3
TC	8	CoilsPer	1.000	NSII	1
Tph	32.000	PPATHS	1	SPP	1.000
Layers	2.000	CSidesPh	8	Z	0.000
MLT	917.191 mm	Ext	0.000 mm	LghOEnd	328.289 mm
MaxSFill	0.492	EndFill	0.500	LaxPack	314.087 mm
SFill	0.492	WDia	10.000	WireSpec	BareDia
WireDia	10.000 mm	Liner	0.400 mm		
SlotArea	2554.242 mm ²	CondArea	78.540 mm ²	ASlotLL	2473.684 mm ²
WdgTemp	25.000 DegC	Rph	6.478E-03 Ohm/Ph	Rterm	0.013 Ohms
PCSlot	3.455	XET	1.000	AxI	75.000 mDeg
ksI	1.000				
kwI	1.000	Nse	40.744		

Table 3. (continued)

4 Magnetic Circuit Design					
BgIOC	0.821 T	PhiM1	8.374 mWb	Bt_pk	1.614 T
Bg_pk	0.821 T	Bf_pk	1.270 T	Bg_pk	1.370 T
				BgBH_pk	3.426 T
5 Inductance Values					
Kc_Rotor	1.054	Kc_Stat	1.007	Kc_Total	1.061
XLq_m	1.000	XLd_m	1.000	XLslot	1.000
XLendf	1.000	LSlot	0.445 mH/Ph	Lendf	0.088 mH/Ph
XLThTip	1.000	LThTip()	0.246 mH/Ph		
MSlot	0.000 mH/Ph	fz	1.020	Xq	0.860 Ohm/Ph
Xm0	1.249 Ohm/Ph	Xsigma	0.223	Xq	0.860 Ohm/Ph
Lq/Ld_1	25.500	L_m	2.982 mH	Ld_1	0.125 mH
Lq/Ld_mU	6.231	Lq_m(U)	2.343 mH	Ld_m	0.376 mH
Lq/Ld_mS	5.150	Lq_m(S)	1.936 mH	Ksat_Lmq	1.210
Lq/Ld(U)	2.491	Lq(Usat)	2.876 mH	Ld	1.154 mH
Lq/Ld(S)	2.139	Lq(Sat)	2.469 mH		
6 Sine-wave static performance [phasor diagram]					
Torque	142.904 Nm	PowerM	29929.669 W	Eff	96.015 %
LossCu_S	1055.105 W	LossFe_R	0.000 W	LossFe_S	187.249 W
LossWF	0.000 W	LossTot	1242.354 W	Jrms	2.967 A/mm ²
IWpk	329.512 A	IWav	209.774 A	IWrms	233.000 A
ILpk	329.512 A	ILav	209.774 A	ILrms	233.000 A
IDclpk	0.000 A	IDclav	0.000 A	IDclrm	0.000 A
IDclnks	69.271 A	LossConv	0.000 W	kVA	82027.629 kVA
Iq1	98.470 A	Id1	-211.170 A	Gamma	65.000 eDeg
Vq1	-79.742 V	Vd1	-86.094 V	Delta	132.806 eDeg
Vs1	350.864 V	Vs1Lin	275.568 V	Phi	67.806 eDeg
Vph1	117.350 V	VLL1	203.256 V	TempRise	37.271 DegC
PF_fund	0.378	PF	0.380	Appt_PF	0.365
7 Mechanical Data					
NumBolts	6	BoltDia	10.000 mm	BoltLgh	66.000 mm
BoltTdDp	0.167 mm	BoltSpec	13.333 mm	BoltHdCl	1.650 mm
BoltInSh	1.650 mm	BtClInSh	64.700 mm	BHdClMin	1.149 mm
BtLoss%	0.600	BoltYStr	230.000 MPa	ShrYStr	300.000 MPa
TensBlt	16879.952 N	ShearThB	2881.233 N	ShearThS	3887.721 N
SpeedMax	2157.190 rpm				
8 Miscellaneous					
WtCu	60.856 kg	WtFe	45.189 kg	WtMag	0.000 kg
WtTot	106.045 kg	RotJ	0.000 kg-m ²	LosFe/Wt	4.144 W/kg
Sigma	3.298 psi	XFe	1.000	Freq1	66.667 Hz
TempCalc	DegCW	DegCW	0.030 degC/W	HTransCo	265.258 W/m ² /C
Ambient	25.000 DegC	HTransCo	0.000 W/m ² /C		
Wf0	0.000 W	RPM0	1000.000 rpm	NWFT	1.000
9 Core loss analysis					
SSteelNa Transl	Bs=1.3T 35				
RSteelNa Transl	Bs=1.3T 35				
WtTeeth	16.823 kg	WtYoke	28.366 kg	WtTrout	4.145 kg
LossTthE	25.082 W	LossTthH	82.736 W	LossTth	107.818 W
LThE/Wt	1.196 W/kg	LThH/Wt	3.946 W/kg	LTh/Wt	5.142 W/kg
LossYkE	20.985 W	LossYkH	58.446 W	LossYk	79.431 W
LYkE/Wt	0.740 W/kg	LYkH/Wt	2.060 W/kg	LYk/Wt	2.800 W/kg
LossE50	0.581 W	LossH50	2.376 W	LossFe50	2.957 W
End of Design sheet					

Both designs have the same overall volume and the same mass of steel. The motor with four stator turns has one-half the mass of copper of the motor with eight turns.

Because of its lower number of turns, the four-turn motor excels at high speeds, while the eight-turn motor is best for low speeds. Specifically, at 2,000 rpm, with the same 400-A_{rms} current limit, the four-turn motor produces 25 kW, while the eight-turn motor produces 55 kW. At 10,000 rpm, with the same voltage limit of 336 V_{dc}, the four-turn motor produces 30 kW, while the eight-turn motor produces only 7.5 kW.

The purely synchronous reluctance motor (no PM) will be large and must be capable of changing the number of active turns to cover the whole range of operation as required by the FreedomCAR specifications. The power density of both motors is one-third of the FreedomCAR goal.

Conclusions from the SPEED Modeling

The power density of synchronous reluctance motors will always benefit from the addition of PM in the rotor; however, adding magnets makes this motor configuration an internal permanent magnet motor, which should be researched with other IPMs. A major reason for studying reluctance motors is to learn how to harvest additional magnet-free torque from them at all speeds. Eliminating magnets could become strategic if their cost rises. Heavy vehicle manufacturers such as LeTorneau have incorporated this type of motor in their loaders and bulldozers because of their sturdy construction, high performance, efficiency, productivity, and simplicity. It is very likely that the synchronous reluctance motor can overcome the torque ripple problems encountered by switched reluctance motors because of its synchronous operation. Some fruitful areas for further research are (1) employing non-sinusoidal waveforms; (2) placing PM materials at symmetrical as well as asymmetrical places on the rotor; and (3) determining how to match the effective number of stator turns to the speed and power requirements of the motor and exploring how to switch the stator turns in and out of the circuit during operation of the motor.

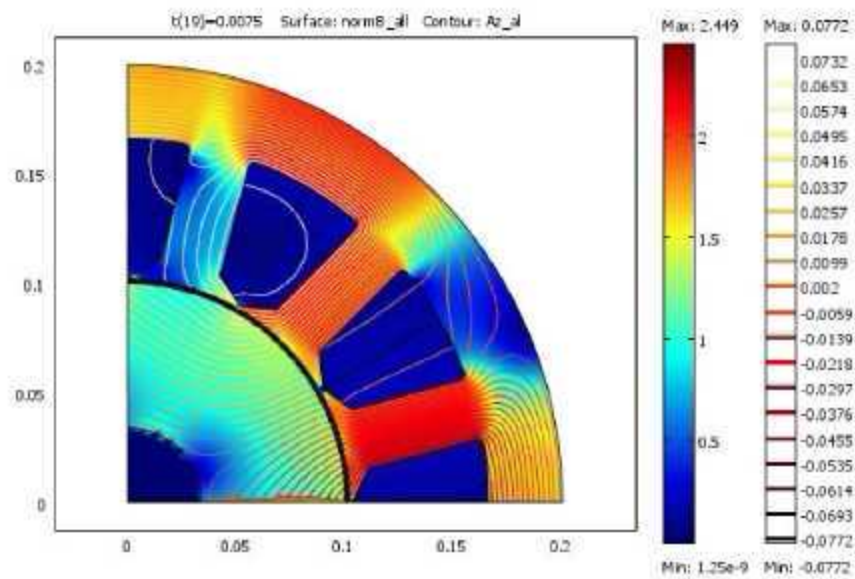
Finite-Element Analysis of Reluctance Motors using COMSOL

Finite-element models of the synchronous reluctance motor were run using stators with and without shoes in their teeth and using several different rotors. To assess the effect of saturation and discreteness of the stator teeth, slot openings, and nonsinusoidal winding distribution on the shape of the rotating magnetic flux produced in the stator and motor, a solid cylindrical rotor was simulated. It was also used to compute the eddy currents induced when the cylinder is a good electrical conductor. The other rotors sported a conventional layered structure with different additions of PM material.

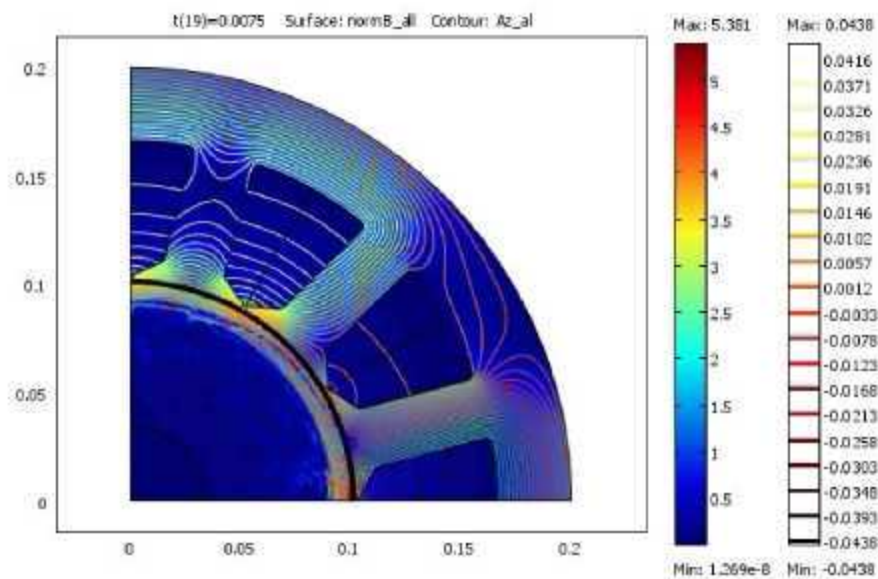
Solid Rotor Study

The colors in Figure 2 show the flux in Tesla, and the contours are lines of constant magnetic potential. Comparing Figures 2(a) and 2(b) illustrates the impact of eddy currents in the rotor. In Figure 2(b) the eddy currents induced in the rotor's surface prevent the stator magnetic flux from crossing the air gap into the rotor, as evidenced by the fact that the contours do not cross the gap.

The effect of magnetic saturation and the stator's heterogeneity on the magnetic flux crossing the air gap is shown in Figure 3. Figure 3(a) shows that the rotor's surface-averaged flux has a trapezoidal ripple of about 6% with a frequency equal to that of the slot-opening crossing. Colored dots correspond to the colored curves in Figure 3(b). The distribution of the flux around the rotor surface is shown in Figures 3(b) and 3(c) to be far from sinusoidal. The generation of torque around the periphery of the solid rotor is shown in Figure 4 to be very small but not uniform.

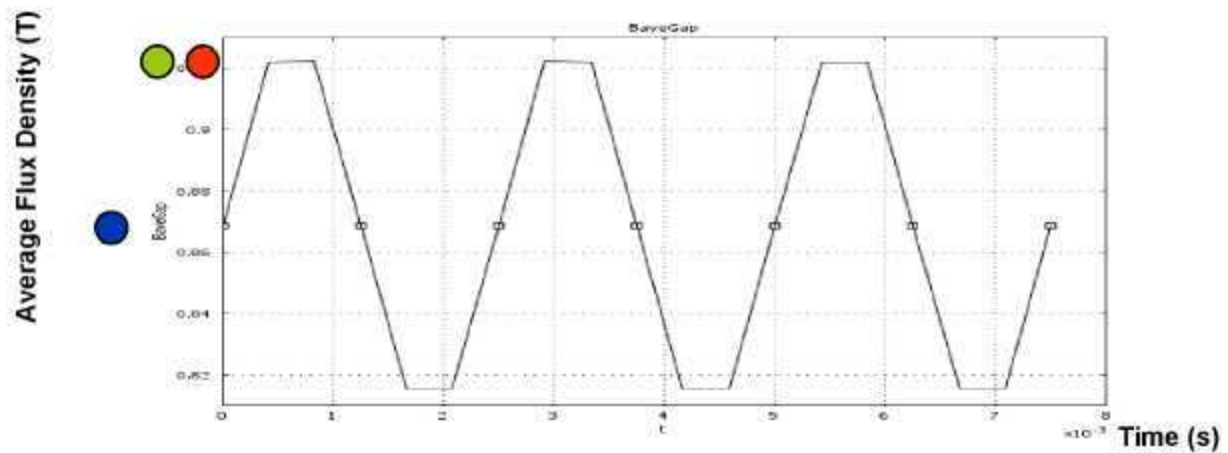


(a) Electrically nonconductive steel rotor.

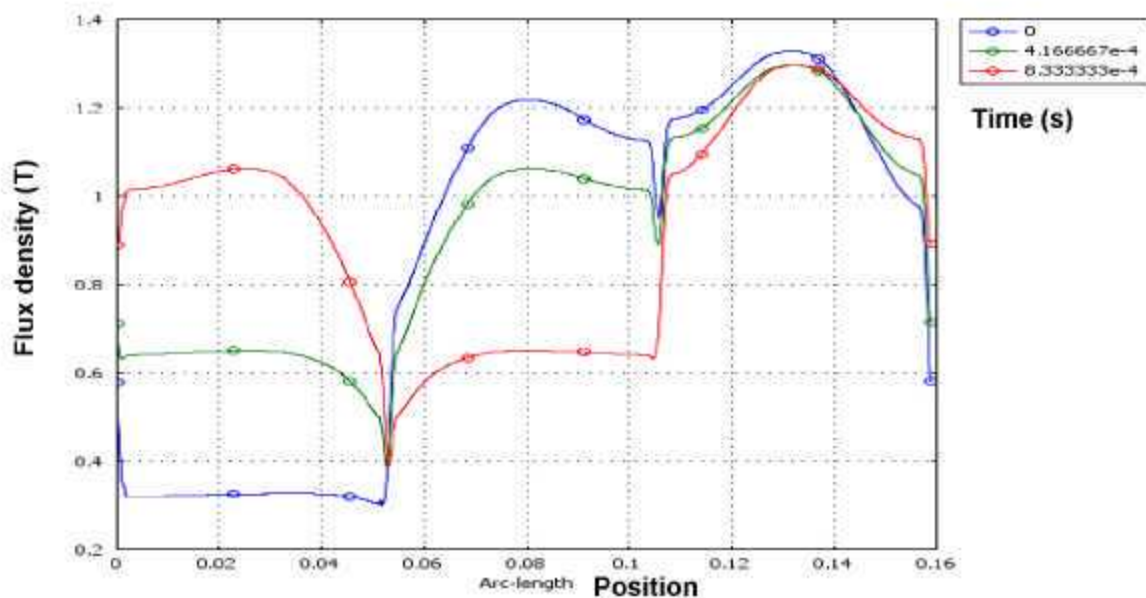


(b) Electrically conductive iron rotor.

Figure 2. Magnetic flux lines generated by the stator's rotating field in a reluctance motor with a solid rotor.

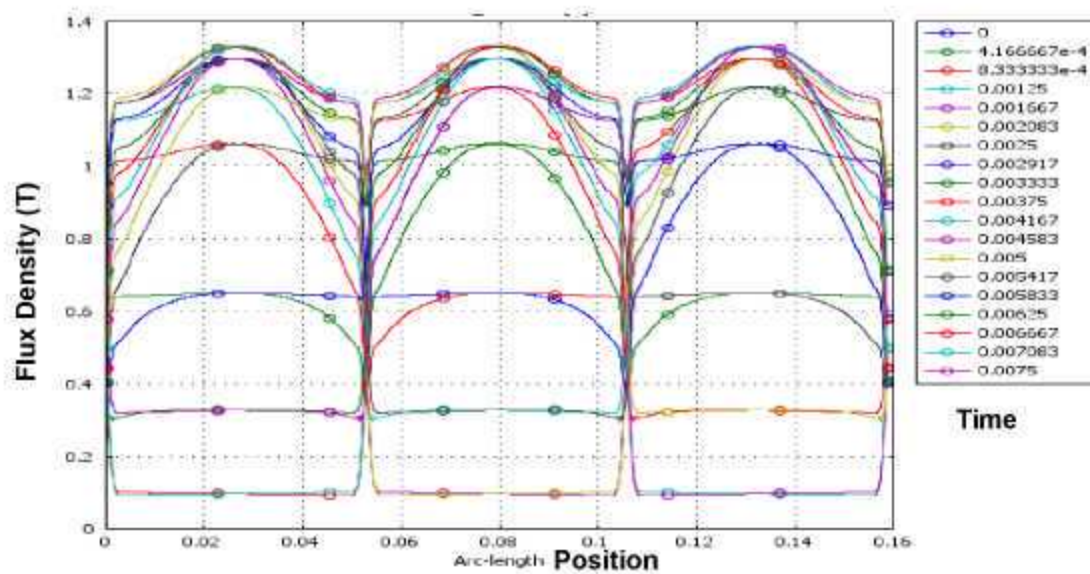


(a) Average air gap flux density for a solid nonconductive steel rotor as a function of time.



(b) Flux density distribution for a nonconductive steel rotor at the three times marked in (a).

Figure 3. Distribution of magnetic flux crossing the air gap generated by the stator's rotating field in a motor with a solid rotor.



(c) Flux distribution for a nonconductive steel rotor at times spanning a quarter turn.

Figure 3. (continued).

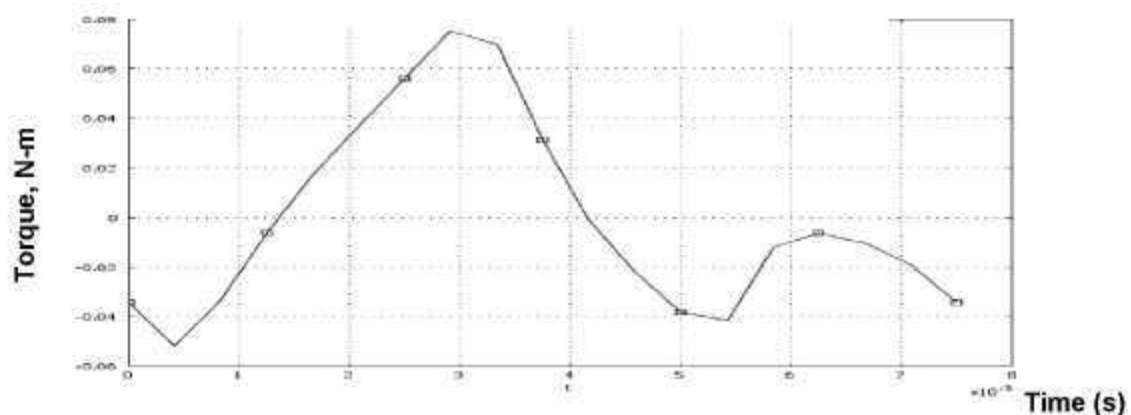


Figure 4. Total torque in the motor with a solid rotor made of nonconductive steel as a function of time for a quarter turn.

Layered Reluctance Rotors

In addition to the stators with and without shoes and the classic rotor shown in Figure 1, several configurations with varying amounts and locations of PM material inserted between the steel layers were simulated. The definitions of these configurations appear in Figure 5.

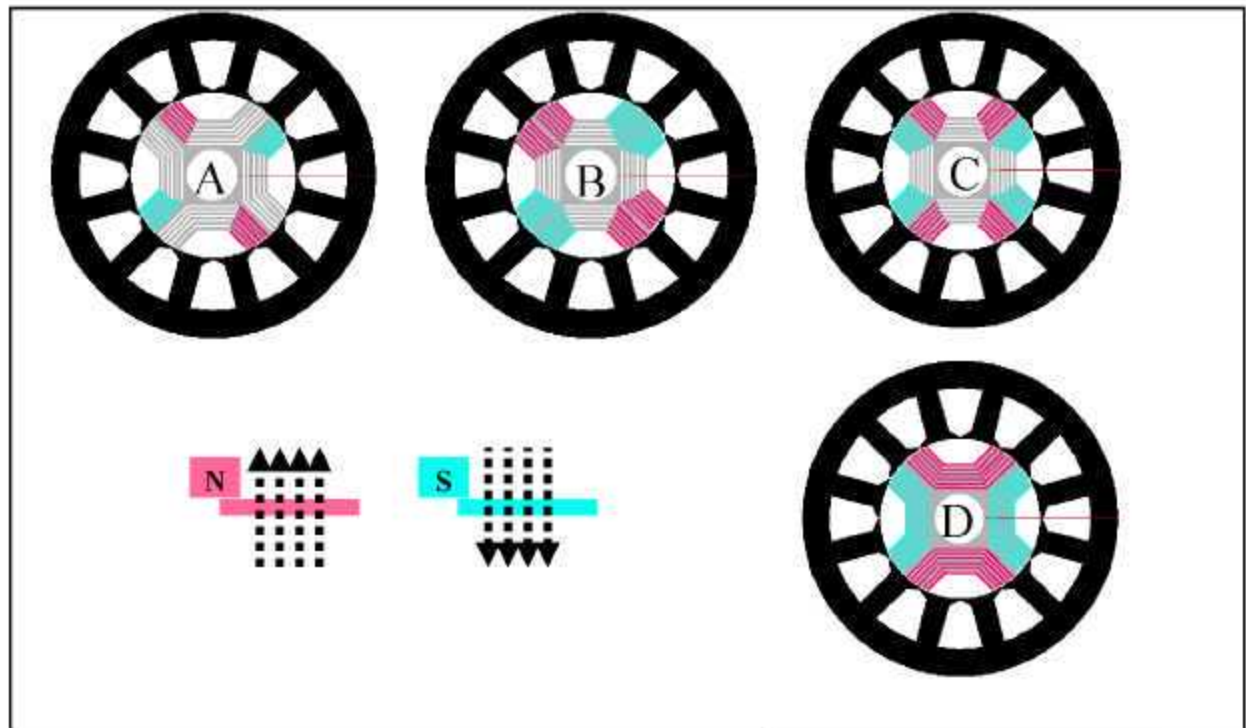


Figure 5. Modified synchronous reluctance motor types with PMs added between the rotor's steel layers. (a) alternating single magnets, (b) back-to-back magnets, (c) alternating dual magnets, and (d) full pole magnets.

Comparison of Torque Generation

In the following figures, the suffix to the rotor type *_s* indicates that the stator teeth had shoes attached, and *_ns* indicates that the teeth had no shoes attached. Figure 6 compares designs B_s and C_s and shows that C, the rotor with consecutive poles partially loaded with PMs of the **same** polarity has the highest peak torque value. For about one-half of the angle range, though, the type B design exhibits higher torque values.

Figure 7 compares the torque as a function of control angle for motors with different rotors for each of the two stator types. The designs fully loaded with PMs, D_{ns} and D_s, have the highest peak torque values. The design without shoes has a slightly higher maximum torque. Although torque is zero for $\gamma = 120$ eDeg, which is the angle where the radial flux is maximum corresponding to the green line in Figure 8, the maximum torque occurs for $\gamma = 265$ eDeg rotating in one direction and 335 eDeg in the other. The notation, eDeg, means electrical degrees. The average flux at 335 eDeg also happens to be a minimum. Comparison of the peaks and valleys in Figures 7 and 8 shows that higher average fluxes do not necessarily produce higher torques at the corresponding control angles.

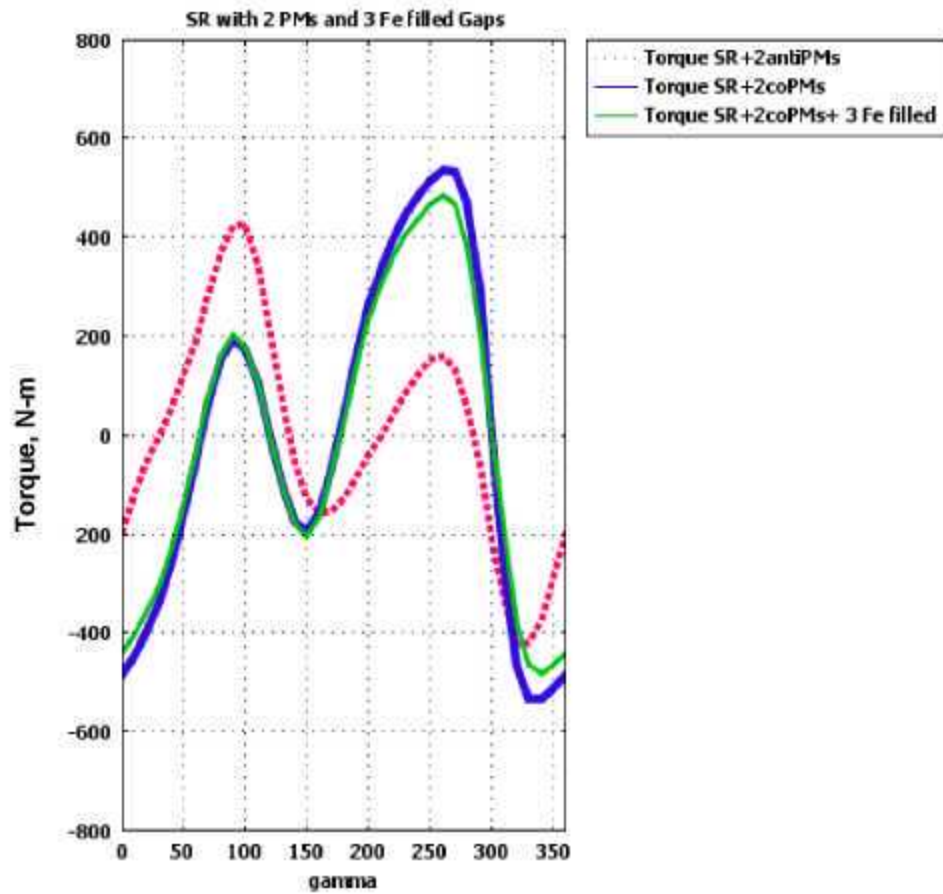


Figure 6. Torque as a function of stator current angle, γ .

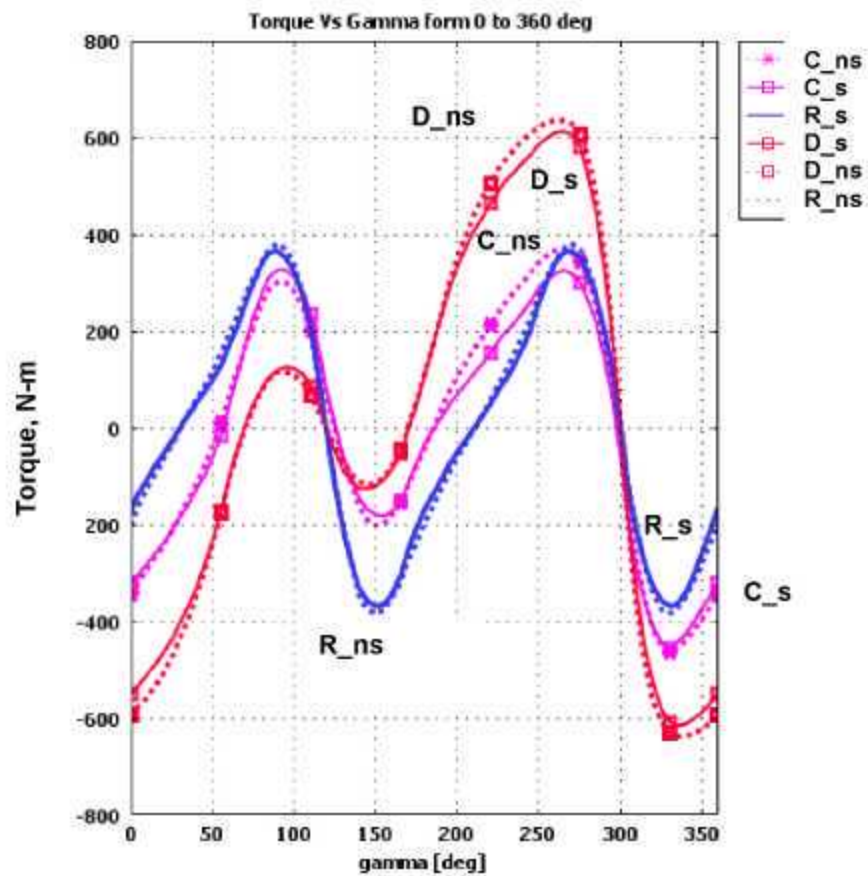


Figure 7. Torque as a function of stator current angles from 0 to 360 eDeg.

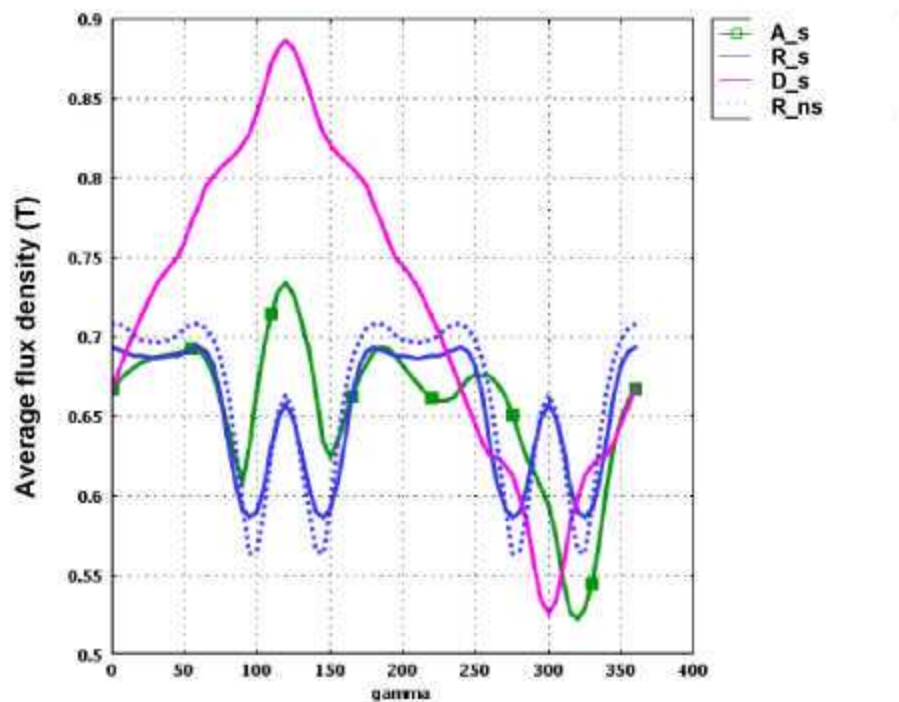


Figure 8. Average flux at the rotor surface for stator current angles from 0 to 360 eDeg.

Flux Shapes along the Rotor Periphery

In this section we illustrate the impact of saturation and stator/rotor nonuniformity on the magnitude and shape of the stator and rotor. Figure 9 shows the permeability dependence on local magnetic flux for the two cases considered: saturating and nonsaturating. The figures below correspond to a motor of type A with no shoes in the stator teeth. The stator current is 400 Arms. Figures 10 and 11 show the dramatic reduction in torque and flux levels and shape distortion when saturation is considered. The peak torque is three times smaller when saturation is considered.

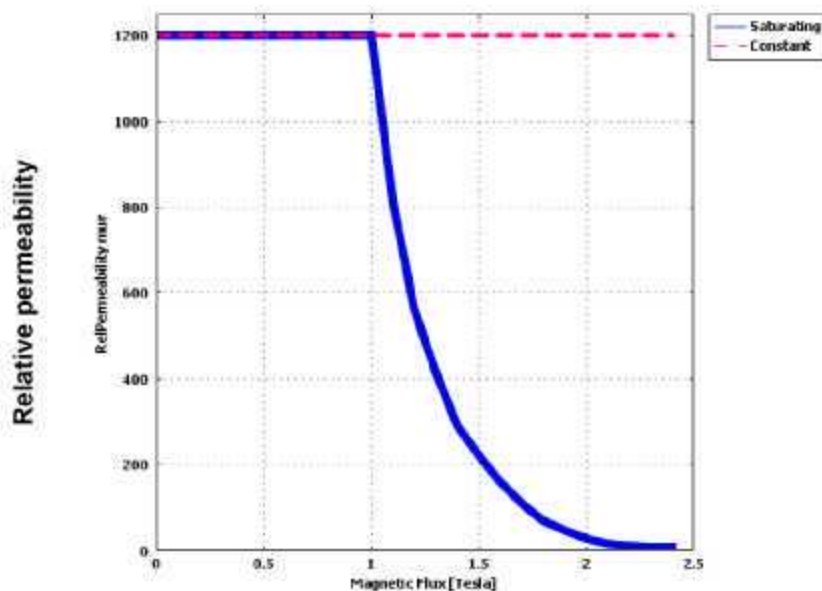


Figure 9. Permeability dependence on flux for study on the effect of saturation.

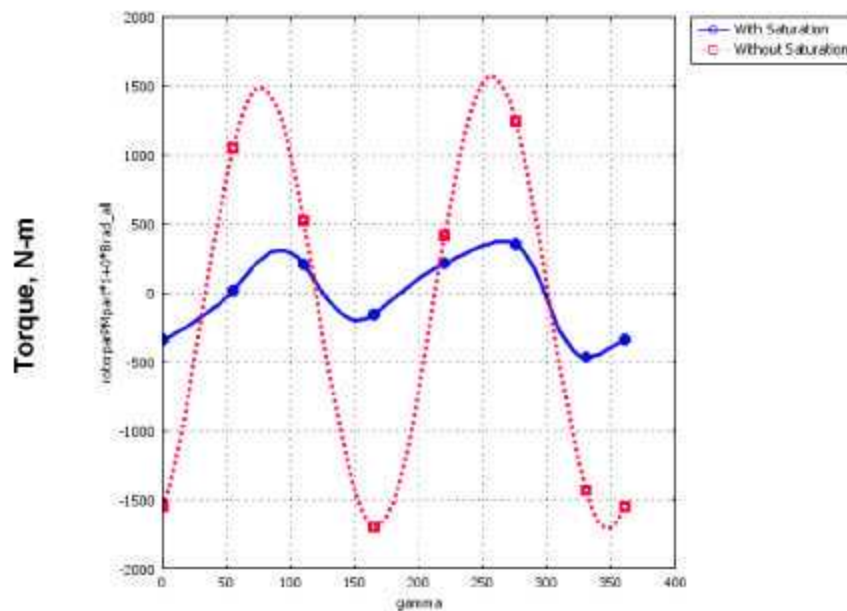


Figure 10. Torque vs control angle, γ , with and without saturation.

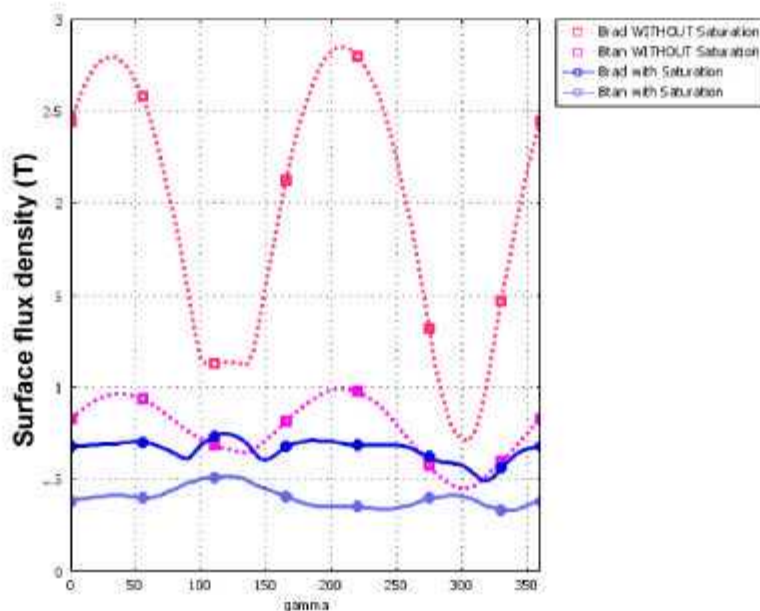


Figure 11. Average radial and tangential rotor surface flux components vs control angle, γ , with and without saturation.

Note that maximum torque corresponds to the situation in which the control angle is such that the two stator teeth close to the rotor iron pieces are unevenly loaded with magnetic energy. In Figure 12(b) the two are heavily loaded, saturated, and because they attract the rotor's iron in opposite directions, they cancel each other and produce no net torque.

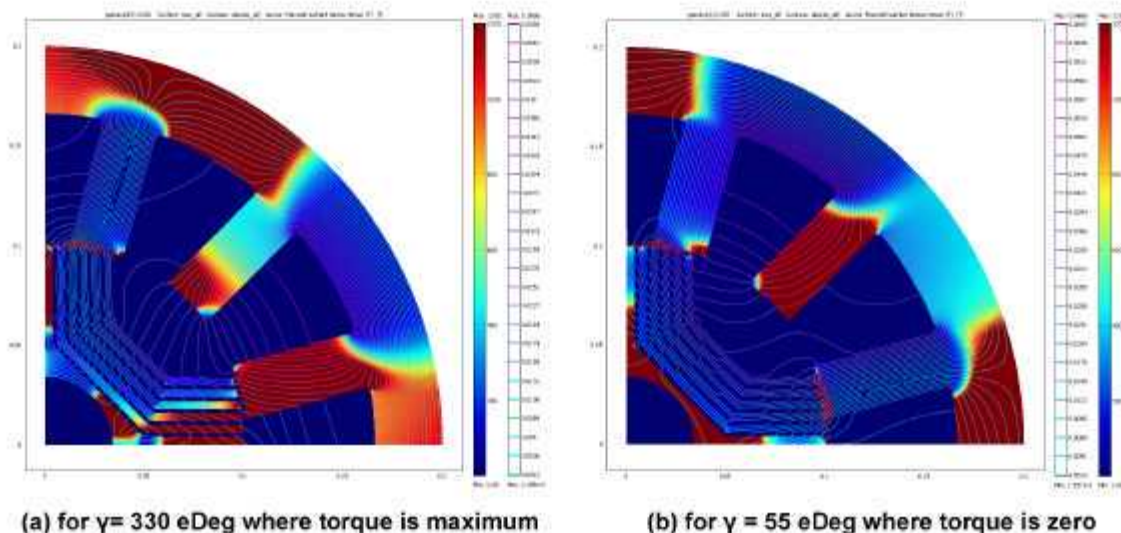


Figure 12. Permeability and flux lines in a type A motor with no shoes on the stator teeth. The bottom of the scale (dark blue) corresponds to $\mu_r = 1$ (saturated iron), and the top of the scale (dark red) corresponds to $\mu_r = 1200$ (unsaturated iron).

In Figures 13 and 14, the envelope created by the shapes of the radial and tangential components of the flux distribution around the rotor surface are shown for all angle control positions from 0 to 360 eDeg. For clarity, the same is shown only for control angles from 0 to 45 eDeg in Figures 15 and 16. Better yet, Figure 17 shows the flux shapes only for the control angle that produces optimal torque in the motor. As can be seen in Figure 10, these angles are 330 eDeg with saturation and 350 eDeg without saturation.

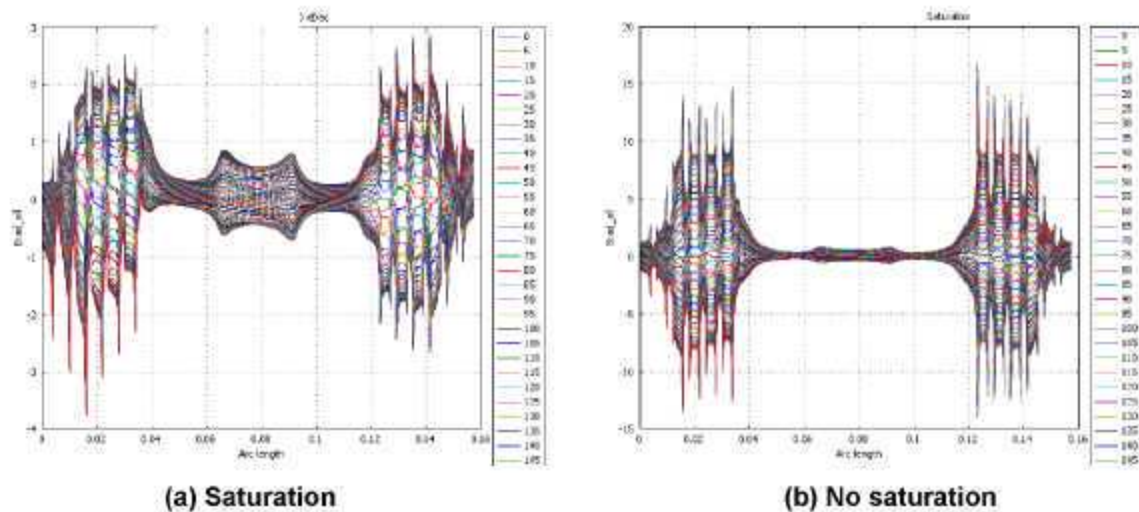


Figure 13. Radial flux distribution along the rotor periphery for $\gamma = 0$ to 360 eDeg. [The Y-axis scale in (b) is much larger for the nonsaturating case.]

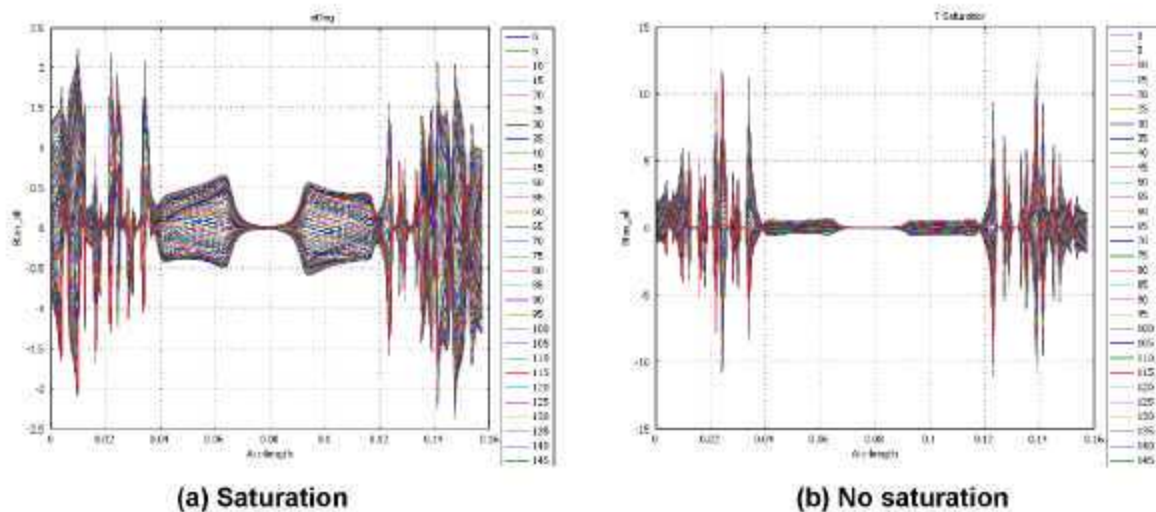
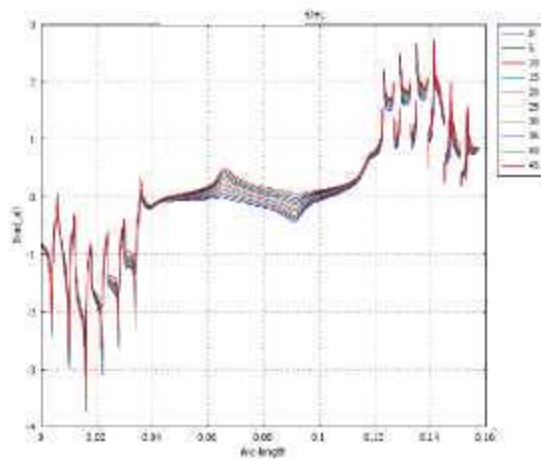
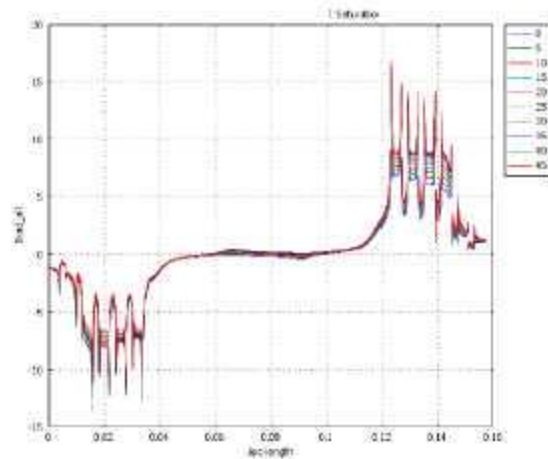


Figure 14. Tangential flux distribution along the rotor periphery for $\gamma = 0$ to 360 eDeg. [The Y-axis scale in (b) is much larger for the nonsaturating case.]

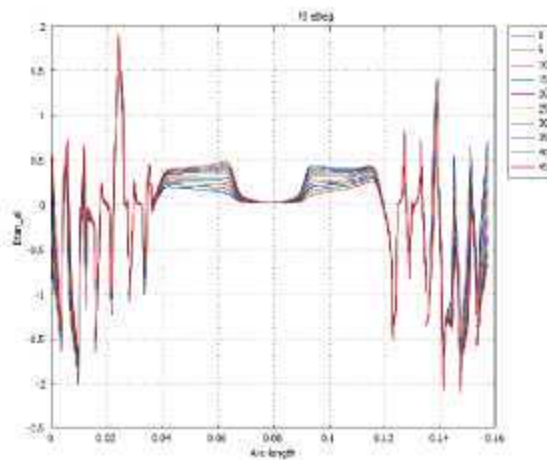


(a) Saturation

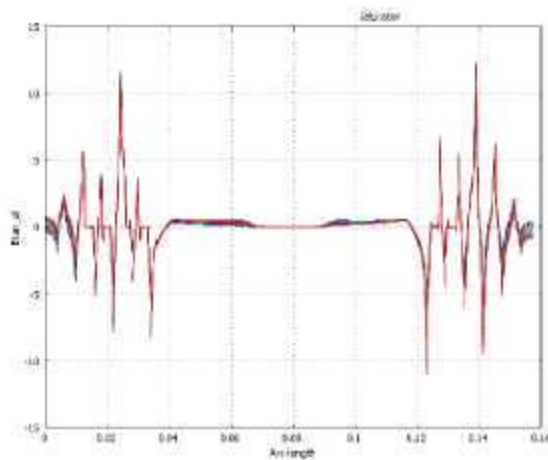


(b) No saturation

Figure 15. Radial flux distribution along the rotor periphery for $\gamma = 0$ to 45 eDeg. [The Y-axis scale in (b) is much larger for the nonsaturating case.]



(a) Saturation



(b) No saturation

Figure 16. Tangential flux distribution along the rotor periphery for $\gamma = 0$ to 45 eDeg. [The Y-axis scale in (b) is much larger for the nonsaturating case.]

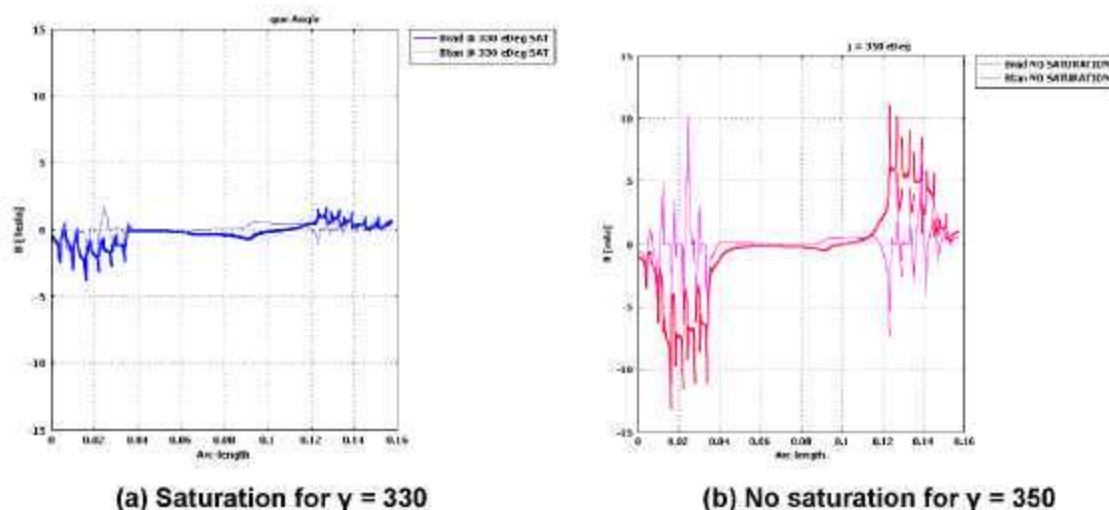


Figure 17. Radial and tangential flux distributions along the rotor periphery for optimal control angle.

Conclusions

Because today's performance of synchronous reluctance motors is below the FreedomCAR targets the potential of the synchronous reluctance motor is often overlooked. These motors exhibit sturdy construction, high performance, efficiency, productivity, and simplicity. It is very likely that the synchronous reluctance motor can overcome the torque ripple problems encountered by switched reluctance motors because of its synchronous operation. For these reasons it is plausible that synchronous reluctance motors may one day be utilized as traction motors if the cost of PMs escalates.

Motor modeling must use actual geometries and solve fundamental equations with as few approximations as possible. At this time finite element analysis seems the best way to directly solve the mathematical equations and account for specific geometric and material properties as well as nonlinear effects such as those introduced by magnetic saturation. Saturation needs to be accounted for as accurately as possible because it affects very significantly the magnitude and shape of the torque and flux distributions.

Because of geometry of stator slots, discreteness of windings, rotor asymmetries, and saturation, actual flux distribution shapes are far from sinusoidal; thus, lumped parameter simulations are always suspect until measured data are available and adjustments are made to the models. This suggests that it will be a challenge to develop a reliable per-phase model of a synchronous reluctance motor.

Our finite-element studies described above have shown that the power density of synchronous reluctance motors will always benefit from the addition of PM in the rotor; however, adding magnets makes this motor configuration an internal permanent magnet motor, which is a different research area. A major reason for studying reluctance motors is to learn how to harvest maximum magnet-free torque from them at all speeds; furthermore, eliminating magnets could become strategic in the future because of market trends.

Although these conclusions come from computations of a reluctance motor, they can be extended generically to modeling electric motors in general because most stators are similar and because saturation is unavoidable for high power densities.

Future Direction

Fruitful areas for further research on synchronous reluctance motors include developing ways to harvest additional torque. Approaches are to drive the motor with a nonsinusoidal waveform, to optimize the control for high-speed operation, and to match the effective number of stator turns to the speed and power requirements of the motor and explore how to switch the stator turns in and out of the circuit

during operation of the motor. It is expected that combining these approaches in a single design can meet the FreedomCAR performance targets as well as the cost targets.

Integrated design and modeling tools are needed to accurately compute the performance of a motor. Traditionally the interfacing between computer-aided drafting (CAD) and finite-element (FE) programs is limited to being able to import the CAD-created geometry to the FE software for analysis. Changes in the geometry require not only reimporting the drawing but also redefining properties, sources, and boundary conditions on the FE side. As a result progress has been slow and tedious. To overcome these interface problems, there is a new approach in which CAD and FE programs interact seamlessly so that changes in the CAD side are automatically incorporated into the FE side, and motor performance can be assessed quickly and effortlessly. Our experience has pointed toward the 64-bit operating system with SolidWorks CAD and COMSOL Multiphysics finite element packages as very promising for the simultaneous solution of electromagnetic, mechanical, and thermal equations of interest in motor design and evaluation computing.

Publications

P. J. Otaduy and J. W. McKeever, *Modeling Reluctance Assisted PM Motors*, ORNL/TM-2005/185, Oak Ridge National Laboratory, Jan. 2006.

References

1. T. J. E. Miller, *SPEED's Electric Motors*, University of Glasgow, 2002.
2. T. J. E. Miller, *SPEED CONSORTIUM PC-BDC Ver. 6 User's Manual*, University of Glasgow, May 1, 2002.
3. *COMSOL Multiphysics User's Manual*, Version 3.2, COMSOL, Inc., 2006.

3.5 Advanced Traction Motor Development

Principal Investigator: Sam Nelson
Oak Ridge National Laboratory
National Transportation Research Center
2360 Cherahala Boulevard
Knoxville, TN 37932
Voice: 865-946-1327; Fax: 865-946-1262; E-mail: nelsonsejr@ornl.gov

DOE Technology Development Manager: Susan A. Rogers
Voice: 202-586-8997; Fax: 202-586-1600; E-mail: Susan.Rogers@ee.doe.gov

ORNL Program Manager: Mitch Olszewski
Voice: 865-946-1350; Fax: 865-946-1262; E-mail: olszewskim@ornl.gov

Objectives

The objective of this task is the development of advanced traction drive motors that would not be pursued by industry alone because of the high risks and uncertainty of long-term earnings. The goal of this task is to develop an advanced traction drive motor with improvements in motor torque capability, efficiency, power density, and cost reductions that will meet the 2010 FreedomCAR goals.

Approach

As a result of a request for proposals, Unique Mobility, Inc. (UQM) was awarded a subcontract to design a state of the art motor to meet FreedomCAR targets. The approach by UQM was to consider the many motor topologies that have been used for traction drive applications, including brushed direct current (dc), permanent magnet (PM) brushless dc (BLDC), alternating current (ac) induction, switched reluctance, and synchronous reluctance machines. Each motor topology was assessed to determine the design that could best meet the 2010 FreedomCAR goals and traction motor technical targets. The advantages and disadvantages of each motor topology were considered, and it was determined that the PM BLDC has consistently demonstrated an advantage in terms of power density and efficiency. After the determination of the motor topology, a design trade study was performed to direct the design approach within that motor topology. A combination of finite-element analysis (FEA) and motor design equations was used to evaluate the design choices. A final design was solidified, and the expected performance of the design was determined.

Major Accomplishments

The technical report, *FreedomCAR Advanced Traction Drive Motor Development Phase 1*, was issued September 2006. This report documents the design effort and conclusions reached by UQM during the Phase 1 task. A 6 pole-pair machine with 36 slots in a 3-slot per pole configuration was determined to be the final design choice. The final design met or exceeded the majority of the 2010 FreedomCAR goals and traction motor technical targets.

Technical Discussion

Of the machine technologies, the PM brushless dc (PMDc) motor has consistently demonstrated an advantage in terms of power density and efficiency. A design trade study was performed for the PMDC motor to determine the motor configuration best suited to meet the motor requirements for the FreedomCAR specification. The three motor configurations that were evaluated in the trade study were the magnet-dominant internal PM machine (IPM), a reluctance-dominant IPM, and a surface-mounted PM machine (see Figure 1). Parametric finite-element models that define the geometry

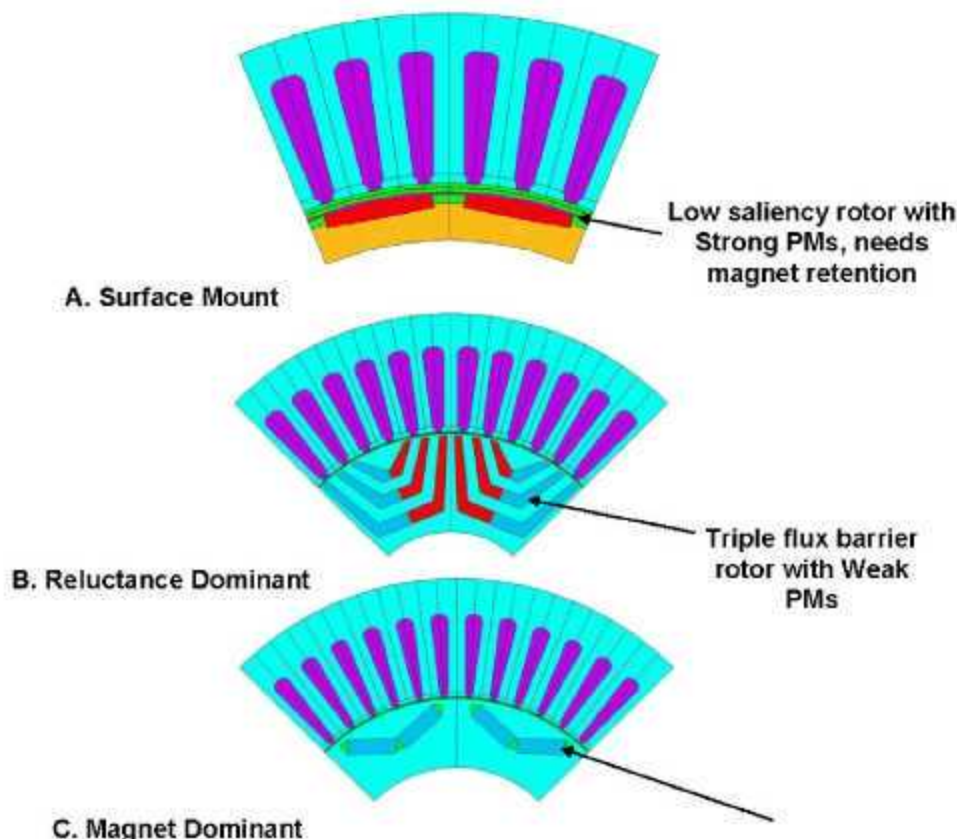


Figure 1. Physical topology, three designs.

of each configuration were created such that the geometry for each design could be quickly manipulated and reevaluated. FEA was used to evaluate motor parameters such as the back-emf constant (K_e) as well as the quadrature axis (q-axis) and direct axis (d-axis) inductance at a variety of currents. The flux density in the stator teeth and return path was also evaluated for use in calculating the iron losses. After the machine parameters were evaluated with FEA, a Mathcad model was used to simulate performance. The Mathcad model is based on the motor design equations and the equations for electric machine vector analysis. This model was used to predict motor performance by utilizing the motor parameters that were determined by FEA. This sequence of design iteration was chosen to provide a quick yet accurate method of design evaluation, given the geometry dependence on the motor parameters. The designs were iterated until each could meet as many of the FreedomCAR motor requirements as possible.

Trade Study

The purpose of the trade study was to identify a design direction for the FreedomCAR advanced traction motor and to identify aspects of each design that should be integrated into the advanced traction motor design. The results of the trade study indicated that the magnet-dominant design configuration would best fit the FreedomCAR specifications. Table 1 compares the performance predictions for each design with the FreedomCAR specifications. In Table 1, the values marked in red type indicate the performance predictions that did not meet the specification. The magnet-dominant design met all specifications except the peak power-to-volume specification (power density).

Table 1. Comparison of three design performances with specification

	Freedom Car Specification	Magnet Dominant Design MGDOM11	Reluctance Dominant Design REDOM*	Surface Mount Design SURMO5
Top Speed (rpm)	10,000	10,000	10,000	10,000
325 Vdc (kW)	55	55	55	55
Battery Operating Range (V)	200-450	same	same	same
Nominal Battery Voltage (V)	325	same	same	same
Maximum Current at motor (Arms)	400	345	480	428
Characteristic Current (Arms)	<400	240.38	272.5	319.4
Efficiency at 10% of maximum Speed and 20% of Rated Torque (1000 rpm, 52.4 Nm)	>93	93.9	93.0	95.0
Efficiency at 20% of maximum Speed and 20% of Rated Torque (2000 rpm, 52.4 Nm)	>93	96.2	95.8	95.9
Efficiency at 100% of maximum Speed and 20% of Rated Torque (10,000 rpm, 52.4 Nm)	>93	95.4	97.2	92.7
Back-EMF at 100% of Maximum Speed (Vpeak, Line to Line)	<600	600	310	670
Peak Power to Volume Ratio (kW/Liter)	>12.5	10.4	8.8	10.0
Torque Pulsations % of peak Torque	<5	??	??	??
Peak Power to weight Ratio (kW/Kg)	>2.75	2.774	2.228	2.795

Magnet Cost Study

A magnet cost study was conducted to get an accurate picture of current magnet prices for NdFeB magnet materials from a variety of magnet sources, domestic and offshore. Because magnets are a relatively significant part of the total cost of a PM machine, it is beneficial to have good cost data for estimating manufacturing costs. UQM decided that the most accurate way to get cost data in volume is to have actual magnet suppliers quote a simple arbitrary shape in various volume quantities. After receiving the quotes, UQM calculated the magnet cost per pound from the official quotations. UQM requested quotes from magnet sources from the United States, Europe, Japan, and China. Also quoted were Chinese magnets distributed through a U.S. company and a U.S. company that processes finished magnets from Japanese magnet materials.

Each magnet manufacturer or distributor was given the same package of material and part specifications to quote pricing. The package included the drawing and magnetic material specifications. Each manufacturer or distributor was asked to quote each magnet specification in quantities of 10K/year to 100M/year. Each magnet manufacturer was asked to quote four different sets of material properties.

The magnet properties were chosen to represent high-energy and a high-coercivity magnet in both a sintered and a bonded NdFeB magnet type.

The conclusion from the magnet cost study supports the conclusion from the trade study that the motor development effort should utilize sintered NdFeB magnets. The reason is that the cost per pound of high-coercivity sintered magnets is the same as that of bonded magnets (i.e., about \$17 to \$20 per pound). The trade study demonstrated that a motor with bonded magnets will utilize significantly more weight in magnets as well as total motor weight for the same performance level. This will significantly increase the cost for the motor.

Rotor Configuration Study

A rotor configuration study was performed with seven different rotor configurations. Characteristics that varied in the study were arranged for magnets (i.e., V-shape and U-shape), number of barriers (single or double), number of bridges (i.e., two, three, and four), and number of magnets per pole (two, three, and four). The stator arrangement, length of rotor, air gap, and current were constant for each configuration. The rotor configuration with U-shape barrier, two bridges, and three magnets per pole was determined to be the best configuration based on significantly more torque for the same size motor and same magnet mass. This rotor configuration will be slated for use in the final design (see Figure 2).

Many design iterations were generated in the development of the final design. The design iterations in this section illustrate the pros and cons of the possible pole count selections. Other design iterations that were not published were generated with a varying amount of analysis. For example, if the torque profile for a given design iteration was not acceptable, the design iteration would be dropped without further analysis. Analysis was performed on a given design iteration until it was found to be unacceptable or it was apparent that improvements could be made to meet the FreedomCAR specification.

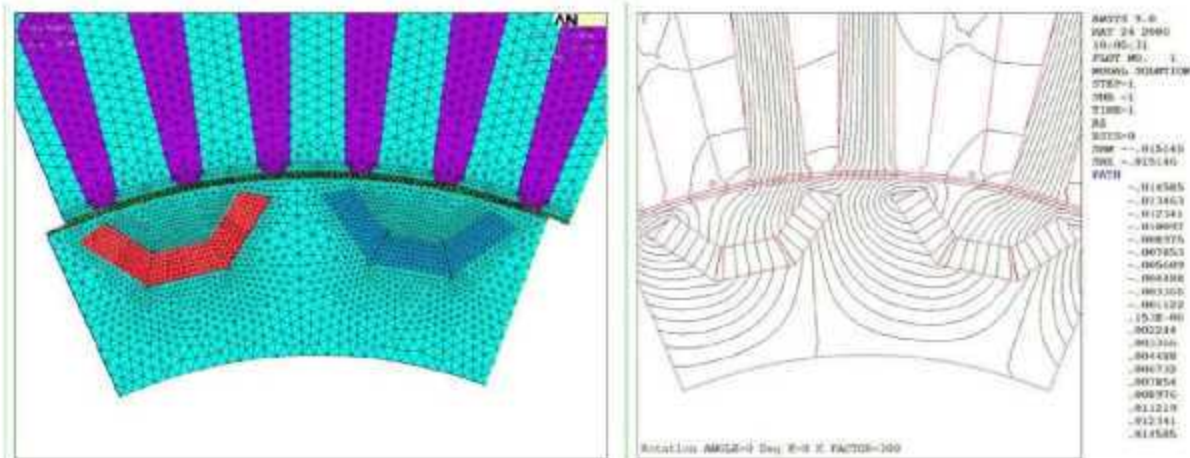


Figure 2. U-barrier, two bridges, three magnets per pole.

Iterative Design Method

All simulations in this section and following sections were conducted assuming an operating temperature of 150°C. This temperature was chosen as a target steady state design point, considering that 105°C is the required maximum inlet temperature and 150°C will allow for a reasonable temperature rise. All design iterations presented here were adjusted so that the maximum required torque, 262 Nm, was reached with 400 Arms leg current. The maximum allowable current according to the specification is 400 Arms. Designs were adjusted in length or turns to make 262 Nm at the maximum current to minimize the inductance and allow peak performance down to 200-V supply voltage. Higher turn counts and inductance will bring down the current but will not allow low-voltage operation.

Motor performance was predicted through means of evaluating the motor parameters, inductance profile (q- and d-axis inductance vs. current), and torque mapping in FEA. These values were then used in conjunction with vector analysis to predict motor performance. The performance models calculated the necessary current at a given operating point from the torque maps. The vector diagram was also evaluated for each point using the inductance values that corresponded to the current demand. The vector analysis determines what phase angle is necessary for operation at a given operating point and if the system will be voltage limited at that point.

The requirement for full-power operation down to 200 V of supply voltage drove the selection of many design features and contributed in determining the pole-pair selection as well. UQM took the approach that the highest pole count that would still allow the efficiency and power requirements to be met would lead to the most compact and power dense design, saving materials and cost. A higher pole count will nearly always give a net benefit in terms of power density so long as the other requirements can be accomplished, such as efficiency and the operating range for voltage, speed, and power.

Six-Pole Pair Design

Meeting the requirements of the specification at a higher power density, but a lower efficiency with the eight pole-pair design as compared with the four pole-pair design, prompted the study of pole-pair combinations between the two. The 6 pole-pair selection was a logical choice, having 36 slots in a 3-slot per pole configuration that allows a simple winding and relatively short end-turns. Iterations of the six pole-pair design led to the final design proving to have a better efficiency and power density than the designs with the other pole combinations.

Table 2 lists the important parameters of the six pole-pair design iteration that became the final design (see Figure 3). This combination yielded short end-turns (0.88 in.) and allowed a relatively short (3.4-in.)

Table 2. Motor parameters, six-pole pair, 3.4 in. (final design)

Overall stator diameter (in.)	8.7
Inner stator diameter (in.)	6.10
Rotor outside diameter (in.)	6.04
Stator stack length (in.)	3.4
End-turn length	0.88
Total axial length (over the end-turns) (in.)	5.165
Tooth thickness (in.)	0.380
Back-iron thickness (magnet return path) (in.)	0.39
Magnet strength (residual induction Br) (T)	1.10
Magnet thickness (in.)	0.165
Magnet weight (lb)	2.21
Minimum bridge thickness (in.)	0.04 (2 bridges)
Torque density (Nm/L) ^a	52.2
Power density (kW/L) ^a	11.0
Winding turns	3
Slots per pole	3
Back-EMF constant (V _{peak} /krpm L-L)	47
Winding fill factor (%) ^b	74
Winding resistance (Ω L-L)	0.011
q-axis inductance (μH L-L) ^c	111
d-axis inductance (μH L-L) ^c	75

^aCalculated using FEA at a 1200 ampere-turn load

^bCalculated using the conservative volume calculation

^cIncludes insulation and copper in magnet wire based sum of square areas

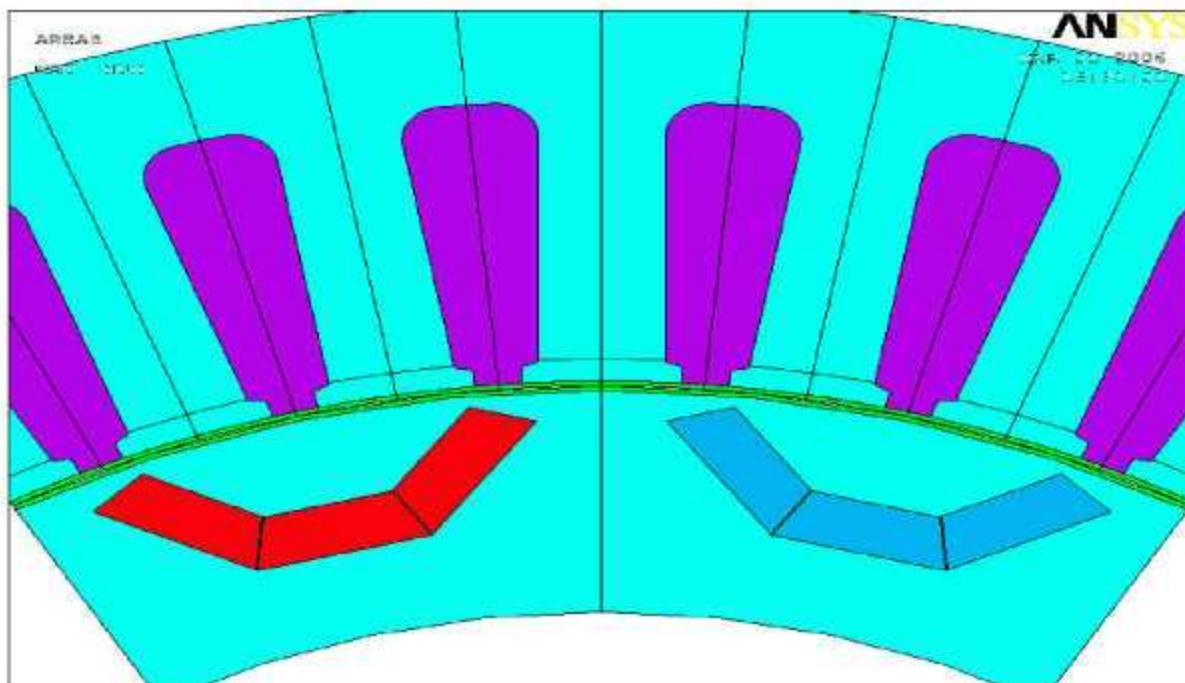


Figure 3. Six-pole pair machine configuration.

stack length as well. At 8.7-in. overall diameter and a total volume of 5 L, the power density is 11 kW/L, better than the design iterations in either of the other pole configurations.

Relatively wide stator teeth (0.380 in.) and back-iron (0.390 in.) reduced flux density and helped to control iron losses, giving good efficiency at high speeds. The motor will be 94.8% efficient at 1000 rpm and 95.6% at 10 krpm, well above the efficiency target of 93%. The peak efficiency, 96.5% is reached at about 4000 rpm and 52 Nm. Also, vector analysis indicated that operation at full power with a 200-V supply would be easily accomplished with this design. The minimum voltage for operation can be maintained below the buss voltage (Vdc) by phase advancing the current to a reasonable angle, and the current never exceeds the maximum allowable current of 400 Arms (see Figure 4).

The eight pole-pair version was able to meet most of the performance specs, but the girth of the iron in the magnetic circuit and the length had to be increased until the weight and volume were higher than expected. The tooth width and return path thickness had to be increased to lower flux density and therefore iron losses. Even so, this design barely met the 93% specification at 10 krpm. In addition, the turn count was dropped from three down to two to lower the inductance and allow performance down to 200 V. The length was increased to compensate for the loss of a turn. Although the end-turns are the shortest of all the designs (0.68 in.), the stack length was the longest (4.2 in.). Unfortunately, with the increased length, the power density of the machine was decreased, and the efficiency was reduced at high speeds. The eight-pole pair machines could not meet the required specification and were eliminated from consideration for the final machine design.

The four-pole pair configuration was evaluated; this configuration has been used in the Prius and other similar applications. The four-pole pair design was able to meet the performance specifications in terms of efficiency, peak power, and voltage range of operation. However, the resulting volume and weight were too high, making the power and torque densities low. Larger volume and weight are partially due to inherently longer end-turns and the requirement for thick stator features. More copper, iron, and magnet are necessary to compensate for less emf because of the lower-frequency operation in comparison to the higher pole counts. Additionally, because there is more magnet weight per pole, more structural support is needed to retain the magnets at high speeds. Consequently, the bridge thickness needed to be greater. With more bridges and/or thicker bridges, more magnet flux is shunted away from

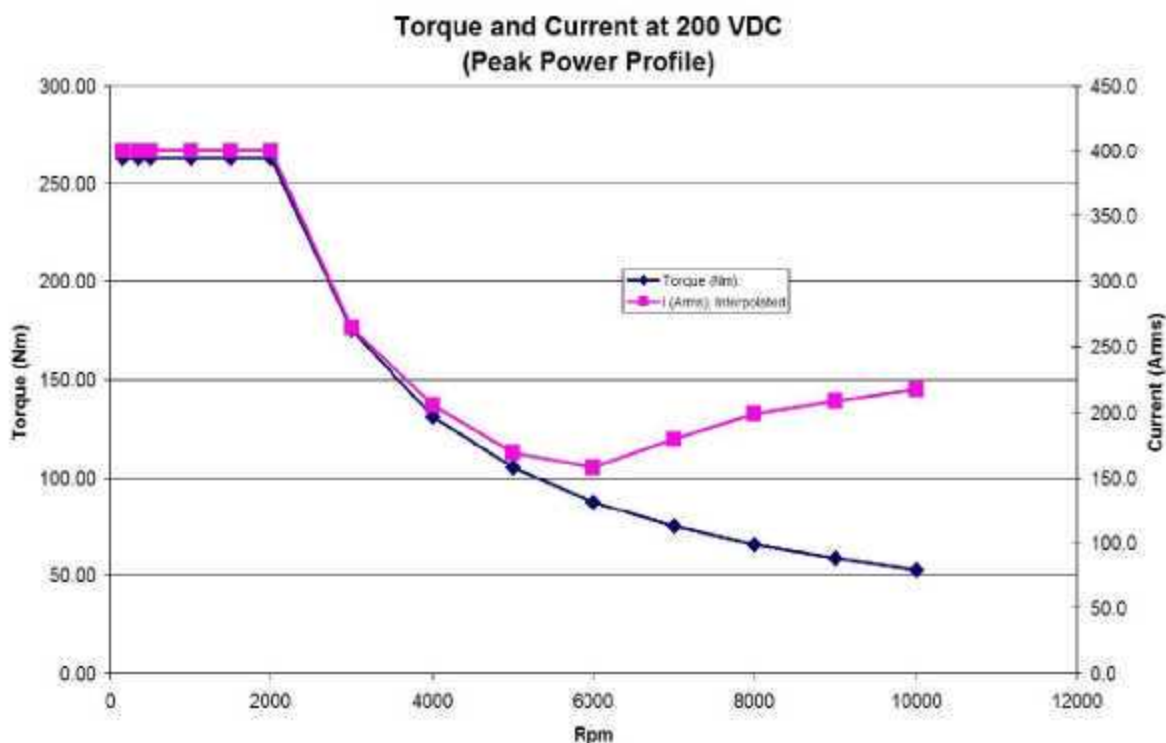


Figure 4. Current and torque profile at 200-Vdc, peak power.

the stator, reducing performance. The four-pole pair design met the efficiency requirements at 52 Nm across the speed range. The efficiency at 1000 rpm was slightly above 95% and slightly below 95% at 10,000 rpm. This four-pole pair design does meet the requirement for full power (i.e., 55 kW) at 200 V across the speed range and was eliminated from consideration for the final design.

During the Phase I design effort, pole-pair combinations between four- and eight-pole pairs were investigated. The six-pole pair configuration proved to be the best choice. Magnet weight was the lowest, and the power density was the best of the three: 11.0 kW/L for six-pole pairs, 10.4 kW/L for eight-pole pairs, and 8.6 kW/L for four-pole pairs. These power densities are based on conservative volume calculations.

Comparison with Prius Motor

The Prius motor is held in high regard in the industry and probably considered state-of-the-art in terms of electric propulsion motors for hybrid electric cars. For this reason, it makes sense to compare the motor design developed in this program with the Prius benchmark, in order to determine the value in continued development of this motor design. Because materials represent the most significant part of the cost in automotive volume production, size reduction is paramount. Figure 5 compares some of the major dimension and figures of merit of the two motors. In this section, all comparisons are made at the active materials level. Note that overall diameter and length are greatly reduced in the FreedomCAR design over the Prius motor design. Overall diameter of the Prius motor is 10.6 in., but the FreedomCAR design is only 8.7 in. The FreedomCAR design is nearly 2 in. smaller in diameter and down from 6.29 to 5.14 in. in overall length. Also, the reduction in the volume of the FreedomCAR design is approximately 40%, and weight is reduced by nearly 50% from the Prius motor. Some of this size reduction is due in part to the difference in operating profiles of the two motors. The FreedomCAR design makes more power, 55 kW as opposed to 50 kW for the Prius motor; however, the Prius motor operates in a lower speed range and

	Prius Motor Design	Final Design (in progress)
Peak Power	50	55
Peak Torque (Nm)	400	262.5
Overall Diameter (in)	10.6	8.7
Rotor Inner Diameter (in)	4.356	3.04
Rotor Outer Diameter (in)	6.315	6.04
Stack Length (in)	3.29	3.4
Endturn Length (in)	1.5	0.87
Slot Length (in)	1.3	0.91
Overall Length (in)	6.29	5.14
Volume* (Liters)	9.10	5.01
Volume** (Liters)	5.50	3.48
Power Density* (kW/Liter)	5.5	11.0
Power Density** (kW/Liter)	9.1	15.8
Torque Density* (Nm/Liter)	44.0	52.4
Torque Density** (Nm/Liter)	72.8	75.4
Stator Weight (lb)	41.2	21.6
Rotor Weight (lb)	11.4	10.1
Magnet Weight (lb)	2.8	2.2
Winding Weight (lb)	24.1	6.6
Total Weight (lb)	79.5	40.5
Total Weight (kg)	36.1	18.4
Specific Power (kW/kg)	1.4	3.0
Specific Torque (Nm/kg)	11.1	14.3

*Utilizes the most conservative method of calculating volume.

**Utilizes the least conservative method of calculating volume.

Figure 5. Power density comparison—FreedomCAR design vs Prius motor.

produces more torque, 400 Nm at 1200 rpm as opposed to 262 Nm at 2000 rpm for the FreedomCAR motor. Because electric motors scale with torque more closely than with power, note that the torque density of the FreedomCAR motor design is still 18% higher than that of the Prius Motor and its power density is 100% higher than that of the Prius.

The difference in motor parameters between the two machines includes a much higher back-emf voltage for the Prius motor, 141 as opposed to 48 V_{peak}/Krpm (see Figure 6). This gives a maximum voltage of 480 V for the FreedomCAR design and 846 V for the Prius, necessitating a higher inverter voltage rating for the Prius system. Conversely, the Prius motor would require a lower current rating for the inverter, having a maximum motor current of 250 A, as opposed to 400 A for the FCVT motor.

	Prius Motor Design	Final Design (in progress)
Pole Pairs	4	6
Slots Per Pole	6	3
Back-EMF Constant @ 20 C	141.7	48
Resistance (Ohms L-L) at 20 C	--	0.011
Phase Inductance Lq (uH)*	--	111
Phase Inductance Ld (uH)*	--	75
Saliency Ratio	--	1.48
Slot Fill Factor	0.84	0.77
Residual Induction (T)	1.12	1.15
Maximum Current (Arms)	250	400
Maximum Speed (rpm)	6000	10000
Minimum Voltage	**200	200
Maximum Voltage	500	450
Max Operating Temp (Celsius)	170	>180
Magnet Retention Sleeve Required	No	No
Flux Barriers	V-Shape	U-Shape
Magnet Shapes	Rectangle	Rectangle

*Boost converter required to achieve this voltage range.

Figure 6. Motor parameter comparison—FreedomCAR design vs Prius motor.

Manufacturing Cost Estimate

UQM chose to estimate the cost of this machine in the most likely automotive production scenario, as a Tier 3 motor manufacturer supplying to a Tier 2 transmission manufacturer. As a result, the gearing cost is not included in the estimate, and the housing is at least partially integrated with the transmission as electric machines are presently being integrated in hybrid vehicles. UQM anticipates this transmission—electric machine integration trend to continue and therefore has chosen to estimate cost as a motor manufacturer would supply to the transmission manufacturer. The water jacket or heat sink is considered part of the motor, which will be included in the cost estimate. The water jacket will encompass the outer diameter of the stator laminations, and the assembly will be pressed into the transmission housing or bolted to the transmission housing as an attachment. The rotor is expected to be coupled and installed on one of the primary shafts of the transmission. Therefore, a hub that supports the rotor ring will be needed to adapt to the shafting of the transmission. Obviously, exact hardware would be application-specific; however, for the purpose of this cost study, a conceptual rendition of the applicable motor parts is depicted in Figure 7. This figure represents a good estimation of the necessary motor parts as supplied to a transmission manufacturer for electric machine integration within a transmission.

The parts and their estimated weights that were considered in this manufacturing cost analysis are listed in Table 3.

Material prices for copper, NdFeB, aluminum, and other materials were based on current market prices.

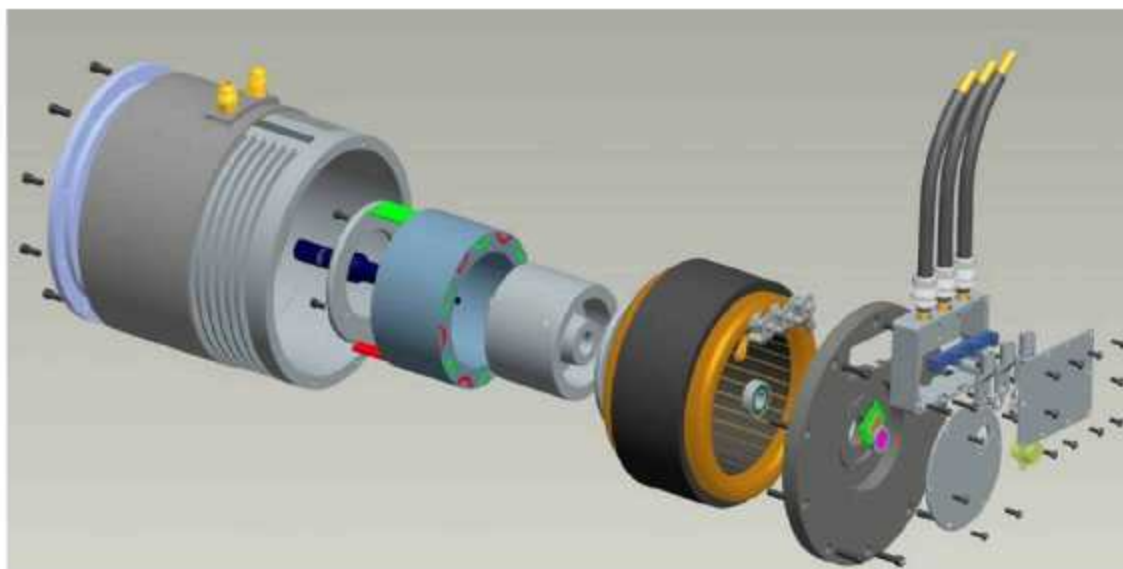


Figure 7. Motor assembly—exploded view.

Table 3. Parts included in manufacturing cost estimate

Part description	Weight of parts/unit (lb)
Stator lamination stack (243 laminations)	21.6
Rotor lamination stack (243 laminations)	10.0
Magnets NdFeB	2.215
Winding magnet wire (copper)	7.0
Bearings	2 ^a
2 piece housing/water jacket (as cast)	5 ^a
Stator finished (wound and insulated)	N/A
Rotor hub (as cast)	4 ^a
Hub machining	N/A
Housing machining	N/A
Circuit board with position sensors (hall effects)	N/A

^aWeights that are estimated, not actual values.

Figure 8, illustrates the results of the cost study generated by the UQM manufacturing group. The cost data presented here represent the cost of the motor and do not include tooling amortization or margin. The estimated unit prices are \$399.60, \$299.73, \$239.78, and \$203.85 at volumes of 100K, 250K, 500K, and 1M per year, respectively. The cost target for the 2010 specification was specified in at \$7/kW. The chart also graphs the cost data in terms of cost/kW. The red horizontal line represents the cost target. At 55-kW peak power, the cost target is met for all quantities slightly over 100K units per year and above. As explained in the report, *FreedomCAR Advanced Traction Drive Motor Development-Phase 1*, the final design will actually be capable of up to 110 kW peak at nominal voltage and 4000 rpm. At 110 kW above 4000 rpm, the cost/kW is reduced well below the target.

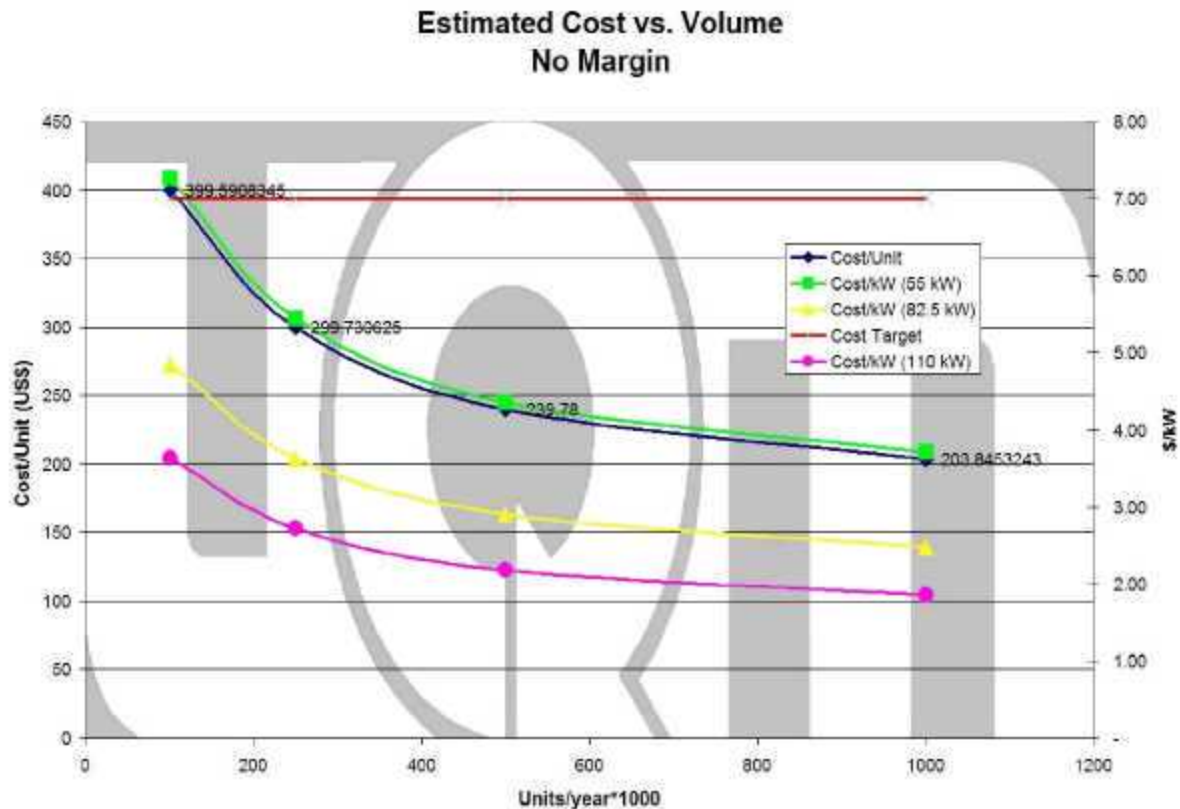


Figure 8. Cost vs volume for the FreedomCAR motor.

Conclusion

A six-pole pair configuration PM motor was determined to be the best choice for the FreedomCAR design. The rotor configuration has U-shaped barriers with two bridges per pole. The stator has 36 slots in a 3-slot per pole configuration that allows a simple winding and relatively short end-turns. Iterations of the six-pole pair design led to a final design with a better efficiency and power density than the designs with other pole combinations.

Table 4 compares the FreedomCAR target with the predicted performance for the FreedomCAR motor design. The motor meets or exceeds the target for power (i.e., continuous and peak) and efficiency. Because the peak power capability of the motor ranges from 55 kW at 2000 rpm to 110 kW at 4000 rpm, power density, specific power, and cost per kilowatt were calculated at both 55 and 100 kW.

Table 4. Comparison of FreedomCAR motor with target

Description	Predicted for FreedomCAR design	FreedomCAR target
Peak power (kW)	55–110 ^a	55 kW
Duration at 55 kW (s)	40	18
Continuous power (kW)	30	30
<i>Quantities based on active materials</i>		
Power density (kW/L)—based on 55 kW	11–15.8 ^b	>12.5
Power density (kW/L)—based on 110 kW	22–31.6 ^b	>12.5
Specific power (kW/kg)—based on 55 kW	3	>2.75
Specific power (kW/kg)—based on 110 kW	6	>2.75
Cost per kW (\$/kW)—based on 55 kW	3.4–6.8 ^c	<3.2
Cost per kW (\$/kW)—based on 110 kW	1.7–3.4 ^c	<3.2
<i>Quantities based on full motor package</i>		
Power density (kW/L)—based on 55 kW	6.6	>5
Power density (kW/L)—based on 110 kW	13.3	>5
Specific power (kW/kg)—based on 55 kW	1.74	>1.3
Specific power (kW/kg)—based on 110 kW	3.47	>1.3
Cost per kW (\$/kW)—based on 55 kW	5–9.5 ^c	<7
Cost per kW (\$/kW)—based on 110 kW	2.5–4.8 ^c	<7
<i>Other motor requirements</i>		
Maximum current (Arms)	400	400
Back-EMF (V)	480	<600
Efficiency (%)	94.8–96.5	>93
Characteristic current (Arms)	344.6	<400
Maximum coolant temperature (°C)	105	105

^aPeak power is 55 kW at 2000 rpm, 82.5 kW at 3000 rpm, and 110 kW at 4000 rpm

^bThe low end of the range is based on the most conservative volume calculation, and the high end of the range is based on the least conservative volume calculation

^cThe range refers to the cost at 100k volume per year to the cost at 1M per year quantities

Future Direction

This task completes the Phase 1 traction drive development task. Development of an advanced traction drive motor will continue with other tasks.

Publications

FreedomCAR Advanced Traction Drive Motor Development—Phase 1—September 2006. ORNL/TM-2006/UQM, Oak Ridge National Laboratory, September 2006.

4. Power electronics Research and Technology Development

4.1 Wide Bandgap Materials

Principal Investigator: Burak Ozpineci

Oak Ridge National Laboratory

National Transportation Research Center

2360 Cherahala Boulevard

Knoxville, TN 37932

Voice: 865-946-1329; Fax: 865-946-1262; E-mail: ozpineci@ornl.gov

DOE Technology Development Manager: Susan A. Rogers

Voice: 202-586-8997; Fax: 202-586-1600; E-mail: Susan.Rogers@ee.doe.gov

ORNL Program Manager: Mitch Olszewski

Voice: 865-946-1350; Fax: 865-946-1262; E-mail: olszewski@ornl.gov

Objectives

- Assess the impact of replacing silicon (Si) power devices in transportation applications with devices based on wide-bandgap (WBG) semiconductors.
- Develop device models for system level simulation studies and analyze the impact of silicon carbide (SiC) devices on the system performance.
- Build high-temperature packages for SiC power devices to operate at 200°C.
- Study the feasibility of building a 55-kW all-SiC inverter.

Approach

- Develop models of WBG semiconductor devices, especially SiC diodes, junction field-effect transistors (JFETs), and metal oxide semiconductor field-effect transistors (MOSFETs).
- Model a 55-kW all-SiC inverter and compare it with similarly rated all-Si and Si-SiC hybrid inverters.
- Build high-temperature packages for SiC power devices to operate at 200°C.
- Survey possible device packaging techniques.

Major Accomplishments

- Acquired several SiC Schottky diodes, JFETs, and GaN Schottky diodes.
- Tested, characterized, and modeled SiC Schottky diodes, JFETs, and GaN Schottky diodes.
- Modeled a 55-kW all-SiC inverter and compared its performance with that of similarly rated all-Si and Si-SiC hybrid inverters.
- Built high-temperature packages for SiC power devices to operate at 200°C.
- Built and tested all-Si and Si-SiC hybrid inverters [Si insulated gate bipolar transistors (IGBTs) and SiC Schottky diodes] and compared the results.

Technical Discussion

A. Device Modeling

Several new WBG devices were acquired this year and were tested, characterized, and modeled. The list of devices includes SiC JFETs, Schottky diodes, and GaN Schottky diodes. All the devices obtained

were experimental samples. A data record of devices tested to date is located in the appendix to this section.

A.1 SiC Schottky Diode

SiC Schottky diodes are majority carrier devices and are attractive for high-frequency switching because they have lower switching losses than pn diodes. However, they have higher leakage currents, which affect the breakdown voltage rating of the devices. Tests were conducted of 600-V/75-A SiC Schottky diodes, and the results are presented in the following subsections.

Static characteristics

I-V characteristics of the 600-V/75-A SiC Schottky diode were obtained at different temperatures in the -50°C to 175°C temperature range (Figure 1). Considering the piece-wise linear (PWL) model of a diode—which includes a dc voltage drop, V_D , and a series resistor, R_D —the diode I-V curves can be approximated with the following equation:

$$V_d = V_D + R_D \cdot I_d \quad (1)$$

where V_d and I_d are the diode forward voltage and current, and V_D and R_D are the diode PWL model parameters.

Figure 2 shows R_D and V_D values of the 600-V /75-A SiC Schottky diodes with respect to temperature. As seen in the figure, V_D decreases with temperature and R_D increases with temperature. The increase in R_D is an effect of the positive temperature coefficient of the SiC Schottky diodes, which enables these devices to be paralleled easily. Equations (2) and (3) show the temperature dependence of the SiC Schottky diode PWL model parameters.

$$V_D = -0.001 \cdot T + 0.94 \text{ (Volts)} \quad (2)$$

$$R_D = 8.9 \times 10^{-5} \cdot T + 0.013 \text{ (Ohms)} \quad (3)$$

where T is the temperature in degrees C.

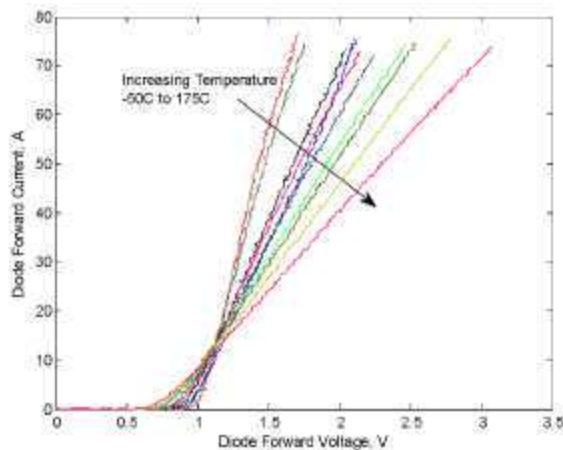


Figure 1. Experimental I-V curves of the 75-A SiC Schottky diode.

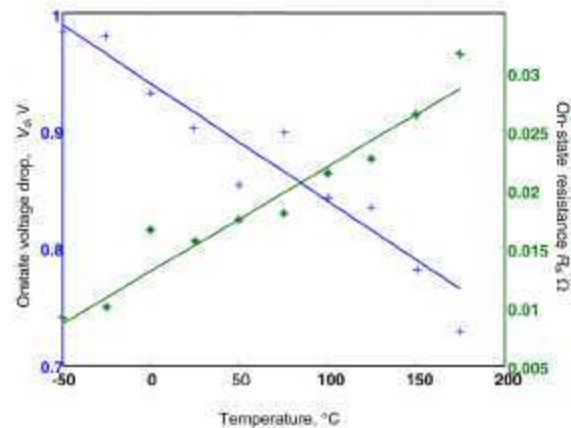


Figure 2. R_D and V_D obtained from the experimental data in Figure 1.

Dynamic characteristics

The SiC Schottky diode was also tested in a chopper circuit (Figure 3) to observe its dynamic characteristics. The IGBT in the circuit was switched at a low switching frequency of 1 Hz to prevent self-heating effects on the diode. The double pulse circuit enables the use of an inductive load instead of the resistive and inductive load together. The current through the inductor builds up during the first pulse and peak forward current is adjusted by changing the width of the first pulse. The switch is turned off and turned on for short periods after the first pulse. The turn-on and turn-off energy losses can be obtained during the short pulse intervals. The double pulse waveforms are shown in Figure 4.

To obtain the switching characteristics at high temperatures, a test set-up was built as shown in Figure 5. The device under test was placed inside the box on a heat sink, and the temperature was controlled using a resistive load paced in the box on the heat sink. The temperature of the heat sink was monitored using a thermistor.

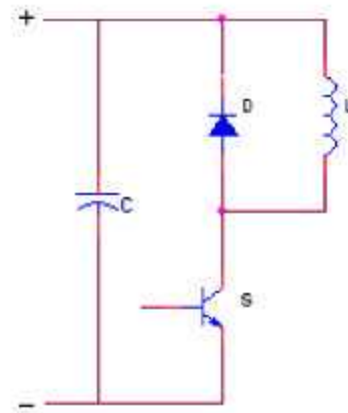


Figure 3. Test circuit for dynamic characterization.

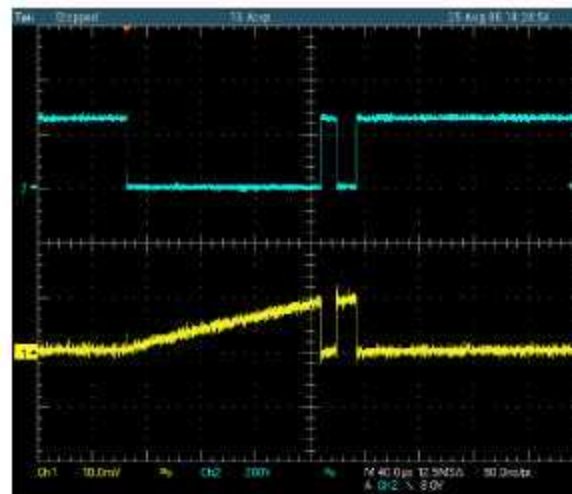


Figure 4. Current and voltage waveforms of SiC JFET S3—double pulse test.

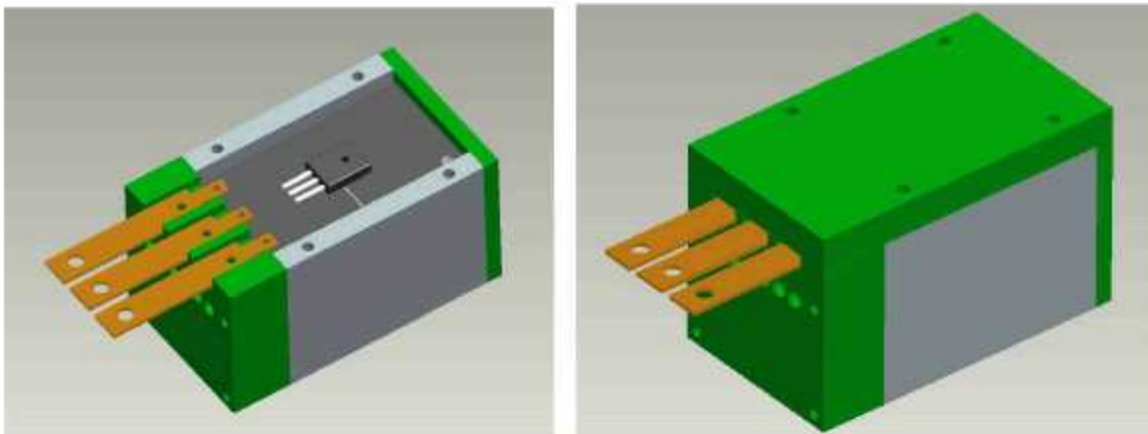


Figure 5. Temperature-controlled box used for high-temperature testing.

The reverse recovery current waveforms obtained for different forward currents at room temperature are shown in Figure 6. The reverse recovery current did not change with forward current. Note that, theoretically, Schottky diodes do not display reverse recovery phenomenon because they are majority carrier devices and do not have a stored charge. The switching losses obtained at different temperatures are shown in Figure 7. The switching loss equation is given below in Equation (4).

$$E_{sw} = -6.5 \times 10^{-9} \cdot I + 3.2 \times 10^{-7} \text{ (Joules)} \quad (4)$$

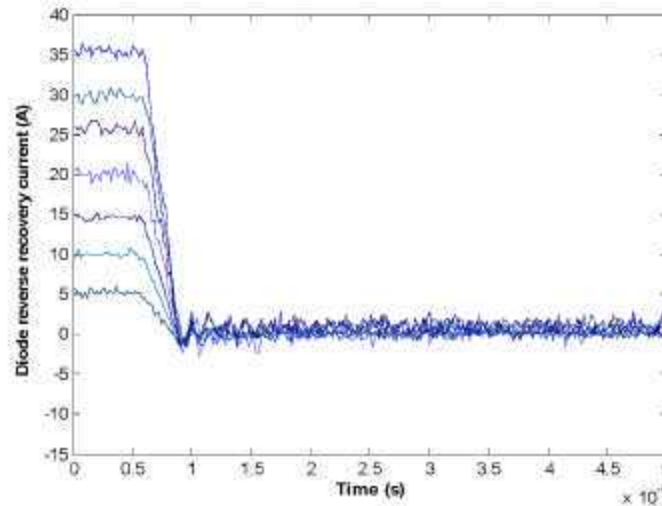


Figure 6. Reverse recovery current waveforms of the SiC Schottky diode for different forward current values.

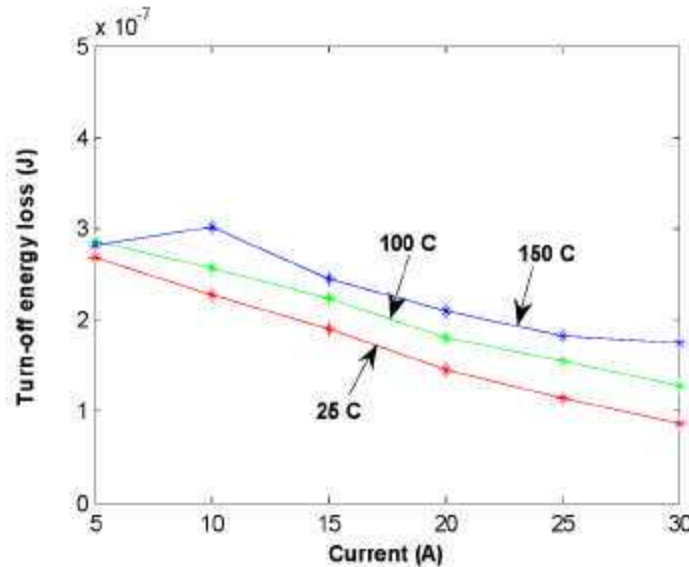


Figure 7. Switching energy losses of SiC diode at different temperatures.

A.2 GaN Schottky Diodes

Static characteristics

The static characteristics of a 600-V/4-A GaN diode in a temperature range of 25 to 175°C are shown in Figure 8. The PWL model parameters were extracted from the static curves (as discussed in the previous section) and plotted in Figures 9 and 10. V_d decreases and R_d increased with an increase in temperature, as expected. The static characteristics of a similarly rated SiC diode are better compared with the GaN diode, as shown in Figure 11. It should be noted that the GaN device is still an experimental sample and SiC Schottky diode technology is more mature.

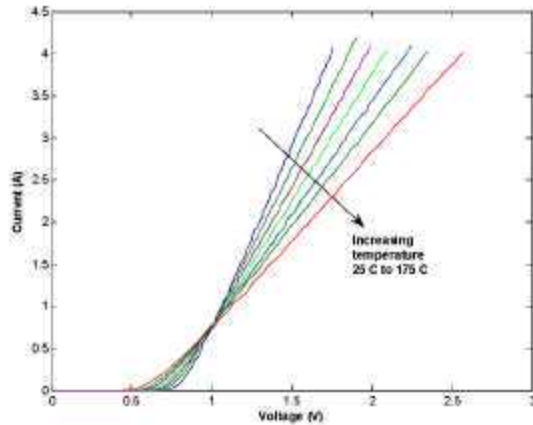


Figure 8. Static characteristics of GaN Schottky diode.

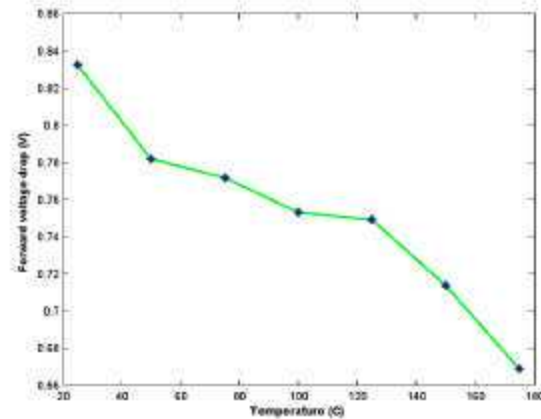


Figure 9. V_d forward voltage drop of GaN Schottky diode.

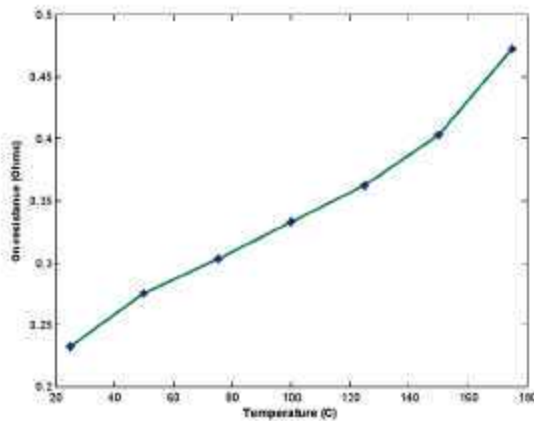


Figure 10. R_d on-state resistance of GaN Schottky diode.

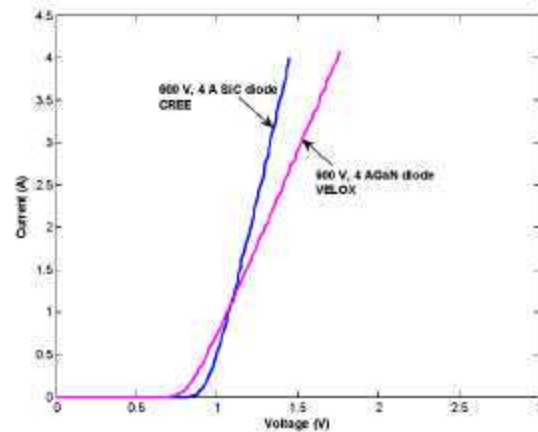


Figure 11. Comparison of i-v curves of SiC and GaN Schottky diodes.

Dynamic characteristics

The dynamic characteristics of the GaN Schottky diode were obtained using the same chopper circuit and high-temperature test set-up as the SiC Schottky diode. Results show that the GaN Schottky diode also has almost zero recovery losses, as expected, similar to the SiC diode (Figure 12). The corresponding turn-off energy losses are shown in Figure 13 for three different temperature conditions. The switching

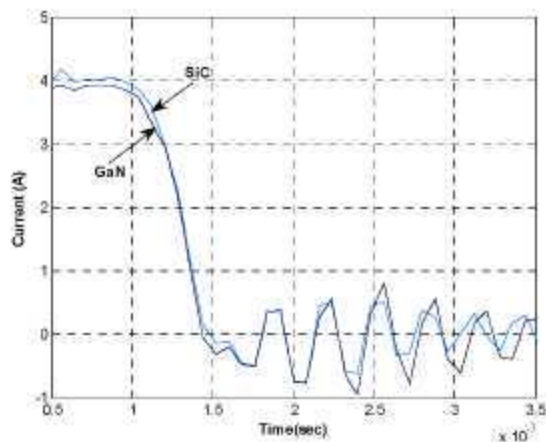


Figure 12. Comparison of reverse recovery currents between SiC and GaN at 25°C.

losses of the GaN diode were compared with those of a similarly rated 600-V, 4-A SiC Schottky diode, shown in Figure 14, for 125°C operation. The losses of the SiC Schottky diode are slightly less than those of the GaN Schottky diode for this operational condition.

A.3 JFETs

Static characteristics

Several experimental JFET samples were obtained from different manufacturers. Static characteristics of three different JFETs—S1 (600-V, 5-A), S2 (1200-V, 15-A), and S3 (1200-V, 10-A)—at different temperatures are shown in Figures 15–17, respectively. SiC JFETs have a positive temperature coefficient, which means that like SiC Schottky diodes, their conduction losses will be higher at higher temperatures. However, positive temperature coefficient makes it easier to parallel these devices and reduce the overall on-resistance.

The on-resistance of the switch S3 increases from 0.25 Ω at -50°C to 0.58 Ω at 175°C , as shown in Figure 18. The on-state resistance can be expressed as a function of temperature as shown in Equation (5).

$$R_D = 7.6 \times 10^{-5} \cdot T^2 + 0.00068 \cdot T + 0.26 \text{ (Ohms)} \quad (5)$$

The transfer characteristics of an SiC JFET are shown in Figure 19. The negative gate pinch-off voltage required to turn off the device is higher than that required for Si devices. The earlier-generation devices had pinch-off voltages that varied between samples, as shown in Figure 20. The pinch-off voltages of the newer-generation devices obtained this year do not vary as much. The transfer characteristics obtained for ten different samples are shown in Figure 20. This is a significant improvement that indicates that SiC JFET technology is maturing.

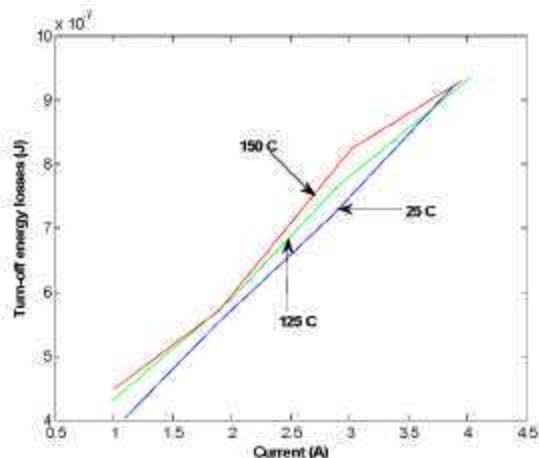


Figure 13. Turn-off energy losses of GaN diode at different temperatures.

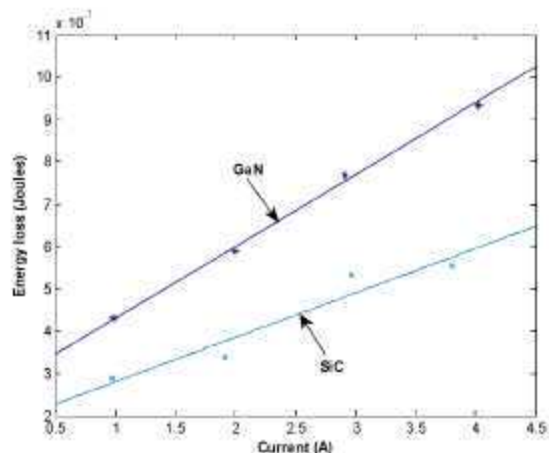


Figure 14. Energy losses comparison between Si and GaN diodes at 125°C.

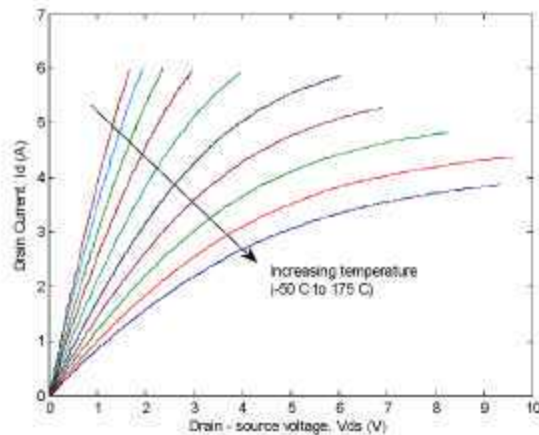


Figure 15. i-v curves of JFET S1.

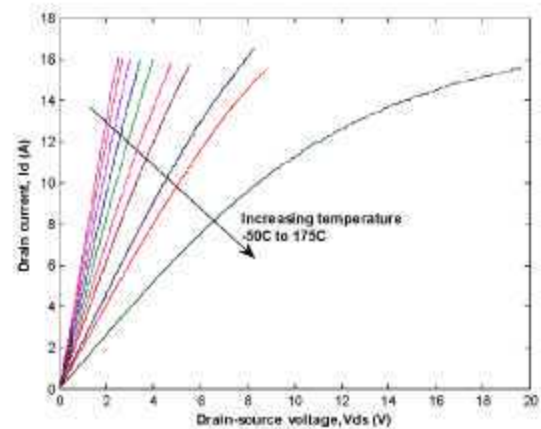


Figure 16. i-v curves of JFET S2.

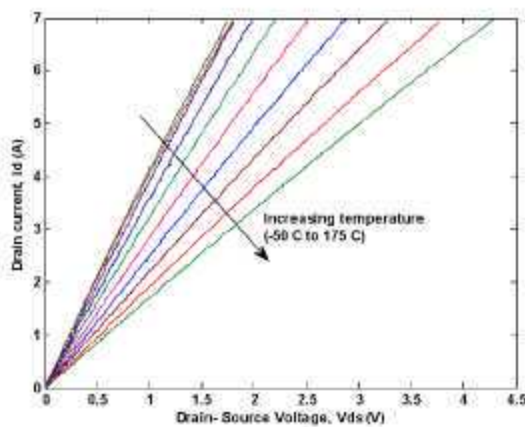


Figure 17. i-v curves of JFET S3.

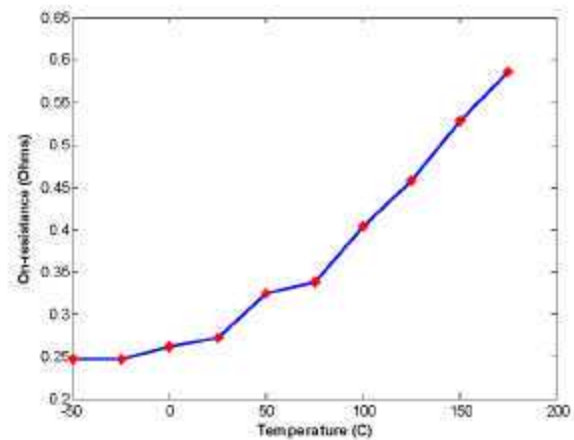


Figure 18. On-resistance of S3.

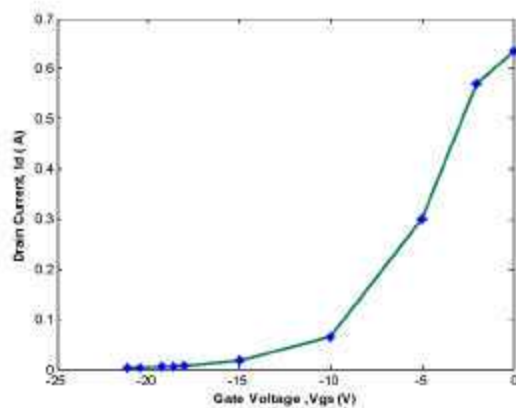


Figure 19. Transfer characteristics of JFET S3.

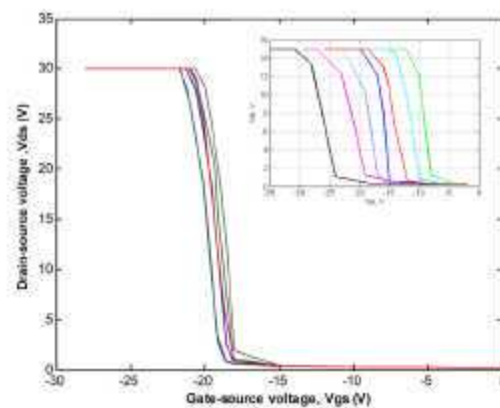


Figure 20. Transfer characteristics of several SiC JFET samples.

Dynamic characteristics

SiC JFETs are normally-on devices, and they can be turned off only by applying a negative voltage. Based on the transfer characteristics (Figure 20), a gate voltage of -22 V has been selected, as that would be enough to turn off most of the samples tested. The dynamic characteristics of the JFET S3 at several temperatures and currents were obtained using the high-temperature set-up and the double pulse circuit test. The total energy losses of the JFET during switching are shown in Figure 21. The losses do not change much with temperature. The switching loss equation is given below in Equation (6).

$$E_{\text{swt}(\text{total})} = 12.2 \times 10^{-5} \cdot I + 1.7 \times 10^{-5} \text{ (Joules)} \quad (6)$$

B. 55-kW Inverter Modeling

Three different inverters were modeled in Simulink to compare and study the system-level benefits of replacing SiC devices with Si devices. The total system-level model with a control system block, device loss model blocks, and a heat sink model block is shown in Figure 22. The power losses of the switches are calculated and fed to the heat sink model, which calculates the junction temperatures of the devices. These temperatures are fed back to the device loss models so that the temperature-dependent device parameters are updated. The blocks in the model will be explained in detail in the next few subsections.

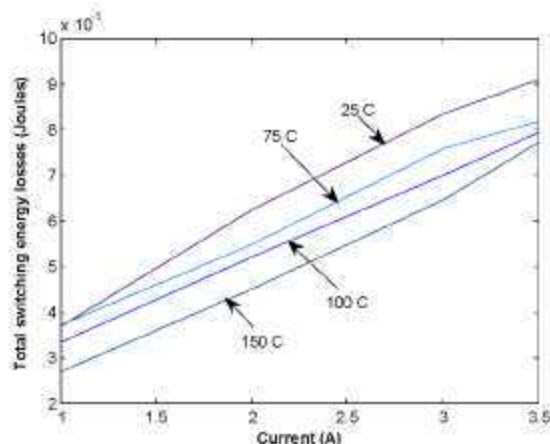


Figure 21. Total switching energy losses of JFET S3 at different currents and temperatures.

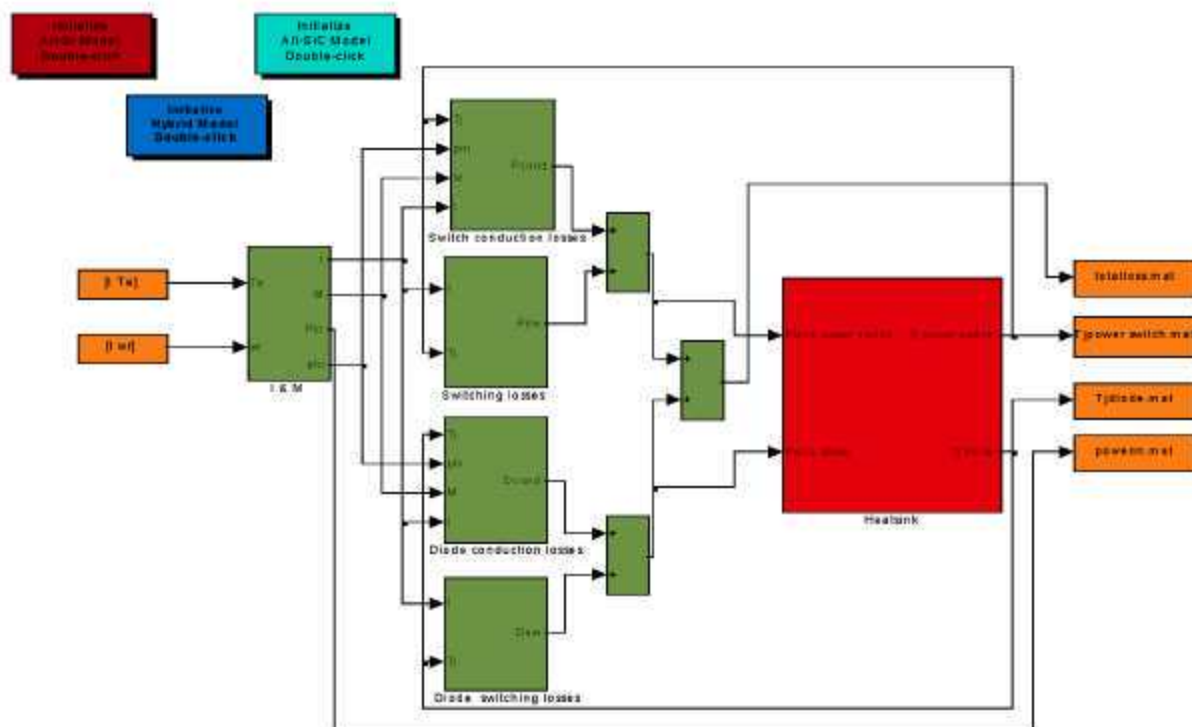


Figure 22. Block diagram of the system level model.

B.1 Control Block Model

The speed and torque profiles for a Federal Urban Driving Schedule (FUDS) cycle were obtained from the power train system analysis toolkit (PSAT), a drive train simulation software developed by Argonne National Laboratory. The speed and torque profiles were fed to the control block, which calculates the peak current, modulation index, input power, and power factor for the average loss model. The control block is explained in detail by Ozpineci.¹

B.2 Device Models

The devices used in three different inverters are listed in Table 1.

Table 1. Ratings of the devices used in the inverters

	Switch	Diode
All-SiC inverter	1200-V/10-A SiC JFET	600-V/75-A SiC Schottky diode
Hybrid inverter	600-V/50-A Si IGBT	600-V/75-A SiC Schottky diode
All-Si inverter	600-V/50-A Si IGBT	600-V/80-A Si pn diode

The devices listed in Table 1 were scaled to a rating of 600 V and 600 A for the power switches and 600 V and 450 A for the diodes to be able to simulate a 55-kW inverter. The device loss models were developed from the static and dynamic characteristics of the devices. The conduction losses were calculated using an average modeling technique that is explained in detail in Ozpineci.¹ The conduction loss parameters derived from the test data were used in the modeling equations. The switching loss models were calculated from total energy losses during switching. The SiC JFET and SiC diode modeling was discussed in earlier sections of this report. Si IGBT and Si pn diode modeling will be presented in the following sections.

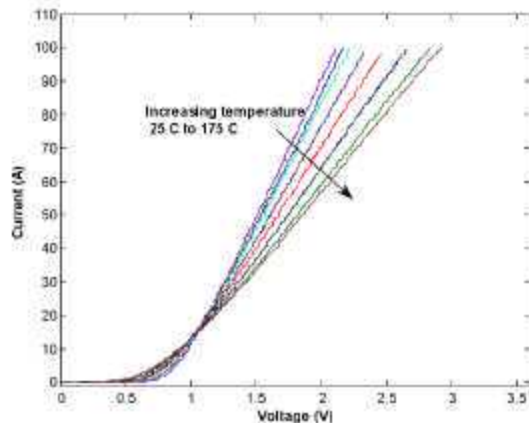


Figure 23. i-v characteristics of IGBT at different temperatures.

as a function of temperature as shown in Equations (7) and (8).

$$V_D = 1.7 \times 10^{-7} \cdot T^3 + 4.3 \times 10^{-5} \cdot T^2 - 0.0032 \cdot T + 0.91 \text{ (Volts)} \quad (7)$$

$$R_D = 1.9 \times 10^{-7} \cdot T^2 + 2.5 \times 10^{-5} \cdot T + 0.012 \text{ (Ohms)} \quad (8)$$

Si IGBT model

A 600-V, 50-A trench-stop technology-based IGBT with a maximum junction temperature specification of 175°C was chosen for the all-Si and hybrid inverter simulations. This IGBT is a commercial device from Infineon, part number IGP60N50T.

Static characteristics

The static characteristics of the IGBT at different temperatures are shown in Figure 23. The IGBT has a positive temperature coefficient similar to that of an SiC diode. The static characteristics of the IGBT are very similar to those of the diode and can be modeled using the PWL model. The PWL model parameters were extracted from the static curves and are derived

Dynamic characteristics

The dynamic characteristics of the IGBT were obtained using the double pulse circuit and the high-temperature setup described earlier with both an SiC Schottky diode and a Si pn diode to model the effects of the reverse recovery on the turn-on current of the IGBT. Figure 24 shows the difference in turn-on losses of the IGBT. The better reverse-recovery characteristics of the SiC diode help in reducing the losses of the IGBT. This is because when a diode in an inverter is turning off, the diode-reverse-recovery current passes through the other IGBT in the same phase leg, causing additional losses. The IGBT turn-off losses do not change much with Si or SiC diodes because the diode affects only the turn-on losses of the IGBT, as shown in Figure 25.

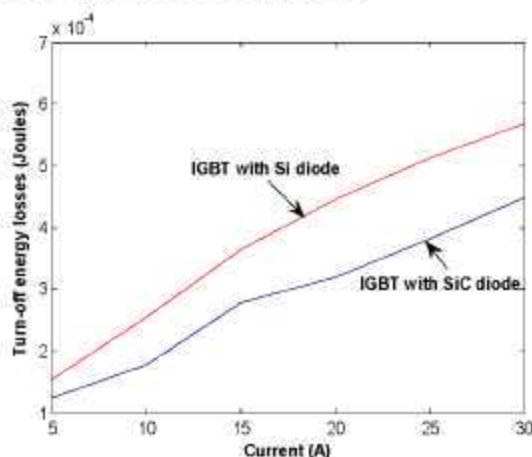


Figure 24. Turn-on switching energy losses of IGBT with Si and SiC diodes at 25°C.

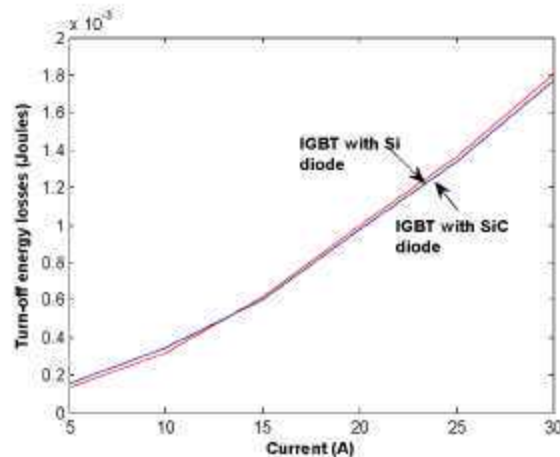


Figure 25. Turn-off switching energy losses of IGBT with Si and SiC diodes at 25°C.

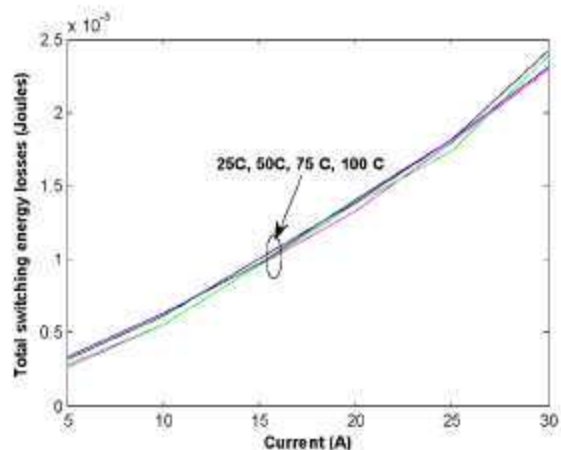


Figure 26. Total switching energy losses of IGBT at different currents and temperatures

Si diode model

A 600-V/ 80-A Si pn diode with a maximum junction temperature specification of 175°C was chosen for the all-Si and hybrid inverter simulations. The diode is a commercial device from Infineon and the part number is RUR8060.

Static characteristics

The static characteristics of the diode at different temperatures are shown in Figure 27. The Si diode has a negative temperature coefficient, as expected, unlike the SiC Schottky diode. The static characteristics of the diode can be modeled using the PWL model. The PWL model parameters were extracted from the static curves and are derived as a function of temperature as shown in Equations (10) and (11).

The diodes in the test were kept outside the temperature-controlled box and hence did not affect the IGBT losses at different temperatures. The turn-off losses of the IGBT dominated the turn-on losses. Since the turn-off losses did not change much with temperature, the total switching losses of the IGBT did not change much with temperature (Figure 26). The variation in switching losses of the IGBT at different temperatures obtained from tests matched the data presented in the data sheet. The switching loss equation is given below in Equation (9).

$$E_{swtotal} = 1.2 \times 10^{-6} \cdot I^2 + 3.8 \times 10^{-5} \cdot I + 3.2 \times 10^{-5} \text{ (Joules)} \quad (9)$$

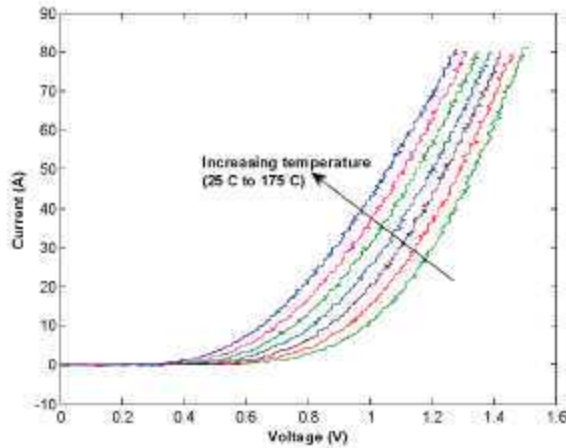


Figure 27. i-v characteristics of Si pn diode at different temperatures.

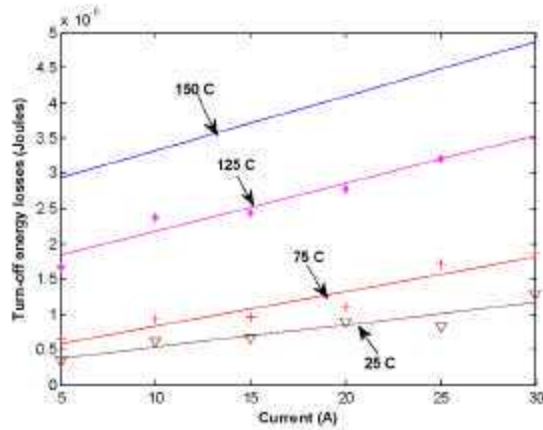


Figure 28. Turn-off energy losses of Si pn diode at different currents and temperatures.

resistance due to heat spreading through the cross section area. A side view of the cross section is shown in Figure 29. The structure, thicknesses, and materials of the layers used in the model were taken from Semikron's SKAI module. The heat sink model was based on the commercially available air-cooled inverter. Note, however, that the heat sink used in the calculation is a model with adjustable fin length and thickness and is designed for natural convection. The equivalent circuit is shown in Figure 30. The model assumes that the temperature along the top of the base plate is uniform. This is a valid assumption because the thermal resistance in the entire cross section is high, from the base plate to the tip of the fins

$$V_D = -0.0012 \cdot T + 0.59 \text{ (Volts)} \quad (10)$$

$$R_D = 1.5 \times 10^{-7} \cdot T^2 + 1.5 \times 10^{-5} \cdot T + 0.0078 \text{ (Ohms)} \quad (11)$$

Dynamic characteristics

The dynamic characteristics of the Si pn diode were obtained using the same chopper circuit and high-temperature set-up as used for the SiC Schottky diode. The switching energy losses due to the reverse recovery current are shown in Figure 28. The reverse recovery losses of the Si pn diode increase with an increase in current and temperature, as seen in Equations (12) and (13)

$$E_{swoff} = a \cdot I + b \text{ (Joules)} \quad (12)$$

$$a = 3.6 \times 10^{-10} \cdot T + 2.3 \times 10^{-8} \quad (13)$$

$$b = 2.1 \times 10^{-10} \cdot T^2 - 1.8 \times 10^{-8} \cdot T + 5.3 \times 10^{-7} \quad (14)$$

where T is in $^{\circ}\text{C}$.

B.3 Thermal Model

The thermal model developed is a 1-dimensional thermal resistance model with 2-dimensional heat spreading effects modeled using finite element analysis. The thermal resistance calculated is a sum of 1-dimensional cross section resistance and the

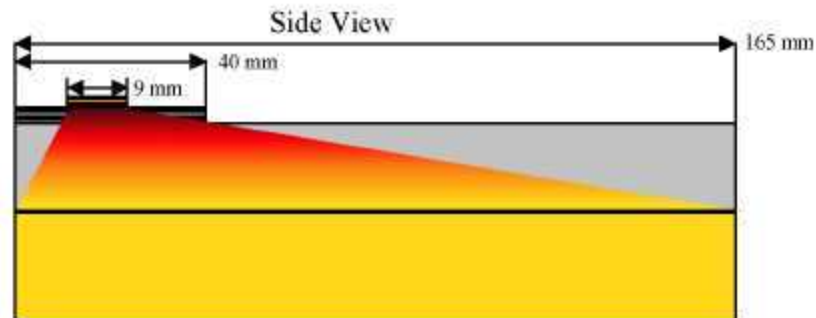


Figure 29. Side view of the cross section of the inverter.

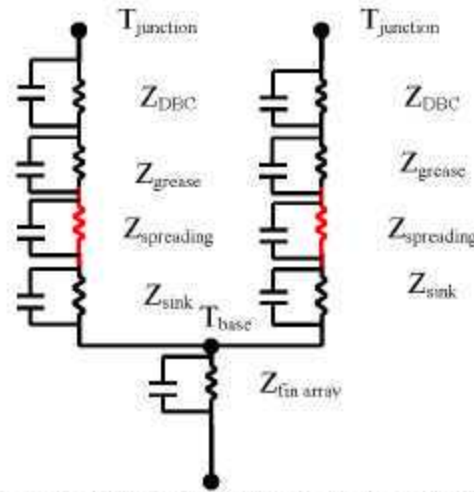


Figure 30. The equivalent circuit of the thermal model.

on the heat sink. The spacing between devices on top of the direct bonded copper is based on the number of devices and the length of the DBC sled and is the same as in the Semikron SKAI unit. The dimensions of each device on top of the DBC can be changed. However, the diodes and the main power switches are assumed to be the same dimensions so that there is a line of symmetry along the cross section.

B.4 Simulation Results

The three different inverter models were simulated for several operating conditions, and some of the results are discussed below. Efficiency vs output power plots for several operating conditions comparing the inverters are shown in Figures 31 and 32. The hybrid inverter and all-SiC efficiencies are higher than those of the all-Si inverter for all operating conditions. The percentage loss reduction was calculated comparing the power loss differences between the hybrid inverter and the all-SiC inverter with respect to the all-Si inverter, as shown in Equation (15).

$$\% \text{loss reduction} = \frac{P_{\text{loss}}^{\text{All-Si}} - P_{\text{loss}}^{\text{All-SiC}}}{P_{\text{loss}}^{\text{All-Si}}} \times 100 \quad (15)$$

The temperature profiles of the JFETs and Schottky diodes in the all-SiC inverter over a FUDS cycle are shown in Figure 33.

The heat sink used in the simulations was designed for 30-kW continuous power. Using the inverter loss model and the thermal model, the junction temperatures calculated for 30-kW operation of the all-Si and all-SiC inverters at different ambient temperatures are shown in Figure 34. The figure also shows the volume of the heat sink required, corresponding to the junction temperature of the device. Figure 34 shows that with natural convection, the all-Si inverter can operate only at 25°C ambient conditions because of the junction temperature limitations. At 105°C ambient, the junction temperatures are beyond the theoretical limits of the Si devices, and even increasing the heat sink volume does not reduce the junction temperatures because the heat sink is saturated. The temperatures of the SiC devices are much lower because of the reduced losses compared with the Si devices. Hence, for the same junction temperature of 150°C, the heat sink volume needed is two-thirds less for an all-SiC inverter than for an all-Si inverter.

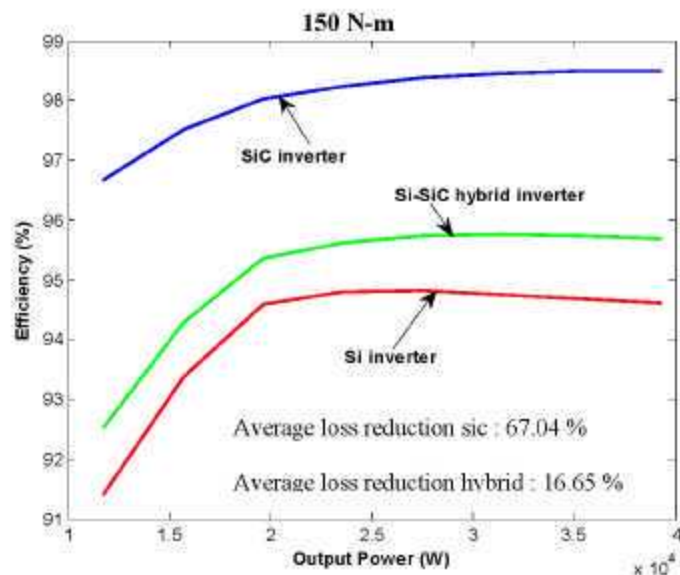


Figure 31. Efficiency vs output power of three different inverters at 150 N-m load.

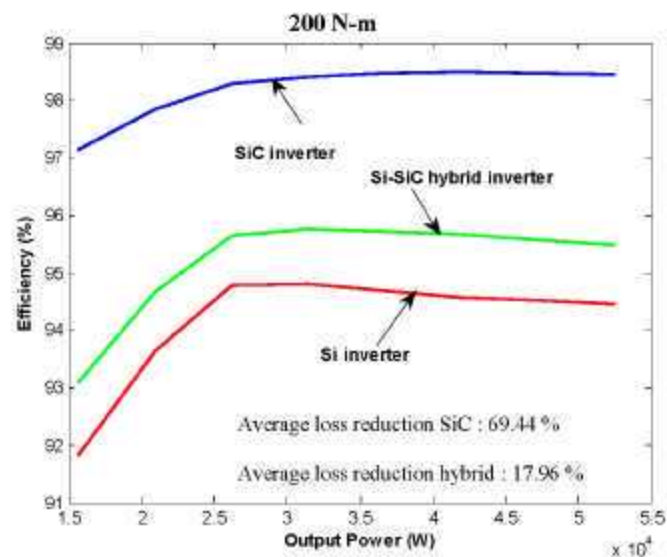


Figure 32. Efficiency versus output power of three different inverters at 200 N-m load.

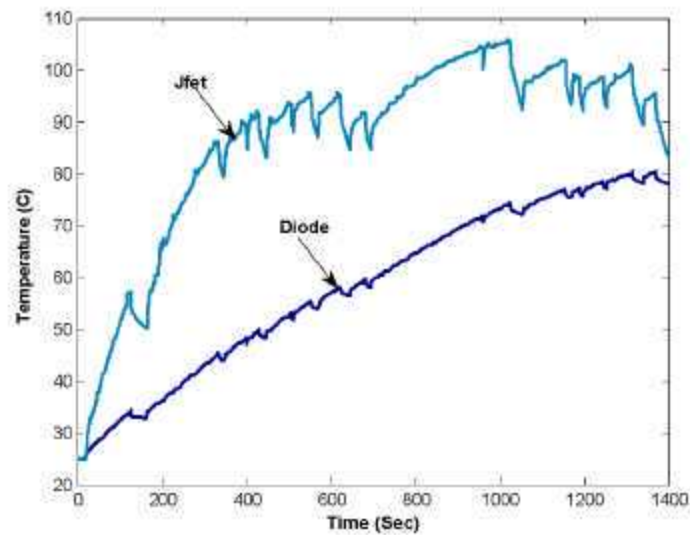


Figure 33. Temperature profile of devices over FUDS cycle.

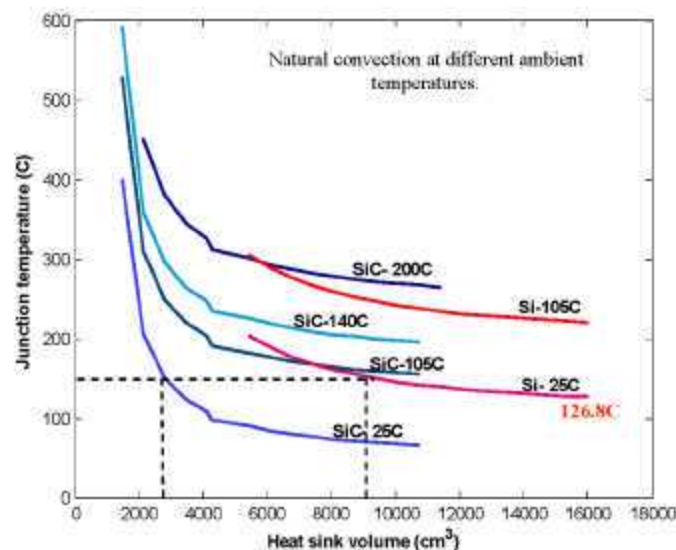


Figure 34. Heat sink volume vs device junction temperatures for all-Si and all-SiC inverters.

C. High-Temperature Packaging Tests

One of the most important characteristics of SiC power devices is that they can operate at much higher temperatures ($>300^{\circ}\text{C}$) than do Si power devices. Presently, SiC devices use Si device packages that limit the operation temperature ($\sim 125^{\circ}\text{C}$). Tests at Oak Ridge National Laboratory (ORNL) have shown that at high temperatures, these packages break open and leave the devices inoperable. This year, ORNL collaborated with the University of Arkansas to build several high-temperature packages to demonstrate packages that can operate at 200°C ambient. Two different packages with SiC Schottky diodes were delivered and tested at ORNL.

- TO-220 package

A single-die 600-V/75-A SiC Schottky diode was packaged in a TO-220 through-hole style package (Figure 35). The package was tested at different current levels at 200°C ambient temperature without a heat sink. The case temperature of the diode was measured using a thermocouple. The diode forward voltage drop was measured at different current levels using a Keithley data acquisition system. The voltage drop of the diode and case temperature as measured are shown in Figures 36 and 37. The diode operated at 361°C at 20 A for over an hour without a failure. However, at 25 A, the diode operated for a short time and then failed by shorting across the junction. This is a significant milestone in terms of operating temperature of the device; it clearly demonstrates the high-temperature operation capability of SiC devices.

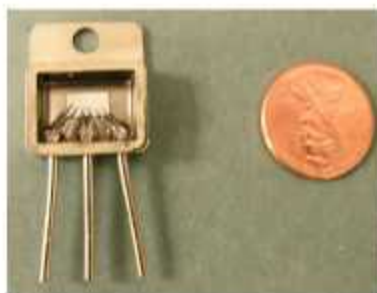


Figure 35. TO-220 through-hole high-temperature package of 75-A SiC Schottky diode.

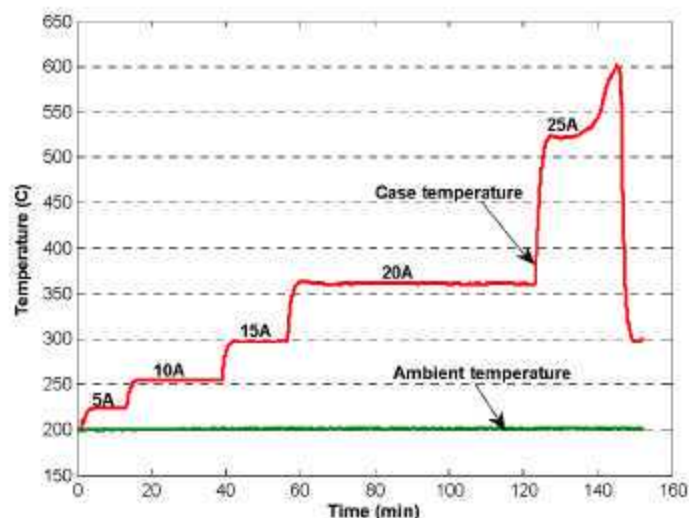


Figure 36. Case temperature of 75-A diode at different current level measured at 200°C ambient.

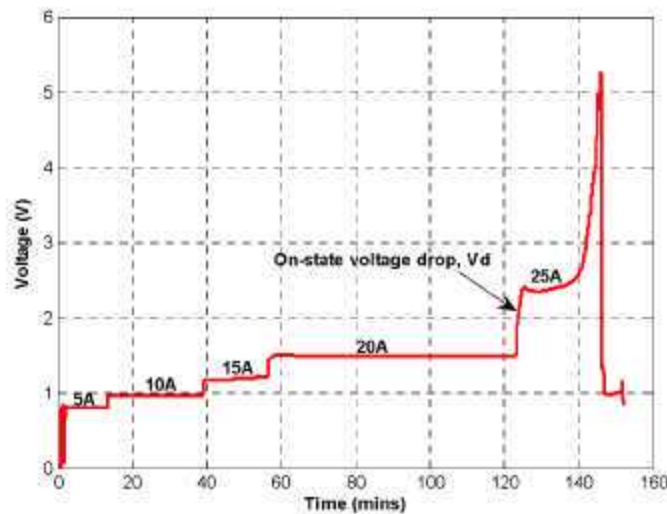


Figure 37. Voltage drop across the diode at different currents.

- 450-A package

Six 600-V/75-A SiC Schottky diodes were packaged in a module yielding a combined rating of 600 V and 450 A, as shown in Figure 38. The static characteristics of the module obtained at different temperatures are shown in Figure 39. The module was also tested at 200°C ambient at different current levels, similar to the testing of the single-die package. The case and ambient temperatures of the diode module were measured using a thermocouple. The forward voltage drop and temperatures are shown in Figures 40 and 41. The module was limited by the contact solder to a maximum operating temperature of 308°C. The upper test temperature limit was set to 282°C so that it would remain below the solder limitation. The operating current corresponding to 282°C was 50 A. The diode operated without any failure for a long duration at this operating point. The effect of the temperature coefficient of the device is evident in the voltage drop plot. The change in current increases the voltage drop, and then the effect of the temperature increase decreases the voltage. Note from Figure 39 that the diode module has a negative temperature coefficient below 120 A and a positive temperature coefficient above that temperature. The maximum current to which the diode module was tested was limited to 50 A.



Figure 38. A 450-A high-temperature SiC diode module with six 75-A Schottky diodes in parallel.

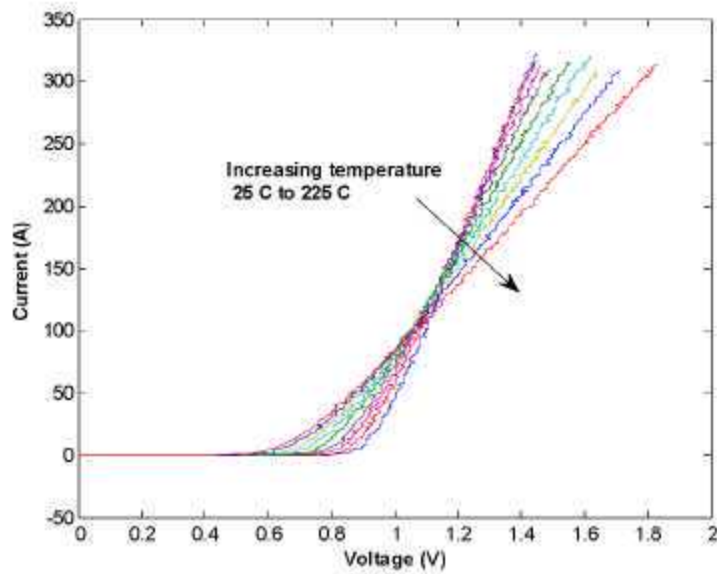


Figure 39. i-v curves of the 450-A diode module.

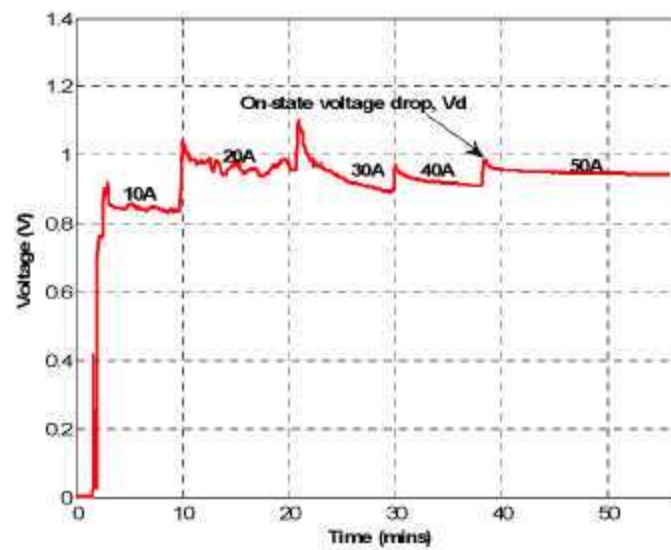


Figure 40. Voltage drop across the diode module at different currents.

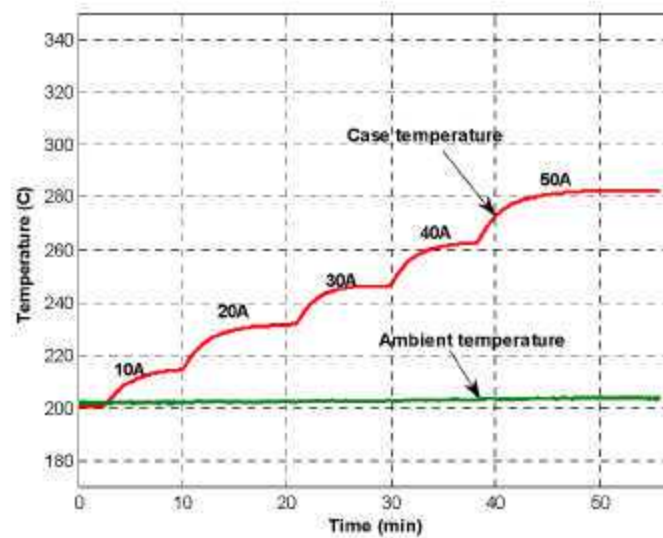


Figure 41. Case temperature of 75-A diode at different current levels measured at 200°C ambient.

D. Hybrid Inverter Tests

The inverter shown in Figure 42 was built at ORNL using power modules delivered by CREE. Two different inverters were built: an all-Si inverter using Si-IGBTs and Si pn diodes, and a hybrid inverter using the same Si IGBTs but SiC Schottky diodes instead of Si pn diodes. The performances of the inverters was compared after an inductive load test. The hybrid inverter and the all-Si inverter were tested with the same test procedure and using the same controller on the same benchtop system.

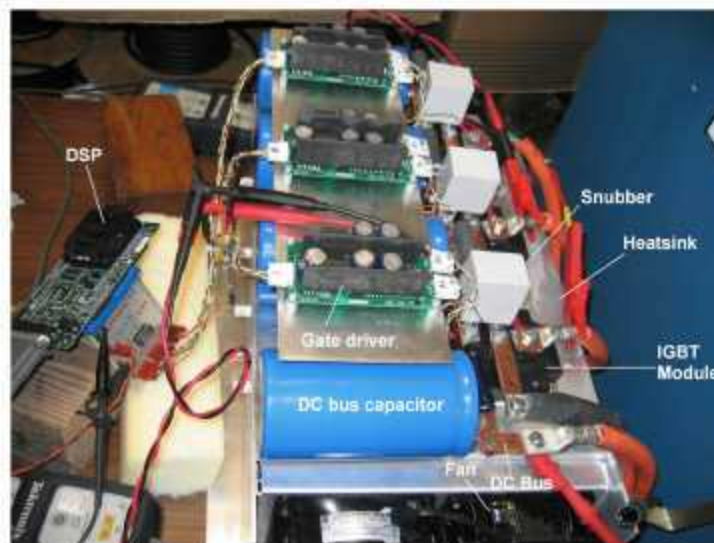


Figure 42. Three-phase inverter built at ORNL.

Test Setup

The output leads of the inverter were connected to a 3-phase star-connected variable resistor bank with a 3-phase inductor in series. The dc inputs were connected to a voltage source capable of supplying

the maximum rated operating voltage and current levels for the inverter. The test setup is shown in Figure 43.



Figure 43. R-L load test setup.

The device modules used in the hybrid inverter were Si IGBT/SiC Schottky diode modules (QID1230009-ES), and the modules used in the all-Si inverter were Si IGBT/Si pn diode modules (CM300DY-24NF). The controls for the inverter were generated using a DSP TMS320F2812. A space vector pulse width modulation technique was used as the control scheme. IGBT modules were driven by a BG2A board (from POWEREX), which used two VLA502-01 gate drivers. The inverter was mounted on a heat sink with fans.

Results

Voltage, current, switching frequency, and the frequency of the output current are important parameters that have significant influences on power losses and efficiency. Thus the tests were conducted under different combinations of these parameters.

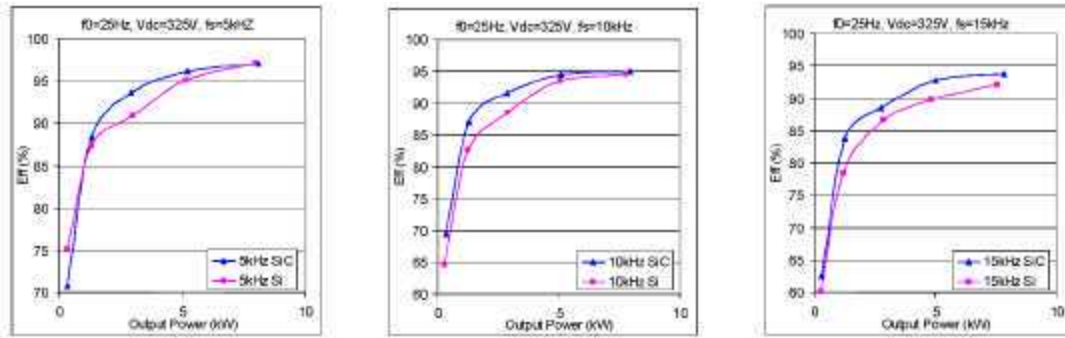
dc voltage: 200 V and 325 V

ac side current (rms): 10 A to 50 A

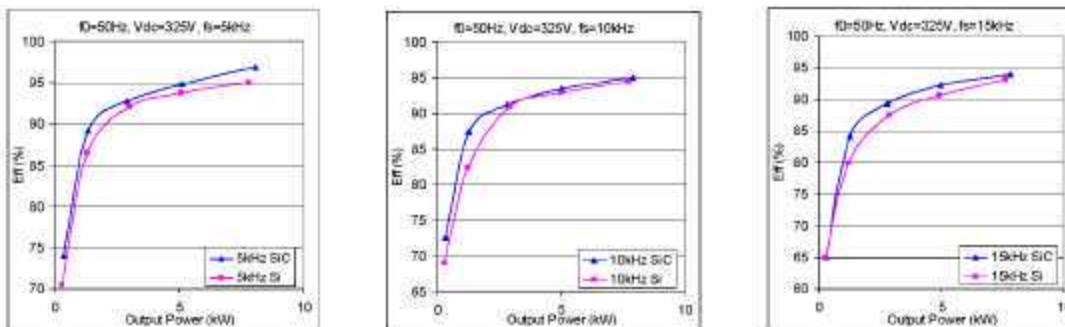
Frequency of output ac current: 25, 50, 75, and 100 Hz

Switching frequency of inverter: 5, 10, and 15 kHz

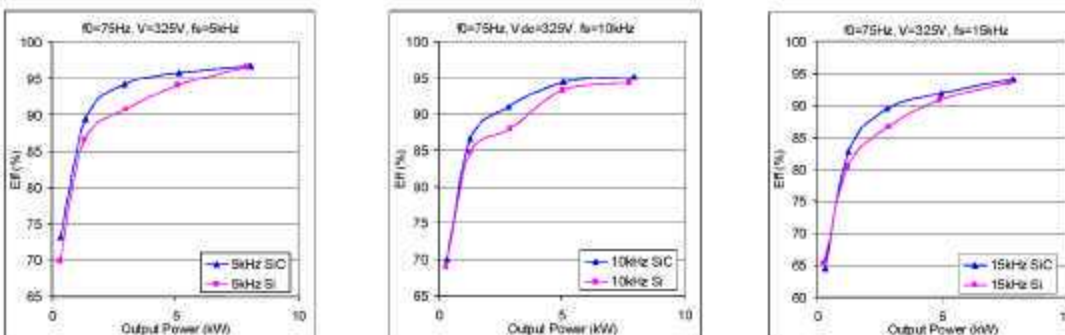
The data obtained for both of the inverters were analyzed and the corresponding efficiencies were calculated. The efficiency versus output power plots for several operating conditions comparing the inverters are shown in Figure 44. The Si-SiC inverter had a higher efficiency than the all-Si inverter. The difference in efficiencies between these two inverters is smaller at low output power and larger at high output power. This is because power losses of both inverters are lower at low output power, and the power losses of the Si inverter increase more quickly as the output power (or current) increases. In some cases, the efficiency of the SiC inverter is even lower than that of the Si inverter at low current levels because the Si pn diode voltage drop is much lower than the SiC Schottky diode voltage drop at low currents; however, most applications will be operating in the higher current regions. The efficiencies of both inverters increase as output power increases (see Figure 44) and decrease as switching frequency increases (see Figure 45), as expected.



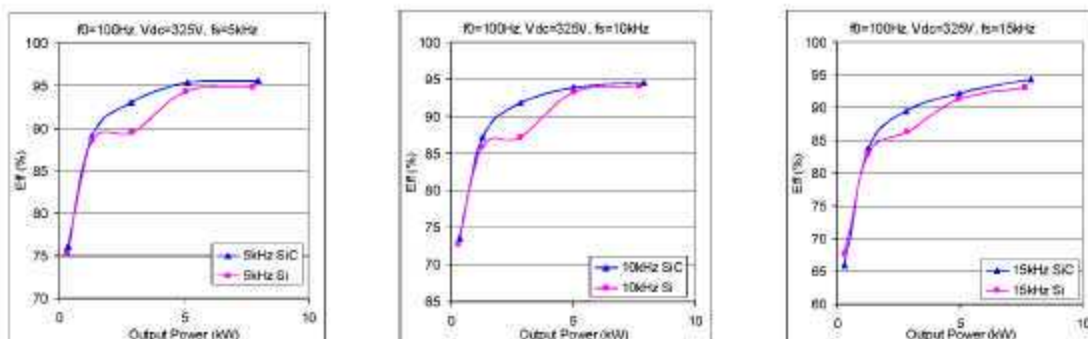
(a) dc voltage 325 V and output frequency 25 Hz



(b) dc voltage 325 V and output frequency 50 Hz



(c) dc voltage 325 V and output frequency 75 Hz



(d) dc voltage 325 V and output frequency 100 Hz

Figure 44. Efficiency vs output power at 325-V dc voltage.

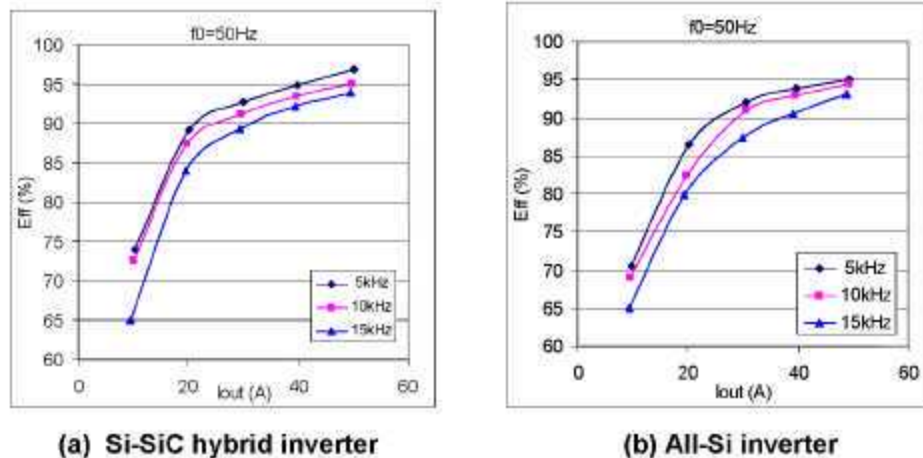


Figure 45. Efficiency of inverters at 325 V dc voltage and 50 Hz output.

Conclusion

Several new devices (SiC Schottky diodes, JFETs and GaN Schottky diodes) were acquired, tested, and modeled. There is a significant improvement in performance of the new-generation JFETs, which indicates that SiC switch technology is maturing. The 55-kW inverter simulations showed reduced losses of up to 69% for the all-SiC inverter and up to 28% for the hybrid inverter compared with the all-Si inverter. The inverters were simulated over a FUDS cycle, and the results showed that with natural convection, a two-thirds reduction in heat sink volume can be realized using an all-SiC inverter rather than an all-Si inverter. Two high-temperature packages delivered by the University of Arkansas were tested to demonstrate a high-temperature packaging technology that can operate at 200°C. The diode operated at a temperature of as high as 361°C at 200°C ambient without any failure.

Future Direction

FY 2007 and Beyond

- Acquire, test, and characterize newer-technology WBG power devices.
- Study the impact of SiC devices on plug-in hybrid vehicles.
- Study the fault current limiting capability of SiC devices for safety and protection.
- Study the possibility of using a thermal boundary in SiC power modules where Si gate drivers can be used.

Publications

M. Chinthavali, L. M. Tolbert, B. Ozpineci, and H. Zhang, "High Temperature Power Electronics—Application Issues of SiC Devices," in *International Conference on High Temperature Electronics (HiTEC 2006)*, International Microelectronics and Packaging Society, Santa Fe, New Mexico, May 15–18, 2006.

B. Ozpineci, M. S. Chinthavali, and L. M. Tolbert, "Enhancing Power Electronic Devices with Wide-Bandgap Semiconductors," *Journal of High Speed Electronics*, in press.

B. Ozpineci, M. S. Chinthavali, L. M. Tolbert, A. Kashyap, and A. H. Mantooth, "A 55-kW Three Phase Inverter with Si IGBTs and SiC Schottky Diodes," *IEEE Annual Applied Power Electronics Conference and Exposition*, March 19–23, 2006, Dallas.

H. Zhang, M. Chinthavali, B. Ozpineci, L. M. Tolbert, "Power Losses and Thermal Modeling of 4H-SiC VJFET Inverter," pp. 2630–2634 in *IEEE Industry Applications Society Annual Meeting*, October 2–6, 2005, Hong Kong, China.

B. Ozpineci, M. S. Chinthavali, and L. M. Tolbert, "A 55-kW Three Phase Automotive Traction Inverter with SiC Schottky Diodes," pp. 541–546 in *IEEE Vehicle Power and Propulsion Conference*, Chicago, September 7–9, 2005.

References

1. B. Ozpineci, "System Impact of Silicon Carbide Power Electronics on Hybrid Electric Vehicle Applications," Ph.D. Dissertation, Department of Electrical Engineering, The University of Tennessee, Knoxville, Tennessee, 2005.

Appendix. List of Devices Tested and Their Parameters

Power Diodes

Device type	Ratings	On-resistance (Ω)	Forward voltage drop (Volts)	Manufacturer	Year tested
SiC Schottky Diode	1200 V, 7.5 A	0.15 Ω at -50°C to 0.32 Ω at 175°C	1.42 V at -50°C to 1.21 V at 175°C	Rockwell	2004
SiC Schottky Diode	300 V, 10 A	0.15 Ω at -50°C to 0.16 Ω at 175°C	1.11 V at -50°C to 0.83 V at 175°C	Infineon	2004
SiC Schottky Diode	600 V, 4 A	0.19 Ω at -50°C to 0.39 Ω at 175°C	1.09 V at -50°C to 0.87 V at 175°C	Cree	2004
SiC Schottky Diode	600 V, 10 A	0.14 Ω at -50°C to 0.25 Ω at 175°C	1.09 V at -50°C to 0.82 V at 175°C	Cree	2004
SiC Schottky Diode	600 V, 75 A	0.01 Ω at -50°C to 0.03 Ω at 175°C	0.91 V at -50°C to 0.61 V at 175°C	Cree	2005
GaN Schottky Diode	600 V, 4 A	0.23 Ω at 25°C to 0.47 Ω at 175°C	0.83 V at 25°C to 0.67 V at 175°C	Velox	2006

Power Switches

Device type	Ratings	On-resistance (Ω)	Voltage drop at rated current @ room temperature (Volts)	Manufacturer	Year tested
SiC JFET	1200 V, 2 A	0.36 Ω at -50°C to 1.4 Ω at 175°C	1.3 V @ $V_{gs} = 0\text{V}$	SiCED	2004
SiC JFET	1200 V, 10 A	0.25 Ω at -50°C to 0.58 Ω at 175°C	2.71 V @ $V_{gs} = 0\text{V}$	SiCED	2006
SiC JFET	1200 V, 15 A	0.15 Ω at -50°C to 2.2 Ω at 175°C	3.2 V @ $V_{gs} = 3\text{V}$	Rockwell	2006
SiC JFET	600 V, 5 A	0.26 Ω at -50°C to 1.87 Ω at 175°C	2.25 V @ $V_{gs} = 3\text{V}$	Semisouth	2006
SiC MOSFET	1200 V, 5 A	(0.48 Ω at -50°C to 0.23 Ω at 50°C) (0.24 Ω at 75°C to 0.29 Ω at 175°C)	1.5 V @ $V_{gs} = 20\text{V}$	Cree	2005

4.2 Integrated dc-dc Converter for Multi-Voltage Bus Systems

Principal Investigator: Gui-Jia Su

Oak Ridge National Laboratory

National Transportation Research Center

2360 Cherahala Boulevard

Knoxville, TN 37932

Voice: 865-946-1330; Fax: 865-946-1262; E-mail: sugj@ornl.gov

DOE Technology Development Manager: Susan A. Rogers

Voice: 202-586-8997; Fax: 202-586-1600; E-mail: Susan.Rogers@ee.doe.gov

ORNL Program Manager: Mitch Olszewski

Voice: 865-946-1350; Fax: 865-946-1262; E-mail: olszewskim@ornl.gov

Objectives

- Develop a dc-dc converter topology that
 - can significantly reduce the component count,
 - is applicable to both triple-voltage and dual-voltage systems with essentially no hardware modifications,
 - provides easy power scaling capability to meet power requirements for varying vehicle sizes, and
 - can incorporate all future advanced components such as silicon carbide (SiC) devices and thermal management technologies as they become available.
- Produce a 4-kW prototype using 2-kW modules as building blocks and testing data to evaluate the prototype's capability to meet the FreedomCAR targets and power scaling capability.
- Establish requirements for dc-dc converters for various power system configurations in fuel cell-powered vehicles (FCVs).

Approach

The following approaches are taken to reduce the cost and size and increase the efficiency and power density of dc-dc converters for multi-bus systems in hybrid electric vehicles (HEVs) and FCVs.

- Increase the level of integration to minimize the number of switches and thus the associated gate drivers in order to reduce component count and still maintain a flexible topology: same circuit applicable to both dual- and triple-voltage systems.
- Increase switching frequency to reduce the weight, size, and volume of passive components.
- Employ soft switching and synchronous rectification to increase efficiency and power density.
- Employ soft switching to lower electromagnetic interference (EMI) noise.
- Use an interleaved modular approach for scaling power up.
- Optimize packaging.
- Conduct a literature search on dc-dc converters for FCV power systems.

Major Accomplishments

- Topology development
 - A half-bridge-based dc-dc converter has been developed that can interconnect the 14-V, 42-V, and high-voltage (HV) buses and can reduce the component count by 50% over conventional full-bridge-based technologies. Further refinements have eliminated the LC filter for the 14-V bus.

- Interleaved modular configurations using the half-bridge as a building block share the capacitor legs and provide a greater degree of component count reduction as the number of modules increases when the power level is scaled up.
- The capacitor leg current in the interleaved configurations can be significantly reduced, thus decreasing the capacitance.
- A novel control scheme has also been devised that can control the power flow among the three buses and reduce the flux density of the transformers.
- Prototype demonstration
 - A 4-kW prototype has been designed and built using two 2-kW modules.
 - The prototype has been successfully tested at load power levels of up to 4.6 kW.
 - Measured efficiencies are between 93.0 and 95.8 % over a wide power range of 0.5 to 4.6 kW.
 - Evaluation of the prototype indicates that it exceeds the 2015 FreedomCAR targets for specific power and power density, and the 2010 cost target.
- dc-dc converter requirements study for FCV applications
 - Several possible power system configurations and the requirements for dc-dc converters have been identified.

Technical Discussion

Background

As the automotive industry moves to drive-by-wire through the electrification of power steering, braking, and suspension, a 42-V net will probably be needed, as the existing 14-V system cannot efficiently power these loads. The HV bus (200–500V) for traction drives will add to the difficulty in meeting the safety requirements and in coping with EMI issues caused by running HV wires throughout the vehicle. While this move is especially needed for FCVs, which have no internal combustion engines to assist with electrification mechanisms, drive-by-wire technology has already been employed in luxury vehicles. For instance, the Toyota RX400h hybrid sport utility vehicle (SUV) uses dc-dc converters to transform the traction battery voltage to 14 V for onboard electronics and to 42 V for electric power steering. In an SUV, the steering load alone demands a 42-V supply. In summary, a triple voltage bus (14-V/42-V/HV) system is likely to be employed in future HEVs and fuel cell-powered vehicles (FCVs).

Figure 1 illustrates a simplified diagram for power management in future FCVs that employs a triple voltage bus (14-V/42-V/HV) system. With presently available technologies, two separate dc-dc converters are needed to fulfill power management demands among the three buses: one for converting high voltage to 42 V and the other for transforming 42 V to 14 V. The cost and volume of this two-converter solution make it difficult to meet the FreedomCAR power density and cost targets. In addition, the dc-dc converters must provide bidirectional power flow control to enable the use of the 14-V or 42-V battery for fuel cell startup and for storing the energy captured by regenerative braking. During vehicle starting, the HV bus is boosted up to around 300 V by the dc-dc converter drawing power from the 14-V

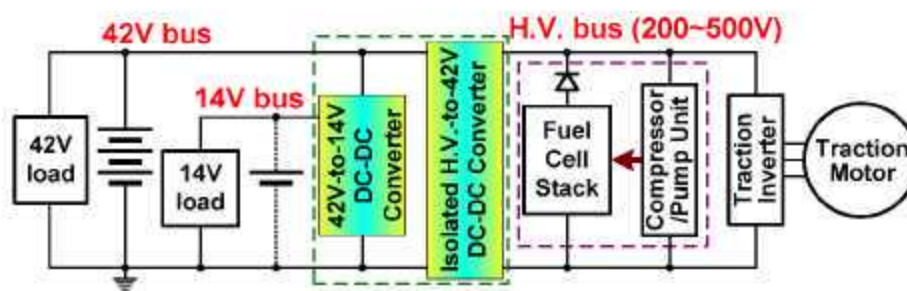


Figure 1. Power management in future fuel cell vehicles.

or 42-V battery. This HV bus then supplies power for the fuel cell compressor motor expanding unit controller and brings up the fuel cell voltage, which in turn feeds back to the HV bus to release the loading from the battery. During normal vehicle operation, power is transferred from the fuel cell stack to the low-voltage nets through the dc-dc converters to supply the vehicle accessory loads. The power management situation is similar in HEVs and plug-in HEVs, where the fuel cell power unit is replaced by an HV battery pack.

Although dc-dc converters are available to interconnect any two of the buses, to reduce component count, size, cost, and volume, it is desirable to employ an integrated dc-dc converter to interconnect the three voltage buses instead of using two separate ones. Aside from the bi-directional power control capability, the converter needs to provide galvanic isolation between the low-voltage and HV buses to meet safety requirements, which dictate the use of a transformer. Further, soft switching is preferred over hard switching because it reduces the level of EMI and switching losses.

In this project, a low-cost, soft-switched, isolated bi-directional dc-dc converter is being developed for interconnecting the three bus nets. The converter is based on a dual half-bridge topology to eliminate half of the switches required in a full-bridge counterpart. Further developments in the topology have led to the elimination of additional components. Figure 2 shows a diagram of the original converter, in which the 14-V bus is connected to the midpoint of the 42-V switch leg through an LC filter. This LC filter is eliminated in the modified topology shown in Figure 3, in which the 14-V bus is derived from the

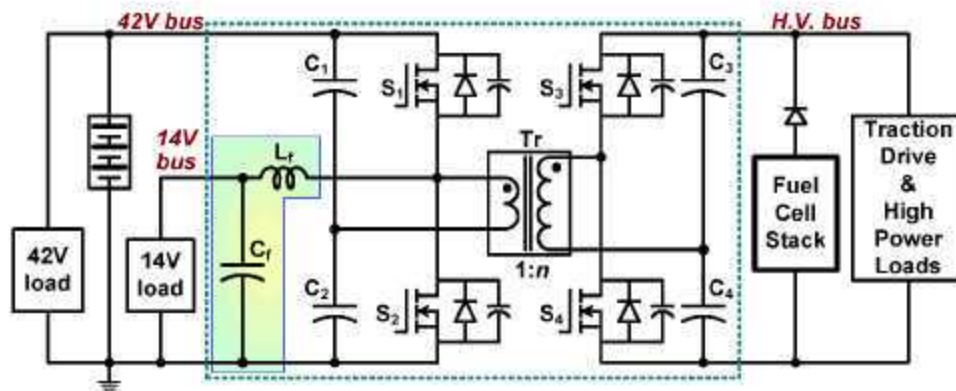


Figure 2. Original topology with LC filter.

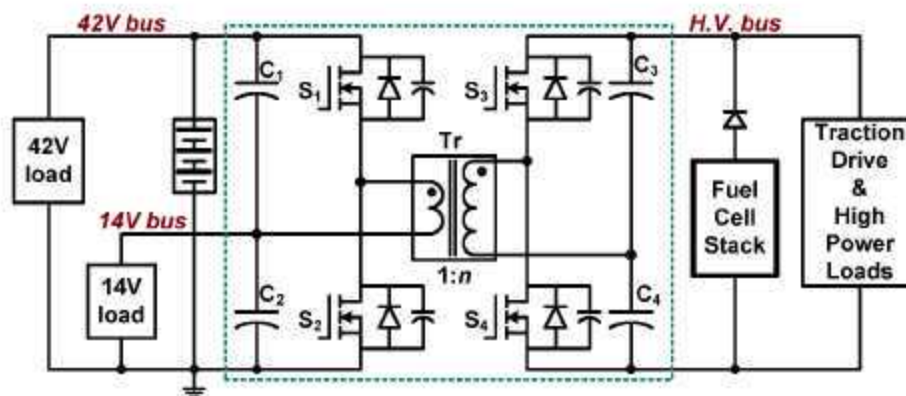


Figure 3. Modified topology that eliminates the LC filter.

capacitor leg. The converter uses the parasitic capacitance of the switches and the transformer leakage inductance to achieve zero-voltage-switching (ZVS). Therefore, no extra resonant components are required for ZVS, further reducing the component count. The inherent soft-switching capability and the low component count of the converter allow high power density, efficient power conversion, and compact packaging. A novel power flow control scheme based on a combined duty ratio and phase shift angle control has also been devised. The operation of the converter at a duty ratio other than the usual 50% reduces the peak flux density of the transformer, and thus a smaller core can be used.

To provide power scaling capability to meet the power requirements of vehicles of various sizes, without incurring the recurring engineering costs, a modular approach employing an interleaved multiphase configuration is the focus of the FY 2006 efforts. To this end, a 4-kW prototype using two 2-kW modules has been designed, built, and tested to evaluate its performance against the FreedomCAR targets.

In FCVs, in addition to the dc-dc converter for power management, higher-power dc-dc converters may be required to interface the fuel cell stack and/or high-power energy storage devices such as batteries and ultracapacitors. A study of dc-dc converter requirements for FCV applications was also performed in FY 2006.

Description of the dc-dc Converter for Triple Voltage Buses

Figure 4 shows a schematic of the 4-kW dc-dc converter, which consists of two half-bridge converter modules with shared capacitor legs. The high-frequency transformers, Tr_a and Tr_b , provide the required galvanic isolation and voltage level matching between the 42-V and the HV buses, while the 14-V and 42-V buses share a common ground. The leakage inductances of the transformers are used as the intermediate energy storage and transferring element between the two low-voltage buses and the HV net. The parasitic capacitors in parallel with the switches in each module resonate with the transformer leakage inductance to provide ZVS for the switches.

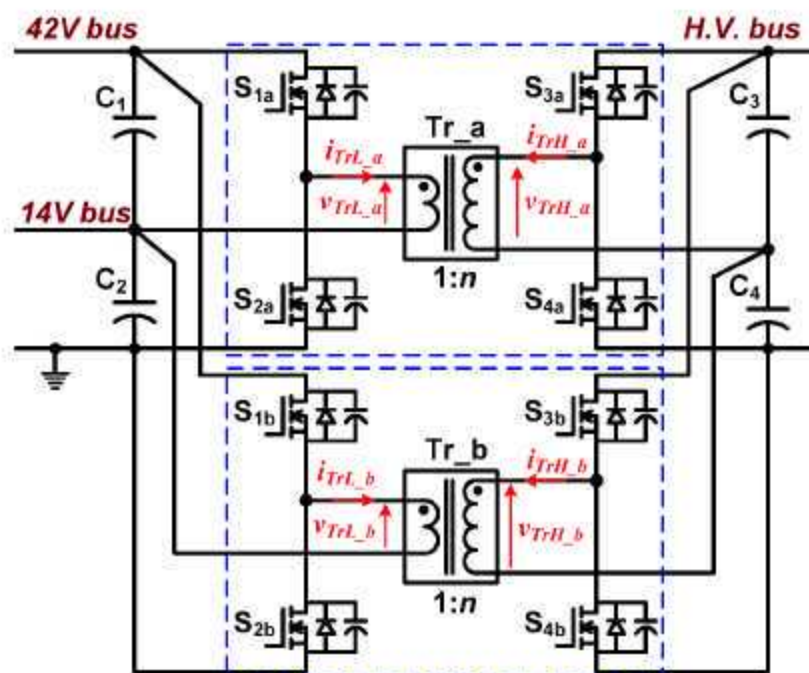


Figure 4. Schematic of the 4 kW dc-dc converter.

Figure 5 shows the transformer terminal voltages and currents waveforms to illustrate the operating principle of the converter. Duty ratio control is used for power flow control between the 14-V and 42-V buses, making the two bus voltages, V_{14V} and V_{42V} , track to each other by $V_{14V} = d \cdot V_{42V}$, where d is the duty ratio of the switches S_{1a} and S_{3a} , and S_{1b} and S_{3b} . It is defined by

$$d = \phi / 2\pi, \quad (1)$$

where ϕ is the conduction angle of the switches S_{1a} and S_{3a} , and S_{1b} and S_{3b} . For 14-V/42-V systems, the duty ratio is fixed at $d = 1/3$, $\phi = 2\pi/3$ at steady state for normal operation and can be changed to adjust the state of charge of the low-voltage batteries if necessary. In addition, a phase shift angle, ϕ , between the primary and secondary voltages of each transformer, v_{TrL_a} and v_{TrH_a} and v_{TrL_b} and v_{TrH_b} , is employed for power flow control between the 42-V and HV buses; $\phi > 0$ for low to high, $\phi < 0$ for high to low power transfer. Moreover, the transformer currents, i_{TrL_a} and i_{TrL_b} and i_{TrH_a} and i_{TrH_b} , are interleaved to reduce the capacitor leg currents, $i_{TrL_a} + i_{TrL_b}$ and $i_{TrH_a} + i_{TrH_b}$, and the capacitance by displacing the voltages of the two transformers by 180° , as shown in Figure 5.

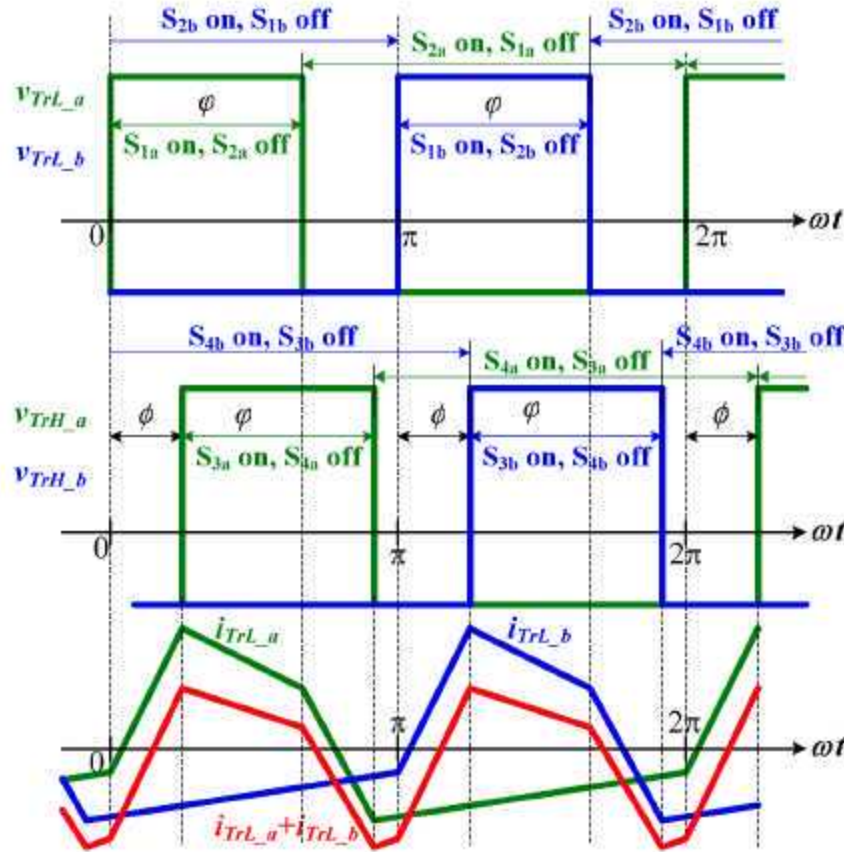


Figure 5. Transformer terminal voltages and currents waveforms illustrating the operating principle.

The power transferred through the transformers at steady state with $d = 1/3$ can be expressed by

$$P = \frac{V_{42V} V_{HV}}{n} \cdot \frac{\phi}{2\pi f_m L_s} \left[\frac{4}{9} - \frac{\phi}{2\pi} \right], \quad (2)$$

where n —transformer turns ratio, L_s —transformer leakage inductance, and f_{sw} —switching frequency. For a given design, the maximum power is determined by

$$P_{\max} = \frac{V_{42V} V_{HV}}{n} \cdot \frac{4}{81 f_{sw} L_s} \text{ at } \phi_{p_{\max}} = \frac{4\pi}{9} \quad (3)$$

For a given bus voltage, V_{42V} , and switching frequency, f_{sw} , varying the duty ratio, d , will change the peak flux linkage, ψ_{peak} , of the transformer but will not introduce a dc bias. This is because the positive transformer terminal voltage, V_P , is $(1-d) \times V_{42V}$ at an interval of $t_P = d/f_{sw}$; and the negative transformer terminal voltage, V_N , is dV_{42V} but at an interval of $t_N = (1-d)/f_{sw}$, leading to the same product of volt \times second of $d(1-d)V_{42V}/f_{sw}$ over the positive cycle and negative cycle. Further, operating at a duty ratio other than the usually employed 50% will decrease the peak flux linkage and thereby the transformer stress. The peak flux linkage is determined by $\psi_{peak} = \pm d(1-d)V_{42V}/(2f_{sw})$. At $d = 50\%$, $\psi_{peak} = \pm V_{42V}/(8f_{sw})$ while at $d = 1/3$ for our converter, the peak flux linkage is reduced to $\psi_{peak} = \pm V_{42V}/(9f_{sw})$ and thus a smaller transformer core can be used at the same switching frequency and number of turns.

Prototype Design and Experimental Results

Simulation study

A detailed circuit simulation was first performed for the 4-kW prototype design. Figure 6 shows simulation results where power is transferred from the 42-V bus to the 14-V and HV net at the level of 4.1 kW. Figure 7 shows simulated waveforms when the power flow is reversed. The simulation results confirm the design goal, that the power rating and the capacitor leg currents can be reduced to half of those in a single channel converter.

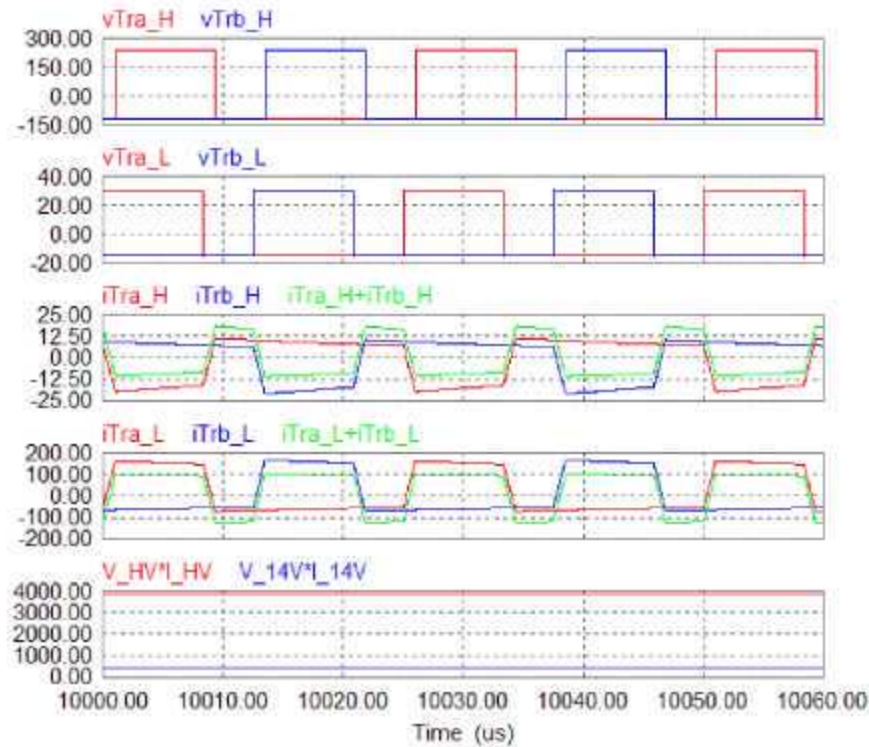


Figure 6. Simulation results showing power transfer from 42 V to 14 V and HV.

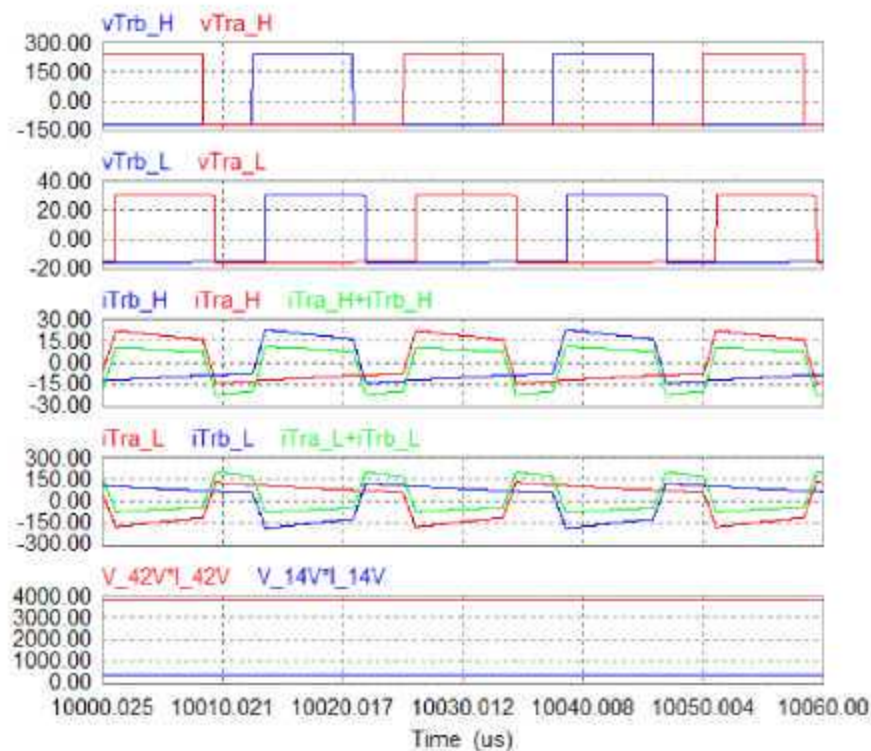


Figure 7. Simulation results showing power transfer from HV to 42 V and 14 V.

Converter design

A 4-kW prototype was then designed and built based on the analytical, simulation, and test results for a single-phase module. The design uses planar transformers, printed circuit power planes, and metal oxide semiconductor field effect transistors (MOSFETs) for both low and high voltages.

- Planar transformer design
 - Core, Ferroxcube E64/10/50
 - 4-layer PCB, 6 oz copper
 - Turns ratio, 1:8
- Power plane, 2-layer PCB
 - Low voltage: 6 oz copper
 - High voltage: 3 oz copper
- Benefits
 - Tight control of the leakage inductance—*important for soft-switching*
 - Easy assembly
- MOSFETS
 - Low-voltage side: SEMIKRON SK 300MB075, 75V/210A
 - High-voltage side: IXYS CoolMOS Power MOSFETVKM40-06P1, 600V/38A

Figure 8 shows a photo of the planar transformer.



Figure 8. Photo of the planar transformer.
Footprint: 4.875×2.125 in.

A new digital signal processor (DSP) control board based on a Texas Instruments chip, TMS320F2812, has been designed and fabricated for controlling the MOSFETs. The DSP chip has two sets of pulse width modulation hardware that can control up to three modules simultaneously. Figure 9 shows a photo of the DSP control board.



Figure 9. Photo of the DSP control board. Size: 7.0×3.5 in.

Figure 10 shows a 3-dimensional assembly layout of the prototype. As clearly indicated in the side view, there are quite large unoccupied spaces. The total converter volume is 203 in.³ with 93 in.³ accounted for by the individual components. This is partly because it was intentionally designed to provide space for easy probing access and partly because commercial-off-the-shelf components were used. It is estimated that 65% of the unoccupied space can be eliminated by optimizing the layout and by using customized packages for the major components.

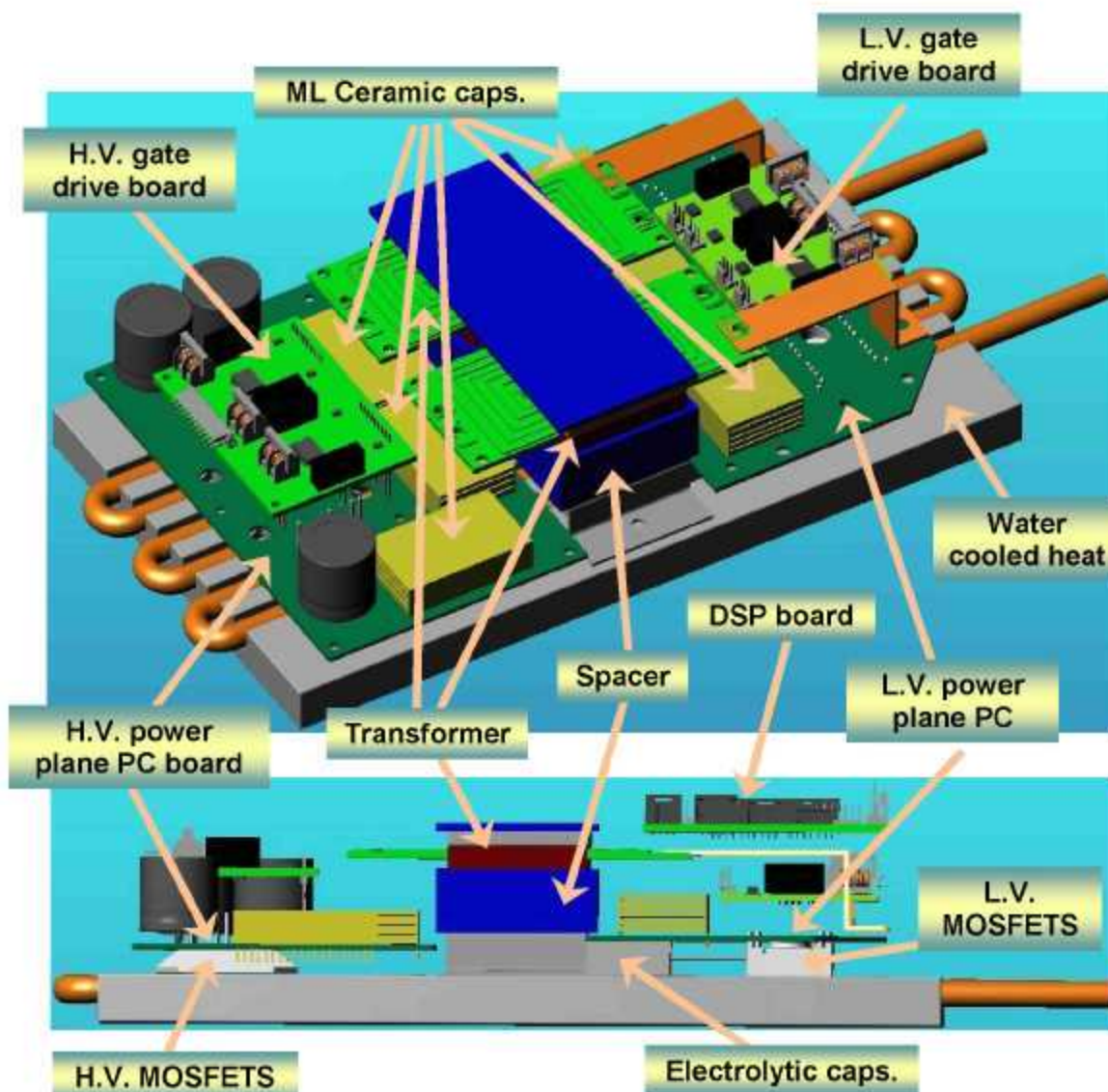


Figure 10. Three-dimensional assembly layout.

Figure 11 shows a photo of the 4-kW prototype. All components are mounted on a water-cooled heat sink 12 in. wide \times 7.0 in. deep. The actual occupied footprint is 10.7 in. wide \times 7.0 in. deep with a maximum height of 2.7 in. Evaluation of the prototype, assuming 65% of the unoccupied space can be removed, yielded performance numbers of 1.1 kW/kg, 2.1 kW/L, and \$60/kW, which exceeds the 2015 FreedomCAR targets for specific power and power density and the 2010 cost target.

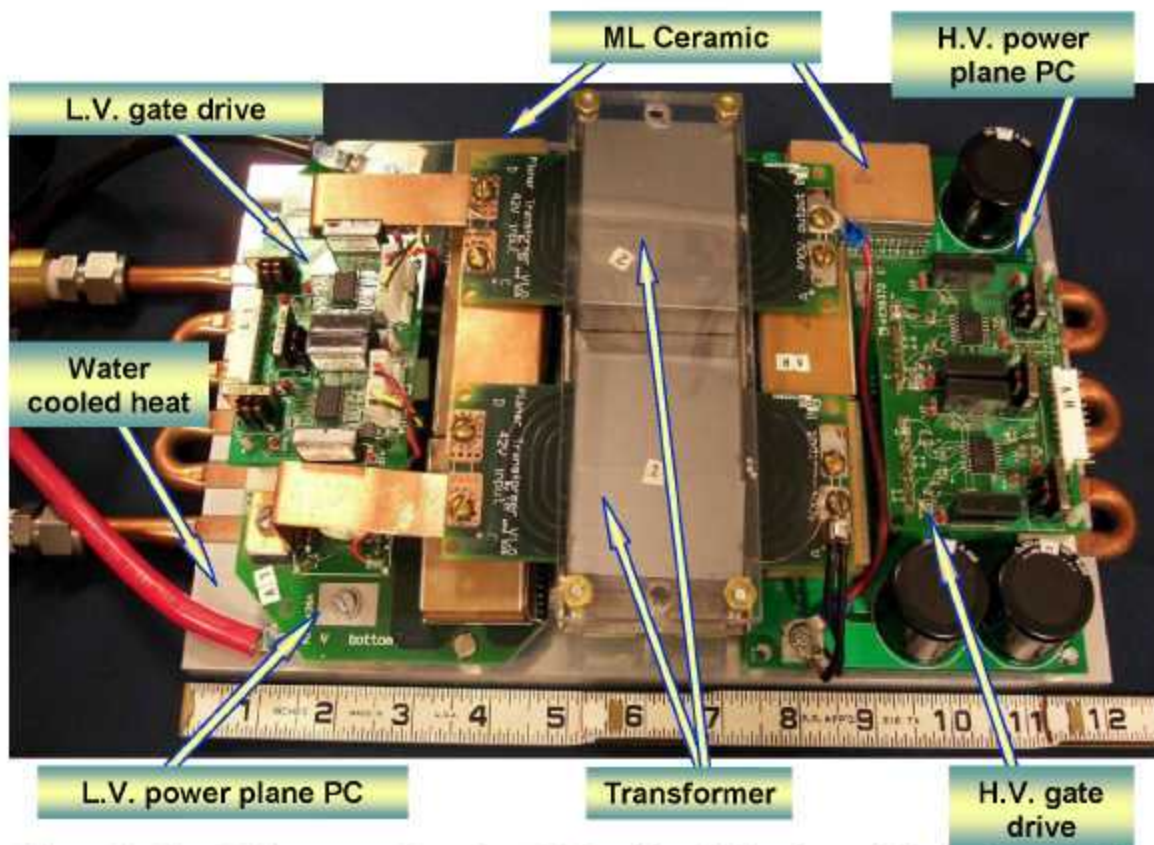


Figure 11. The 4-kW prototype. Footprint: 10.7 in. wide \times 11.0 in. deep \times 2.7 in. maximum height.

Experimental results

The prototype was fully tested at power levels of up to 4.6 kW. Figures 12 and 13 show typical testing waveforms at different load power levels when power was transferred from the 42-V bus to the 14-V and HV buses, and from the HV bus to the 14-V and 42-V buses, respectively. The smooth rising and falling edges of the transformer voltages indicate soft-switching operation.

Figure 14 plots power conversion efficiency against the load power for both low-to-high and high-to-low conversion. Measured efficiencies are between 93.0 and 95.8 % over a wide power range of 0.5 to 4.6 kW for low-to-high conversion, against 93.0 to 95.7 % over a power range of 0.7 to 4.2 kW for high-to-low conversion.

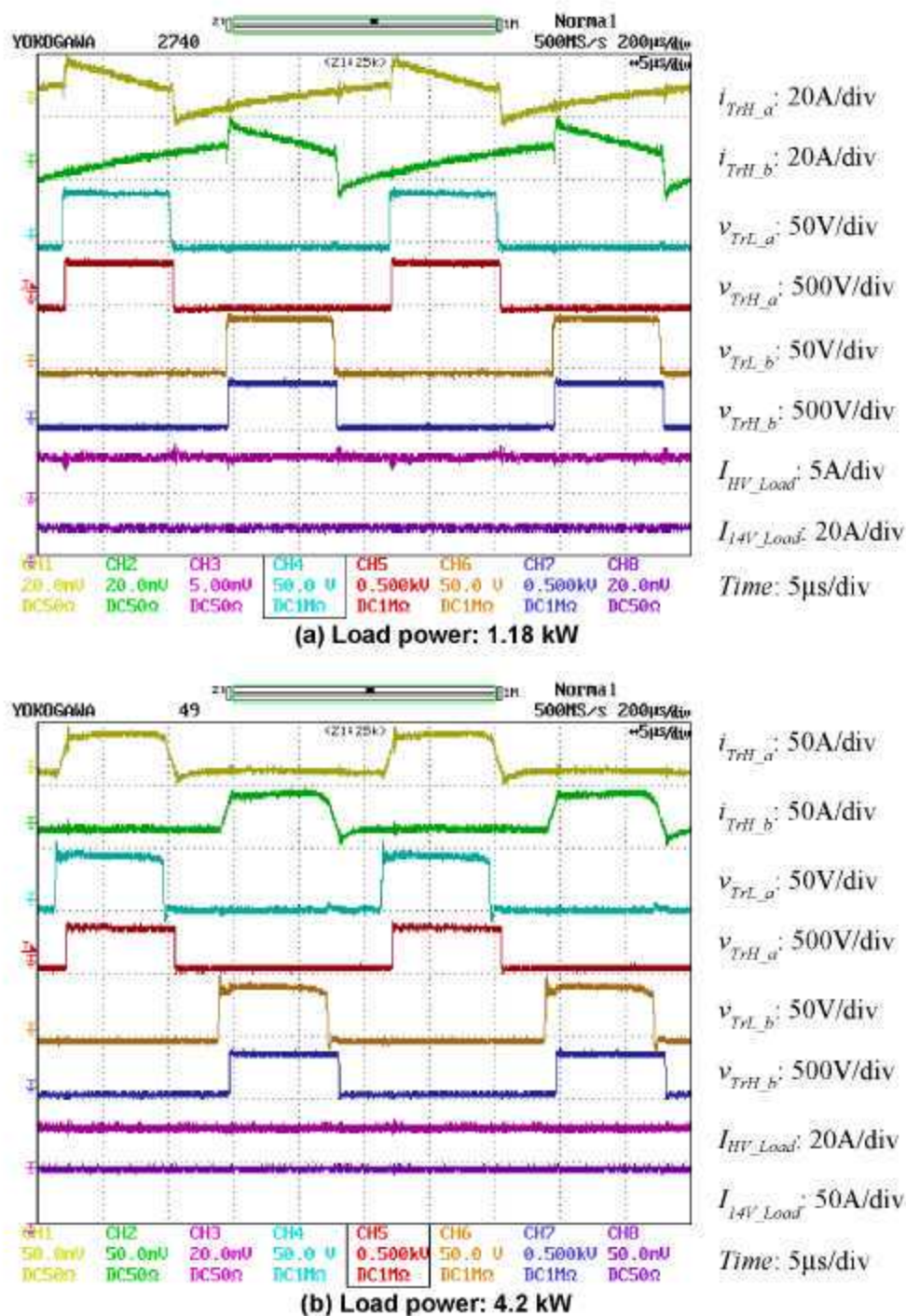


Figure 12. Typical testing waveforms for power transfer from 42 V to 14 V and HV.

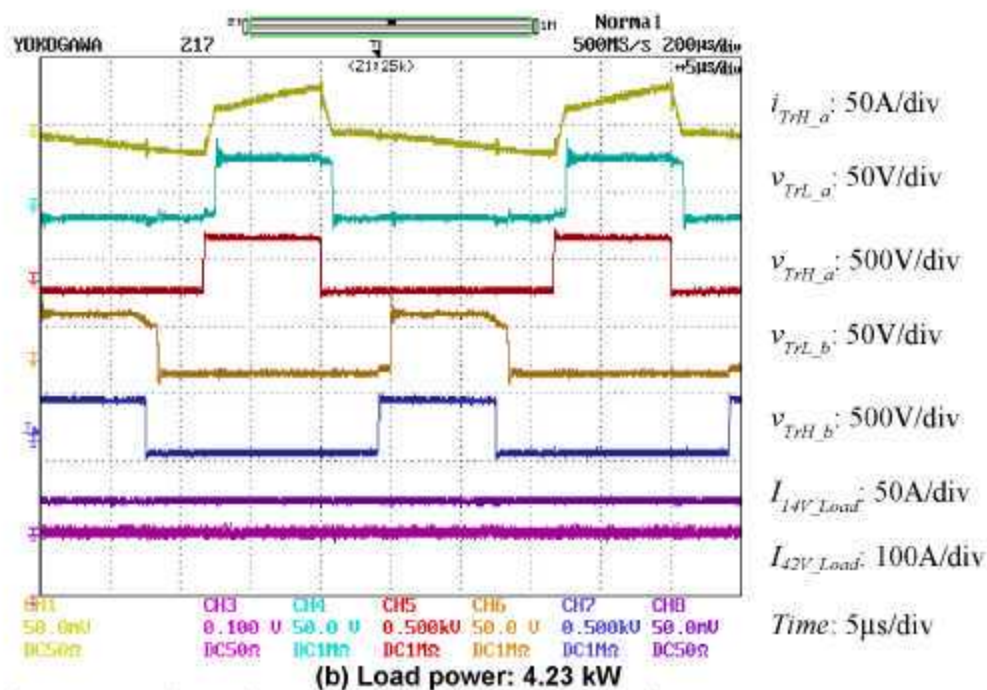
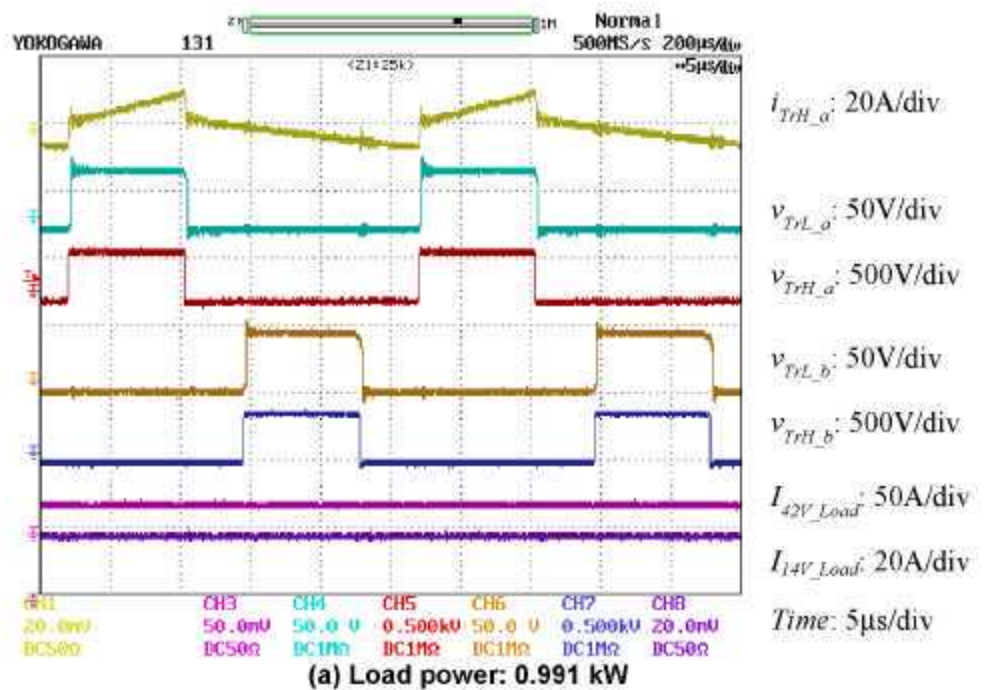


Figure 13. Typical testing waveforms for power transfer from HV to 42 V and 14 V.

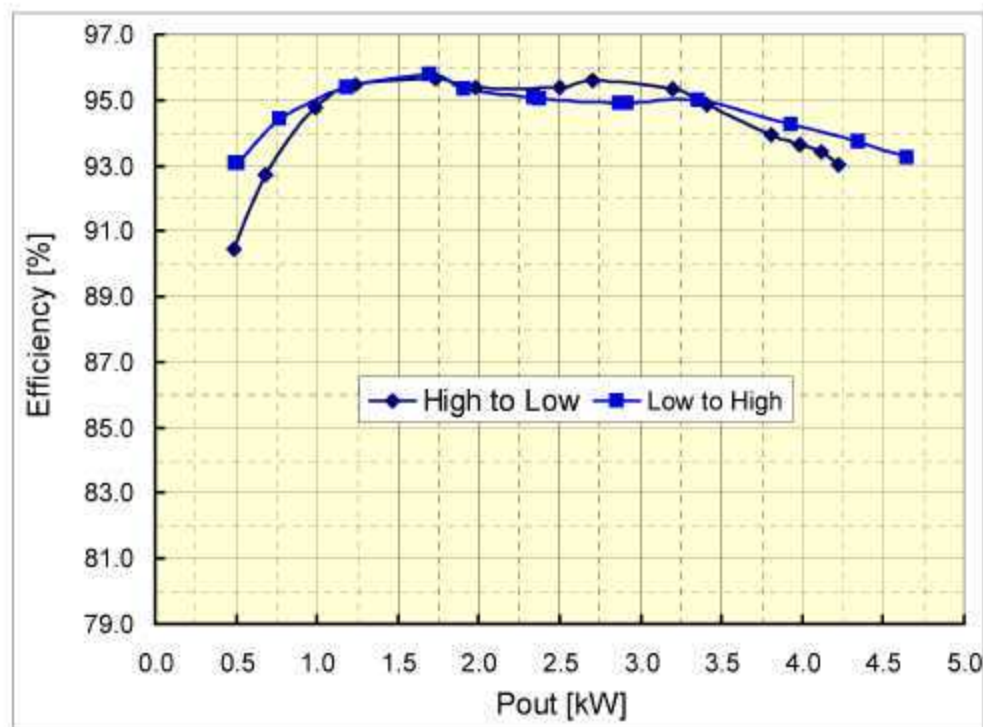
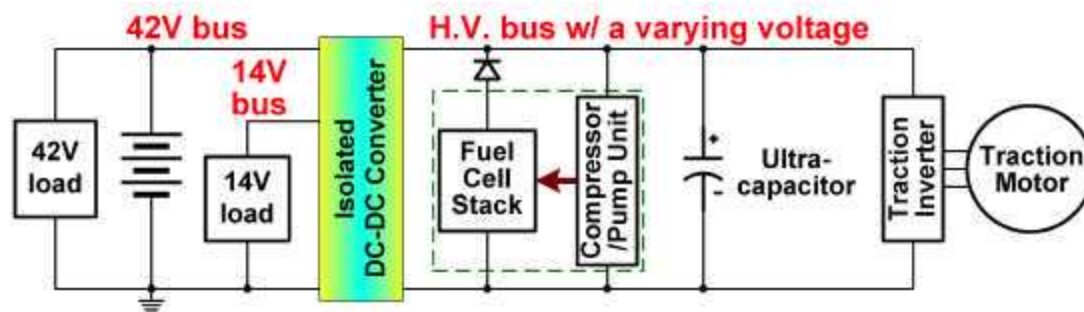


Figure 14. Efficiency chart.

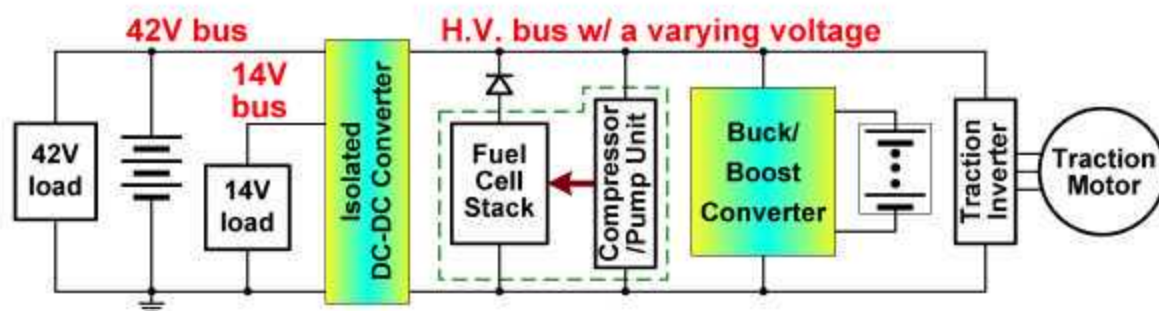
dc-dc Converter Requirements Study for Fuel Cell Vehicle Applications

A literature search was conducted to determine what power system architectures are being considered by original equipment manufacturers. While a few publications did turn up data on the Hyundai Tucson fuel cell electric vehicle, Honda FCX, and Toyota fuel cell hybrid vehicle, published information is presently quite scarce. Based on the limited findings, several possible power system configurations are identified in Figure 15, along with the requirements for the dc-dc converter needed in each architecture.

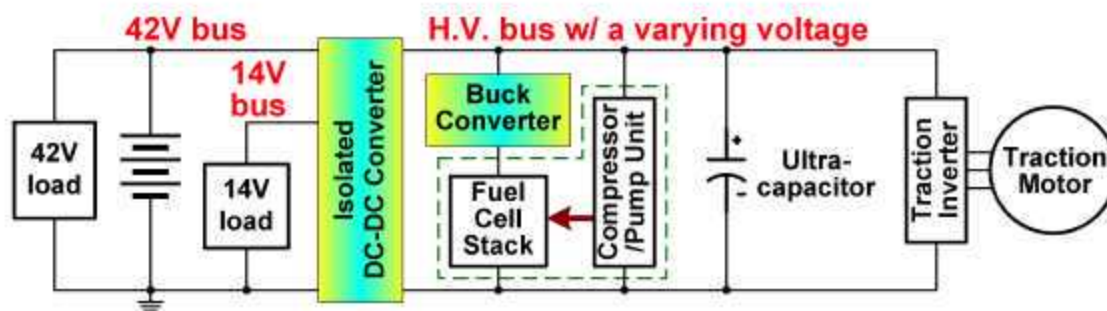


- (a) This topology uses the capability of ultracapacitors to operate over a widely fluctuating bus voltage produced by the fuel stack as load power changes. The ultracapacitors compensate for the slow response of the fuel cell stack and store regenerative power during braking. The isolated dc-dc converter must be bi-directional to power the compressor/pump unit for startup of the fuel cell stack and needs to provide a peak power of several kilowatts, typically around 5 kW.

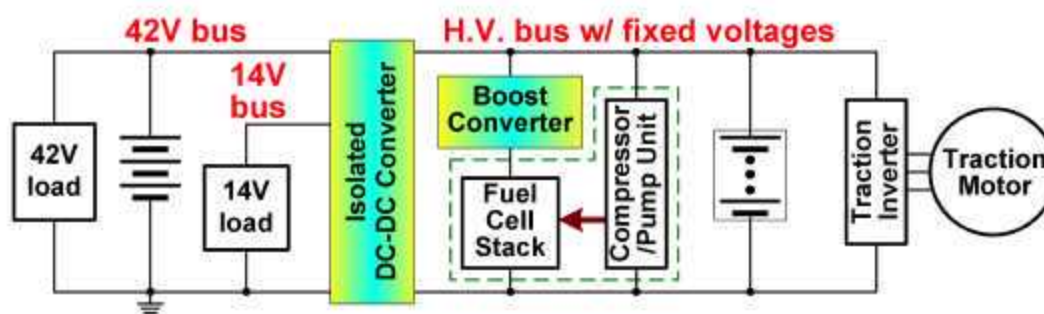
Figure 15. Possible electrical power system architectures for fuel cell vehicles.



- (b) In this topology, a buck/boost converter is required to employ batteries at the high-voltage bus because batteries cannot operate at the widely fluctuating bus voltage produced by the fuel stack as load power changes. The peak power rating of the buck/boost is in the range of several tens of kilowatts, typically around 30 kW.



- (c) A buck converter is employed in this scenario to control the power of the fuel stack. The benefits of doing so are twofold: it enables the ultracapacitors to capture more regenerative power during braking while keeping the bus voltage below a safe level, and it keeps the bus voltage below a safe level at light load conditions under which the fuel cell stack output voltage rises significantly. The buck converter needs to handle the peak power of the fuel cell stack, typically in the range of 80–100 kW. The isolated dc-dc converter must be bi-directional to power the compressor/pump unit for startup of the fuel cell stack and needs to provide a peak power of several kilowatts, typically around 5 kW.



- (d) A boost converter is employed in this topology to regulate the output voltage of the fuel cell stack to provide a stable bus voltage so the batteries can be directly connected to the dc bus. The peak power rating of the boost converter is the same as that of the fuel cell stack, typically 80–100 kW. If desired, a buck/boost converter can be used to interface a lower-voltage battery as in configuration (b), possibly reducing the battery cost and facilitating the use of a higher bus voltage optimized for a more efficient traction drive system.

Figure 15. (continued).

Conclusion

The integrated dc-dc converter for triple-voltage-bus systems (14-V/42-V/HV) for HEVs and FCVs applications has the following features:

- Employs interleaved half-bridge modules with each one using only four switching devices and all modules sharing the capacitor legs, leading to significant cost savings and higher power density.
- Requires no LC filter for the 14-V bus.
- Employs soft switching and synchronous rectification for high efficiency and low EMI.
- Requires no auxiliary circuit or complex control dedicated for soft switching.
- Provides flexible power flow management owing to the capability to transfer power among all three voltage buses by employing the combined duty ratio and phase shift angle control scheme, which also reduces the flux density of the transformers.

A 4-kW prototype has been designed and built using two 2-kW modules and has been successfully tested at load power levels all the way up to 4.6 kW. Measured efficiencies are between 93.0 and 95.8% over a wide power range of 0.5 to 4.6 kW. Evaluation of the prototype indicates that it exceeds the 2015 FreedomCAR targets for specific power and power density and the 2010 cost target.

The information on the possible power system configurations and the requirements of dc-dc converters identified in this report is useful to guide future dc-dc converter development for FCV applications.

Future Direction

- Develop control algorithms to reduce the capacity of the 42-V battery or eliminate it and test with the 4-kW prototype
- Further improve the efficiency through optimization of the topology and packaging

Publications and Presentations

G. J. Su, L. Tang, and X. Huang, "Control of Two Permanent Magnet Machines Using a Five-Leg Inverter for Automotive Applications," presented at IEEE IAS 2006, October 8–12, 2006.

L. Tang, G. J. Su, and X. Huang, "Experimental High Performance Control of Two Permanent Magnet Synchronous Machines in an Integrated Drive for Automotive Applications," presented at IEEE COMPEL 2006 Workshop, July 16–19, 2006.

G. J. Su and J. S. Hsu, "A Five-Leg Inverter for Driving a Traction Motor and a Compressor Motor," *IEEE Trans. on Power Electronics* 21(3), 687–692 (May 2006).

G. J. Su, "Pulse-Width-Modulation Schemes for an Integrated Traction and Compressor Drive System," pp. 640–645 in *IEEE APEC 2006*, vol. 2, March 19–23, 2006.

Patents

G. J. Su, "Multi-Level DC Bus Inverter for Providing Sinusoidal and PWM Electrical Machine," U.S. No. 6,969,967, November 29, 2005.

G. J. Su, "Integrated Inverter for Driving Multiple Electrical Machines," U.S. Patent No. 7,023,171, April 4, 2006.

G. J. Su, "Triple Voltage dc-to-dc Converter and Method," U.S. Patent Office Disclosure No. 1300001646, October 28, 2005.

References

1. G. J. Su and F. Z. Peng, "A Low Cost, Triple-Voltage Bus DC/DC Converter for Automotive Applications," pp. 1015–1021 in *IEEE Applied Power Electronics Conference and Exposition (APEC)*, vol. 2, Austin, Texas, March 6–10, 2005.
2. G. J. Su, D. J. Adams, F. Z. Peng, and H. Li, "A Soft-Switched DC/DC Converter for Fuel Cell Applications," *SAE 2002 Transactions—Journal of Passenger Cars: Electronic and Electrical Systems*, ISBN 0-7680-1291-0, pp. 757–764, September 2003.

3. G. J. Su, F. Z. Peng, and D. J. Adams, "Experimental Evaluation of a Soft-Switching DC/DC Converter for Fuel Cell Vehicle Applications," pp. 39–44 in *Seventh IEEE Workshop on Power Electronics in Transportation (WPET2002)*, DaimlerChrysler Technical Center, Auburn Hills, Michigan, October 24–25, 2002.
4. D. M. Divan and O. Patterson, "A Pseudo-resonant Full Bridge dc/dc Converter," pp. 424–430 in *Conf. Rec. 1987 IEEE Power Electronics Specialist Conf.*, 1987.
5. M. H. K. Wang et al., "Bi-directional dc to dc Converters for Fuel Cell Systems," pp. 47–51 in *Conf. Rec. 1998 IEEE Power Electronics In Transportation*, 1998.
6. T. Ishikawa, S. Hamaguchi, and T. Shimizu, "Development of Next Generation Fuel Cell Hybrid System—Consideration of High Voltage Systems," SAE technical paper 2004-01-1304, Society of Automotive Engineers 2004 World Congress and Exhibition, Detroit, March 2004.
7. S-H. Choi and S-K. Kim, "Development of Fuel Cell Hybrid Vehicle by Using Ultra-Capacitors as a Secondary Power Source," SAE technical paper 2005-01-0015, Society of Automotive Engineers 2005 World Congress and Exhibition, Detroit, April 2005.
8. S. H. Kim and J. A. Ferro, "Development of Hyundai's Tucson FCEV," SAE technical paper 2005-01-0005, Society of Automotive Engineers 2005 World Congress and Exhibition, Detroit, April 2005.
9. A. Ohkawa, "Electric Power Control System for a Fuel Cell Vehicle Employing Electric Double-Layer Capacitor," SAE technical paper 2004-01-1006, Society of Automotive Engineers 2004 World Congress and Exhibition, Detroit, March 2004.

4.3 Cascaded Multilevel Inverter

Principal Investigator: Burak Ozpineci

Oak Ridge National Laboratory

National Transportation Research Center

2360 Cherahala Boulevard

Knoxville, TN 37932

Voice: 865-946-1329; Fax: 865-946-1262; E-mail: ozpineci@ornl.gov

DOE Technology Development Manager: Susan A. Rogers

Voice: 202-586-8997; Fax: 202-586-1600; E-mail: Susan.Rogers@ee.doe.gov

ORNL Program Manager: Mitch Olszewski

Voice: 865-946-1350; Fax: 865-946-1262; E-mail: olszewskim@ornl.gov

Objectives

- To produce a cascade multilevel inverter that combines inverter and converter functions.
- To eliminate the magnetics required for the dc-dc boost converter, therefore reducing the weight, volume, and cost of the system while increasing its efficiency.

Approach

- Assess the performance and cost trade-offs to come up with a viable design.
- Simulate the inverter/converter in PSpice for circuit operation.
- Design simulation of the electric traction drive system (inverter/converter/motor) in Simulink.
- Design a 1.2-kW unit.

Major Accomplishments

- Developed a control algorithm to keep the capacitors charged.
- Simulated the inverter/converter in PSpice and Simulink.
- Developed a design simulation of an electrical drive system with the inverter/converter.
- Designed a 1.2-kW prototype.

Technical Discussion

A cascade multilevel inverter is a power electronic device built to synthesize a desired ac voltage from several levels of dc voltages. Such inverters have been the subject of research in the last several years,¹⁻⁴ where the dc levels were considered to be identical because all of them were batteries, solar cells, etc. In Reference 5, a multilevel converter was presented in which the two separate dc sources were the secondaries of two transformers coupled to the utility ac power. Corzine et al.⁶ have proposed using a single dc power source and capacitors for the other dc sources. A method was given to transfer power from the dc power source to the capacitor in order to regulate the capacitor voltage. A similar approach was later (but independently) proposed by Du et al.⁷ These approaches required a dc power source for each phase. Similar methods have also been proposed by Veenstar and Rufer.^{8,9} The approach here is very similar to that of Corzine et al.⁶ and Du et al.⁷ with the important exception that only a single standard three-leg inverter is required as the power source (one leg for each phase) for the three-phase multilevel inverter.

Specifically, the interest here is in using a single dc power source connected to a standard three-leg inverter, which in turn is connected to capacitors to form a three-phase five-level cascade multilevel inverter to be used as a drive for a permanent magnet (PM) traction motor. The five-level inverter consists of a standard three-leg inverter (one leg for each phase) and an H-bridge in series with each inverter leg

and using a capacitor as a dc source. It is shown that one can simultaneously maintain the regulation of the capacitor voltage while achieving an output voltage waveform that is 25% higher than that obtained using a standard three-leg inverter by itself.

Multilevel Inverter Architecture

Figure 1 shows a dc source connected to a single leg of a standard three-leg inverter.

The output voltage v_1 of this leg (with respect to the ground) is either $+V_{dc}/2$ (S_5 closed) or $-V_{dc}/2$ (S_6 closed). This leg is connected in series with a full H-bridge, which in turn is supplied by a capacitor voltage. If the capacitor is kept charged to $V_{dc}/2$, then the output voltage of the H-bridge can take on the values $+V_{dc}/2$ (S_1 and S_4 closed), 0 (S_1 and S_2 closed or S_3 and S_4 closed), or $-V_{dc}/2$ (S_2 and S_3 closed). An example output waveform that this topology can achieve is shown in Figure 2.

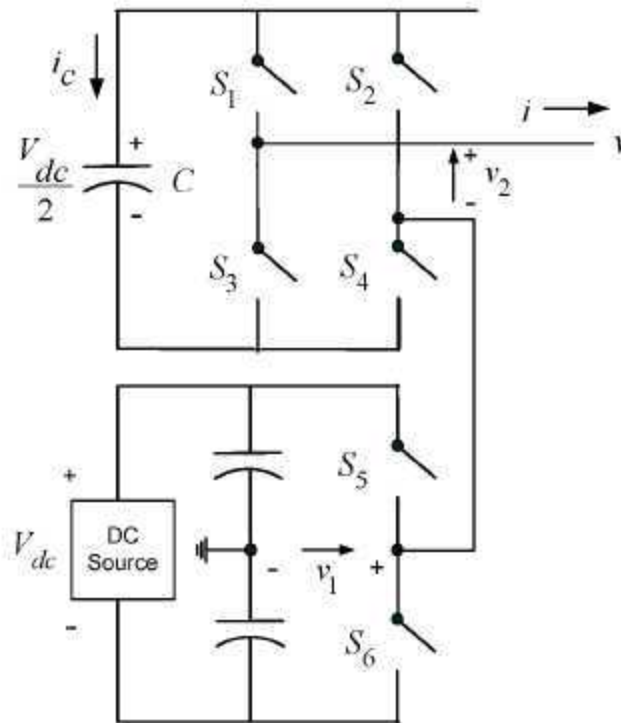


Figure 1. One leg of a three-leg inverter connected to a full H-bridge with a capacitor dc source.

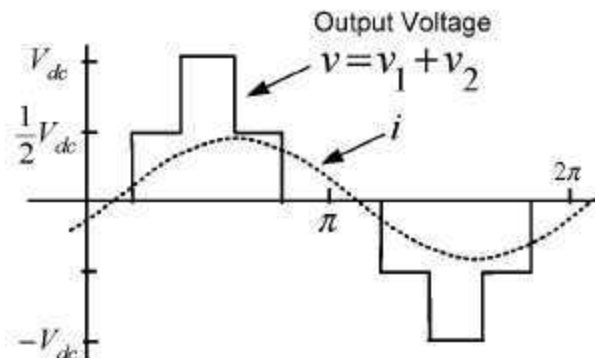


Figure 2. Five-level output waveform of the multilevel inverter.

When the output voltage $v = v_1 + v_2$ is required to be zero, one can either set $v_1 = +V_{dc}/2$ and $v_2 = -V_{dc}/2$ or $v_1 = -V_{dc}/2$ and $v_2 = +V_{dc}/2$. It is this flexibility in choosing how to make that output voltage zero that is exploited to regulate the capacitor voltage. In more detail, consider Figure 3.

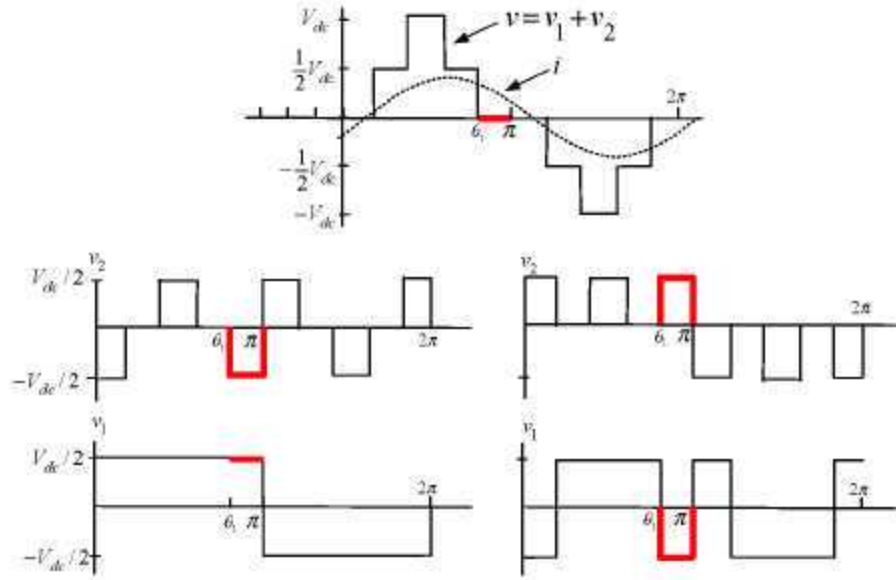


Figure 3. To make the output voltage zero for $\theta_1 \leq \theta \leq \pi$, one can either set $v_1 = +V_{dc}/2$ and $v_2 = -V_{dc}/2$ (bottom left) or $v_1 = -V_{dc}/2$ and $v_2 = +V_{dc}/2$ (bottom right).

In the interval $\theta_1 \leq \theta \leq \pi$, the output voltage in Figure 3 is zero, and the current $i > 0$. If S_1 and S_4 are closed (so that $v_2 = +V_{dc}/2$) along with S_6 closed (so that $v_1 = +V_{dc}$), then the capacitor is discharging ($i_c = -i < 0$; see Figure 1) and $v = v_1 + v_2 = 0$. On the other hand, if S_2 and S_3 are closed (so that $v_2 = -V_{dc}/2$) and S_5 is also closed (so that $v_1 = -V_{dc}/2$), then the capacitor is charging ($i_c = i > 0$; see Figure 1) and $v = v_1 + v_2 = 0$.

The case $i < 0$ is accomplished by simply reversing the switch positions of the $i > 0$ case for charge and discharge of the capacitor. Consequently, the method consists of monitoring the output current and the capacitor voltage so that during periods of zero voltage output, either the switches S_1 , S_4 , and S_6 are closed or the switches S_2 , S_3 , and S_5 are closed depending on whether it is necessary to charge or discharge the capacitor.

Remark

As Figure 3 illustrates, this method of regulating the capacitor voltage depends on the voltage and current not being in phase. That is, one needs positive (or negative) current when the voltage is passing through zero to charge or discharge the capacitor. Consequently, the ability to regulate the capacitor voltage depends on the power factor.

Simulation Results Using Multilevel PWM

A simulation of the multilevel converter driving a PM synchronous machine was carried out. The basic block diagram for the simulation is shown in Figure 4.

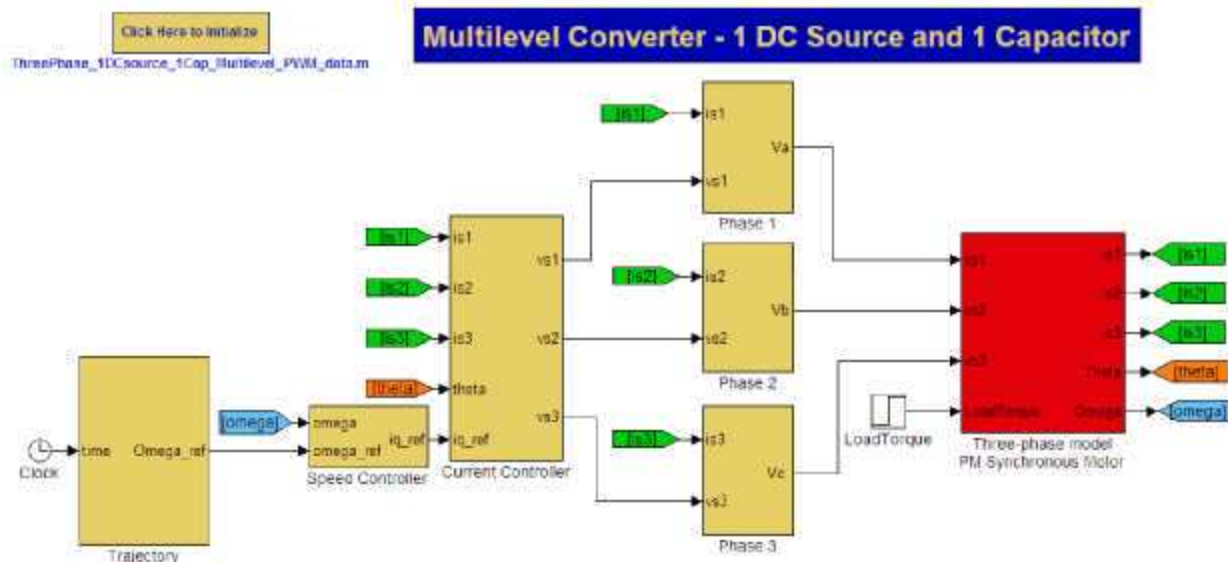


Figure 4. Top level Simulink block diagram.

The motor is controlled using a standard field-oriented controller.¹⁰ The blocks marked phase 1, phase 2, and phase 3 contain the modeling of the multilevel converter. The switching scheme is based on the standard multilevel pulse width modulation (PWM) scheme.¹¹ The scheme is modified so that during those time periods when the multilevel inverter has an output of zero volts, either the switches S_1 , S_4 , and S_6 are closed or the switches S_2 , S_3 , and S_5 are closed, depending on whether the current is positive or negative and whether it is necessary to charge or discharge the capacitor.

The dc link voltage V_{dc} was set to 200 V so that the three-leg inverter supplies ± 100 V. The capacitors were regulated to 100 V. The motor's inertia is $J = 0.1 \text{ kg-m}^2$, the motor has $n_p = 4$ pole-pairs, the stator resistance is $R_s = 0.065 \text{ } \Omega$, the stator inductance is $L_s = 3 \text{ mH}$, the torque/back-emf constant $K_T = K_b = 0.37 \text{ Nm/A (V/rad/s)}$ and the load torque $\tau_L = 19 \text{ Nm}$. The capacitor value is $C = 0.01 \text{ F}$.

For comparison purposes, simulations were performed using both the multilevel inverter of Figure 1 capable of supplying up to ± 200 V and a standard three-leg inverter (i.e., only the bottom half of Figure 1) capable supplying ± 100 V. Though the multilevel inverter can supply up to ± 200 V, it cannot do this and maintain regulation of the capacitor voltages. As pointed out earlier, the ability to regulate the capacitor voltage depends on the power factor of the load. The PM motor was run to achieve the highest possible speed under the given load and available voltage. This is shown in Figure 5. The standard three-leg inverter could only achieve a maximum speed of 212 rad/s, while the proposed multilevel inverter could get the motor up to 275 rad/s using the same dc source voltage.

The corresponding voltages for the speed trajectories of Figure 5 are shown in Figure 6. The standard three-leg inverter is supplying a nearly six-step wave form of $V_{dc}/2 = 100$ V maximum corresponding to a fundamental voltage of $(4/\pi)V_{dc}/2 = 127$ V peak, while the multilevel inverter output is 170 V peak in steady state and up to 180 V before steady state.

The corresponding torques for the above trajectories are shown in Figure 7. The chattering shown in the torque response of the standard three-leg inverter results from the voltage undergoing saturation (see the left side of Figure 6).

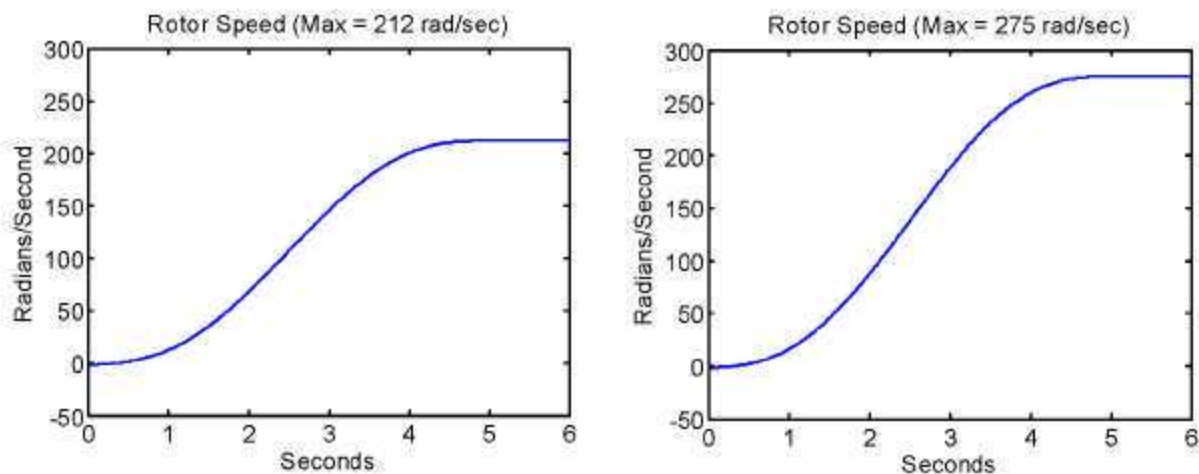


Figure 5. Rotor speeds achievable using a standard three-leg inverter (left) and the proposed multilevel inverter (right).

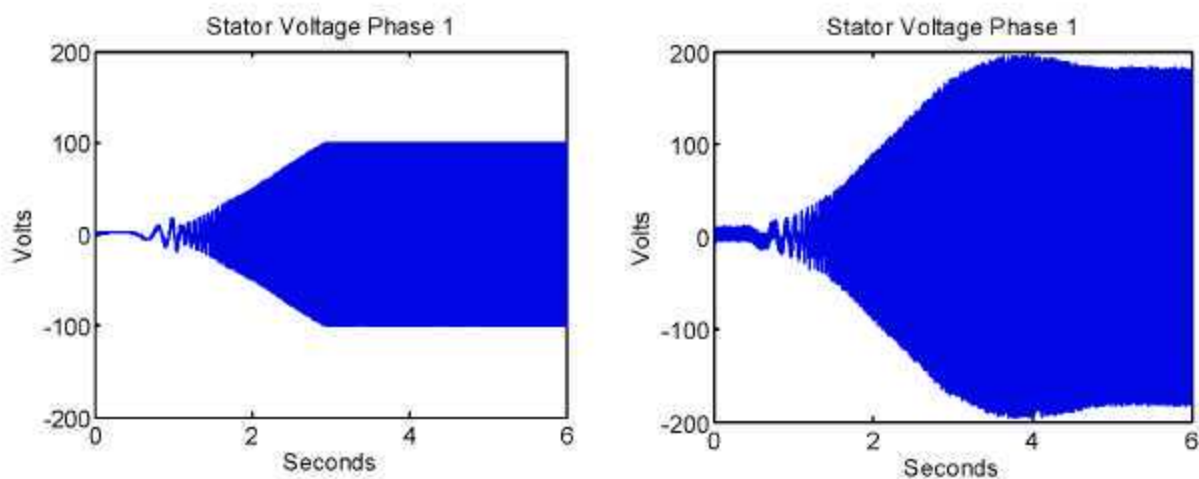


Figure 6. Left: Voltage using a standard three-leg inverter. Right: Voltage obtained using the proposed multilevel inverter.

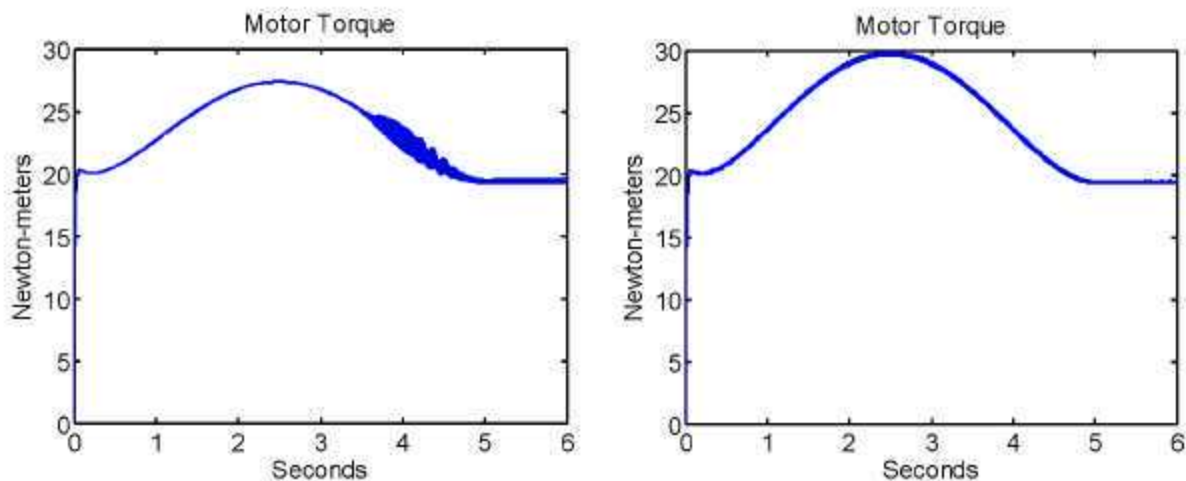


Figure 7. Left: Motor torque using standard three-leg inverter. Right: Motor torque using proposed multilevel inverter.

The stator currents are shown in Figure 8. The current used in the multilevel inverter is higher because it requires more torque to accelerate the motor to its higher speed (see Figure 5).

The capacitor voltage as a function of time is plotted in Figure 9, showing that it is kept within about 2 V of the desired value.

An enlarged view of the capacitor voltage is shown in Figure 10, showing the regulation of the voltage in more detail. The variation in the voltage will be less if a larger value of capacitance is used ($C = 0.01$ F in the simulation).

Note that the capacitor voltage decreases during those times when the inverter is supplying ± 100 V, is constant during those times the inverter is supplying ± 50 V, and is increasing (recharging) during those times the inverter is supplying 0 V. For example, a little after $t = 5.577$ s, the current becomes positive, and the inverter is required to put out (up to) 200 V (only 100 in the figure due to the scaling) by the PWM scheme. The capacitor voltage (red) then decreases. Then shortly before $t = 5.579$ s, the inverter is only required to supply up to 100 V (only 50 in the figure due to the scaling), and the capacitor voltage is constant. At about $t = 5.579$ s, the multilevel PWM scheme is having the inverter supply 0 V for significant time intervals, so the capacitor voltage increases.

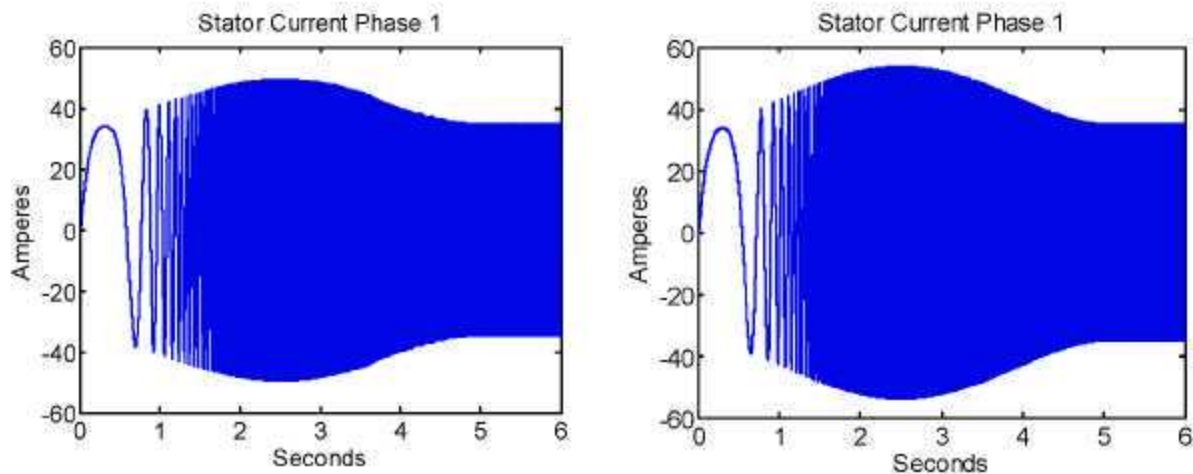


Figure 8. Left: Stator current for the standard three-leg inverter. Right: Stator current for the proposed multilevel inverter.

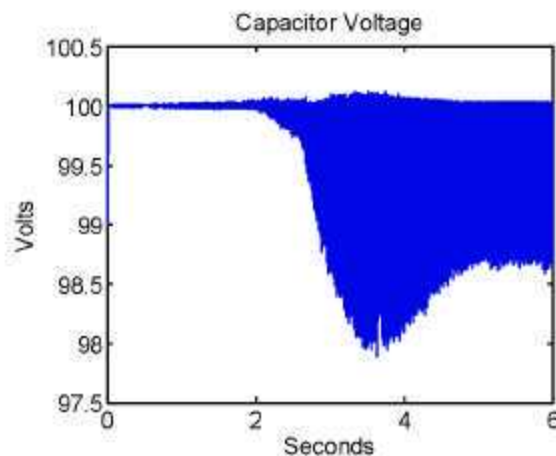


Figure 9. Capacitor voltage vs time.

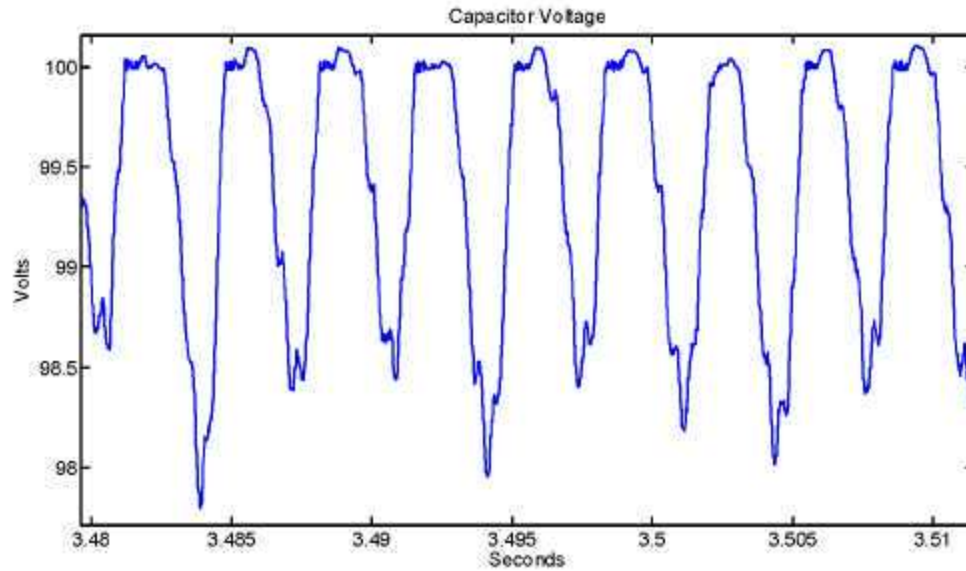


Figure 10. Expanded view of the capacitor voltage as a function of time.

Simulation Results—Fundamental Frequency Switching

In this section a fundamental frequency switching scheme is used. By fundamental frequency switching, it is meant that each device switches once per cycle in contrast to a PWM scheme for which each device turns on and off several times a cycle. Typically a fundamental switching scheme results in a higher harmonic content in the lower frequency spectrum (closer to the fundamental) than a PWM method, but has lower switching losses. In the five-level multilevel inverter under consideration here, a fundamental switching scheme is implemented by choosing two angles θ_1 and θ_2 for when the devices are to be switched on as indicated in Figure 11. By symmetry of the waveform, the rest of the switching occurs at $\pi - \theta_1$, $\pi - \theta_2$, $\pi + \theta_1$, $\pi + \theta_2$, $2\pi - \theta_1$, and $2\pi - \theta_2$.

With the nominal capacitor voltage chosen as $V_{dc}/2$, one computes the switching angles θ_1 and θ_2 as in References 12 and 13. Briefly, the Fourier series expansion of the (staircase) output voltage waveform of the multilevel inverter as shown in Figure 11 is

$$V(\omega t) = \frac{4}{\pi} \frac{V_{dc}}{2} \times \sum_{n=1,3,5,\dots}^{\infty} \frac{1}{n} \left(\cos(n\theta_1) + \cos(n\theta_2) \right) \sin(n\omega t) \quad (1)$$

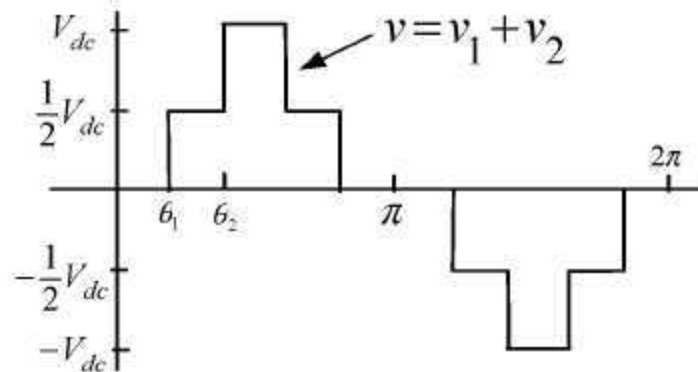


Figure 11. Fundamental frequency waveform.

Ideally, given a desired fundamental voltage V_1 , one wants to determine the switching angles θ_1 and θ_2 so that (FS) becomes $V(\omega t) = V_1 \sin(\omega t)$. In practice, one is left with trying to do this approximately. For three-phase systems, the triplet harmonics in each phase need not be canceled as they automatically cancel in the line-to-line voltages. In this case, where there are two dc sources, the desire is to cancel the fifth order harmonic as it tends to dominate the total harmonic distortion. The mathematical statement of these conditions is then

$$\begin{aligned} \cos(\theta_1) + \cos(\theta_2) &= m = \frac{V_1}{\frac{4}{\pi} \frac{V_{dc}}{2}} \\ \cos(5\theta_1) + \cos(5\theta_2) &= 0 \end{aligned} \quad (2)$$

This is a system of two transcendental equations in the two unknowns θ_1 and θ_2 . There are many ways one can solve for the angles (see, for example, References 14–16). Here the approach in Reference 12 and Reference 17 is used. It is found that a solution to (conditions1) exists for $0.6 \leq m \leq 1.909$, and these solution angles are plotted in Figure 12. Note that the fundamental is given by

$$V_1 = m \frac{4}{\pi} \frac{V_{dc}}{2} \quad (3)$$

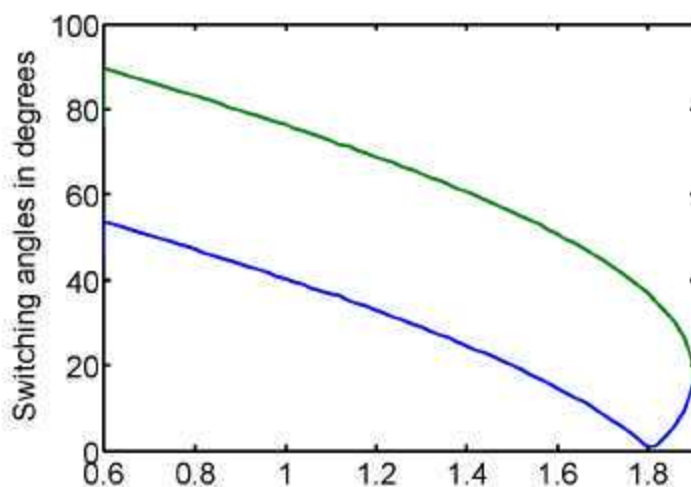


Figure 12. θ_1 and θ_2 vs m .

In the simulations presented here, the same PM motor as chosen for the multilevel PWM scheme was used, but the motor was driven open-loop rather than closed-loop. The voltage magnitude was ramped from 90 V to 180 V during the time interval from 0 to 3 s. The stator electrical frequency f_s was brought up smoothly from 0 to 175 Hz in 5 s resulting in a peak speed of $2\pi f_s / n_p = 275$ rad/s. This is the same speed trajectory as used in the closed-loop multilevel PWM implementation above. The resulting speed response is shown in Figure 13, which is somewhat oscillatory due to the open-loop control. Because it is driven open loop, it is much more difficult to have the machine go up in speed with a significant load torque at the start. As a result, only a viscous friction load torque was used with the viscous friction coefficient chosen as $f = 0.07$ so that at maximum speed the load torque is $f\omega_{\max} = f(2\pi f_s / n_p) = 0.07 * 275 = 19$ Nm, giving the same steady-state load-torque as in the multilevel PWM case.

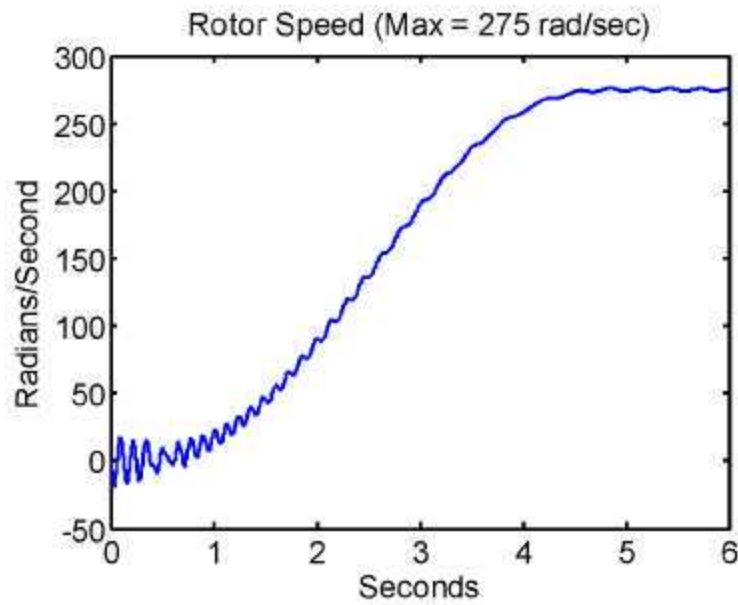


Figure 13. Rotor speed in rad/s vs time in seconds.

The commanded voltage magnitude [see (fund)] and the computed fundamental of the inverter output are given in Figure 14.

The computed fifth harmonic of the voltage is plotted vs time in Figure 15. During the end of the run when the speed is close to being constant, the fifth-harmonic is about 0.7 V compared with the 180 V of the fundamental.

The motor torque is shown in Figure 16, which is oscillatory as a result of the open-loop control. Note that at the end of the run, the torque is oscillating about 19 Nm to counteract the (viscous-friction) load torque.

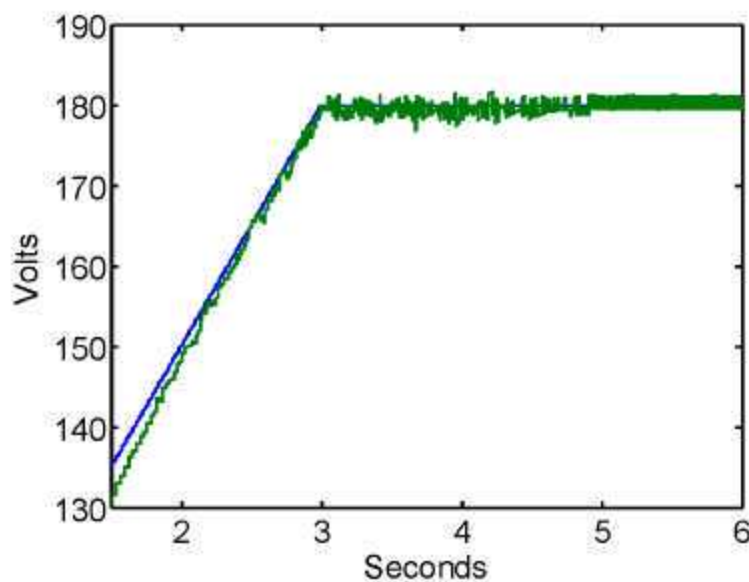


Figure 14. Commanded and computed fundamental voltage in volts vs time in seconds.

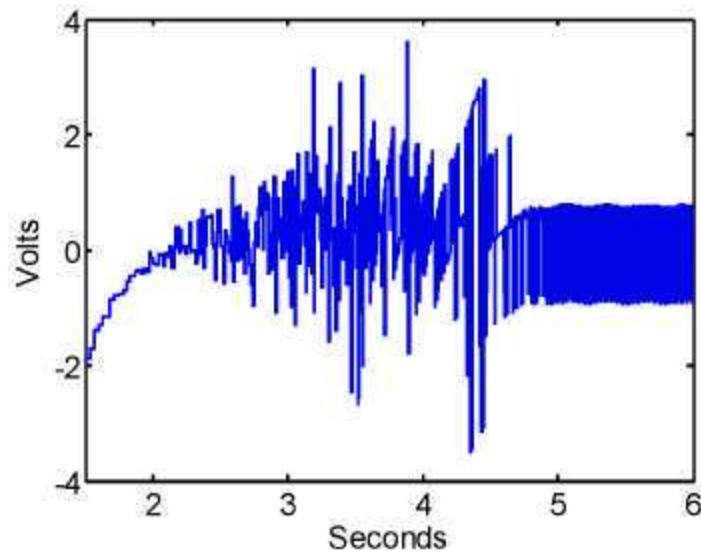


Figure 15. Computed fifth-harmonic of the voltage in volts vs time in seconds.

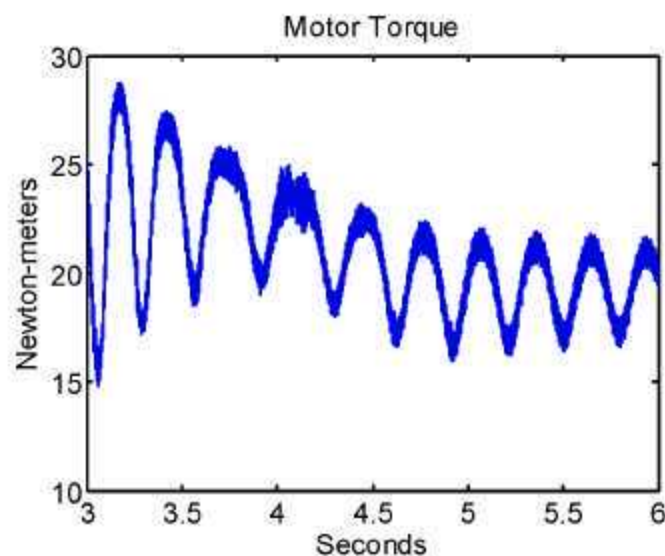


Figure 16. Torque in N-m vs time in seconds.

An enlarged section of the inverter output voltage of phase 1 is given in Figure 17 and shows the fundamental switching scheme for a stator frequency of $f_s = 175$ Hz.

The stator current response of phase 1 is plotted in Figure 18 and uses somewhat more current than the closed-loop PWM scheme (see Figure 8).

The capacitor voltage is shown in Figure 19, showing that the scheme regulates the voltage within 3 V of the nominal value. The value of the capacitance is $C = 0.01$ F as in the multilevel PWM case. An enlarged view of the capacitor voltage for $5.5 \leq t \leq 5.525$ is shown in Figure 20.

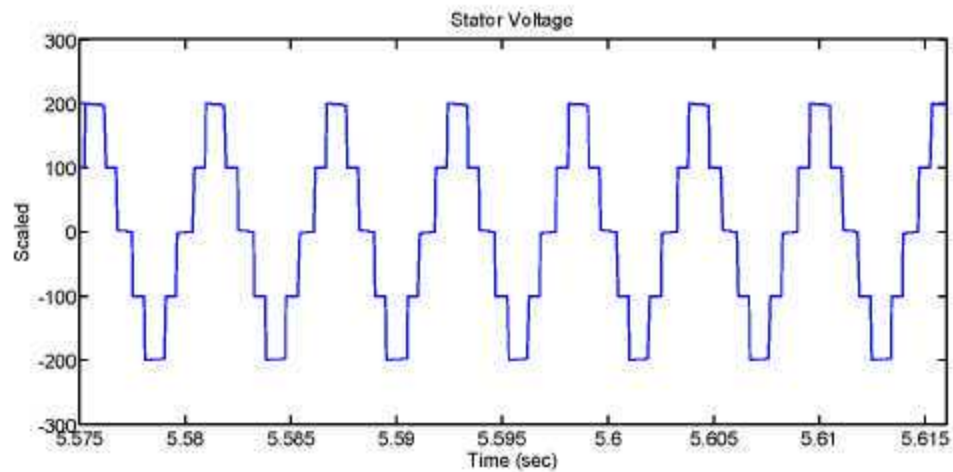


Figure 17. Enlarged view of the phase 1 voltage in volts vs time in seconds.

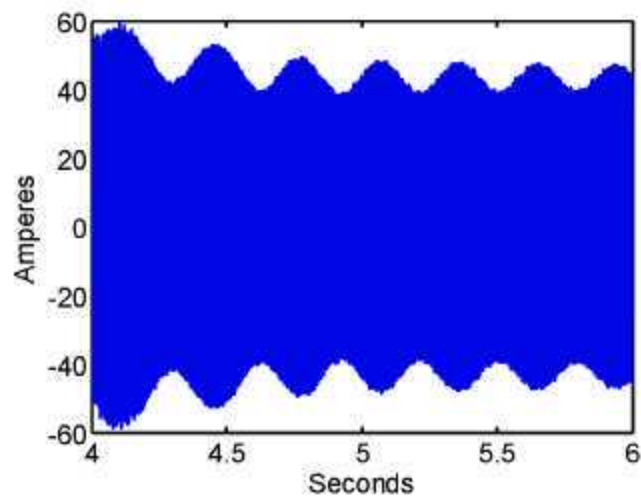


Figure 18. Phase 1 stator current vs time.

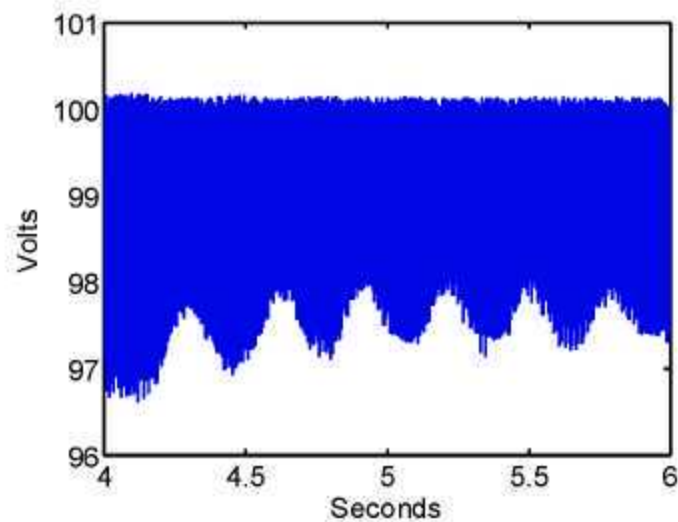


Figure 19. Capacitor voltage in volts vs time in seconds.

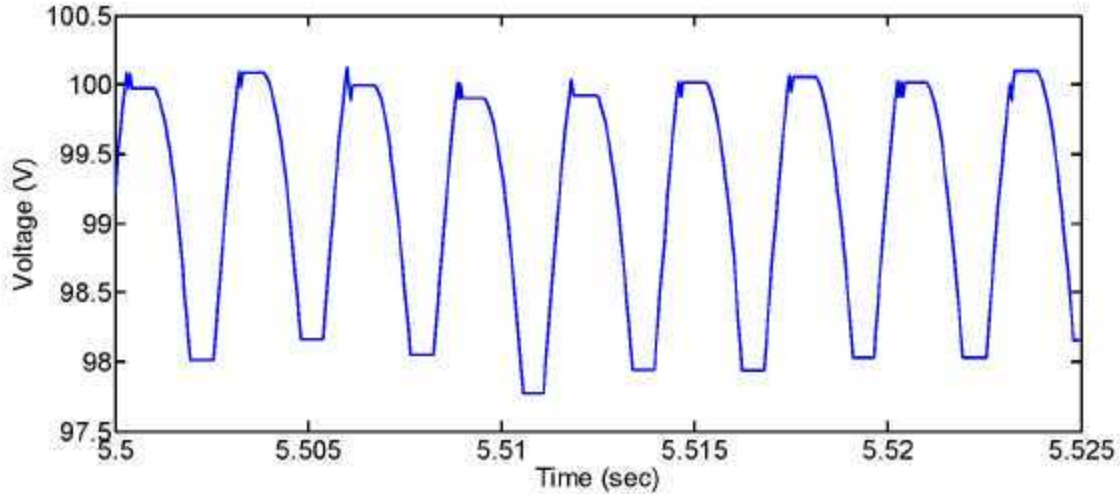


Figure 20. An enlarged view the capacitor voltage in volts vs time in seconds.

Scaled versions of the capacitor voltage, stator current, and stator voltage vs time are shown in Figure 21. Note that the capacitor discharges when the inverter is supplying ± 200 V, stays constant when the inverter is supplying ± 100 V, and recharges when the inverter is supplying 0 V.

For example, a little after $t = 5.575$ s, the stator current becomes positive, and the inverter is required to supply 200 V. The capacitor voltage then decreases. Following this, when the inverter is only required to supply 100 V, the capacitor voltage is constant. Next, the inverter is putting out 0 V so that the capacitor is charging and its voltage increases.

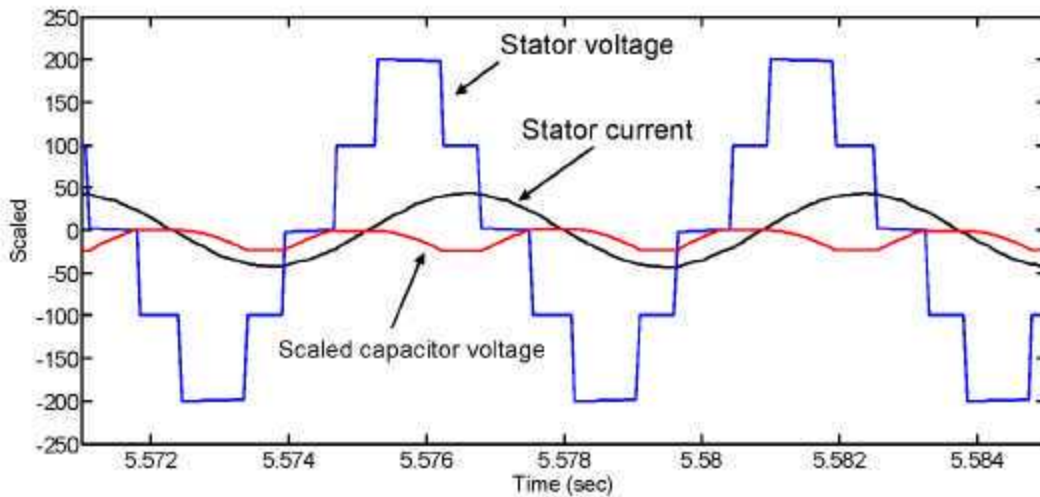


Figure 21. Scaled capacitor voltage, stator current, and stator voltage vs time in seconds.

Conditions for Capacitor Voltage Regulation

Let

$$\begin{aligned} v_f(\theta) &= V \sin(\theta) , \\ i(\theta) &= I \sin(\theta - \phi) , \end{aligned} \tag{4}$$

where $v_f(\theta)$ is the fundamental component of the voltage, $i(\theta)$ is the current, and ϕ is the power factor angle. The objective here is to compute the conditions on θ_1 , θ_2 , and ϕ to ensure the capacitor can be regulated to a desired value.

Interval 1: $0 < \phi < \theta_1$

Consider the case where $0 < \phi < \theta_1$ as illustrated in Figure 22. During the interval $\theta_2 < \theta < \pi - \theta_2$, the capacitor loses the amount of charge $\int_{\theta_2}^{\pi-\theta_2} I \sin(\theta - \phi) d\theta$, while during the intervals $0 < \theta < \theta_1$ and $\pi - \theta_1 < \theta < \pi$ the capacitor can be recharged (by choosing the switch positions appropriately) by the amounts $\int_0^{\theta_1} I |\sin(\theta - \phi)| d\theta + \int_{\pi-\theta_1}^{\pi} I \sin(\theta - \phi) d\theta$ and $\int_{\pi-\theta_1}^{\pi} I \sin(\theta - \phi) d\theta$, respectively.

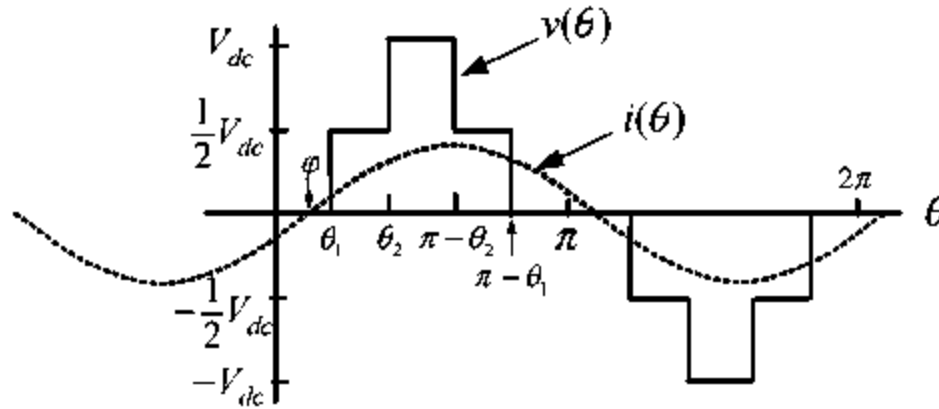


Figure 22. $0 < \phi < \theta_1$.

In this case, keeping the capacitor charged requires

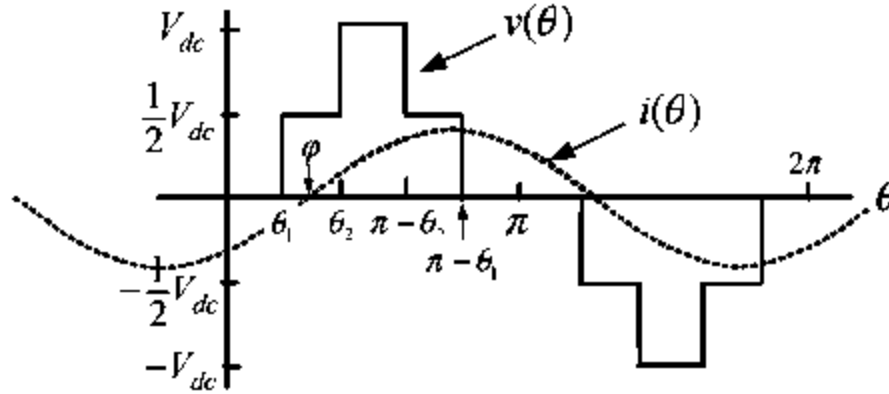
$$\begin{aligned}
 \int_{\theta_2}^{\pi-\theta_2} I \sin(\theta - \phi) d\theta &< \int_0^{\theta_1} I |\sin(\theta - \phi)| d\theta + \int_{\pi-\theta_1}^{\pi} I \sin(\theta - \phi) d\theta + \int_{\pi-\theta_1}^{\pi} I \sin(\theta - \phi) d\theta \\
 I \cos(\theta_2 + \phi) + I \cos(\theta_2 - \phi) &< (I \cos(0) - I \cos(\phi)) + (-I \cos(\theta_1 - \phi) + I \cos(0)) + \\
 &\quad (I \cos(\phi) - I \cos(\theta_1 + \phi)) \\
 \cos(\theta_2) \cos(\phi) &< \cos(0) - \cos(\theta_1) \cos(\phi),
 \end{aligned} \tag{5}$$

or finally, the condition in this case is

$$\cos(\phi) < \frac{1}{\cos(\theta_1) + \cos(\theta_2)}. \tag{6}$$

Interval 2: $\theta_1 < \phi < \theta_2$

Consider the case $\theta_1 < \phi < \theta_2$ as in Figure 23. During the interval $\theta_2 < \theta < \pi - \theta_2$, the capacitor loses the amount of charge $\int_{\theta_2}^{\pi-\theta_2} I \sin(\theta - \phi) d\theta$, while during the intervals $0 < \theta < \theta_1$ and $\pi - \theta_1 < \theta < \pi$ the capacitor can be recharged (by choosing the switch positions appropriately) by the amount $\int_0^{\theta_1} I |\sin(\theta - \phi)| d\theta + \int_{\pi-\theta_1}^{\pi} I \sin(\theta - \phi) d\theta$.

Figure 23. $\theta_1 < \varphi < \theta_2$.

Thus, keeping the capacitor voltage regulated requires

$$\int_{\theta_2}^{\pi-\theta_2} I \sin(\theta - \varphi) d\theta < \int_0^{\theta_1} I |\sin(\theta - \varphi)| d\theta + \int_{\pi-\theta_1}^{\pi} I \sin(\theta - \varphi) d\theta \quad (7)$$

Expanding

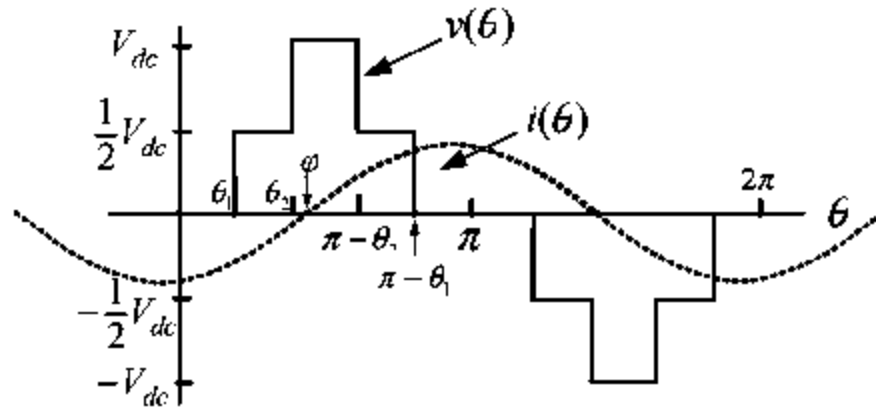
$$\begin{aligned} I \cos(\theta_2 + \varphi) + I \cos(\theta_2 - \varphi) &< (I \cos(\theta_1 - \varphi) - I \cos(\varphi)) + (I \cos(\varphi) - I \cos(\theta_1 - \varphi)) \\ 2I \cos(\theta_2) \cos(\varphi) &< 2I \sin(\theta_1) \sin(\varphi). \end{aligned} \quad (8)$$

or finally, the condition is

$$\frac{\cos(\theta_2)}{\sin(\theta_1)} < \tan(\varphi) \quad (9)$$

Interval 3: $\theta_2 < \varphi < \pi/2$

Finally, consider the case where $\theta_2 < \varphi < \pi/2$ as shown in Figure 24. During the subinterval $\theta_2 < \theta < \varphi$, the capacitor is being charged as the current is negative while it is discharging in subinterval $\varphi < \theta < \pi - \theta_2$. Thus the total discharge in the interval $\theta_2 < \theta < \pi - \theta_2$ is $\int_{\theta_2}^{\pi-\theta_2} I \sin(\theta - \varphi) d\theta$.

Figure 24. $\theta_2 < \varphi < \pi/2$.

Thus, keeping the capacitor voltage regulated requires

$$\int_{\theta_2}^{\pi-\theta_2} I \sin(\theta - \varphi) d\theta < \int_0^{\theta_1} I |\sin(\theta - \varphi)| d\theta + \int_{\pi-\theta_1}^{\pi} I \sin(\theta - \varphi) d\theta \quad (10)$$

Expanding

$$\begin{aligned} I \cos(\theta_2 + \varphi) + I \cos(\theta_2 - \varphi) &< (I \cos(\theta_1 - \varphi) - I \cos(\varphi)) + (I \cos(\varphi) - I \cos(\theta_1 + \varphi)) \\ 2I \cos(\theta_2) \cos(\varphi) &< 2I \sin(\theta_1) \sin(\varphi), \end{aligned} \quad (11)$$

or finally, the condition is

$$\frac{\cos(\theta_2)}{\sin(\theta_1)} < \tan(\varphi) \quad (12)$$

which has the same form as the previous case.

Capacitor voltage regulation as a function of m and φ

In summary, the conditions for capacitor voltage regulation in terms of θ_1 , θ_2 , and φ are

$$\begin{aligned} 0 < \varphi < \theta_1 \quad \cos(\varphi) &< \frac{1}{\cos(\theta_1) + \cos(\theta_2)} = \frac{1}{m} \\ \theta_1 < \varphi < \pi/2 \quad \frac{\cos(\theta_2)}{\sin(\theta_1)} &< \tan(\varphi) \end{aligned} \quad (13)$$

Notice at the boundary of the two conditions where $\varphi = \theta_1$, the two conditions are identical. These conditions can be rewritten as

$$\begin{aligned} 0 < \varphi < \theta_1 \quad \varphi &> \cos^{-1}(1/m) \\ \theta_1 < \varphi < \pi/2 \quad \varphi &> \tan^{-1}\left(\frac{\cos(\theta_2)}{\sin(\theta_1)}\right) \end{aligned} \quad (14)$$

Figure 12 is a plot of θ_1 and θ_2 in degrees vs m (the modulation index is $m/2$). For any given value of m and φ , the values of θ_1 and θ_2 are found via Figure 12, and thus whether or not the capacitor voltage can be regulated is straightforwardly checked using the conditions (conditions2). What these conditions say is, for any given value of m in the interval $0.6 \leq m \leq 1.909$ [i.e., where conditions (conditions1) have a solution], the capacitor voltage can be regulated provided the power factor angle is large enough.

Conclusions

A cascade multilevel inverter topology has been proposed that requires only a single standard three-leg inverter and capacitors as the power sources. The capacitors obtain their power from the three-leg inverter, allowing the cascade multilevel inverter to put out significantly more voltage from a given dc power source than just a three-leg inverter alone. Both multilevel PWM and fundamental frequency

switching schemes were considered. Finally, subject to conditions in terms of the power factor and modulation index ($= m/2$), it was shown that the capacitor voltages could be regulated.

Future Direction

- A 1.2-kW prototype will be built to demonstrate the operation of the converter with a fuel cell (FY 2007).
- More simulation studies will be done to add plug-in hybrid capabilities to the cascaded multilevel inverter (FY 2007).
- If the 1.2-kW prototype is successful, a full-power 105-kW unit will be built (FY 2008–2009).

Publications

Z. Du, L. M. Tolbert, J. Chiasson, and B. Ozpineci, "A Cascade Multilevel Inverter Using a Single DC Source," *Applied Power Electronics Conference, APEC 2006*, Dallas, Texas.

Z. Du, L. M. Tolbert, J. Chiasson, B. Ozpineci, H. Li, and A.Q. Huang, "Hybrid Cascaded H-bridges Multilevel Motor Drive Control for Electric Vehicles," *Power Electronics Specialists Conference, PESC 2006*, Jeju Korea.

References

1. M. Klabunde, Y. Zhao, and T. A. Lipo, "Current control of a 3-level Rectifier/Inverter Drive System," pp. 2348–2356 in *Conference Record 1994 IEEE IAS Annual Meeting*, 1994.
2. W. Menzies, P. Steimer, and J. K. Steinke, "Five-level GTO Inverters for Large Induction Motor Drives," *IEEE Transactions on Industry Applications*, **30**(4), 938–944 (July 1994).
3. J. K. Steinke, "Control Strategy for a Three Phase AC Traction Drive with Three Level GTO PWM Inverter," pp. 431–438 in *IEEE Power Electronic Specialist Conference*, 1988.
4. J. Zhang, "High Performance Control of a Three Level IGBT Inverter Fed AC Drive," pp. 22–28 in *Conf. Rec. IEEE IAS Annual Meeting*, 1995.
5. M. Manjrekar, P. K. Steimer, and T. Lipo, "Hybrid Multilevel Power Conversion System: A Competitive Solution for High-Power Applications," *IEEE Transactions on Industry Applications*, **36**(3), 834–841 (May/June 2000).
6. K. A. Corzine, F. A. Hardrick, and Y. L. Familant, "A Cascaded Multi-level H-bridge inverter Utilizing Capacitor Voltage Sources," pp. 290–295 in *Proceedings of the IASTED International Conference*, Palm Springs, California, 2003.
7. Z. Du, L. M. Tolbert, J. N. Chiasson, and B. Ozpineci, "Cascade Multilevel Inverter Using a Single dc Source," pp. 426–430 in *Proceedings of the Applied Power Electronics Conference*, Dallas, Texas, 2006.
8. M. Veenstra and A. Rufer, "Non-equilibrium State Capacitor Voltage Stabilization in a Hybrid Asymmetric Nine-level Inverter: Non-linear Model-predictive Control," in *Proceedings of the European Control Conference, Toulouse, France*, 2003.
9. M. Veenstra and A. Rufer, "Control of a Hybrid Asymmetric Multilevel Inverter for a Competitive Medium-voltage Industrial Drive," *IEEE Transactions on Industry Applications*, **IAS-41**(2), 655–664 (March/April 2005).
10. J. Chiasson, *Modeling and High-Performance Control of Electric Machines*, John Wiley & Sons, New York, 2005.
11. D. G. Holmes and T. Lipo, *Pulse Width Modulation for Power Electronic Converters*, Wiley Interscience, 2003.
12. J. Chiasson, L. M. Tolbert, K. McKenzie, and Z. Du, "Control of a Multilevel Converter Using Resultant Theory," *IEEE Transactions on Control System Technology*, **11**(3), 345–354 (May 2003).
13. L. M. Tolbert, F. Z. Peng, and T. G. Habetler, "Multilevel Converters for Large Electric Drives," *IEEE Transactions on Industry Applications*, **35**(1), 36–44 (Jan./Feb. 1999).

14. P. N. Enjeti, P. D. Ziogas, and J. F. Lindsay, "Programmed PWM Techniques to Eliminate Harmonics: A Critical Evaluation," *IEEE Transactions Industry Applications*, **26**(2), 302–316 (March/April 1990).
15. J. Vassallo, P. W. Wheeler, and J. C. Clare, "Optimal Waveform Generation for Utility-connected Multilevel Converters," in *European Power Electronics Conference*, September 2003.
16. T. Kato, "Sequential Homotopy-based Computation of Multiple Solutions for Selected Harmonic Elimination in PWM Inverters," *IEEE Transactions on Circuits and Systems 1: Fundamental Theory and Applications*, **46**(5), 586–593 (May 1999).
17. J. Chiasson, L. Tolbert, K. McKenzie, and Z. Du, "Elimination of Harmonics in a Multilevel Converter Using the Theory of Symmetric Polynomials," *IEEE Transactions on Control Systems Technology*, **13**(2), 216–223 (March 2005).

4.4 Advanced Converter Systems for High-Temperature HEV Environments

Principal Investigator: Leon M. Tolbert

Oak Ridge National Laboratory

National Transportation Research Center

2360 Cherrahala Boulevard

Knoxville, TN 37932

Voice: 865-946-1332; Fax: 865-946-1262; E-mail: tolbertlm@ornl.gov

DOE Technology Development Manager: Susan A. Rogers

Voice: 202-586-8997; Fax: 202-586-1600; E-mail: Susan.Rogers@ee.doe.gov

ORNL Program Manager: Mitch Olszewski

Voice: 865-946-1350; Fax: 865-946-1262; E-mail: olszewskam@ornl.gov

Objectives

The goal of this project is to develop a new and unique bidirectional dc-dc power converter that incorporates high-temperature power devices and capacitors with a high-temperature packaging technology and gate drives that will enable the converter to operate in high ambient temperature conditions. This project will develop a converter that has greatly reduced weight/mass, volume, and maintenance/service with high system efficiency, performance, and reliability compared with existing dc-dc converters for hybrid electric vehicles (HEVs).

Air-cooled high-temperature capacitors and SiC power electronics will lead to smaller thermal management systems, which will increase the peak power-to-weight ratio. Reduction of thermal management systems and lack of magnetic devices should offset the higher cost for SiC devices and high-temperature capacitors. Lower switching losses in a multilevel dc-dc converter will increase the efficiency to >97%. The converter topology will allow the battery pack to be subdivided into smaller modules in which the failure of a single cell does not disable the entire battery pack and only a single battery module need be replaced instead of the entire pack.

Approach

Several design tasks are being conducted in parallel by different organizations. These products will be integrated during the final year of this project to achieve a dc-dc converter that can operate at high temperatures. The other reason for the parallel design approach is that some technologies, such as the multilevel converter topologies, can be fabricated and tested now with conventional cooling techniques while other technologies, such as high-temperature packaging, SiC switches, and high-temperature capacitors, mature.

Multiple institutions are involved in this project to draw on the strengths of the particular institutions. Michigan State University, The University of Tennessee (UT), and Oak Ridge National Laboratory (ORNL) have devised two different magnetic-less dc-dc converter topologies. The Pennsylvania State University (Penn State) has used its experience in high-temperature capacitors to determine a figure of merit for new capacitor materials. UT and ORNL have designed a high-temperature gate drive.

Major Accomplishments

During FY 2006, there were major several accomplishments.

1. Michigan State University designed and fabricated a 10-kW dc-dc converter module based on some of its earlier topologies.

2. UT and ORNL devised an alternative dc-dc converter topology and fabricated a low-power proof-of-concept circuit to demonstrate its feasibility. More details on these accomplishments are given in the next section.
3. UT and ORNL designed a high-temperature gate drive using a new silicon-on-insulator (SOI) process by Atmel.
4. Penn State evaluated capacitors for high-temperature applications.

Each of these tasks is further elucidated in the next section.

Technical Discussion

Bidirectional dc-dc Converter Module

The design and fabrication of a 10-kW bidirectional dc-dc converter module was initiated during FY 2006. The converter module is able to output either the battery voltage or twice the battery voltage. Thus a power conversion system with n modules is able to output 1 to $2n$ different voltages with an increment of 42 V, as shown in Figure 1.

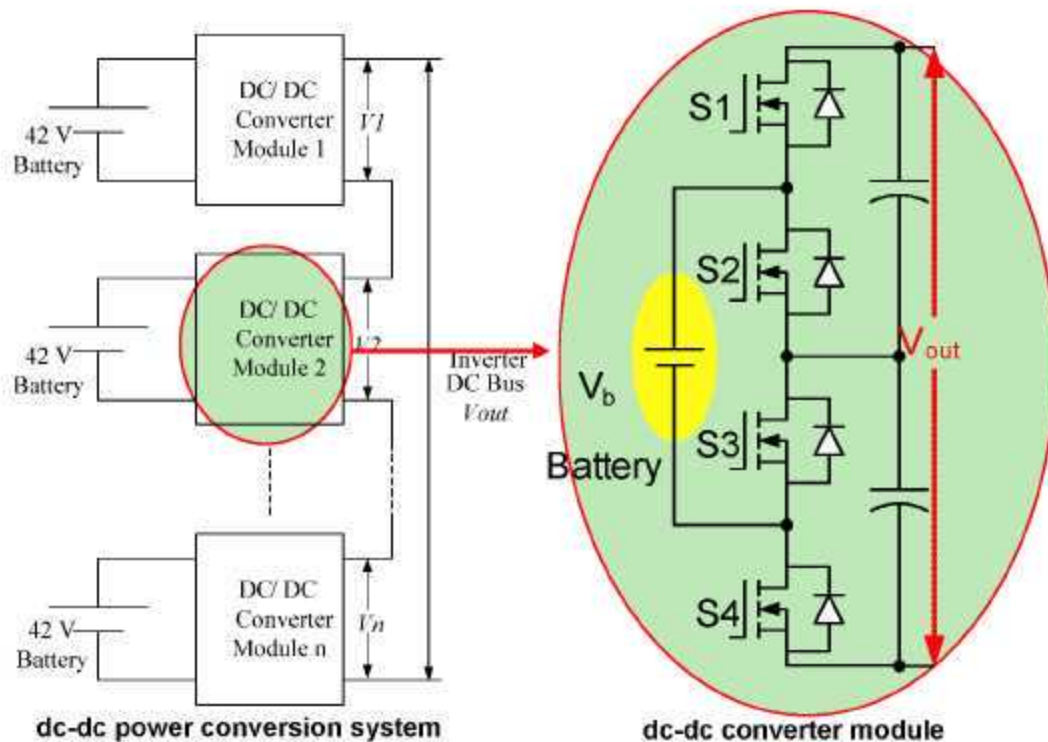


Figure 1. The dc-dc power conversion system and dc-dc converter module.

An individual module has been fabricated and is pictured in Figure 2. Specifications are as follows:

- nominal input voltage—42 V
- minimum input voltage—25 V
- maximum input voltage—45 V
- output voltage—42V/80V for nominal input voltage,
- nominal input current—240 A
- maximum input current—350 A,
- nominal output current—120 A

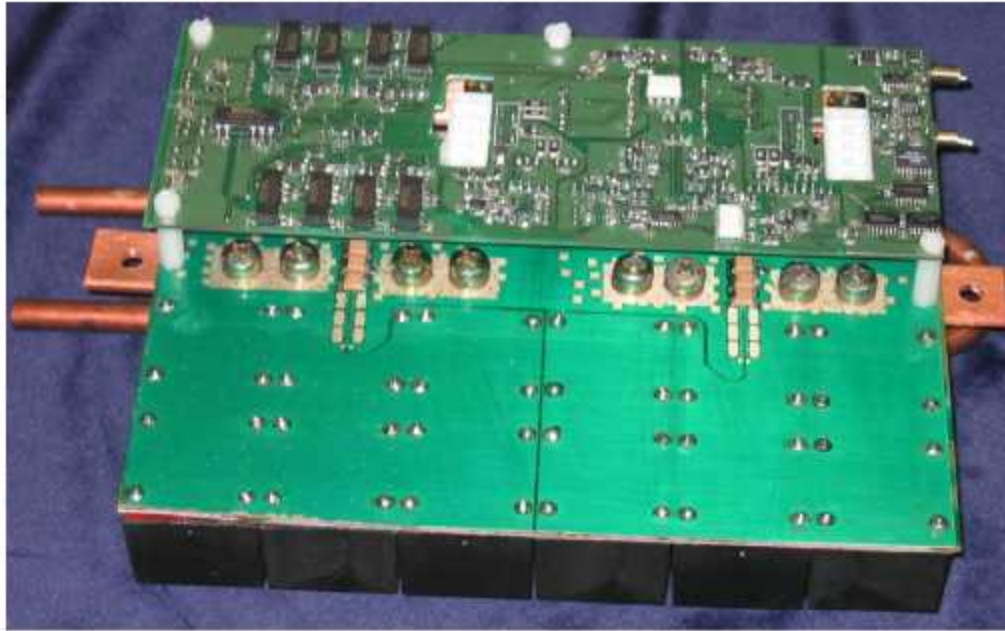


Figure 2. 10-kW dc-dc converter module.

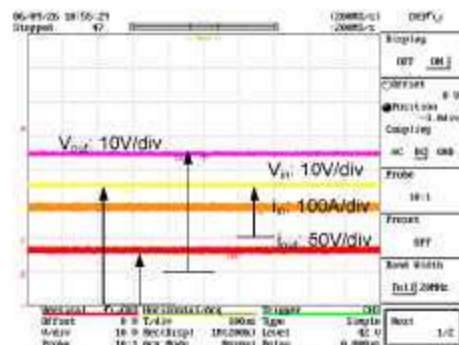
- maximum output current—180 A
- heat-sink—liquid cooled
- devices—2 metal oxide semiconductor field effect transistors (MOSFET) Modules: FM600TU-07A

A custom bus bar was fabricated to reduce the output voltage noise. Some initial tests of the converter were done with conventional car batteries, and converter efficiency was measured. Some experimental results are shown in Figure 3. The efficiency test was conducted using a YOKOGAWA power meter WT1600. The measured efficiency when output voltage equals input voltage was 99.4%, including the losses in the gate drive power supplies; the efficiency when output voltage equaled twice the input voltage was 98.1%, including the gate drive power losses. During the test, the battery voltage was around 30 V. When the input voltage increases to 42 V, the efficiency should be higher because the conduction loss will be less at this higher voltage level and it is the major loss.

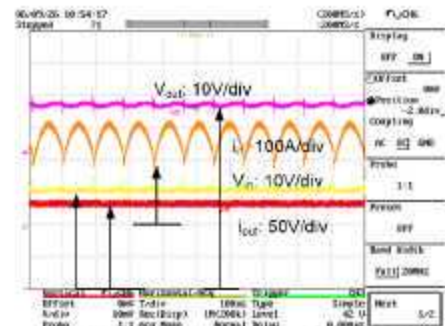
Additional testing of the converter will be conducted during FY 2007 to characterize its efficiency over a wide load and temperature range. The use of high-temperature devices in place of the conventional silicon switches will be made and a high-temperature module will be designed.

Multilevel modular capacitor clamped dc-dc converter (MMCCC)

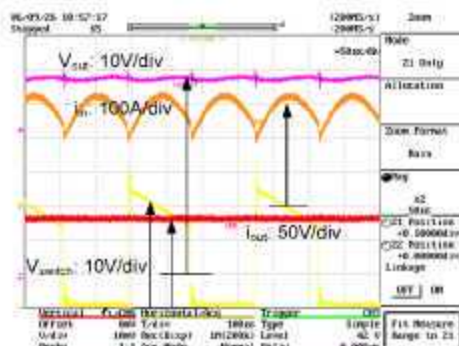
A second magnetic-less dc-dc converter topology explored as part of this project is the multilevel modular capacitor clamped dc-dc converter. The proposed 5-level MMCCC shown in Figure 4 has an inherent modular structure and can be designed to achieve any conversion ratio. For the schematic shown in Figure 4 with four modular blocks, the high-voltage side of the converter will be a factor of 5 greater than the low voltage side. Each modular block has one capacitor and three transistors leading to three terminal points. A modular block is shown in Figure 5. The terminal V_{in} is connected to either the high-voltage battery or to the output of the previous stage. One of the output terminals V_{next} is connected to the input of the next stage. The other output terminal V_{LB} is connected to the low-voltage side + battery terminal. Figure 6 shows the proof-of-concept 6-level MMCCC.



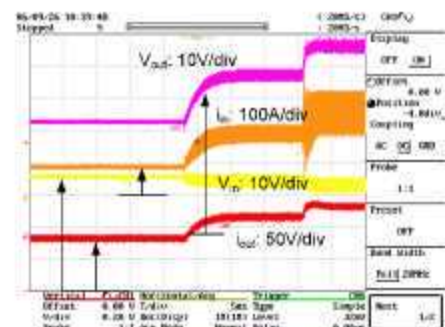
(a) Steady state waveform when outputting 1X



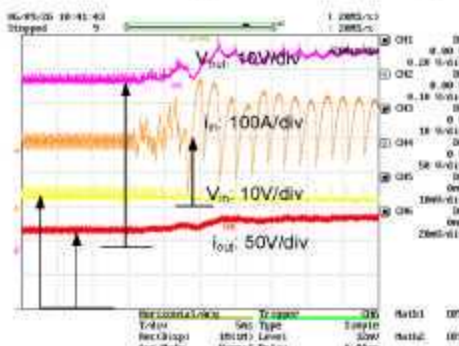
(b) Steady state waveform when outputting 2X



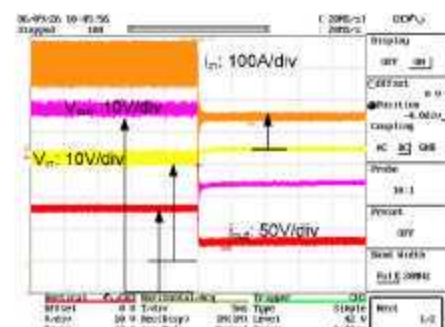
(c) Switch voltage when outputting 2X



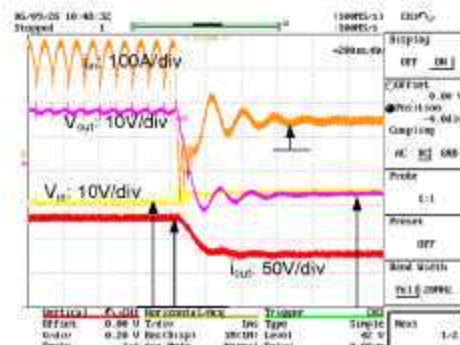
(d) Transition from 1X to 2X



(e) Details of transition from 1X to 2X



(f) Transition from 2X to 1X



(g) Details of transition from 2X to 1X

Figure 3. Experimental results of the converter. 1X means the output voltage equals to input voltage; 2X means the output voltage is twice the input voltage.

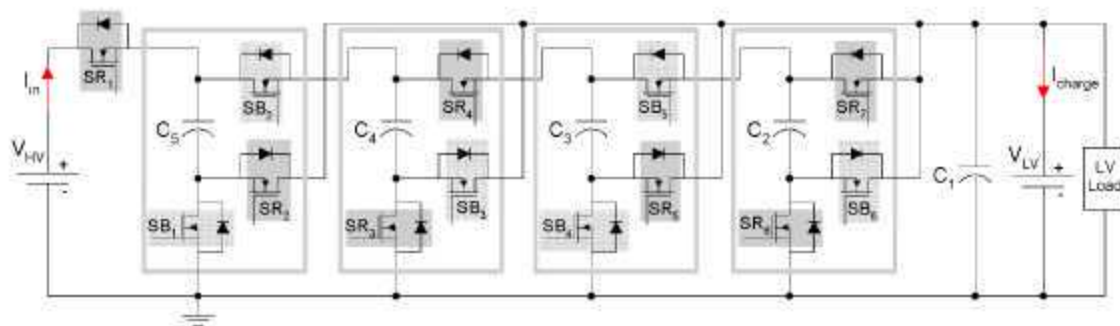


Figure 4. The proposed 5-level MMCCC with four modular blocks.

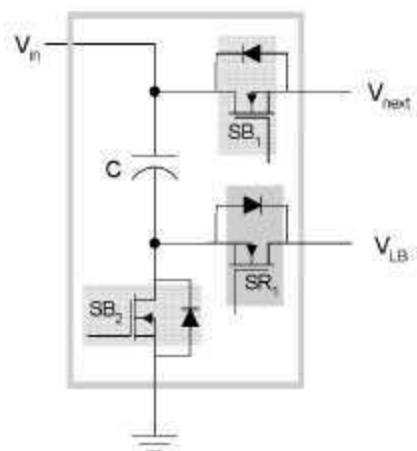


Figure 5. The modular block.

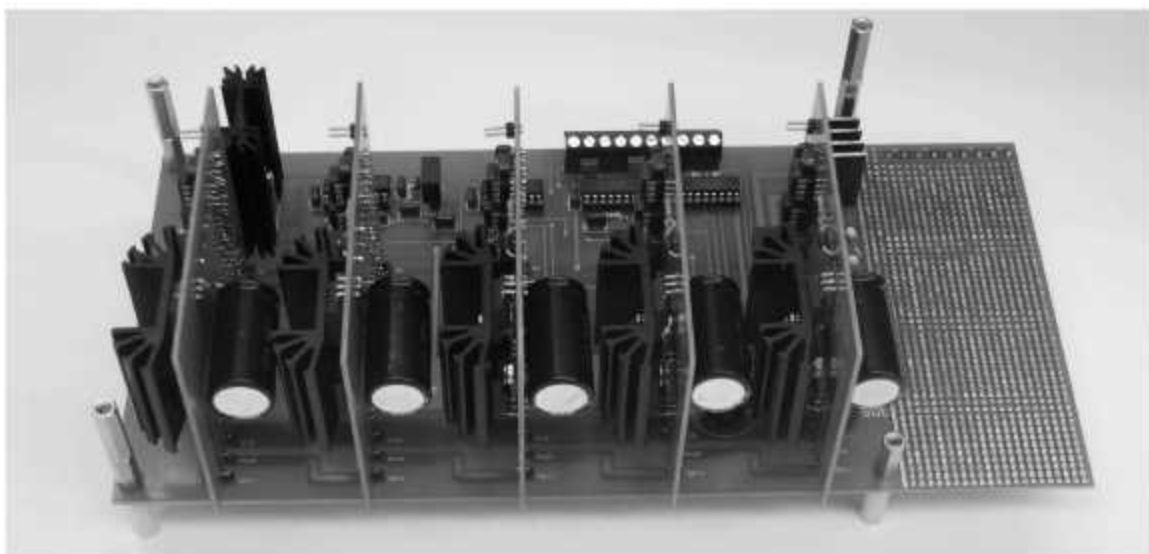


Figure 6. The proof-of-concept six-level MMCCC.

The new converter has much better voltage regulation compared with the conventional converter. In up conversion mode, the conventional converter's input current flows through (N-1) series connected transistors and one diode. The situation will be worse when the conventional converter attempts to deliver current from the high-voltage side to the low-voltage side. During this time the current flows through (N-1) diodes and only one transistor. Usually the voltage drop across the diode is higher than the voltage drop across any transistor, and thereby the regulation is very poor during this time. In contrast, the current flows through at most three transistors or diodes in the new converter irrespective of the conversion ratio. The reduced number of series connected devices in the new converter is responsible for less voltage drop and better regulation.

The new circuit suffers from one limitation. The MMCCC uses more transistors than are required for the conventional flying capacitor multilevel dc/dc converter with the same conversion ratio. For an N-level design, the conventional converter requires $2N$ transistors, whereas the new converter needs $(3N-2)$ transistors. Thus, for a five-level design, the conventional converter needs 10 transistors; 13 transistors are needed for the new converter. However, the use of more transistors is truly compensated by obtaining all the desirable features from the new converter.

A new topology of the modular multilevel dc-dc converter has been proposed and validated by both simulation and experimental results. The new converter outperforms the conventional converters by having complete modular construction, high power transfer capability, simpler gate drive circuit requirements, high-frequency operation capability, onboard fault bypassing, and bi-directional power management capability. By virtue of the modular topology, the circuit obtains redundancy and the reliability can be increased significantly. The modular nature also introduces the use of one additional level to establish the fault bypassing and bidirectional power flow management. Thus this converter could be a suitable choice in various applications to establish a bidirectional power management between buses having different voltages.

High-Temperature Gate Driver

Layout of a gate driver chip capable of operating from -50 to 200°C was completed and submitted to Atmel for fabrication in September 2006. Figure 7 is the schematic of the circuit, and Figure 8 shows the complete layout. The process used by Atmel is referred to as a BCD (bipolar-CMOS-DMOS) on SOI commonly known as SMARTIS. The total size of the chip is 5 mm^2 ($2240\text{ }\mu\text{m} \times 2240\text{ }\mu\text{m}$).

Figure 9 shows the layout of the logic part of the gate driver chip, and Figure 10 shows the layout of the high-voltage (45-V) output stage of the gate driver chip. Two negative channel MOSs (NMOSs) in the output stage are made large enough (total $W = 24,000 \mu\text{m}$) to provide enough load current to get acceptable rise and fall times. Each of these NMOSs comprises six hundred 45-V NMOSs ($W = 40 \mu\text{m}$)

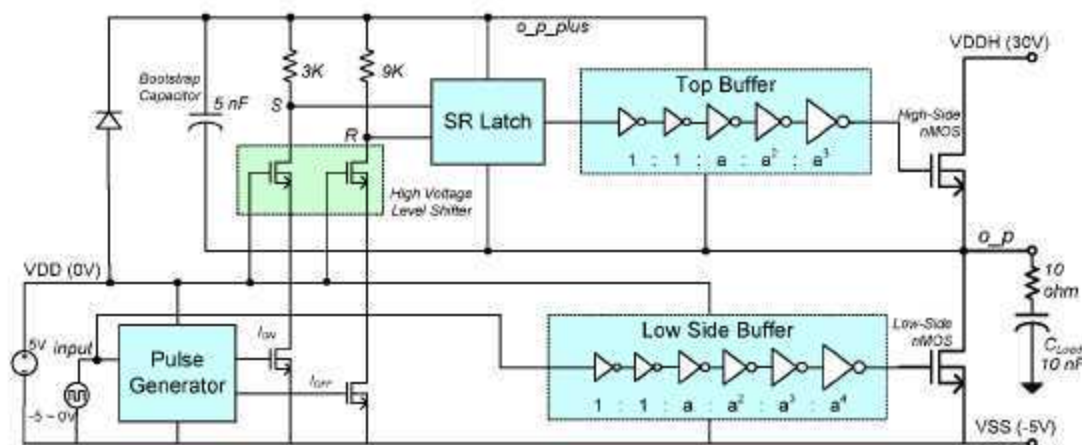


Figure 7. Schematic of the gate driver circuit.

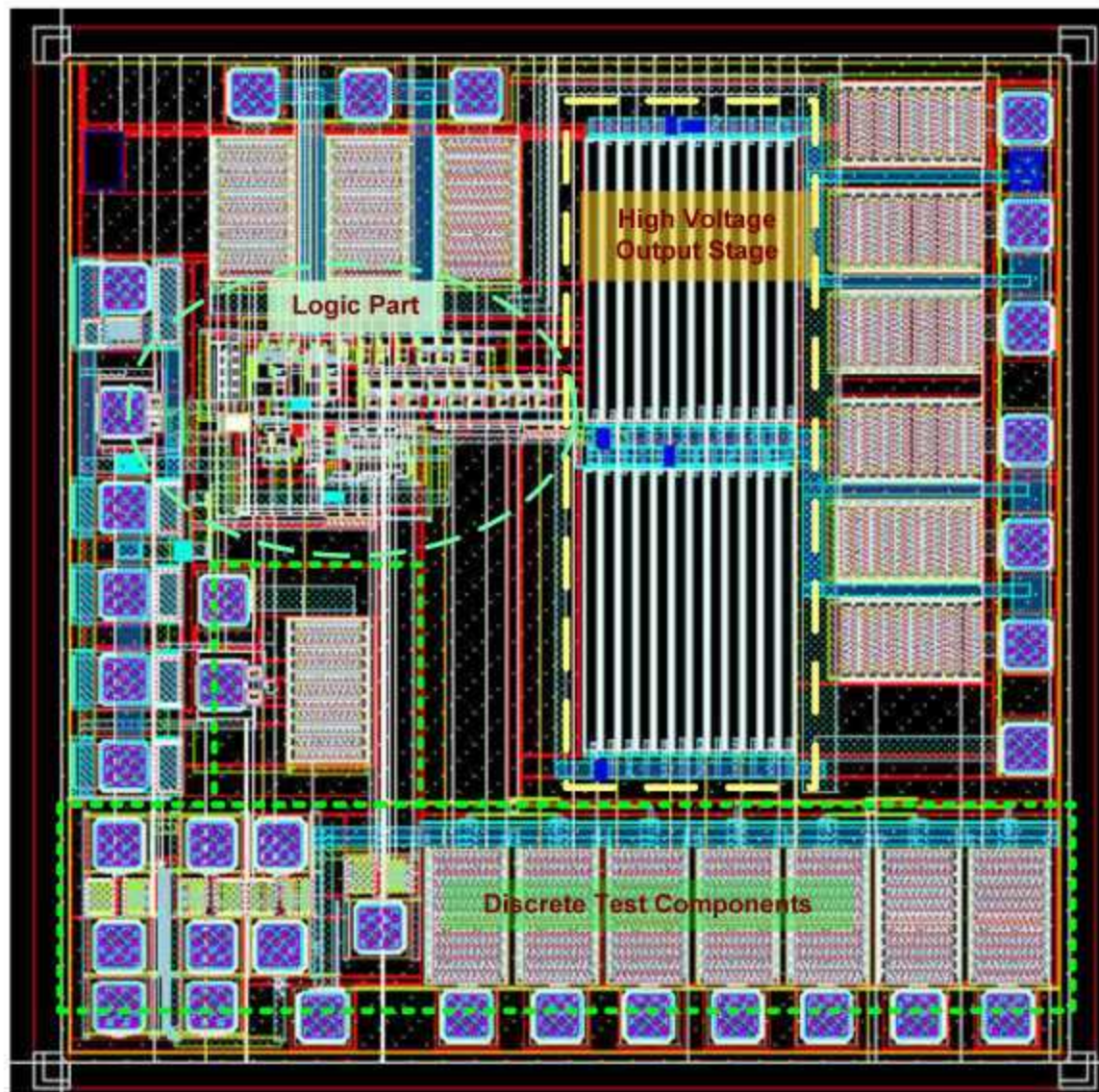


Figure 8. Complete layout of the gate driver chip.

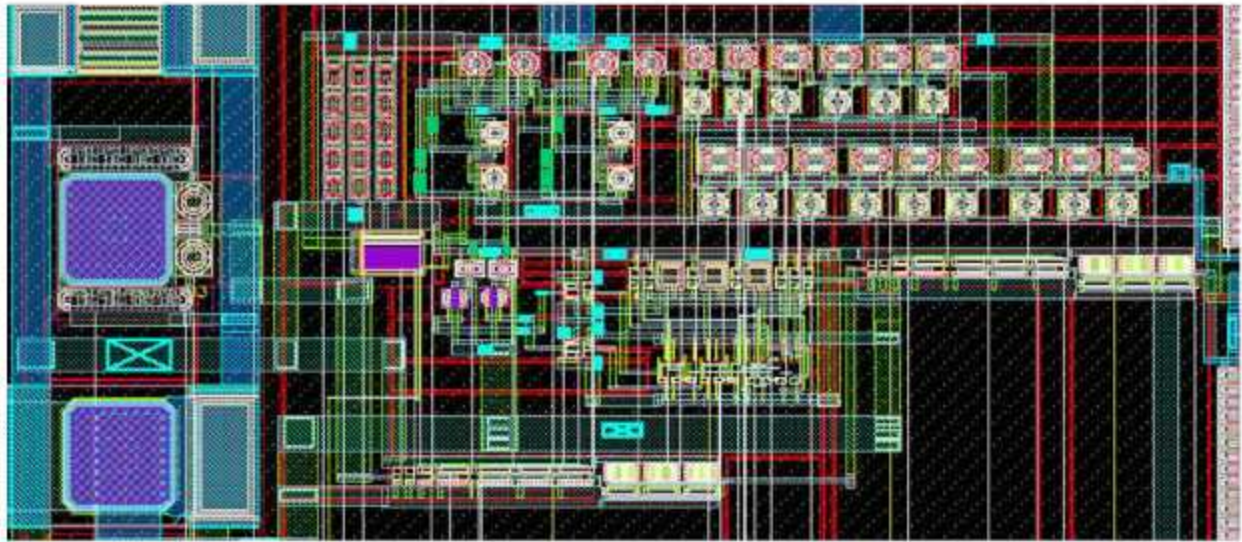


Figure 9. Layout of the logic part of the gate driver chip.

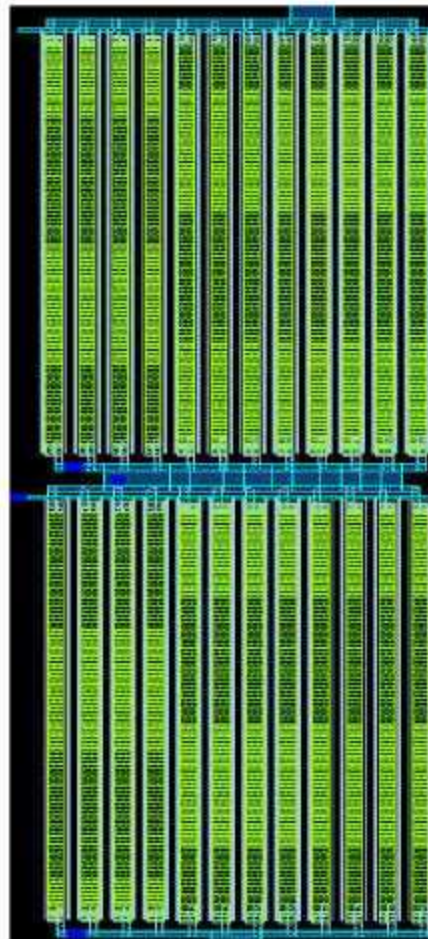


Figure 10. Layout of the high-voltage output stage.

connected in parallel. In the layout, the high-voltage output stage and low-voltage logic sections are carefully laid separately for the safety of the chip. Gate and power supply protections are also ensured in the pad frame. Post-layout simulations were performed to check the functionality of the layout.

Other than the gate driver circuit, some discrete components [45-V NMOS, 5-V NMOS and p-channel MOS (PMOS), 25 NMOS and PMOS] are also added in the layout for testing and characterization at high temperature so that after these are characterized, we will know if these can be used in future chips.

Fabrication of the gate drive chip by Atmel will occur during the last 3 months of 2006 (first quarter of FY 2007). High-temperature printed circuit boards will be evaluated for use with the gate drive chip.

High-Temperature Capacitors

Penn State contacted a number of capacitor companies and procured samples from several sources. A list of capacitors is shown in Table 1.

Table 1. U.S. capacitor industry products for high-temperature capacitors

Company	Capacitance value (μF)	Temperature range ($^{\circ}\text{C}$)	Voltage rating (V)	Comments	Size $W \times H \times T$ (cm)
Johansen Dielectric	0.22	Up to 200	100	NPO type	$1.2 \times 1.27 \times 0.38$
	2.70		100	X7R type	
Kemet	0.033	Up to 200	100	NPO type	$0.78 \times 0.78 \times 0.38$
	1.0		100	X7R type	
Wright Capacitors	0.082	Up to 200	500	NPO type	$1.57 \times 1.68 \times 0.64$
	2.75		500	X7R type	
Dearborn Electronics	1.0	Up to 125	50	Metallized film	$1.8(\text{h}) \times 0.625$ (diam)
	1.0		250		$2.5(\text{h}) \times 1.5$ (diam)
Electronic Concepts	150	Up to 100	500	Metallized film	$4.0(\text{h}) \times 8.3$ (diam)
K Systems	<1.0	Up to 300	50	Diamondlike	Not specified
TRS Technologies	1	Up to 300	500	Almost X7R	$1.6 \times 1.6 \times 0.7$
	50	Up to 600	2000	Almost NPO	

The largest multilayer ceramic capacitors (MLCCs) are 1 μF , and they need to be stacked in parallel to achieve the total capacitance that is required by the power converter. The highest-temperature polymer film capacitors were found to be 125 $^{\circ}\text{C}$, and MLCCs have substantially higher temperature capability (600 $^{\circ}\text{C}$).

In addition to ac characterization of commercial capacitors, the dc performance was evaluated for commercial capacitors and prototype capacitors made at TRS Technologies and Penn State. An “RC figure-of-merit” which combines capacitance and dc resistance results was established. High dc resistance is important for component reliability, and high capacitance is important for volume-efficient inverters. The “figure-of-merit” was derived from the following:

$$R = \frac{\rho d}{A} \quad , \quad (1)$$

$$C = \frac{\epsilon_r \epsilon_0 A}{d} \quad , \quad (2)$$

$$RC = \rho \epsilon_0 \epsilon_r \quad , \quad (3)$$

where A is the capacitor area, d is the capacitor thickness, ϵ_0 is the permittivity of free space, ρ and ϵ_r are the resistivity and relative permittivity (same as dielectric constant) of the dielectric material, respectively. Note that the “ RC ” value only contains material parameters and that the capacitor geometry is factored out of Equation (3). The “ RC ” value shown in Equation (3) is not the standard “time constant” for capacitor discharge, but a figure-of-merit related to capacitor reliability and volumetric efficiency. Low leakage current in a material represents a high R -value and is important for capacitor reliability. A high C -value is important for shrinking capacitor size. Penn State surveyed more than 50 materials, including polymer film and ceramic, and the RC values ranged from 10^{-4} to 100 at 200°C. Table 2 shows that the best material was found to be BaZrO₃.

**Table 2. Summary of high-temperature materials survey
(taken from a study of more than 50 materials)**

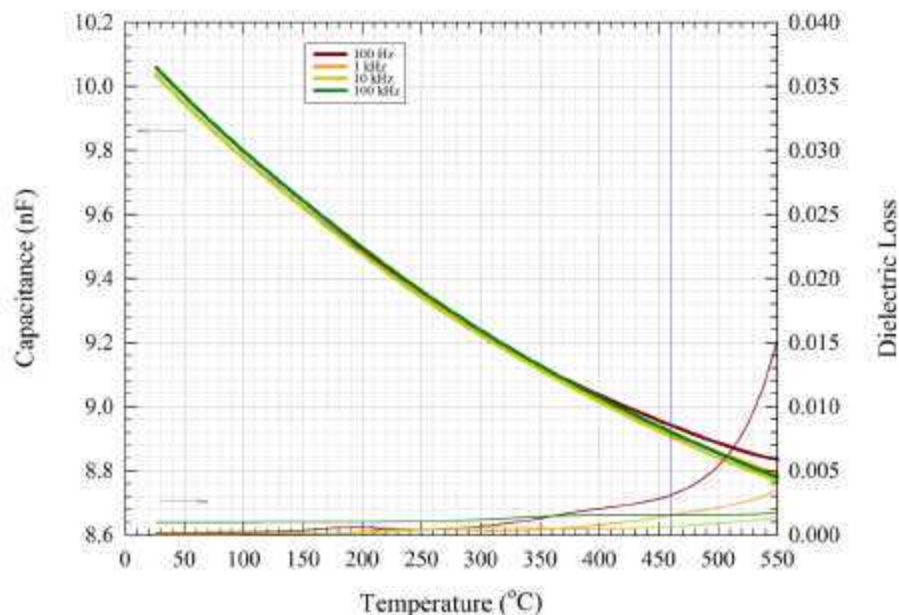
Material	RC at 200°C	RC at 300°C	RC at 400°C
Polypropylene	0.000081	Too low to measure	Too low to measure
BaZrO ₃	103	59	0.33
JDI NPO	90	Bad terminations	Bad terminations
Average PLZT	280	13	0.04

The RC value is very low at 200°C for commercial polypropylene, which is used in film capacitors for pulsed-power applications. As temperature is increased, the resistance “ R ” drops for all dielectric materials. Therefore the RC product also decreases for all dielectric materials as temperature is increased. A commercial high-temperature capacitor material, JDI NPO, has a high RC value at 200°C; however, we were unable to measure the electrical properties at higher temperatures. The terminations of this commercial capacitor did not work at 300°C.

Experimental materials PLZT and BaZrO₃ were explored, and both have excellent RC values at 200°C. BaZrO₃ is the best overall dielectric material at higher temperatures. The capacitance and loss of a prototype BaZrO₃ capacitor is shown in Figure 11. Penn State and TRS Technologies have been collaborating on high-temperature capacitor development, and the results show that BaZrO₃ has low losses up to 350°C, well above the DOE FreedomCAR specification of 140°C.

Researchers from Penn State University and TRS Technologies visited Wright Patterson Air Force Base to deliver high-temperature capacitors to its power electronic group. Jim Scofield and coworkers have assembled an all-SiC converter, operating at 2 kW, 200 V, and 200°C. They are presently using commercial Y5V 4.7- μ F multilayer ceramic capacitors for the dc bus capacitors. These capacitors are only rated to 125°C and 50 V, but they perform well above these specifications. However, these capacitors were only operated for a short time at these elevated temperature and voltage ratings, and it is expected that the lifetime of the capacitor would be significantly reduced. A summary of commercial capacitor temperature specifications for consumer electronics is shown in Table 3.

Figure 12 shows a typical response for commercial Y5V multilayer ceramic capacitors, and the industry specifications are shown in Table 3 for common capacitor types. Typically NPO capacitors are used for high-temperature operation. Figure 13 shows the dielectric response of the commercial Kemet capacitors under a 200-V bias (which is four times the voltage rating). The capacitance has a peak value of 0.35 μ F at 200°C, which is the operating temperature of the SiC converter at Wright Patterson Air Force Base.

ML-387: RB-0604 BLZ MLCC sintered 1650°C/1 h (10C pm) 6/5/6

Edward F. Alberta
TRS Technologies, Inc.

06/07/2006(3)
Heating 2°C/min

Figure 11. Capacitance and loss for a BaZrO₃ prototype capacitor manufactured at TRS Technologies. Note that the capacitance changes approximately 10% from room temperature to 550°C. The loss value at 100 Hz exceeds the DOE FreedomCAR specification at 350°C. High dielectric loss at low frequency suggests that dc conduction is an important factor at high temperature.

Table 3. General commercial capacitor classes (Note the trade-off between dielectric constant and temperature dependence of dielectric constant)

Capacitor specification	Y5V	X7R	NPO
Dielectric constant	6000	2000	60
Temperature range °C	10 to 85	-55 to 125	-55 to 125
Δ°C over temperature range	80%	30%	30 ppm

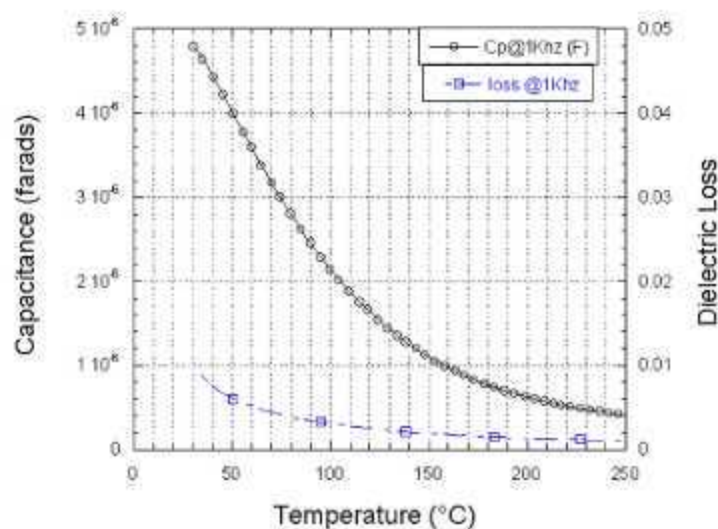
4.7 ~ 5.2 μF Kemet capacitors under 0 voltage

Figure 12. Temperature dependence of capacitance and loss for a commercial multilayer ceramic capacitor. The capacitor is "Y5V" specified and is designed to have a maximum capacitance at room temperature.

Kemet capacitor
4.7 μF = 5.2 μF under 200 V

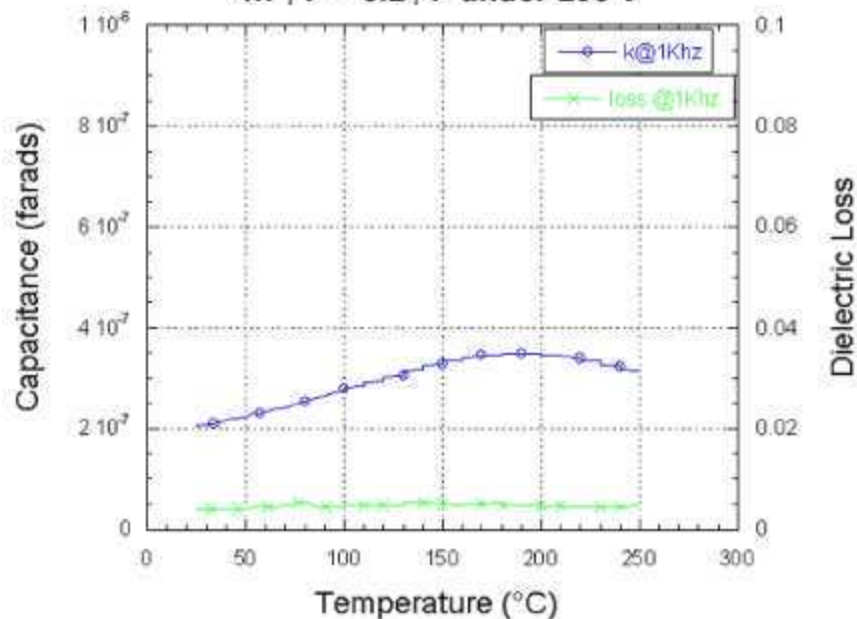


Figure 13. Temperature dependence of capacitance and loss for a commercial multilayer Y5V ceramic capacitor under an applied dc voltage of 200 V.

Both ac and dc tests of commercial and experimental capacitors were carried out as a collaborative effort between Penn State, ORNL, and industrial partners. It was found that high-temperature polymer film capacitors had very low dielectric loss up to temperatures of 120°C. The ac properties of commercial MLCCs were characterized up to 180°C, and the dielectric properties improved continuously as temperature was increased. dc tests were also performed and an RC figure-of-merit was used to compare capacitors. A new dielectric BaZrO₃, developed in collaboration with TRS Technologies, was found to have the best high-temperature properties. dc bus capacitors in an all-SiC power inverter which operates at 200°C, are presently being explored at Wright Patterson Air Force Base. Presently, an array of commercial 5-μF MLCCs is employed in a parallel array for the dc bus capacitor. Penn State characterized the high-temperature and high-voltage dielectric properties of these capacitors.

Conclusion

This challenging project involves the development and demonstration of several novel technologies to achieve a converter that can operate at high ambient temperatures. Novel magnetic-less dc-dc converter topologies will result in reduced volume and weight compared with conventional topologies. The multilevel design of these converters will also allow segregation of the battery pack into multiple modules. This will allow only a portion of the battery pack to be replaced if there is a failure. It may also result in an increase in reliability and availability of the battery power, as the converter designs will allow for a damaged or failed battery module or power electronics module to be bypassed.

A high-temperature gate drive has been designed and will be tested in the upcoming year. High-temperature packaging of SiC-based power electronics will transition from diodes to controllable switches in the upcoming year as another step toward a complete high-temperature module. Gains made from this project will likely impact other power electronics projects that need high-temperature packaging, gate drives, or modular conceptual designs.

Future Direction

During FY 2007, detailed design, fabrication, and testing will be conducted of two different magnetic-less dc-dc converters to demonstrate the feasibility of the topologies. These will have conventional packaging and heat transfer technology. The development of converter control will be done during FY 2007 of the necessary algorithms to control power flow in both directions while regulating the voltage at the receiving end of the converter.

In addition, a high-temperature gate drive fabricated in SOI that was submitted for fabrication in September 2006 will be manufactured by Atmel during the first quarter of FY 2007 and then tested to determine its characteristics over a wide temperature range (-50 to 200°C). Based upon the results of the testing, a revised gate drive design will be done and submitted for fabrication.

A high-temperature power module will be designed and fabricated that leverages some of the high-temperature packaging techniques that were used in the Wide Bandgap Semiconductor project at ORNL. This module will likely consist of several SiC junction field effect transistors, SiC Schottky diodes, and high-temperature capacitors. The module will be a building block of one of the two dc-dc converter topologies that are being tested during FY 2007. The selection of the topology will be based on availability of components (SiC switches and high-temperature capacitors) and which converter looks most promising in terms of meeting FreedomCAR goals after testing.

Upon successful testing of these power modules and gate drives, these will then be ready for a system assembly using five of these units to complete the fabrication of a dc-dc converter capable of bidirectional power transfer. The complete converter assembly and testing will be done during FY 2008.

Publications

F. H. Khan and L. M. Tolbert, "A Multilevel Modular Capacitor Clamped DC-DC Converter," *IEEE Industry Applications Society Annual Meeting, Tampa, Florida*, October 8-12, 2006.

L. M. Tolbert, H. Zhang, M. Chinthavali, and B. Ozpineci. "SiC-based Power Converters for High Temperature Applications," *European Conference on Silicon Carbide and Related Materials (ECSCRM)*, Newcastle, United Kingdom, September 3–7, 2006.

H. Zhang, M. Chinthavali, B. Ozpineci, and L. M. Tolbert, "System Modeling and Characterization of SiC Schottky Power Diodes," *IEEE Workshop on Computers in Power Electronics*, Troy, New York, July 16–19, 2006.

F. H. Khan, L. M. Tolbert, and F. Z. Peng, "Deriving New Topologies of DC-DC Converters Featuring Switching Cells," *IEEE Workshop on Computers in Power Electronics*, Troy, New York, July 16–19, 2006.

M. Chinthavali, L. M. Tolbert, B. Ozpineci, and H. Zhang, "High Temperature Power Electronics—Application Issues of SiC Devices," *IMAPS International Conference on High Temperature Electronics*, Santa Fe, New Mexico, May 15–18, 2006.

References

1. Z. Pan, F. Zhang, and F. Z. Peng, "Power Losses and Efficiency Analysis of Multilevel DC-DC Converters," pp. 1393–1298 in *IEEE Applied Power Electronics Conference*, March 2005.
2. F. Zhang, F. Z. Peng, and Z. Qian, "Study of Multilevel Converters in DC-DC Application," pp. 1702–1706, in *IEEE Power Electronics Specialists Conference*, June 2004.
3. F. Z. Peng, F. Zhang, and Z. Qian, "A Novel Compact DC-DC Converter for 42V Systems," pp. 33–38, in *IEEE Power Electronics Specialists Conference*, June 2003.
4. K. D. T. Ngo and R. Webster, "Steady-State Analysis and Design of a Switched-Capacitor DC-DC Converter," *IEEE Transactions on Aero. and Elec. Systems*, **30**(1), 92–101 (Jan. 1994).
5. W. Harris and K. Ngo, "Power Switched-Capacitor DC-DC Converter, Analysis and Design," *IEEE Transactions on Aero. and Elec. Systems*, **33**(2), 386–395 (April 1997).
6. S. V. Cheong, H. Chung, and A. Ioinovici, "Inductorless DC-to-DC Converter with High Power Density," *IEEE Transactions on Industrial Electronics*, **41**(2), 208–215 (April 1994).
7. O. Mak, Y. Wong, and A. Ioinovici, "Step-up DC Power Supply Based on a Switched-Capacitor Circuit," *IEEE Transactions on Industrial Electronics*, **42**(1), 90–97 (February 1994).
8. C. K. Tse, S. C. Wong, and M. H. L. Chow, "On Lossless Switched-Capacitor Power Converters," *IEEE Transactions on Power Electronics*, **10**(3), 286–291 (May 1995).
9. E. Bayer, "Optimized Control of the 'Flying'-Capacitor Operating Voltage in 'Gear-Box'-Charge Pumps—The Key Factor for a Smooth Operation," pp. 610–615, in *IEEE Power Electronics Specialists Conference*, June 2003.
10. R. D. Middlebrook, "Transformerless DC-to-DC Converters with Large Conversion Ratios," *IEEE Transactions on Power Electronics*, **3**(4), 484–488 (October 1988).
11. L. Cheng, I. Sankin, J. N. Merrett, V. Bondarenko, R. Kelley, S. Purohit, Y. Koshka, J. R. B. Casady, J. B. Casady, and M. S. Mazzola, "Cryogenic and High Temperature Performance of 4H-SiC Vertical Junction Field Effect Transistors (VJFETs) for Space Applications," *International Symposium on Power Semiconductor Devices & ICs*, May 23–26, 2005.
12. D. C. Hopkins, D. W. Kellerman, R. A. Wunderlich, C. Basaran, and J. Gomez, "High-temperature, High-density Packaging of a 60-kW Converter for >200°C Embedded Operation," pp. 871–877 in *IEEE Applied Power Electronics Conference*, Dallas, March 19–23, 2006.
13. D. Katsis, B. Geil, T. Griffin, G. Koebke, S. Kaplan, G. Ovrebø, and S. Bayne, "Silicon Carbide Power Semiconductor Module Development for a High Temperature 10-kW ac Drive," pp. 399–403 in *IEEE Industry Application Society Annual Meeting*, Hong Kong, China, October 2–6, 2005.
14. T. Funaki, J. C. Balda, J. Junghans, A. S. Kashyap, F. D. Barlow, H. A. Mantooth, T. Kimoto, and T. Hikiyara, "Power Conversion with SiC Devices at Extremely High Ambient Temperatures," pp. 2030–2035 in *IEEE Power Electronics Specialists Conference*, Recife, Brazil, June 12–16, 2005.

15. S. Mounce, B. McPherson, R. Schupbach, and A. B. Lostetter, "Ultra-lightweight, High Efficiency SiC Based Power Electronic Converters for Extreme Environments," *IEEE Aerospace Conference*, March 4–11, 2006.
16. M. Chinthavali, B. Ozpineci, and L. M. Tolbert, "High Temperature and High Frequency Performance Evaluation of 4H-SiC VJFET and Schottky Diodes," pp. 322–328 in *IEEE Applied Power Electronics Conference*, Austin, Texas, March 6–10, 2005.

4.5 dc/dc Converter for Fuel Cell and Hybrid Vehicle

Principal Investigator: Lizhi Zhu

Ballard Power Systems

15001 Commerce Drive North

Dearborn, MI 48120

Voice: 313-354-5973; Fax: 313-583-5990; E-mail: lizhi.zhu@ballard.com

DOE Technology Development Manager: Susan A. Rogers

Voice: 202-586-8997; Fax: 202-586-1600; E-mail: Susan.Rogers@ee.doe.gov

ORNL Program Manager: Mitch Olszewski

Voice: 865-946-1350; Fax: 865-946-1262; E-mail: olszewskim@ornl.gov

Objectives

The goal of this project is to develop and fabricate a 5-kW dc/dc converter with a baseline 14-V output capability for fuel cell and hybrid vehicles. The major objectives for this dc/dc converter technology are to provide

- higher efficiency (92%)
- high coolant temperature capability (105°C)
- high reliability (15 years/150,000 miles)
- smaller volume (5 L)
- lower weight (6 kg)
- lower cost (\$75/kW)

Approach

The key technical challenge for this converter is the 105°C coolant temperature. The power switches and magnetics must be designed to sustain higher operating temperatures reliably, without a large cost/mass/volume penalty. The following key technologies are proposed to break through technical barriers to achieve a high-temperature, high-power-density, and lower-cost design.

1. Converter topology

A novel interleaved dc/dc converter topology is proposed as shown in Figure 1. The key merits of the converter are

- lower rms current stresses on components due to interleaving
- reduced ripple current on capacitors due to interleaving
- lower power losses due to low R_{ds_on} and soft-switching
- smaller magnetics due to high switching frequency
- low EMI due to integrated power devices and magnetics

2. Integrated module-based dc/dc converter

Power module-based integration technology has been employed in this design. The thermal requirements are a challenge. The coolant temperature is 105°C. To meet the junction temperature 125°C design criteria, the thermal impedance has to be very small. Power module integration simplifies thermal stack-up layers, obtaining smaller thermal resistance. Furthermore, the customized power module optimizes the high-current interconnection path, reducing conduction losses. By using wirebonds in the

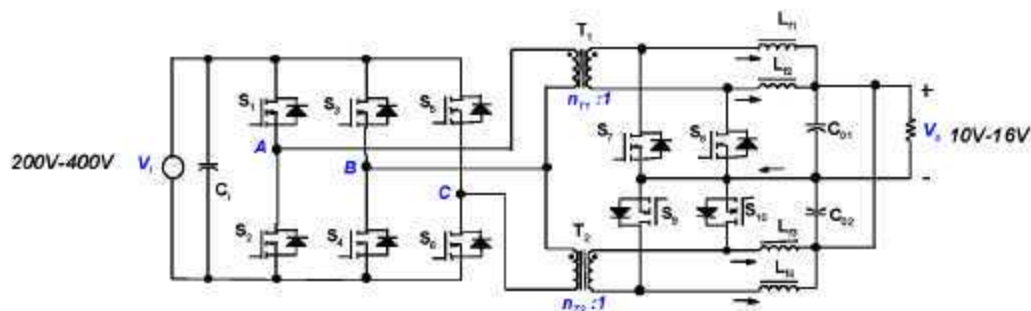


Figure 1. The novel interleaved dc/dc converter topology.

transformer design, rather than the traditional bolts and busbars, the reliability is also improved. The major advantages of the power module based dc/dc converters are

- enhanced thermal performance
- reduced number of devices
- increased reliability
- higher level of integration

3. Planar magnetics with enhanced cooling

This converter has also been designed using planar magnetics, a technology that Ballard thinks is critical for reliable and cost-effective high-volume production of such products. The benefits from this technology are

- lower leakage inductance due to shorter winding termination and smaller circuit paths
- elimination of discrete contacts' Ohmic loss
- reduction of Ohmic loss due to shorter conduction paths
- lower ac loss due to flat winding structure
- higher core window utilization ratio
- smaller core volume and weight
- higher surface to volume ratio for improved heat conduction
- direct cooling of core by direct contact to heat sink
- higher power density

Major Accomplishments of FY 2006

In FY 2006, Ballard focused on the production Beta design to address differences between the DOE goals and the Alpha design results. The major achievement in FY 2006 was the design and verification of the final Beta unit to meet the targets. Tasks included

- electrical improvements over the Alpha design
- cost reduction
- volume reduction
- weight reduction
- thermal design improvement
- manufacturing process improvements

The project timing consisted of four phases: Phase I: Key technologies prove-out; Phase II: Full function Alpha design and test; Phase III: Final Beta prototype design; Phase IV: Final build, DV test, delivery, and report. In FY 2005, we have finished Phase I and part of Phase II. The results have been reported as shown in Table 1.

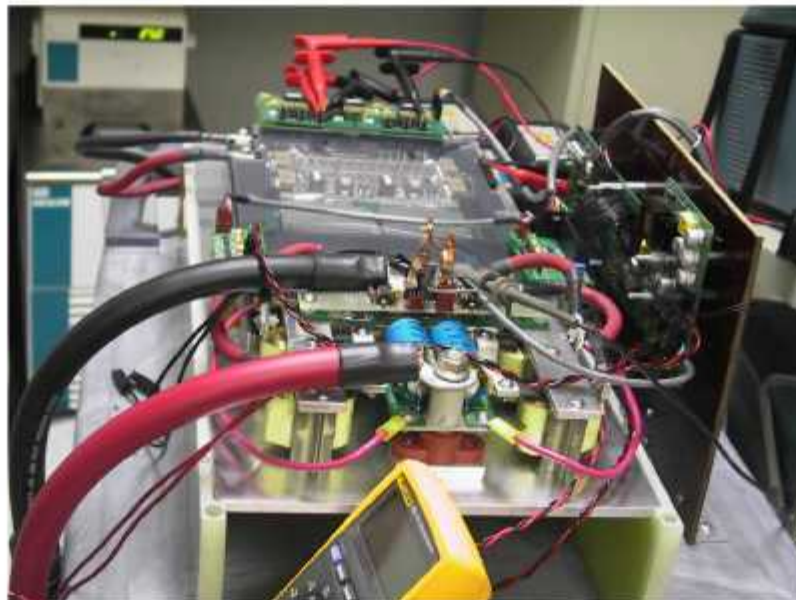
Table 1. The percentage of goals achieved as of FY 2005 through Alpha design

	Alpha Design	DOE Goal	% Target
Output Power	5.1kW	5kW	102%
Efficiency	93%	92%	101%
Cost Estimation	\$545	\$375 total, (\$75/kW)	69%
Coolant Temperature	90 Deg C	105 Deg C	86%
Volume	6.5 Liter	5 Liter	77%
Weight	7.6kg	6kg	79%
Coolant Pressure Drop	2.3 PSI	0.73PSI (5kPa)	32%

In FY 2006, we continued working on the Alpha prototype testing work, completed the Beta design and part purchasing, and developed the manufacturing process to produce the final prototype. The major tasks follow:

I. Continued electrical evaluation testing on Alpha prototype:

Figure 2 shows the test implementation for the Alpha prototype. At the end of FY 2005, we had finished the efficiency tests at $V_i = 200\text{ V}$, 300 V , 350 V up to 5 kW , and achieved the 92% efficiency target. The remaining issue was when the input voltage reached $\sim 400\text{ V}$, the efficiency dropped substantially, and excessive switching noise appeared in the synchronized rectifier switches. This problem prevented the dc/dc converter from delivering full power at 400 V .

**Figure 2. Alpha dc/dc converter under test.**

Troubleshooting of the noise problem had been done in early FY 2006 to solve the switching noise problem. It turned out to be that a higher Q_{rr} loss occurred under hot coolant test conditions. When coolant was raised to 90°C , the ambient temperature surrounding the die and gate drive circuit rose. It

caused a small change in signal delay. However, the delay was big enough to cause a higher reverse recovery current in the rectifier turn on/off transitions, leading to excessive Q_{rr} losses on the rectifiers. An improvement was made in the gate drive circuit to compensate the delay due the high-temperature operation. The dc/dc passed the full-input voltage ($V_i = 400$ V) and full-power ($P_o = 5$ kW) operation with 90°C coolant. The overall efficiency kept above 92%, as shown in the final test results in Figure 3.

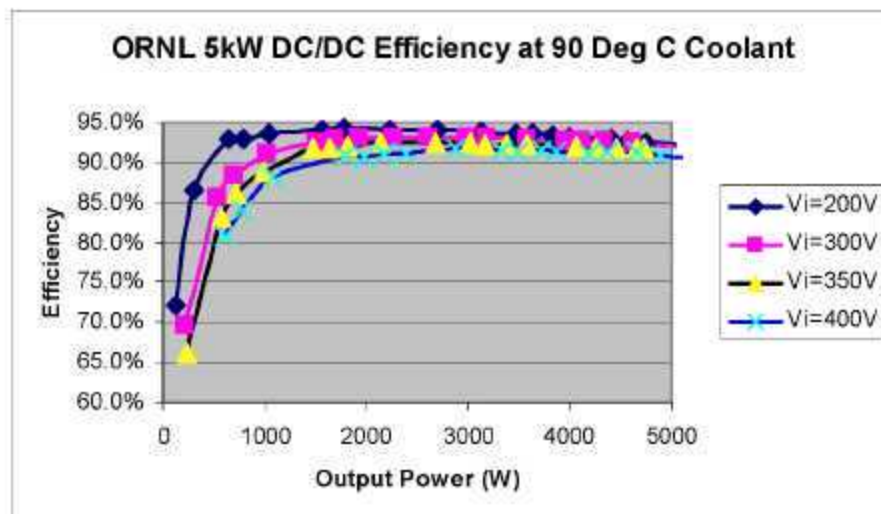


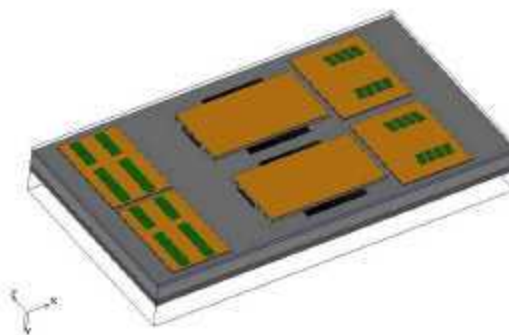
Figure 3. Efficiency test results at $V_i = 200$ V, 300 V, 350 V, and 400 V.

2. Cost reduction—Beta design

The cost of the customized power module is a major portion of the dc/dc converter costs, making up more than 50% of the total. In the Beta design, a new lead frame design concept was adopted to eliminate signal pin inserts. As a result, the power module baseplate width was reduced by 33 mm. Figure 4 depicts the Alpha and Beta power module design. The reduction of the power module width reduces the power module cost by 7%. The improved lead frame design also saves in the tooling costs. The high-volume cost estimation based on the Beta design is \$458 at high volume; this is 82% of the DOE goal.



a) Alpha (203 X 315 mm)



b) Beta (170 X 315 mm)

Figure 4. Alpha and Beta power module layout.

3. Volume and weight reduction

The 33-mm saving in power module width dimension also contributes to volume and weight reduction in the final packaging. To pass the environmental requirements, an aluminum cast housing was designed for the Beta prototype. The total volume was reduced to 5.1 L in the Beta design, down from the 6.5-L Alpha prototype design. Figure 5 shows the final Beta dc/dc converter packaging without cover.

The adoption of the final power module design greatly simplified the interconnection of the dc/dc converter. The part count was reduced to a total of 42 parts, including 2 wire harnesses and 11 types of fasteners. Table 2 lists the bill of materials of the Beta design and the weight estimation. The total weight is 7.4 kg. Although the aluminum housing is included, the total weight is 0.2 kg less than the Alpha prototype.

Figure 6 illustrates the bottom view of the Beta packaging. It shows the interfaces between the dc/dc converter and the end-user. The high-voltage connector connects the high-voltage input (200–400 V) to the dc/dc converter; the LV studs are the 12-V output to deliver the low-voltage power to the 12-V battery and loads in a vehicle. The coolant in/outlet ports bring a circulating coolant into the unit to remove the heat generated in the dc/dc converter. The signal connector is the control path between the dc/dc converter and vehicle controller. It includes the voltage command and enable signals through a controller area network interface.

4. Thermal design improvement

Two major design improvements have been made in the Beta design: the lead frame material and baseplate material.

To meet 105°C coolant operation requirements, AMODEL A-4133 L had been selected for the high-temperature plastic lead frame. It has high heat resistance, high strength and stiffness over a broad temperature range, low moisture absorption, excellent chemical resistance, and excellent electrical properties. It has been advantageously used for many automotive electrical and electronics applications. Its heat deflection temperature is as high as 300°C. An injection mold was required to manufacture the plastic lead frame. It added a substantial tooling cost for the Beta prototype development.

To design for a 15-year reliability requirement, aluminum silicon carbide (AlSiC) had been selected for the power module baseplate material. The AlSiC composite materials are designed to have a high thermal conductivity and a controlled thermal expansion (CTE) behavior that provides better CTE matching between the substrate and baseplate. A baseplate and substrate assembly was built to perform the thermal cycle test. It passed the thermal shock tests (–40°C to +125°C) 100 times without delaminating.

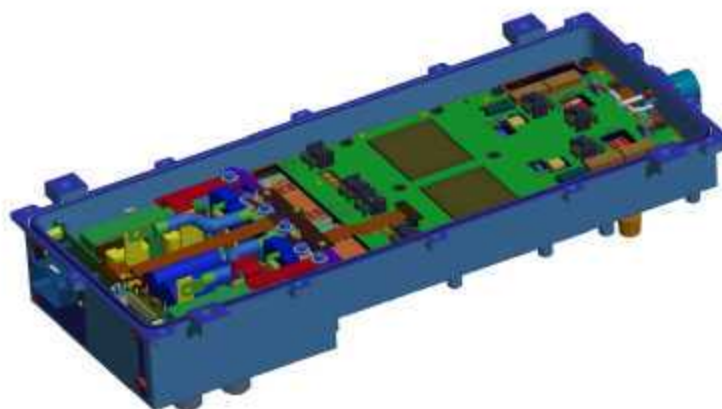


Figure 5. The Beta version of dc/dc converter (5.1 L).

Table 2. The BOM and weight of Beta design

	Part Description/Remarks	Ballard Part No.	Drawing No.	Qty /Per M	Weight* (kg)
1	Fasteners, M4X8, (Inductor Bracket to Housing)	5109167		10	0.001
2	Fasteners, M3X10, (HV connector to Housing)	5109391		4	0.002
3	Fasteners, M5X12, (Cover to Housing)	5109393		17	0.002
4	Sealing Washer, Fastener to Housing	5109394		8	
5	Inductor, 4.5uH, 125A, 100Vpk, 100KHz Ripple	5109397		4	0.295
6	Pad, Silicon Gel Gasket, Inductor Bracket, ORNL	5109605	DRW5106205	2	
7	Fasteners, M5X8, (Control BRD to Stand-off)	5110338		4	0.001
8	Fastener, Hi-Low, Gate DRV to Plastic Bracket	5110602		13	0.001
9	Fasteners, M4X12, (LV Positive Busbar to PCB Capacitor ASY)	100330-PAA		4	0.002
10	Connector, 2Pin, 1 Row	101666-PAA		1	
11	Fastener, Hi-Low, Control Board to Housing	102264-PAA		4	0.005
12	Capacitor, Ceramic, 200V, 0.01uF, 10%, Radial	5106357-s		2	
13	Fasteners, M5X14, (LV Connections to Power Module)	5108401-s		6	0.003
14	Fasteners, M5X10, (Inductor Cables to Inductor)	5108404-s		2	0.002
15	Capacitor, Ceramic, 200V, 0.15uF, 10%, Radial	5106359-s		1	
16	Gasket, HV Connector to Housing	5109392		1	0.005
17	Fasteners, M6X16, (AC Connector, Negative)	5109511-s		2	0.005
18	Brass Hose Fitting, Barb X Male Pipe for 3/4" Hose Id, 3/4" Pipe	5110760		2	0
19	HEX Nut, M5, (Inductor Cable to Inductor)	5110481-S		6	0.005
20	LV Positive Busbar Cable, Inductor(3&4) to Power Module, ORNL	5109603	DRW5106203	2	0.01
21	Connector, High Voltage, ITT Cannon ORNL	5111030		1	0.07
22	O-ring, Inside coolant channel, ORNL	5110400	DRW5106911	1	0.005
23	O-ring, Outside, Cooling Channel, ORNL	5110407	DRW5106911	1	0.005
24	O-Ring, Electronic Housing, ORNL	5110528	DRW5106911	1	0.005
25	O-Ring Seal, Divider Coolant, ORNL	5110550	DRW5106913	1	0.005
26	Harness, 2-Pin, Control BRD to Capacitor BRD	5109387	DRW5105907	1	0.005
27	Current Sensor	5109144		2	0.023
28	Electronic Box Cover - Oakridge	5109098	DRW5105707	1	0.76
29	Capacitor, Electrolytic, 8200uF, 25V, 150Deg C	5109637		2	
30	Busbar Assembly, LV Positive	5109105	DRW5105712	1	0.09
31	LV Positive Busbar, Inductor(1) to Power Module, ORNL	5109600	DRW5106199	1	0.025
32	LV Positive Busbar, Inductor(2) to Power Module, ORNL	5109601	DRW5106200	1	0.025
33	Busbar Assembly, LV Negative	5109102	DRW5105709	1	0.023
34	HSG - ELEC BOX	5109101	DRW5105708	1	2.295
35	AC Connector, LV Positive	5109808-s		2	0.145
36	Inductor Bracket, ORNL	5109104	DRW5105711	2	0.01
37	Stand-off, Female-Female, 15mm Body, M5 thread	5109504	DRW5106204	4	0.005
38	Fastener, M5X30, (Power Module to Housing)	5108406-s		15	0.006
39	Flex Circuit, Gate Drive Board to Control Board, ORNL	5109141	DRW5105742	1	0.05
40	PCB Bare Board, LV Capacitors, ORNL	5109650		1	0.1
41	Power Module			1	1.535
42	PCB Assembly, Control Board, ORNL	5109173	DRW5105735	1	0.55

Weight (kg)	7.378
DOE Target (kg)	6
% of Target	81%

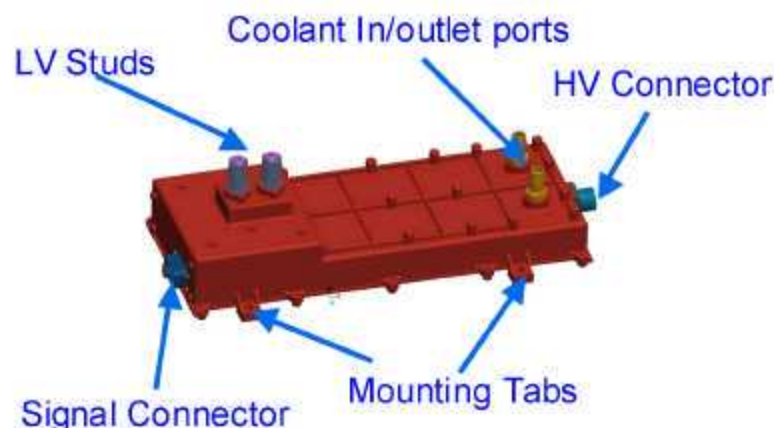


Figure 6. Beta dc/dc converter interfaces.

5. Coolant channel final design

The 105°C coolant operation requirement poses a significant challenge to the thermal design. The junction temperature is targeted at 125°C to allow metal oxide semiconductor field effect transistor switches to operate at a higher efficiency. There is only 20°C of temperature rise budgeted from die to coolant. In the Alpha design, a pin-fin pattern was designed in the coolant channel to achieve lower thermal impedance, as shown in Figure 7.

The pin-fin structure increases the surface area of the baseplate and increases the velocity of fluid in the coolant channel. As a result, the thermal resistance can be very low. However, the test result for the Alpha baseplate design revealed that the pressure drop with the pin-fin design was as high as 2.3 psi at 7 L/min, which is three times higher than the DOE goal (0.73 psi). In the Beta design, a decision was made to eliminate all pin-fins to meet the pressure drop target. The baseplate was redesigned as shown in Figure 8. A sample plate was made to test the pressure drop. The test result verified that the pressure drop in the baseplate coolant channel drops to 0.25 psi at 25°C with a 7-L/min coolant flow rate. This meets the DOE target of 0.73 psi.

The location of inlet and outlet ports was also adjusted accordingly to minimize the turbulence of the coolant inside the channel. A 15-mm chamfer was added to the inlet/outlet chamber. The simulation result of the fluid field is shown in Figure 9.



Figure 7. Alpha baseplate pin-fin design with pin-fin.

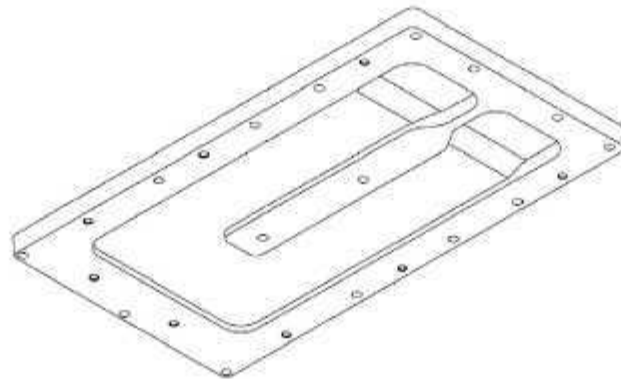


Figure 8. Beta baseplate design without pin-fin.

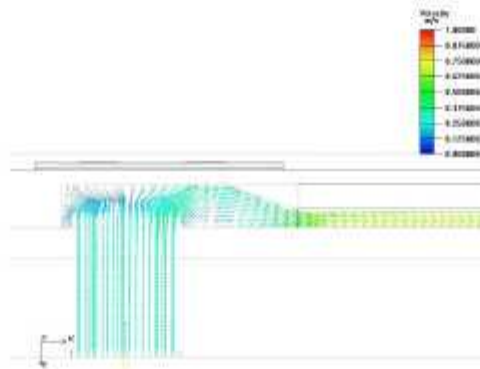


Figure 9. Coolant channel fluid simulation.

Thermal simulations were also performed using ICE pack to verify the junction temperature was within the 125 °C limit. The maximum junction temperature is 122.4°C for the worst case, as shown in Figure 10.

6. Solving practical issues

Given the coolant temperature range of -40°C to +105°C, a coolant pressure peak was detected as high as 60 psi. It broke the O-ring seal of the baseplate and caused leaking of coolant. Figure 11 illustrates

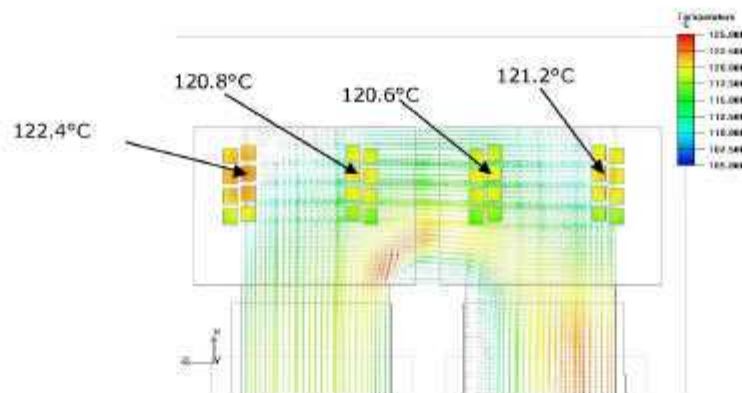
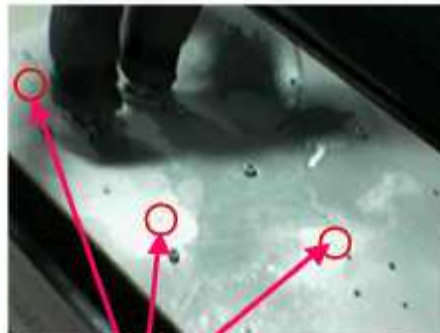


Figure 10. The thermal simulation results.



Figure 11. Baseplate leak test setup.

the baseplate coolant leak test setup. Figure 12 demonstrates the initial seal design leaked at -18°C . After a few iterations, the seal design was improved and passed the leakage test over the entire range of -40°C to $+105^{\circ}\text{C}$.



O-ring seal leaks at -18°C and 60 psi

Figure 12. Baseplate leaks with initial seal design.

Technical Discussion

In FY 2006, the Beta version of dc/dc converter design has been completed. Several improvements have been made to meet DOE targets; however, there are still some gaps existing in the weight and cost goals.

1. Weight target—6 kg

The Beta design is 7.4 kg, which is 1.4 kg over the target. There are two opportunities to meet the weight target. The first opportunity is in housing weight reduction. Currently, we use sand casting for the Beta housing design to reduce the development costs. The housing itself occupies 3.1 kg. Using die casting in high-volume production instead of sand casting, we will be able to reduce the wall thickness from 4 mm to 2.5 mm, resulting in 30% weight reduction. The second opportunity is in power module baseplate weight reduction. The power module baseplate is 1.2 kg. Because the pin-fin is removed from the coolant channel, we can move the coolant channel into the molded housing, allowing us to make a thinner flat baseplate. This change will gain 45% weight reduction in the baseplate. The above two improvements will potentially lead to a 1.47-kg weight saving, which will eventually meet the DOE 6-kg target in high-volume production.

2. Cost target—\$375 for the 5-kW dc/dc converter

The Beta design result reached 82% of the DOE target. The use of two expensive materials in this design can be revisited to reduce the cost. They are (1) AlSiC power module baseplate and (2) silicon nitride planar transformer windings. The opportunities are to (1) improve the material utilization factor and (2) work with the supplier to identify the major cost driver and improve the yield.

Conclusion

In the FY 2006, the testing of the Alpha prototype was completed. Based on the Alpha test results, we have implemented dramatic improvements in the design of the production Beta design. The status summary of the Beta design is presented in Table 3.

Table-3. Status summary from the Beta design during FY 2006

	DOE Goal	Beta Design Results (7/25/06)	Beta Design % Target
Output Power	5kW	5.1kW	102%
Efficiency	92%	93%	101%
Cost Estimation	\$375 total, (\$75/kW)	\$458	82%
Coolant Temperature	105 Deg C	105 Deg C	100%
Volume	5 Liter	5.1 Liter	98%
Weight	6kg	7.4kg	81%
Coolant Pressure Drop	0.73PSI (5kPa)	0.25 PSI	292%

Publications and Presentations

Presentation on U.S. Council for Automotive Research meeting, Southfield, Michigan, March 30, 2006.

Presentation on 2006 DOE FreedomCAR APEEM Annual Review, Pollard Technology Conference Center, Oak Ridge, Tennessee, August 16, 2006.

Presentation on Industrial Power Converter Products and Services Session in IEEE IAS 2006, Tampa, Florida, October 12, 2006.

Patents

“An Interleaved High Power DC/DC Converter,” PAT0589-01US, filed on June 4, 2004.

“Integration of Planar Magnetics Transformer and Power Switching Devices in a Liquid-cooled High Power DC/DC Converter,” PAT0588-02US, filed on October 12, 2004.

5. Systems Research and Technology Development

5.1 Fully Integrated HEV Traction Motor Drive Development Using Thermoelectrics and Film Capacitor Innovations

Principal Investigator: C. W. Ayers

Oak Ridge National Laboratory

National Transportation Research Center

2360 Cherahala Boulevard

Knoxville, TN 37932

Voice: 865-946-1342; Fax: 865-946-1400; E-mail: cayerscw@ornl.gov

DOE Technology Development Manager: Susan A. Rogers

Voice: 202-586-8997; Fax: 202-586-1600; E-mail: Susan.Rogers@ee.doe.gov

ORNL Program Manager: Mitch Olszewski

Voice: 865-946-1350; Fax: 865-946-1262; E-mail: olszewskam@ornl.gov

Objectives

The intent of this project is to produce an integrated motor and inverter with special heat transfer paths that promote and improve operation at high power density in a high-temperature environment. It is intended to apply thermoelectric (TE) device innovations to form temperature-controlled islands within the system. These temperature islands will allow high- and low-temperature devices to function side by side, for example, high-temperature silicon carbide (SiC) power electronics in close proximity with silicon electronics and film capacitors.

Silicon-based electronics need their core temperature to be controlled at or below 125°C, and polypropylene capacitors operate best at or below 85°C. SiC components are being tested at temperatures above 300°C, so there is a strong application of the temperature-controlled island concept with this combination of components.

Approach

The first task was to perform literature research on TEs, evaluate what devices were commercially available, and compare different devices to see which devices would be most applicable to our intended applications. It would be important as well to evaluate what new devices are emerging on the market or under development in order to augment or redirect design ideas for an integrated motor and inverter.

Oak Ridge National Laboratory (ORNL) would then procure TE devices that best fit the design ideas, as well as film capacitors, to aid in conceptualizing an integrated motor/inverter traction drive for building and testing the following year.

Major Accomplishments

The TE research that was performed was used to produce a comparison chart of commercially available TE devices. Many manufacturers' products were evaluated, and the data have been pulled together for comparison of costs and capabilities. Informative results were obtained that provide good insight into how the available TEs perform and how some emerging TE technologies are improving performance in some helpful areas.

A motor type was chosen to provide a tangible basis for design concepts and packaging innovations. The design chosen was a commercially available General Electric 5-kW induction motor.

Physical packaging design ideas were introduced and developed. These ideas resulted in the concept of the layered SiC/TE packaging that allows silicon electronics and film capacitors to be packaged closely with the SiC. This idea utilizes TEs to keep the silicon and film capacitors cool while allowing the SiC to operate at much higher ambient temperatures.

The higher operational temperature environment enabled by this technology provides a pathway for the possibility of air cooling the entire traction drive system. The primary problems involved with air cooling a high-power system are the volume required for the system-to-ambient heat sink and the typical high air flow rate. The simplicity of air cooling is an attractive option for traction drives if the volume can be kept to a minimum, and the higher operating temperatures that can be used with SiC power devices promotes reduced volume with reasonable air flow quantities.

Technical Discussion

Thermoelectric Comparison Chart

TEs were researched extensively, looking at ongoing development, commercially available components, and emerging products or near-market technologies. The results of this research are tabulated in a spreadsheet to provide a quick means of comparing sizes, costs, heat flux, etc., for the devices. It was interesting to find that essentially all of the commercially available TE products are produced using bismuth-telluride junctions; the only differences between the products seem to be packaging shapes, thickness, bonding methods, etc. The packaging and bonding methods seem to be where the near-term innovations will be found. These parameters are the controlling factors in TE temperature limitation. Packaging and thickness seem to be the parameters that are being studied and improved to provide better efficiencies for the devices. Heat losses in TE packaging are major contributors to their low coefficient of performance (COP).

See Table 1 for an abbreviated list of manufacturers and key parameters of the TE devices. A more exhaustive list of TE devices presently available on the market is presented in Appendix A.

Emerging TE Devices

Thin film devices are an emerging technology, with products such as the MicroPelt® Peltier Coolers coming onto the market this year. The manufacturing technology for thin film TE devices, based on methods used in the semiconductor industry, produces very small and thin discrete devices. MicroPelt® device thickness is on the order of 0.4 mm. The conventional devices are thicker (such as the Advanced Thermoelectrics devices) and are built up using subcomponents with solder joints connecting the layers together, producing devices that are 2–3 mm thick. The thin film devices ORNL has evaluated are very expensive at first glance, but as a result of a much higher heat flux capability than the conventional bismuth-telluride devices, thicker, the relative price to handle a certain heat load looks much better. When cost is normalized to their ability to remove heat (i.e., dollars per unit of heat flux), the new thin-film devices are actually the cheapest devices on the market. This cost comparison is highlighted in Table 2. If the physical configuration of these can be adapted to match the application, then the thin film devices are a good cost-effective candidate for near-term development of temperature-controlled islands that can be used in our motor and inverter integration concept. With another year or two of maturity, and assuming reasonable manufacturing quantities, the cost of these devices is expected to drop much lower than the present prices.

Motor and Inverter Integration Concepts

The motor chosen earlier this fiscal year was a 5-kW induction motor (General Electric model # 5KE184AC105) that provided an easy platform for procurement, laboratory handling, and measuring/modeling. The motor model developed from this physical motor served as a productive tool for developing the SiC/TE/silicon/film capacitor layering design. It is not necessarily suggested that an induction motor is the motor of choice; this motor was simply chosen for expediency at this stage of the

Table 1. TE device manufacturer comparison data

Advanced Thermoelectrics	ST-127-1 4-6 0	25.00	40.00	40.00	4.20	3.50	71.00	8.48	150.00	97.86
	ST-127-1 4-8 5	25.00	40.00	40.00	3.95	5.00	72.00	12.66	150.00	95.60
ADV Engineering	A-TM-S 5-127-1 4	25.00	40.00	40.00	3.70	4.50	72.00	12.16	150.00	
ALTEC	Altec-CM-1-S-IE -127-2 6x2 D-1 15	27.00	40.00	40.00	4.70	9.38	70.00	19.95	150.00	
BMCE	TEC1-161 1ST125	27.00	40.00	40.00	3.00	11.78	60.00	39.25	150.00	
Custom Thermoelectric	12711-4L31-09R1	50.00	40.00	40.00	3.80	4.69	68.00	12.35	150.00	
Fardis	TM1-12740B5	25.00	40.00	40.00	3.40	4.50	71.00	13.24	150.00	
Ferrotec (Thin Film)	9502X065X018MP		11.20	12.10	1.79	5.31	65.00	29.65	135.00	
INB Products	intOT-1 2	27.00	40.00	40.00	3.60	7.19	69.00	19.97	150.00	\$3.90
	intOT-1 15	27.00	40.00	40.00	3.40	7.50	69.00	22.06	150.00	\$3.73
	intOT-1 05	27.00	40.00	40.00	3.30	8.19	69.00	24.31	150.00	\$3.42
	intOT-0 8	27.00	40.00	40.00	3.20	10.75	69.00	33.59	150.00	\$2.60
INTERM	TECB-32-110- [24 7.25-400]-62-69	25.00	62.00	62.00	4.80	10.41	69.00	21.69		
Marlow	OT12-8	27.00	40.00	40.00	4.01	3.38	66.00	8.42	150.00	UA
	OT12-9	27.00	40.00	40.00	3.63	4.44	66.00	12.57	150.00	UA
Melsar	HTB-12-40	26.00	44.00	40.00	3.30	4.09	63.00	12.40	225.00	\$5.69
	CP 2-127-10L	26.00	62.00	62.00	6.60	2.01	68.00	3.69	80.00	\$20.79
	CP 2-127-06L	26.00	62.00	62.00	4.60	3.12	67.00	6.79	80.00	\$12.63
	CP 6-31-06L	26.00	65.00	65.00	4.90	4.13	67.00	8.43	80.00	UA
Micropet (Thin Film)	MPC-C901-M44	25.00	0.72	0.72	0.43	42.05	22.80	982.53	85.00	90.68
	MPC-C901-M44	25.00	4.80	4.80	0.43	62.93	21.90	1463.58		
TE Technologies	HT-199-1 4-0 8	27.00	40.00	40.00	3.20	10.75	67.00	33.59	150.00	\$2.95
	HT-199-1 4-1 15	27.00	40.00	40.00	3.40	7.50	69.00	22.06	150.00	\$3.63
	HT-199-1 4-1 5	27.00	40.00	40.00	3.30	5.88	70.00	15.06	150.00	\$4.26
	HP-199-1 4-1 15	25.00	40.00	40.00	3.60	7.50	69.00	20.83	80.00	\$2.65
	HP-199-1 4-1 05	25.00	40.00	40.00	3.50	8.19	69.00	23.38	80.00	\$3.00

Table 2. TE comparisons showing normalized cost per unit of heat flux

Manufacturer	Qmax W/cm ²	Delta Tmax C	Price/cm ²	Price/(W/cm ²)
Advanced Thermoelectrics	5.00	72.00	\$1.24	\$5.60
INB Products	10.75	69.00	\$1.75	\$2.60
Marlow	4.44	66.00	UA	UA
Melcor - (high temperature series)	4.09	63.00	\$1.32	\$5.68
Micropelt (Thin Film)	60.00	31.90	\$3,495.84	\$0.62
TE Technologies (high temperature series)	10.75	67.00	\$1.98	\$2.95
Tellurex	4.09	79.00	\$1.22	\$5.26

conceptual development (better availability, easier handling and testing, etc.). Permanent magnet motors are an equally acceptable candidate for this concept and are typically the preferred traction motor in most HEV developments. Scalability of the concept is not expected to be an issue when designing for larger motors (50- to 100-kW capacity).

The primary concept was developed based on the motor platform, film capacitor shaping, and TE in an attempt to provide very tight integration of the inverter into the motor. Figure 1 shows a cutaway isometric view of the motor concept. This motor concept is based on SiC power electronics and an air-

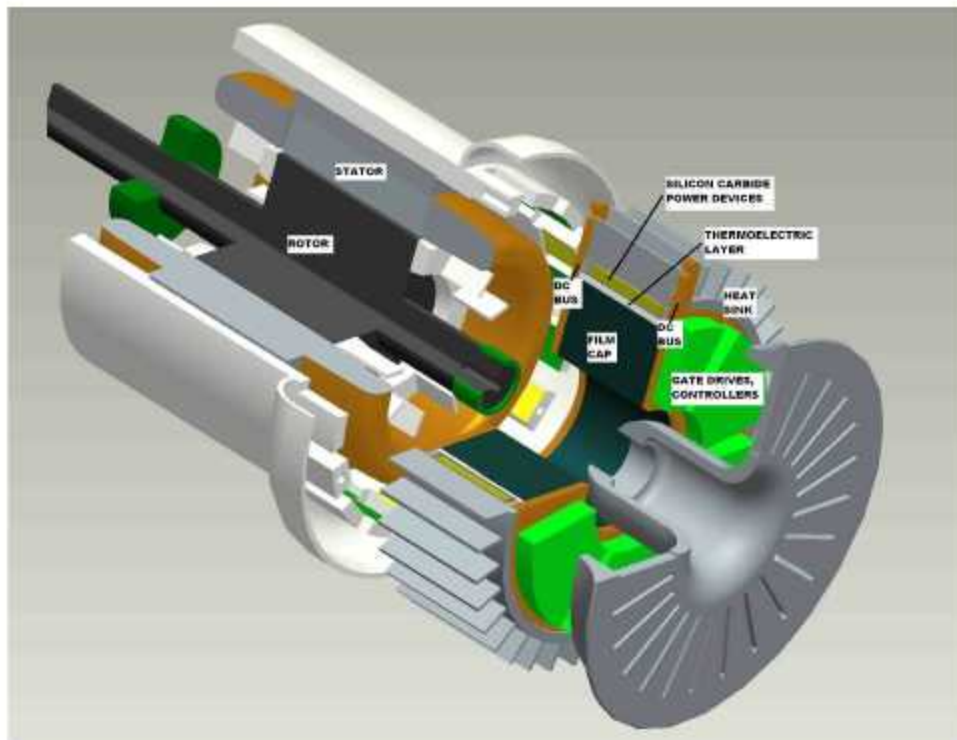


Figure 1. Cutaway view of integrated motor and inverter utilizing silicon carbide power electronics, thermoelectric temperature boundaries, silicon electronics and film capacitors.

cooled motor and inverter housing. The inverter is attached to the end of the motor casing. Although packaging the inverter into the end of the motor is not necessarily a new idea, the TE application enables much tighter packaging than before and promotes air cooling through the use of high-temperature SiC.

Figure 2 shows a view of the power electronics section of the motor concept design. This proposed arrangement shows heat flow paths from the various components in the system, in which the components that need to remain cooler are embedded in and surrounded by the warmer motor environment. The white band wrapped around the lower side of the SiC power electronics (yellow) represents the TE temperature control boundary that protects the silicon and film capacitor from the very hot SiC. The lower perimeter of these components is protected from the warmer motor environment using passive insulation techniques. The reason that passive insulation is not used on the top perimeter of these components is the need to promote heat flow up and out of their core (i.e., the "cool zone"); in other words, the capacitor and control electronics produce some minimal heat. The heat removal for the capacitor and controls can only be accomplished with a heat pumping action (TEs) to draw the heat from this area and remove it through the hotter zone.

There can be several arrangements of electronics in this situation, and this is one embodiment of the concept. The main point to be made is that as integration increases, there is an increased likelihood that components with incompatible heat capacities will be adjacent to each other. This method of integration requires a small amount of power, but it can potentially greatly increase the power density of the traction drive while simultaneously enabling air cooling for the whole system.

The simplicity of air cooling is a desirable characteristic for vehicle traction drive cooling because it offers a continuously available low-temperature source, no problem with leaks, and no need for pumps or piping (probably only a fan and some ducting would be required). Although heat sink volume will continue to be the critical issue, an air-cooling method would allow simplification of the system and reduction of active components and weight.

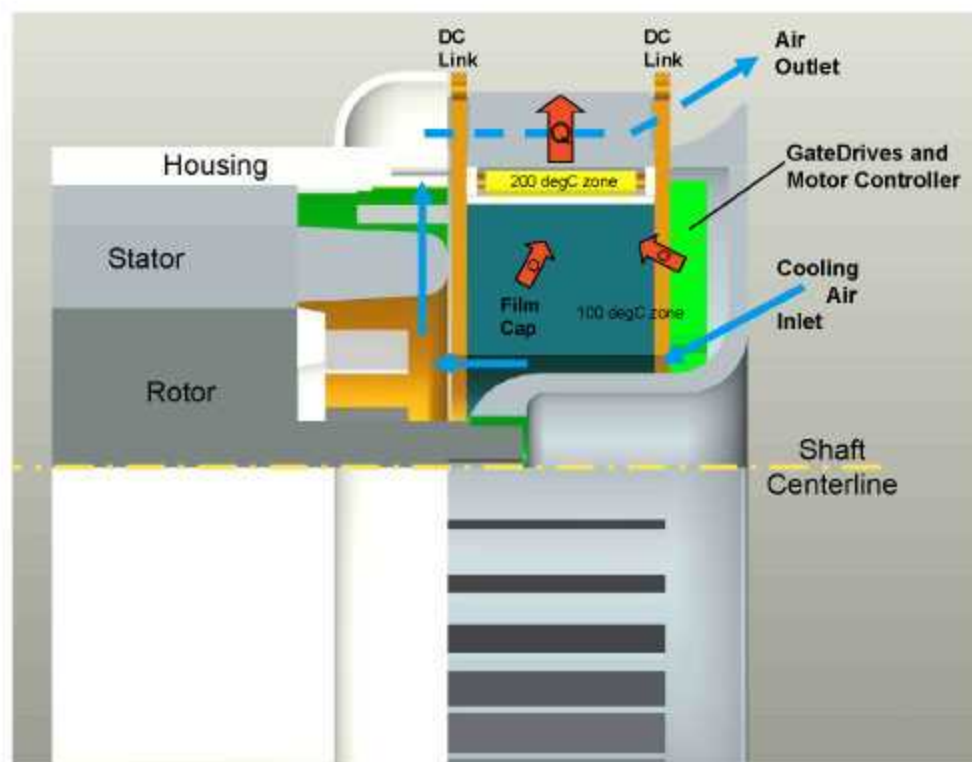


Figure 2. Motor concept section view showing detail of component arrangement and proposed heat flow path.

Thermal Mechanical Modeling of the Concept

ORNL has performed some basic thermal modeling to validate several ideas:

- show air-cooling viability for the integrated package
- show feasibility of use of TEs in relation to system COP
- evaluate temperature profiles throughout the layers to indicate if the packaging/layering concept allows reasonable temperatures in the cold zone and at the TE interfaces

Mechanical models developed with ProEngineer Wildfire software have been thermally analyzed using ProEngineer Mechanical finite element software. Figure 3 shows the mechanical model produced in Wildfire, exploded and labeled to show the subcomponents of the assembly. The primary subcomponents, starting at the bottom of the assembly, are (1) the cold-zone components (silicon-based gate drivers, digital signal processor controller, and film capacitor), (2) the thermoelectric device layer, and (3) the SiC power electronics devices. This design was modeled using the specific material properties for each layer or component, and the heat generated in each section was calculated and input into the software. Using data acquired from research on the TE devices, power consumption for the TE boundary layer was calculated and used as input into the thermal model (i.e., the losses that are incurred in the TE devices as a result of their inefficiencies). Also, based on TE research, it was established that the TE boundary layer can maintain certain temperature differences at corresponding heat flux values. Based on these findings, temperature boundary constraints were established for the upper and lower surfaces of the TE boundary. The TE device itself was not modeled in detail but is basically assumed to control upper and lower surface temperature, generate a certain amount of internal heat, and provide a conduit for the heat flux coming from the lower components.

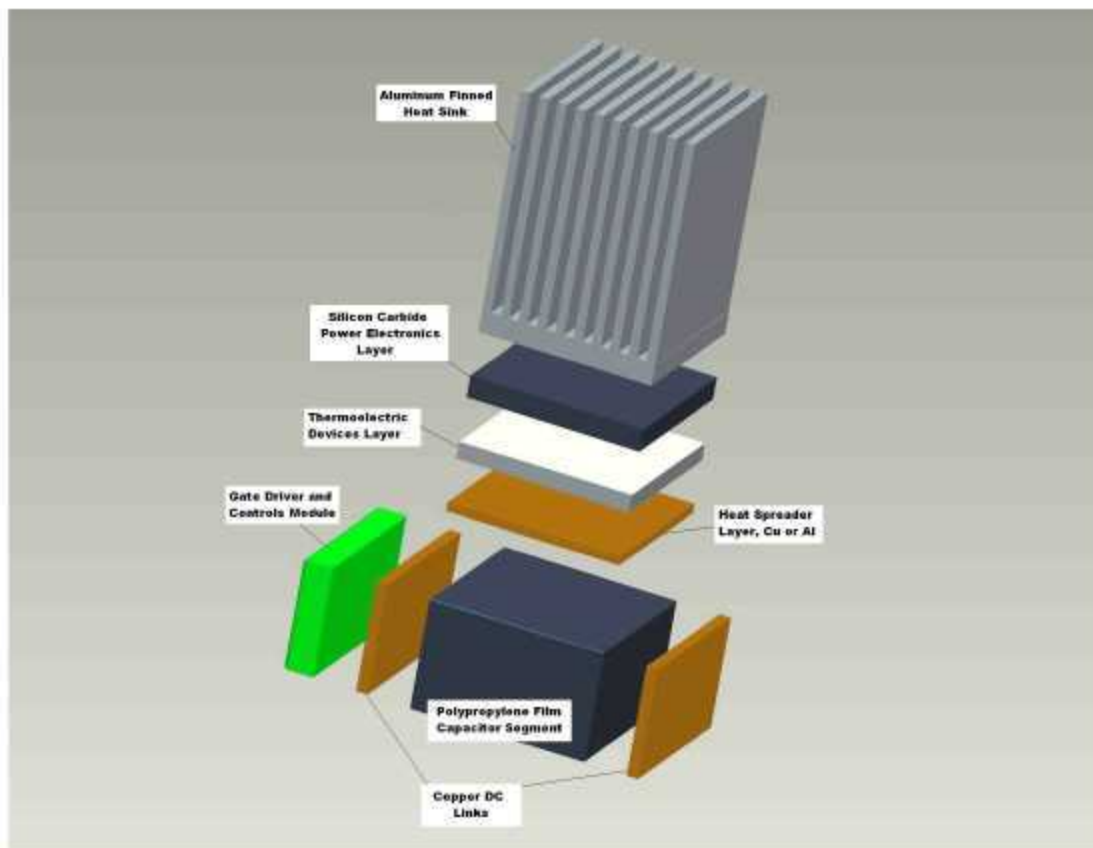


Figure 3. Exploded view of ProEngineer mechanical model used to analyze the thermal performance of the ORNL SiC-TE motor/inverter integration concept.

The model constraints and assumptions are listed in Table 3. Volumetric heat generation values were calculated for potted-module style components such as gate drivers, digital signal processors, and SiC power sections, based on estimated heat losses and their approximate sizes and shapes. The modeling was performed in three stages with two simplified models of upper and lower sections and a third model as an entire cross-section of the concept. This was done to provide a validation of how the TE device interacts with the system without having to actually model the internal conditions of the TE itself—in other words, to treat the TE as a black box.

Table 3. Thermal model calculations and assumptions

Subcomponent description	Constraint	Material
Gate drive and controller module	280,000 W/m ³	Thermal potting mixture
Film capacitor	5,000 W/m ³	Polypropylene
Silicon carbide power electronics	750,000 W/m ³	Thermal potting mixture
TE boundary layer	5.2 W	Ceramic (approximation)
TE cold surface	100°C	—
TE hot surface	200°C	—
Ambient temperature	120°C	—
Heat transfer coefficient	100 W/m ² K	—
DC links	—	Copper

The first thermal model (shown in Figure 4) is made up of the cold zone components, configured in the way the laboratory model was designed, and is used to evaluate heat flows and temperature distribution in the lower section. The copper dc links for the inverter design make up two sides of the model, sandwiching the film capacitor block in between. This design places the electronics, that is, digital

First Model - Lower Section: Assumes TE keeps top surface at 100 C

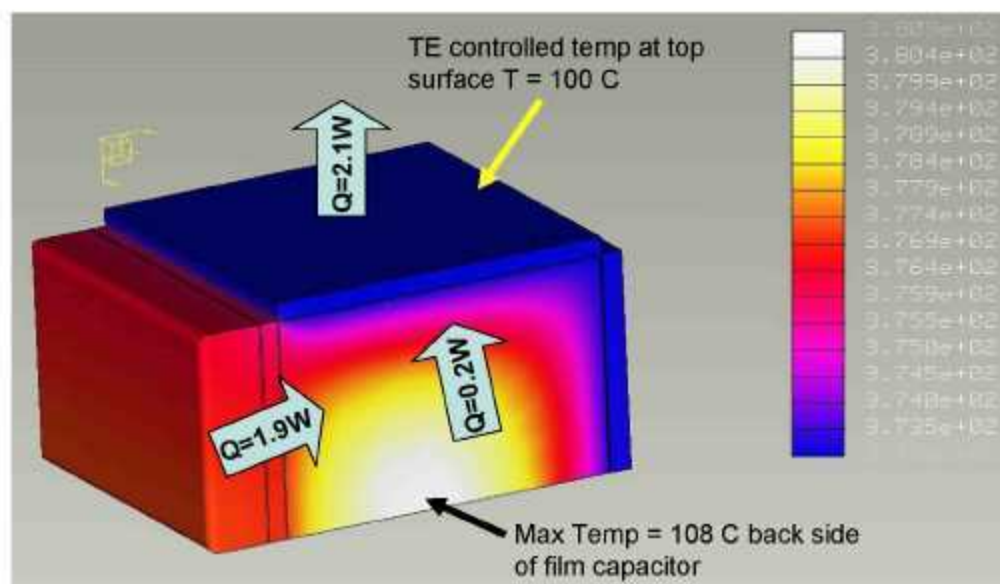


Figure 4. First model analyzed showing the “cold zone” heat flows—the top layer (just a copper heat spreader) interfaces with the rest of the system through the TE layer (not in this model). The silicon electronics are shown on the lower left and the film capacitor cross-section is the major component in the lower middle portion. This model shows temperature distribution for these estimated heat flows.

signal processor controller and gate drivers, on the outside of one of the dc links (left side). Heat in this zone is generated in the silicon electronics section (about 1.9 W) and in the film capacitor (lower middle, about 0.2 W). The constraints in this model consist of insulation all around the unit, except on the top surface, which removes a total heat flux of 2.1 W (up through the TE “black box” device, next layer). The specifications for these subcomponents can be found in Table 3. The TE device is not needed in this model and is omitted to keep the analysis simple.

The second model seen in Figure 5 was developed to look at heat flow and temperature for the upper or “hot zone” components. This unit includes the SiC power device module and a finned heat sink to transfer heat to the ambient air. The constraints for this model consist of (1) heat flux entering the bottom surface (lower section’s heat plus TE device losses) of 7.3 W, (2) SiC module losses of 7.1 W, and (3) insulation all around except for the finned heat sink surfaces. The heat sink surfaces are given a heat transfer coefficient of $100 \text{ W/m}^2\text{K}$; for a fourth condition, the ambient air temperature is set at 120°C for these analyses. The TE device is not included in this model segment for simplicity.

The third model (Figure 6) represents the entire cross-section of the SiC/silicon/film cap layering concept. The TE device is included in this model, but is represented by a “black box” with boundary constraints. Except for the addition of the TE device, this model is basically made up of Model 1 and Model 2. The boundary constraints for these two models are included as required with the addition of the TE device. The results from this thermal model closely match the results from the first two models, in temperature distribution and maximum temperatures seen at critical parts of the system, and these results provide good validation for the total system model. In future work, this model can be used to perform “what-if” cases for different designs or other concepts.

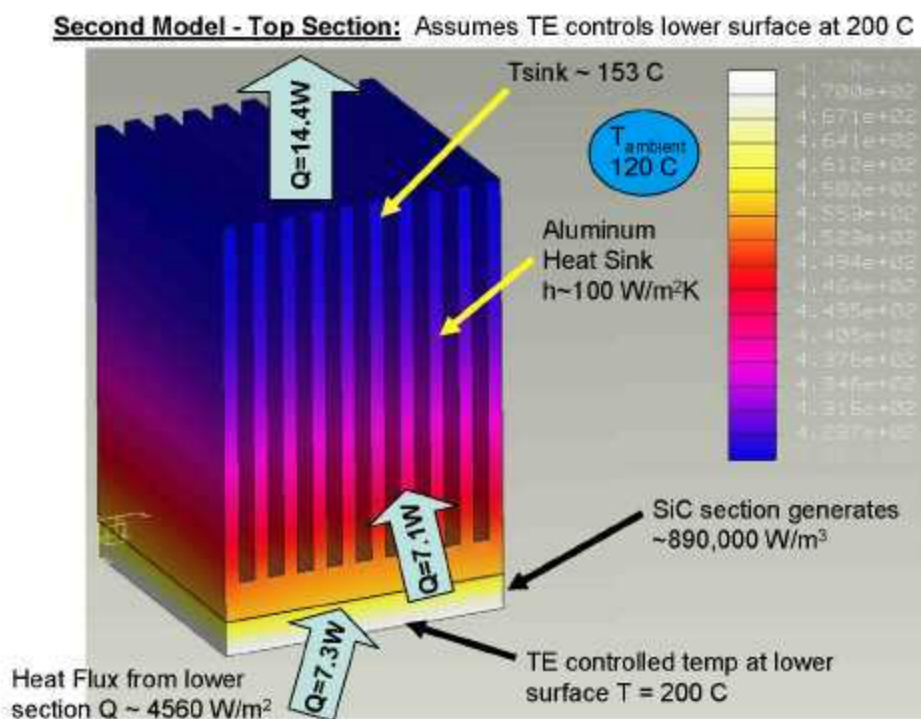


Figure 5. Second model showing the “hot zone” heat flows. The lower surface (SiC section) rests on top of the TE device. The heat from the SiC and the lower section moves upward to the heat sink and then to ambient. This model shows the temperature distribution for the upper section using the heat generated in the SiC and the heat flux from the lower section (Model 1).

Third Model - Total Assembly: Assumes TE holds its upper surface at 200 °C and its lower surface at 100 °C, and generates 5.2 W (for this segment)

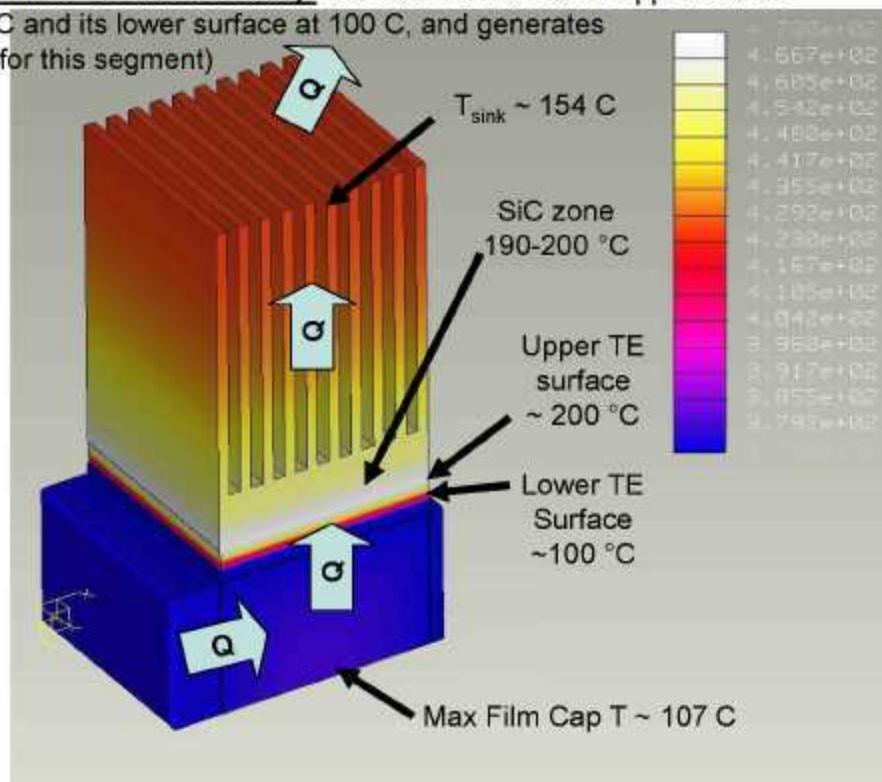


Figure 6. This third model shows the whole assembly where Model 1 and Model 2 structures are basically joined together using the TE boundary layer. This more complex model (with assumptions about the TE boundary layer) is validated by observing the temperature profile and seeing a close match with the system temperatures in Models 1 and 2.

TEs in general are found to have a relatively low heat flux carrying capability and in single layers have a limited temperature rise/drop capability across their boundaries. The low heat flux (i.e., ~5–10 W/cm²) capability makes them unsuitable for use directly to remove heat from conventional power electronics, which require on the order of 50–100 W/cm² in conventional inverter designs. It was originally desired to produce a concept where power electronics were cooled directly as needed in a high-integration design, but the heat flux numbers proved to be too small for this idea. Thin film TE devices are rapidly approaching the required heat flux numbers, however, and in the near future may be suitable to be incorporated into various applications of direct power electronics high flux cooling with reasonable efficiencies.

This understanding of TE heat flux limitations influenced the design ideas that were evaluated during this project. The main result of that has been the development of the concept of temperature-controlled islands that allow silicon electronics and film capacitors to be used in close proximity with SiC power electronics. In this design scenario, the SiC power electronics can be allowed to operate at much higher than conventional temperatures (>200°C), which makes the use of air cooling much more viable (reasonable heat sink size would then be possible). What limits the use of high-temperature SiC in a tightly integrated motor drive is the relatively low-temperature environment required for the silicon control electronics and dc filtering capacitors. These devices need an environment much closer to 80–90°C. Figure 7 depicts a basic layout of the integration concept and shows how the TE layers provide a lower-temperature island to protect the silicon and film capacitor. This lower-temperature island allows

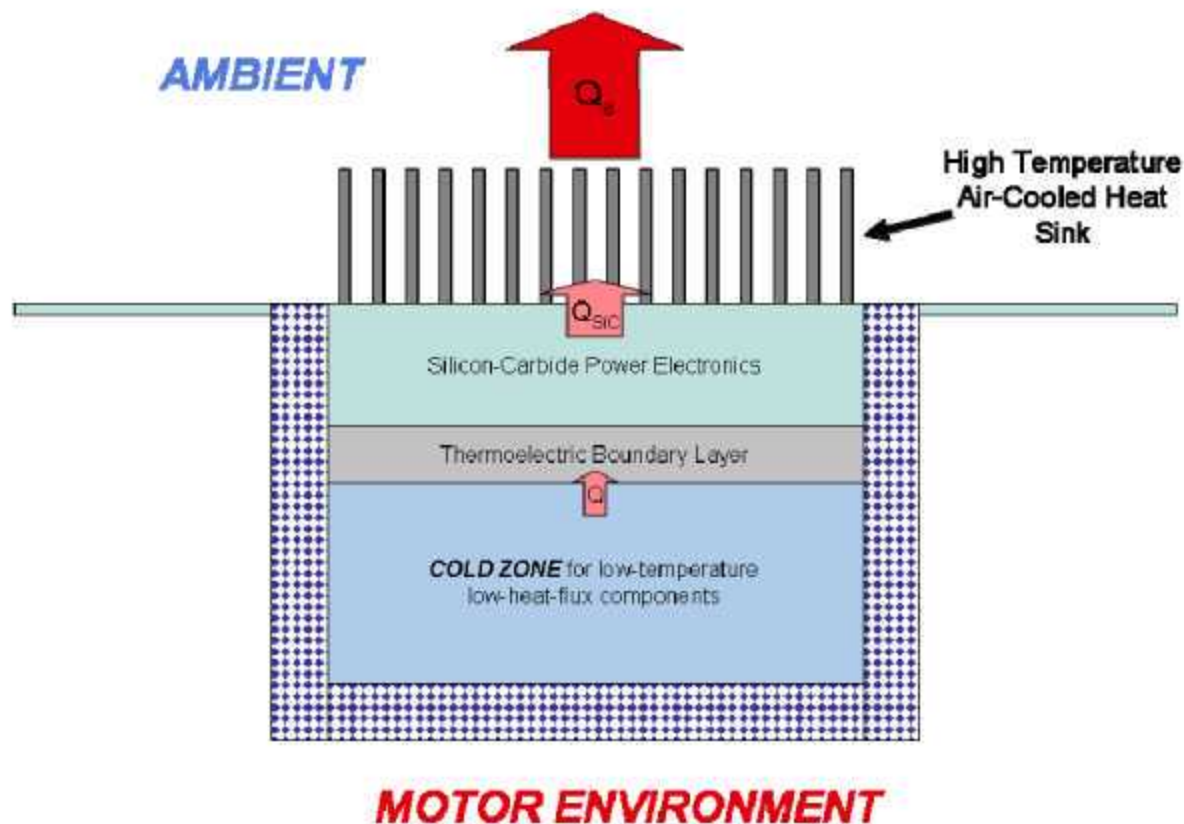


Figure 7. Cold zone produced by TE layer. Cold zone components are protected from high-temperature SiC and motor zones by the heat pumping action of the TEs.

for improved reliability, better utilization of the silicon and much reduced volume/weight for the film capacitor.

Although the heat flux is low, the internal heat must be removed from the silicon electronics and film capacitor(s). Otherwise, the internal temperature of these components will rise to excessive levels and result in failure. This packaging concept requires that this heat energy be transferred out to the ambient zone by traveling through a higher-temperature zone. Because this is against the natural flow of heat, the TEs are used to provide a heat pumping action to remove the energy from the cold zone (80–90°C) out through the hot zone (>200°C).

Thermoelectric Performance and Multilayer Benefits Modeling:

Because of the high heat flux capabilities of the Micropelt TE devices and the project initiative to perform analysis on the most advanced thermoelectric technology, a model of this device was constructed using Matlab. The model is based on data provided by the manufacturer specifications and consists of analysis of the cooling capability of the device in relation to temperature and input current. This provides a COP relationship to temperature and cooling capability per TE device.

The requirements to maintain the silicon control devices and dc filtering capacitors at or below 100°C and to allow the SiC to reach temperatures exceeding 150°C produce temperature gradients in excess of 50°C. This condition necessitated the use of a multilayer strategy as seen in Figure 8. Using the model developed in Matlab and combining the concept of layering, the maximum obtainable COP was determined for each load based on a particular temperature difference and a number of layers.

The analysis conducted with the Matlab model revealed that an increase in the maximum temperature difference and COP could be obtained with increased layers as seen in Figure 9. There seems to be a

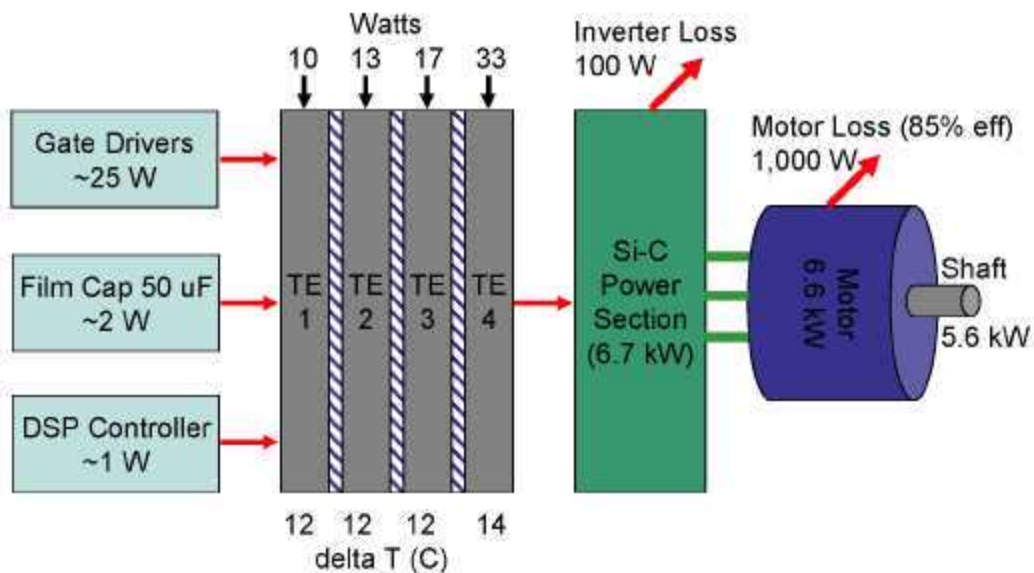


Figure 8. Power flow schematic in the SiC/TE/silicon/film capacitor integration concept.

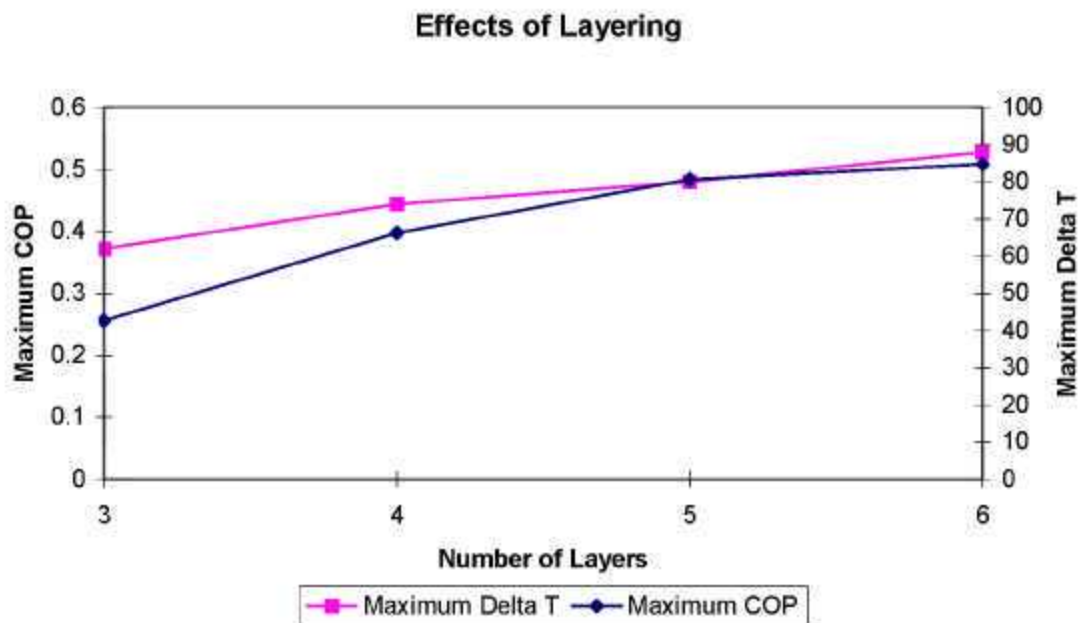


Figure 9. The effect of layering on maximum temperature difference.

diminishing return on increasing the number of layers, as seen in Figure 9, but we have limited data at this point. Continued research must be done to fully understand this phenomenon. If this is a real phenomenon, it would be of great interest to determine what part of the system causes this drop in COP/layer as the number of layers increases. Understanding this effect could direct future research and development for TE devices.

To make use of this data, a value for the heat load was necessary. For the motor assembly developed, the heat load stems from the gate drivers, dc filter capacitor, and digital signal processor controller. The gate drivers were estimated to produce a maximum of 4 W each or a total of 24 W. The DSP controller from manufacturer specifications produces a maximum of approximately 1W. The capacitor heat load is a more difficult estimate and was determined through a voltage-power factor matrix provided in Table 4. For this matrix, a 6.6-kW motor is assumed, and the inverter is expected to be operating in full-over modulation. The capacitor expected to be used in the motor assembly has a capacitance of 500 μ F and an ESR of 0.0031 at 10 kHz. From this table, the maximum heat load is approximately 2 W.

From these calculations, the final heat flux is expected to be extremely low with less than 1-W/cm² cooling requirements. Using this heat flux number and varying the temperature gradient, Table 5 was created. This table demonstrates the COP in terms of the number of layers and temperature difference.

Table 4. Capacitor power dissipation (W) due to voltage and power factor effects

Voltage	PF								
	0.6	0.65	0.7	0.75	0.8	0.85	0.9	0.95	1
130	0.193	0.296	0.685	0.998	1.254	1.466	1.644	1.795	1.923
150	0.145	0.223	0.514	0.749	0.942	1.101	1.235	1.348	1.445
170	0.113	0.173	0.400	0.583	0.733	0.857	0.961	1.050	1.125
190	0.090	0.139	0.320	0.467	0.587	0.686	0.770	0.840	0.900
210	0.074	0.114	0.262	0.382	0.481	0.562	0.630	0.688	0.737
230	0.062	0.095	0.219	0.319	0.401	0.468	0.525	0.573	0.614
250	0.052	0.080	0.185	0.270	0.339	0.396	0.445	0.485	0.520
270	0.045	0.069	0.159	0.231	0.291	0.340	0.381	0.416	0.446
290	0.039	0.060	0.138	0.200	0.252	0.295	0.330	0.361	0.387
310	0.034	0.052	0.120	0.175	0.221	0.258	0.289	0.316	0.338
330	0.030	0.046	0.106	0.155	0.195	0.228	0.255	0.279	0.298
350	0.027	0.041	0.094	0.138	0.173	0.202	0.227	0.248	0.265
370	0.024	0.037	0.085	0.123	0.155	0.181	0.203	0.222	0.237
390	0.021	0.033	0.076	0.111	0.139	0.163	0.183	0.199	0.214
410	0.019	0.030	0.069	0.100	0.126	0.147	0.165	0.180	0.193
430	0.018	0.027	0.063	0.091	0.115	0.134	0.150	0.164	0.176
450	0.016	0.025	0.057	0.083	0.105	0.122	0.137	0.150	0.161
470	0.015	0.023	0.052	0.076	0.096	0.112	0.126	0.137	0.147
490	0.014	0.021	0.048	0.070	0.088	0.103	0.116	0.126	0.135
510	0.013	0.019	0.044	0.065	0.081	0.095	0.107	0.117	0.125
530	0.012	0.018	0.041	0.060	0.075	0.088	0.099	0.108	0.116
550	0.011	0.017	0.038	0.056	0.070	0.082	0.092	0.100	0.107
570	0.010	0.015	0.036	0.052	0.065	0.076	0.086	0.093	0.100
590	0.009	0.014	0.033	0.048	0.061	0.071	0.080	0.087	0.093
610	0.009	0.013	0.031	0.045	0.057	0.067	0.075	0.082	0.087

Table 5. COP in terms of number of layers and temperature gradient

Temperature	Layers			
	3 layers	4 layers	5 layers	6 layers
50	0.049	0.075		0.111
60	0.023	0.043		0.07
70	X	0.022		0.044
80	X	X		
88	X	X	X	0.0154

Conclusions

Tighter integration of conventional electronics into a SiC based motor/traction drive, which creates thermal compatibility problems, can be aided by embedding TE layers strategically into the package. Combining SiC power electronics with conventional silicon controls and polypropylene film dc link capacitors, utilizing TE thermal control "islands," enables air cooling of the entire traction drive. The viability of air cooling is further enhanced when this concept is used in combination with higher temperature motor windings and advanced magnets.

Research indicates presently available TE maximum temperature rating/gradient and maximum heat flux are a little low. Emerging devices show great promise to make this concept highly attractive, so the project has been put on hold for the following year to evaluate these devices as they become available. Thin film TE cost on the surface appears very high, but their ability to produce high heat flux at a reasonable delta T brings the relative cost down lower than conventional TEs that do not perform as well.

Future Direction

When the project resumes, prototype models need to be built to validate the information that is being seen in the models. Further modeling needs to be performed to evaluate the entire traction drive heat removal system. Data from these models will indicate viability of air cooling of the whole system including motor/gears, SiC power electronics, silicon controls, and the dc link film capacitor.

When the technology of thin film TEs matures to a greater degree, ORNL will pursue further development of this or similar system concepts, possibly in partnership with a company such as MicroPelt®. Their work in the area of thin film devices looks very promising for the next year.

The need is to produce a geometry suitable for integration into the SiC/TE/silicon/film capacitor, using an array of devices in a flexible/conformable substrate. Multiple layering of the devices can be achieved by a coiled TE layer wrapped around the capacitor and electronics core, which can be made with a flexible circuit board containing thin film TE devices.

Three Areas Particular Interest as TEs Mature

1. Maximum temperature limitations presently are approximately 80–150°C. This temperature needs to approach 200°C and higher to make this concept most feasible.
2. Heat flux numbers with good delta T need to improve above the present ~10 W/cm² at a few degrees C delta T. The multiple layering concept helps mitigate the problem with limited delta T, but higher numbers are still needed such that a maximum of 2–3 layers can produce a total delta T of ~150–200°C.
3. Efficiency of the devices needs to improve. Thin film technology appears to be improving the COP of the TE device. This is definitely of interest and will benefit this concept, but it is not a critical path for this type of motor/inverter integration.

Publications

M. Starke, "Thermoelectrics for Cooling Power Electronics," Masters Thesis, University of Tennessee, August 2006

Patents

"Motor and Inverter Drive Design Concept Integrating Silicon Carbide Power Devices with Silicon Controls and Capacitors Utilizing Thermoelectrics," provisional patent filed July 8, 2006, with the U.S. Patent and Trademark Office.

References

1. J. Vandersande and J. Fleurial, "Thermal Management of Power Electronics using Thermoelectric Coolers," pp. 253–255 in *15th International Thermoelectrics Conference, March 1996*.
2. D. M. Rowe, *CRC Handbook of Thermoelectrics*, G. S. Nolas, J. Sharp, H. J. Goldsmid, *Thermoelectrics: Basic Principles and New Materials Developments*, Springer-Verlag Berlin Heidelberg, 2001.
3. G. W. Sutton, *Direct Energy Conversion*, McGraw-Hill, 1966.
4. D. T. Morelli, "Potential Applications of Advanced Thermoelectrics in the Automobile Industry," pp. 383–386 in *15th International Conference on Thermoelectrics, March 1996*.
5. G. Min, D. M. Rowe, and F. Volklein, "Integrated Thin Film Thermoelectric Cooler," *Electronics Letters*, **34**, p. 222–223 (January 1998).
6. H. Bottner, "Micropelt Miniaturized Thermoelectric Devices: Small Size, High Cooling Power Densities, Short Response Time," pp. 1–8 in *24th International Conference on Thermoelectrics, June 2005*.
7. H. Bottner, J. Nurnus, M. Braun, J. Wollenstein, F. Volkert, and A. Schubert, "Micropelt: State of the Art, Road Map and Applications," Infineon Technologies AG, München, Germany, 2004.
8. <http://www.illinoiscapacitor.com/techcenter/lifecalculators.asp>, Illinois Capacitor, Inc., 2006.
9. A. M. Hava, R. J. Kerkman, and T. A. Lipo, "Simple Analytical and Graphical Methods for Carrier-Based PWM-VSI Drives," *IEEE Transactions on Power Electronics*, **14**(1), 49–61 (January 1999).

Appendix A. Thermoelectric Device Manufacturer Comparison Data

MANUFACTURERS

Manufacturer	Product	Dimensions				Gmax W/cm ²	Delta Tmax C	Power Density kW/L	Max Operating Th	Price/Wcm ²
		Operating Th C	L mm	W mm	H mm					
J. Stone Company (Hong Kong)	TES1-0401A	25.00	3.40	1.80	2.40	3.59	67.00	14.98		\$2.23
	TES1-0801A	25.00	3.40	3.40	2.40	3.72	67.00	15.50		\$2.29
	TES1-1201A	25.00	5.00	3.40	2.40	3.82	67.00	15.93		\$2.35
	TES1-1801A	25.00	5.00	5.00	2.40	3.88	67.00	16.17		\$2.84
	TES1-3201A	25.00	5.60	5.60	2.40	3.95	67.00	16.45		\$3.04
	TES1-0401B	25.00	4.20	2.20	2.70	3.46	67.00	12.83		\$2.31
	TES1-0801B	25.00	4.20	4.20	2.70	3.68	67.00	13.85		\$2.31
	TES1-1201B	25.00	6.20	4.20	2.70	3.73	67.00	13.80		\$2.42
	TES1-1801B	25.00	6.20	6.20	2.70	3.80	67.00	14.07		\$2.80
	TES1-3201B	25.00	8.30	8.30	2.70	3.76	67.00	13.92		\$3.19
	TES1-0401C	25.00	2.20	4.20	2.40	4.33	67.00	18.04		\$1.85
	TES1-0801C	25.00	4.20	4.20	2.40	4.59	67.00	19.13		\$1.85
	TES1-1201C	25.00	4.20	6.20	2.40	4.65	67.00	19.36		\$1.94
	TES1-1801C	25.00	6.20	6.20	2.40	4.73	67.00	19.73		\$2.32
	TES1-3201C	25.00	8.30	8.30	2.40	4.68	67.00	19.54		\$2.56
	TES1-0402D	25.00	2.20	4.20	2.20	5.84	67.00	26.56		\$1.37
	TES1-0802D	25.00	4.23	4.20	2.20	6.08	67.00	27.83		\$1.40
	TES1-1202D	25.00	4.20	6.20	2.20	6.18	67.00	28.10		\$1.46
	TES1-1802D	25.00	6.20	6.20	2.20	6.32	67.00	28.73		\$1.74
	TES1-3202D	25.00	8.30	8.30	2.20	6.27	67.00	28.50		\$1.91
	TES1-0401E	25.00	1.80	3.40	2.40	3.59	67.00	14.98		\$2.23
	TES1-0801E	25.00	3.40	3.40	2.40	3.72	67.00	15.50		\$2.29
	TES1-1201E	25.00	3.40	5.00	2.40	3.82	67.00	15.93		\$2.35
	TES1-1801E	25.00	5.00	5.00	2.40	3.88	67.00	16.17		\$2.84
	TES1-3201E	25.00	5.60	5.60	2.40	3.95	67.00	16.45		\$3.04
	TES1-0401F	25.00	2.20	4.20	2.70	3.46	67.00	12.83		\$2.31
	TES1-0801F	25.00	4.20	4.20	2.70	3.68	67.00	13.85		\$2.31
	TES1-1201F	25.00	4.20	6.20	2.70	3.73	67.00	13.80		\$2.42
	TES1-1801F	25.00	6.20	6.20	2.70	3.80	67.00	14.07		\$2.80
	TES1-3201F	25.00	8.30	8.30	2.70	3.76	67.00	13.92		\$3.19
	TES1-0401G	25.00	2.20	4.20	2.40	4.33	67.00	18.04		\$1.85
	TES1-0801G	25.00	4.20	4.20	2.40	4.59	67.00	19.13		\$1.85
	TES1-1201G	25.00	4.20	6.20	2.40	4.65	67.00	19.36		\$1.94
	TES1-1801G	25.00	6.20	6.20	2.40	4.73	67.00	19.73		\$2.32
	TES1-3201G	25.00	8.30	8.30	2.40	4.68	67.00	19.54		\$2.56
	TES1-0402H	25.00	2.20	4.20	2.20	5.84	67.00	26.56		\$1.37
	TES1-0802H	25.00	4.20	4.20	2.20	6.12	67.00	27.83		\$1.39
	TES1-1202H	25.00	4.20	6.20	2.20	6.18	67.00	28.10		\$1.46
	TES1-1802H	25.00	6.20	6.20	2.20	6.32	67.00	28.73		\$1.74
	TES1-3202H	25.00	8.30	8.30	2.20	6.27	67.00	28.50		\$1.91
	TES1-3202H	25.00	6.60	13.20	2.20	4.13	67.00	18.78		
	TES1-0701I	25.00	1.80	3.40	2.40	6.21	67.00	25.87		\$1.37
	TES1-1101I	25.00	3.40	6.00	2.40	2.63	67.00	14.71		\$2.65
	TES1-1701I	25.00	3.40	5.00	2.40	5.41	67.00	22.56		\$2.03
	TES1-3101I	25.00	5.00	5.60	2.40	5.06	67.00	21.09		\$2.37
	TES1-0701J	25.00	4.20	4.20	2.40	3.23	67.00	13.46		\$2.63
	TES1-1101J	25.00	4.20	6.20	2.70	3.42	67.00	12.86		\$2.63
	TES1-1701J	25.00	6.20	6.20	2.70	3.56	67.00	13.20		\$3.09
	TES1-3101J	25.00	8.30	8.30	2.70	3.64	67.00	13.48		\$3.29
	TES1-0701K	25.00	4.20	4.20	2.70	4.02	67.00	14.91		\$2.11
	TES1-1101K	25.00	4.20	6.20	2.70	4.28	67.00	15.79		\$2.11
	TES1-1701K	25.00	6.20	6.20	2.40	4.47	67.00	16.54		\$2.46
	TES1-3101K	25.00	8.30	8.30	2.40	4.54	67.00	16.93		\$2.64
	TES1-0702L	25.00	4.20	4.20	2.20	5.39	67.00	24.45		\$1.58
	TES1-1102L	25.00	6.20	6.20	2.20	3.88	67.00	17.62		\$2.32
	TES1-1702L	25.00	6.20	6.20	2.20	5.98	67.00	27.20		\$1.84
	TES1-1702L	25.00	6.60	6.60	2.20	5.92	67.00	27.24		\$1.84
	TES1-3102L	25.00	8.30	8.30	2.20	6.07	67.00	27.54		\$1.98
	TES1-0702M	25.00	6.00	6.00	3.40	2.78	67.00	8.17		\$2.24
	TES1-1702M	25.00	12.00	9.00	3.40	2.22	67.00	6.54		\$3.60
	TES1-3102M	25.00	12.00	12.00	3.40	3.06	67.00	8.89		\$2.78
	TES1-6302M	25.00	18.00	25.00	3.40	2.00	67.00	5.88		\$5.00
	TES1-7102M	25.00	8.90	18.00	3.40	7.01	67.00	20.63		\$1.43

	TES1-0702N	25.00	12.00	8.00	4.00	1.25	67.00	3.13	\$4.80
	TES1-1702N	25.00	15.00	12.00	4.00	1.61	67.00	4.03	\$4.03
	TES1-3102N	25.00	20.00	15.00	4.00	1.77	67.00	4.42	\$3.68
	TES1-4802N	25.00	20.00	20.00	4.00	1.98	67.00	4.94	\$4.05
Advanced Thermoelectrics	ST-71-1 0-3 0	25.00	22.40	22.40	3.20	3.14	71.00	9.61	\$5.22
	ST-127-1 0-3 0	25.00	30.00	30.00	3.95	3.11	71.00	7.88	\$5.32
	ST-71-1 0-4 0	25.00	22.40	22.40	4.20	3.85	71.00	9.16	\$4.32
	ST-127-1 0-4 0	25.00	30.00	30.00	3.95	4.22	72.00	10.69	\$3.97
	ST-127-1 4-4 0	25.00	40.00	40.00	4.20	2.38	72.00	5.65	\$7.63
	ST-71-1 4-6 0	25.00	30.00	30.00	4.20	3.56	72.00	8.47	\$4.73
	ST-127-1 4-6 0	25.00	40.00	40.00	4.20	3.56	71.00	8.48	\$5.26
	ST-71-1 4-8 5	25.00	30.00	30.00	3.95	5.00	72.00	12.66	\$3.62
	ST-127-1 4-8 5	25.00	40.00	40.00	3.95	5.00	72.00	12.66	\$3.96
ADV Engineering (Russia)	A-TM 85-127-1 4	40.00	40.00	3.70	4.50	72.00	12.16	150.00	
	A-TM 60-127-1 4	40.00	40.00	4.20	3.31	72.00	7.89	150.00	
	A-TM 35-127-1 4	40.00	40.00	5.10	3.31	73.00	6.50	150.00	
	A-TM 35-127-1 0	30.00	30.00	3.90	3.78	71.00	9.69	150.00	
	A-TM 37 5-49-3 0	40.00	40.00	4.30	8.13	71.00	16.90	150.00	
	A-TM 60-31-1 4	20.00	20.00	4.20	3.13	72.00	7.44	150.00	
Amec (Ukraine)	Altec-CM-1-S-SQ-7-0 8x0 8-2 5	6.00	6.00	4.40	1.67	72.00	3.79	200.00	
	Altec-CM-1-S-SQ-17-0 8x0 8-2 5	9.00	9.00	4.00	1.65	72.00	0.42	200.00	
	Altec-CM-1-S-SQ-31-0 8x0 8-2 5	12.00	12.00	4.40	1.88	72.00	4.26	200.00	
	Altec-CM-1-S-SQ-63-0 8x0 8-2 5	12.00	24.00	4.40	1.88	72.00	4.26	200.00	
	Altec-CM-1-S-SQ-71-0 8x0 8-2 5	18.00	18.00	4.40	1.88	72.00	4.26	200.00	
	Altec-CM-1-S-SQ-127-0 8x0 8-2 5	24.00	24.00	4.40	1.91	72.00	4.34	200.00	
	Altec-CM-1-S-SQ-7-0 8x0 8-2 0	6.00	6.00	3.90	1.94	71.00	4.99	200.00	
	Altec-CM-1-S-SQ-17-0 8x0 8-2 0	9.00	9.00	3.90	2.22	71.00	5.70	200.00	
	Altec-CM-1-S-SQ-31-0 8x0 8-2 0	12.00	12.00	3.90	2.28	71.00	5.88	200.00	
	Altec-CM-1-S-SQ-63-0 8x0 8-2 0	12.00	24.00	3.90	2.33	71.00	5.97	200.00	
	Altec-CM-1-S-SQ-71-0 8x0 8-2 0	18.00	18.00	3.90	2.35	71.00	6.01	200.00	
	Altec-CM-1-S-SQ-127-0 8x0 8-2 0	24.00	24.00	3.90	2.34	71.00	6.01	200.00	
	Altec-CM-1-S-SQ-7-0 8x0 8-1 5	6.00	6.00	3.40	2.78	70.00	8.17	200.00	
	Altec-CM-1-S-SQ-17-0 8x0 8-1 5	9.00	9.00	3.40	2.96	70.00	8.71	200.00	
	Altec-CM-1-S-SQ-31-0 8x0 8-1 5	12.00	12.00	3.40	2.99	70.00	8.78	200.00	
	Altec-CM-1-S-SQ-63-0 8x0 8-1 5	12.00	24.00	3.40	3.06	70.00	8.99	200.00	
	Altec-CM-1-S-SQ-71-0 8x0 8-1 5	18.00	18.00	3.40	3.16	70.00	9.40	200.00	
	Altec-CM-1-S-SQ-127-0 8x0 8-1 5	24.00	24.00	3.40	3.09	70.00	9.09	200.00	
	Altec-CM-1-S-SQ-7-0 8x0 8-1 3	6.00	6.00	3.20	3.06	69.00	9.55	200.00	
	Altec-CM-1-S-SQ-17-0 8x0 8-1 3	9.00	9.00	3.20	3.33	69.00	10.42	200.00	
	Altec-CM-1-S-SQ-31-0 8x0 8-1 3	12.00	12.00	3.20	3.40	69.00	10.63	200.00	
	Altec-CM-1-S-SQ-63-0 8x0 8-1 3	12.00	24.00	3.20	3.47	69.00	10.85	200.00	
	Altec-CM-1-S-SQ-71-0 8x0 8-1 3	18.00	18.00	3.20	3.49	69.00	10.90	200.00	
	Altec-CM-1-S-SQ-127-0 8x0 8-1 3	24.00	24.00	3.20	3.51	69.00	10.96	200.00	
	Altec-CM-1-S-SQ-7-0 8x0 8-1 15	6.00	6.00	3.10	3.61	68.00	11.65	200.00	
	Altec-CM-1-S-SQ-17-0 8x0 8-1 15	9.00	9.00	3.10	3.70	68.00	11.95	200.00	
	Altec-CM-1-S-SQ-31-0 8x0 8-1 15	12.00	12.00	3.10	3.82	68.00	12.32	200.00	
	Altec-CM-1-S-SQ-63-0 8x0 8-1 15	12.00	24.00	3.10	3.89	68.00	12.54	200.00	
	Altec-CM-1-S-SQ-71-0 8x0 8-1 15	18.00	18.00	3.10	3.88	68.00	12.54	200.00	
	Altec-CM-1-S-SQ-127-0 8x0 8-1 15	24.00	24.00	3.10	3.91	68.00	12.60	200.00	
	Altec-CM-1-S-SQ-7-1 0x1 0-2 5	8.00	8.00	4.50	1.41	72.00	3.13	200.00	
	Altec-CM-1-S-SQ-17-1 0x1 0-2 5	12.00	12.00	4.50	1.53	72.00	3.40	200.00	
	Altec-CM-1-S-SQ-31-1 0x1 0-2 5	15.00	15.00	4.50	1.78	72.00	3.95	200.00	
	Altec-CM-1-S-SQ-63-1 0x1 0-2 5	15.00	30.00	4.50	1.82	72.00	4.05	200.00	
	Altec-CM-1-S-SQ-71-1 0x1 0-2 5	23.00	23.00	4.50	1.74	72.00	3.86	200.00	
	Altec-CM-1-S-SQ-127-1 0x1 0-2 5	30.00	30.00	4.50	1.83	72.00	4.07	200.00	
	Altec-CM-1-S-SQ-7-1 0x1 0-2 0	8.00	8.00	4.00	1.72	71.00	4.30	200.00	
	Altec-CM-1-S-SQ-17-1 0x1 0-2 0	12.00	12.00	4.00	1.88	71.00	4.69	200.00	
	Altec-CM-1-S-SQ-31-1 0x1 0-2 0	15.00	15.00	4.00	2.22	71.00	5.56	200.00	
	Altec-CM-1-S-SQ-63-1 0x1 0-2 0	15.00	30.00	4.00	2.24	71.00	5.61	200.00	
	Altec-CM-1-S-SQ-71-1 0x1 0-2 0	23.00	23.00	4.00	2.16	71.00	5.39	200.00	
	Altec-CM-1-S-SQ-127-1 0x1 0-2 0	30.00	30.00	4.00	2.27	71.00	5.67	200.00	
	Altec-CM-1-S-SQ-7-1 0x1 0-1 5	8.00	8.00	3.50	2.34	70.00	6.70	200.00	
	Altec-CM-1-S-SQ-17-1 0x1 0-1 5	12.00	12.00	3.50	2.50	70.00	7.14	200.00	
	Altec-CM-1-S-SQ-31-1 0x1 0-1 5	15.00	15.00	3.50	2.68	70.00	8.26	200.00	
	Altec-CM-1-S-SQ-63-1 0x1 0-1 5	15.00	30.00	3.50	2.96	70.00	8.44	200.00	

Altec-CM-1-S-SQ-71-1 0x1 0-1 5	23 00	23 00	3 50	2 84	70 00	8 10	200 00
Altec-CM-1-S-SQ-127-1 0x1 0-1 5	30 00	30 00	3 50	2 98	70 00	8 51	200 00
Altec-CM-1-S-SQ-71-1 0x1 0-1 3	8 00	8 00	3 30	2 66	69 00	8 06	200 00
Altec-CM-1-S-SQ-17-1 0x1 0-1 3	12 00	12 00	3 30	2 85	69 00	8 83	200 00
Altec-CM-1-S-SQ-31-1 0x1 0-1 3	15 00	15 00	3 30	3 33	69 00	10 10	200 00
Altec-CM-1-S-SQ-63-1 0x1 0-1 3	15 00	30 00	3 30	3 40	69 00	10 30	200 00
Altec-CM-1-S-SQ-71-1 0x1 0-1 3	23 00	23 00	3 30	3 25	69 00	9 85	200 00
Altec-CM-1-S-SQ-127-1 0x1 0-1 3	30 00	30 00	3 30	3 42	69 00	10 37	200 00
Altec-CM-1-S-SQ-71-1 0x1 0-1 15	8 00	8 00	3 20	2 97	68 00	9 28	200 00
Altec-CM-1-S-SQ-17-1 0x1 0-1 15	12 00	12 00	3 20	3 13	68 00	9 77	200 00
Altec-CM-1-S-SQ-31-1 0x1 0-1 15	15 00	15 00	3 20	3 64	68 00	11 39	200 00
Altec-CM-1-S-SQ-63-1 0x1 0-1 15	15 00	30 00	3 20	3 73	68 00	11 67	200 00
Altec-CM-1-S-SQ-71-1 0x1 0-1 15	23 00	23 00	3 20	3 67	68 00	11 16	200 00
Altec-CM-1-S-SQ-127-1 0x1 0-1 15	30 00	30 00	3 20	3 76	68 00	11 74	200 00
Altec-CM-1-S-SQ-71-1 0x1 0-2 5	8 00	8 00	4 50	1 41	72 00	3 13	200 00
Altec-CM-1-S-SQ-17-1 0x1 0-2 5	12 00	12 00	4 50	1 53	72 00	3 40	200 00
Altec-CM-1-S-SQ-31-1 0x1 0-2 5	15 00	15 00	4 50	1 79	72 00	3 96	200 00
Altec-CM-1-S-SQ-63-1 0x1 0-2 5	15 00	30 00	4 50	1 62	72 00	4 05	200 00
Altec-CM-1-S-SQ-71-1 0x1 0-2 5	23 00	23 00	4 50	1 74	72 00	3 86	200 00
Altec-CM-1-S-SQ-127-1 0x1 0-2 5	30 00	30 00	4 50	1 83	72 00	4 07	200 00
Altec-CM-1-S-SQ-71-1 0x1 0-2 0	8 00	8 00	4 00	1 72	71 00	4 30	200 00
Altec-CM-1-S-SQ-17-1 0x1 0-2 0	12 00	12 00	4 00	1 89	71 00	4 59	200 00
Altec-CM-1-S-SQ-31-1 0x1 0-2 0	15 00	15 00	4 00	2 22	71 00	5 56	200 00
Altec-CM-1-S-SQ-63-1 0x1 0-2 0	15 00	30 00	4 00	2 24	71 00	5 51	200 00
Altec-CM-1-S-SQ-71-1 0x1 0-2 0	23 00	23 00	4 00	2 16	71 00	5 39	200 00
Altec-CM-1-S-SQ-127-1 0x1 0-2 0	30 00	30 00	4 00	2 27	71 00	5 87	200 00
Altec-CM-1-S-SQ-71-1 0x1 0-1 5	8 00	8 00	3 50	2 34	70 00	6 70	200 00
Altec-CM-1-S-SQ-17-1 0x1 0-1 5	12 00	12 00	3 50	2 50	70 00	7 14	200 00
Altec-CM-1-S-SQ-31-1 0x1 0-1 5	15 00	15 00	3 50	2 89	70 00	8 25	200 00
Altec-CM-1-S-SQ-63-1 0x1 0-1 5	15 00	30 00	3 50	2 96	70 00	8 44	200 00
Altec-CM-1-S-SQ-71-1 0x1 0-1 5	23 00	23 00	3 50	2 84	70 00	8 10	200 00
Altec-CM-1-S-SQ-127-1 0x1 0-1 5	30 00	30 00	3 50	2 95	70 00	8 51	200 00
Altec-CM-1-S-SQ-71-1 0x1 0-1 3	8 00	8 00	3 30	2 66	69 00	8 06	200 00
Altec-CM-1-S-SQ-17-1 0x1 0-1 3	12 00	12 00	3 30	2 85	69 00	8 83	200 00
Altec-CM-1-S-SQ-31-1 0x1 0-1 3	15 00	15 00	3 30	3 33	69 00	10 10	200 00
Altec-CM-1-S-SQ-63-1 0x1 0-1 3	15 00	30 00	3 30	3 40	69 00	10 30	200 00
Altec-CM-1-S-SQ-71-1 0x1 0-1 3	23 00	23 00	3 30	3 25	69 00	9 85	200 00
Altec-CM-1-S-SQ-127-1 0x1 0-1 3	30 00	30 00	3 30	3 42	69 00	10 37	200 00
Altec-CM-1-S-SQ-71-1 0x1 0-1 15	8 00	8 00	3 20	2 97	68 00	9 28	200 00
Altec-CM-1-S-SQ-17-1 0x1 0-1 15	12 00	12 00	3 20	3 13	68 00	9 77	200 00
Altec-CM-1-S-SQ-31-1 0x1 0-1 15	15 00	15 00	3 20	3 64	68 00	11 39	200 00
Altec-CM-1-S-SQ-63-1 0x1 0-1 15	15 00	30 00	3 20	3 73	68 00	11 67	200 00
Altec-CM-1-S-SQ-71-1 0x1 0-1 15	23 00	23 00	3 20	3 57	68 00	11 16	200 00
Altec-CM-1-S-SQ-127-1 0x1 0-1 15	30 00	30 00	3 20	3 76	68 00	11 74	200 00
Altec-CM-1-S-SQ-71-1 2x1 2-2 5	8 00	8 00	4 90	2 03	72 00	4 15	200 00
Altec-CM-1-S-SQ-17-1 2x1 2-2 5	12 00	12 00	4 90	2 22	72 00	4 54	200 00
Altec-CM-1-S-SQ-31-1 2x1 2-2 5	15 00	15 00	4 90	2 58	72 00	5 26	200 00
Altec-CM-1-S-SQ-63-1 2x1 2-2 5	15 00	30 00	4 90	2 62	72 00	5 36	200 00
Altec-CM-1-S-SQ-71-1 2x1 2-2 5	23 00	23 00	4 90	2 51	72 00	5 13	200 00
Altec-CM-1-S-SQ-127-1 2x1 2-2 5	30 00	30 00	4 90	2 64	72 00	5 40	200 00
Altec-CM-1-S-SQ-71-1 2x1 2-2 0	8 00	8 00	4 40	2 50	71 00	5 68	200 00
Altec-CM-1-S-SQ-17-1 2x1 2-2 0	12 00	12 00	4 40	2 79	71 00	6 31	200 00
Altec-CM-1-S-SQ-31-1 2x1 2-2 0	15 00	15 00	4 40	3 16	71 00	7 17	200 00
Altec-CM-1-S-SQ-63-1 2x1 2-2 0	15 00	30 00	4 40	3 29	71 00	7 47	200 00
Altec-CM-1-S-SQ-71-1 2x1 2-2 0	23 00	23 00	4 40	3 16	71 00	7 17	200 00
Altec-CM-1-S-SQ-127-1 2x1 2-2 0	30 00	30 00	4 40	3 31	71 00	7 53	200 00
Altec-CM-1-S-SQ-71-1 2x1 2-1 5	8 00	8 00	3 90	3 44	70 00	8 81	200 00
Altec-CM-1-S-SQ-17-1 2x1 2-1 5	12 00	12 00	3 90	3 61	70 00	9 26	200 00
Altec-CM-1-S-SQ-31-1 2x1 2-1 5	15 00	15 00	3 90	4 27	70 00	10 94	200 00
Altec-CM-1-S-SQ-63-1 2x1 2-1 5	15 00	30 00	3 90	4 31	70 00	11 06	200 00
Altec-CM-1-S-SQ-71-1 2x1 2-1 5	23 00	23 00	3 90	4 14	70 00	10 62	200 00
Altec-CM-1-S-SQ-127-1 2x1 2-1 5	30 00	30 00	3 90	4 36	70 00	11 17	200 00
Altec-CM-1-S-SQ-71-1 2x1 2-1 3	8 00	8 00	3 70	3 91	69 00	10 56	200 00
Altec-CM-1-S-SQ-17-1 2x1 2-1 3	12 00	12 00	3 70	4 17	69 00	11 26	200 00
Altec-CM-1-S-SQ-31-1 2x1 2-1 3	15 00	15 00	3 70	4 84	69 00	13 09	200 00
Altec-CM-1-S-SQ-63-1 2x1 2-1 3	15 00	30 00	3 70	4 93	69 00	13 33	200 00
Altec-CM-1-S-SQ-71-1 2x1 2-1 3	23 00	23 00	3 70	4 74	69 00	12 82	200 00
Altec-CM-1-S-SQ-127-1 2x1 2-1 3	30 00	30 00	3 70	4 98	69 00	13 45	200 00

	Altec-CM-1-S-SQ-7-1 2x1 2-1 15	8 00	8 00	3 50	4 22	68 00	12 06	200 00
	Altec-CM-1-S-SQ-17-1 2x1 2-1 15	12 00	12 00	3 50	4 58	68 00	13 10	200 00
	Altec-CM-1-S-SQ-31-1 2x1 2-1 15	15 00	15 00	3 50	5 33	68 00	15 24	200 00
	Altec-CM-1-S-SQ-63-1 2x1 2-1 15	18 00	30 00	3 50	5 44	68 00	15 56	200 00
	Altec-CM-1-S-SQ-71-1 2x1 2-1 15	23 00	23 00	3 50	5 22	68 00	14 01	200 00
	Altec-CM-1-S-SQ-127-1 2x1 2-1 15	30 00	30 00	3 50	5 43	68 00	15 55	200 00
	Altec-CM-1-S-SQ-7-1 4x1 4-2 5	10 00	10 00	4 90	1 80	72 00	3 87	200 00
	Altec-CM-1-S-SQ-17-1 4x1 4-2 5	15 00	15 00	4 90	1 96	72 00	3 89	200 00
	Altec-CM-1-S-SQ-31-1 4x1 4-2 5	20 00	20 00	4 90	2 03	72 00	4 13	200 00
	Altec-CM-1-S-SQ-63-1 4x1 4-2 5	20 00	40 00	4 90	2 05	72 00	4 18	200 00
	Altec-CM-1-S-SQ-71-1 4x1 4-2 5	30 00	30 00	4 90	2 06	72 00	4 20	200 00
	Altec-CM-1-S-SQ-127-1 4x1 4-2 5	40 00	40 00	4 90	2 06	72 00	4 21	200 00
	Altec-CM-1-S-SQ-7-1 4x1 4-2 0	10 00	10 00	4 40	2 30	71 00	5 23	200 00
	Altec-CM-1-S-SQ-17-1 4x1 4-2 0	15 00	15 00	4 40	2 40	71 00	5 45	200 00
	Altec-CM-1-S-SQ-31-1 4x1 4-2 0	20 00	20 00	4 40	2 48	71 00	5 63	200 00
	Altec-CM-1-S-SQ-63-1 4x1 4-2 0	20 00	40 00	4 40	2 53	71 00	5 74	200 00
	Altec-CM-1-S-SQ-71-1 4x1 4-2 0	30 00	30 00	4 40	2 53	71 00	5 76	200 00
	Altec-CM-1-S-SQ-127-1 4x1 4-2 0	40 00	40 00	4 40	2 54	71 00	5 78	200 00
	Altec-CM-1-S-SQ-7-1 4x1 4-1 5	10 00	10 00	3 90	3 00	70 00	7 89	200 00
	Altec-CM-1-S-SQ-17-1 4x1 4-1 5	15 00	15 00	3 90	3 16	70 00	8 09	200 00
	Altec-CM-1-S-SQ-63-1 4x1 4-1 5	20 00	40 00	3 90	3 31	70 00	8 49	200 00
	Altec-CM-1-S-SQ-71-1 4x1 4-1 5	30 00	30 00	3 90	3 32	70 00	8 52	200 00
	Altec-CM-1-S-SQ-127-1 4x1 4-1 5	40 00	40 00	3 90	3 34	70 00	8 57	200 00
	Altec-CM-1-S-SQ-7-1 4x1 4-1 3	10 00	10 00	3 70	3 40	69 00	9 19	200 00
	Altec-CM-1-S-SQ-31-2 0x2 0-2 5	20 00	20 00	4 90	4 08	72 00	8 32	200 00
	Altec-CM-1-S-SQ-63-2 0x2 0-2 5	20 00	40 00	4 90	4 15	72 00	8 47	200 00
	Altec-CM-1-S-SQ-71-2 0x2 0-2 5	30 00	30 00	4 90	4 17	72 00	8 50	200 00
	Altec-CM-1-S-SQ-127-2 0x2 0-2 5	40 00	40 00	4 90	4 19	72 00	8 55	200 00
	Altec-CM-1-S-SQ-7-2 0x2 0-2 0	10 00	10 00	4 80	4 60	71 00	9 58	200 00
	Altec-CM-1-S-SQ-17-2 0x2 0-2 0	15 00	15 00	4 80	4 69	71 00	10 19	200 00
	Altec-CM-1-S-SQ-31-2 0x2 0-2 0	20 00	20 00	4 80	5 03	71 00	10 47	200 00
	Altec-CM-1-S-SQ-63-2 0x2 0-2 0	20 00	40 00	4 80	5 10	71 00	10 63	200 00
	Altec-CM-1-S-SQ-71-2 0x2 0-2 0	30 00	30 00	4 80	5 11	71 00	10 65	200 00
	Altec-CM-1-S-SQ-127-2 0x2 0-2 0	40 00	40 00	4 80	5 14	71 00	10 72	200 00
	Altec-CM-1-S-SQ-7-2 0x2 0-1 5	10 00	10 00	4 60	5 00	70 00	13 04	200 00
	Altec-CM-1-S-SQ-17-2 0x2 0-1 5	15 00	15 00	4 60	5 44	70 00	14 01	200 00
	Altec-CM-1-S-SQ-31-2 0x2 0-1 5	20 00	20 00	4 60	5 63	70 00	14 40	200 00
	Altec-CM-1-S-SQ-63-2 0x2 0-1 5	20 00	40 00	4 60	5 74	70 00	14 65	200 00
	Altec-CM-1-S-SQ-71-2 0x2 0-1 5	30 00	30 00	4 60	5 77	70 00	14 71	200 00
	Altec-CM-1-S-SQ-127-2 0x2 0-1 5	40 00	40 00	4 60	5 80	70 00	14 78	200 00
	Altec-CM-1-S-SQ-7-2 0x2 0-1 3	10 00	10 00	4 70	6 50	69 00	14 68	200 00
	Altec-CM-1-S-SQ-17-2 0x2 0-1 3	15 00	15 00	4 70	7 33	69 00	15 50	200 00
	Altec-CM-1-S-SQ-31-2 0x2 0-1 3	20 00	20 00	4 70	7 55	69 00	16 06	200 00
	Altec-CM-1-S-SQ-63-2 0x2 0-1 3	20 00	40 00	4 70	7 68	69 00	16 33	200 00
	Altec-CM-1-S-SQ-71-2 0x2 0-1 3	30 00	30 00	4 70	7 70	69 00	16 38	200 00
	Altec-CM-1-S-SQ-127-2 0x2 0-1 3	40 00	40 00	4 70	7 74	69 00	16 45	200 00
	Altec-CM-1-S-SQ-7-2 0x2 0-1 15	10 00	10 00	4 70	8 10	68 00	17 23	200 00
	Altec-CM-1-S-SQ-17-2 0x2 0-1 15	15 00	15 00	4 70	8 62	68 00	18 35	200 00
	Altec-CM-1-S-SQ-31-2 0x2 0-1 15	20 00	20 00	4 70	8 90	68 00	18 54	200 00
	Altec-CM-1-S-SQ-63-2 0x2 0-1 15	20 00	40 00	4 70	9 03	68 00	19 20	200 00
	Altec-CM-1-S-SQ-71-2 0x2 0-1 15	30 00	30 00	4 70	9 07	68 00	19 29	200 00
	Altec-CM-1-S-SQ-127-2 0x2 0-1 15	40 00	40 00	4 70	9 11	68 00	19 35	200 00
Custom Thermoelectrics	00901-9G30-11D	5 89	4 00	2 92	2 71	65 00	9 29	225 00
	01801-9G30-11B	8 13	5 10	2 92	2 62	65 00	8 88	225 00
	03601-9G30-11B	13 46	10 16	2 92	1 90	65 00	5 51	225 00
	00901-9G30-15D	5 89	4 00	2 46	3 67	65 00	14 93	225 00
	03601-9G30-15B	13 46	10 16	2 46	2 59	65 00	10 52	225 00
	00901-9G30-18D	5 99	4 00	2 24	4 17	63 00	18 63	225 00
	01801-9G30-18B	8 13	5 10	2 24	4 23	63 00	18 50	225 00
	03601-9G30-18B	13 46	10 16	2 24	3 14	63 00	14 04	225 00
	04101-9G30-20B	19 05	12 19	3 94	2 33	63 00	5 90	225 00
	04101-9G30-27B	19 05	12 19	3 43	3 14	63 00	9 18	225 00
	00901-9L31-04B	19 05	15 75	5 28	0 79	68 00	1 49	225 00
	01701-9L31-04B	23 11	23 11	5 28	0 86	68 00	1 82	225 00
	03101-9L31-04B	31 75	31 75	5 28	0 81	68 00	1 53	225 00
	04901-9L31-04B	38 10	38 10	5 28	0 89	65 00	1 68	225 00
	0711-9L31-04B	29 72	29 72	4 57	2 10	65 00	4 50	225 00

	12601-9L31-04B		49.78	49.78	5.28	1.34	68.00	2.53	225.00
	12701-9L31-04B		42.67	42.67	5.28	1.83	68.00	3.47	225.00
	12701-9L31-04C		50.80	50.80	5.28	1.29	68.00	2.46	225.00
	00901-9L31-06B		19.05	15.75	4.70	1.18	68.00	2.52	225.00
	01701-9L31-06B		23.11	23.11	4.70	1.25	68.00	2.87	225.00
	03101-9L31-06B		31.75	31.75	4.70	1.21	68.00	2.57	225.00
	04901-9L31-06B		38.10	38.10	4.70	1.33	68.00	2.83	225.00
	0711-9L31-06B		29.72	29.72	4.06	3.17	68.00	7.81	225.00
	12601-9L31-06B		49.78	49.78	4.70	2.00	68.00	4.26	225.00
	12701-9L31-06B		42.67	42.67	4.70	2.75	68.00	6.84	225.00
	12701-9L31-06C		50.80	50.80	4.70	1.94	68.00	4.12	225.00
	00901-9L31-09B		19.05	15.75	5.28	1.77	68.00	3.36	225.00
	01701-9L31-09B		23.11	23.11	5.28	1.89	68.00	3.58	225.00
	03101-9L31-09B		31.75	31.75	5.28	1.82	68.00	3.44	225.00
	04901-9L31-09B		38.10	38.10	5.28	2.00	68.00	3.78	225.00
	0711-9L31-09B		29.72	29.72	3.56	4.78	68.00	13.36	225.00
	12601-9L31-09B		49.78	49.78	5.28	3.01	68.00	6.69	225.00
	12701-9L31-09B		42.67	42.67	5.28	4.12	68.00	7.81	225.00
	12701-9L31-09C		50.80	50.80	5.28	2.91	68.00	5.51	225.00
	00901-9L31-14B		19.05	15.75	4.70	2.77	68.00	5.89	225.00
	01701-9L31-14B		23.11	23.11	4.70	2.92	68.00	6.21	225.00
	03101-9L31-14B		31.75	31.75	4.70	2.83	68.00	6.02	225.00
	04901-9L31-14B		38.10	38.10	4.70	3.11	68.00	6.61	225.00
	12601-9L31-14B		49.78	49.78	4.70	4.67	68.00	9.94	225.00
	12701-9L31-14C		50.80	50.80	4.70	4.53	68.00	9.83	225.00
Huimao (Beijing)	TEC1-007106T150	27.00	30.00	30.00	3.90	3.51	65.00	9.00	150.00
	TEC1-007110T150	27.00	30.00	30.00	3.30	5.86	62.00	17.74	150.00
	TEC1-007112T150	27.00	38.00	38.00	3.90	4.38	63.00	11.22	150.00
	TEC1-007118T150	27.00	38.00	38.00	3.40	6.57	60.00	19.31	150.00
	TEC1-007106T200	27.00	30.00	30.00	3.90	3.51	65.00	9.00	200.00
	TEC1-007110T200	27.00	30.00	30.00	3.30	5.86	62.00	17.74	200.00
	TEC1-007112T200	27.00	38.00	38.00	3.90	4.38	63.00	11.22	200.00
	TEC1-007118T200	27.00	38.00	38.00	3.40	6.57	60.00	19.31	200.00
	TEC1-007106T250	27.00	30.00	30.00	3.90	3.51	65.00	9.00	250.00
	TEC1-007110T250	27.00	30.00	30.00	3.30	5.86	62.00	17.74	250.00
	TEC1-007112T250	27.00	38.00	38.00	3.90	4.38	63.00	11.22	250.00
	TEC1-007118T250	27.00	38.00	38.00	3.40	6.57	60.00	19.31	250.00
	TEC1-12706T150	27.00	40.00	40.00	3.90	3.53	65.00	9.05	150.00
	TEC1-12710T150	27.00	40.00	40.00	3.30	5.89	62.00	17.84	150.00
	TEC1-12712T150	27.00	50.00	50.00	3.90	4.52	63.00	11.59	150.00
	TEC1-12718T150	27.00	50.00	50.00	3.40	6.78	60.00	19.95	150.00
	TEC1-12706T200	27.00	40.00	40.00	3.90	3.53	65.00	9.05	200.00
	TEC1-12710T200	27.00	40.00	40.00	3.30	5.89	62.00	17.84	200.00
	TEC1-12712T200	27.00	50.00	50.00	3.90	4.52	63.00	11.59	200.00
	TEC1-12718T200	27.00	50.00	50.00	3.40	6.78	60.00	19.95	200.00
	TEC1-12706T250	27.00	40.00	40.00	3.90	3.53	65.00	9.05	250.00
	TEC1-12710T250	27.00	40.00	40.00	3.30	5.89	62.00	17.84	250.00
	TEC1-12712T250	27.00	50.00	50.00	3.90	4.52	63.00	11.59	250.00
	TEC1-12718T250	27.00	50.00	50.00	3.40	6.78	60.00	19.95	250.00
	TEC1-03140T150	27.00	40.00	40.00	5.00	5.34	63.00	10.69	150.00
	TEC1-03140T200	27.00	40.00	40.00	5.00	5.34	63.00	10.69	200.00
	TEC1-03140T250	27.00	40.00	40.00	5.00	5.34	63.00	10.69	250.00
Fandis (Italy)	TM1-1273030-NX	25.00	30.00	30.00	3.80	2.94	71.00	7.75	150.00
	TM1-1273039-NX	25.00	30.00	30.00	3.60	3.78	71.00	10.49	150.00
	TM1-1274039-NX	25.00	40.00	40.00	4.70	2.13	69.00	4.52	150.00
	TM1-1274060-NX	25.00	40.00	40.00	3.80	3.31	71.00	8.72	150.00
	TM1-1274085-NX	25.00	40.00	40.00	3.40	4.50	71.00	13.24	150.00
	TM2-1274060-N	25.00	40.00	40.00	11.70	1.05	95.00	0.91	150.00
	TM2-1274065-N	25.00	40.00	40.00	7.50	2.19	86.00	2.92	150.00
Ferrotec	9500018012 M P		6.05	6.05	2.09	3.55	66.00	16.99	135.00
	9502031012 M P		7.97	7.97	2.09	3.62	66.00	17.32	135.00
	9502065012 M P		12.10	11.20	2.09	3.64	66.00	16.95	135.00
	9500018018 M P		6.05	6.05	1.79	5.19	66.00	29.00	135.00
	9502031018 M P		7.97	7.97	1.79	5.35	66.00	29.90	135.00
	9502065018 M P		12.10	11.20	1.79	5.31	66.00	29.68	135.00

	9501/126/030 B	29.70	29.70	3.94	3.29	72.00	6.34	135.00	
	9501/127/030 B	29.70	29.70	3.94	3.29	72.00	6.34	135.00	
	9501/071/030 B	22.40	22.40	3.18	2.19	72.00	10.03	135.00	
	9501/031/030 B	15.10	15.10	3.18	3.07	72.00	9.85	135.00	
	9501/023/030 B	7.39	22.40	3.18	3.14	72.00	9.88	135.00	
	9501/017/030 B	11.50	11.50	3.18	2.87	72.00	9.04	135.00	
	9501/128/040 B	29.70	29.70	3.94	4.31	72.00	10.93	135.00	
	9500/128/040 B	39.70	39.70	4.16	2.41	72.00	5.80	135.00	
	9501/127/040 B	29.70	29.70	3.94	4.31	72.00	10.93	135.00	
	9500/127/040 B	39.70	39.70	4.16	2.41	72.00	5.80	135.00	
	9501/071/040 B	22.40	22.40	3.18	4.19	72.00	13.16	135.00	
	9500/071/040 B	29.80	29.80	4.16	2.36	72.00	5.68	135.00	
	9501/063/040 B	21.10	39.70	4.16	2.15	72.00	5.17	135.00	
	9500/035/040 B	15.10	29.80	4.16	2.22	72.00	5.34	135.00	
	9501/031/040 B	15.10	15.10	3.18	4.08	72.00	12.83	135.00	
	9500/031/040 B	20.00	20.00	4.16	2.33	72.00	5.59	135.00	
	9501/023/040 B	7.39	22.40	3.18	4.17	72.00	13.11	135.00	
	9501/017/040 B	11.50	11.50	3.18	3.86	72.00	12.13	135.00	
	9500/017/040 B	15.01	15.10	4.16	2.25	72.00	5.41	135.00	
	9500/035/060 B	15.10	29.80	4.16	3.56	72.00	8.55	135.00	
	9500/031/060 B	20.00	20.00	4.16	3.50	72.00	8.41	135.00	
	9500/017/060 B	15.10	15.10	4.16	3.33	72.00	8.01	135.00	
	9500/071/060 B	29.80	29.80	4.16	3.60	72.00	8.66	135.00	
	9500/127/060 B	39.70	39.70	4.16	3.62	72.00	8.69	135.00	
	9501/127/060 B	29.70	29.70	3.61	6.46	72.00	17.90	135.00	
	9500/128/060 B	39.70	39.70	4.16	3.62	72.00	8.89	135.00	
	9500/017/085 B	15.10	15.10	3.94	4.82	72.00	12.24	135.00	
	9500/031/085 B	20.00	20.00	3.94	5.00	72.00	12.69	135.00	
	9500/035/085 B	15.10	29.80	3.94	4.89	72.00	12.41	135.00	
	9500/063/085 B	39.70	39.70	3.94	2.54	72.00	6.44	135.00	
	9500/071/085 B	29.80	29.80	3.94	5.07	72.00	12.86	135.00	
	9500/127/085 B	39.70	39.70	3.94	5.05	72.00	12.88	135.00	
	9500/128/085 B	39.70	39.70	3.94	5.08	72.00	12.88	135.00	
	9500/031/090 B	29.80	29.80	4.00	2.48	72.00	5.39	135.00	
	9500/071/090 B	29.80	29.80	3.94	5.29	72.00	13.43	135.00	
	9500/097/090 B	29.80	29.80	3.56	7.32	72.00	20.62	135.00	
	9501/063/100 B	20.10	39.70	3.64	5.89	72.00	16.18	135.00	
	9500/127/100 B	39.70	39.70	3.64	6.03	72.00	16.56	135.00	
	9504/071/120 B	40.10	40.10	4.65	3.92	72.00	8.43	135.00	
	9504/017/150 B	22.00	22.00	4.65	2.93	72.00	8.44	135.00	
	9500/031/150 B	29.80	29.80	4.60	3.94	72.00	8.57	135.00	
	9504/071/150 B	40.10	40.10	4.65	4.91	72.00	10.57	135.00	
	9504/031/240 B	39.70	39.70	4.62	3.49	72.00	7.55	135.00	
	9504/031/400 B	55.00	55.00	4.85	3.04	72.00	6.27	135.00	
HB	TEC1-07103HTS	30.00	30.00	4.90	1.33	65.00	2.72	225.00	\$3.74
	TEC1-07108HT	30.00	30.00	3.60	4.22	65.00	11.11	225.00	\$1.13
	TEC1-12703HT	40.00	40.00	4.70	1.59	65.00	3.39	225.00	\$3.76
	TEC1-12703HTS	40.00	40.00	4.70	1.34	65.00	2.86	225.00	\$4.65
	TEC1-12705HT	40.00	40.00	4.20	2.69	65.00	6.40	225.00	\$2.04
	TEC1-12706HTS	40.00	40.00	3.80	2.83	65.00	6.91	225.00	\$2.19
	TEC1-12707HT	40.00	40.00	3.70	3.69	65.00	9.97	225.00	\$1.62
	TEC1-12707HTS	40.00	40.00	3.70	3.16	65.00	8.53	225.00	\$1.98
	TEC1-12708HTS	40.00	40.00	3.60	3.56	65.00	10.15	225.00	\$1.75
	TEC1-12710HT	40.00	40.00	3.30	5.28	65.00	16.00	225.00	\$1.19
	TEC1-12710HTS	40.00	40.00	3.30	4.44	65.00	13.45	225.00	\$1.47
	TEC1-12715HT	50.00	50.00	4.30	5.12	65.00	11.91	225.00	\$3.75
	TEC1-12715HTS	50.00	50.00	4.30	4.32	65.00	10.05	225.00	\$4.61
	TEC1-12730HT	62.00	62.00	4.80	6.61	65.00	13.77	225.00	\$2.71
	TEC1-12730HTS	62.00	62.00	4.80	5.54	65.00	11.54	225.00	\$3.34
Hitech	QTEC 2-017.03	27.00	15.00	15.00	4.90	1.73	65.00	3.54	200.00
	QTEC 2-031.03	27.00	20.00	20.00	4.90	1.80	65.00	3.67	200.00
	QTEC 2-035.03	27.00	30.00	15.00	4.90	1.81	65.00	3.70	200.00
	QTEC 2-048.03	27.00	25.00	25.00	4.90	1.81	65.00	3.69	200.00
	QTEC 2-083.03	27.00	40.00	20.00	4.90	1.81	65.00	3.70	200.00
	QTEC 2-071.03	27.00	30.00	30.00	4.90	1.82	65.00	3.72	200.00
	QTEC 2-127.03	27.00	40.00	40.00	4.90	1.83	65.00	3.74	200.00

	QTEC 2-017.04	27.00	15.00	15.00	4.70	2.00	65.00	4.26	200.00
	QTEC 2-031.04	27.00	20.00	20.00	4.70	2.05	65.00	4.36	200.00
	QTEC 2-035.04	27.00	30.00	15.00	4.70	2.04	65.00	4.35	200.00
	QTEC 2-049.04	27.00	25.00	25.00	4.70	2.06	65.00	4.39	200.00
	QTEC 2-063.04	27.00	40.00	20.00	4.70	2.08	65.00	4.39	200.00
	QTEC 2-071.04	27.00	30.00	30.00	4.70	2.08	65.00	4.42	200.00
	QTEC 2-127.04	27.00	40.00	40.00	4.70	2.09	65.00	4.44	200.00
	QTEC 2-017.05	27.00	15.00	15.00	4.00	2.44	65.00	6.11	200.00
	QTEC 2-031.05	27.00	20.00	20.00	4.00	2.50	65.00	6.25	200.00
	QTEC 2-035.05	27.00	30.00	15.00	4.00	2.51	65.00	6.28	200.00
	QTEC 2-049.05	27.00	25.00	25.00	4.00	2.53	65.00	6.32	200.00
	QTEC 2-063.05	27.00	40.00	20.00	4.00	2.53	65.00	6.31	200.00
	QTEC 2-071.05	27.00	30.00	30.00	4.00	2.53	65.00	6.33	200.00
	QTEC 2-127.05	27.00	40.00	40.00	4.00	2.56	65.00	6.41	200.00
	QTEC 2-017.06	27.00	15.00	15.00	3.80	3.07	65.00	8.07	200.00
	QTEC 2-031.06	27.00	20.00	20.00	3.80	3.13	65.00	8.22	200.00
	QTEC 2-035.06	27.00	30.00	15.00	3.80	3.16	65.00	8.30	200.00
	QTEC 2-049.06	27.00	25.00	25.00	3.80	3.20	65.00	8.42	200.00
	QTEC 2-063.06	27.00	40.00	20.00	3.80	3.19	65.00	8.39	200.00
	QTEC 2-071.06	27.00	30.00	30.00	3.80	3.19	65.00	8.39	200.00
	QTEC 2-127.06	27.00	40.00	40.00	3.80	3.21	65.00	8.45	200.00
	QTEC 2-017.08	27.00	15.00	15.00	3.30	4.09	65.00	12.39	200.00
	QTEC 2-031.08	27.00	20.00	20.00	3.30	4.20	65.00	12.73	200.00
	QTEC 2-035.08	27.00	30.00	15.00	3.30	4.22	65.00	12.79	200.00
	QTEC 2-049.08	27.00	25.00	25.00	3.30	4.24	65.00	12.85	200.00
	QTEC 2-063.08	27.00	40.00	20.00	3.30	4.28	65.00	12.95	200.00
	QTEC 2-071.08	27.00	30.00	30.00	3.30	4.28	65.00	12.96	200.00
	QTEC 2-127.08	27.00	40.00	40.00	3.30	4.30	65.00	13.03	200.00
	QTEC 2-031.09	27.00	30.00	30.00	5.60	1.17	65.00	2.06	200.00
	QTEC 2-049.09	27.00	36.00	36.00	5.60	2.28	65.00	4.06	200.00
	QTEC 2-071.09	27.00	44.00	44.00	5.60	2.23	65.00	3.98	200.00
	QTEC 2-127.09	27.00	62.00	62.00	5.60	2.02	65.00	3.60	200.00
	QTEC 2-031.14	27.00	30.00	30.00	4.60	3.28	65.00	7.13	200.00
	QTEC 2-049.14	27.00	36.00	36.00	4.60	3.56	65.00	7.73	200.00
	QTEC 2-071.14	27.00	44.00	44.00	4.60	3.47	65.00	7.55	200.00
	QTEC 2-127.14	27.00	62.00	62.00	4.60	3.13	65.00	6.81	200.00
<hr/>									
INB Products	inbC2-040-085-31-17	27.00	11.50	11.50	6.60	2.34	85.00	3.55	200.00
	inbC2-055-085-31-17	27.00	15.00	15.00	7.20	2.69	85.00	3.73	200.00
	inbC2-055-085-71-31	27.00	20.00	20.00	7.20	3.16	85.00	4.39	200.00
	inbC2-040-050-127-63	27.00	30.00	30.00	7.10	1.79	85.00	2.52	200.00
	inbC2-055-045-127-63	27.00	40.00	40.00	7.50	2.15	85.00	2.88	200.00
	inbC1-017.03	27.00	15.00	15.00	4.90	1.73	65.00	3.54	150.00
	inbC1-031.03	27.00	20.00	20.00	4.90	1.80	65.00	3.67	150.00
	inbC1-035.03	27.00	30.00	15.00	4.90	1.81	65.00	3.70	150.00
	inbC1-049.03	27.00	25.00	25.00	4.90	1.81	65.00	3.69	150.00
	inbC1-063.03	27.00	40.00	20.00	4.90	1.81	65.00	3.70	150.00
	inbC1-071.03	27.00	30.00	30.00	4.90	1.82	65.00	3.72	150.00
	inbC1-127.03	27.00	40.00	40.00	4.90	1.83	65.00	3.74	150.00
	inbC1-017.04	27.00	15.00	15.00	4.70	2.00	65.00	4.26	150.00
	inbC1-031.04	27.00	20.00	20.00	4.70	2.05	65.00	4.36	150.00
	inbC1-035.04	27.00	30.00	15.00	4.70	2.04	65.00	4.35	150.00
	inbC1-049.04	27.00	25.00	25.00	4.70	2.08	65.00	4.39	150.00
	inbC1-063.04	27.00	40.00	20.00	4.70	2.06	65.00	4.39	150.00
	inbC1-071.04	27.00	30.00	30.00	4.70	2.08	65.00	4.42	150.00
	inbC1-127.04	27.00	40.00	40.00	4.70	2.09	65.00	4.44	150.00
	inbC1-017.05	27.00	15.00	15.00	4.00	2.44	65.00	6.11	150.00
	inbC1-031.05	27.00	20.00	20.00	4.00	2.50	65.00	6.25	150.00
	inbC1-035.05	27.00	30.00	15.00	4.00	2.51	65.00	6.28	150.00
	inbC1-049.05	27.00	25.00	25.00	4.00	2.53	65.00	6.32	150.00
	inbC1-063.05	27.00	40.00	20.00	4.00	2.53	65.00	6.31	150.00
	inbC1-071.05	27.00	30.00	30.00	4.00	2.53	65.00	6.33	150.00
	inbC1-127.05	27.00	40.00	40.00	4.00	2.56	65.00	6.41	150.00
	inbC1-017.06	27.00	15.00	15.00	3.80	3.07	65.00	8.07	150.00
	inbC1-035.06	27.00	30.00	15.00	3.80	3.16	65.00	8.30	150.00
	inbC1-049.06	27.00	25.00	25.00	3.80	3.20	65.00	8.42	150.00
	inbC1-063.06	27.00	40.00	20.00	3.80	3.19	65.00	8.39	150.00
	inbC1-071.06	27.00	30.00	30.00	3.80	3.19	65.00	8.39	150.00

inbC1-127.06	27.00	40.00	40.00	3.80	3.21	65.00	6.46	150.00
inbC1-017.08	27.00	15.00	15.00	3.30	4.09	65.00	12.39	150.00
inbC1-031.08	27.00	20.00	20.00	3.30	4.20	65.00	12.73	150.00
inbC1-035.08	27.00	30.00	15.00	3.30	4.22	65.00	12.79	150.00
inbC1-049.08	27.00	25.00	25.00	3.30	4.24	65.00	12.85	150.00
inbC1-063.08	27.00	40.00	20.00	3.30	4.28	65.00	12.95	150.00
inbC1-071.08	27.00	30.00	30.00	3.30	4.28	65.00	12.96	150.00
inbC1-127.08	27.00	40.00	40.00	3.30	4.30	65.00	13.03	150.00
inbC1-031.09	27.00	30.00	30.00	5.60	2.09	65.00	3.73	150.00
inbC1-049.09	27.00	36.00	36.00	5.60	2.28	65.00	4.06	150.00
inbC1-071.09	27.00	44.00	44.00	5.60	2.23	65.00	3.98	150.00
inbC1-127.09	27.00	62.00	62.00	5.60	2.02	65.00	3.60	150.00
inbC1-031.14	27.00	30.00	30.00	4.60	3.28	65.00	7.13	150.00
inbC1-049.14	27.00	36.00	36.00	4.60	3.56	65.00	7.73	150.00
inbC1-071.14	27.00	44.00	44.00	4.60	3.47	65.00	7.85	150.00
inbC1-127.14	27.00	62.00	62.00	4.60	3.13	65.00	6.81	150.00
inbC1-127.14-50	27.00	50.00	50.00	4.70	4.82	65.00	10.26	150.00

Intarm	TECB-1-1-(15.4-6.0-51.4)-40-71	25.00	40.00	40.00	3.60	3.21	71.00	8.92	250.00
	TECB-1-3-(15.4-8.5-68.8)-40-69	25.00	40.00	40.00	3.30	4.30	69.00	13.03	250.00
	TECB-1-14-(15.4-3.9-33.4)-40-72	25.00	40.00	40.00	4.70	2.09	72.00	4.44	250.00
	TECB-1-28-(15.4-10-86)-40-71	25.00	40.00	40.00	3.50	5.38	71.00	15.36	250.00
	TECB-1-33-(15.4-1.0-8.6)-40-72	25.00	40.00	40.00	4.80	0.64	72.00	1.12	250.00
	TECB-1-34-(15.4-11.4-97)-40-70	25.00	40.00	40.00	3.30	6.09	70.00	18.47	250.00
	TECB-2-2-(15.4-3.9-33.4)-30-71	25.00	30.00	30.00	3.20	3.71	71.00	11.60	250.00
	TECB-2-43-(15.4-4.8-41.0)-30-69	25.00	30.00	30.00	3.00	4.56	69.00	15.19	250.00
	TECB-2-44-(15.4-3.5-30.2)-30-70	25.00	30.00	30.00	3.40	3.36	70.00	9.87	250.00
	TECB-2-45-(15.4-2.4-29.7)-30-71	25.00	30.00	30.00	4.10	2.30	71.00	5.61	250.00
	TECB-13-13-(8.6-3.9-18.7)-30-72	25.00	30.00	30.00	4.60	2.08	72.00	4.52	250.00
	TECB-13-46-(8.6-4.2-21.0)-30-72	25.00	30.00	30.00	4.40	2.33	72.00	5.30	250.00
	TECB-13-47-(8.6-4.7-23.0)-30-71	25.00	30.00	30.00	4.20	2.56	71.00	6.08	250.00
	TECB-13-48-(8.6-5.1-25.2)-30-70	25.00	30.00	30.00	4.00	2.80	70.00	7.00	250.00
	TECB-13-49-(8.6-5.0-29.6)-30-70	25.00	30.00	30.00	3.70	3.29	70.00	8.89	250.00
	TECB-14-88-(12.6-40)-40-71	25.00	40.00	40.00	3.50	2.00	71.00	7.14	250.00
	TECB-14-81-(12.6-5.44)-40-71	25.00	40.00	40.00	3.40	2.75	71.00	8.09	250.00
	TECB-14-82-(12.7-47)-40-71	25.00	40.00	40.00	3.30	2.94	71.00	8.90	250.00
	TECB-15-15-(24.7-11.4-173)-40-69	25.00	40.00	40.00	3.00	10.81	69.00	36.04	250.00
	TECB-15-16-(24.7-7.9-120)-40-69	25.00	40.00	40.00	3.40	7.50	69.00	22.06	250.00
	TECB-15-26-(24.0-3.9-52)-40-71	25.00	40.00	40.00	4.20	3.25	71.00	7.74	250.00
	TECB-15-56-(24.7-9.5-130)-40-69	25.00	40.00	40.00	3.30	8.13	69.00	24.62	250.00
	TECB-15-101-(24.7-14.5-220)-40-69	25.00	40.00	40.00	2.90	13.75	69.00	47.41	250.00
	TECB-16-89-(24.2-7-100)-30-70	25.00	30.00	30.00	3.10	11.11	70.00	35.84	250.00
	TECB-16-93-(24.2-6.3-90)-30-70	25.00	30.00	30.00	3.20	10.00	70.00	31.25	250.00
	TECB-16-94-(24.2-5.7-81)-30-70	25.00	30.00	30.00	3.30	9.00	70.00	27.27	250.00
	TECB-17-17-(15.4-14.0-120)-62-71	25.00	62.00	62.00	5.00	3.12	71.00	6.24	250.00
	TECB-17-21-(15.4-8.3-72)-62-71	25.00	62.00	62.00	5.90	1.87	71.00	3.17	250.00
	TECB-17-51-(15.4-9.3-81)-62-71	25.00	62.00	62.00	5.70	2.11	71.00	3.70	250.00
	TECB-17-52-(15.4-11.1-94.4)-62-71	25.00	62.00	62.00	5.50	2.45	71.00	4.47	250.00
	TECB-17-53-(15.4-12.6-107)-62-70	25.00	62.00	62.00	5.30	2.78	70.00	5.25	250.00
	TECB-18-18-(8.6-2.5-12)-23-71	25.00	23.00	23.00	3.60	2.27	71.00	6.30	250.00
	TECB-18-54-(8.6-2.1-9.9)-23-72	25.00	23.00	23.00	4.00	1.87	72.00	4.68	250.00
	TECB-18-55-(8.6-2.3-10.6)-23-71	25.00	23.00	23.00	3.80	2.00	71.00	5.27	250.00
	TECB-18-56-(8.6-3.3-15.0)-23-71	25.00	23.00	23.00	3.40	2.84	71.00	8.34	250.00
	TECB-18-57-(8.6-3.9-15.1)-23-71	25.00	23.00	23.00	3.20	3.42	71.00	10.69	250.00
	TECB-18-87-(8.2-3.7-20)-23-71	25.00	28.00	23.50	3.30	3.04	71.00	9.21	250.00
	TECB-21-102-(42-12-300)-55-69	25.00	55.00	55.00	4.00	9.92	69.00	24.79	250.00
	TECB-21-103-(42-15-330)-50-69	25.00	55.00	55.00	4.00	10.91	69.00	27.27	250.00
	TECB-21-104-(42-16.7-350)-50-69	25.00	55.00	55.00	3.80	11.57	69.00	30.45	250.00
	TECB-21-105-(42-20-400)-50-68	25.00	55.00	55.00	3.50	13.22	68.00	37.78	250.00
	TECB-22-22-(17.4-6.0-57)-40-71	25.00	40.00	40.00	3.80	3.56	71.00	9.38	250.00
	TECB-22-58-(17.4-4.0-39)-40-71	25.00	40.00	40.00	4.30	2.44	71.00	5.67	250.00
	TECB-23-59-(17.4-4.5-45.5)-40-71	25.00	40.00	40.00	4.10	2.84	71.00	6.94	250.00
	TECB-22-60-(17.4-5.5-52.2)-40-70	25.00	40.00	40.00	3.90	3.26	70.00	8.37	250.00
	TECB-22-61-(17.4-7.3-70.0)-40-70	25.00	40.00	40.00	3.50	4.38	70.00	12.50	250.00
	TECB-22-62-(17.4-8.1-77.4)-40-70	25.00	40.00	40.00	3.30	4.84	70.00	14.66	250.00
	TECB-25-25-(15.4-6.5-72)-70-71	25.00	70.00	70.00	5.70	1.47	71.00	2.58	250.00
	TECB-25-30-(15.4-11.4-100)-70-70	25.00	70.00	70.00	5.50	2.04	70.00	3.71	250.00
	TECB-25-35-(15.4-14-125)-70-70	25.00	70.00	70.00	5.00	2.55	70.00	5.10	250.00

	TECB-25-63-(15.4-17-150)-70-70	25.00	70.00	70.00	4.00	3.06	70.00	7.65	250.00
	TECB-25-64-(15.4-10-2-88)-70-71	25.00	70.00	70.00	5.70	1.80	71.00	3.15	250.00
	TECB-26-90-(30-19-300)-70-69	25.00	70.00	70.00	5.70	6.12	71.00	10.74	250.00
	TECB-26-95-(30-17.5-275)-70-69	25.00	70.00	70.00	5.80	5.61	71.00	9.88	250.00
	TECB-26-96-(30-16.4-280)-70-69	25.00	70.00	70.00	5.90	5.31	71.00	8.90	250.00
	TECB-27-27-(19-14-147)-40-70	25.00	40.00	40.00	3.10	9.19	70.00	29.64	250.00
	TECB-27-65-(19-11.6-123)-40-70	25.00	40.00	40.00	3.30	7.50	70.00	22.73	250.00
	TECB-27-66-(19-9.8-108)-40-70	25.00	40.00	40.00	3.50	6.63	70.00	18.93	250.00
	TECB-27-67-(19-8.6-93.3)-40-71	25.00	40.00	40.00	3.70	5.83	71.00	15.76	250.00
	TECB-27-68-(19-7.6-83.0)-40-71	25.00	40.00	40.00	3.90	5.19	71.00	13.30	250.00
	TECB-28-28-(2.5-3.9-5.4)-20-72	25.00	20.00	20.00	4.70	1.35	72.00	2.87	250.00
	TECB-28-69-(2.5-4.4-6.0)-20-71	25.00	20.00	20.00	4.60	1.50	71.00	3.33	250.00
	TECB-28-70-(2.5-5.0-6.9)-20-71	25.00	20.00	20.00	4.30	1.73	71.00	4.01	250.00
	TECB-28-71-(2.5-5.4-7.5)-20-71	25.00	20.00	20.00	4.10	1.88	71.00	4.57	250.00
	TECB-29-109-(24.7-11.5-175)-50-69	25.00	50.00	50.00	4.00	7.00	69.00	17.50	250.00
	TECB-32-32-(24.7-19.0-300)-62-69	25.00	62.00	62.00	5.10	7.80	69.00	15.30	250.00
	TECB-32-72-(24.7-17.0-270)-62-69	25.00	62.00	62.00	5.30	7.02	69.00	13.25	250.00
	TECB-32-73-(24.7-15.0-240)-62-69	25.00	62.00	62.00	5.50	6.24	69.00	11.35	250.00
	TECB-32-74-(24.7-13.0-200)-62-70	25.00	62.00	62.00	5.70	5.20	70.00	9.13	250.00
	TECB-32-110-(24.7-25.0-400)-62-69	25.00	62.00	62.00	4.80	10.41	69.00	21.68	250.00
	TECB-39-97-(30-15.2-270)-50-69	25.00	50.00	50.00	5.50	10.80	69.00	19.64	250.00
	TECB-39-98-(30-14.0-255)-50-69	25.00	50.00	50.00	5.60	10.20	69.00	18.21	250.00
	TECB-39-99-(30-12.7-240)-50-69	25.00	50.00	50.00	5.70	9.60	69.00	16.84	250.00
	TECB-39-100-(30-12.7-240)-50-69	25.00	50.00	50.00	6.10	4.40	70.00	7.21	250.00
	TECB-40-40-(17.4-6.0-58)-50-71	25.00	50.00	50.00	4.00	2.32	71.00	5.80	250.00
	TECB-40-75-(17.4-4.0-38)-50-71	25.00	50.00	50.00	4.60	1.52	71.00	3.30	250.00
	TECB-40-76-(17.4-4.6-45.2)-50-71	25.00	50.00	50.00	4.40	1.81	71.00	4.11	250.00
	TECB-40-77-(17.4-5.5-52.3)-50-71	25.00	50.00	50.00	4.20	2.09	71.00	4.98	250.00
	TECB-40-78-(17.4-6.9-68.0)-50-70	25.00	50.00	50.00	3.80	2.64	70.00	6.95	250.00
	TECB-41-41-(30-3.0-50)-40-71	25.00	40.00	40.00	3.20	3.13	71.00	9.77	250.00
	TECB-41-79-(30-2.7-45)-40-71	25.00	40.00	40.00	3.40	2.81	71.00	8.27	250.00
	TECB-41-80-(30-2.5-42.3)-40-71	25.00	40.00	40.00	3.60	2.64	71.00	7.34	250.00
	TECB-41-81-(30-2.3-37.8)-40-72	25.00	40.00	40.00	3.80	2.38	72.00	6.22	250.00
	TECB-41-82-(30-2.1-34.5)-40-72	25.00	40.00	40.00	4.00	2.16	72.00	5.39	250.00
Kryotherm	TB-7-1,0-2,5	8.00	8.00	4.80	1.55	70.00	3.26	150.00	\$5.62
	TB-17-1,0-2,5	11.50	11.50	4.80	1.89	70.00	3.94	150.00	\$5.21
	TB-31-1,0-2,5	14.80	14.80	4.80	2.05	70.00	4.28	150.00	\$5.66
	TB-63-1,0-2,5	15.00	15.00	4.80	4.04	70.00	8.43	150.00	\$3.14
	TB-71-1,0-2,5	23.00	23.00	4.80	1.93	70.00	4.02	150.00	\$6.72
	TB-83-1,0-2,5	22.00	19.00	4.80	2.87	70.00	5.98	150.00	\$4.70
	TB-127-1,0-2,5	30.00	30.00	4.80	2.03	70.00	4.24	150.00	\$6.98
	TB-7-1,0-2,0	8.00	8.00	4.30	2.03	70.00	4.72	150.00	\$3.15
	TB-17-1,0-2,0	11.50	11.50	4.30	2.34	70.00	5.45	150.00	\$3.58
	TB-31-1,0-2,0	14.80	14.80	4.30	2.56	70.00	5.95	150.00	\$3.99
	TB-63-1,0-2,0	15.00	30.00	4.30	2.53	70.00	5.89	150.00	\$4.42
	TB-71-1,0-2,0	23.00	23.00	4.30	2.42	70.00	5.63	150.00	\$4.96
	TB-83-1,0-2,0	22.00	19.00	4.30	3.56	70.00	8.29	150.00	\$3.65
	TB-127-1,0-2,0	30.00	30.00	4.30	2.64	70.00	5.92	150.00	\$5.34
	TB-71-1,4-3,175	30.00	30.00	5.60	1.83	72.00	3.27	150.00	\$9.88
	TB-7-1,0-1,5	8.00	8.00	3.80	2.68	69.00	6.99	150.00	\$2.35
	TB-17-1,0-1,5	11.50	11.50	3.80	3.02	69.00	7.96	150.00	\$2.71
	TB-31-1,0-1,5	14.80	14.80	3.80	3.33	69.00	8.77	150.00	\$3.00
	TB-63-1,0-1,5	15.00	30.00	3.80	3.29	69.00	8.65	150.00	\$3.28
	TB-71-1,0-1,5	23.00	23.00	3.80	3.16	69.00	8.31	150.00	\$3.64
	TB-83-1,0-1,5	22.00	19.00	3.80	4.67	69.00	12.28	150.00	\$2.63
	TB-127-1,0-1,5	30.00	30.00	3.80	3.32	69.00	8.74	150.00	\$4.06
	TB-7-1,0-1,3	8.00	8.00	3.60	2.97	69.00	8.25	150.00	\$2.11
	TB-17-1,0-1,3	11.50	11.50	3.60	3.48	69.00	9.66	150.00	\$2.36
	TB-23-1,0-1,3	30.00	5.00	3.60	4.13	69.00	11.48	150.00	\$2.36
	TB-31-1,0-1,3	14.80	14.80	3.60	3.83	69.00	10.65	150.00	\$2.82
	TB-63-1,0-1,3	15.00	30.00	3.60	3.80	69.00	10.66	150.00	\$3.09
	TB-71-1,0-1,3	23.00	23.00	3.60	3.65	69.00	10.13	150.00	\$3.15
	TB-83-1,0-1,3	22.00	19.00	3.60	5.38	69.00	14.95	150.00	\$2.23
	TB-127-1,0-1,3	30.00	30.00	3.60	3.83	69.00	10.65	150.00	\$3.29
	TB-32-1,0-0,8	40.00	6.00	3.10	5.88	69.00	18.95	150.00	\$1.91
	TB-127-1,0-0,8	30.00	30.00	3.10	6.22	69.00	20.07	150.00	\$2.31
	TB-195-1,0-0,8	50.00	25.00	3.10	6.88	69.00	22.19	150.00	\$4.62

	TB-7-1,4-2,5	10.00	10.00	4.90	2.10	72.00	4.29	150.00	\$4.12
	TB-17-1,4-2,5	15.00	15.00	4.90	2.22	72.00	4.54	150.00	\$4.77
	TB-31-1,4-2,5	20.00	20.00	4.90	2.28	72.00	4.64	150.00	\$5.45
	TB-63-1,4-2,5	20.00	40.00	4.90	2.33	72.00	4.74	150.00	\$5.85
	TB-71-1,4-2,5	30.00	30.00	4.90	2.32	72.00	4.74	150.00	\$6.24
	TB-127-1,4-2,5	40.00	40.00	4.80	2.34	72.00	4.87	150.00	\$6.31
	TB-71-1,4-1,8	30.00	30.00	4.20	3.10	70.00	7.38	150.00	\$4.65
	TB-7-1,4-1,5	10.00	10.00	4.00	3.30	70.00	8.25	150.00	\$2.48
	TB-17-1,4-1,5	15.00	15.00	4.00	3.56	70.00	8.89	150.00	\$2.87
	TB-31-1,4-1,5	20.00	20.00	4.00	3.65	70.00	9.13	150.00	\$3.12
	TB-63-1,4-1,5	20.00	40.00	4.00	3.71	70.00	9.28	150.00	\$3.39
	TB-71-1,4-1,5	30.00	30.00	4.00	3.71	70.00	9.28	150.00	\$3.72
	TB-127-1,4-1,5	40.00	40.00	3.90	3.75	70.00	9.62	150.00	\$4.48
	TB-127-1,4-1,2	40.00	40.00	3.60	4.09	70.00	13.02	150.00	\$3.71
	TB-7-1,4-1,15	10.00	10.00	3.60	4.20	69.00	11.67	150.00	\$2.06
	TB-17-1,4-1,15	15.00	15.00	3.60	4.53	69.00	12.59	150.00	\$2.54
	TB-31-1,4-1,15	20.00	20.00	3.60	4.65	69.00	12.92	150.00	\$2.89
	TB-63-1,4-1,15	20.00	40.00	3.60	4.74	69.00	13.16	150.00	\$2.91
	TB-71-1,4-1,15	30.00	30.00	3.60	4.78	69.00	13.27	150.00	\$3.14
	TB-127-1,4-1,15	40.00	40.00	3.40	4.75	69.00	13.97	150.00	\$4.06
	TB-127-1,4-1,05	40.00	40.00	3.30	5.25	69.00	15.91	150.00	\$4.11
	TB-7-2,0-2,5	14.80	14.80	4.80	1.92	72.00	3.99	150.00	\$4.69
	TB-17-2,0-2,5	22.00	22.00	4.80	2.11	72.00	4.39	150.00	\$5.74
	TB-31-2,0-2,5	30.00	30.00	4.80	2.08	72.00	4.33	150.00	\$6.59
	TB-71-2,0-2,5	40.00	40.00	4.80	2.69	72.00	6.60	150.00	\$11.39
	TB-127-2,0-2,5	48.00	48.00	4.80	3.30	72.00	6.87	150.00	\$14.85
	TB-127-2,0-2,5	55.00	55.00	4.80	2.51	72.00	5.23	150.00	\$19.50
	TB-127-2,0-2,5	62.00	62.00	4.80	1.98	72.00	4.32	150.00	\$24.78
	TB-127-2,0-1,65	48.00	48.00	4.00	4.82	70.00	12.04	150.00	\$9.91
	TB-7-2,0-1,5	14.80	14.80	3.80	3.05	70.00	8.95	150.00	\$4.12
	TB-17-2,0-1,5	22.00	22.00	3.80	3.37	70.00	8.86	150.00	\$4.16
	TB-31-2,0-1,5	30.00	30.00	3.80	3.31	70.00	8.71	150.00	\$4.32
	TB-71-2,0-1,5	40.00	40.00	3.80	4.25	70.00	11.18	150.00	\$6.92
	TB-127-2,0-1,5	48.00	48.00	3.80	5.30	70.00	13.93	150.00	\$9.29
	TB-127-2,0-1,5	55.00	55.00	4.80	4.03	70.00	8.40	150.00	\$12.20
	TB-127-2,0-1,5	62.00	62.00	3.90	3.17	70.00	8.14	150.00	\$15.00
	TB-127-2,0-1,15	48.00	48.00	3.40	6.77	69.00	19.91	150.00	\$6.76
	TB-32-2,8-1,5	40.00	40.00	4.00	3.75	70.00	9.38	150.00	\$5.15
	TB-31-5,0-2,5	55.00	55.00	6.00	3.70	70.00	6.17	150.00	\$10.16
	TB-31-5,0-1,5	55.00	55.00	5.00	6.15	70.00	12.30	150.00	\$5.81
Marlow	DT12-2-5	27.00	30.00	30.00	4.04	2.55	66.00	6.33	150.00
	DT12-2.5-01L	27.00	30.00	30.00	4.04	2.56	66.00	6.33	150.00
	DT12-4	27.00	30.00	30.00	3.43	4.00	66.00	11.66	150.00
	DT12-4-01	27.00	30.00	30.00	3.43	4.00	66.00	11.66	150.00
	DT12-4-01L	27.00	30.00	30.00	3.43	4.00	66.00	11.66	150.00
	DT12-4-01S	27.00	30.00	30.00	3.43	4.00	66.00	11.66	150.00
	DT12-4-06LS	27.00	30.00	30.00	3.43	4.00	66.00	11.66	150.00
	DT12-6	27.00	40.01	40.01	4.01	3.37	66.00	8.41	150.00
	DT12-6-01L	27.00	40.01	40.01	4.01	3.37	66.00	8.41	150.00
	DT12-6-01LS	27.00	40.01	40.01	4.01	3.37	66.00	8.41	150.00
	DT12-6-01S	27.00	40.01	40.01	4.01	3.37	66.00	8.41	150.00
	DT12-6-05	27.00	40.01	40.01	4.01	3.37	66.00	8.41	150.00
	DT12-8	27.00	40.01	40.01	3.53	4.44	66.00	12.56	150.00
	DT12-8-01L	27.00	40.01	40.01	3.53	4.44	66.00	12.56	150.00
	DT3-2-5	27.00	16.00	16.00	4.04	2.34	65.00	5.80	150.00
	DT3-2.5-01	27.00	16.00	16.00	4.04	2.34	65.00	5.80	150.00
	DT3-4	27.00	16.00	16.00	3.43	3.52	65.00	10.25	150.00
	DT3-4-01L	27.00	16.00	16.00	3.43	3.52	65.00	10.25	150.00
	DT3-6	27.00	19.99	19.99	4.01	3.25	65.00	8.11	150.00
	DT3-6-01	27.00	19.99	19.99	4.01	3.25	65.00	8.11	150.00
	DT3-6-01LS	27.00	19.99	19.99	4.01	3.25	65.00	8.11	150.00
	DT3-6-01S	27.00	19.99	19.99	4.01	3.25	65.00	8.11	150.00
	DT3-8	27.00	19.99	19.99	3.63	4.25	65.00	11.72	150.00
	DT6-2-5	27.00	23.50	23.50	4.04	2.35	65.00	5.83	150.00
	DT6-2.5-01L	27.00	23.50	23.50	4.04	2.35	65.00	5.83	150.00
	DT6-2.5-01LS	27.00	23.50	23.50	4.04	2.35	65.00	5.83	150.00
	DT6-4	27.00	23.50	23.50	3.43	3.62	65.00	10.56	150.00

	DT6-4-01	27.00	23.50	23.50	3.43	3.62	65.00	10.56	150.00
	DT6-4-01L	27.00	23.50	23.50	3.43	3.62	65.00	10.56	150.00
	DT6-4-01LS	27.00	23.50	23.50	3.43	3.62	65.00	10.56	150.00
	DT6-6	27.00	30.00	30.00	4.01	3.33	65.00	8.31	150.00
	DT6-6-01L	27.00	30.00	30.00	4.01	3.33	65.00	8.31	150.00
	DT6-8	27.00	30.00	30.00	3.63	4.33	65.00	11.94	150.00
	DT6-8-01L	27.00	30.00	30.00	3.63	4.33	65.00	11.94	150.00
	MI1010T	27.00	3.96	3.96	2.41	3.00	61.00	12.44	150.00
	MI1011T	27.00	6.90	6.90	2.41	2.30	61.00	9.53	150.00
	MI1012T	27.00	8.79	8.79	2.41	2.72	61.00	11.28	150.00
	MI1012T-01AC	27.00	8.79	8.79	2.41	2.72	61.00	11.28	150.00
	MI1013T	27.00	13.16	13.16	2.41	2.77	61.00	11.50	150.00
	MI1015T	27.00	8.79	10.97	2.39	2.70	61.00	11.28	150.00
	MI1020T	27.00	3.91	3.91	2.16	5.89	64.00	27.25	150.00
	MI1020T-02AC	27.00	3.91	3.91	2.16	5.89	64.00	27.25	150.00
	MI1021T	27.00	6.80	6.80	2.16	5.05	64.00	23.38	150.00
	MI1021T-02AC	27.00	6.80	6.80	2.16	5.05	64.00	23.38	150.00
	MI1022T	27.00	8.79	8.79	2.16	5.18	64.00	23.97	150.00
	MI1023T	27.00	13.16	13.16	2.16	5.31	64.00	24.59	150.00
	MI1023T-02AC	27.00	13.16	13.16	2.16	5.31	64.00	24.59	150.00
	MI1025T	27.00	8.79	10.97	2.16	5.39	64.00	24.97	150.00
	NL1010T	27.00	3.96	3.96	2.41	3.00	61.00	12.44	150.00
	NL1011T	27.00	6.90	6.90	2.41	2.30	61.00	9.53	150.00
	NL1012T	27.00	8.79	8.79	2.41	2.72	61.00	11.28	150.00
	NL1013T	27.00	13.16	13.16	2.41	2.77	61.00	11.50	150.00
	NL1015T	27.00	8.79	10.97	2.39	2.70	61.00	11.28	150.00
	NL1020T	27.00	3.96	3.96	2.16	5.74	64.00	26.57	150.00
	NL1021T	27.00	6.80	6.80	2.16	5.05	64.00	23.38	150.00
	NL1022T	27.00	8.79	8.79	2.16	5.18	64.00	23.97	150.00
	NL1023T	27.00	13.16	13.16	2.16	5.31	64.00	24.59	150.00
	NL1025T	27.00	8.79	10.97	2.16	5.39	64.00	24.97	150.00
	RC12-2.5	27.00	30.00	30.00	4.04	2.58	66.00	6.33	150.00
	RC12-4	27.00	30.00	30.00	3.43	4.00	66.00	11.56	150.00
	RC12-6	27.00	40.13	40.13	4.01	3.35	66.00	8.36	150.00
	RC12-8	27.00	40.13	40.13	3.63	4.41	66.00	12.15	150.00
	RC3-2.5	27.00	16.00	16.00	4.04	2.34	65.00	5.80	150.00
	RC3-4	27.00	16.00	16.00	3.43	3.52	65.00	10.25	150.00
	RC3-6	27.00	19.99	19.99	4.01	3.25	65.00	8.11	150.00
	RC3-8	27.00	19.99	19.99	3.63	4.25	65.00	11.72	150.00
	RC6-2.5	27.00	23.50	23.50	4.04	2.35	65.00	5.83	150.00
	RC6-4	27.00	23.50	23.50	3.43	3.62	65.00	10.56	150.00
	RC6-6	27.00	30.00	30.00	4.01	3.33	65.00	8.31	150.00
	RC6-8	27.00	30.00	30.00	3.63	4.33	65.00	11.94	150.00
	SP1507	27.00	11.28	11.28	2.44	4.24	64.00	17.39	150.00
	SP1848	27.00	25.40	25.40	4.88	3.26	62.00	6.67	150.00
	SP1848-03AC	27.00	25.40	25.40	4.88	3.26	62.00	6.67	150.00
	SP5025	27.00	5.97	5.22	2.51	5.12	64.00	20.39	150.00
	SP5162	27.00	5.99	5.15	1.65	5.24	65.00	37.84	150.00
	SP5255	27.00	6.02	6.18	1.65	5.70	63.00	40.61	150.00
	SP5445	27.00	5.99	12.19	1.65	5.95	65.00	41.50	150.00
Motor	HOT 1 2-18-F2A	25.00	7.20	6.00	2.70	3.38	64.00	12.52	225.00
	HOT 1 2-24-F2A	25.00	10.80	6.00	2.50	2.78	64.00	11.05	225.00
	HOT 1 2-30-F2A	25.00	12.30	6.20	2.40	3.19	64.00	13.28	225.00
	HOT 1 2-31-F2A	25.00	11.00	8.80	2.70	2.59	64.00	9.60	225.00
	HOT 1 2-65-F2A	25.00	13.20	13.20	2.70	3.05	64.00	11.35	225.00
	HOT 1 5-30-F2A	25.00	12.30	5.20	2.20	3.97	64.00	18.06	225.00
	HOT 1 5-31-F2A	25.00	11.00	8.90	2.40	3.23	64.00	13.47	225.00
	HOT 1 5-65-F2A	25.00	13.20	12.10	2.40	4.11	64.00	17.14	225.00
	HOT 2 0-30-F2A	25.00	12.30	10.30	1.90	3.19	64.00	17.72	225.00
	HOT 2 0-65-F2A	25.00	13.20	13.20	2.20	5.03	64.00	22.85	225.00
	HT2-12-30	25.00	34.00	30.00	3.60	1.95	63.00	6.45	225.00
	HT3-12-30	25.00	34.00	30.00	3.20	2.35	63.00	7.35	225.00
	HT4-12-40	25.00	34.00	30.00	3.20	3.24	63.00	10.11	225.00
	HT5-12-40	25.00	34.00	30.00	3.80	2.84	63.00	7.48	225.00
	HT6-7-30	25.00	44.00	40.00	3.60	2.90	63.00	8.05	225.00
	HT8-12-40	25.00	44.00	40.00	3.30	4.09	63.00	12.40	225.00
	HT9-3-25	25.00	29.00	25.00	4.90	2.75	66.00	5.63	225.00

Microcell (Thin Film)	MPC-D301-M44	25.00	0.72	0.72	0.43	42.05	22.50	982.53	55.00	50.88
	MPC-D301-M44	25.00	4.80	4.80	0.43	62.93	21.90	1463.58		
TE Technologies	VT-127-1 0-1 3-71	27.00	30.00	30.00	3.60	4.00	71.00	11.11	200.00	
	VT-127-1 4-1 15-71	27.00	40.00	40.00	3.40	5.00	71.00	14.71	200.00	
	VT-127-1 4-1 5-72	27.00	40.00	40.00	3.90	3.68	72.00	9.94	200.00	
	VT-199-1 4-0 8	27.00	40.00	40.00	3.20	10.75	67.00	33.59	200.00	
	VT-199-1 4-1 15	27.00	40.00	40.00	3.40	7.50	69.00	22.06	200.00	
	VT-199-1 4-1 5	27.00	40.00	40.00	3.90	5.88	70.00	15.06	200.00	
Telumex	CZ-1 0-127-1 27	50.00	34.00	31.00	3.20	3.67	79.00	11.47	100.00	
	CZ-1 4-127-1 65	50.00	40.00	40.00	3.70	3.50	79.00	9.46	100.00	
	CZ-1 4-127-1 14	50.00	44.00	40.00	3.20	4.58	79.00	14.31	100.00	
	CZ-1 4-219-1 14	50.00	54.00	54.00	3.20	4.77	79.00	14.90	100.00	
Thermon	1MCD4-004-03		1.60	3.20	1.70	14.65	70.00	86.17	175.00	
	1MCD4-006-03		3.20	3.20	1.70	14.65	70.00	86.17	175.00	
	1MCD4-012-03		3.20	4.80	1.70	14.97	70.00	88.08	175.00	
	1MCD4-018-03		4.80	4.80	1.70	14.76	70.00	86.81	175.00	
	1MCD4-032-03		6.40	6.40	1.70	14.65	70.00	86.17	175.00	
	1MCD4-064-03		9.60	8.00	1.70	14.32	70.00	84.25	175.00	
	1MCD4-004-02		3.20	1.60	1.60	21.45	68.00	134.28	175.00	
	1MCD4-006-02		3.20	3.20	1.60	21.45	68.00	134.28	175.00	
	1MCD4-012-02		4.80	3.20	1.60	21.45	68.00	134.28	175.00	
	1MCD4-018-02		4.80	4.80	1.60	21.70	68.00	135.63	175.00	
	1MCD4-032-02		6.40	6.40	1.60	21.45	68.00	134.28	175.00	
	1MCD4-060-02		9.60	8.00	1.60	20.83	68.00	130.21	175.00	

5.2 Studies of Competitive Products

5.2.1 Benchmarking of Competitive Technologies

Principal Investigator: Robert Staunton

Oak Ridge National Laboratory

National Transportation Research Center

2360 Cherahala Boulevard

Knoxville, TN 37932

Voice: 865-946-1351; Fax: 865-946-1262; E-mail: stauntonrh@ornl.gov

DOE Technology Development Manager: Susan A. Rogers

Voice: 202-586-8997; Fax: 202-586-1600; E-mail: Susan.Rogers@ee.doe.gov

ORNL Program Manager: Mitch Olszewski

Voice: 865-946-1350; Fax: 865-946-1262; E-mail: olszewskim@ornl.gov

Objectives

The Benchmarking of Competitive Technologies project is intended to conduct electrical and mechanical studies of hybrid electric vehicle (HEV) and plug-in hybrid electric vehicle (PHEV) systems as new system innovations are developed and introduced into the automotive market. The testing produces valuable data on efficiency, torque, speed, and voltage-current relationships that cannot be obtained from other open-literature sources. The full inspection and characterization of the electric motors and inverters also defines their thermal system performance in terms of temperature and corresponding sustainable power levels. Testing of these systems helps to rapidly advance the domestic technology base of electric traction drive systems suitable for HEV/PHEV applications.

The Oak Ridge National Laboratory (ORNL) testing program documents how the systems are manufactured and packaged and what performance limitations exist. These data are obtained by (1) thorough design inspections/assessments, (2) instrumenting the motor/inverter system, and (3) conducting locked-rotor, back-electromotive force (back-emf), thermal, and performance tests over the entire design envelope. These data permit ORNL to determine mechanical and electrical losses and map the inverter and/or motor efficiencies over the entire torque-speed domain.

Approach

Benchmarking of HEV traction drive systems provides detailed electrical and mechanical data from known permanent magnet synchronous motors (PMSMs) and inverters and yields information concerning their thermal performance. The overall approach of this project is to thoroughly define the systems and then perform a detailed evaluation of their performance in a controlled laboratory environment. This approach has proved to be technically sound and quite successful.

During the year, the efficiency mapping tests of the Prius were completed using a test plan developed in the prior year. This same methodology was duplicated for the evaluation of Accord subsystems. Accord activities included preparing the motor with a new rotor shaft design and motor end plates; preparing the inverter through analysis of the circuit and the construction of an auxiliary circuit; and tests that included back-emf, locked rotor, and efficiency mapping.

The technical approach for performing benchmarking evaluations during the year included the following tasks:

- Complete Prius subsystem testing, share detailed test data, and fully document the benchmarking activities. (Completed: May 2006)

- Test the performance of the Accord motor, inverter, and components in the laboratory to generate baseline performance data. (Completed: July 2006)
- Provide the auto company partners with a consistent, open-literature source for complete characterization of Accord technology recently introduced in the marketplace. (Completed: September 2006)
- Query DOE and industry partners regarding emerging technology issues and which competitive technologies hold the greatest technical interest. (Completion: duration of project)
- Based on resources, complete additional limited benchmark assessments of emerging hybrid technology selected by the FCVT program and/or FCVT technical partners. (Completed: September 2006)
- Continue to apply benchmarking information to assist in program planning efforts, developing and executing specific projects, and to support the partnership with the original equipment manufacturers at U.S. Council for Automotive Research. (Completion: duration of project)
- Confirm the realism of performance goals for the technologies and components and identify technology gaps. (Completion: duration of project)
- Use benchmarking data to validate/refine multiproject R&D modeling efforts so that they may be better used in developing new prototype designs to support research. (Successfully completed by some researchers—ongoing as new results are published)
- Use results to confirm the validity of the project technology thrust and avoid duplication of existing efforts. (Completion: duration of project)
- Provide technical insights that can be used to guide research efforts. (Completion: corresponds to presentation and report dates)

Major Accomplishments

The FY 2006 accomplishments have made it possible to combine test data with design, packaging, and fabrication assessments to enable analysts to determine how various commercial HEV traction systems, such as the Accord and the Prius, compare with system and program technology targets (peak-power-to-weight and -volume ratios). ORNL and other researchers have used data from the benchmarking project in motor models such as Motorsoft SPEEDCAD, Flux2D (FEA), and PSAT (ORNL/Sentech). Other researchers at ORNL have used the data to (1) perform fabrication and cost analyses for the Prius motor and (2) conduct thermal control studies using ORNL's HEATING 7.3, a general-purpose, finite-difference conduction heat transfer model. Ongoing work on another model, developed as part of the benchmarking project, is described in "Future Direction."

The following summarize other major accomplishments of the project during the year:

- The efficiency mapping tests of the Prius PMSM and inverter were completed in a specially prepared test cell using an ORNL controller system developed for this project.
- The benchmarking design and packaging evaluation were completed for the Accord subsystems.
- The Accord motor was prepared with a new rotor shaft design and motor end plates, and the inverter was prepared through analysis of the circuit and the construction of auxiliary circuitry.
- Tests were completed on the Accord subsystems that included back-emf, locked rotor, and efficiency mapping.
- Prius and Accord technical evaluations and test results were documented, and technical reports were issued for both during the year.
- Special by-request benchmarking evaluations were also completed and are documented in this report (see Technical Discussion).

Technical Discussion

The 2005 hybrid Accord is an example of how the automotive industry is introducing hybrid technology to preexisting vehicle models. This Accord design is considered to be a "mild hybrid" because

of the small power rating of the integrated motor assist (IMA) and the fact that it is used only for acceleration assist to the engine. The PMSM/inverter system is not used for acceleration without engine power as in the case of a "strong hybrid." After the vehicle reaches highway speeds, the IMA is used to contribute torque during moderate or strong accelerations.

In contrast, the Prius was designed from the beginning to be a hybrid vehicle and is considered to be a "strong hybrid." Many of the significant Accord vs Prius design differences are summarized in Table 1.

The Accord PMSM casing is very narrow (68 mm) to allow it to be inserted between the engine and torque converter. Consequently, the motor was designed without a full casing (ends are missing), and the rotor was designed without a shaft and bearings. In preparation for motor operation in the ORNL laboratory, a shaft was designed and installed in the rotor, and end plates with bearings were designed and installed. The completed, stand-alone motor assembly is shown in Figure 1. The completed test stand is shown in Figure 2.

Locked Rotor Test

A series of locked rotor tests were performed to determine the torque-producing behavior of the PMSM motor. A motorized mechanical-gear mechanism was used to precisely position and lock the rotor based on readings from the absolute position sensor in the motor.

A motor-driven gear mechanism was used to rotate the motor incrementally every 5 electrical degrees, and the fixture remained rigidly locked each time a set level of dc current was applied. Torque values were obtained from an in-line shaft torque sensor when the motor windings were energized. The resulting Accord and Prius data were used to produce torque-vs-shaft-angle plots, which are shown in Figure 3 for various current levels and more than one-half an electrical cycle. The levels of torque that were produced reflect the absolute maximum torque obtainable from the motor for each current (magnetic

Table 1. Differences between the hybrid Accord and the Prius

Design feature	Hybrid Accord	Prius
Motor peak power rating, kW	12.4 @ 840 rpm	50 @ 1200–1540 rpm
Motor peak torque rating, Nm	136	400
Separate generator	No	Yes (although the motor also serves as a generator)
PMSM used for initial acceleration	Engine assist	Exclusively
Source of power to PMSM	Battery	Generator and battery
Purpose of the hybrid system	Primarily performance	Primarily improved fuel economy
PMSM rotor design	Interior permanent magnets embedded near the rotor surface	Interior permanent magnets with "V" configuration at each pole
Number of rotor poles	16	8
Boost converter used	No	Yes
Inverter bus voltage	144	200–500
PMSM cooling	Passive cooling	Water/glycol loop
Inverter cooling	Forced air convection	Water/glycol loop
Location of inverter	Behind rear seat in passenger compartment	Engine compartment
Physical integration of the PMSM	Flat (68-mm) motor-only assembly located between engine and torque converter; the rotor shaft is replaced by dual rotor hubs with bolt flanges	PMSM is included in an engine-mounted casing ("axle assembly") that contains the generator and planetary gear/reduction gear assemblies

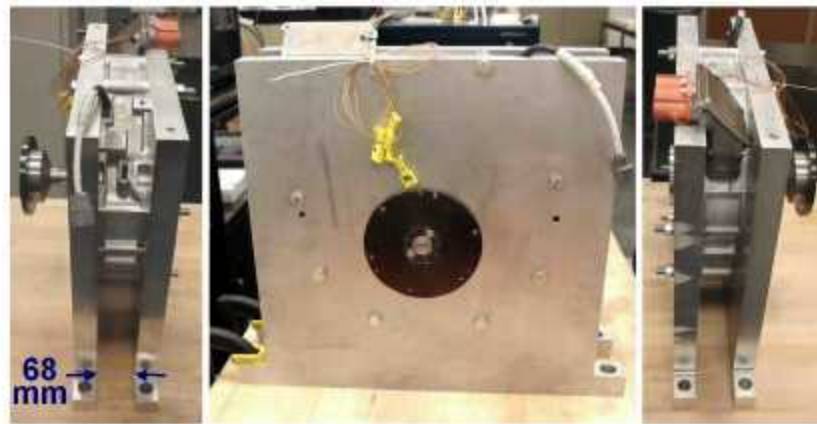


Figure 1. Accord motor with custom-designed end plates and shaft.

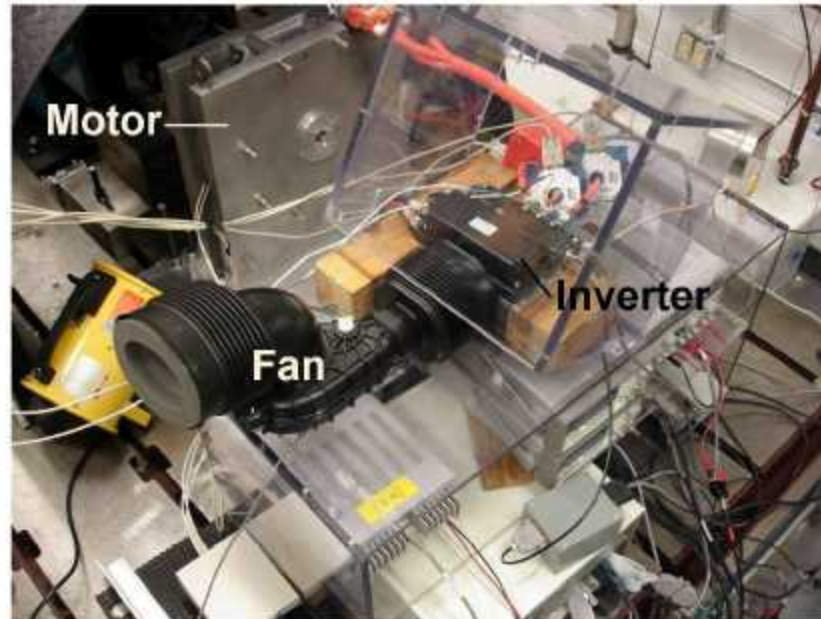


Figure 2. Preparation of test cell for Accord performance testing.

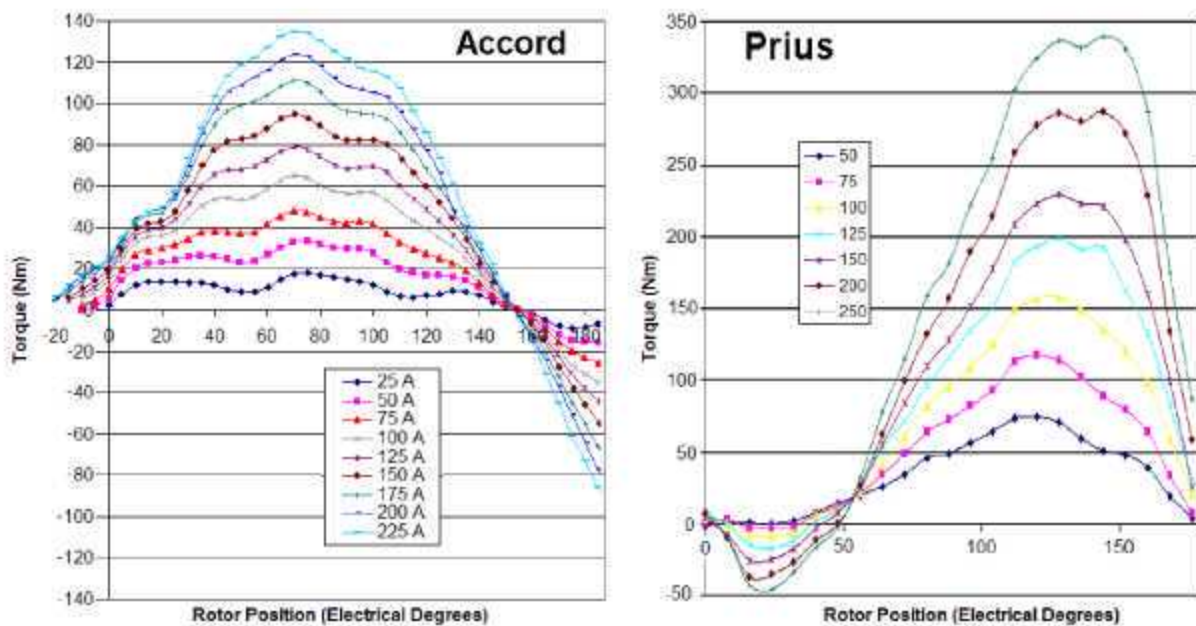


Figure 3. Accord/Prius locked-rotor torque vs electrical position at varying levels of stator current.

torque and reluctance torque). In contrast to an operating motor, there are no eddy current core losses, losses due to windage, and bearing friction.

Prius testing did not continue to the full torque specification of 400 Nm because of rapidly escalating stator winding temperatures. To collect several sets of data for averaging, it was necessary to remain at each speed-torque combination for about 20 s.

Accord/Prius Efficiency Mapping Data

Figures 4 through 6 show comparisons of the Accord and Prius Efficiency contour maps for the motor, inverter, and motor plus inverter, respectively. In each case, the bottom plot is for the Prius, and it shows comments pertaining to how the Prius efficiency compares with Accord efficiency for the designated area of the map. These comments are “broad-brush” comparisons and should not be taken in a precise, mathematical sense. For instance, very narrow contour regions of the map may be disregarded in the interest of placing emphasis on the larger, more significant areas.

The most important conclusion to be drawn from these figures is the fact that, in terms of efficiency, the Prius inverter excels, the Accord motor excels (except in the high-speed, low-torque region), and the combined HEV system efficiency is essentially the same except at the low-speed (<1000 rpm), high-torque region* where the Accord efficiency excels and the high-speed range where the Prius excels.

*Expressions such as “low-speed, high torque” for the Accord and Prius systems simply refer to corresponding areas or domains in the speed-load maps, even though the actual torque values may be quite different.

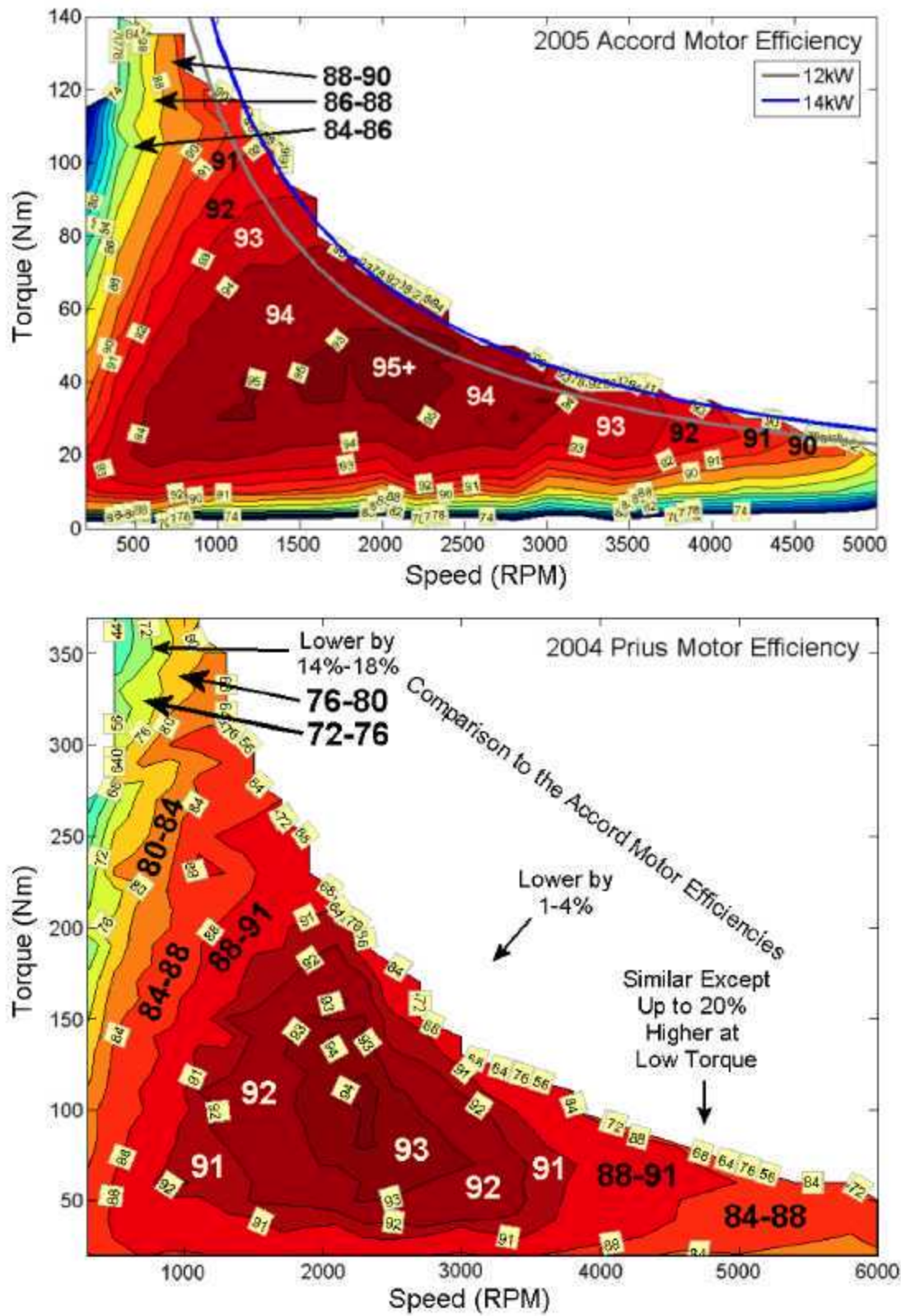


Figure 4. Comparison of Accord and Prius motor efficiency contour maps.

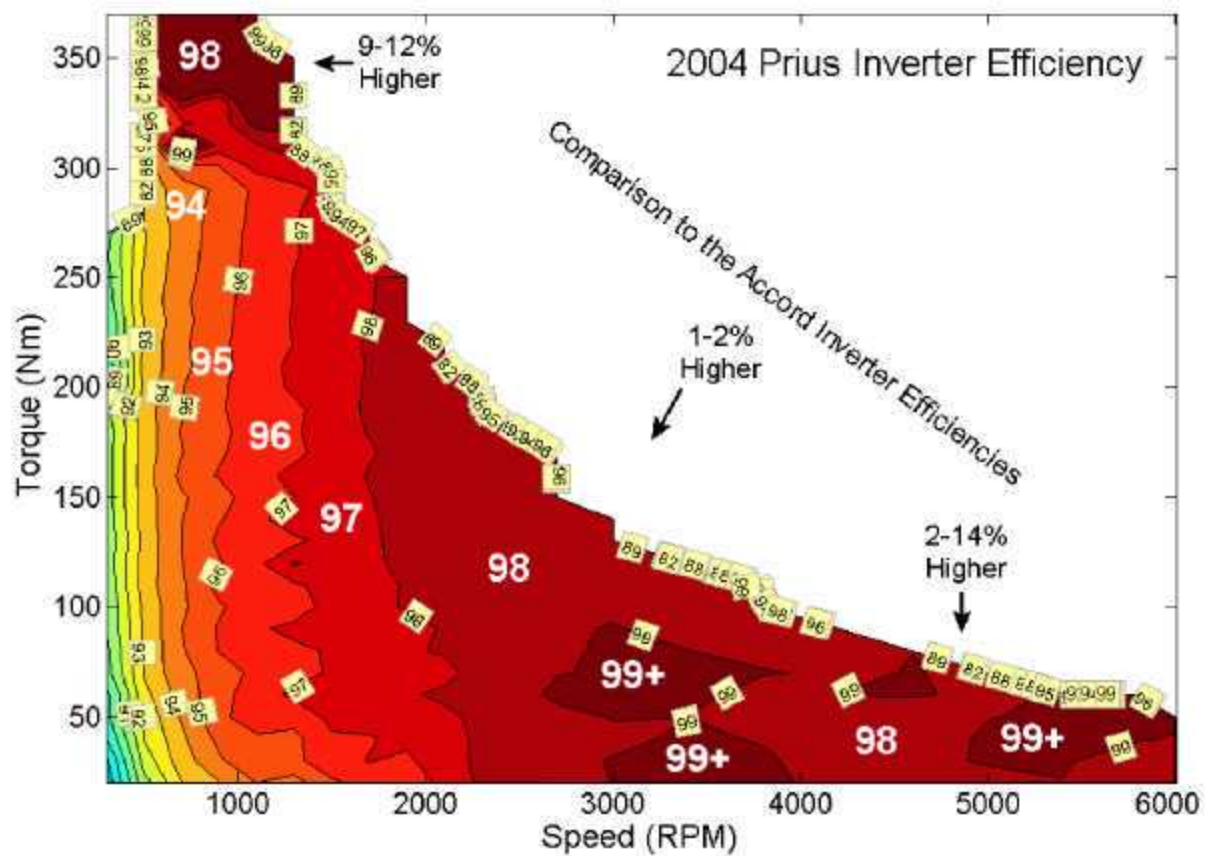
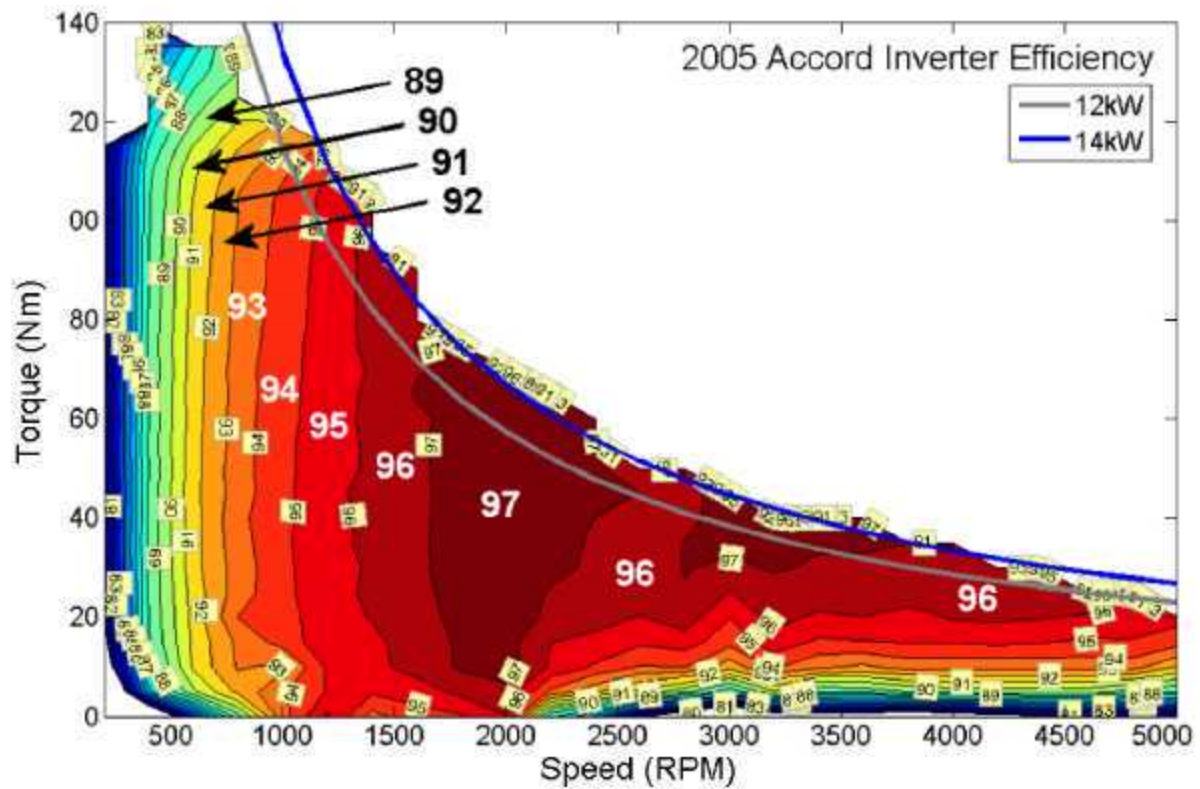


Figure 5. Comparison of Accord and Prius inverter efficiency contour maps.

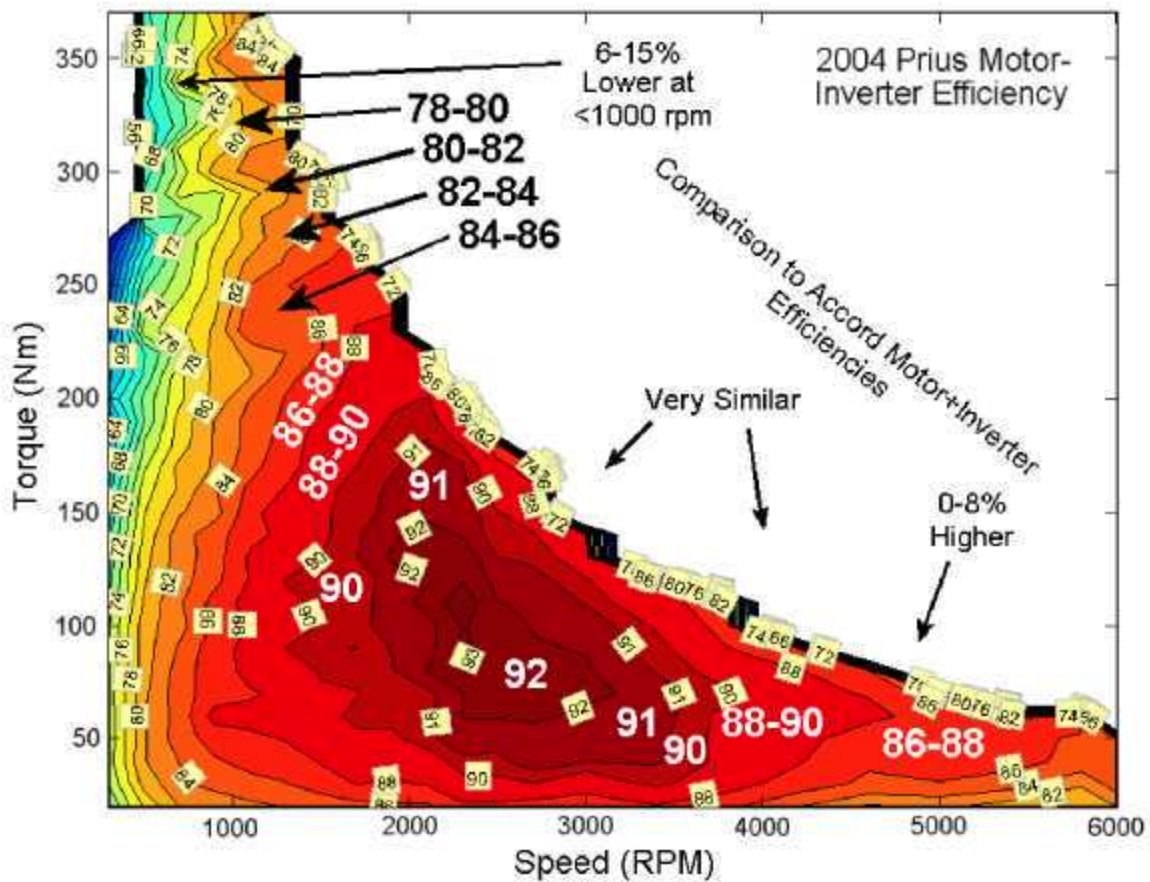
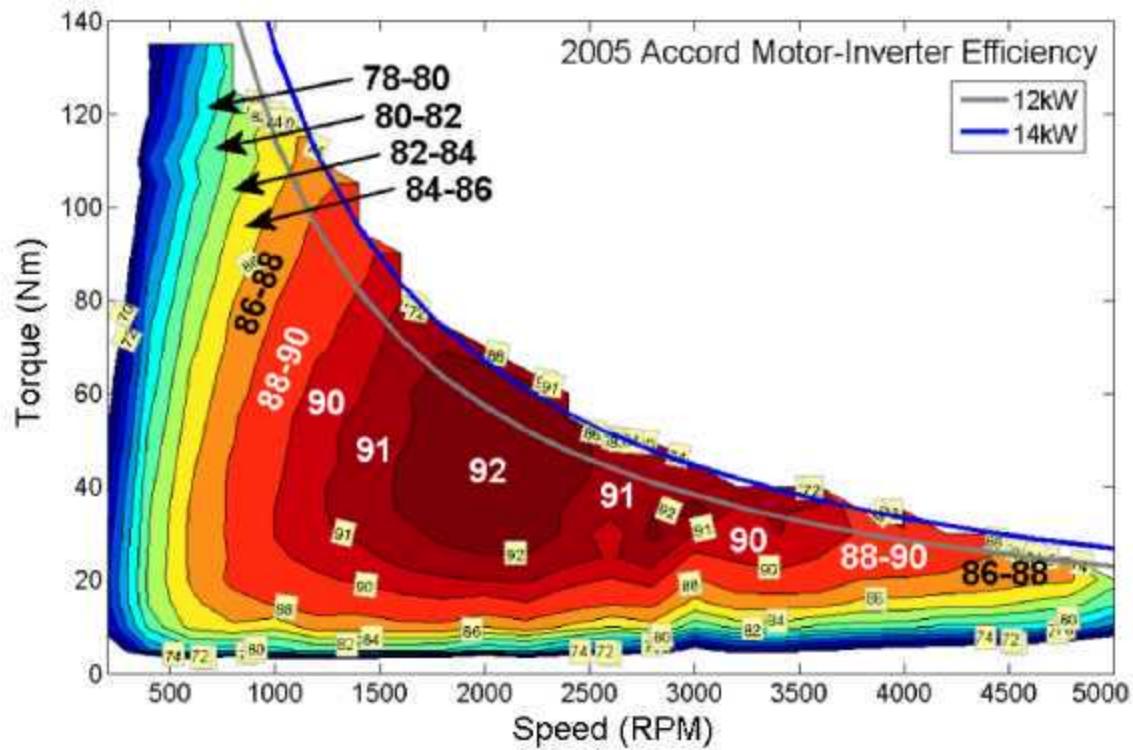


Figure 6. Comparison of Accord and Prius motor plus inverter efficiency contour maps.

Design Parameters for Prius/Accord

Table 2 summarizes the motor design and inverter insulated gate bipolar transistor (IGBT) ratings for the original Prius, the 2004 Prius, and the 2005 hybrid Accord designs. Included in the table are several design parameters describing each PMSM stator and rotor assembly and the PM volume and mass. Figure 7 provides clarification regarding the PM configurations used in each of the vehicle designs.

Table 2. Comparison of design parameters for Prius and Accord

Parameter	Prius I	Prius II	Accord	Comments
Stator OD, mm	269	269	315.5	
Stator ID, mm	162	162	232	
Rotor OD, mm	160	160	230	
Rotor ID, mm	115.6	111	188	
Rotor stack length, mm	90.7	83.6	41.2	Lamination only
Stator stack length, mm	89	84	40.1	Lamination only
Air gap, mm	1	1	1	
Lamination thickness, mm	0.356	0.33	0.343	
End-turn length, mm	83	80	35	Approx middle line
End-turn length (phase lead side), mm	83	80	35	Approx middle line
End turn arc extension, mm	31.8	30.5	~6.5–10	
Stator turns per coil	9	9	52	
Parallel circuit per phase	2	0	8	
Turns in series per phase	4	8	0	
Number of poles	8	8	16	
Number of stator slots	48	48	24	
Number of wires in parallel	13	13	0	
Wire diameter	Awg 19	Awg 19	1.55 mm	
Slot depth, mm	33.5	33.5	30.6	
Slot opening, mm	1.93	1.93	4.75	
Slot area, mm	–	–	307	
Phase resistance at 21°C, Ω /un	0.017	0.069	0.0097	
Stator winding mass, kg	7.48	6.8	3.01	
Stator core mass, kg	19.7	19.05	7.704	Laminations only
Rotor mass, kg	10.2	10.2	8.02	Prius I/II included bearings; Accord without bearings
Magnet width, mm	34.8	18.9	18.45	Individual magnets or bonded pairs as applicable
Magnet thickness, mm	6.15	6.5	4.46	Individual magnets or bonded pairs as applicable
Magnet length, mm	90.3	83.1	40.4	Individual magnets or bonded pairs as applicable
Magnet volume, mm	19330	10210	3320	For a pole, double Prius II and Accord volumes
Magnet mass, g	144	76	25	For a pole, double Prius II and Accord masses
IGBT current rating, A	Not tested	~195	~175	Max i during tests (per phase or IGBT pair)
IGBT voltage rating, V	600	1200	300 or 600	Assumed rating based on peak V

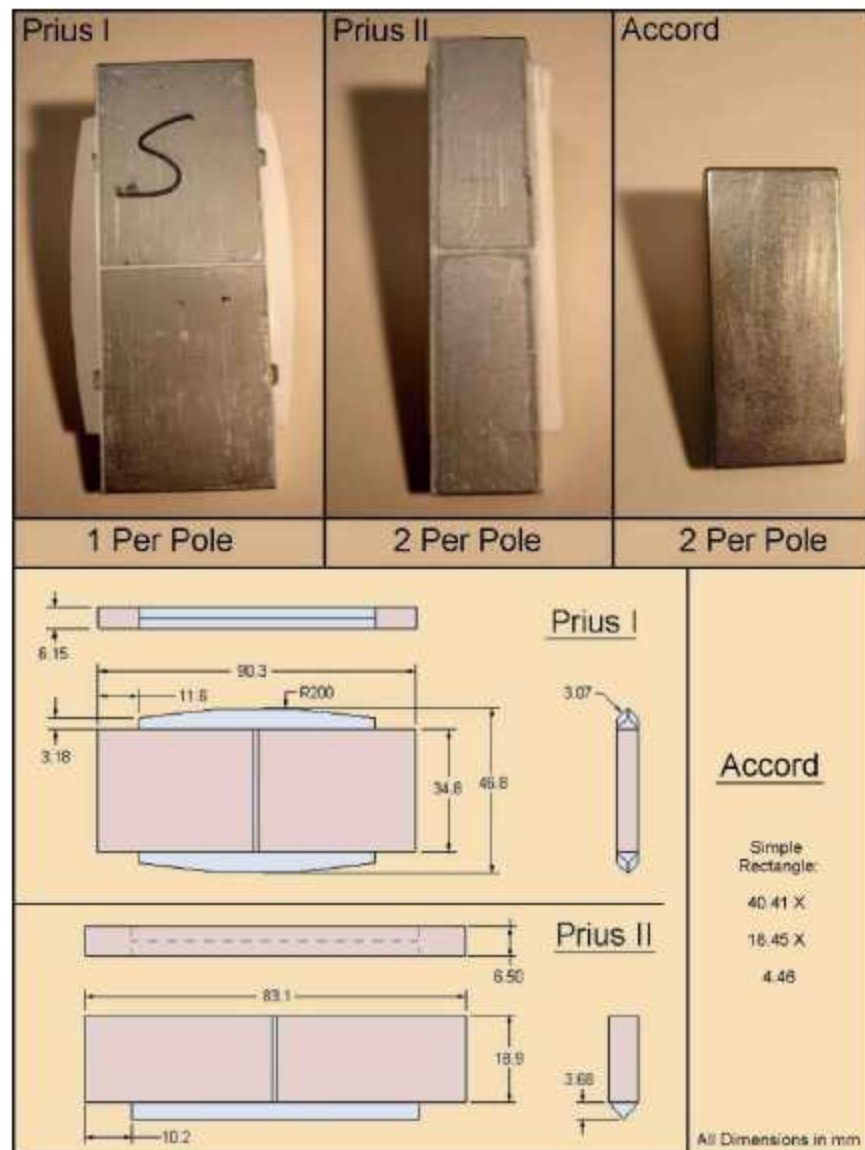


Figure 7. PM configurations and dimensions for three hybrid rotor designs.

Prius Inverter-only Mass and Volume Estimates

This section derives the inverter and casing mass and volume estimates for the Prius as if the buck/boost converter and generator-related circuitry did not exist. This has not been previously documented in any benchmarking report. The total volume of the Prius inverter/converter casing is 17.8 L as depicted in Figure 8.

The total volume of the Prius “inverter only” with resized casing is 9.9 L and is derived as follows:

- The midsection volume is reduced by 55% to account for the exclusion of the converter components, the generator portion of the inverter board (a 1/2 reduction), the generator portion of the power module (a 1/3 reduction), and the corresponding portion of the cold plate (a 60% reduction). See the change in the size of the cold plate in Figure 9 as a visualization aid.
- The casing is also reduced by the deletion of the bottom compartment (unrelated circuitry).
- The “cap” volume (or lid and capacitor volume) is retained in full.

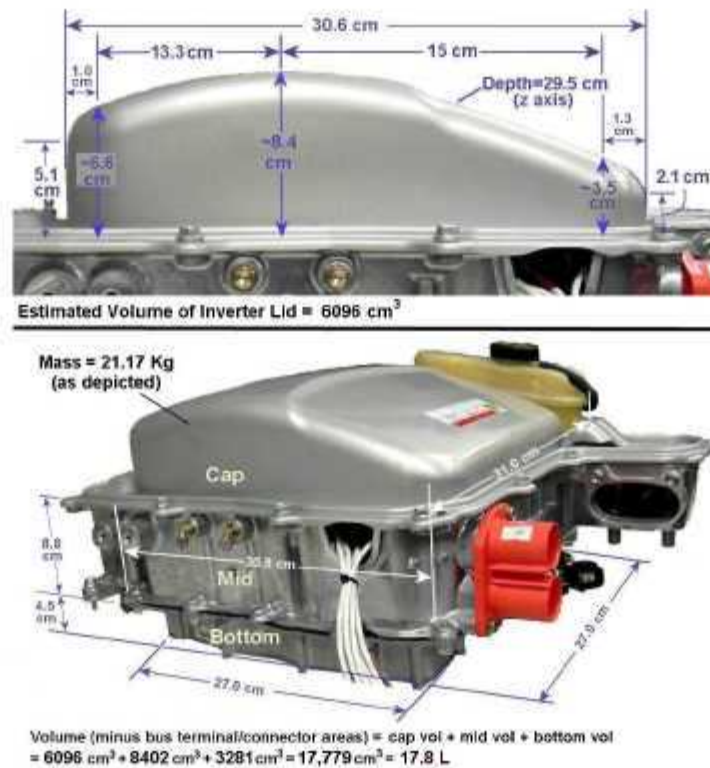


Figure 8. Volume of entire Prius inverter/converter assembly.



Figure 9. Conceptual change to inverter/converter casing for excluding the buck/boost converter.

The total mass of inverter/converter casing as depicted in Figure 8 is 21.2 kg.

The total mass of the “inverter *only*” is 9.4 kg and is derived in a similar manner to the volume (100% of cap mass, 45% of midsection mass, and 0% of bottom section mass). To be more precise, the mass of the converter transformer and converter power module were first fully excluded before the 45% was applied to the remainder of the midsection. This is quite significant considering that the converter transformer has a mass of 2.57 kg.

Prius Planetary Gear Packaging

The 2004 Prius has a planetary gear assembly that is integral to the motor/generator casing, and it is linked to reduction gears and a differential. Figure 10 shows the gear assembly with number-of-teeth



Figure 10. 2004 Prius gear assembly in an open casing.

labels on each gear. The planetary gear system uses the chain depicted in the figure to drive a series of reduction gears that power the differential and the axles. Because of the integral design, certain assumptions and estimates must be made to determine approximate mass and volume of the planetary gear system. The information provided in this section will include certain details on discrete components.

Figure 11 lays out the same gearing components as shown in Figure 10 and supplies masses associated with each. The fasteners represent an approximation because they were not fully inventoried.



Figure 11. Components making up the Prius gear box.

The casing for the assembly is not shown, and because of the two-piece design that is shared with the generator and motor, mass and volume estimates are difficult to produce with precision. Nevertheless, it is estimated from mass measurements of selected and modified Prius gear/motor casing parts that the entire gear assembly could be housed in an ~8-kg casing with a 17-L volume [also see Figure 12(a)].

A close-up of the partially disassembled planetary gear assembly with the top and bottom plates removed is shown in Figure 12(b).

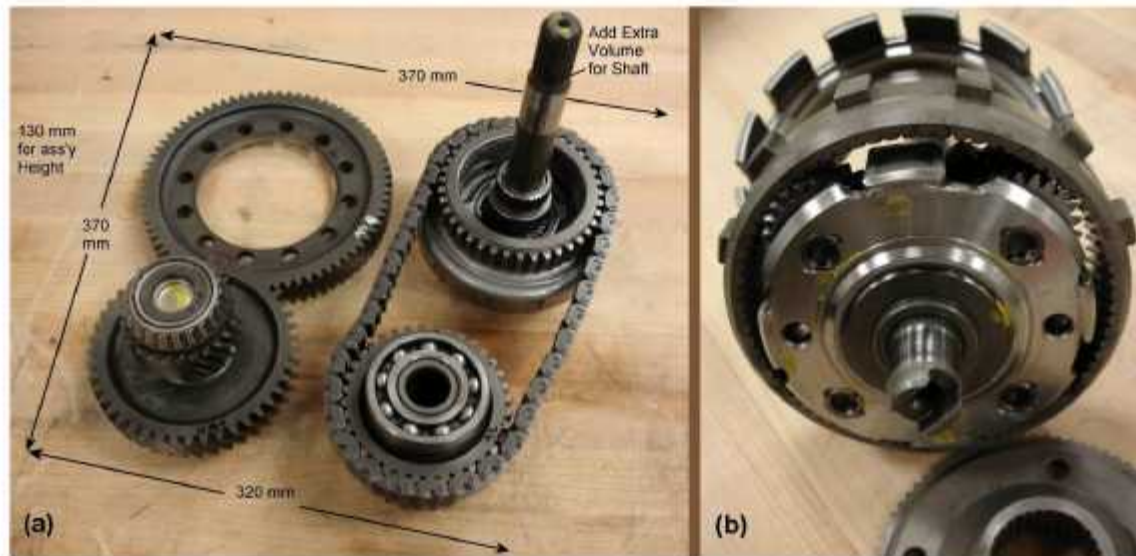


Figure 12. Approximate volume estimation and planetary gear assembly.

Additional information regarding dimensions for both components and the assembly are given in Figure 13.

Core loss tests

The core losses can be determined from energized spin tests where the motor shaft is uncoupled. Figure 14 provides the ac electrical power vs speed plot for the Accord PMSM.



Figure 13. Dimensions for planetary gear, the first reducer gear, and extension.

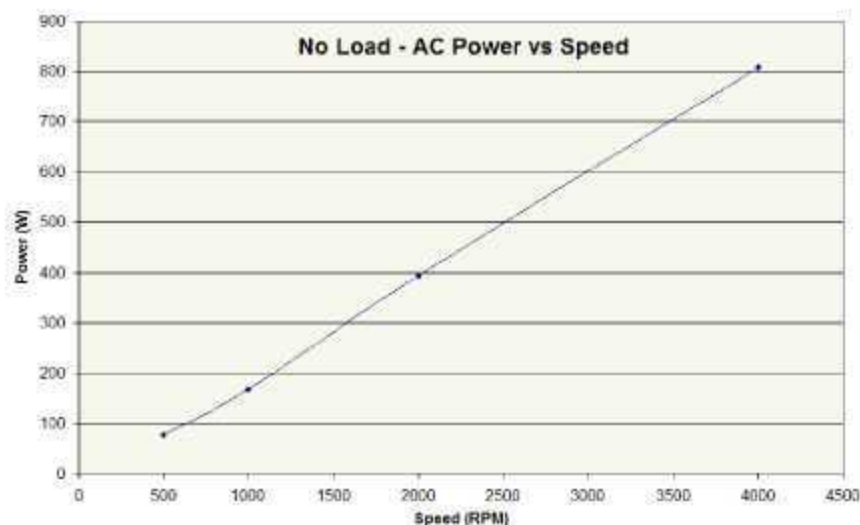


Figure 14. Uncoupled, energized spin test of the Accord motor to assess core losses.

Conclusion

The benchmarking project has been very successful in assessing the Prius and Accord designs and completing a full range of tests, including back-emf, locked-rotor, and efficiency mapping tests. The sets of data obtained from these tests have (1) helped to provide a technical basis for the FCVT management to determine program targets/direction and (2) enabled researchers to improve/refine their analytical models so that greater accuracy is obtained for high-power density PMSMs.

Future Direction

The FY 2007 goal of the benchmarking project is to complete testing of various traction drive subsystems that would be useful to the FCVT program integration/management. The design, packaging, and fabrication assessments will be combined with comprehensive performance mapping test results to enable analysts to determine how each HEV/PHEV traction drive subsystem compares with the other and with program technology targets (thermal efficiency, peak power density, and peak specific power goals). The project will focus on inverters, converters, and PMSMs. Since FY 2006, the impact of the collective data obtained from each vehicle has impacted the broader program, including program planning. This is expected to continue in FY 2007.

One specific test planned for FY 2007 is an assessment and performance evaluation of a high-speed PMSM such as used in the Toyota Highlander and the Lexus GS450 and RX400h. High-speed operation, up to 12,500 rpm, is clearly the most recent hybrid technology that has been successfully introduced into the market.

The Benchmarking project will continue its efforts to improve the accuracy of a PMSM model using data obtained from no-load and back-emf tests. Because the empirical approaches used in the performance tests ensure optimal operation, high-quality data are obtained that are well suited for this purpose. The model will effectively incorporate effects of saturation and the impact of variance in other parameters such as stator resistance and inductance, all of which fluctuate with speed, current, or temperature. The efforts to improve the motor model will aid in understanding the operational behavior of the 2006 Accord motor and other interior PM motors of similar design.

If capital funding is obtained in FY 2007, the project will upgrade the test cell with a larger dynamometer to permit the testing of high-power motors. The need for this can be underscored by considering that if the Prius motor had actually been capable of providing 400 Nm without rapid thermal

escalation beyond short-term limits, the ORNL dynamometer would have proved to be inadequate to support thorough testing.

Limited evaluation of state-of-the-art capacitors and magnetic materials will be performed to ascertain their applicability for use in high-power, high-temperature FreedomCAR automotive applications.

Publications

R. H. Staunton, C. W. Ayers, J. Chiasson, T. A. Burrell, and L. D. Marino, *Evaluation of 2004 Toyota Prius Hybrid Electric Drive System*, ORNL/TM-2006-423, Oak Ridge National Laboratory, May 16, 2006.

R. H. Staunton, T. A. Burrell, and L. D. Marino, *Evaluation of 2005 Honda Accord Hybrid Electric Drive System*, ORNL/TM-2006-535, Oak Ridge National Laboratory, UT-Battelle, LLC, September 2006.

5.2.2 Component Characterization

*Principal Investigator: Larry Seiber
Oak Ridge National Laboratory
National Transportation Research Center
2360 Chertala Boulevard
Knoxville, TN 37932*

Voice: 865-946-1334; Fax: 865-946-1400; E-mail: seiberle@ornl.gov

*DOE Technology Development Manager: Susan A. Rogers
Voice: 202-586-8997; Fax: 202-586-1600; E-mail: Susan.Rogers@ee.doe.gov*

*ORNL Program Manager: Mitch Olszewski
Voice: 865-946-1350; Fax: 865-946-1262; E-mail: olszewskam@ornl.gov*

Objective

As capacitor and magnet technologies mature, it is important to ascertain the limitations of these new technologies by subjecting the components to testing that will evaluate their capabilities and limitations. The object of this project is to test and characterize new capacitor and magnet components to determine their ability to provide improvements in power electronics and motor designs to meet the FreedomCAR goals.

Approach

- Capacitor performance data were acquired by testing over temperature in both static and dynamic modes of operation. A data acquisition system (DAQ) was developed and used to log the test results for the capacitor parameter evaluations.
- A full four-quadrant hysteresis graph was used to evaluate the new magnet technologies over an expanded temperature range.

Major Accomplishments

- Commercial film and ceramic capacitor benchmarks were defined and characterized. Capacitor test samples were tested in two modes, statically and dynamically. Capacitor testing in the static mode requires a thermal cycling process that must continue uninterrupted for extended periods of time. Capacitor testing in the dynamic mode requires testing at thermal extremes and requires ripple current and bias voltage input from the operator.
- Magnet benchmarks for bonded and sintered magnets were defined and characterized.
- Magnet test samples were tested over a temperature range from 20 to 235°C.
- The development of a DAQ using LABView was completed to control the environmental chamber and log data from the measuring instruments for capacitor evaluations.

Technical Discussion

Data Acquisition System

The DAQ consists of a Dell Precision 380 Workstation running LABView 7.1. In the static mode the instruments used are an Espec environmental chamber and an Agilent 4284 LCR meter. Figure 1 shows the input screen for the static test.

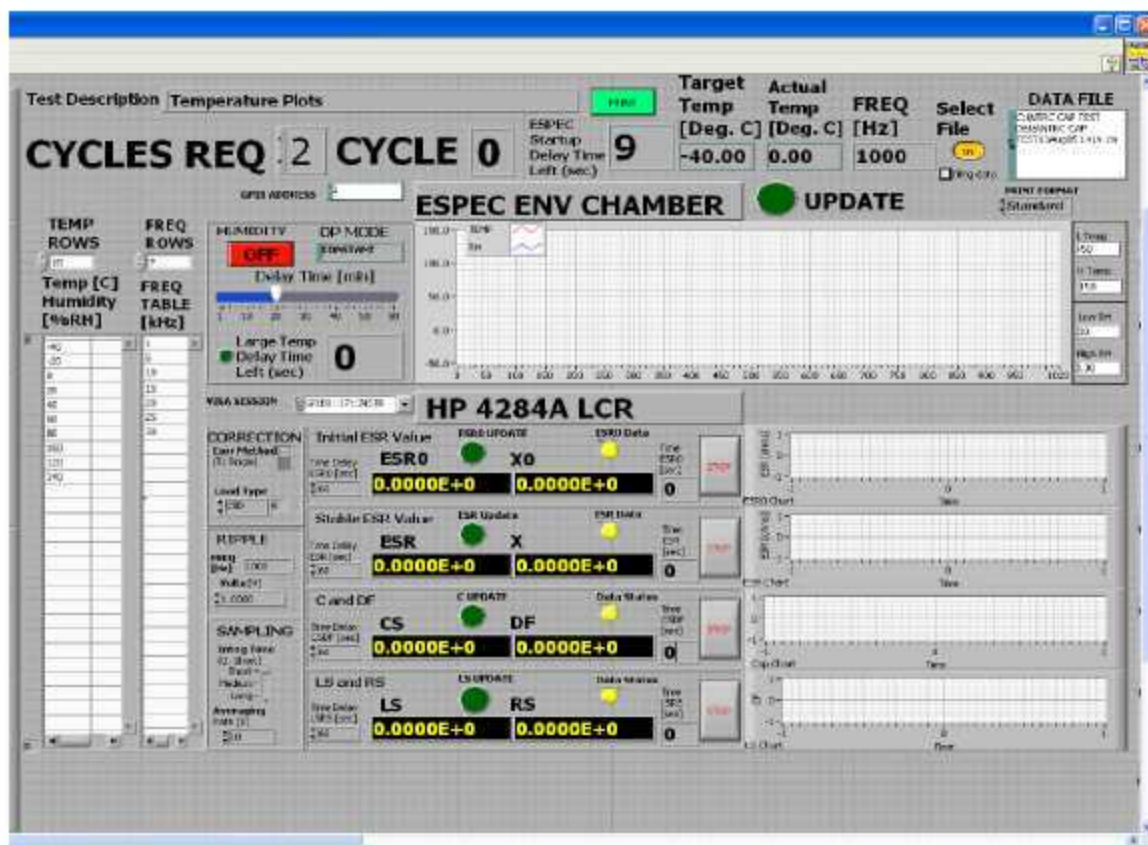


Figure 1. Static test input screen.

At the beginning of the static thermal cycling test, temperature steps and test frequencies are entered in the tables on the left of the screen. A test description is entered at the top of the screen, and the number of cycles requested is also entered. A delay time is set using the slider bar in the large temperature delay time window. This preprogrammed delay is to ensure that the temperature of the dielectric has equalized once the target temperature of the environmental chamber has been reached. When the temperature difference between the ambient temperature of the chamber and the target temperature of the chamber is 40°C or greater, the preprogrammed delay is invoked after the target temperature is reached. The amount of delay is determined by the operator and is based on the size of the capacitor. A larger capacitor will require a larger delay to ensure that the temperature of the dielectric is uniform.

Once data have been entered, the program turns on the environmental chamber and commands a target temperature to the chamber. After the target temperature is reached and the preprogrammed delay time is met, the program sends a command to the LCR meter to output the first test frequency and then begin to monitor the equivalent series resistance (ESR) from the capacitor under test. When that value is stable, the ESR is recorded, and the next parameter is measured and recorded. After the ESR, the dissipation factor (DF), and capacitance value are recorded at the first test frequency, the command is given to the LCR meter to output the next test frequency and the monitoring and recording process is repeated. After all data are recorded at all test frequencies, the next temperature step is commanded to the environmental chamber, and the process is repeated.

Capacitor testing in the dynamic mode also uses the DAQ. Figure 2 shows the dynamic test input screen.

The screenshot displays a software interface for configuring a dynamic test. At the top, it shows the 'Present State' as 'PZ4000' and 'Step No.' as '2'. A large green 'PRINT' button is visible. Below this, a 'Test Description' field contains 'Prus Dynamic Test (-40 to 140)'. A prominent message 'Select OK to continue ...' is displayed with 'OK', 'Cancel', and 'STOP' buttons. The main area is a grid of controls for steps 0 through 7. Each step includes a 'SHUTDOWN' toggle, 'Power Supply' settings (VDC, Ripple Freq., Ripple Vp), 'ESPEC' settings (Temp., RH), 'LCR' settings (VDC, Ripple Freq.), 'Wattmeter', 'Megohmmeter', 'Thermocouples', and 'IR Camera' status indicators. For example, in Step 0, VDC is 200, Ripple Freq. is 15000, and Temp. is -40. The interface is designed for precise control and monitoring of the test parameters across multiple temperature steps.

Figure 2. Dynamic test input screen.

Capacitor testing in the dynamic mode requires a dc bias voltage to be applied to the capacitor under test along with a ripple current. The maximum bias voltage value is 75% of the maximum rated dc voltage of the capacitor. The dc bias voltage is applied in series with the secondary of a transformer and across the capacitor under test. The primary of the transformer is connected to the output of an ac amplifier, and a signal generator is connected to the ac amplifier. This configuration will provide a ripple current that is at a dc level similar to what would be seen in an inverter. The signal generator also allows the ripple current frequency to be adjusted. The ripple current value in amps can be adjusted by adjusting the gain of the ac amplifier.

Thermocouples are attached at three different locations on the capacitor, one on each end and one in the middle to monitor temperature rise as ripple current values increase.

After the bias voltage and ripple current have been adjusted, the DAQ dynamic mode is activated, and temperature limits and steps are entered. Ripple current amplitude and frequency can be changed along with the dc bias voltage at each temperature step if needed. Different measuring instruments can also be selected or turned off at each temperature step. Instruments can be selected or deselected by clicking on the toggle switch located on the front panel of the dynamic test input screen in Figure 2.

After all temperature step values, dc voltage values, and test frequencies have been entered, the program turns on the environmental chamber, commands a target temperature, and begins monitoring the chamber temperature. When the target temperature is reached, the program waits for operator input before logging ripple current, chamber temperature, and thermocouple data. The next temperature step will then be commanded.

Static Testing

Single Prius film capacitor

A single 140- μ F 600-Vdc film capacitor was extracted from the 2004 Prius capacitor module to use as a benchmark for film capacitor evaluations. The module was taken to a materials lab to be x-rayed to identify the layout of the ten capacitors in the module. The film was brought back to the Power Electronics on Electric Machines Research Center lab, and several single capacitors were extracted for testing. Figure 3 shows the test configuration used to evaluate the single Prius capacitor, in the static and dynamic mode, inside the environmental chamber.

The capacitor was placed in a vise with copper strips on each end bent to allow connection to a cable capable of carrying high ripple currents. Electrically insulating material was added between the vise and the copper strips. This material also provided some thermal insulation in an effort to keep the vise from becoming a heat sink during the ripple current vs temperature evaluation.

Figure 4 shows the results of the static test on the single Prius film capacitor.



Figure 3. Single Prius film capacitor test set up.

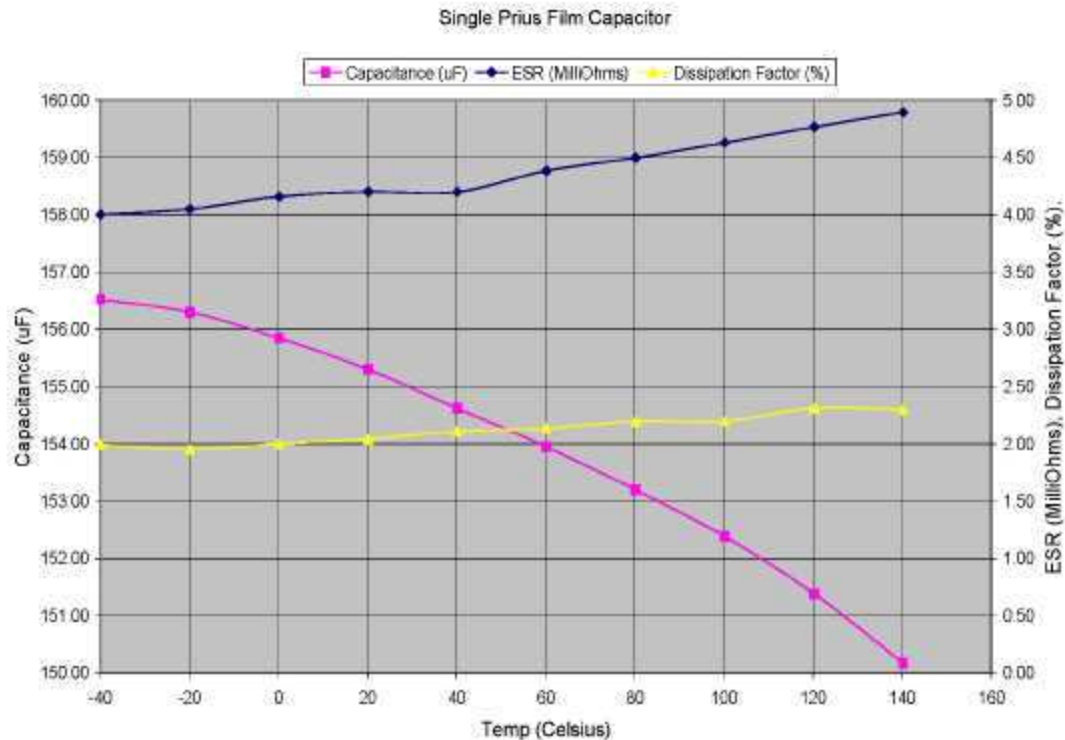


Figure 4. Single Prius film capacitor tested in the static mode at 5 kHz.

When tested at 5 kHz, the DF increased less than 0.5% over the entire temperature test range of -40°C to 140°C . The capacitance value decreased less than 5%, and the ESR increased less than 1 m Ω .

The ESR, DF, and capacitance values of the single Prius capacitor were evaluated at frequencies of 1 kHz, 2 kHz, 5 kHz, 10 kHz, and 15 kHz at three different temperatures: -40°C , 20°C , and 120°C . Figures 5–7 show these results.

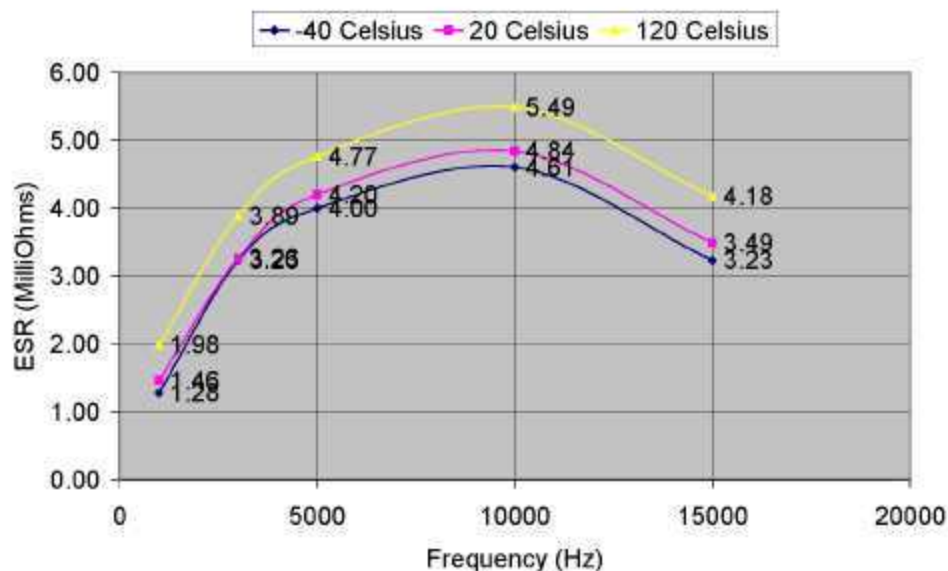


Figure 5. Single Prius film capacitor ESR frequency response.

The ESR peaked at 10 kHz at all temperatures and increased from an average of 1.57 m Ω at 1 kHz to an average of 4.98 m Ω at 10 kHz. The average at 5 kHz was 4.32 m Ω .

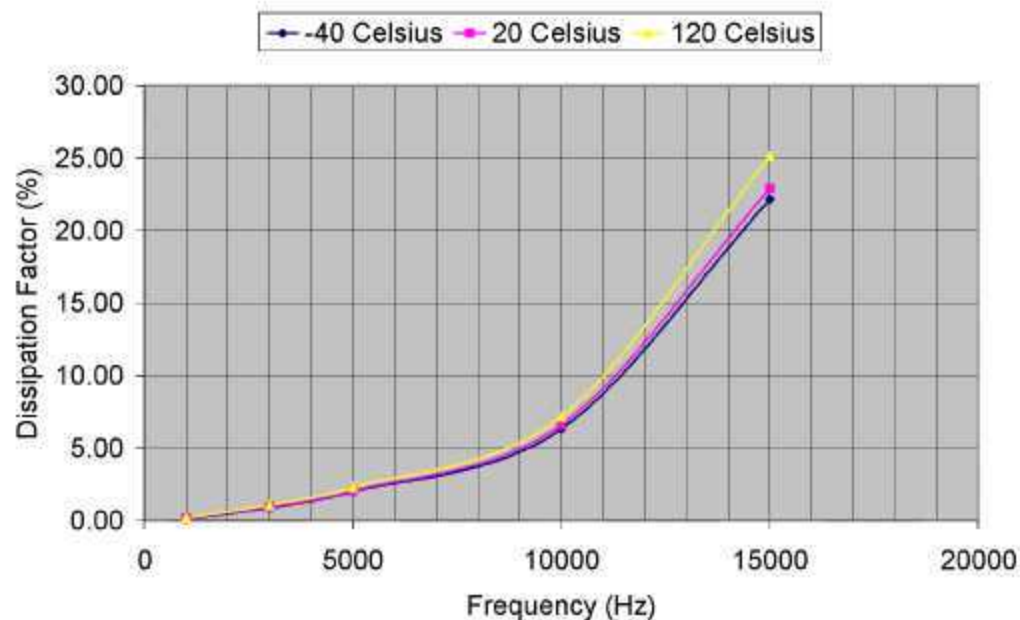


Figure 6. Single Prius film capacitor DF frequency response.

The DF increased from a value of 0.14% at 1 kHz to a value of 2.04% at 5 kHz. At 10 kHz, the average value was 6.7%. The increase was substantial above 10 kHz.

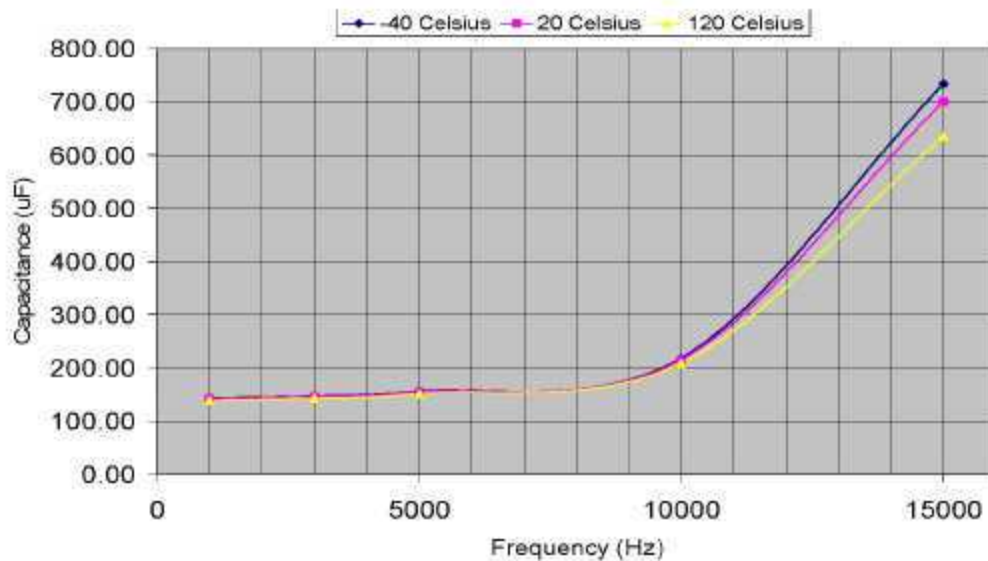


Figure 7. Single Prius film capacitor frequency response.

The capacitance value increased 9% from 1 kHz to 5 kHz at all three temperatures. Above 10 kHz, there was a very substantial increase in capacitance that was evident up to 15 kHz.

Kemet ceramic capacitor

A Kemet 1- μF 500-Vdc ceramic capacitor was tested in the static mode as a ceramic benchmark. The capacitor is rated at 200°C. Figure 8 shows ESR, DF, and capacitance values over the temperature range of -40°C to 180°C.

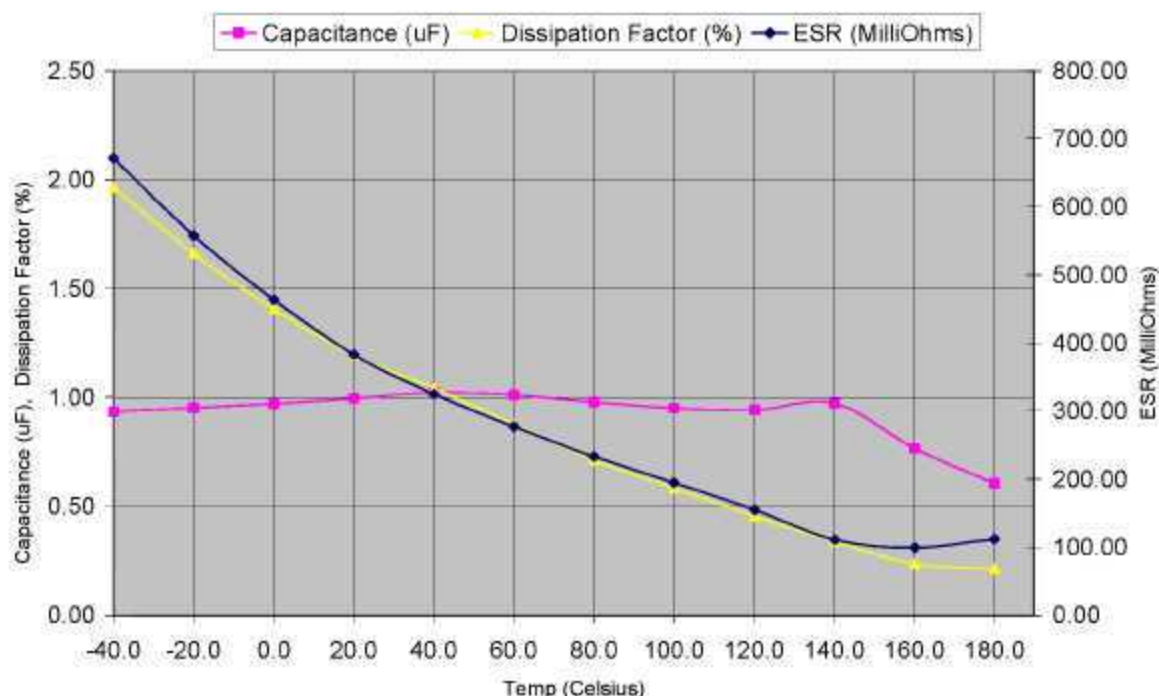


Figure 8. Kemet ceramic capacitor static test at 5 kHz.

The Kemet 1- μF ceramic capacitor was tested over the temperature range of -40°C to 180°C. The DF decreased from 1.96% to 0.21%, and the ESR changed from 671 m Ω to 111 m Ω . The capacitance value was basically flat up to 140°C; at that point it changed from 0.93 μF to 0.61 μF at 180°C.

Penn State multilayer ceramic capacitor

Pennsylvania State University (Penn State) supplied a 90-nF 500-Vdc high-temperature prototype multilayer ceramic capacitor for evaluation. The capacitor is rated at 300°C. The static test of this capacitor at 5 kHz is shown in Figure 9.

The Penn State 300°C prototype multilayer ceramic capacitor was tested in the static mode at 5 kHz over the temperature range of -40°C to 180°C. The DF decreased from 6.39% to 1.8%, and the ESR decreased from 144 Ω to 8.68 Ω . The capacitance value increased from 14.1 nF to 66.5 nF.

This capacitor did not function well at lower temperatures, but as the temperature increased it continued to improve. The capacitor was rated at 300°C, but the evaluation was made to 180°C because of the limitations of the environmental chamber.

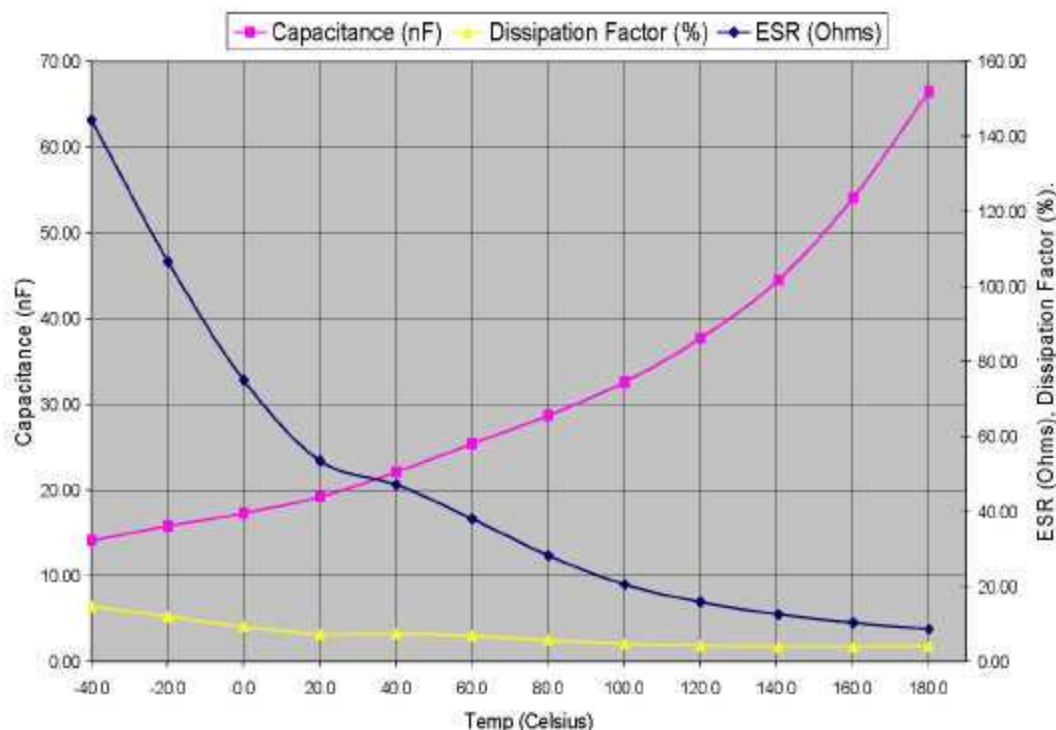


Figure 9. Penn State ceramic high-temperature static test at 5 kHz.

Dynamic Testing

The single film capacitors extracted from the Prius capacitor module were also tested in the dynamic mode. The bias voltage was 250 Vdc. Maximum ripple current was determined at several different ambient temperatures; leakage current and effective series inductance (ESL) were also measured. No prototype film capacitors were supplied to Oak Ridge National Laboratory for dynamic tests during this reporting period.

Because of the size and the fact that they will not be used as a dc bus filtering capacitors, the smaller value ceramic capacitors were not tested in the dynamic mode.

Single Prius film capacitor ripple current

Figure 10 shows the results of a single 140- μ F Prius film capacitor's ripple current test. This capacitor was extracted from the Prius capacitor module and was tested by increasing the ripple current and measuring the temperature rise above an ambient temperature of 22°C. The test was repeated at an ambient temperature of 100°C.

The maximum ripple current was determined by increasing the current in 5-A steps until the capacitor failed. After each increase, the temperature on the surface of the capacitor was allowed to stabilize before increasing the ripple current to the next value. At 100°C ambient, the capacitor failed after 20 min at 70 A of ripple current. The ambient temperature was raised to 140°C, and another single film capacitor was tested from the Prius module. This capacitor failed at 20 A ripple current after 30 min. The ambient temperature was decreased to -40°C, and another single film capacitor was tested from the Prius module. This capacitor failed at 100 A of ripple current after 35 min. Table 1 lists these ripple current limits. All tests were done at 5 kHz. The capacitors failed when their film melted and thus shorted.

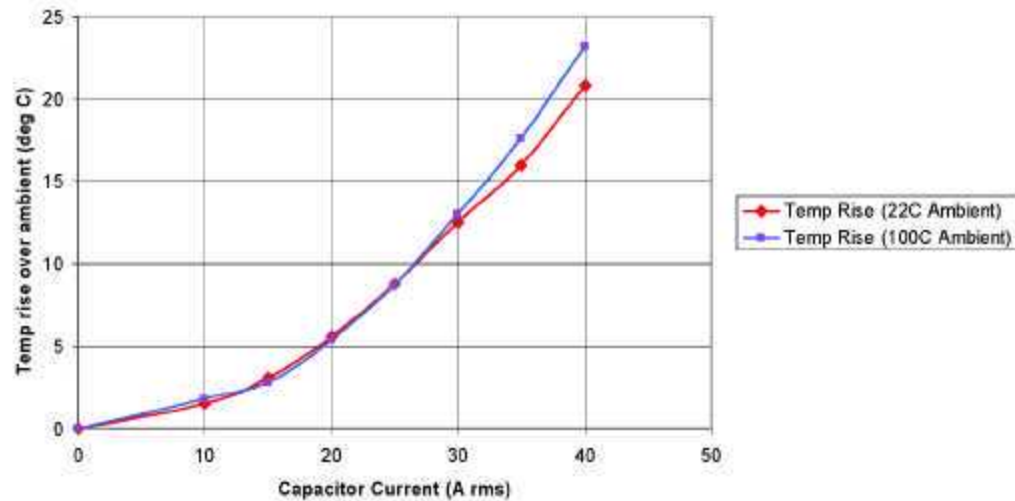


Figure 10. Temperature rise over ambient at 5 kHz.

Table 1. Maximum ripple current for the single Prius film capacitor

Ambient temperature	20 A	70 A	100 A
-40°C			Failure after 35 min
100°C		Failure after 20 min	
140°C	Failure after 30 min		

Single Prius film capacitor leakage current

Leakage current test results measured on a single Prius film capacitor using a Danbridge 621 megohmmeter are listed in Figure 11. The capacitor was placed in the environmental chamber, and leakage current was measured at five different temperatures: 25°C, 40°C, 60°C, 80°C, and 100°C.

Leakage current increased through the single Prius film capacitor from 16 nA to 16 μ A over the test range of 25°C to 100°C.

Single Prius film capacitor ESL

ESL was measured on the single Prius film capacitor using a method and circuit configuration offered by Electronic Concepts, Inc. This circuit is shown in Figure 12.

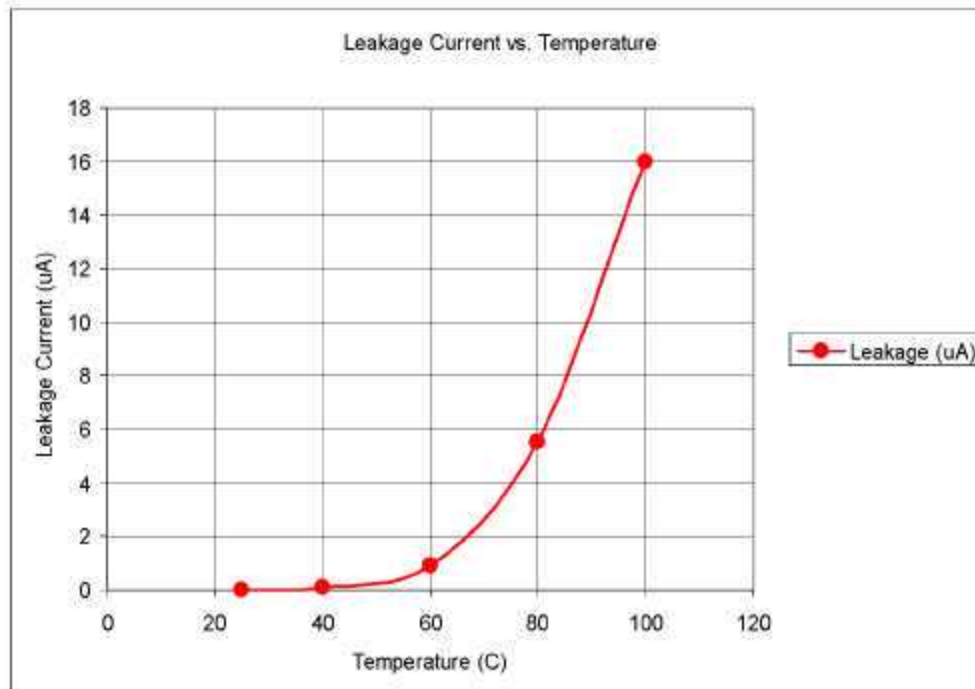


Figure 11. Single Prius film capacitor leakage current vs temperature.

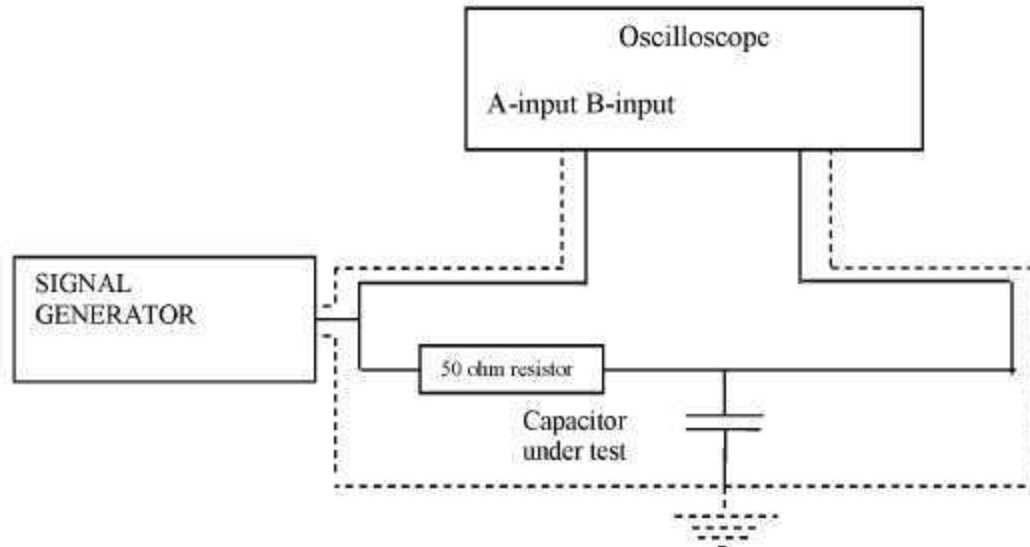


Figure 12. Circuit used to calculate ESL.

After the resonant frequency was found using the circuit in Figure 12, the ESL was derived as a function of the inductive reactance (X_L) and the capacitive reactance (X_C). At resonant frequency, the two are equal so that $X_L = X_C$; therefore, $2\pi fL = 1/(2\pi fC)$, and from this the equation for inductance is $ESL = L = 1/(4\pi^2 f^2 C)$. The ESL of the single Prius film capacitor was found to be 147 nH at an ambient temperature of 22°C.

Magnet Evaluation

Magnet samples were evaluated using a Walker Scientific AMH-40 automatic hysteresisgraph. This computer-controlled system is used for testing, analyzing, and evaluating the hysteresis properties of magnetic materials. The system consists of a PC-based control console, two computer-interfaced integrating flux meters, a gauss meter, B and B-H coil sets, two 7-in.-diam variable-gap water-cooled electromagnets with cobalt-iron tipped poles, and a 5-kW 50-A programmable power supply. The 1200-lb electromagnets are capable of generating demagnetizing forces up to 30,000 Oersteds. This system allows the operator to perform five different types of tests: (1) manual H-Field sweep, (2) second-quadrant demagnetization curves, (3) complete four-quadrant full hysteresis loops, (4) recoil minor loops after saturation in the first quadrant, and (5) first-quadrant saturation or demagnetization of the samples. Also complementing the system is a pulse charger capable of saturating very hard magnetic materials and a Model TCS2 temperature-controlled, water-cooled fixture for testing materials at temperatures ranging from -100 to +300°C. This fixture is used with a compatible, high-temperature coil set with integral thermocouples.

The basic magnetic properties measured using the AMH-40 automatic hysteresisgraph are residual induction (Br), coercive force (Hc), intrinsic coercivity (Hci), and energy product (BHmax).

Sintered magnets

A Prius magnet was evaluated as the sintered magnet benchmark using the AMH-40 Hysteresisgraph, four-quadrant full hysteresis loop. Two other sintered magnets were evaluated against the Prius benchmark using the same four-quadrant full hysteresis loop: Shin-Etsu's N43TS and a magnet developed at Argonne National Laboratory (ANL).

Table 2 shows that the Hci value for the Shin-Etsu N43TS sintered magnet is 30% less than the Prius benchmark magnet at 183°C. The intrinsic coercivity (Hci) parameter, is used as an indication of a magnet's resistance to demagnetization. The hysteresis plot of the N43TS will show the knee of the demagnetization curve in the second quadrant. If the operating point of the magnet falls below the knee of this curve, the magnet will have an irreversible loss of magnetization. The Prius magnet had better resistance to demagnetization at elevated temperatures than other sintered magnets tested. The maximum energy product (BHmax) of the N43TS magnet is 12% better than the Prius at 183°C, and the residual induction (Br) of the N43TS is 6% better than the Prius.

The magnet developed at ANL was not tested beyond 175°C because it falls far below the Prius benchmark in all areas except Br. In this area, the ANL magnet is 3% better than the benchmark.

Figures 13–15 show the full four-quadrant hysteresis graph of the Prius sintered magnet, the Shin-Etsu N43TS sintered magnet, and the ANL sintered magnet at elevated temperatures.

Table 2. Sintered magnet test results

Magnet type	Residual induction (Br) (kG)	Coercivity (Hc) (kOe)	Intrinsic coercivity (Hci) (kOe)	Energy product (BHmax) (MGOe)
Prius (sintered)	12.55 (ambient)	12.18 (ambient)	>24 (ambient)	38.19 (ambient)
"	10.42 (183°C)	9.13 (183°C)	9.87 (183°C)	26.17 (183°C)
"	9.37 (235°C)	5.44 (235°C)	5.63 (235°C)	20.83 (235°C)
Shin-Etsu	13.33 (ambient)	12.92 (ambient)	>24 (ambient)	42.95 (ambient)
N43TS (sintered)	11.09 (182°C)	6.79 (182°C)	6.87 (182°C)	29.43 (182°C)
"	12.91 (ambient)	11.85 (ambient)	15.01 (ambient)	38.68 (ambient)
ANL (sintered)	10.75 (175°C)	3.05 (175°C)	3.07 (175°C)	19.6 (175°C)

^aBold indicates benchmark magnet

Br = 10.42 kG
Hc = 9.13 kOe
Hci = 9.87 kOe
BHmax = 26.17 MGoe

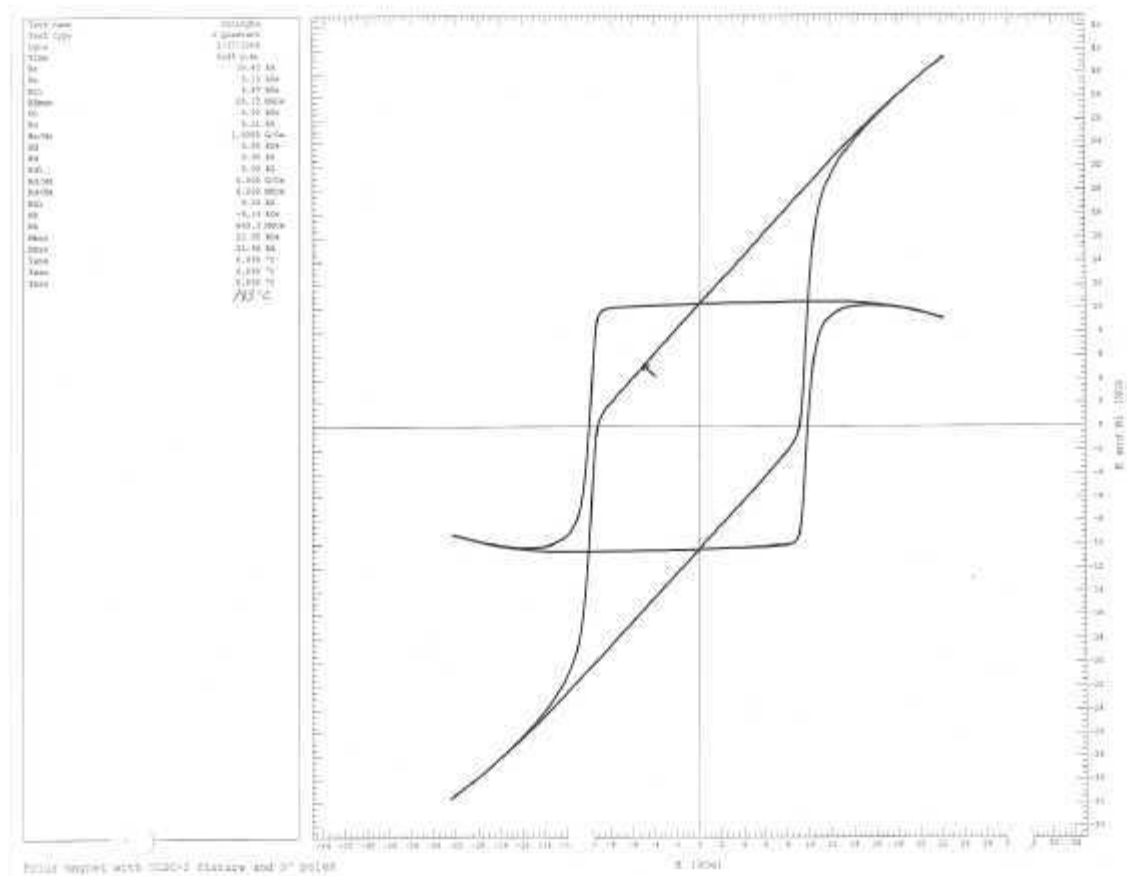


Figure 13. Hysteresis plot of the Prius sintered benchmark magnet at 183°C.

$B_r = 11.09 \text{ kG}$
 $H_c = 6.79 \text{ kOe}$
 $H_{ci} = 6.87 \text{ kOe}$
 $BH_{\max} = 29.43 \text{ MGOe}$

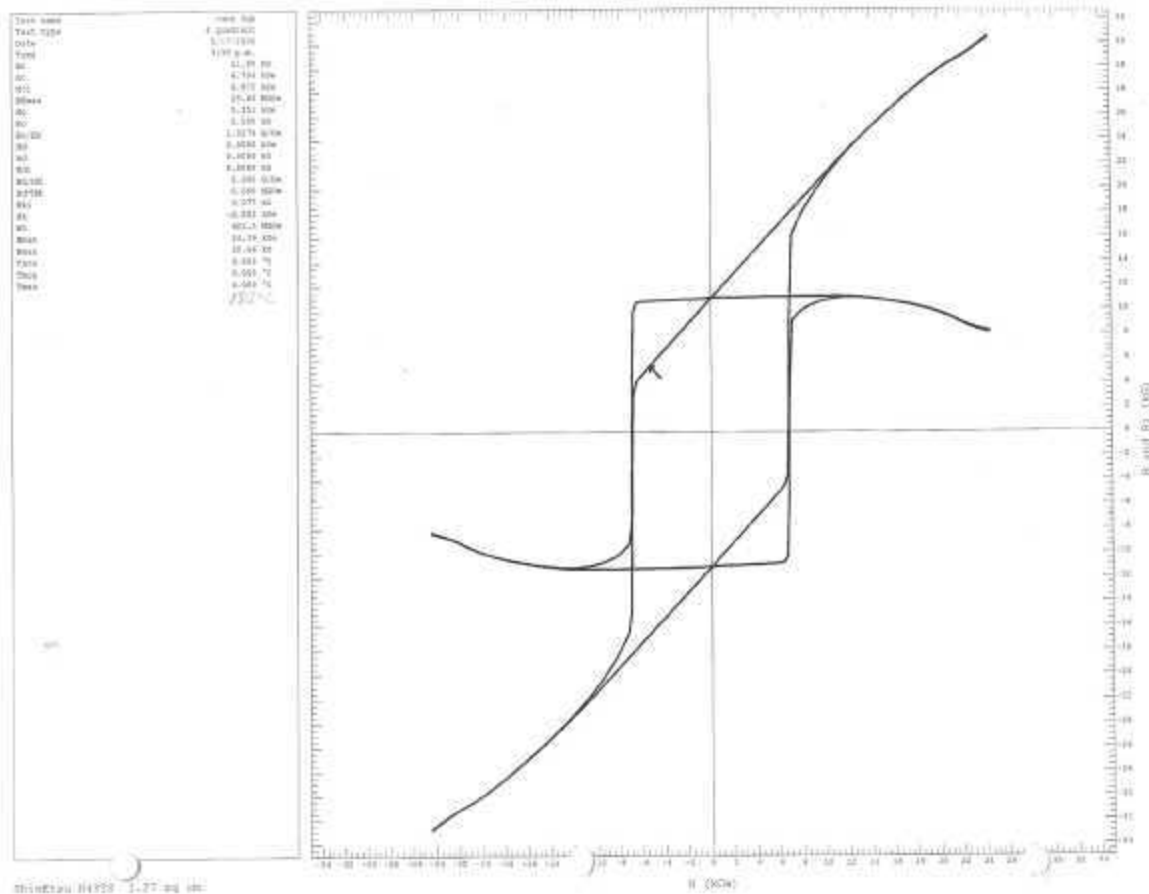


Figure 14. Hysteresis plot of the Shin-Etsu N43TS sintered magnet at 182°C.

$B_r = 10.75 \text{ kG}$
 $H_c = 3.05 \text{ kOe}$
 $H_{ci} = 3.07 \text{ kOe}$
 $BH_{\max} = 19.60 \text{ MGOe}$

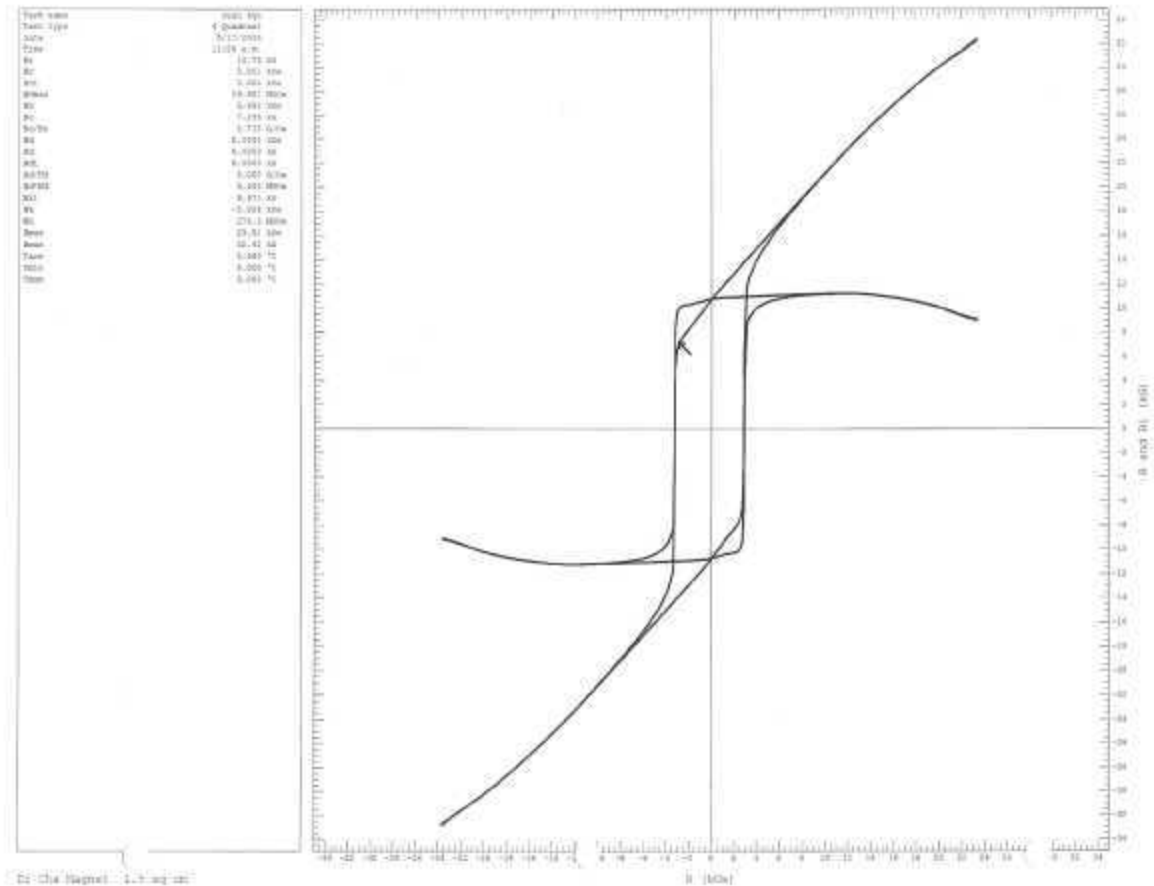


Figure 15. Hysteresis plot of the ANL sintered magnet at 175°C.

Bonded magnets

Arnold Magnetics Plastiform 2205 was evaluated as the bonded magnet benchmark using the AMH-40 Hysteresisgraph, four-quadrant full hysteresis loop. Two other bonded magnets were evaluated against the Arnold Magnetics benchmark using the same four-quadrant full hysteresis loop: Ames Laboratory (Ames) MQP-11 HTP and Ames MQP-O. The Ames MQP-O bonded magnet was made from the same alloy powder used to make the plastiform 2205 benchmark magnet. However, this magnet was fabricated using a hot-pressed process instead of being extruded. The Ames MQP-11 HTP magnet was fabricated with the same process, but it used an alloy powder developed by Iver Anderson at the Ames Lab. Table 3 lists the test results.

Table 3. Bonded magnet test results

Magnet type	Residual induction (Br) (kG)	Coercivity (Hc) (kOe)	Intrinsic coercivity (Hci) (kOe)	Energy product (BHmax) (MGOe)
Arnold Magnetics Plastiform 2205 (bonded)^a	5.03 (ambient) 3.70 (200°C)	4.24 (ambient) 2.85 (200°C)	11.49 (ambient) 5.10 (200°C)	5.29 (ambient) 2.68 (200°C)
Ames MQP-11HTP (bonded)	3.93 (ambient) 3.41 (200°C)	3.56 (ambient) 2.89 (200°C)	11.87 (ambient) 5.72 (200°C)	3.49 (ambient) 2.51 (200°C)
Ames MQP-O (bonded)	4.46 (ambient) 3.15 (200°C)	4.03 (ambient) 2.55 (200°C)	12.23 (ambient) 5.25 (200°C)	4.53 (ambient) 2.03 (200°C)

^aBold indicates benchmark magnet.

At 200°C, the Ames MQP-11 HTP magnet has a 12% higher Hci than the benchmark, indicating a superior resistance to demagnetization at elevated temperatures. The BHmax of the MQP-11 HTP is 6% less than the benchmark at 200°C. The Br of the MQP-11 HTP is just under 8% less than the benchmark at 200°C.

At 200°C, the Ames MQP-O magnet has a 3% higher Hci than the benchmark, indicating a slightly better ability to resist demagnetization at elevated temperatures. The BHmax of the MQP-O magnet is 24% less than that of the benchmark at 200°C. The Br of the MQP-O magnet is 15% less than that of the benchmark at 200°C.

Figures 16–18 show the full four-quadrant hysteresis graph of the Arnold Magnetics Plastiform 2205 bonded benchmark magnet, the Ames MQP-11 HTP bonded magnet, and the Ames MQP-O bonded magnet at 200°C.

$B_r = 3.70 \text{ kG}$
 $H_c = 2.85 \text{ kOe}$
 $H_{ci} = 5.10 \text{ kOe}$
 $BH_{max} = 2.68 \text{ MGOe}$

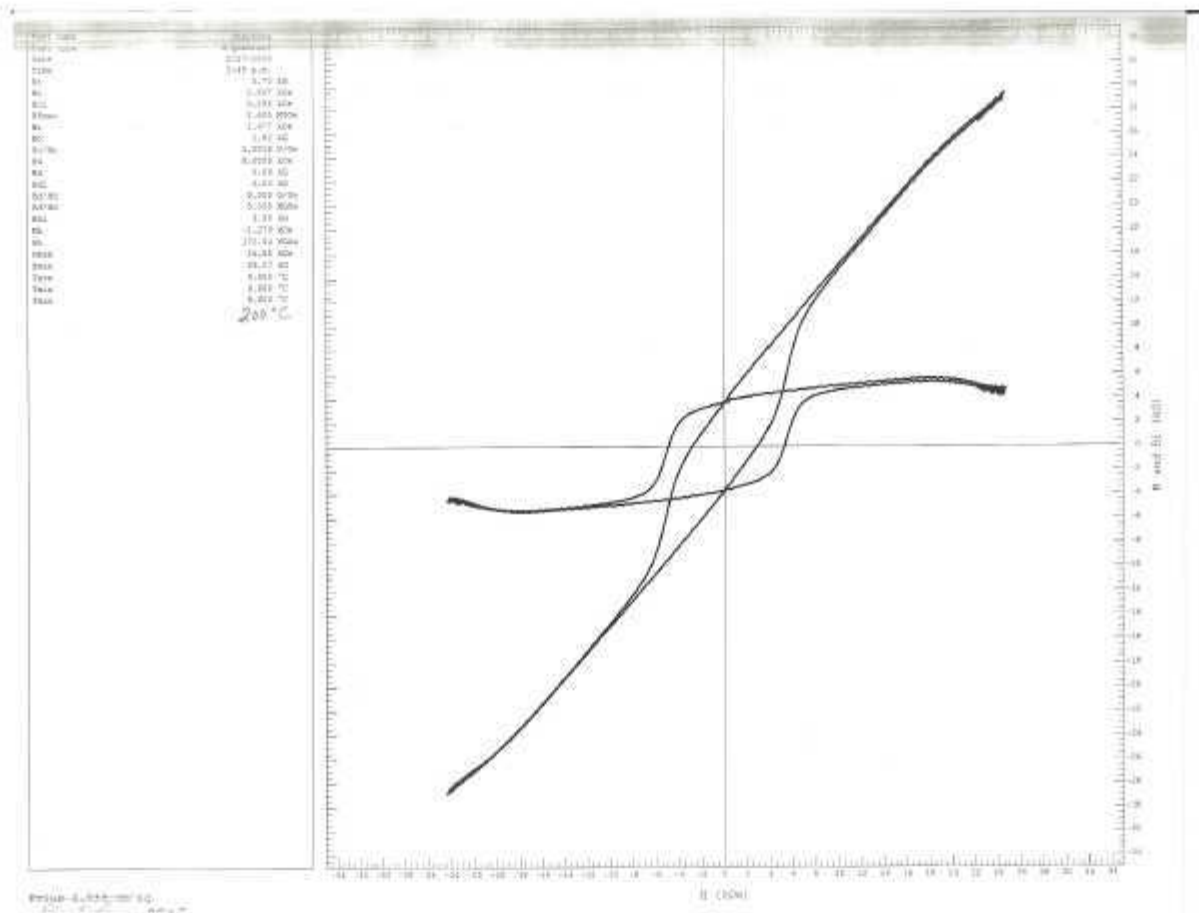


Figure 16. Hysteresis plot of Arnold Magnetics Plastiform 2205 bonded benchmark magnet at 200°C.

Br = 3.41 kG
Hc = 2.89 kOe
Hci = 5.72 kOe
BHmax = 2.51 MG Oe

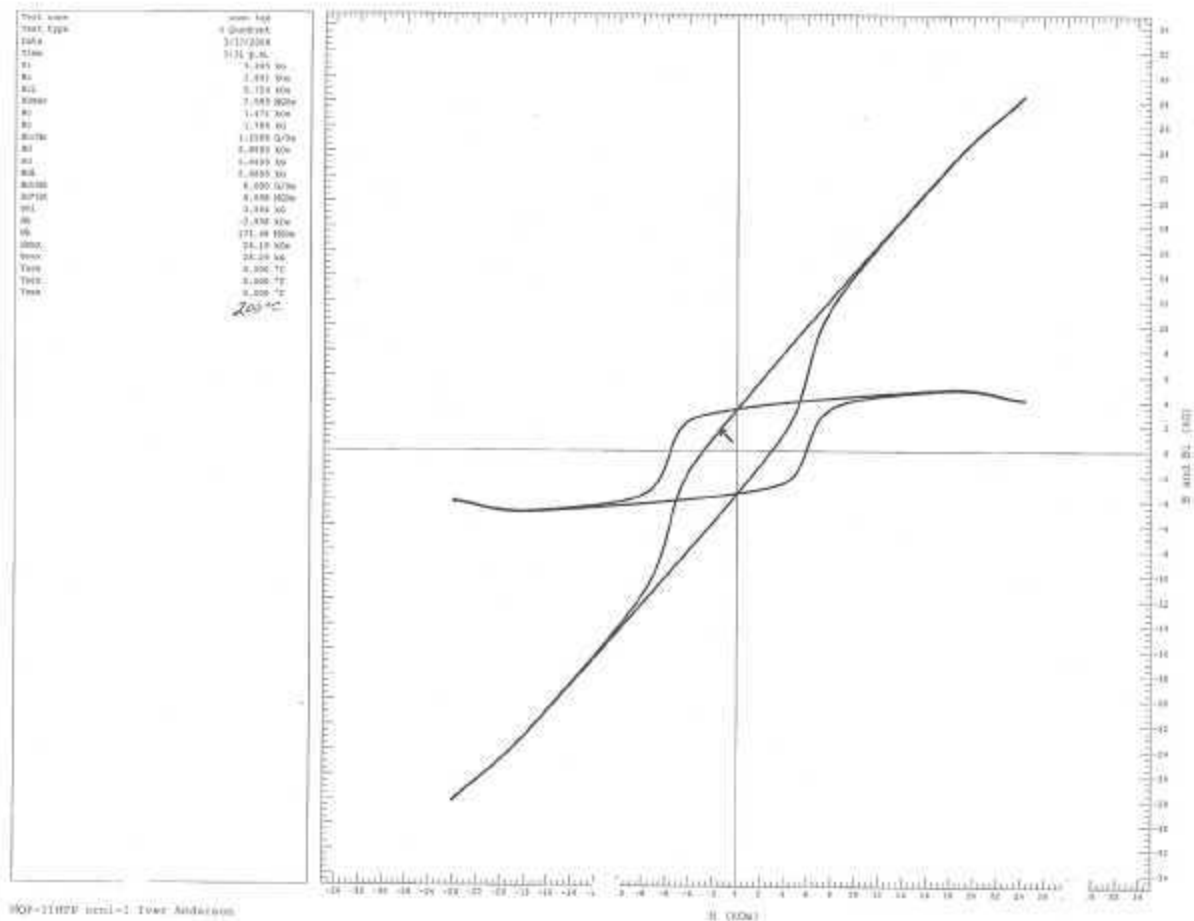


Figure 17. Hysteresis plot of the Ames MQP-11 HTP magnet at 200°C.

Br = 3.15 kG
Hc = 2.55 kOe
Hci = 5.25 kOe
BHmax = 2.03 MGOe

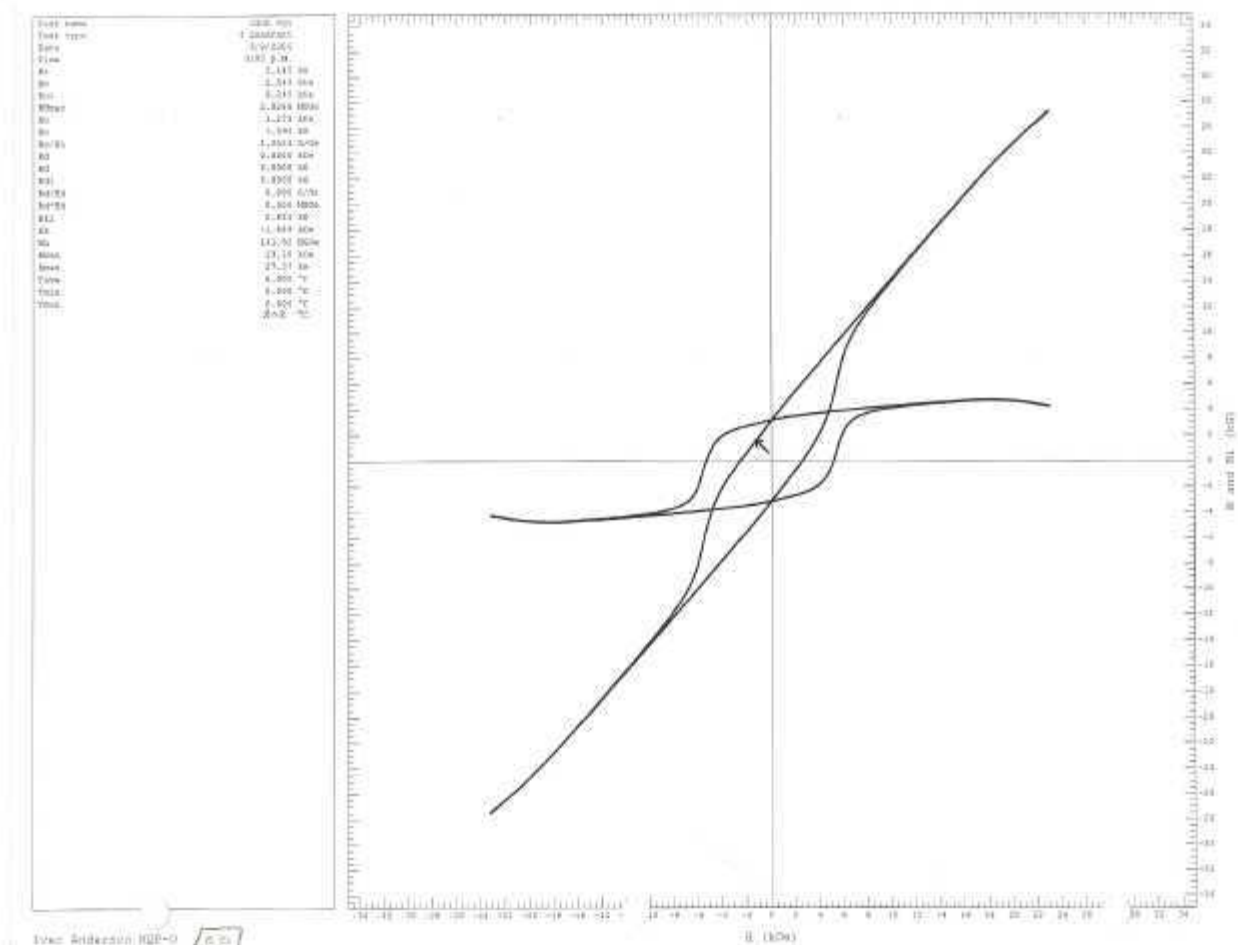


Figure 18. Hysteresis plot of the Ames MQP-O bonded magnet at 202°C.

Conclusion

The evaluation and characterization of capacitor and magnet technologies was accomplished through the testing of these components at elevated temperatures and in simulated operating conditions. All components that were received were evaluated. No prototype film capacitors were received for evaluation during this reporting period.

The film capacitor evaluated as the benchmark was taken from the Prius HEV capacitor module. The Prius capacitor module contains ten film capacitors in parallel. Several of these were extracted and used in the evaluation process.

A Kemet 1- μ F 500-Vdc ceramic capacitor was evaluated as the ceramic benchmark. Penn State supplied a prototype 90-nF 500-Vdc ceramic capacitor for evaluation. No other prototype ceramic capacitors were received from developers for evaluation during this reporting period.

The Kemet capacitor performed worse in the area of capacitance value and ESR as the temperature approached its rated value. The Penn State capacitor started out poorly in both of those areas at lower

temperatures, but as the temperature increased the ESR improved by over 70%, and the capacitance value improved by over 370%.

Benchmark characterizations of anisotropic sintered and isotropic bonded rare earth magnets were performed to determine the basic properties of these very hard magnetic materials. Magnets taken from the Prius motor were used as the sintered benchmark, and commercial Arnold Plastiform bonded magnets were used as the bonded magnet benchmark.

Tests included pulse charging the magnetic samples to saturation and performing second quadrant demagnetization curves. Sintered magnets from Shin-Etsu as well as bonded magnets from Ames Laboratory were tested. Several samples of both types of magnets were evaluated and compared with the benchmarks. The performance of all the magnets varied with temperature and was unique for each sample. The actual performance of any magnet in a magnetic circuit depends on the geometric design and operating conditions such as temperature and demagnetizing fields. The basic properties of the Shin-Etsu magnet indicate it could possibly be used with good results if the temperature can be kept low.

Future Direction

Evaluation of prototype components will be done on a case-by-case basis as the need arises.

DISTRIBUTION

Internal

- | | |
|-------------------|-----------------------|
| 1. D. J. Adams | 4. L. D. Marlino |
| 2. K. P. Gambrell | 5. M. Olszewski |
| 3. E. C. Fox | 6. Laboratory Records |

External

7. R. Al-Attar, DCX, raa9@dcx.com.
8. T. Q. Duong, U.S. Department of Energy, EE-2G/Forrestal Building, 1000 Independence Avenue, S.W., Washington, DC 20585.
9. R. R. Fessler, BIZTEK Consulting, Inc., 820 Roslyn Place, Evanston, Illinois 60201-1724.
10. K. Fiegenschuh, Ford Motor Company, Scientific Research Laboratory, 2101 Village Road, MD-2247, Dearborn, Michigan 48121.
11. V. Garg, Ford Motor Company, 15050 Commerce Drive, North, Dearborn, Michigan 48120-1261.
12. G. Hagey, Sentech, Inc., 501 Randolph St., Williamsburg, Virginia 23185.
13. E. Jih, Ford Motor Company, Scientific Research Laboratory, 2101 Village Road, MD-1170, Rm. 2331, Dearborn, Michigan 48121.
14. K. J. Kelly, National Renewable Energy Laboratory, 1617 Cole Boulevard, Golden, CO 80401.
15. A. Lee, Daimler Chrysler, CIMS 484-08-06, 800 Chrysler Drive, Auburn Hills, Michigan 48326-2757.
16. F. Liang, Ford Motor Company, Scientific Research Laboratory, 2101 Village Road, MD1170, Rm. 2331/SRL, Dearborn, Michigan 48121.
17. M. W. Lloyd, Energetics, Inc., 7164 Columbia Gateway Drive, Columbia, Maryland 21046.
18. M. Mehall, Ford Motor Company, Scientific Research Laboratory, 2101 Village Road, MD-2247, Rm. 3317, Dearborn, Michigan 48124-2053.
19. Jean A. Montemarano-Naval Surface Warfare Center, Carderock Division, Code 642, NSWCD, 9500 MacArthur Boulevard, West Bethesda, Maryland 20817.
20. N. Olds, United States Council for Automotive Research (USCAR), nolds@uscar.org.
21. J. Rogers, Chemical and Environmental Sciences Laboratory, GM R&D Center, 30500 Mound Road, Warren, Michigan 48090-9055.
22. S. A. Rogers, U.S. Department of Energy, EE-2G/Forrestal Building, 1000 Independence Avenue, S.W., Washington, DC 20585.
23. G. S. Smith, General Motors Advanced Technology Center, 3050 Lomita Boulevard, Torrance, California 90505.
24. E. J. Wall, U.S. Department of Energy, EE-2G/Forrestal Building, 1000 Independence Avenue, S.W., Washington, DC 20585.
25. B. Welchko, General Motors Advanced Technology Center, 3050 Lomita Boulevard, Torrance, California 90505.
26. P. G. Yoshida, U.S. Department of Energy, EE-2G/Forrestal Building, 1000 Independence Avenue, S.W., Washington, DC 20585.